Non-Local Modeling of the Compressive Strength of Composite Structures

Anil Bettadahalli Channakeshava

THESE

Pour l'obtention du Grade de
DOCTEUR DE L'ECOLE NATIONALE SUPERIEURE DE MECANIQUE ET D'AEROTECHNIQUE
(Diplôme National – Arrêté du 25 mai 2016)

Ecole Doctorale :
Sciences et Ingénierie en Matériaux, Mécanique, Energétique et Aéronautique

Secteur de Recherche : Mécanique des solides, des Matériaux, des Structures et des Surfaces

Présentée par :

Anil BETTADAHALLI CHANNAKESHAVA

****

MODELISATION NON-LOCALE DE LA RESISTANCE EN COMPRESSION DES COMPOSITES ARCHITECTURES
-
NON-LOCAL MODELING OF THE COMPRESSIVE STRENGTH OF COMPOSITE STRUCTURES

****

Directeur(s)de thèse : Jean-Claude GRANDIDIER

****
Soutenue le *17th Décembre 2020*

devant la Commission d'Examen

****

JURY

Président :
DRAPIER Sylvain, Professeur, Ecole des Mines de Saint-Etienne, Saint-Etienne
Rapporteurs :
PIMENTA Soraia, Senior lecturer, Imperial College London (UK)
GANGHOFFER Jean- François, Professeur, Université de Lorraine, Lorraine
Membres du jury :
DRAPIER Sylvain, Professeur, Ecole des Mines de Saint-Etienne, Saint-Etienne
KERYVIN Vincent, Professeur, Université Bretagne Sud, Lorient
MECHIN Pierre-Yves, Directeur de Recherche, Dassault Systèmes
GRANDIDIER Jean-Claude, Professeur, ISAE-ENSMA, Poitiers

ACKNOWLEDGEMENTS

First and foremost, I would like to express my sincere gratitude to Prof. Jean-Claude GRANDIDIER for giving me this PhD opportunity with Institute Pprime/ISAE-ENSMA and his immense support, encouragement, patience and motivation throughout my thesis. His vast experience in the field of finite elements brings lots of insight to my computational knowledge. It was really a great pleasure to work under him. Also, I would like to thank all my friends and other colleagues in the laboratory who contributed to the success of finishing my thesis.

A special thanks to my parents, my brother and my beloved wife Anusha for their love and support continuously throughout my thesis. Without their motivation and support it would not be possible for me to complete my work.

ABSTRACT

The compressive failure of long carbon fiber composites is due to complex mechanisms. The knowledge of these mechanisms is important for the design of composite structures because the compressive strength and stiffness of laminates are assumed less than their tensile strength. Further, compressive failure is a mechanism of non-local ruin that depends on the composite structure (layer thickness, load gradient) which makes it a peculiarity. The mechanism has been described and modelled in the literature with suitable numerical tools and experiments that accounted for this effect. There are many articles in the literature regarding the modelling of composites compressive behavior, particularly the microbuckling phenomenon / local instability. But only a few researchers modelled the mechanism at the structural/mesoscopic scale. For example, Drapier et al., [D3] proposed a 2D homogenized model, which takes into account fiber initial alignment defects, matrix plasticity and structural parameters. The model is successful in predicting the elastic microbuckling modes and to predict the failure. But the model is built for 2D unidirectional laminates and assumes microbuckling is periodic in the fiber direction, just one gradient in the thickness direction is taken into account and the influence of the misalignment is not completely described [D4]. Therefore, to extend the developments of these works ([D1],[D3],[G1],[G4]), new non-local finite element models are developed: one with using ABAQUS® in-built structural elements, named Beam Non-Local (BNL) model and the other with User Element (UEL) subroutine of ABAQUS®, named Homogenized Non-Local Model (HOMNL), implemented in the user element (NL U32), which can be applied with the aim to predict the compressive strength of unidirectional plies/laminates and also for woven composites (2D and 3D). Both the non-linear geometrical and material effects are taken into account in this model. With the BNL model, it is possible to capture the mechanism in 2D and 3D space for laminates of unidirectional composites. Results of the bibliography have been confirmed and new results are presented, for example, the elastic mode in 3D or the mechanism under bending. The width and angle of the kink band are determined by this model. In the framework of more general, the validation of the NL U32 element has been performed with respect to ABAQUS® classical elements for both linear and non-linear (geometry and material) cases. The classical (elastic and plastic) and non-local material properties (elastic) are identified by comparison to the responses of a Representative Volume Element (RVE) of full heterogenous microstructures. Some results have been validated with the bibliography. The developed non-local user element (NL U32) is 2D in this thesis and it can be extended easily to a 3D case, which remains one of the future perspectives.

In this work, ABAQUS® v2017, DAKOTA v6.10.0, PARAVIEW v5.8.0 are the softwares used and FORTRAN, Python are the programming languages used.

Keywords : Compressive strength, Long carbon fiber composites, Non-Local model, Finite Element, Microbuckling.

RÉSUMÉ

La rupture en compression des composites à fibers de carbone longues est due à des mécanismes complexes. La connaissance de ces mécanismes est importante pour la conception des structures composites car la résistance à la compression et la rigidité des stratifiés sont supposées inférieures à leur résistance à la traction. De plus, la rupture en compression est un mécanisme de ruine non locale qui dépend de la structure du composite (épaisseur de la couche, gradient de charge), ce qui en fait une particularité. Ce mécanisme a été décrit et modélisé dans la littérature avec des outils numériques appropriés et des expériences qui ont pris en compte cet effet. Il existe de nombreux articles dans la littérature intégrant le phénomène de microflambage pour capter l'instabilité locale. Mais uniquement quelques chercheurs ont modélisé le mécanisme à l'échelle structurelle dite mesoscopique. Par exemple, Drapier et collaborateurs ont proposé un modèle homogénéisé en 2D, qui prend en compte les défauts d'alignement initial des fibers, la plasticité de la matrice et les paramètres structurels. Le modèle permet de prédire les modes de microflambage élastique et de prévoir la défaillance en compression. Mais le modèle est construit pour des stratifiés unidirectionnels 2D et suppose que le microflambage est périodique dans la direction des fibers, un seul gradient dans la direction de l'épaisseur est pris en compte et l'influence du désalignement n'est pas complètement appréhendée.Par conséquent, pour étendre les développements de ces travaux, de nouveaux modèles d'éléments finis non locaux sont développés dans cette thèse : l'un avec des éléments de structures proposés de base par ABAQUS®, appelé modèle BNL (Beam Non-Local) et l'autre avec le sous-programme UEL (User Element) d'ABAQUS®, appelé modèle HOMNL (Homogenized Non-Local Model), mis en œuvre sous la forme d'un élément utilisateur (NL U32), qui peut être utilisé dans le but de prédire la résistance à la compression des plis stratifiés unidirectionnels mais également pour les composites tissés (2D voire 3D). Les effets de non linéarités géométriques et matériels sont bien évidemment pris en compte dans cette modélisation. Avec le modèle BNL, il est possible d'appréhender le mécanisme en 2D et 3D dans des stratifiés de composites unidirectionnels. Les résultats de la bibliographie ont été confirmés et de nouveaux résultats ont été générés, comme par exemple, le mode élastique en 3D ou le mécanisme de microflambage en flexion dans un stratifié. La largeur et l'angle de la bande de pliage sont déterminés automatiquement par ce modèle. Dans un cadre plus général, la validation de l'élément NL U32 a été effectuée par rapport aux éléments classiques ABAQUS® pour les cas linéaires et non linéaires (géométrie et matériau). Les propriétés classiques (élastiques et plastiques) et non locales des matériaux (élastiques) sont identifiées par comparaison avec les réponses d'un élément de volume représentatif (RVE) de microstructures totalement hétérogènes. Certains résultats de résistances ont été validés avec la bibliographie. L'élément utilisateur non local développé (NL U32) est en 2D dans cette thèse mais il peut être étendu très facilement à un cas en 3D, ce qui reste une des perspectives futures.

Dans ce travail, ABAQUS® v2017, DAKOTA v6.10.0, PARAVIEW v5.8.0 sont les logiciels utilisés et FORTRAN, Python sont les langages de programmation.

Mots-clés : Résistance en compression, Composites à fibers longues, modèle non local, élément fini, microflambage.

Table of Contents

LIST OF FIGURES

LIST OF TABLES

1 Introduction

The general context of this work is the modelling of the compressive behavior of unidirectional laminate and woven fabrics. This topic has been the subject of numerous researches since many years (starting from 1964) and regularly papers bring new results or confirm the results of the previous ones. The difficulty of this problem lies in the very mechanism of ruin. Its peculiarity is that the compressive strength cannot be only a 'material' quantity, but the mechanism is the joint consequence of material nonlinearities of the initial state of the material (initial defects) and structural parameters at the mesoscopic scale. To illustrate this point, pure compression tests are very difficult to handle because the material failure depends not only on the stress concentrations in the jaws, their intensity but also certainly on their gradients. The compressive strength under bending stress is higher than that of measured under pure compression.

From a more concrete point of view, faced with this rapid observation, engineers dimension in compression with coefficients that are not always in agreement with what the material is able to withstand. Grandidier et al., (2012) has proposed a simple criterion to ameliorate the dimensioning under compression. Besides, additional questions arise about the notions of damage tolerance or fatigue. How can we predict the compressive strength in structures that are tired or have damage inherent to severe use? These are all open questions that call for a little more work in modelling the behavior and resistance in compression. The work of this thesis should contribute to this problem. Based on this reflection and current knowledge, it appeared an opportunity to create theoretical and numerical tools to answer the questions of engineers.

More precisely, the global objective of the thesis is to: *'Develop a Continuous Homogenized Non-Local Finite Element model/ tool (2D and 3D), which is capable of predicting the compressive strength of the complex composite structures'.* The objective defined is actually linked to the past research works of Grandidier, Drapier et al., (1992,1996,1999). The clear definitions of the local objectives and the necessity to develop this model are explained comprehensively in Chapter 4. To have a clear vision of the problems and definition of objectives, it is recommended for the reader to have a prior understanding of the literature review on the general mechanical behavior of composites, especially under compression (Chapter section 2.6), various experimental investigations, theoretical and numerical models developed by many researchers over the years to modelize and predict the compressive strength (Chapter 3).

2 About Composites

Composite materials continue to gain popularity in various industries like aerospace, automotive, naval, medical, etc. primarily due to their ability to reduce weight. One of the main advantages of composite materials is that they can be designed to obtain a wide range of properties by altering the type and ratios of constituent materials, their orientations, process parameters, and so on. Composites also have high mechanical properties with a low weight which makes them ideal materials for automotive and aerospace applications. Other advantages of composites include high fatigue resistance, toughness, thermal conductivity, and corrosion resistance. The main disadvantage of composites is the high processing costs which limit their wide-scale usage.

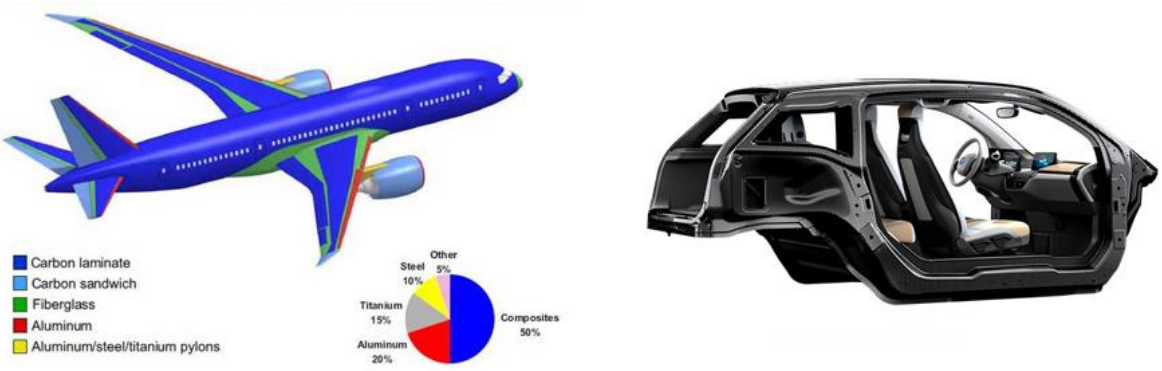

Figure 1: Applications of composite materials. [D7],[B21]

Components of Composite Materials:

A composite material consists of different phases called reinforcements (fibers) and matrix. When the composite material is undamaged, the latter two are perfectly bonded and consequently there can be no sliding or separation between the different phases. The reinforcements are in the form of continuous or discontinuous fibers. The main function of the matrix in a composite is to support the fibers. It must transfer the stress to the fibers and protect the fibers from environmental influences.

The requirements on the fibers in the composite are a high stiffness and strength because their function is to bear the loading. Fibers have normally a higher tensile strength and stiffness than the material in its bulk form. The arrangement of the fibers and their orientation permit to reinforce the mechanical properties of the structure.

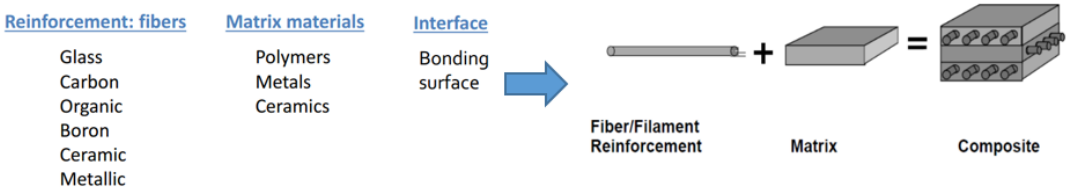

Figure 2: Architecture of composite materials.

2.1 Classification of composites

Different materials are used in industrial structures, these ones can be classified as follows:

2.1.1 First Level (Matrix Material)

Different materials are used in industrial structures, which can be classified as follows:

a) Polymer Matrix Composites (epoxydes, polyesters, nylons, etc.);
b) Ceramic Matrix Composites (SiC, glass ceramics, etc);
c) Metal Matrix Composites (aluminium alloys, magnesium alloys, titanium, etc).

2.1.2 Second Level (Reinforcement form)

For the reinforcement many possibilities are proposed to engineers to design composites, many kinds of materials exist and different shapes are proposed:

a) Fiber-short or long fiber (S-glass, R-glass, carbon fibers, born fibers, ceramic fibers and aramid fibers);
b) Yarn;
c) Fabric/Textile Composites (Woven, knitted, non-woven and braided).

The choice of an association between a reinforcement (fibers) and a matrix is very delicate and this work remains the responsibility of the chemists. Indeed, the interface resulting from the intimate association of two different constituents must have good mechanical performance. Examples of the association between reinforcement and resin commonly used in the aeronautical and space industry are:

- composites with carbon fiber and thermosetting epoxy matrix: carbon/epoxy: T300/5208, T300/914, IM6/914, GY/70M55J/M18, AS4/3501-6;
- composites with carbon fiber and thermoplastic epoxy matrix: carbon/polyamide IM7/K3B, C6000/PMR-15, AS4/PEEK (APC-2);
- composites with carbon fiber and carbon matrix: 3D C/C, 3D EVO, 4D C/C;
- composites with ceramic fiber and ceramic matrix: SiC/SiC, Sic/Mas-L;
- composites with metallic matrix: SCS-6/Ti-15-3.

In the present work, *composite with long carbon fiber and thermosetting epoxy matrix: T300/914"* (widely used in aircraft industries in the past) is considered because many data in the literature are proposed without restriction by the industry.

The reinforcements used during manufacturing maybe in form of laminates which are combined to get certain thickness or in the form of thick woven cloth. Soon the basis of reinforcement composites can be categorized in two categories: laminated composites; 2D or 3D woven composites.

2.2 Laminated Composites

In laminar composites, the layers of reinforcement are stacked in a specific pattern (unidirectional or bi-directional) to obtain required properties in the resulting composite piece. These layers are called plies or laminates (see Figure 3). These layers are formed of long fiber reinforcements bonded by resin. The individual layers consist of high-modulus, high-strength fibers in a polymeric, metallic or ceramic matrix material. Typical fibers used include glass, carbon, boron, silicon carbide and matrix materials, such as epoxies, polyamides, aluminium, titanium and

alumina. Layers of different materials may be used, resulting in a hybrid laminate. The individual layers generally are orthotropic (that is, with principal properties in orthogonal directions) or transversely isotropic(with isotropic properties in the transverse plane) with the laminate then exhibiting anisotropic (with variable direction of principal properties), orthotropic, or quasi-isotropic properties. Quasi-isotropic laminates exhibit isotropic (that is, independent of direction) in-plane response but are not restricted to isotropic out-of-plane (bending) response. Depending upon the stacking sequence of the individual layers, the laminate may exhibit coupling between in-plane and out-of-plane response ([M1], [A3] and [B1]).

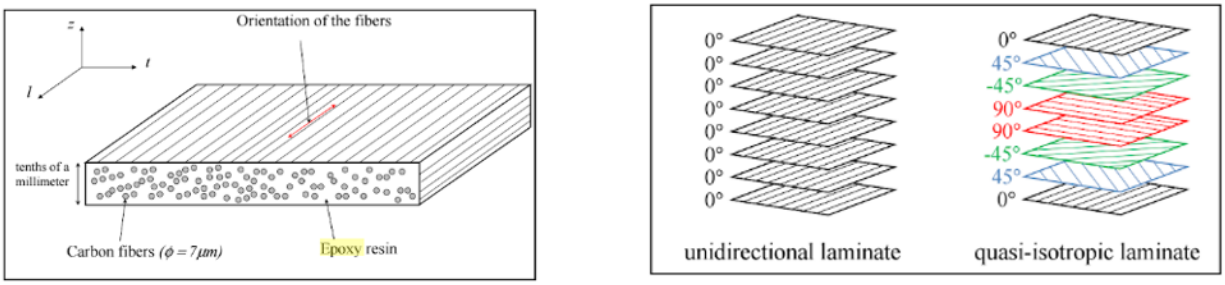

Figure 3: Long carbon fiber composite UD ply (left) and laminate (right). [B5]

2.3 Woven composites

Woven fabrics/ textile reinforced composites, characterized by the interlacing of two or more yarns (called, warp and weft) systems, are currently the most widely used textile reinforcement with glass, carbon and aramid reinforced. The use of woven fibers was originally introduced mainly to solve the problem of the high anisotropic behavior of unidirectional composites. Woven fabric reinforced composites are orthotropic and they have similar properties in the length and width directions, i.e., the warp and weft directions. They are increasingly used in various industries such as aerospace, construction, automotive, medicine, and sports due to their distinctive advantages over traditional materials such as metals and ceramics. They have good fatigue and impact resistance. Their directional and overall properties can be tailored to fulfil specific needs of different end uses by changing constituent material types and fabrication parameters such as fiber volume fraction and fiber architecture. A variety of fiber architectures can be obtained by using two- (2D) and three-dimensional (3D) fabric production techniques such as *weaving, knitting, braiding, stitching, and nonwoven methods*. (Note: Only weaving technique is discussed here) Each fiber architecture/textile form results in a specific configuration of mechanical and performance properties of the resulting composites and determines the end-use possibilities and product range. The mechanical properties of woven fabric-reinforced composites are dominated by the type of fiber used, the weaving parameters and the stacking and orientation of the various layers.

The first textile structure to be used in composite reinforcement was *2D biaxial fabric* to produce carbon-carbon composites for aerospace applications. However, multi-layered 2D fabric structures suffer from poor inter-laminar properties and damage tolerance due to lack of through-the-thickness fibers (z-fibers). *3D textile fabrics* with through-the-thickness fibers have improved inter-laminar strength and damage tolerance. Therefore, 3D textile composites have attracted great interest in the aerospace industry since the 1960s in order to produce structural parts that can

withstand multidirectional mechanical and thermal stresses. Advantages of 3D textile-reinforced composites are their high toughness, damage tolerance, structural integrity and handle ability of the reinforcing material, and suitability for net-shape manufacturing. 3D woven composites have a distinct advantage over 2D woven composites due to their enhanced inter-laminar and flexure properties. Today, composites reinforced with 2D and 3D fabrics are in common use in various industries including aerospace, construction, automotive, sports, and medicine [K2].

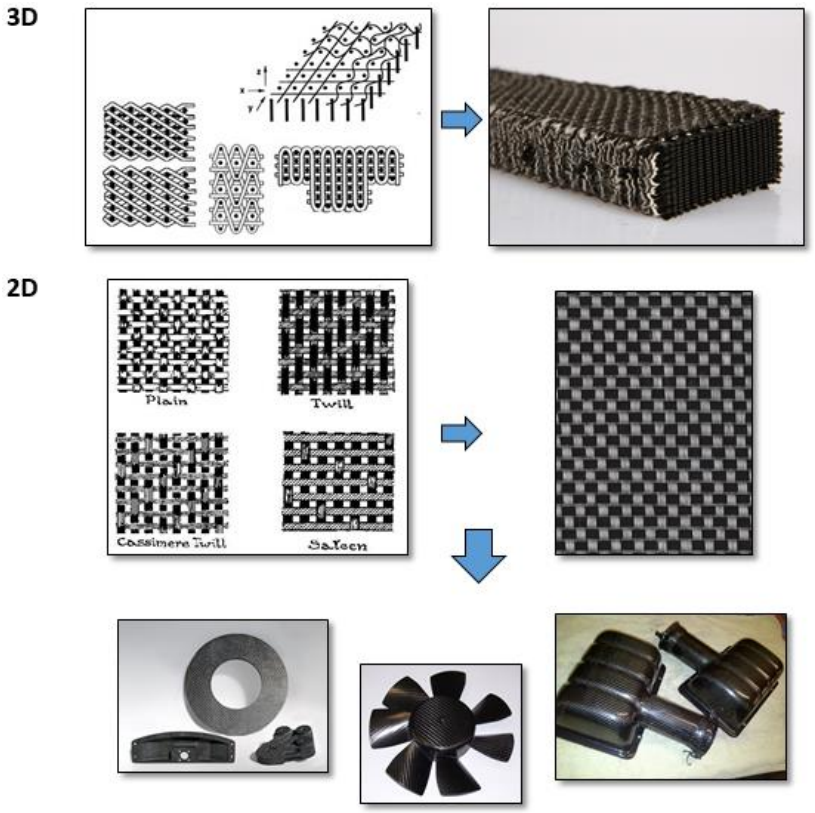

Figure 4: Woven Composites and its parts (2D and 3D). [D8],[B22]

2.3.1 2D Woven fabrics

A woven fabric consists of two or more sets of yarns interlaced together to form a continuous 2D surface. The most common 2D woven fabric is the biaxial (orthogonal) fabric/ plain weave fabric which is composed of longitudinal (warp) yarns and transverse (weft or filling) yarns interlaced at right angles (see Figure 5). Different types of 2D woven fabrics and its configuration can also be seen in Figure 5.

It is produced by conventional 2D weaving process (see Figure 6). The fundamental operations constituting the weaving process are, in their sequential order, *shedding*, *picking*, *beating up* and *taking up*. The shedding operation displaces the warp yarns using healds (a heald is a flat steel strip or wire, with one or more eyes in which warp yarns are threaded) to create a shed (a gap). The shedding operation is followed by the picking operation whereby the weft yarns are inserted in the created shed. The weft that is laid in the shed is beaten-up by the reed (reed- a metal comb fixed in the loom used for beating up) to the fabric-fell position, and thereby completing the fabric

formation. To achieve continuity in the process, the produced fabric is advanced forward by the take-up operation. This cycle of operations is continued repeatedly to obtain the woven fabric [F8].

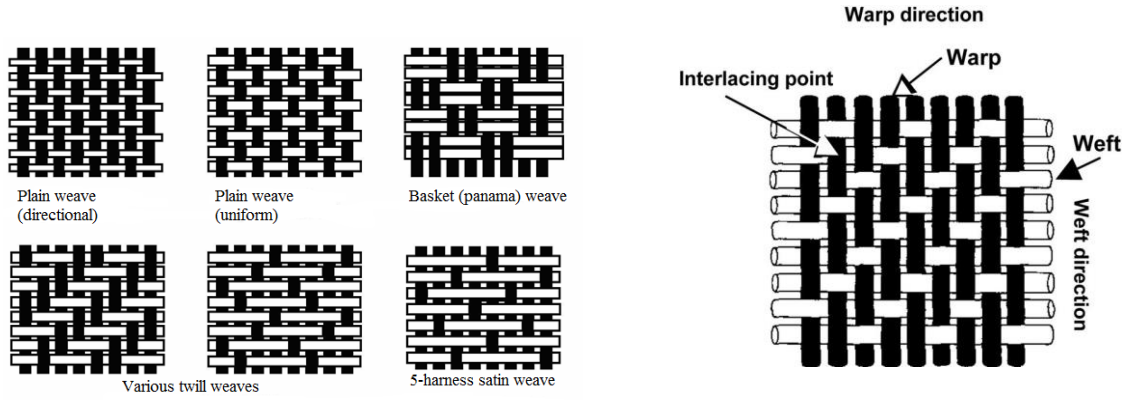

Figure 5: Types of 2D woven fabrics and its configuration. Ref: Textile Reinforced structural composites for advanced applications, [Chap 4, Karaduman, (2017)]

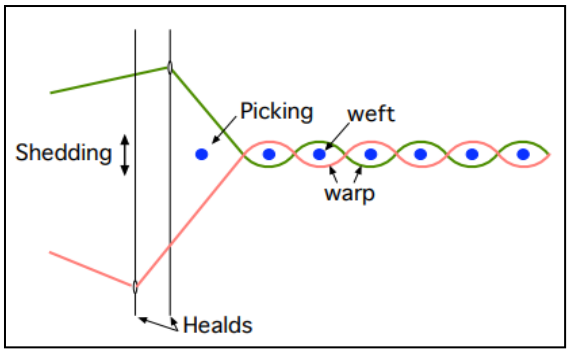

Figure 6: Illustration of 2D weaving principle for 2D fabrics. [Fredrik et al., (2009)]

Biaxial woven fabric has a good dimensional stability and balanced properties in the fabric plane. Another advantage of this fabric type is the ease of handling and low fabrication cost. Disadvantages include poor in-plane shear resistance, lack of through-the-thickness reinforcement, and poor fiber-to-fabric tensile strength translation

2.3.2 3D Woven fabrics

3D woven fabrics are produced using multiple warp layers. The movement of each group of warp yarns is governed by separate harnesses so that some are formed into layers, while others weave these layers together. The most common classes of 3D weaves are *angle-interlock*, *orthogonal*, and *fully interlaced weaves* (see Figure 7). Angle-interlock fabrics fall into two main categories depending on the number of layers that the warp weavers travel such as through-the-thickness angle interlock and layer-to-layer angle interlock. In through-the-thickness fabric, warp weavers pass through the entire thickness of the preform, while in layer-to-layer structure, they bind only two filling layers. Orthogonal interlock weaves, on the other hand, are characterized by warp weavers oriented from orthogonal to other in-plane directions and run through the thickness of the preform. 3D weaving is capable of producing a wide range of architectures [K2]. The main

limitations of 3D woven fabrics include the lack of in-plane bias reinforcement and long preparation and processing times.

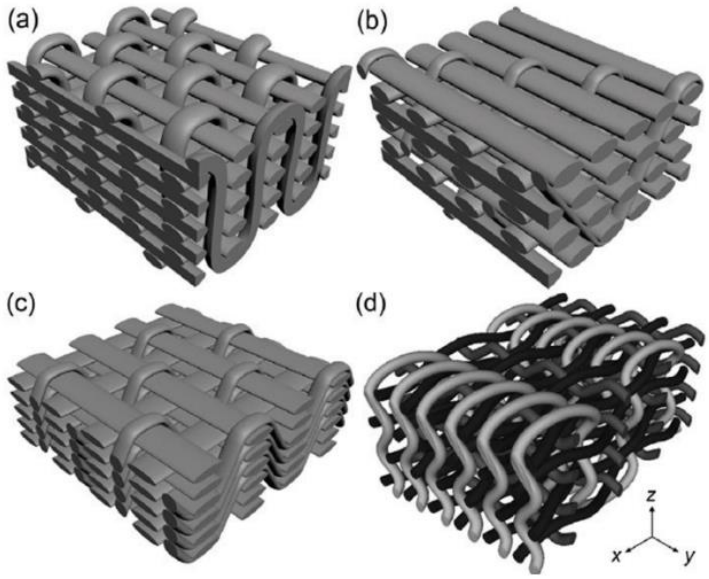

Figure 7: Types of 3D woven composites: (a) orthogonal, (b) through the thickness angle interlock, (c) layer-to-layer angle interlock, and (d) fully interlaced (plain 3D weave). [Fredrik et al., (2009)]

2.3.3 3D woven production techniques

3D woven fabrics can be manufactured both with 2D and 3D weaving. The produced 3D fabrics are different from the properties point of view due to the differences in weaving methods. With 2D weaving, pleated or plissé fabric, terry fabrics, velvet fabrics and multilayer woven fabrics can be manufactured with machines used in clothes industry. Orthogonal 3D weave structures, fully interlaced 3D weave structures can be manufactured only by using special designed 3D weaving machines.

2.3.3.1 *2D weaving*

The manner in which the 2D-weaving process is employed for producing 3D-fabrics is illustrated in Figure 8. Two mutually perpendicular sets of yarns, the warps and the wefts, are used. The warp yarns run in the length-wise direction of the fabric, and the weft yarns in the transverse direction, using fundamental weaving operations (as discussed earlier). This arrangement remains unchanged whether a single warp sheet is used (to produce sheet-like 2D-fabrics) or multiple warp sheets are used (to produce 3D-fabrics). For more details refer Fredrik et al., [F8]. The two most common 2D-woven 3D-fabrics are: *the layer-to-layer angle interlock weave* and *through-the-thickness angle interlock weave* (also known as 3-X weave). The 2D-woven 3D-frabrics are usually produced as wide sheets for use in manufacturing conveyor belts, paper clothing, double cloth etc. The 2D weaving technique also allows indirect production of a few, relatively simple, shell type profiled 3D-fabrics.

3D Fabrics could also be produced by 2D techniques, with different sets of warp yarns in the ways mentioned below [G6]:

1. By effective utilisation of warp and weft in single layer;
2. By the use of multi-layer warp and weft or multi-layer ground warp, binder warp and weft;
3. Conventional 2D process can also produce pile fabrics by utilising three sets of yarns, namely, single-layer ground warp, pile warp and weft.

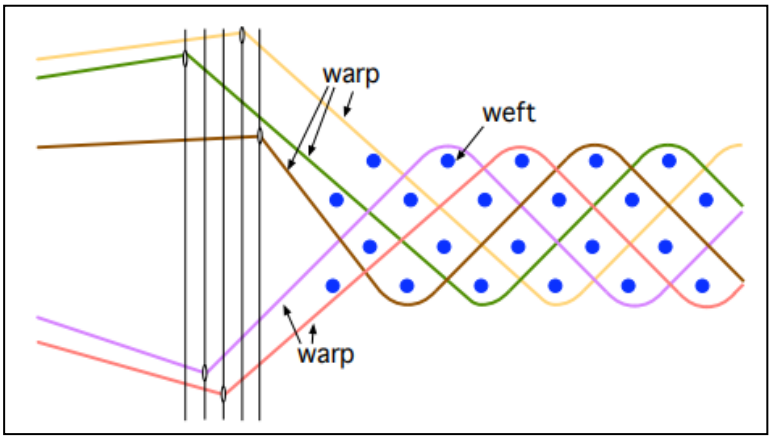

Figure 8: Illustration of 2D weaving principle for 3D fabrics. [Fredrik et al., (2009)]

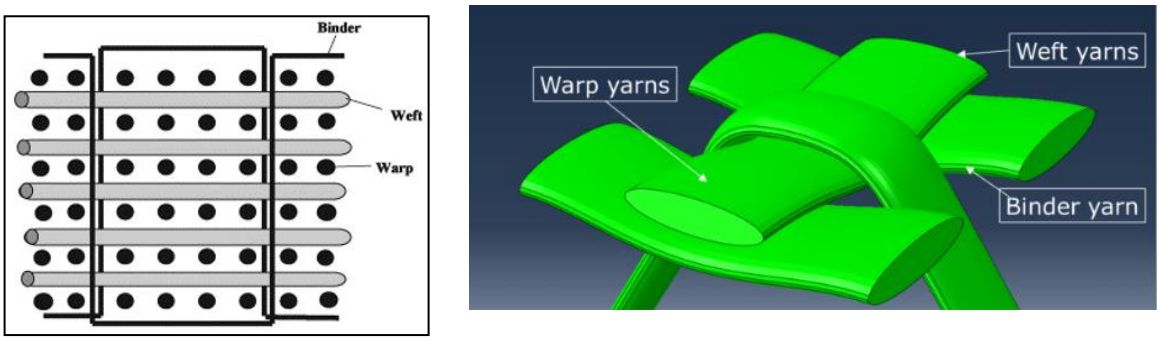

Figure 9: Schematic representation of warp and weft yarns with a crossover of binder yarn in 3D woven fabrics (orthogonal). [Elsaid et al., (2014)]

2.3.3.2 ***3D weaving***

3D-weaving is a relatively new weaving development, invented by Khokar in 1997 [K4]. The 3D-weaving process is characterised by the incorporation of the dual directional shedding operation. Such a shedding system enables the warp yarns to interlace with the horizontal and the vertical sets of weft yarns. Khokar [K3] defines the 3D-weaving process as: *"the action of interlacing a grid-like multiple-layer warp with the sets of vertical and horizontal wefts"*.

The schematic representation of the 3D-weaving process is illustrated in Figure 10 for a plain 3D-weave (fully interlaced). As shown, the warp yarns are arranged and supplied in a grid-like arrangement (Figure 10a), warps are displaced in the vertical direction to create multiple horizontal

sheds (Figure 10b), corresponding number of horizontal wefts are inserted into the created sheds (Figure 10c), the multiple horizontal sheds are then closed (Figure 10d), whereby the warp yarns become interlaced with the horizontal weft yarns. The warps are at their level positions (Figure 10e) in the weaving cycle. Next, the warp yarns are displaced in the horizontal direction to create multiple vertical sheds (Figure 10f), corresponding number of vertical wefts are inserted into the created sheds (Figure 10g), the multiple vertical sheds are then closed (Figure 10h), whereby the warp yarns become interlaced with the vertical weft yarns. These sequences of operations are repeated once more to insert the wefts in the respective opposite directions to complete one cycle of the 3D-weaving process to obtain the woven structure in Figure 10i.

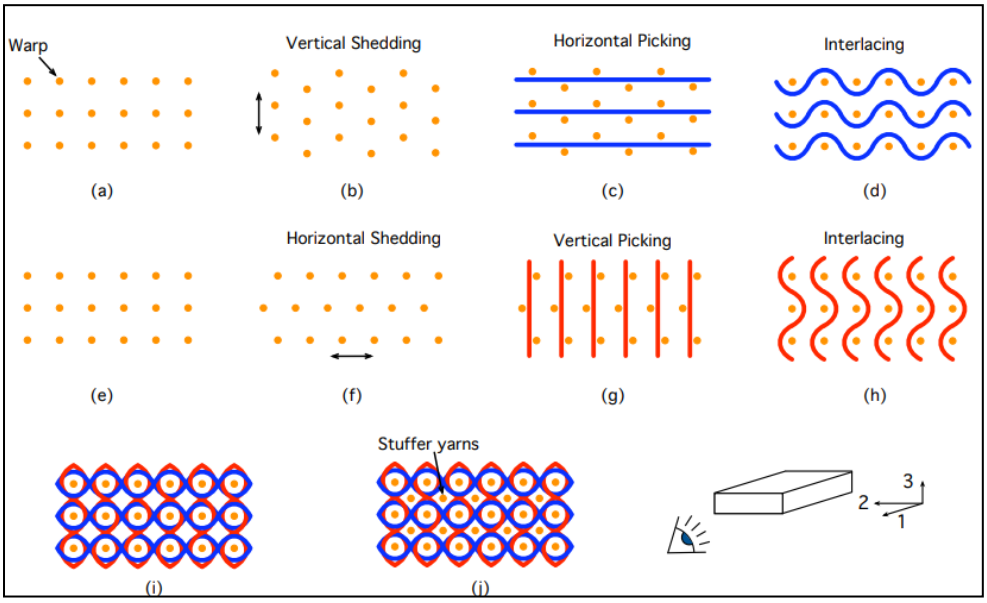

Figure 10: Illustration of 3D weaving principle for 3D fabrics, seen from the warp or 1-direction. [Fredrik et al., (2009)]

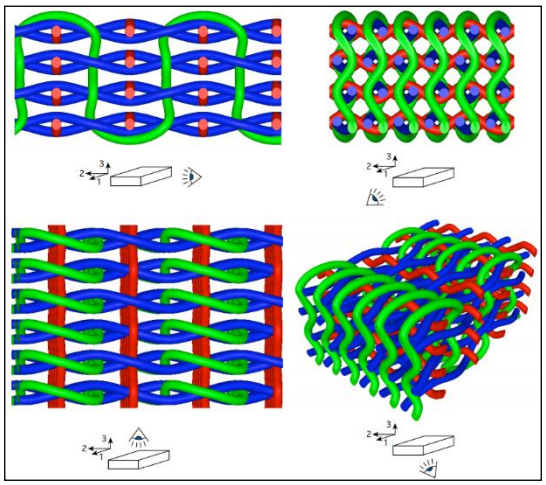

Figure 11: A plain 3D-weave without stuffer yarns seen from its three principle planes and from an isometric view. Warp yarns are blue, horizontal weft yarns red and vertical weft yarns green in the illustrations. [Fredrik et al., (2009)]

In order to have better picture of the weave illustration given in Figure 10i, the views from the three principle planes and from an isometric view are shown in Figure 11. For more comprehensive overview on fabrication methods of 3D textile composites refer Chen et al., (2011).

2.3.3.3 *General production methods of composites*

The type of matrix material, i.e., thermosetting or thermoplastic, is the main factor that determines the manufacturing technique used for the production of composites. Other parameters include: the matrix material used, reinforcement form, fiber volume fraction, dimensions of the part to be produced, and complexity of the part shape. In the thermosetting resin-based methods, the matrix material is generally used in liquid resin form, whereas thermoplastic-based composite processing requires the melting of the polymer material. Thermosetting composites can be manufactured using a range of methods such as *hand lay-up*, *Resin Transfer Molding (RTM)*, *Autoclave molding*, *Compression molding*, *Filament winding*, *Vacuum infusion,* and *Pultrusion*. For thermoplastic matrix-based composites, *Injection molding* and *Thermo-forming* are the most commonly used techniques [K2].

2.4 Defects from process/manufacturing techniques

The manufacturing process has the potential for causing a wide range of defects, the most common of which is "porosity," the presence of small voids in the matrix. Porosity can be caused by incorrect, or non-optimal, cure parameters such as duration, temperature, pressure, or vacuum bleeding of resin. Porosity levels can be critical, as they will affect mechanical performance parameters, such as compressive strength, transverse tensile strength and inter-laminar shear stress. More recent low-cost manufacturing techniques, involving the infusion of resin into pre-formed dry fibers in moulds, have introduced other potential defects such as fiber misalignment, or waviness, both in the plane of the material and out-of-plane. Sandwich structures with honeycomb or foam cores can suffer from poor bonding of the skin to the core. Delamination can occur at the skin-to-adhesive interface or at the adhesive to-core interface[S10]. Other defects include matrix cracking, laminate warping and buckling from build-up of thermal residual stresses during the curing etc., [W5]. In case of woven composites: crimp, tow waviness, and fiber breakage during processing are the main factors leading to property reduction, such as in-plane and fatigue performance [T7].

2.5 Specific case: long carbon fiber reinforced composites

The superior mechanical properties of long carbon fiber reinforced composites make them an ideal substitute for metals. Some of major advantages of long carbon fiber reinforced composites include[B5]:

- High strength-to-weight ratio;
- Resistant to deformation and crack propagation;
- Superb load carrying ability;
- Exceptional long-term creep resistance;
- Cyclical fatigue endurance;

- Outstanding dimensional stability;
- Performance maintained at low and elevated temperatures;
- Low coefficient of thermal expansion;
- Dampen vibrations and sound.

One of the *main disadvantages* of this type of composites is the '*high processing costs'*, which limit their wide scale usage. In the present work, as discussed in the earlier sections, we mainly focus on *composite with long carbon fiber and thermosetting epoxy matrix* which is widely used in aircraft industries and in specific custom applications: racing cars, racing yachts, etc,. Typical representation of UD long Carbon Fiber Reinforced Plastic (CFRP) composites is illustrated in Figure 12.

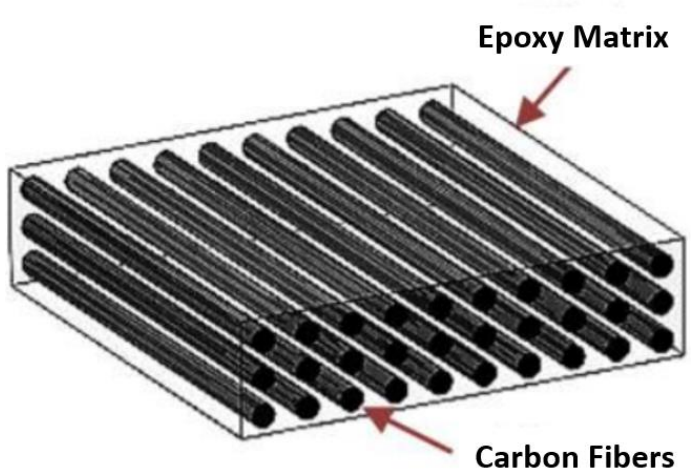

Figure 12: UD Carbon/Epoxy (CFRP) Composite. [Thirumalai et al., (2017)]

2.6 Behavior of composite materials

The section contains brief overview of general mechanical behavior of composite materials, for example: static and fatigue under different loading conditions. And then focused with respect to particularly UD and woven composites, followed by explaining the specific problem of compression, the need of modelling the rupture/failure under compression.

2.6.1 General behavior

The composite materials are generally treated as a heterogenous anisotropic continuum. Materials whose properties at a point vary in different directions are anisotropic; those with properties which vary from point to point are heterogenous. This physical property significantly increases the number of parameters that determine rigidity, strength, thermal effects, etc., (generally there are at least three elasticity modulus, three Poisson's ratios and three shear moduli). Thus, there are two concepts, heterogeneity and anisotropy, which are pertinent to the study of composite materials. A composite can be one or both or neither of these depending upon the constituents and the scale of interest. Fox example, consider a fiber composite material; that is a mixture of fibers contained in a matrix material which binds the fibers together. The two phases may individually be isotropic or

anisotropic materials. When the fibers are oriented within the matrix - for example, a set of filaments, all parallel to a given line, embedded in an otherwise isotropic and homogenous matrix - the composite material is heterogenous but isotropic. This is on a small scale; however, for contemporary filaments whose cross-sectional dimensions are extremely small, practical interest focusses on the average of stresses and strains over a dimension which is large compared to this cross-sectional dimension. For that purpose, it is possible to consider the materials response in an average way to be anisotropic but homogenous; that is, one may consider a material which has the same average properties as a given fiber composite material. This new average or "effective", material will have properties in the fiber direction which differ substantially from those in a direction transverse to the filaments. This makes it an anisotropic material. Since one is not concerned with the local perturbations associated with the individual filaments, this may be considered to be a homogenous material. This replacement of “actual” by “effective” material provides the transition from “micromechanics” to “macromechanics”. On a microscopic scale, the composite is a heterogenous isotropic material; whereas on a macroscopic scale, it is an anisotropic but homogenous material [R2].

For anisotropic materials like composites, application of a normal stress leads not only extension in the direction of the stress and contraction perpendicular to it, but to shearing deformation. Conversely, application of shear stress causes extension and contraction in addition to the distortion of shearing deformation, i.e., shear-extension coupling, which is also characteristic of orthotropic materials subjected to normal stress in a non-principal material direction [J1].

The main factors that could cause fractures on composite part or structure are numerous [J2]:

- Environment: temperature, contact with chemicals, humidity (influence on mechanical properties mainly at low number of cycles);
- Inadequate or faulty design: over-estimation of the strength of the material, underestimation of actual stress;
- Type of stress: especially compression and shear;
- Presence of manufacturing defects.

The different stages in the damage (microscale) process occur earlier or later depending on the type and direction of the reinforcement and also depending on the type of mechanical stresses applied. However, the damage process is always driven by the same process: the first damage occurring requires low energy consumption (interface or matrix failure), while the last stages (fiber breakage) require more significant energy level.

More precisely the first step of damage begins logically in zones of lower strength such as the matrix fiber interfaces and the matrix itself, with failure over small distances called intralaminar cracks. Intralaminar damages mainly appear in the areas where fibers are not oriented in the axis of the load, when the strain in the matrix reaches its breaking strain. In general, intralaminar cracks are parallel and regularly spaced [J2]. It is necessary to underline that under static loading, the engineers think that the composite materials generally have a lower compression resistance than tensile resistance.

In the case of a laminated composite, in addition to the intralaminar damage, the interlaminar damage called delamination occurs. When cracks develop in a ply, the propagation is stopped by

the adjacent plies. At the intralaminar crack tip, the singularities of stress make the cracks propagate at the interface between two adjacent plies layers. In the case of a laminated composite with different directions plies, delamination can also initiate because of differences of stiffness of the different plies forming the laminate. This damage can also develop from sources like manufacturing defects and impact events.

Finally, when the volume ratio of the matrix damage reaches a certain level, the final stage of damage corresponds to the failure of the fibers, called translaminar failure. This type of damage is mainly involved in the final stages of ruin in areas where fiber orientation more or less coincides with the axis of stress. This is usually the case in the high stress-applying region of the parts [J2].

2.6.2 Unidirectional case

The unidirectional composites behave as an effective anisotropic material. In the most general case, it may be an orthotropic material having nine independent elastic constants. For a random distribution of fibers over a given cross section, the transverse plane may be considered to be an isotropic plane and the composite itself is then a transversely isotropic composite having five independent elastic constants. With the desired loading conditions defined, it is possible to determine the properties analytically or experimentally [R2].

The understanding of the influence of constituent properties upon composite strength is not as definitive as of the results obtained in the literature for the other physical properties. The primary reason for this is the influence of material heterogeneity. When simple problem of assessing the tensile strength of unidirectional fiber composites under a unidirectional load parallel to the fiber axes is considered, a range of complexities can occur. First, since the fibers are generally brittle materials, their strength varies from point to point and fiber strength can only be defined by statistical measures. As a result of this, when tensile load is applied to the composite, some fractures of fibers will occur, at relatively low load levels, at weak points of the fibers. In the vicinity of these fractures there will be perturbations of the stress field. The resulting stress concentrations can cause a multiplicity of other failure modes. Thus, we may have interface separation, matrix yielding, or matrix cracking, or the stress concentration may cause crack propagation. It is to be expected in the general case that a combination of these possible failure modes will occur. Thus, under increasing load there will be a continual increase in the number of damaged regions and in the size of these damaged regions. This growth of internal damage will continue until either a crack propagation becomes unstable causing failure, or until the interaction of the large number of damaged regions causes overall failure of the material [R2].

A load in other direction generate many damages under the form of crack inside the ply in the matrix and interfaces. Moreover, the composite can exhibit a nonlinear behavior with plasticity and viscous phenomena. The evolution and scenario of damage is complex and many articles deal with this subject.

2.6.3 Woven case

Due to their complex structural characteristics, woven composites (2D and 3D) display different mechanical properties and failure modes from traditional composite laminates. The relations between the weaving geometry and main mechanical properties of composites can be obtained by studying the internal structures of woven textiles. 3D woven composites provide sufficiently high in-plane mechanical properties, is delamination-free, and can obviously improve transverse strength, fracture toughness, damage tolerance, and impact and blast performances [H8]. Many researchers have conducted numerous studies on tension in 3D woven composites. For example, Huang [H9] studied the effect of Z yarn in 3D orthogonal woven composites and found that the tensile modulus and strength increased only in the thickness direction with increasing Z yarn size, but dropped in the in-plane warp and weft directions. Tsai [T5] compared the fatigue properties and damage processes between three layers and five layers of 3D angle interlock woven composites under tensile cyclic loading. Transverse cracks in warp yarns existed first. Debonding between the warp and weft yarns, debonding extension and deflection into the matrix, and weft fiber breakages were then observed. Brandt [B20] tested the interlaminar shear strength of 3D through-the-thickness angle-interlock woven composites and 3D orthogonal woven composites. The strength of former composites was higher than that of latter one because of the load carrying of Z yarn. Gerlach [G10] discussed the interlaminar shear properties of the 3D angle interlock woven composites of carbon. The stress in the warp direction decreased to a lower level than that in the weft direction. The existence of binder yarns, which remained connected, caused high residual strength. Refer [H8] for comprehensive details. Compression in 3D woven composites has been also extensively studied. The bending of warp fibers seems to be the main reason for the failure in axial compression. Explicit details regarding the experimental investigations are found in the following chapter (Chapter 3).

2.6.4 Specific problem of compression

In short, the damage to composite material is a combination of crack in matrix, debonding of interface and breaking of fibers. The damage of yarns is the consequence of these modes. Under complex loads, the damage of a composite or a structure should be described by a scenario given the evolution, localization and propagation of each mode. The delamination is a crack which go through the resin of the interface and sometime jumps on interface between fibers and matrix, which are close to each lip of interface.

It is the same for the failure under a compression applied in the fiber direction. This is the consequence of a complex mechanisms, which is discussed in detail in following chapter. The knowledge of these mechanisms is important for the design of composite structures [M5], because the compressive strength and stiffness of laminates is assumed less than their tensile strength.

Two examples are shown in Figure 13, to explain the necessity to modelize the compressive behavior/failure of composites. First example corresponds to an aeroplane wing, which is subjecting to constant compressive load while flying, which may result in compressive failure near the junction (as highlighted in the figure) over the period of time. Second example is a sailing/racing yacht. Mast of sailing/racing yacht can expect a compressive failure due to the

continuous application of compressive load, which is induced by tensioning of the rigging(forestay/backstay) and the mass of the mast and rigging itself.

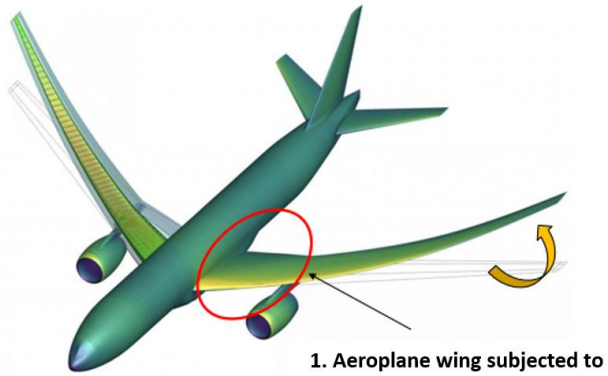

1. Aeroplane wing subjected to compressive load

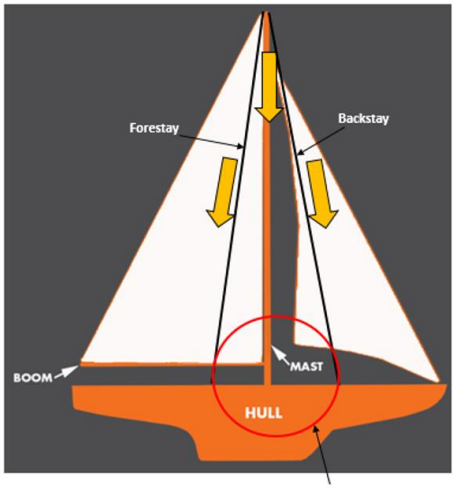

2. Mast of Sail boat subjecting to compressive load

Figure 13: Examples of Compressive failures at structural scale

Likewise, there are numerous examples of compressive failures occurring on structural scale to demonstrate the need of modelling compressive behavior/failure. Many Researches over the years confirmed that one of the major causes for this compressive failure, especially in long carbon fiber composites is due to the '*local plastic microbuckling phenomenon*', which is discussed explicitly in the following chapter. However, these examples clearly depict the need to understand and modelize the compressive behavior of composites, thereby improving their strength predictions.

3 Strength of composite materials under compression (experiments and models)

This chapter focus on various compression tests available and bibliography of experimental results by various researchers, followed by the analytical and numerical models developed over the years at different length scales to modelize the compressive strength, in particular failure of composites.

3.1 Compression tests

Until the mid-1970s, compression testing of composite materials received relatively little attention. Up to that point, it had generally been assumed that the compressive stiffness was approximately equal to the tensile stiffness (which is not a reasonable assumption now [M5]), and thus tensile stiffness testing was adequate to identify the stiffness. However, the industry soon realized that a similar assumption regarding compressive strength was definitely not valid [A2]. The compressive strength of many composites, when measured, appeared to be significantly lower than the tensile strength.

The American Society for Testing and Materials (ASTM) adopted two standard test procedures for compression tests of composite materials. These are: i) Test Method for Compressive Properties of Rigid Plastics (D 695-89) and ii) Test Method for Compressive Properties of UD of Crossply Fiber-Resin Composites (D 3410-87). The standard ASTM D 3410-87 includes the: a) Celanese and b) the Illinois Institute of Technology Research Institute (IITRI) test methods (see Figure 14). The main difference between these two test methods is the grip design. The Celanese test methods uses ‘conical’ wedge grips, whereas the IITRI test involves ‘trapezoidal’ wedge grips. The Celanese fixture weighs approximately 10 lb, whereas the IITRI fixture weighs about 95 lb. The fabrication cost of the Celanese fixture, due to its complexity, was high relative to other types of fixtures and also the cost of the IITRI fixture was about twice as high. Due to these limitations, both the fixtures are not widely in use [A2].

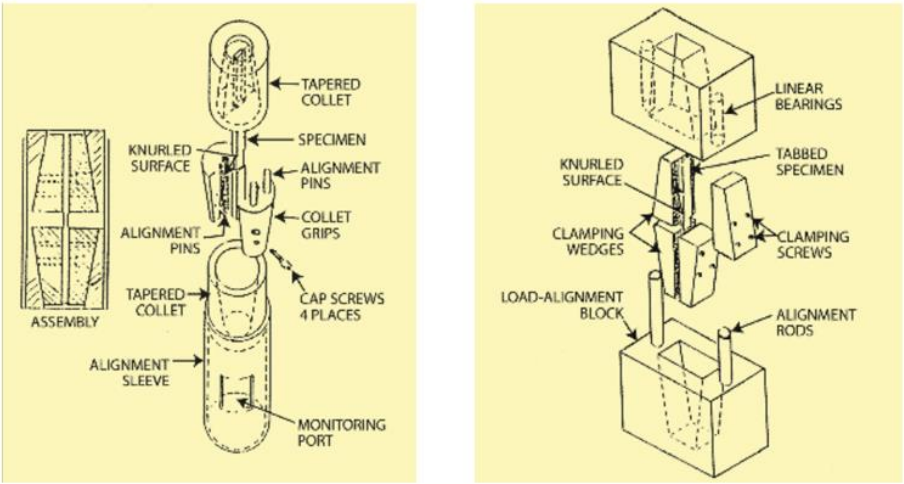

Figure 14: Celanese Fixture (left) and IITRI Fixture (right). [A2]

As a result, in part, of these nontechnical considerations, it was not until 12 years later, in 1987, that the IITRI test method was added to ASTM D 3410, as Method B. Incidentally, a Method C also was added at the same time, viz., a flexural test of a sandwich beam with the test coupon being the face sheet on the compressive surface of the beam (The Sandwich Beam method). In 1993, this seldom-used Method C was removed to its own standard, ASTM D 5467, where it still languishes today. The Celanese method was then deleted in 2003, so that presently ASTM D 3410 contains only the IITRI method. However, the IITRI method (ASTM D 3410) is used much less frequently nowadays.

A major research effort at the University of Wyoming during the 1990s led to the development of ASTM D 6641, the Combined Loading Compression (CLC) Test Method (Figure 15), first issued in 2001. The fixture is relatively small (10 lb) and inexpensive, easy to use and favorably combines loading modes. This often permits the use of simple untapped, straight-sided specimens, and very reliable results are usually obtained [A2].

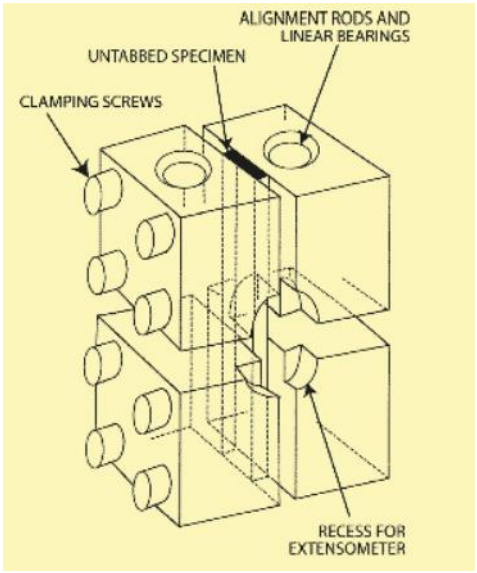

Figure 15: Combined Loading Compression test Fixture. [A2]

3.2 Four Point Flexion Compression Fixture

One of the most widely used test fixture nowadays in order to assess the flexural properties of the composites is *Four Point Flexion Compression fixture*. The Four Point Flexion Compression fixture/Four Point Flexural test fixture (ASTM D6272) measures the force required to bend a plastic beam under a four point loading system. This test method covers the determination of flexural properties of unreinforced and reinforced plastics, and is used for reinforced or unreinforced materials including high modulus composites and for materials that do not fail within the limits of ASTM D790 (a three point loading test). The major difference between the three point and four point flexural tests is the location of the bending moment. The four-point bending method allows for uniform distribution between the two loading noses, whilst the three point bending method's stress is located under the loading nose [I1].

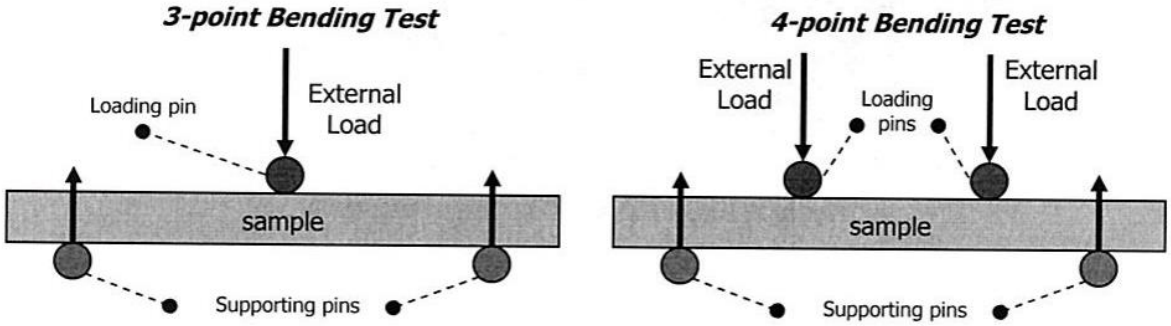

Figure 16: Schematic of Flexure tests (3-point and 4-point test). [I1]

For the four-point flexural test, the specimen lies on a span and stress is uniformly distributed between the loading noses (see Figure 16). There are two procedures within the ASTM D6272 method. Procedure A is followed for materials with smaller deflection and for measuring modulus. It shall be used for measurement of flexural properties, particularly flexural modulus, unless the material specification states otherwise. Procedure B is followed for materials with larger deflections and used for measuring strength. Procedure B, designed particularly for those materials that undergo large deflections during testing. It is suitable for measurement of flexural strength. In general, a rectangular cross section bar rests on two supports and is loaded at two points. The test specimen and loading members are symmetrically placed relative to the central axis. The load is increased until failure or rupture occurs at the outside edge of the plastic test specimen. The test method for conducting this test usually involves a specified test fixture on a universal testing machine. Flexural properties determined by this test method are especially useful for quality control and specification purposes.

3.3 Strength of long fiber UD composites

The compressive failure of long fiber composites is of major concern for the design of composite structures since the compressive strength of practical laminates is significantly less than their tensile strength[M5]. Competing modes of compressive failure exist, including *delamination, fiber failure and elastic and plastic microbuckling*. '*Elastic microbuckling'* is a shear buckling instability and the matrix deforms in simple shear, whereas '*Plastic microbuckling'* is a shear buckling instability, which occurs at sufficiently large strains for the matrix to deform in non-linear manner [H2].

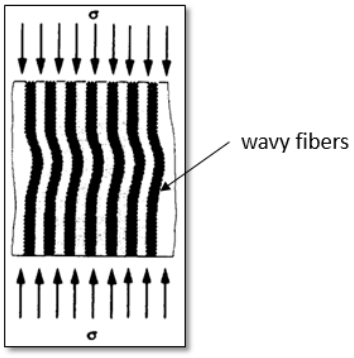

Figure 17: Initial fiber waviness. [Sun et al., (1994)]

A common failure mechanism for engineering composites is imperfection-sensitive plastic microbuckling from *pre-existing fiber waviness*, fiber misalignment (see Figure 17). Initial fiber waviness is a manufacturing defect that is created by fiber movement in the matrix during the prepreg and curing processes (as discussed in earlier sections [S4].

Many experimental investigations conducted by various researchers over the years confirmed that, composite with fibers having initial misalignments, when loaded under compression, the shear

stresses are induced due to angle between fibers and loading directions. Resin (epoxy matrix) maintains the fiber misalignment. But, when the misalignment increases due to higher shear strains, the fiber transmits to the matrix a non-linear shear load, consequently matrix assumes non-linear behavior which corresponds to the loss of stiffness. When fiber deformation reaches higher than critical value, microbuckling phenomenon starts and formation of kink band/shear band occurs (see Figure 18). Consequently, this leads to decrease in compression strength and failure of composite. Therefore, the main parameters that influence the microbuckling and kink band formation are: a) Matrix physical non-linearity and b) Presence of fiber initial wavy imperfection/undulation.

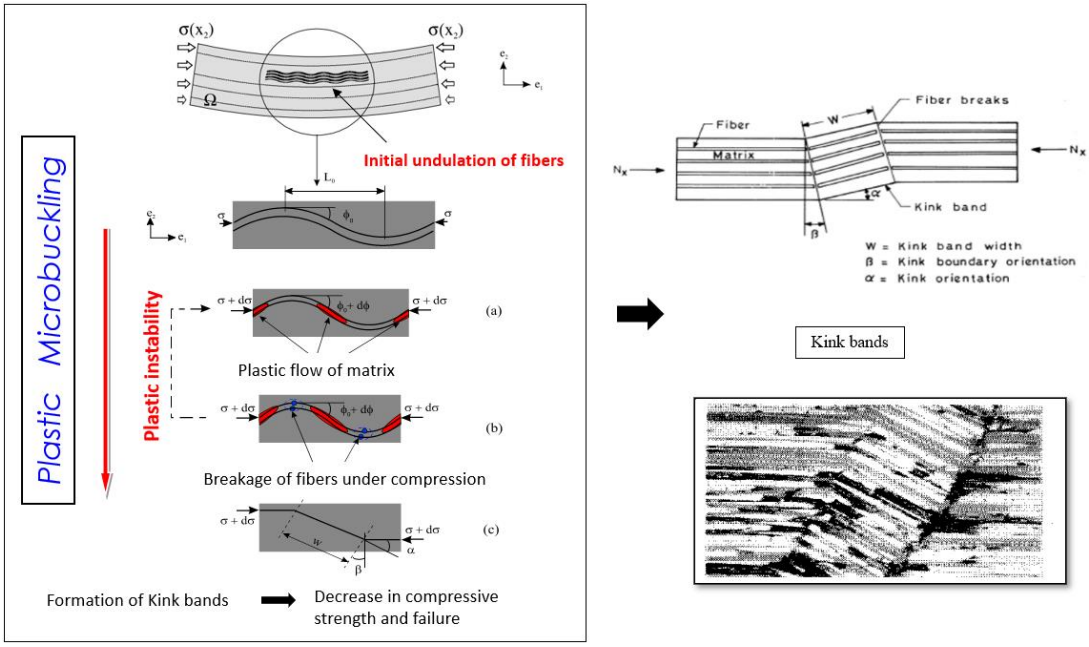

Figure 18: Formation of kink bands (plastic microbuckling phenomenon). [Drapier et al., (1999)]

Microbuckling phenomenon is strongly influenced from many factors. As discussed earlier, mainly fibers alignment defect inside the material and the plastic behavior of the matrix, which are the most significant parameters of the mechanism. The knowledge about geometrical characteristics for fibers positioning defect appears, therefore essential for the prediction of compression rupture. Other important factors play a major role on this mechanism, they are: *i) Effects of stacking sequence ii) Type of loading and iii) Ply thickness***,** which represent "*the structural effect"*, the term coined during the experimental investigations of Wisnom, (1991), Grandidier et al., (1992) and Grandsire-Vinçon, (1993) , which has been proved later to be the key to improve the failure criteria.. Taking into consideration all these parameters, several failure/ microbuckling models have been developed over the years to predict the composite failure under compression, which is discussed in detail in the following sections.

3.4 Strength of Woven composites

It was found during the experiments conducted by Abdel Ghafaar et al., (2006), who studied the mechanical behavior of 2D woven fabric composites under bending and compression that, when

carbon fiber woven composite with epoxy resin is loaded under compression, the composite (with different volume fractions) showed a non-linear elastic behavior and the mechanical properties are increased, as the reinforcement volume fraction is increased. It was observed that, the main cause for the fracture of the carbon fiber woven composite with epoxy resin is the "*inter-laminar shearing between matrix and fibers"* (see Figure 19). The compression test was conducted in a universal testing machine. The specimen geometry and dimensions were made according to ASTM D 3410-75(1987).

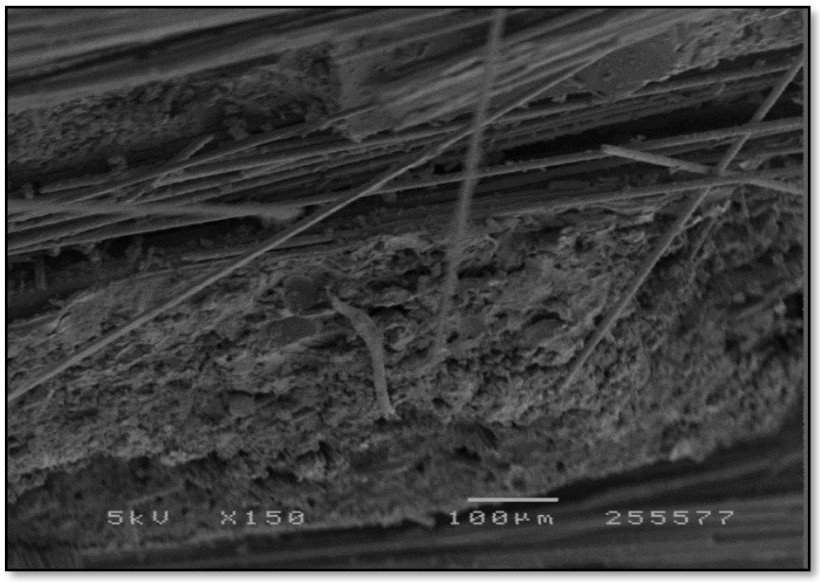

Figure 19: SEM fractograph of woven carbon fiber epoxy composite after fracture under compression (36.8% vol). [Ghafaar et al., (2006)]

In another experiments conducted by Cox et al., (1994), where they observed the failure mechanisms for *carbon/epoxy composite containing three-dimensional (3D) interlock weave reinforcement* (layer-to-layer angle, through-the-thickness angle and orthogonal interlock), loaded under monotonic loading (compression, tension and bending). Two types of processed composites were used for experiments: 1) lightly compacted and 2) heavily compacted. The major differences between them is that, the former one is loosely wovened with minimal compaction pressure applied through thickness and the latter on is tightly wovened with higher compaction pressure, during processing. They reported that the key phenomenon that leads to failure of composite under compression was '*delamination'* and '*kink band formation'* (see Figure 20). Compression tests were displacement controlled, dogbone and cuboidal specimens were used for the experiments.

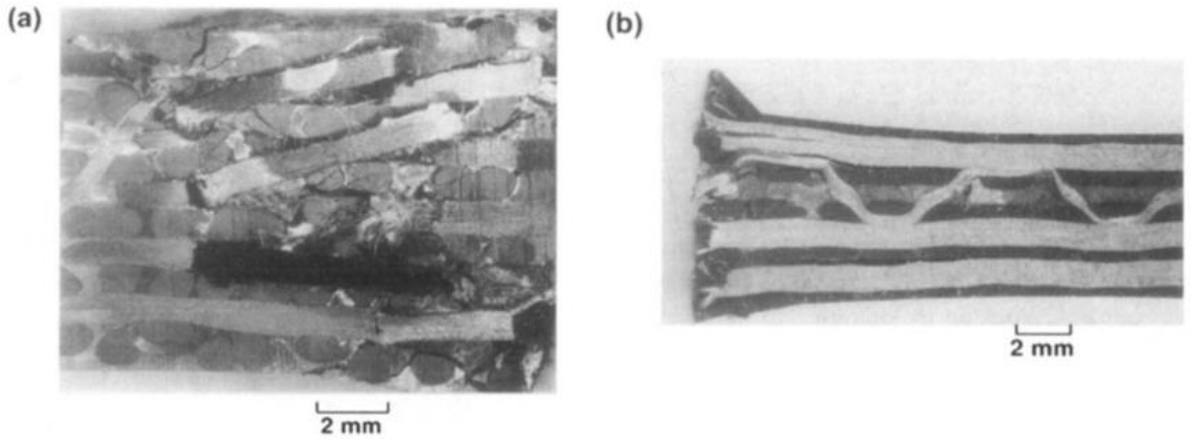

Figure 20: Comparison of compressive failure of cuboidal specimens of (a) lightly compacted composites, and (b) a heavily compacted composite, that failed by delaminating. [Cox et al. (1994)]

Fredrik et al., (2009) in their research assessed the mechanical performance of a 3D woven-fabric composite by determining its tensile, compressive, out-of-plane, shear, and flexural properties. Flat beam specimens of rectangular cross section with four different configurations: (3D-fully interlaced weave, 2×2 twill, noncrimp (NC) $[0, 90]_{3S}$, and noncrimp $[90, 0]_{3S}$) were tested at room temperature. They concluded that the '*3D woven material had better out-of-plane, but worse in-plane properties than the traditional 2D laminates*. The 3D and twill specimens were found to have lower in-plane stiffnesses and compressive strengths than NC ones. Young's moduli for all the specimens were evaluated between 0.2 and 0.3% strains. The compressive failure mode of all

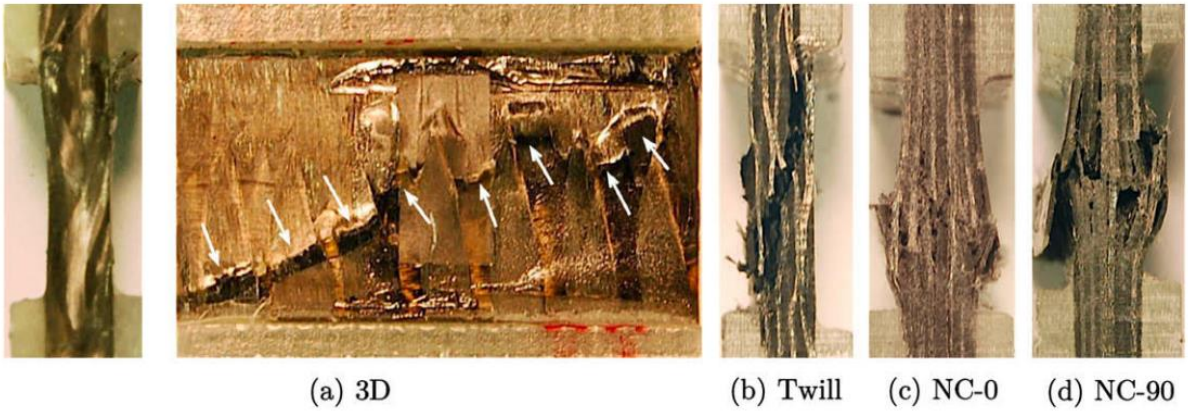

Figure 21: Failure modes in compression. (a) The warp yarns in the 3D specimens fail locally at an angle, see the right hand image, (b) fiber failure in the Twill and (c) + (d) brooming fiber failure of the two non-crimp laminates. [Fredrik et al., (2009)]

material types can be seen in Figure 21. It was reported that, the failure in the 3D specimens occurs at an angle with respect to the 2-axis and the failure pattern is believed to be related to in-plane crimp, the Twill failure mode was through-thickness fiber failure and NC specimens all showed a brooming failure mode. The compressive tests was performed according to standards of ASTM D3410.

Warren et al., (2015a) performed experimental study of composites reinforced with three dimensional woven preforms subjected to tensile, compressive and in-plane shear loading. Three innovative three-dimensional woven architectures were examined that utilize large 12 K and 24 K IM7 carbon tows, including two ply to ply angle interlock architectures and one orthogonal architecture. The combined loading compression (CLC) fixture was used to evaluate materials in compression in accordance with ASTM D6641. Experiments were conducted in displacement control.

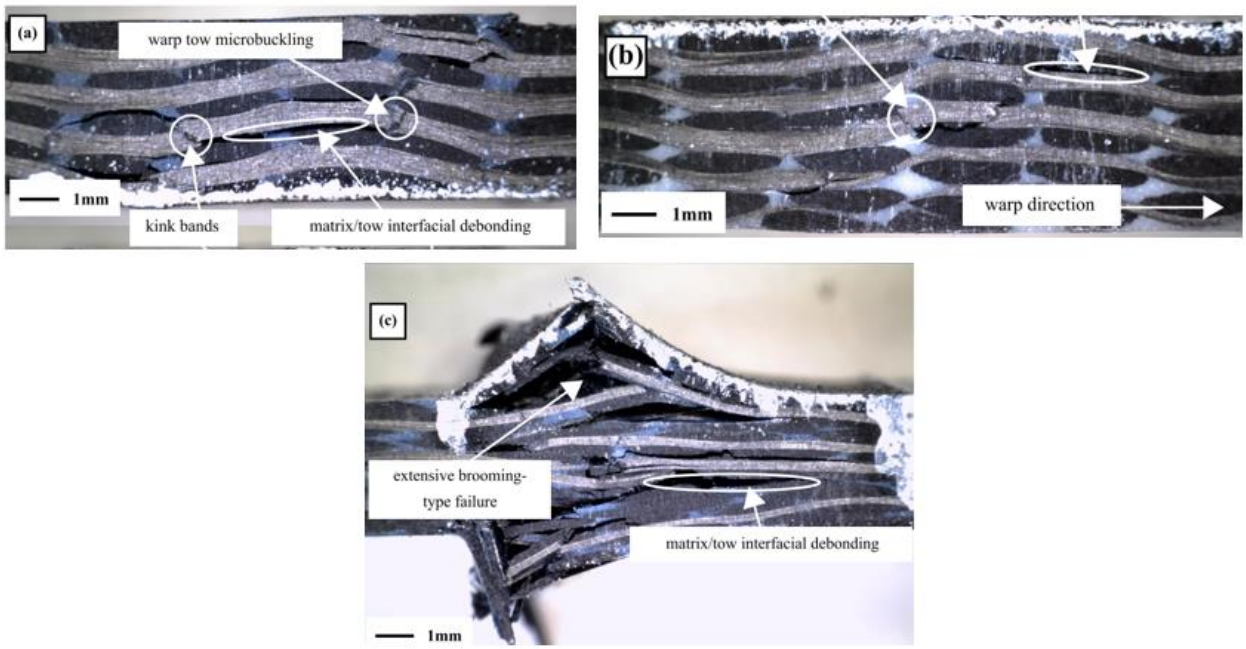

Figure 22: longitudinal compressive failure for (a) ply to ply 12 K/24 K, (b) ply to ply 24 K/24 K and (c) quasi-isotropic 2D woven fiber architectures. [Warren et al., (2015)]

Compressive failure modes were found to be largely a concurrent *debonding between the matrix and the surrounding tows coupled with tow/yarn microbuckling* and *isolated kink band formation* for both the 3D ply to ply architectures (see Figure 22). Failure modes and fracture paths found in samples loaded in the weft direction were similar to those found in warp direction loading. They also reported that, 3D orthogonal woven architecture experienced a similar response and failure mechanism to the two 3D woven ply to ply architectures. Finally, they concluded that, ***'****Kink band formation'* as a primary compressive failure mode, comparing their results with works of Kuo et al., (2000) and Cox et al., (1994).

Turner et al., (2016), performed experimental and numerical investigation to characterize the collapse of *3D orthogonal woven carbon fiber composites* under the load cases of: in-plane tension, in-plane compression and out-of-plane bending.

Two different fiber architectures (see Figure 23). varying only by the density of through-thickness reinforcement, were investigated, i.e., 3D orthogonal woven carbon fiber reinforcements with two through-the-thickness (TTT) binder densities was used. The in-plane compression experimental procedure was performed according to methodology of ASTM D3140/B. *The compression test showed elastic–brittle fracture both in the warp and weft directions* (as observed in SEM). Fracture occurred at the location of the TTT-reinforcement of samples orientated along the y-direction (weft). No significant delamination, and no buckling of plies was recorded during these tests, according to them. However, more details on different compressive failure modes were not reported in detail in their research article.

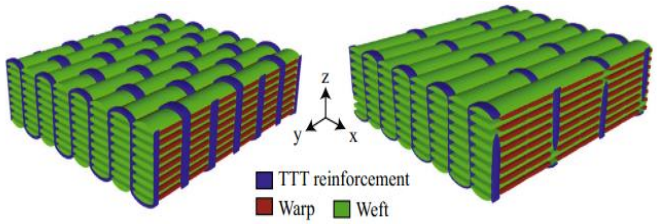

Figure 23: 3D orthogonal woven carbon composites: Full TTT reinforcement (left) and Half TTT reinforcement (right). [Turner et al. (2016)]

3.5 Models for compression of composite materials – Theoretical Background

3.5.1 Microbuckling models for unidirectional composite

3.5.1.1 *Local models*

As compressive failure in unidirectional composites is normally catastrophic, with little apparent damage before failure, it is difficult to determine from post-mortem examinations the precise sequence of events leading to failure. Hence models of microbuckle initiation have a valuable role to play. Over the years, starting from 60's, significant work has been done by many researchers to calculate longitudinal compressive strength of UD composites triggered by different failure mechanism. The first model of microbuckling was developed by Rosen (Rosen, 1964). In his opinion, elastic microbuckling is due to the appearance of local instability process: *'fiber microbuckling'*. The composite was schematized as a superimposition of hard and soft layers representing the fibers and the matrix. Under a compressive load parallel to the direction of the layers, two modes of instability may occur: i) in-phase mode/Shear mode ii) out-of-phase / Extension mode (see Figure 24). Extension mode microbuckling typically occurs in composites, which have very low fiber volume fraction. In such unidirectional composites, the distance between two adjacent fibers are fairly large. Shear mode microbuckling typically occurs in composites, which have very moderate or high fiber volume fraction. In such UD composites, the distance between two adjacent fibers are small, and thus transverse deformation of one fiber has a significant influence on that of the adjacent fiber. Rosen equations for two possible modes of fiber microbuckling within the composites:

$$\sigma_c = \frac{G_m}{1-f} \qquad \text{(Shear mode)} \qquad (3\text{-}1)$$

$$\sigma_c = 2f\left(\frac{fE_mE_f}{3(1-f)}\right)^{1/2} \qquad \text{(Extension mode)} \qquad (3\text{-}2)$$

Where,
σ_c = compressive stress at failure;
G_m= matrix shear modulus ;
f = fiber volume fraction;
E_m= matrix Young's modulus ;
E_f= fiber Young's modulus.

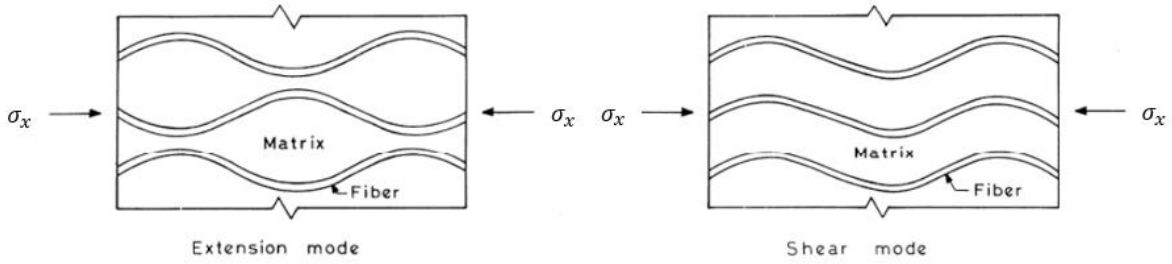

Figure 24: Microbuckling modes. [Rosen, 1964]

But, the major drawback of Rosen's model equations (Eq. 3-1 and Eq. 3-2) is that, the compressive strength predictions obtained was higher than one from measured experimental values. This is clearly due to the negligence of *'fiber initial misalignment/undulation'* and the *'matrix non-linear behavior'*. After Rosen, many authors have tried to take into account initial fiber misalignments, matrix physical non-linearity and/ or damage at the interface. Argon (Argon, 1972), observing that practical fiber composites have regions of fiber misalignment angle, considered kinking of an infinite band of inextensible fibers with a small initial fiber misalignment angle,$\bar{\emptyset}$. For the case where the normal to the band is inclined at an angle, $\beta = 0$ to the principal fiber direction, simple expression for the compressive strength, σ_c of unnotched material is derived by Argon as:

$$\sigma_c = \frac{\tau_y}{\bar{\emptyset}} \qquad (3\text{-}3)$$

Where, τ_y is the shear yield stress of the rigid, ideally plastic composite. This infinite band model has been later extended by Budiansky and Fleck (Budiansky and Fleck, 1983, 1993) for the case of elastic-perfectly plastic, who presented a failure criterion, which includes the effects of both the fiber initial misalignment and matrix plasticity. Matrix plasticity is of Ramberg-Osgood strain-hardening type. They derived the compressive strength as:

$$\sigma_c = \frac{G}{1+n\cdot\left(\frac{3}{7}\right)^{\frac{1}{n}}\cdot\left(\frac{\frac{\bar{\emptyset}}{\gamma_y^C}}{n-1}\right)^{\frac{n-1}{n}}} \qquad (3\text{-}4)$$

Where,
G = composite longitudinal shear modulus;
γ_y= composite shear yield strain;
$\bar{\emptyset}$ = initial inclination of the kink band;
n = strain hardening exponent (Ramberg-Osgood type constitutive law).

Later to improve upon this, Fleck et al., (1995) proposed an infinite band analysis, including *fiber bending*, to estimate the compressive strength of fiber composites. They assumed that the fiber behaves as linear elastic beams embedded within a non-linear dilatant matrix. The bending stiffness of individual fibers was homogenized by treating the composite as a Cosserat continuum capable of bearing couple stresses; the fiber diameter, d acts as the pertinent length scale. Their results showed that inclusion of fiber bending increases the predicted compressive strength above kinking theory when the band width is less than about $30d$. And also, since the stress tensor is unsymmetrical (in case of Cosserat Couple stress theory), thereby making implementation of model into commercial FE codes very challenging. Hence model is not very feasible.

Later in 2004, Fleck et al., (2004), removed the restriction of this assumption of fiber distribution as infinite band and argued that, in reality, the composites possess random waviness, and there is a need to determine the relationship between the distribution of compressive strength and the underlying statistical distribution of fiber waviness (2D), and hence they investigated compressive strength of composites containing 2D random distribution of fibers, using theoretical and FE model of Fleck et al., (1995) ,where the characterization of fiber misalignment angle is done by using a '*power spectral density function'* and prediction of statistical distribution of compressive strengths is found using Monte Carlo Method. Their approach provided the sensitivity analysis of statistics of macroscopic strength to micromechanical details. Meanwhile, Sun and Jun (Sun and Jun, 1994), also investigated this microbuckling phenomenon and presented a model, similar to Rosen, including effects of initial fiber misalignment and non-linearity in matrix (matrix elastic shear model is replaced by elastic-plastic shear modulus), also studied effect of temperature and made a conclusion that fiber misalignments or matrix plasticity alone cannot alter the elastic microbuckling strength. In the year 1996, Hsiao and Daniel (Hsiao and Daniel, 1996), developed analytical models using lamination theory and Tsai Wu failure criteria for predicting compressive strength of composites for different type of waviness: uniform, graded and localized. They concluded with results that, compressive strength decreases as fiber waviness increases and also material anisotropy too has influence in decrease in stiffness and strength along with fiber waviness in carbon/epoxy unidirectional composites. Pimenta et al., (2009) derived a closed form expression for the longitudinal compressive strength and predict the post failure response of UD lamina. The model is built using the approach of Hahn and Williams, (1984) (model based on equilibrium of an initially misaligned fiber in a matrix with a nonlinear shear response). An initial fiber misalignment was given by $y_0(x) = \overline{y_0} \cdot (1 - \cos\left(\frac{\pi x}{L}\right))$is assumed where the fiber axis is along the x direction and the parameters $\overline{y_0}$ and L define initial imperfection. The expression for compressive strength is given by:

$$\sigma_c = \tau_Y \frac{G_{2D}^m\, d + \frac{\pi^2}{L^2} E_1^f I_x^f}{\tau_Y + \pi \frac{\bar{y}_0}{L} G_{2D}^m} \qquad (3\text{-}5)$$

Where superscript (f) indicates quantities associated with fibers and $G_{2D}^m = G_m/\left(1 - V_{2D}^f\right)$ with $V_{2D}^f = d/(d + t^m)$ where t^m is the thickness of matrix in 2D approximation and d is the diameter of fiber. The results with this model was consistent against Fleck et al., [F9].

Even though, the correlation between the predictions given by above discussed models and some experimental failure stresses is good, these models are local and cannot take into account the

'structural effect', that is established during experiments (as discussed in earlier sections), in particular it is not possible to estimate the microbuckling wavelength. For this reason, the microbuckling approach must be carried out at the scale of the ply thickness, also referred to as the mesoscopic scale.

3.5.1.2 *Models at the mesoscopic scale*

Different models (Schaeffers, 1976, Swanson, 1992 and Grandidier et al., 1992), express the critical compressive stress and the wavelength in the direction of fibers as explicit functions of the boundary conditions imposed at the mesoscopic scale, but in these studies the shape of the mode through ply thickness is given a priori. This restriction has been removed by Drapier et al., (1996), who clearly established the influence of the ply thickness, the stacking sequence and the loading on elastic microbuckling. They developed a 2D heterogenous numerical model, where they discretized complete 2D microstructure of the laminate. However, they calculated exactly the elastic microbuckling modes, which is influenced by structural effects, the limitations were that the increase of degrees of freedom, which resulted in increase in computational time. And also, their numerical model does not take into account fiber initial defects and matrix plasticity and is limited to just elastic instability/microbuckling. In the study conducted by Kyriakides et al., (1995), the entire microstructure is also discretized, consisting of a 2D representation with a layered composite of alternating imperfect isotropic elastic fibers and J2 flow theory elasto-plastic matrix. The domain of each problem is discretized with FE using ABAQUS® with eight noded biquadratic elements. The layers followed a sinusoidal curve representing the initial fiber misalignment (ϕ_0). Microsections of finite width with imperfections of various spatial distributions were analysed. Even though, they could predict well the sequence of events leading to the formation of kink bands and realistic values for kink band angle (β), determined by fiber failure, the computation times required to solve these non-linear problems are very large because of the high number of degrees of freedom.

In order to remove these limitations, later Drapier et al., (1999), proposed a 2D *'Homogenized model (HOM)'*, which takes into account fiber initial alignment defects, matrix plasticity and structural parameters. Microstructural behavior is represented through homogenous continuum medium, in which bending stiffness of fibers are distributed. The homogenized numerical model/formulation of the plastic microbuckling problem, built at mesoscopic scale with the help of works of Grandidier et al., (1992) in the form of variational formulation using (PVW) is given as:

$$-\int_{\Omega}\Big\{\underbrace{fE_f r_{gf}^2 v''\delta v''}_{\text{I}}+\underbrace{\mathbf{S}\cdot\delta\boldsymbol{\gamma}}_{\text{II}}\Big\}d\Omega+\underbrace{\langle\mathbf{F},\delta\mathbf{u}\rangle}_{\text{III}}=0\quad\forall\delta\mathbf{u}, \tag{3-6}$$

Where,

f = fiber volume fraction;

E_f = fiber Young's modulus;

$r_{gf}=\sqrt{\frac{I}{S_f}}$ = fiber gyration radius;

$I=\pi\cdot\frac{\left(\frac{d_f}{2}\right)^4}{4}$

$$\gamma(\mathbf{u})=\varepsilon(\mathbf{u})+\gamma(\mathbf{u})^{NL}=\begin{pmatrix}\frac{\partial u}{\partial x_1} & \frac{1}{2}\left(\frac{\partial u}{\partial x_2}+\frac{\partial v}{\partial x_1}\right)\\ \frac{1}{2}\left(\frac{\partial u}{\partial x_2}+\frac{\partial v}{\partial x_1}\right) & \frac{\partial v}{\partial x_2}\end{pmatrix}+\begin{pmatrix}\frac{1}{2}\left(\frac{\partial v}{\partial x_1}\right)^2+\frac{\partial v}{\partial x_1}\frac{\partial v_0}{\partial x_1} & 0\\ 0 & 0\end{pmatrix}$$

Geometrical non-linearities + fiber initial undulation

$S_f = \pi \cdot \frac{{d_f}^2}{4}$
v'' = fiber curvature field;
$\boldsymbol{S}$ = Second Piola Kirchoff stress tensor;
$\boldsymbol{\gamma}$ = Green Lagrange strain tensor;
$v_0(x_1)$ = fiber initial position;
$\boldsymbol{F}$ = External loading.

In the equation (Eq. 3-6), I term represents work done by the internal fiber bending effort, II term corresponds to the work developed by internal in-plane efforts and III term represents the work of external efforts. Fiber misalignment is represented by function, $v_0(x_1)$, defining the initial position of fibers. The constitutive law: $\boldsymbol{S}(\gamma) = \boldsymbol{D}(\boldsymbol{\gamma}) \cdot \boldsymbol{\gamma}$ is of anisotropic type, the secant modulus tensor, $\boldsymbol{D}$ being obtained from explicit homogenization formulas based upon the constituent's behavior (Gardin and Potier-Ferry, 1992). Plasticity is defined at the microscopic scale to describe the anisotropy induced by fiber microbuckling. Matrix is considered non-linear and follows an isotropic J2 deformation type. Ritz basis functions are selected for displacement approximation to obtain the microbuckling elastic modes, similar to one from Draper et al., (1996). However, even though, the model was successful in predicting the elastic microbuckling modes, w.r.t complete heterogenous model of Draper et al., (1996), the model is 2D and assumes microbuckling is periodic in fiber direction (just one gradient in thickness direction). Consequently, not possible to compare test results obtained with real structures. And also, prediction of both the 'distribution' and 'amplitudes' of 'fiber initial imperfection' is still not well known, which was confirmed later by Drapier et al., (2001), where they compared the predictions obtained by this HOM model with experimental and theoretical results from the literatures, and also investigated and refined the understanding of plastic microbuckling.

3.5.1.3 *Various additional approaches over the years at different scales*

Basu et al., (2006) proposed a mechanism based lamina level modeling approach, based on Schapery Theory(ST) (Schapery, 1995) to study fiber kinking by validating against micromechanical model (Basu, 2005) for UD laminate in the state of plane stress loaded under compression. The model uses the non-linear stress-strain relations for the lamina in shear and in transverse tension/compression input, with readily available lamina level inputs measured. The energy associated with damage (matrix microcracks) is included in the constitutive relation as *Internal State Variable (ISV).* The model is implemented in User material subroutine, UMAT subroutine for simulation in ABAQUS® using CPS8 element with different mesh size. Fiber is assumed linear isotropic elastic and matrix modeled as J2 elasto-plastic material with a Mises yield criterion and isotropic hardening. Non-linear geometrical effects are included in the response analysis through the RIKS option available in ABAQUS®. Fiber initial misalignment is also taken into account. The study was performed with different mesh sizes, fiber inclination angles and also with different load levels in comparison with micromechanical model (Basu, 2005). Even though the model is validated with respect to the reference model with less computational cost and parameters to capture kink band, it is limited to just UD laminate, it cannot be used to asses complex mirco/mesostructures.

Nezamabedi, Poitier-Ferry et al., (2015) modelled compressive failure of long fiber composites by considering *Multiscale Finite Element approach*, also called *computational homogenization*

approach, where it involves double scale analysis, by coupling instabilities at microscopic level(RVE) with macroscopic structural analysis. With this model, plastic microbuckling phenomenon is analyzed. *'Loss of ellipticity'* is considered as failure criterion at the macroscale and Kink band model of Budiansky and Fleck (Budiansky and Fleck, 1993) is considered at microscale to analyze the evolution of microbuckling and kink bands clearly. Fiber is considered as isotropic and Ramberg-Osgood relation was used to account for matrix plasticity. Linear material behavior and nonlinear deformation theory of plasticity in finite strain framework is assumed. The solutions of nonlinear multiscale problem were sought using *'Asymptotic Numerical Method (ANM)'*, where ANM is a path following technique where each step is represented by Taylor series with respect to path parameter. The FE analysis is performed in plane stress framework, at the two scales. The macrostructures were meshed with 8-noded quadrangular elements and microstructures were meshed with 9-noded quadrangular elements, and solved using 3X3 gauss integration scheme with periodic boundary condition. The weak point of this approach is that, the instability wavelength is prescribed using the choice of width of unit cell. Also, even though the predictions obtained by combining multiscale FE and loss of ellipticity was in good agreement with the predictions obtained by shear band analysis, the approach leads to high computational cost and is only limited to 2D models.

A 2D micro-mechanical Finite Element (FE) model was proposed by Sun et al., (2017), to analyze the compressive failure of UD composite, where the initial imperfection of the fiber ($y_0 = \delta\, cos\frac{\pi x}{\lambda}$; $\delta = 2d - amplitude\ and\ \lambda - wavelength$) , Weibull distribution of the fiber strength, the matrix plasticity (Ramberg Osgood + linear Drucker-Prager criterion) and ductile damage (to simulate matrix plastic damage and failure) were taken into account. Equivalent elastic properties of UD composite are obtained by using back stepping method, based on the analysis of Representative Volume Element (RVE) model of UD composite with fiber volume fraction of 0.6 and hexagonal distribution, where fiber was meshed with C3D8R and matrix is meshed with C3D6 element with periodic boundary conditions based on control points. Later, 2D micromechanical model was built with T300 carbon fiber and epoxy 914 matrix, using 2D element type CSPS4R for analysis, with fiber diameter, $d = 7\mu m$ and length of FE model, $l = \lambda$. Large deformation and strong nonlinear behavior of UD composite under compressive was considered and solved using ABAQUS/Explicit solver. The predicted numerical results with their model were good agreement with the experimental, and they concluded that fiber initial imperfection and matrix plasticity, instead of fiber failure are the two main factors to affect the compressive strength. However, the model is restricted to 2D and cannot be used to simulate complex 3D structures and also bending stiffness of fibers is clearly not well established.

Naya et al., (2017) proposed a coupled experimental-computational micromechanics approach (framework based on RVE) to determine the longitudinal compression properties of UD CFRP plies (AS4/8852) under different environmental conditions. 3D micromechanical numerical model includes a coupled plasticity-damage model for matrix and a cohesive-frictional behavior for the fiber/matrix interface. The microstructure of 3D RVE of a UD composite was idealized as a random dispersion of parallel and circular fibers in the matrix. C3D8 element was used to model fiber and matrix for simulation in ABAQUS ® within the framework of finite deformations. Carbon fibers were assumed to be linear elastic and transversely isotropic solid and matrix as linear isotropic elastic solid. The fiber initial imperfection is also taken into account by using a sinusoidal shaped fiber and allowing the prediction of sensitivity function. The debonding between fibers and

matrix was modeled by means of classical cohesive zone method coupled with frictional behavior. The input constitutive properties measured by tensile test are used for the simulation with different environmental conditions (dry/wet). It was found out that with different fiber misalignment angles, there was no significant effect on the longitudinal compression strength which was clearly due to usage of fiber properties measured under tensile loads. Even though the model predicted well the ply behavior with respect to the chosen reference, it leads to a high computational cost. Moreover, fiber distribution, cohesive frictional fiber/matrix interface properties have not been yet investigated properly. The model is just limited to UD plies.

Two microbuckling criteria for UD composites (micromechanical models) was proposed by Brieman et al., (2017). First one is the modified failure criteria of Lo and Chim, (1992), which is based on compressive strength formulation using buckling of Timoshenko's beam and the second one is the modified criteria of Aboudi and Gilta, (2006), which is based on buckling-wave propagation analogy using the solution of an eigenvalue problem. The modified criterions are obtained by a fitting approach for wide range of volume fractions and applied to four classes of UD composites. The major limitations of these proposed models are that: they are local and cannot take into account the structural effects and limited to elastic. And also, it is difficult to fit one set of universal parameters value for all groups of composites used.

Bishara M et al., (2017) See B[18][19] proposed a "*hybrid micro meso modeling*" strategy in context of 3D finite element analysis to investigate the progressive failure of multidirectional laminates under compressive loading. Two sets of laminated composites are studied: i) 5 plies with $90^0/0^0/90^0/0^0/90^0$ distribution and ii) 16 plies with $45^0/90^0/-45^0/0^0$ …$/45^0$ distribution. Micro model is used to resolve the regions which are prone to fiber kinking. It is applied only to just 0^0 plies in order reduce the numerical cost. Isotropic elasto-plastic constitutive law [Ernst et al., (2010)] is used for the matrix and an orthotropic elasticity model with linear damage [Hashin, (1980) and Puck and Schrmann, (1998)] is used for fibers. In all other regions, UD plies ($45^0/90^0$) are considered as a homogenized continuum using a transversely isotropic elastic-plastic constitutive model [Vogler et al., (2013)] for each ply in order to predict the nonlinear behavior and cracks in 45^0 *and* 90^0 plies. An explicit 3D finite element analysis is performed in ABAQUS ® using C3D8 element. Material models were used via user material subroutine, VUMAT in ABAQUS/Explicit. Mechanical properties of fiber and epoxy matrix are taken from Kaddour et al., (2013). Fiber misalignments are added only in 0^0 plies using a python subroutine. The fiber path is created by a spline curve running through a sequence of points which are located on a sinusoidal function. In the region where micro model is used, matrix yielding, damage initiation, fiber bending and breakage and development of kink bands has been investigated, and in the region where meso-meso and micro-meso model is used, matrix cracks and delamination has been investigated. The results indicated that the ultimate failure occurs by i*nteractions between matrix yielding*, *splitting*, *fiber kinking*, *delamination* and *matrix cracking*. All the numerical results, including predicted compressive strength are validated against the experimental results of Pinho et al., (2006) for multidirectional laminate with 5 plies and Lee and Soutis, (2007) for multidirectional laminate with 16 plies.

Even though the model is capable to study and analyze the complex compressive failure behavior of CFRP composites, it neglects the effect of local fiber bending stiffness, which is also one of the key parameters for predicting good compressive strength and microbuckling/local instability

phenomenon. And also, it seems that this modeling strategy is efficient for just UD composites and is computational expensive for complex micro/meso structures (woven composites).

3.5.2 Modelling of woven composite in compression

Modelling of woven fabric/textile composites is challenging, as the mechanical properties of such composites depends upon various factors such as *fiber orientation*, *fiber architecture*, *fiber bundles*, *fiber volume fraction*, *yarn stacking sequence*, *yarn spacing* and *yarn size* (Dixit et.al., 2013). Several methods are employed by many researchers for the analysis and mechanical modeling of woven/textile structure. The mechanical modeling of such structures can be briefly classified as "*analytical"* and "*computational"* approaches, each having its own merits and demerits. The other important classification of the modeling aspects, which is based on the scale of models, is "*micromechanical"*, "*mesomechanical"*, and "*macromechanical"* modeling. The micromechanical modeling scale involves the study of orientation and mechanical properties of the constituent fibers. The mesomechanical modeling, on the other side, follows the concept of homogenization and evaluates the mechanical properties of a fabric unit cell, which in turn is used to calculate the effective material properties of the textile composite. Finally, the macromechanical modeling deals with predicting the mechanical properties of textile fabrics under complex deformations, assuming the fabric to be a continuous medium.

Another approach (computational) is the modelling of woven composites using Numerical methods. Many numerical methods, such as *boundary element method (BEM)*, *the finite-element method (FEM*), *the finite-difference method (FDM)*, and *meshless methods*, such as the element-free Galerkin method, are available for analyzing orthotropic composite materials. Among all the methods, the FEM is most promising, as it allows to analyse non-linear systems with general boundary conditions and can be adapted to complex geometries. The general procedure to predict the mechanical properties of a textile composite using the FEM includes: (i) dividing the composite into repeating unit cells or the representative volume elements (RVE's) and calculating properties of the unit cell, followed by homogenization and (ii) predicting the mechanical properties of the entire textile structure from properties of the unit cell. Hence, the ability of a FEA model to accurately predict the mechanical properties of a textile composite depends upon the accuracy of modelling of fiber geometry in unit cell (Dixit et.al., 2013). However, even FEM has its own limitations, mainly large computational time, when analyzing complex woven structures.

The mechanical behavior (tensile/compression) of textile composite is a multi-scale problem. In the multi-scale modeling approach, the behavior on a lower level is calculated and the results extrapolated to the higher level. In fiber-based modeling techniques, the hierarchical structure as shown in Figure 25 is taken into account by a multi-scale modeling. The macroscopic behavior is very much dependent on the interactions of fibers at the *meso-scale (scale of the woven unit cell)* and at the *micro-scale (level of the fibers constituting yarns)*. The fiber-fiber interactions inside of composite structures are usually neglected as they have only sub ordinary influence in respect to the yarn-yarn interaction and would considerably raise the computation costs.

The modeling of mechanical behavior of even relatively simple plain-weave fabrics is complex due to the intricate interactions of the yarns that constitute the fabric ''mesostructure''. Despite of a great amount of work in the field, there is no widely accepted model that accurately describes all

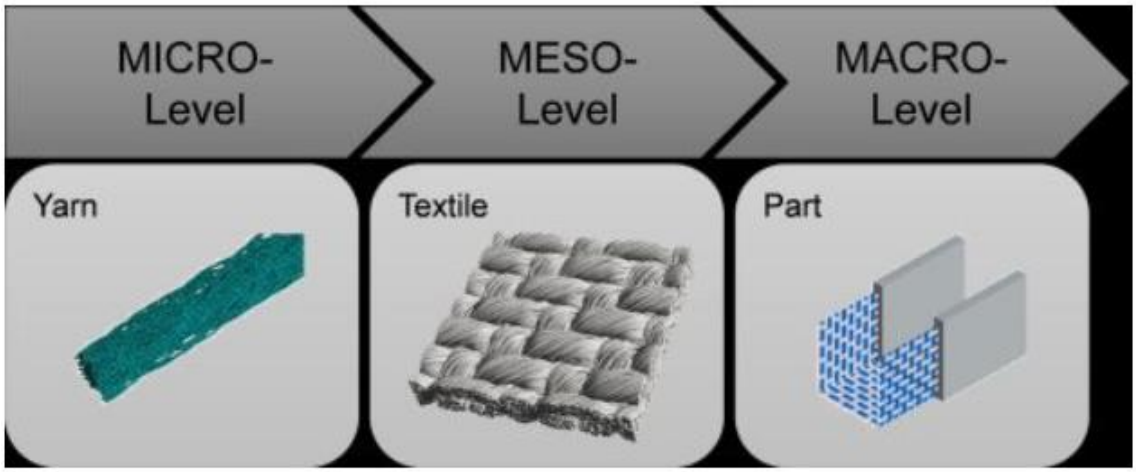

Figure 25: Hierarchical levels of woven/textile-based composites. [M6]

main aspects of fabric mechanical behavior. This is due in part to the variability of requirements for fabric models in different applications (King et al., 2005).

King et al., (2005) proposed a new approach for developing mesostructurally based continuum models for the mechanical behavior of woven fabrics in-planar deformation that can both simulate quasi-static, in-plane tensile behavior (locking, shear deformation, crimp interchange and yarn bending) of a plain weave ballistic fabric, Kevlar® S2706, manufactured by DuPoint. Kevlar® S2706 is a plain weave fabric composed of multifiber untwisted yarns. In their continuum description, yarns are not modelled explicitly, rather, the woven fabric is treated as a homogenized anisotropic material (see Figure 26(left)). Geometry was adopted similar to the one proposed by Kawabata (1973) as shown in the Figure 26(right) below, where the *yarns are represented as a network of trusses connected by pin-joints at the crossover points*.

The drawback of the model proposed by King et al., (2005) is that, it captures only in-plane tensile response of the fabric, and cannot be used to predict out-of-plane displacements or bending, transverse shear responses, or changes in fabric thickness. And also, it does not predict the failure or yarn slippage. However, the model is focused only on the in-plane tensile behavior of the woven fabric, it gives an idea about the ideas to define the geometry for the modelling the compressive behavior of the woven fabric (carbon fiber).

Similar to model developed by King et al., (2005), there are many articles in the literatures regarding modelling of tensile behavior of woven composites, out of which works of Boisse et al., (1997,2001,2006) are interesting, where they focused mainly on the Finite element simulations (meso/macro scale) of textile composite forming including the biaxial fabric(glass fiber plain weave) behavior. Four node finite element (made of ncell woven unit cells/RVE's) has been developed for simulating the woven fabric response. The yarn directions evolve as the elements deform and the yarn-direction behaviors are based on Kawabata's analytical model Kawabata (1973). The major drawback in their FE model is that they do not consider fiber (yarn) bending effects.

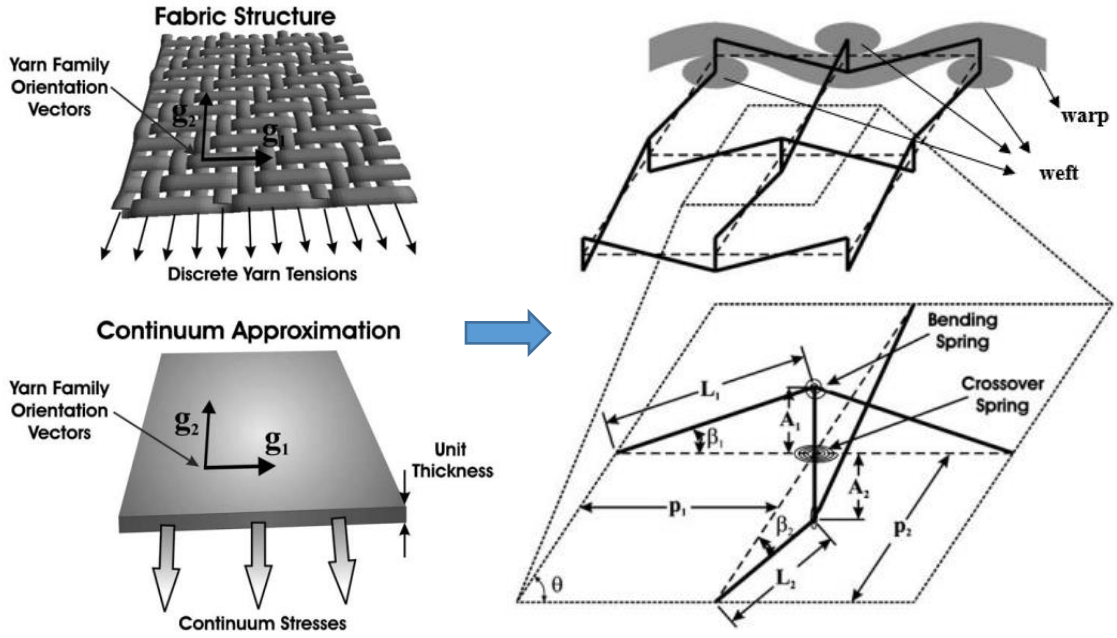

Figure 26: Approximation of woven fabric as anisotropic continuum medium (left); fabric model geometry (right) [King et al., (2005)]

For more different approaches on modelling the tensile behavior of the woven composites over the years, refer King et al., (2005). However, there are very few works related to modelling the compressive behavior of woven composites, especially predicting the failure.

3.5.3 Discussion

We have seen in this chapter, the literature review on various experimental investigations to study compressive strength/failure, numerous analytical and numerical models developed over the years by many researchers at different length scales to modelize the compressive strength of composites. It gave us a broad spectrum of different experimental and modeling approaches, its limitations and idea as to what are the important aspects to be considered in modeling this compressive behavior. However, on a global point of view it can be understood that there is no single model, which can predict well the compressive behavior of complex composite micro/mesostructures, both in UD and Woven (involving complex deformation gradients in all possible directions), or in other words there is a lack of 'generalized model'. With consideration of all these factors, the following chapter is now dedicated to the definition of '*Scope of the thesis work*', with definite information on global and local objectives.

4 Scope of work and outline

Although, many nonlocal theories and various FE approaches, based on the nonlocal theories (to assess the nonlocal phenomenon), that has been developed over the years to solve the problems at the microscopic/mesoscopic scale, each model is restricted to some limitations and only few models, that has been developed to assess the compressive strength (particularly microbuckling phenomenon/local instability) of the carbon/epoxy long fiber composite materials at the structural scale/ mesoscopic scale. For example, Drapier et al., (1999), proposed a 2D homogenized model (as discussed in chapter 3), which takes into account fiber initial alignment defects, matrix plasticity and structural parameters. The model is successful in predicting the elastic microbuckling modes, but the model is 2D and assumes microbuckling is periodic in fiber direction, just one gradient in thickness direction is taken into account. Consequently, not possible to compare test results obtained with real complex structures (for example: woven composites, structure with hole near the clamped edge). Moreover, the prediction of both the 'distribution' and 'amplitudes' of fiber initial imperfection is still not well known [D4]. Hence, it is necessary to extend the models and more specifically, the one proposed by Drapier et al., (1999), because all parameters are taken into account.

Further, there is no particular works found on the literature, which deals with nonlocal modelling of compressive behavior of UD ply and woven composites (2D and 3D) and no simulation of instabilities at scale of a real structure has been performed. Consequently, a single model should be developed to assess the compressive strength on complex structure with UD and woven composites (2D and 3D), which takes into account the effects of gradients in all possible directions. With this model, it is necessary to develop a nonlocal numerical model at the structural scale that can assess/simulate the microbuckling phenomenon of the carbon/epoxy long fiber composites, taking into account the matrix(epoxy) plasticity and bending energy of the fibers due to fiber waviness/undulations (the main causes for the compressive failure of carbon/epoxy long fiber composites).

Therefore, with the motivation of works of Grandidier, Drapier et al., (1992,1996,1999), the scope/aim of the thesis work is to *'Develop a Continuous Homogenized Non-Local Finite Element model/ tool (2D and 3D), which is capable of predicting the compressive strength of the complex composite structures'*. In more detail:

- Build a new modelisation of microbuckling, more general that of works of Drapier et al., (1996,1999);
- Take into account:
    - Non-linear behavior of resin/matrix;
    - Geometrical non-linear effects;
    - Defects in the modeling (ex: fiber initial misalignment).
- Develop the control parameters for 2D and 3D calculation;
- Extend the model to assess complex mesoscopic structures (ex: woven composites).

4.1 Work package/Outline

The work package/outline of the research work includes mainly 2 parts:

1. Development of Non-local model with structural elements of ABAQUS® for UD composites in order to evaluate the possibility to solve the microbuckling in 2D and 3D structure;
2. Development of generalized Homogenized Non-local Finite Element model/tool using User Element (UEL) subroutine of ABAQUS® to asses UD and woven composites:
    a. Formulation and Validation for linear isotropic elastic case;
    b. Formulation and Validation for non-linear geometry (isotropic elastic) case;
    c. Formulation and Validation for non-linear material and non-linear geometry case;
    d. Identification of Elastic and Non-Local parameters;
    e. Identification of Non-linear material parameters.

In particular, the Chapter 5 is associated with part-1 of thesis, where it consists the detailed information regarding development of the non-local model using ABAQUS® in-built elements, followed by validation with respect to the results of some of the past research works. Chapter 6 is devoted to some of the important theoretical backgrounds and research works developed over the years on various non-local models and its applications with respect to finite elements which permits to modelize the compressive behavior of composites with complex architectures, followed by theoretical and numerical development of generalized Homogenized Non-local Finite Element model (HOMNL), and its implementation for 2D case in User Element (UEL) subroutine of ABAQUS® to asses UD and woven composites.

Chapter 7, 8 and 9 deals with the validation of HOMNL model, implemented in 2D user element (NL U32) for the case of linear isotropic elastic, non-linear geometry + isotropic elastic and non-linear geometry and material cases respectively. The results are compared with in-built classical elements of ABAQUS®.

Chapter 10 is associated with detailed procedure or protocol to identify the elastic, non-local and non-linear material parameters with geometrical non-linearity in 2D HOMNL model respectively. Chapter 11 comprise some results of compressive response of composites with HOMNL model, followed by a closing chapter, i.e., Chapter 12, which includes conclusions and future perspectives.

5 Non-Local model for UD composites with structural elements of Abaqus®

5.1 Introduction

The numerical model proposed in this part is built in order to determine the three-dimensional field of instability generated by a compressive stress. This should have the capability to take into account more realistically all the effects mentioned before, and to analyze the phenomenon of compression at mesoscopic scale. It is inspired by the homogenous model of Gardin et al., (1992) and Drapier et al., (1996) where the non-linear formulation of the microbuckling problem can be seen as a continuum media stiffener by beams (named Beam Non-Local Model with contraction BNL). The bending energy relative to the fibers, induce the effect of non-locality. BNL model is similar to a model developed by Wisnom, (1993), which consisted a bidimensional analysis of a composite UD ply modelled through ABAQUS®. In previous studies, the option REBAR was exploited to define the uniaxial reinforcements layers as membrane, shell and surface elements in which the geometry is defined with respect to a local orientation system. However, unlike Wisnom's model, these studies did not take into account the bending stiffness. In this latest model the Bernoulli's beam B23 (2-node cubic beam in a plane) provided the axial and bending stiffness of fibers and continuum elements CPS4 (4-node bilinear plane stress quadrilateral) were used to represent the transverse and shear properties of the composite structure. The continuum elements have only in-plane degree of freedom, whereas the beams also have rotation out of plane. The properties of shear are not influenced by the beams and they are allocated only to the continuum elements. Wisnom's model is suitable for accurate modeling of shear instability even if it has some limitations. In fact, this author undertook an analysis limited in two-dimensional field and consequently he considered the waviness only in a plane. Furthermore, only a single wave was taken into account and from considerations of symmetry, it was necessary to model half the wavelength. The width modelled did not affect the results since a continuous domain was represented, consequently just one element was used along this direction, whereas, in fiber direction 17 elements were considered sufficient to achieve accurate results.
For the need of a more advanced modeling, the BNL model is developed in order to:

- take into account the bending stiffness;
- take into account the width effect (hence, not just one element along this direction);
- extend three-dimensional modelling;
- permit to evaluate the microbuckling phenomenon, not only in the microscale but also in the scale of the structure (macroscale), by using a hypothesis on boundary conditions, which allow to assess the structural effect;
- permit to evaluate the microbuckling phenomenon through the buckle protocol proposed by ABAQUS's solver (subspace iteration eigen solver);
- microbuckling is evaluated through: i) global critical strain: $\epsilon_{cr} = \frac{U_{cr}}{l_0} = \frac{\lambda^c U^{buckle} + U^{step1}}{l_0}$; where λ^c is critical eigen value, U^{buckle} is buckling load, U^{step1} is pre-load (level very close to instability), l_0 is initial length of the structure. ii) observing eigen/buckling modes.

Remark: For this part, a student in internship carried out part of the simulations and I received a strong support from my thesis director.

5.2 Beam Non-Local Model: Building the model

The BNL model is developed in ABAQUS® software without subroutine for the elastic case and USDFLD ('USerDefinedFieLD') subroutine for nonlinear behavior. It is constituted by the superimposition of:

- a continuum medium, which can be a homogenous solid (3D) or a plane stress or plane strain (2D) assumption, that has mechanical characteristics close to the matrix, that have been obtained with a specific protocol, which is described in the following sections;
- beams: one-dimensional elements in space or in plane, representing the stiffness of fibers (1D reinforcements on ABAQUS®).

5.2.1 Definition of properties

The type of beam elements both in the case of 2D and 3D are chosen carefully in order to be compatible with respect to the nodes of elements used for the continuum medium. In 2D case, a mesh is chosen with the superimposition of CPS8 (An 8-node biquadratic plane stress quadrilateral), representing the continuum medium, and B22 (A 3-node quadratic beam in a plane), standing for the beams. The edges of the CPS8 element parallel with the fiber direction are associated with the beams by binding and matching the three nodes of each type of element. While, in 3D case, the superimposition of C3D8 (An 8-node linear brick), representing the continuum medium, and B33 (A 2-node linear beam in space with cubic formulation), is chosen. In this way all the nodes are in coincidence.

In the formulation $\boldsymbol{x_1}$ denotes the fiber direction (0°), $\boldsymbol{x_2}$ the transverse direction across the thickness, $\boldsymbol{x_3}$ the transverse direction across the width, *u* the displacement on direction $\boldsymbol{x_1}$ and *v,w* the displacements on direction $\boldsymbol{x_2}$ and $\boldsymbol{x_3}$ respectively. Derivatives with respect to $\boldsymbol{x_1}$ are denoted by (.)'. Stresses are expressed with the second Piola-Kirchhoff stress tensor denoted $\overline{\overline{\boldsymbol{S}}}$. For strains, Green-Lagrange tensor is used, denoted $\overline{\overline{\boldsymbol{\epsilon}}}$, corresponding to moderate rotations in small strain hypothesis. In this formulation, the equilibrium of the medium is characterized by the principle of virtual works, where the components of the virtual displacement field $\boldsymbol{\delta u}$ are noted $\delta u, \delta v, \delta w$ and the virtual strain tensor is noted $\delta\overline{\overline{\boldsymbol{\epsilon}}}$:

$$-\int_{\Omega\to 3D}\left\{f E_f r_{gf2}^2 v''\delta v'' + f E_f r_{gf3}^2 z w''\delta w'' + \overline{\overline{\boldsymbol{S}}}:\delta\overline{\overline{\boldsymbol{\epsilon}}}\right\}d\Omega + < \boldsymbol{F}, \boldsymbol{\delta u} > = 0, \ \forall\, \delta\boldsymbol{u} \qquad (5\text{-}1)$$

In this expression:

- Ω is the volume, *f* is the volume fraction of fiber and $mf = f E_f r_{gf2}^2 v''$ is distributed micro-moment;
- the first term represents the work done by the fiber bending effort which have been distributed on the whole domain;
- the second term corresponds to the work developed by the external efforts, it is a linear form of the vector **F** standing for the whole efforts applied on the structure;
- the behavior law is assumed linear elastic, consequently $\overline{\overline{\boldsymbol{S}}} = \overline{\overline{\overline{\overline{\boldsymbol{L}}}}} \cdot \overline{\overline{\boldsymbol{\epsilon}}}$ in which $\overline{\overline{\overline{\overline{\boldsymbol{L}}}}}$ is the matrix of elastic constants;

- fibers are assumed to have linear elastic behavior and E_f is the Young modulus of fiber in fiber direction;
- $r_{gf2} = \sqrt{\frac{I2}{S_f}}$ and $r_{gf3} = \sqrt{\frac{I3}{S_f}}$ are the fiber gyration radius, with the fiber cross section defined by $S_f = \pi \cdot \frac{d_f^2}{4}$ and the moment of the second order (or inertial moments) is defined by the classical expression $I_2 = I_3 = \pi \cdot \frac{\left(\frac{d_f}{2}\right)^4}{4}$ where d_f is the diameter of fiber.

In BNL model, beams stand for the bending and the tension of the fibers in their direction, and a continuum medium represent the behavior of composite without bending and tension of fibers (matrix transverse behavior of composite and its shear). Therefore, the energy inside the beams must be equal to the energy of the fibers. For this reason, the formulation (Eq. 5-1) is again modified to the following form:

$$\begin{aligned} &-\sum_{i=1}^{n_{beam}} \int_0^{l_{beam_i}} E^{B_i} I_1^{B_i} v'' \delta v'' dl_i^B - \sum_{i=1}^{n_{beam}} \int_0^{l_{beam_i}} E^{B_i} I_2^{B_i} w'' \delta w'' dl_i^B \\ &\quad - \sum_{i=1}^{n_{beam}} \int_0^{l_{beam_i}} E^{B_i} S^{B_i} u' \delta u' dl_i^B - \int_\Omega S_{11}^{CM} \delta\epsilon_{11} d\Omega - \int_\Omega S_{22}^{CM} \delta\epsilon_{22} d\Omega \\ &\quad - \int_\Omega S_{33}^{CM} \delta\epsilon_{33} d\Omega - 2\int_\Omega S_{12}^{CM} \delta\epsilon_{12} d\Omega - 2\int_\Omega S_{13}^{CM} \delta\epsilon_{13} d\Omega - 2\int_\Omega S_{23}^{CM} \delta\epsilon_{23} d\Omega + \\ &\quad < \boldsymbol{F}, \boldsymbol{\delta u} > = 0 \end{aligned} \tag{5-2}$$

where, E^{B_i} is the Young's modulus of beam, $I_1^{B_i} et\ I_2^{B_i}$ are quadratic moments of beam, $I_1^{B_i} = I_2^{B_i}$ for a circular section. The components of stress tensor in continuum media, noted S_{ij}^{CM} are linked with strains by a constitutive law of composite material, which is assumed transverse isotropy:

$$\begin{cases} S_{11}^{CM} = L_{1111}^{CM}\epsilon_{11} + L_{1122}^{CM}\epsilon_{22} + L_{1133}^{CM}\epsilon_{33} \\ S_{22}^{CM} = L_{2211}^{CM}\epsilon_{11} + L_{2222}^{CM}\epsilon_{22} + L_{2233}^{CM}\epsilon_{33} \\ S_{33}^{CM} = L_{3311}^{CM}\epsilon_{11} + L_{3322}^{CM}\epsilon_{22} + L_{3333}^{CM}\epsilon_{33} \\ S_{12}^{CM} = L_{1212}^{CM}\epsilon_{12} \\ S_{13}^{CM} = L_{1313}^{CM}\epsilon_{13} \\ S_{23}^{CM} = L_{2323}^{CM}\epsilon_{23} \end{cases} \tag{5-3}$$

L_{ijkl}^{CM} are the elastic coefficient of continuum medium.
The first term of Eq. (5-3) correspond to fiber direction and is explored below:

$$-\int_\Omega S_{11}^{CM} \delta\epsilon_{11} d\Omega = -\int_\Omega \left(L_{1111}^{CM}\epsilon_{11}\delta\epsilon_{11} + L_{1122}^{CM}\epsilon_{22}\delta\epsilon_{11} + L_{1133}^{CM}\epsilon_{33}\delta\epsilon_{11}\right) d\Omega \tag{5-4}$$

for small displacement theory, the strain-displacement relations are given as follows:

$$\epsilon_{11} = u', \epsilon_{22} = v', \epsilon_{33} = w' \tag{5-5}$$

thus:

$$-\int_{\Omega} S_{11}^{CM} \delta\epsilon_{11} d\Omega = -\int_{\Omega} \left(L_{1111}^{CM} u' \delta u' + L_{1122}^{CM} v' \delta u' + L_{1133}^{CM} w' \delta u'\right) d\Omega \tag{5-6}$$

Now, developing the first term of Eq. (5-6) for a unidirectional composite, which is obtained with the mixture rule:

$$-\int_{\Omega} \left(L_{1111}^{CM} \epsilon_{11} \delta\epsilon_{11}\right) d\Omega = -\int_{\Omega} f L_{1111}^{f} u' \delta u' d\Omega - \int_{\Omega} (1-f) L_{1111}^{matrix} u' \delta u' d\Omega \tag{5-7}$$

From the Hooke's law and in particular from the rigidity formulation for transverse isotropic materials, with notations as defined in [G9]:

$$L_{1111}^{CM} = \frac{1 - \nu_{23}\nu_{32}}{E_2 E_3 \Delta} \quad where\ \Delta = \frac{1 - \nu_{12}\nu_{21} - \nu_{23}\nu_{32} - 2\nu_{21}\nu_{32}\nu_{12} - \nu_{31}\nu_{13}}{E_1 E_2 E_3} \tag{5-8}$$

where, E_i and ν_{ij} are the Young's modulus in different directions and Poisson's coefficient respectively.
Hence, by substituting Δ and by manipulating the equation:

$$L_{1111}^{CM} = E_1 \cdot \frac{1}{\left[1 - \frac{(\nu_{12}\nu_{21} + \nu_{31}\nu_{13} + 2\nu_{21}\nu_{32}\nu_{12})}{1 - \nu_{23}\nu_{32}}\right]} \ (noted \frac{E_1}{A}) \tag{5-9}$$

With the mixture rule, Young's modulus in fiber direction, $E_1 = fE_f + (1-f)E_m$, consequently:

$$L_{1111}^{CM} = \frac{fE_f}{A} + \frac{(1-f)E_m}{A} = fL_{1111}^{f} + (1-f)L_{1111}^{'matrix'} \tag{5-10}$$

Thus, the first term of Eq. (5-7) becomes:

$$\int_{\Omega} f L_{1111}^{f} u' \delta u' d\Omega = \int_{\Omega} \frac{fE_f}{A} u' \delta u' d\Omega \tag{5-11}$$

Turning to fibers domain Ω_f and then to the domain of a single fiber Ω_{f_i}, it easy to obtain:

$$\int_{\Omega} \frac{fE_f}{A} u' \delta u' d\Omega = \int_{\Omega_f} \frac{E_f}{A} u' \delta u' d\Omega_f = \sum_{i=1}^{n_f} \int_{\Omega_{f_i}} \frac{E_{f_i}}{A} u' \delta u' d\Omega_{f_i} \tag{5-12}$$

It is assumed that the cross section of each fibers and also the elastic modulus are constant:

$$\sum_{i=1}^{n_f}\int_{\Omega_{f_i}}\frac{E_{f_i}}{A}u'\delta u' d\Omega_{f_i} = \sum_{i=1}^{n_f}\int_0^{l_{f_i}} E_{f_i}\frac{S_{f_i}}{A}u'\delta u' dl_{f_i} = \sum_{i=1}^{n_f}\frac{E_{f_i}S_{f_i}}{A}\int_0^{l_{f_i}} u'\delta u' dl_{f_i} \quad (5\text{-}13)$$

If the axial energy of fiber is equivalent to energy of a single beam, this means that:

$$\int_0^{l_{f_i}} u'\delta u' dl_{f_i} \sim \int_0^{l_{beam_i}} u'\delta u' dl_{beam_i} \quad (5\text{-}14)$$

By applying this approximation to the formulation and by taking into account that the modulus of beam is identical to fibers, one can also use $E^{B_i} = E_{f_i}$ and consequently:

$$\sum_{i=1}^{n_f}\frac{E_{f_i}S_{f_i}}{A}\int_0^{l_{f_i}} u'\delta u' dl_{f_i} = \sum_{i=1}^{n_{beam}} E^{B_i}S^{B_i}\int_0^{l_{beam_i}} u'\delta u' dl_{beam_i} \quad (5\text{-}15)$$

Which permits to define the section of beam:

$$\frac{n_{fibers}S_{f_i}}{A}E_{f_i} = n_{beam}E^{B_i}S^{B_i} \;\; and \;\; S^{B_i} = \frac{n_{fibers}}{n_{beams}}\cdot\frac{S_{f_i}}{A} \quad (5\text{-}16)$$

This equality makes it possible to derive the section of the single beam such that the energy condition of BNL model is respected.

In 3D case the volume of a single fiber is defined as follows:

$$V_{f_i} = S_f l_f = \frac{\pi d_f^2}{4}h \quad (5\text{-}17)$$

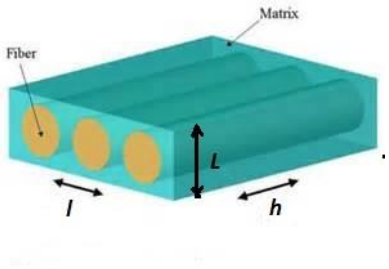

Knowing that the volume fraction $f = \frac{V_f}{V}$ and the total volume of the composite defined as: $V = h \cdot l \cdot L$, the number of fibers inside the composite is:

$$n_f = \frac{flL}{\frac{\pi d_f^2}{4}} \quad (5\text{-}18)$$

Consequently, the section of the beam can be calculated.

$$\sum_{i=1}^{n_{beam}} \int_0^{l_{beam_i}} E^{B_i} I_1^{B_i} v'' \delta v'' dl_i^B + \sum_{i=1}^{n_{beam}} \int_0^{l_{beam_i}} E^{B_i} I_2^{B_i} w'' \delta w'' dl_i^B = \int_{\Omega \to 3D} \{ f E_f r_{gf2}^2 v'' \delta v'' + f E_f r_{gf3}^2 w'' \delta w'' \} d\Omega$$

$$\sum_{i=1}^{n_{beam}} \int_0^{l_{beam_i}} E^{B_i} I_1^{B_i} v'' \delta v'' dl_i^B - \sum_{i=1}^{n_{beam}} \int_0^{l_{beam_i}} E^{B_i} I_2^{B_i} w'' \delta w'' dl_i^B = \int_l \int_{\Omega - 1} \{ f E_f r_{gf2}^2 v'' \delta v'' + f E_f r_{gf3}^2 w'' \delta w'' \} d\Omega^{-1} dl \quad \textit{(5-19)}$$

If it is considered equality of bending stiffness:

$$\sum_{i=1}^{n_{beam}} E^{B_i} I_1^{B_i} = \int_{\Omega - 1} \{ f E_f r_{gf2}^2 \} d\Omega^{-1} \quad and \quad \sum_{i=1}^{n_{beam}} E^{B_i} I_2^{B_i} = \int_{\Omega - 1} \{ f E_f r_{gf3}^2 \} d\Omega^{-1} \quad \textit{(5-20)}$$

The inertia is thus determined. With both section and inertia, the profile of the beams is defined in section module of ABAQUS ®. In 3D case, it appears necessary to use a pipe section in order to obtain an equivalence between beam and fibers.

In 2D case this expression is simplified, therefore it is just necessary to calculate the thickness, w_{beam_i} and width of a single beam l_{beam_i}, case where the beam section is set $S^{B_i} = l_{beam_i} \cdot w_{beam_i}$ and the fiber section is set $S_{f_i} = d_{f_i} \cdot 1$ and from Eq. (5-16), the beam thickness is achieved:

$$w_{beam_i} l_{beam_i} = \frac{n_f d_{f_i}}{n_{beams} A} \quad \textit{(5-21)}$$

As the volume of the whole model V and the volume of all fibers V_f are respectively:

$$V = l_z \cdot 1 \cdot l; \quad V_f = 1 \cdot d_f \cdot n_f \cdot l_z \quad \textit{(5-22)}$$

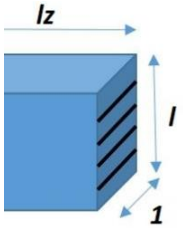

The volume fraction ensuing is: $= \frac{V_f}{V} = \frac{d_f n_f}{l}$. Finally, by reversing this last equation, the number of fibers inside ply with thickness, l is defined by:

$$n_f = \frac{l \cdot f}{d_f} \quad \textit{(5-23)}$$

As previous, the equality on bending stiffness permits to determine section of beam in 2D case:

$$\sum_{i=1}^{n_{beam}} E^{B_i} I_1^{B_i} = \int_{\Omega-1} \{f E_f r_{gf2}^2\} d\Omega^{-1} \qquad (5\text{-}24)$$

5.2.2 2D Validation of stiffness in elastic

To validate, the properties of 2D continuum media in this non-local model is identified through a comparison with a heterogenous media, which consist of stack of layers of matrix and fibers. The mechanical characteristics of the unidirectional T300/914 ply of Drapier et al., [D1] are chosen.

Table 1: Properties of heterogenous media for validation

Isotropic matrix	***Isotropic fiber***	***Geometry***
E_m= 4.5 *GPa*	E_f =240 *GPa*	*Volume fraction,* f = 0.625
G_m= 1.6 *GPa*	G_f= 92 *GPa*	*Diameter of fiber,* d_f =10 *µm*
v_m= 0.4	v_f= 0.3	*Ply thickness,* h = 400 *µm*
		Length of ply, l = 1600*µm*

Anisotropy properties of non-local homogenous medium can be defined through the classical mixture rules in unidirectional composite, the terms of stiffness matrix properties are:

Table 2: Properties of non-local homogenous media for validation

L_{1111} *(MPa)*	L_{1122} *(MPa)*	L_{2222} *(MPa)*	L_{1133} *(MPa)*	L_{2233} *(MPa)*	L_{3333} *(MPa)*	L_{1212} *(MPa)*	L_{1313} *(MPa)*	L_{2323} *(MPa)*
2008.9	2142.9	14285.7	2142.9	5831.2	14285.7	4266.7	4266.7	4382.1
E_{beam} *(GPa)*	v_{beam}	*Thickness Beam (mm)*	*Width Beam (mm)*					
240	0.3	0.397	0.01					

Three loads are investigated on a square structure:

- compression in fiber direction and transverse shear;
- traction in transverse fiber direction and transverse shear;
- shear.

The comparison of response between both models are presented in figures following. The curves link the global force with global displacement (referent point). It appears that the stiffness is very close under these specific loads, thereby validating BNL model for elastic case.

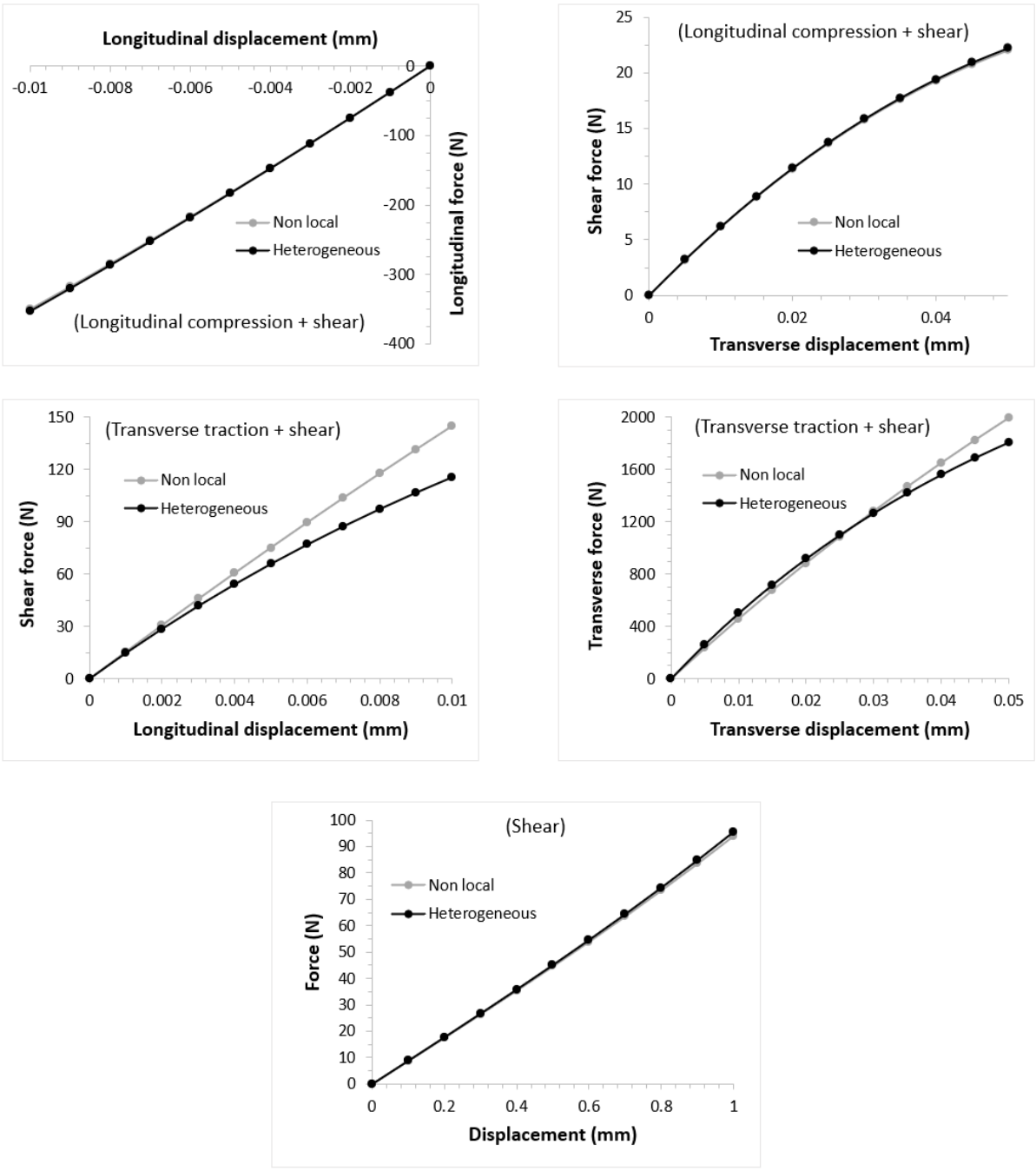

Figure 27: Comparison of global stiffness calculated with heterogenous model and non-local BNL model

5.2.3 Effect of number of beams

The '*number of beams'* is one of the important parameters of this numerical model. The distribution of energy is better when the number of beams is increased. A convergence study has

been performed in 2D (1500µm x 400µm) and 3D (1500µm x 100µm x 400µm) on one unidirectional ply. This test is performed under compression with transverse faces (top and bottom) are considered clamped and load is applied on the right edge/face (clamped-clamped condition).

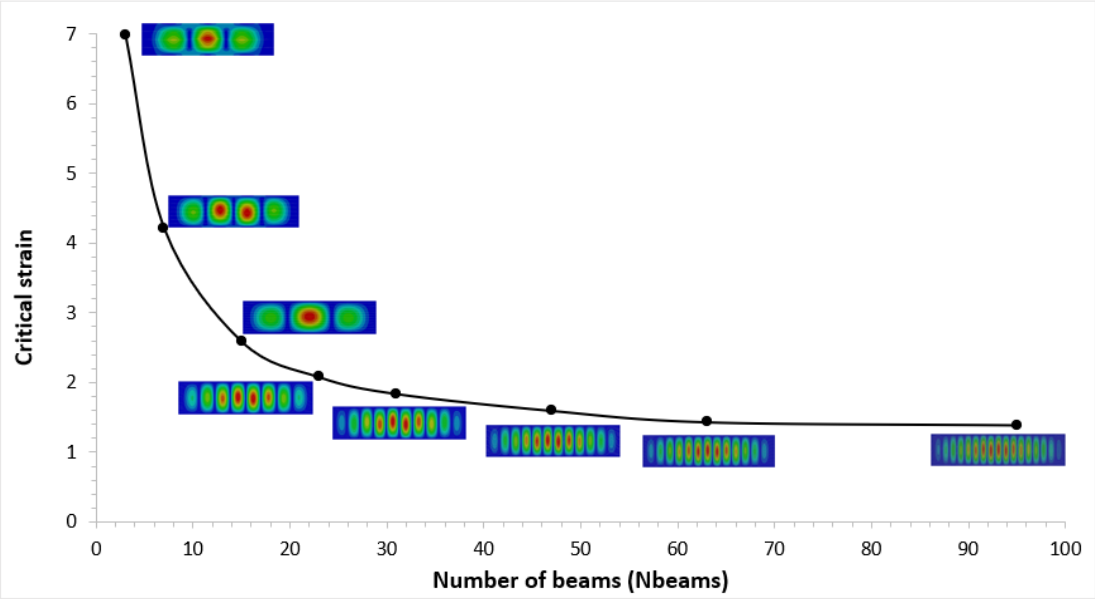

Figure 28: Influence of number of beams in 2D case (extract to internship of Roberta Maziotta)

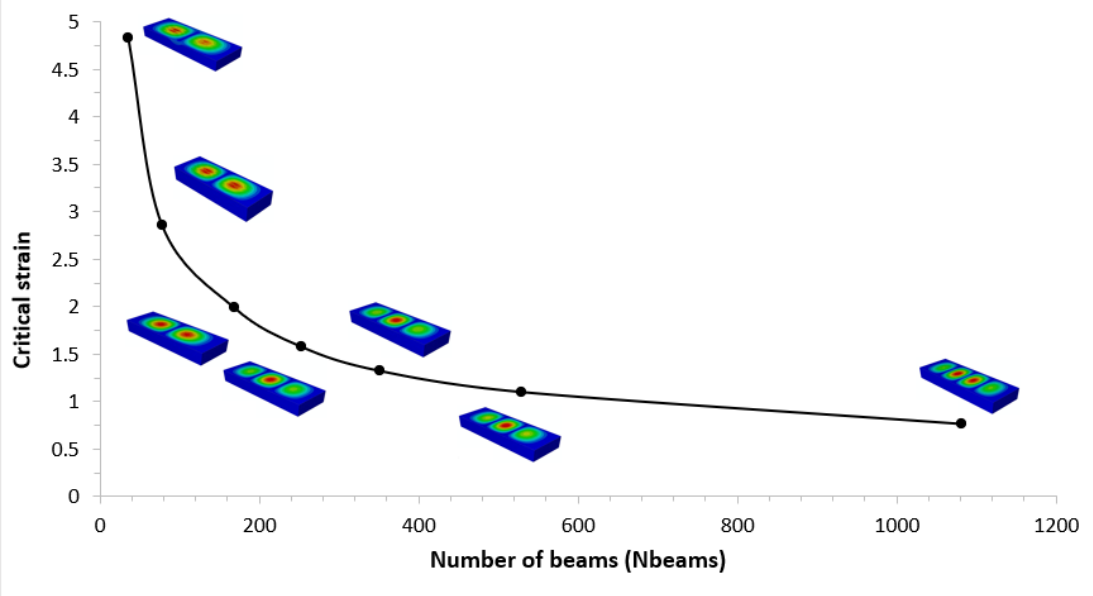

Figure 29: Influence of number of beams in 3D case (extract to internship of Roberta Maziotta)

It can be observed from Figure 28 and Figure 29 that, if the number of beams inside the model increases, the wave number increases and the eigenvalue decreases, thereby decrease in critical strain until an asymptotic value, thereby approaching the solution close to continuum of non-local media. With a smaller number of beams, the mode change and influence the solution. When the number of beams increases inside the model; they have a smaller section, then the local stiffness and the heterogeneity gradients decrease and the structure tends to the continuum gradient

medium. In this particular case, a good compromise between computational time and results is to choose the model with 63 beams, for 2D case, and 441 beams, for 3D case.

5.2.4 Effect of the length of ply

Two sets of Boundary Conditions (BC's) are used: i) Clamped-Clamped(CC) and ii) Clamped-Free(CF), as shown in Figure 30, where the former one represents ply inside a laminate and the latter on represents the case of ply at the free face of laminate (the hypothesis proposed by Grandidier et al., [G3] to describe the interaction of neighboring plies onto the UD ply, to replicate the same scenario as UD composite at macroscale). The thickness of ply is equal to 400µm and the length vary between 400µm (square) to 6400µm. The results are shown in Figure 31. It can be realized that an asymptotic value of critical eigenvalue, thereby critical strain is obtained with increase of length of ply. The shape of mode is similar but number of waves depends on the length of interest in the structure. This result is new and it completes the developments proposed by Drapier et al., [D1].

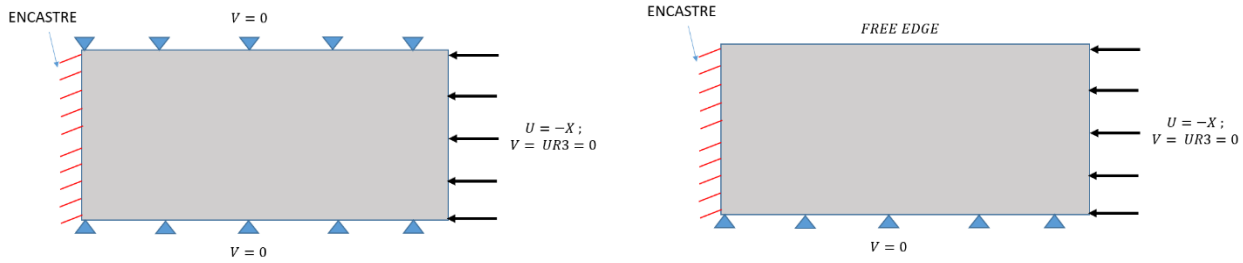

Figure 30: Clamped-Clamped (left) and Clamped-Free BC's (right)

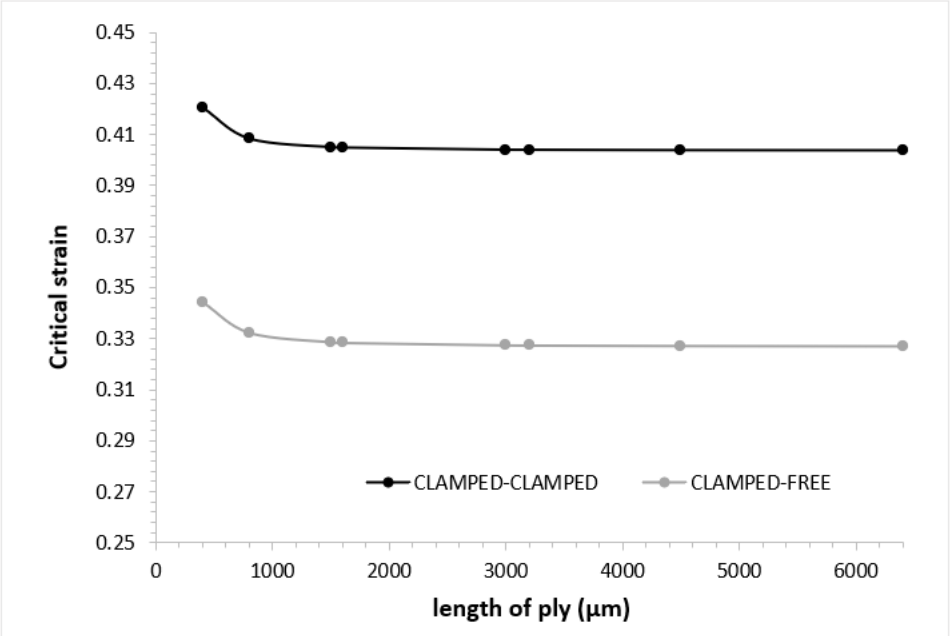

Figure 31: Critical stain in function of length of ply

5.2.5 Structural effect on elastic mode – comparison with bibliography

In this part, different critical load calculations were performed on a unidirectional ply, loaded under compression with a length equal to 1600µm and with a variable thickness. Two models are used: one with BNL configuration and another with a complete description of the microstructure (2D heterogenous model). In BNL model, a density of 63 beams for a thickness of 400µm is chosen and is declined for the other thickness with constant density. The results are compared with those obtained by Drapier et al., [D1] and [D3]. These authors obtained the critical deformations as a function of thickness with a heterogenous and homogenous non-local description by searching for the solution in the form of an amplitude multiplied by a sinusoidal base. This Ritz method allowed them to obtain a critical deformation and a wavelength dependent on the thickness of the fold. As it can be seen in the Figure 32, the new approach gives very good results in accordance with past work. The results of Rosen's model [R1] for very thick plies correspond to non-local predictions. In addition, the power of the combination of ABAQUS® elements allows to provide the elastic modes in the 2D domain where we can perceive the amplitude modulation created by the boundary conditions at each end of the ply (See Figure 33 and Figure 34).

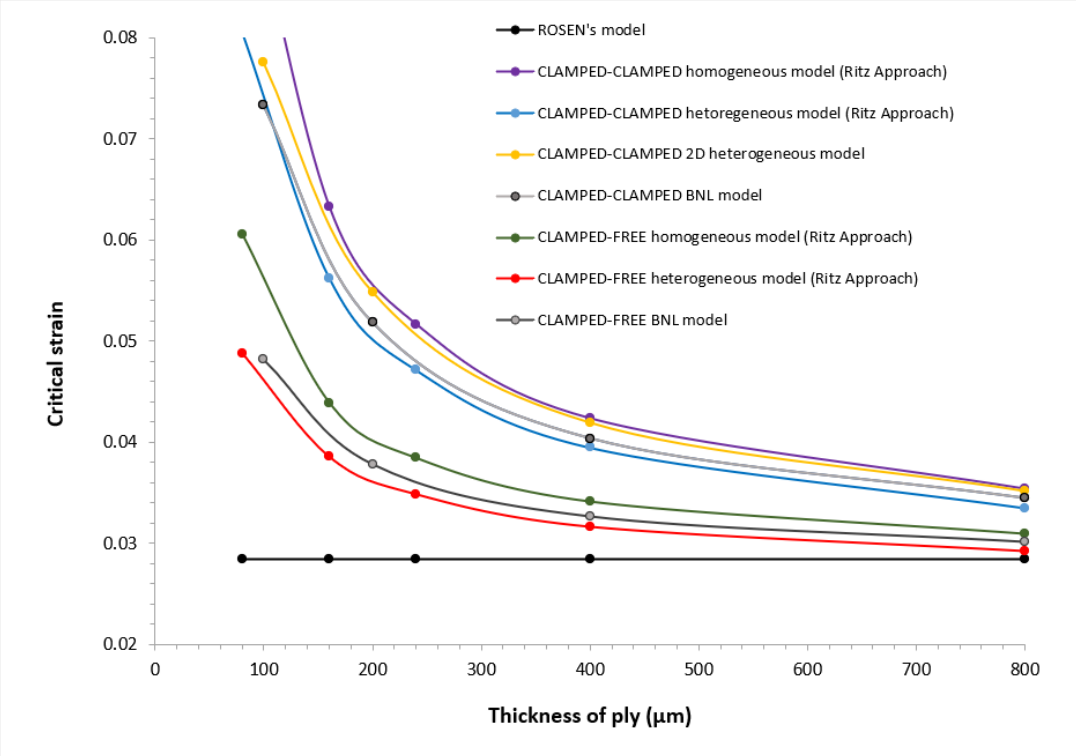

Figure 32: Critical stain in function of thickness of ply

The influence of the length of the structure is comparatively much less. In the papers of Drapier et al., [D1] and [D3], it has been shown that the wavelength of microbuckling is influenced by these previous parameters (thickness and boundary conditions). With the BNL model, this effect appears clearly and the level of critical strain is very close to previous studies. The comparison of mode for both the boundary conditions permits us to understand the influence of neighborhood plies. The “clamped-clamped” condition corresponds to a ply inside a laminate and consequently, the maximal amplitude appears at the center of the ply (Figure 33). Unlike the situation “clamped-

free" which represents a ply close to the free surface, the maximal of amplitude is close to this free surface (Figure 34). The number of waves changes with the thickness, it increases when the thickness decrease. The modulation in the longitudinal direction is similar, perhaps a spread of the maximum amplitude can be observed when the thickness decreases. Moreover, the structural effect is confirmed without the assumption of infinite mode in longitudinal direction (assumption made by some authors in the literature as discussed in earlier chapters), thereby proving the capability of the model.

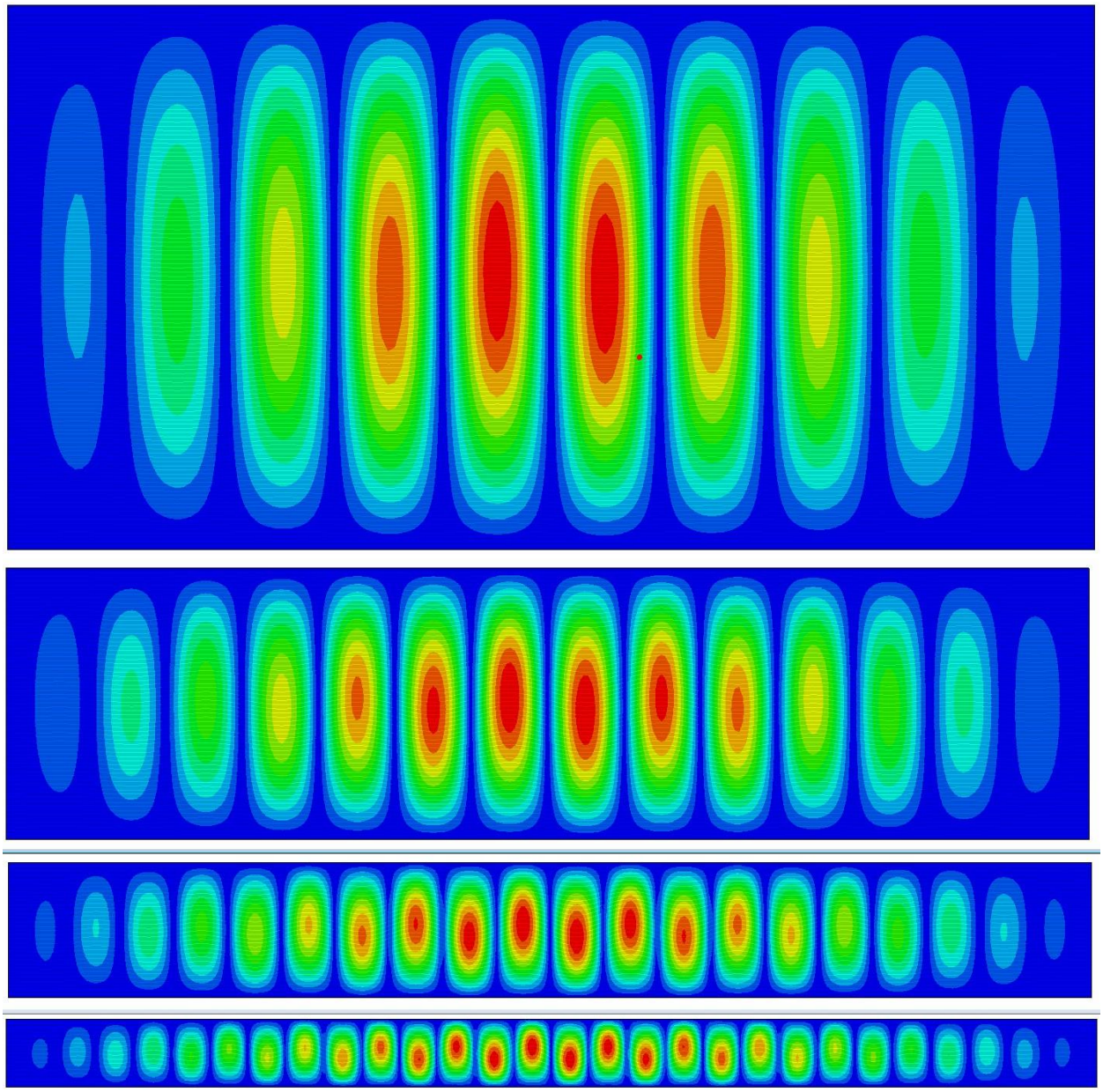

Figure 33: Critical mode in function of thickness of ply (Clamped-Clamped BC's)

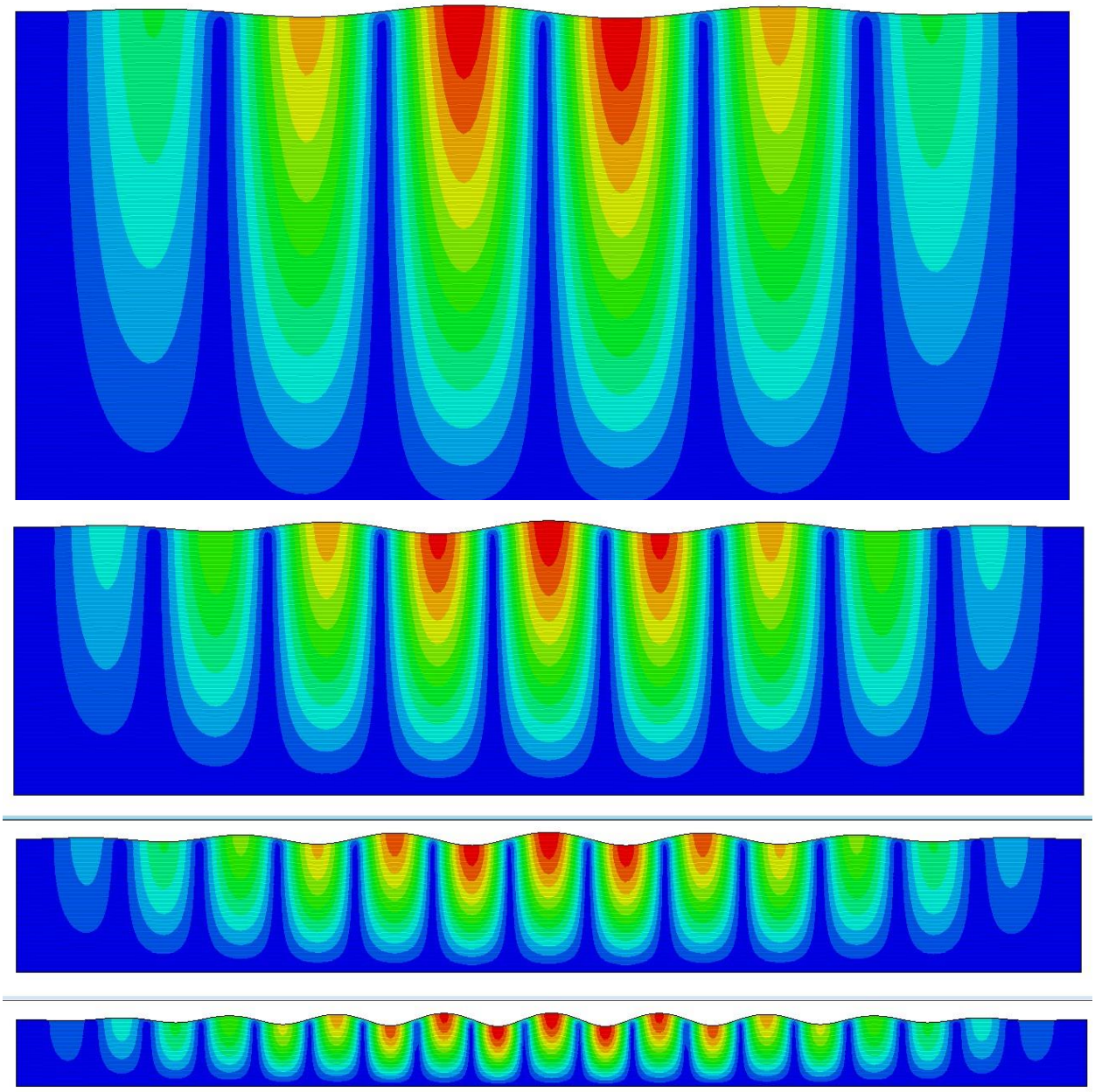

Figure 34: Critical mode in function of thickness of ply (Clamped-Free BC's)

The comparison of modal displacements/amplitudes over the ply thickness permits to validate the previous conclusions, the distributions of modal amplitudes are very close to previous papers (For Ex. Drapier et al., (1996)) as illustrated in Figure 35.

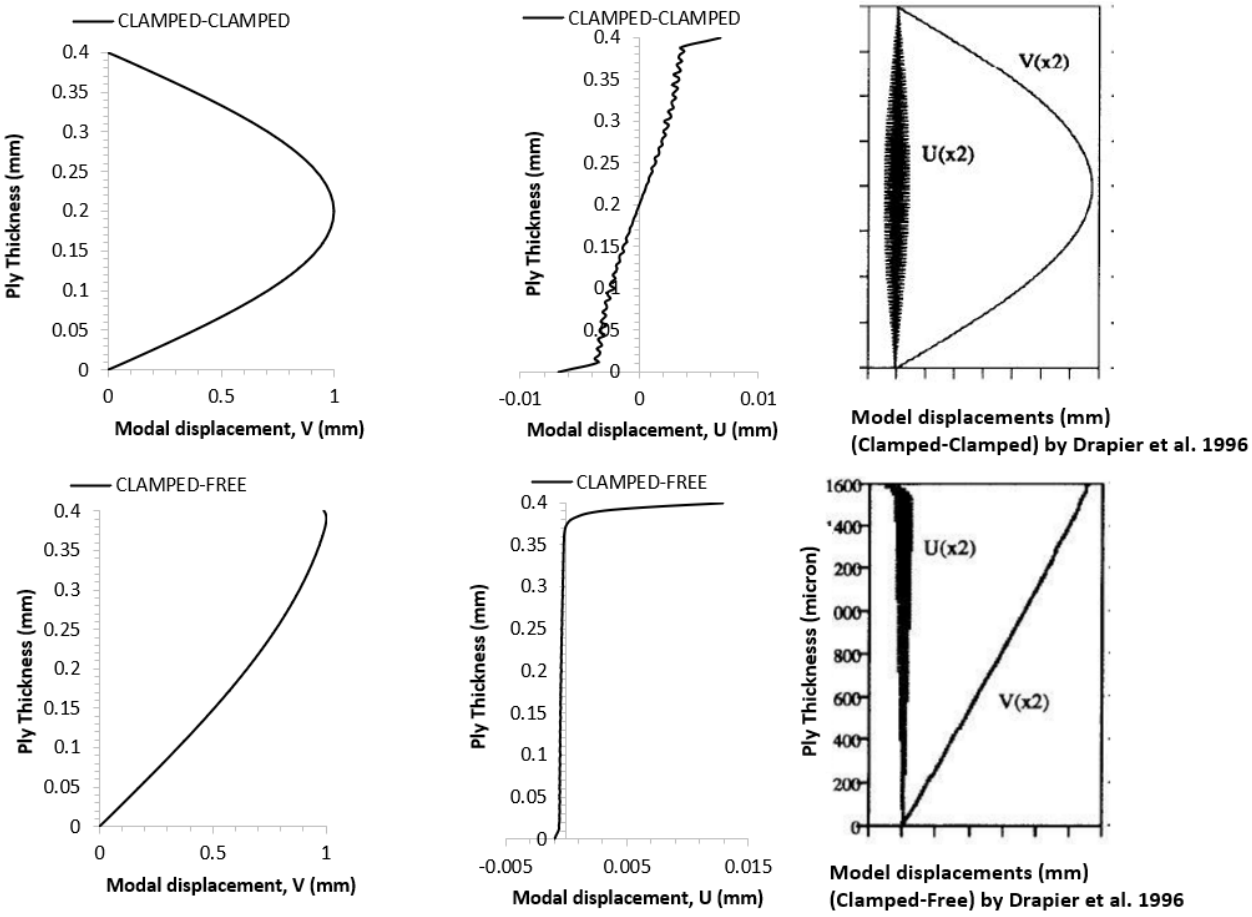

Figure 35: Comparison of modal displacements over ply thickness with Drapier et al., (1996) for clamped-clamped and clamped-free condition under pure compression

5.2.6 Other structural effects

The model permits to solve structures under compression, the possibilities are infinite. Two examples are shown in order to evaluate the tool. The first one permits validation of the "effect of external load", where unidirectional ply is subjected under bending, a transverse displacement is imposed on one extremity and opposite extremity is clamped (Figure 36). The compressive area appears on a part of the thickness and a gradient of stress is present and depends on membrane force and bending moment. The mode localizes in area where compressive stress is higher (see Figure 36 zoom area). The shape depends on boundary conditions, the left extremity is clamped, where all degrees of freedom are null. It is not a symmetry condition; this point explains why the maximal displacement is not in plane of symmetry. The number of waves is equal to 3. In the thickness, only part under compression is affected by the microbuckling. The maximum amplitude appears next to the free surface, as expected.

Secondly, to investigate the "effect of stacking sequence", same simulation is performed on laminate [90°,0°,90] under compression and bending:

- a compressive displacement is applied with left, top and bottom faces are clamped to avoid global buckling;
- a transverse displacement on one extremity with other embeddings to simulate a global bending (Figure 38). In the laminate, the behavior of 90° plies are identical to 0° ply without beam but with a transverse stiffness taking into account the fibers.

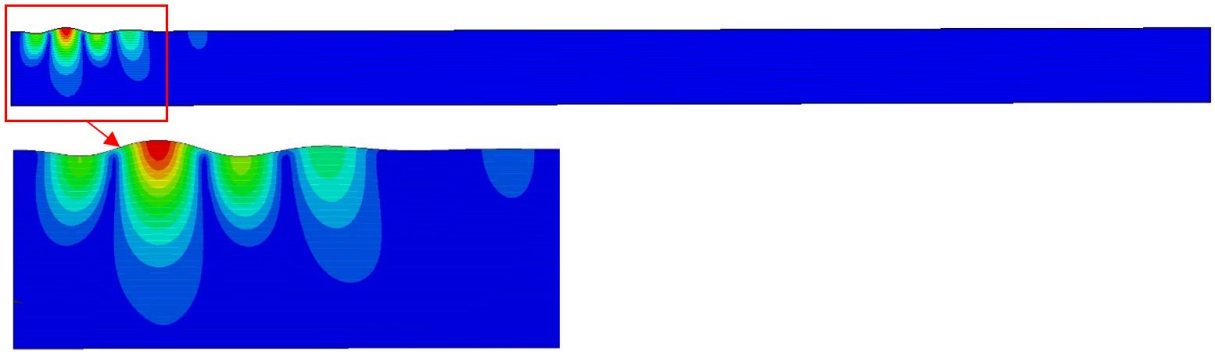

Figure 36: Elastic microbuckling mode in unidirectional ply under bending; clamped at left edge

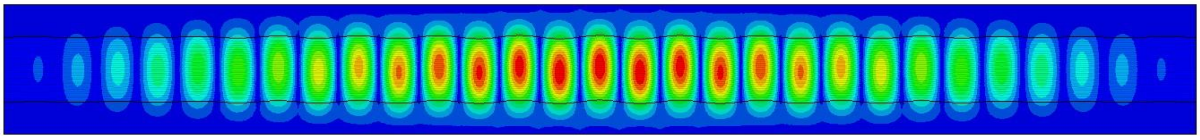

Figure 37: Elastic microbuckling mode in [90°,0°,90°] laminate under compression; upper, lower and left edges are clamped

Under compression, the mode localizes in area where compressive stress is higher in unidirectional ply (Figure 37). The mode which appears in 0° ply inside the laminate is very close to the one calculated with clamped-clamped conditions (Figure 33). However, it appears that there is an influence of 90° ply stiffness, the amplitude spread inside the 90° plies and the interfaces undulate along the entire length of the specimen. The interactions between the ply are obtained by the simulation without assumption.

Under bending of laminate [90°,0°,90] similar to unidirectional ply, the mode is localized close to clamped edge, four bumps seem to appear in the 0° ply in the part of thickness under compression (Figure 38). The length of the phenomenon in longitudinal direction is approximately at the scale of the thickness of the ply. The 90° ply is impacted by the mode, a bump is visible next to the free surface and the amplitude of mode spread on all the thickness of the 90° ply and repercussions can be observed in the traction layers.

The model proposed by Drapier et al., [D3] cannot apprehend such a result, because of the assumption of cellular microbuckling. The gradient of compression in the thickness combine with the gradient generated by the boundary conditions determine the shape of the elastic mode in the restrictive area. This result is new and permits correctly now to quantify the effect of the gradient in the 2D structure.

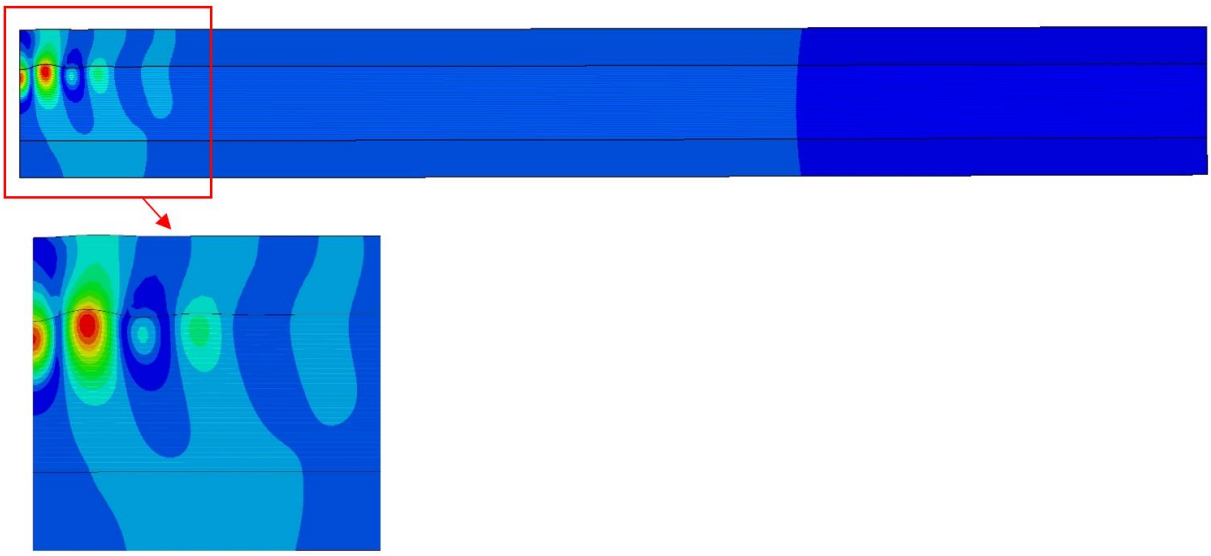

Figure 38: Elastic microbuckling mode in [90°,0°,90°] under bending; clamped at left edge

5.2.7 3D microbuckling

In this part, microbuckling in 3D case is investigated. The number of cases is very limited because the time of simulations is high on personal computer. The cluster does not permit to use parallel calculations for extraction of mode under ABAQUS®. Some results are shown to quantify the capabilities of the model. A rectangular box is subjected to compression (Figure 39), all transverse faces are clamped (clamped-clamped). The field of modal displacements are show in the following figures:

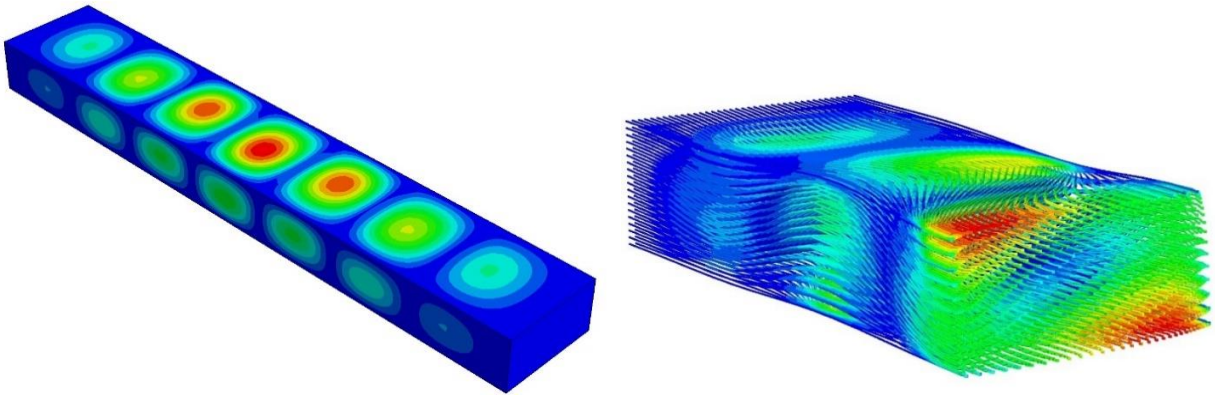

Figure 39: Elastic microbuckling mode in unidirectional case under compression just beams are represented in the right picture and a transverse cut is applied)

In comparison to 2D case, a similar undulation along the structure is obtained. But this one evolves in the 3D space. More precisely the direction of transverse displacement of beam turn around the center when you go along the bar.
In case of [90°,0°,90°] laminate under compression (Figure 40) with upper and lower faces clamped, the mode appears in unidirectional ply with 3 waves, because length is too short. Similar

to 2D case, the microbuckling mode has an impact on the 90° plies, it is possible to observe a field of displacement in 90° plies next to the clamped upper surface.

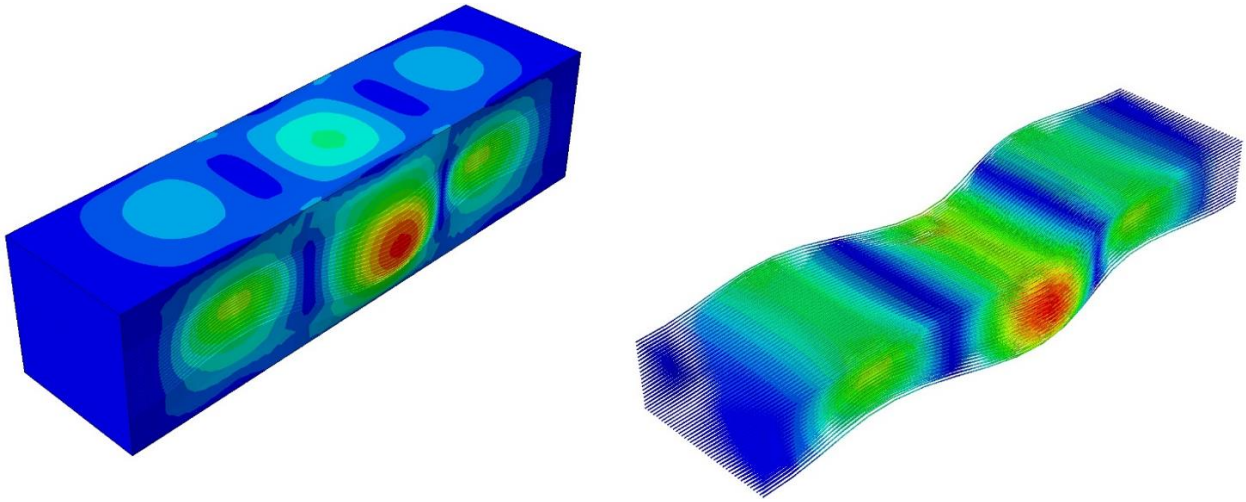

Figure 40: Elastic microbuckling mode in [90°,0°,90°] under compression; upper, lower and left faces are clamped (just beams are represented in right picture)

Under bending (Figure 41), we obtain the mode for this structure (left face is clamped; right face displaces in transverse direction). This figure answers the question on direction of the mode in 3D space under bending in a laminate with a small width. It will be very interesting to increase this width, but the computer that I have been using do not have enough capability to perform these simulations. To summarize, the external boundary conditions (upper and lower face of unidirectional ply) determine the mode and it is clear that results presented in the bibliography in 2D cases are consistent.

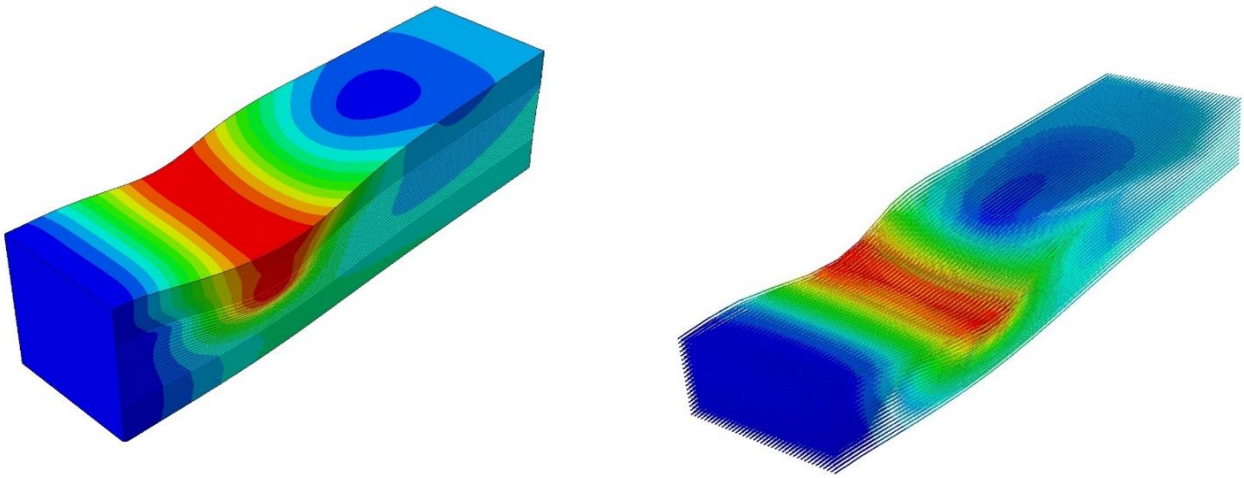

Figure 41: Elastic microbuckling mode in [90°,0°,90°] under bending; left face clamped (just beams in UD ply are represented in right picture)

5.2.8 Material nonlinearity effect and initial defects

Even though, if the elastic mode gives many information of structural effect on microbuckling, we know that the compressive failure is due to the nonlinearity of matrix and the initial defects in positioning of fibers. The aim of this part is to show the capability to take into account this both parameters in this model.

5.2.8.1 *Nonlinear behavior*

To introduce the evolution of matrix stiffness, the subroutine USDFLD combined with GETVAR tool are used. USDFLD permits to define a field in the structure, which evolves in function of equivalent strain. During the simulation at each point of Gauss, the components of tensor LE (logarithm of tensor **V** – classical decomposition of the deformation gradient matrix, **F** = **V**· **R** with rotation matrix) are obtained with GETVAR tools. Then equivalent strain is calculated and recorded in field. The stiffness parameters are defined in function to the equivalent strain (function to the field) with a table. To build this dependency, the response of a heterogenous structure under different loads is compared to the responses of BNL model. The table is obtained by a manual identification based on shear response and mixture rule. Geometrical nonlinearities are taken into account during the simulation. The external loads are applied as a simple ramp.

For the heterogenous model, it is assumed the behavior law of matrix is defined by a Ramberg Osgood (RO) law and the fiber is elastic; the properties are defined in following table:

Table 3: Properties of heterogenous media to build a non-linear law (RO law)

Isotropic matrix	***Isotropic fiber***	***Geometry***
$E_m = 4.5\ GPa$	$E_f = 240\ GPa$	*Volume fraction,* $f = 0.625$
$G_m = 1.6\ GPa$	$G_f = 92\ GPa$	*Diameter of fiber,* $d_f = 10\ \mu m$
$v_m = 0.4$	$v_f = 0.3$	*Ply thickness,* $h = 400\ \mu m$
Yield stress, $\sigma_y = 50\ MPa$		*Traction length of ply:* $800\mu m$
Exponent, $n = 4$		*Shear length of ply:* $200\mu m$
Yield Offset, $\alpha = 0.06$		

All anisotropic properties evolve (Figure 42-top left), the transverse stiffness is most impacted by the nonlinearity of the matrix. The shear stiffness is low but the evolution is similar to the construction of the model. The longitudinal stiffness is very low because it corresponds only to the contribution of the matrix. The contribution of the fibers is taken into account by the beams. Square structure is investigated, three loads are applied by a reference point as previous case and the global response is compared (Figure 42). The curves link global force applied on reference point with global displacement of this point. The responses under transverse shear and longitudinal traction are very close between heterogenous model and BNL model. As shown in many articles, very

good shear matching is essential for the modelling of the local bending fibers, which is the origin of instability. In the transverse traction direction, the comparison is not so good as a deviation is observed, but it remains rather limited. However, it can be improved by using good optimization tool.

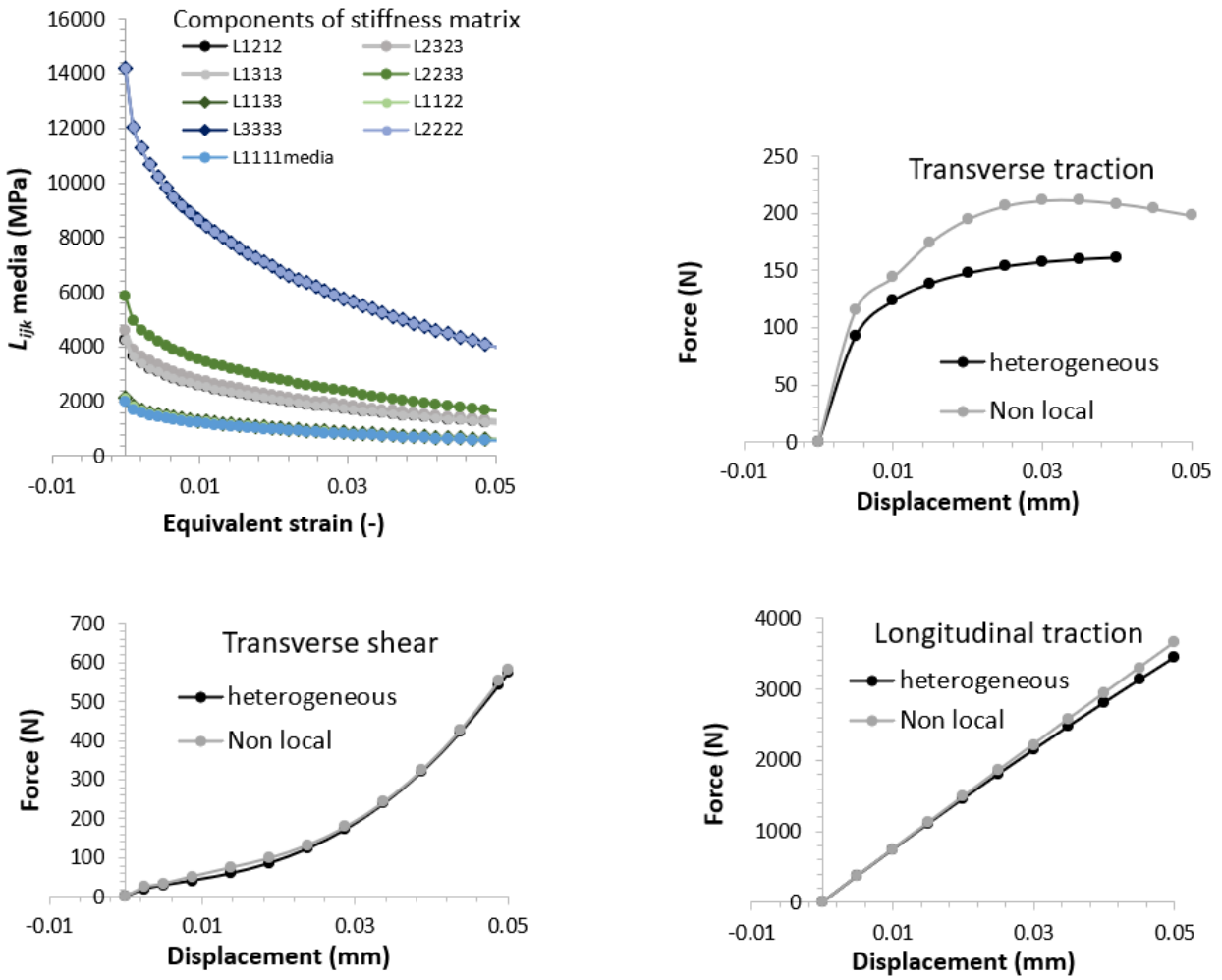

Figure 42: Evolution of components of stiffness matrix in function of equivalent strain and comparison of nonlinear behavior under three different loads

5.2.8.2 *Effect of the thickness and boundary conditions on upper and lower faces*

In this part, a unidirectional ply with a sinusoidal defect is investigated. The Geometrical nonlinearity, the material nonlinearity and a defect are taken into account. The defect has an amplitude equal to 0.002mm and the wave length equal to 0.6mm, which generate a maximal angle of misalignment equal to 1.152°. Lower face is clamped and upper is clamped or free. For the thick ply, the effect of a defect is studied, a hole is introduced with the radius equal to 50µm. The simulations are carried out until divergence, the critical displacement is recorded when ABAQUS® calculation is aborted. The structural effect is confirmed with critical value in the order of experimental data, the difference between a ply next to free surface and inside a laminate

is obtained. This porosity greatly influences the result, the critical strain decreases. The critical value decreases by 40% for a ply inside the ply and 34% for a ply next to free surface.

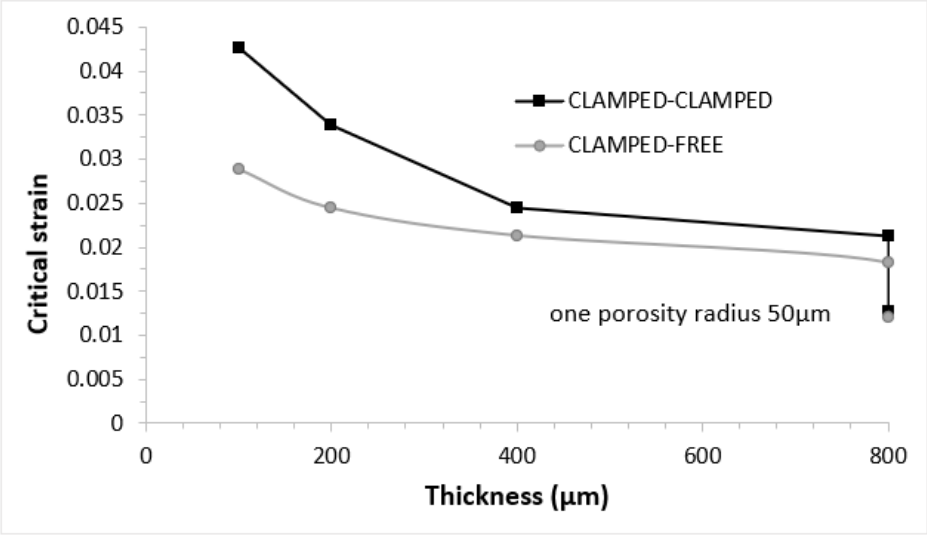

Figure 43: Critical strain for different thickness on unidirectional ply under compression with two boundary conditions

The state of stress at instability can be presented in order to confirm the birth of kink band in function of the thickness and boundary conditions, which are shown in the following figures.

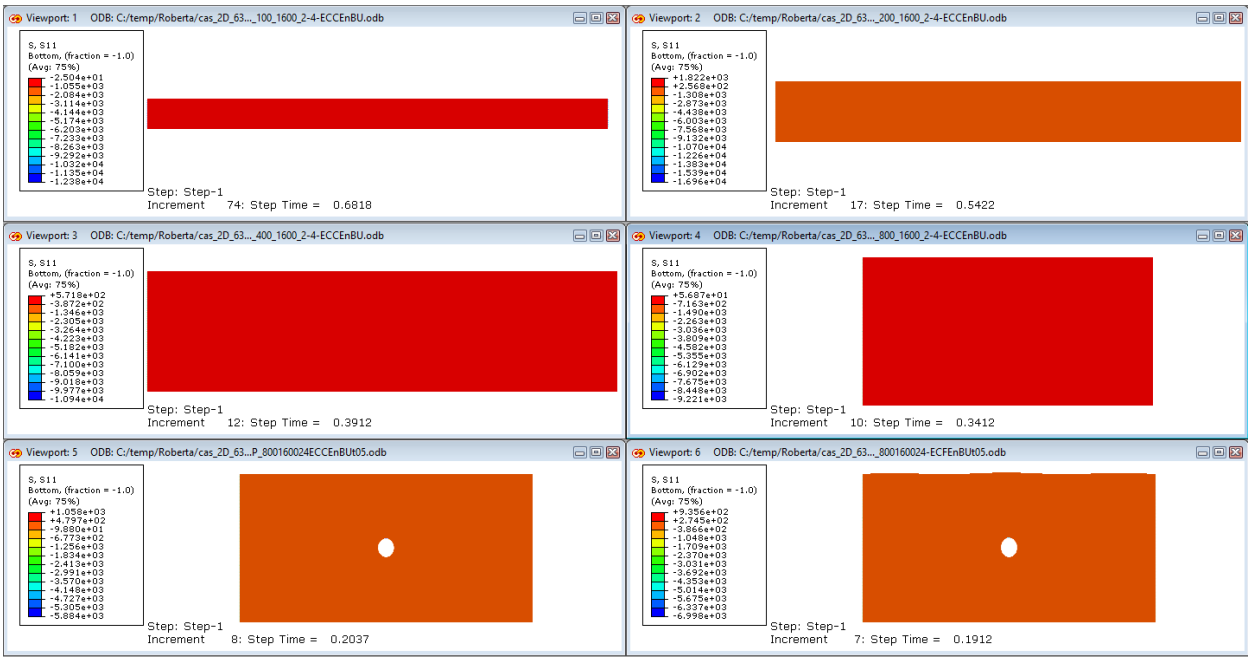

Figure 44: Fields of longitudinal stress at instability for a unidirectional ply under compression (clamped-clamped) – bottom right (clamped-free)

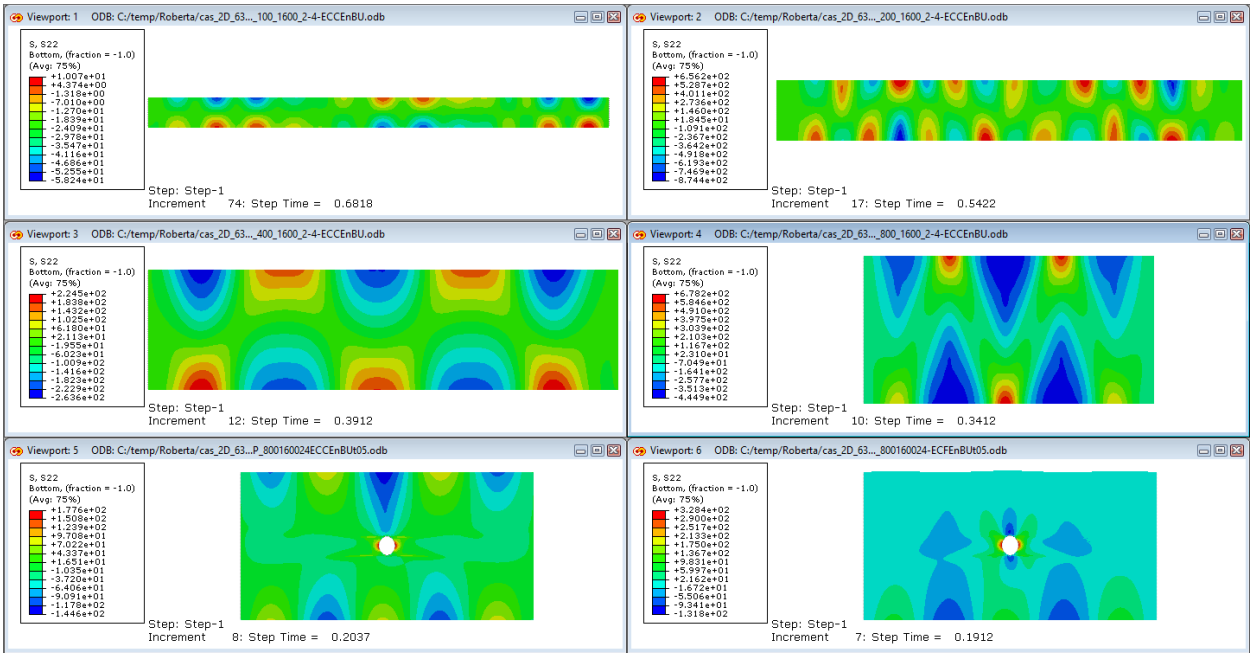

Figure 45: Fields of transverse stress at instability for a unidirectional ply under compression (clamped-clamped) – bottom right (clamped-free)

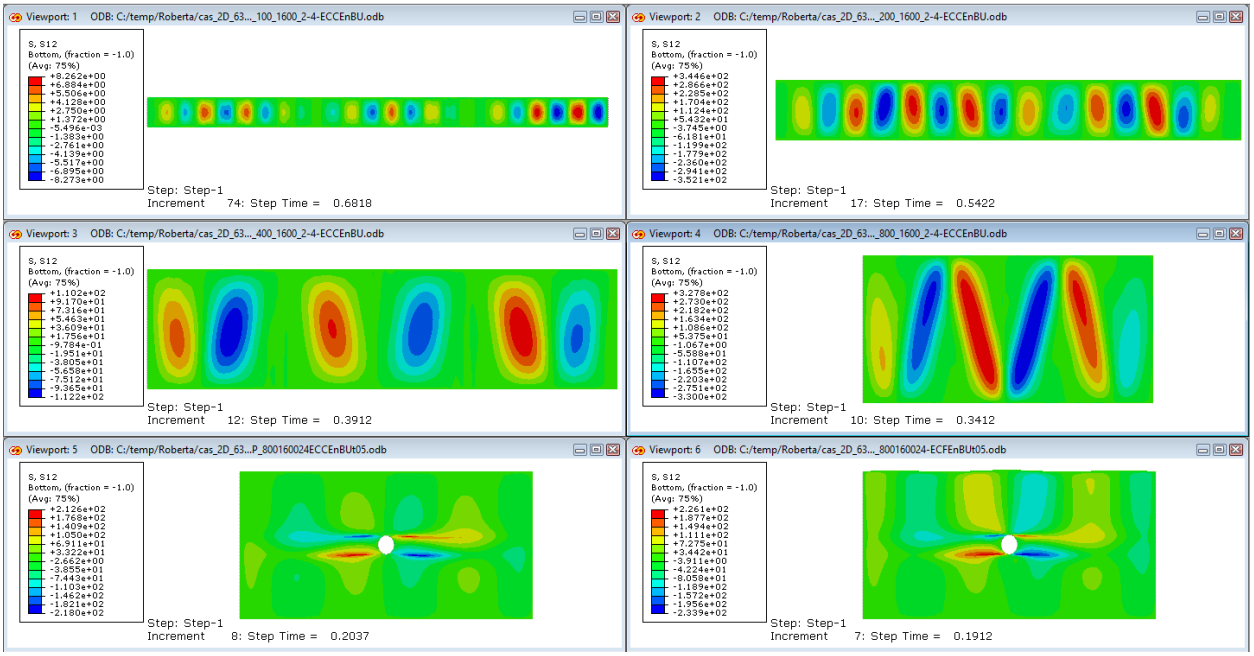

Figure 46: Fields of shear stress at instability for a unidirectional ply under compression (clamped-clamped) – bottom right (clamped-free)

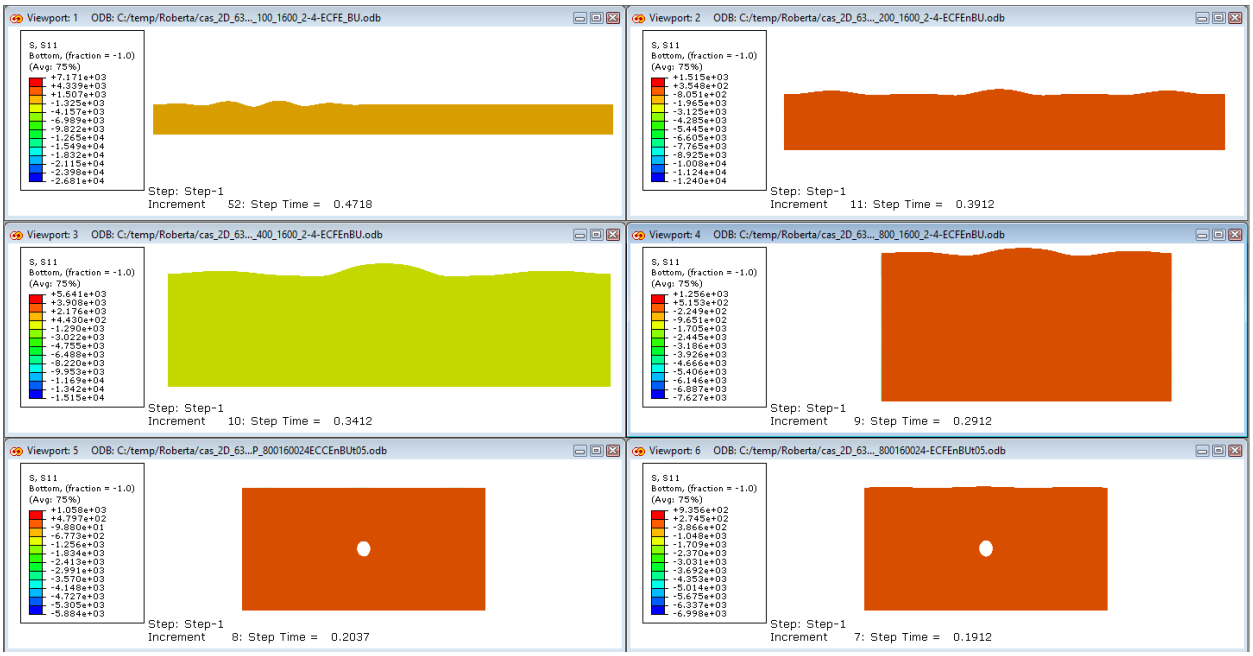

Figure 47: Fields of longitudinal stress at instability for a unidirectional ply under compression (clamped-free) – bottom left (clamped-clamped)

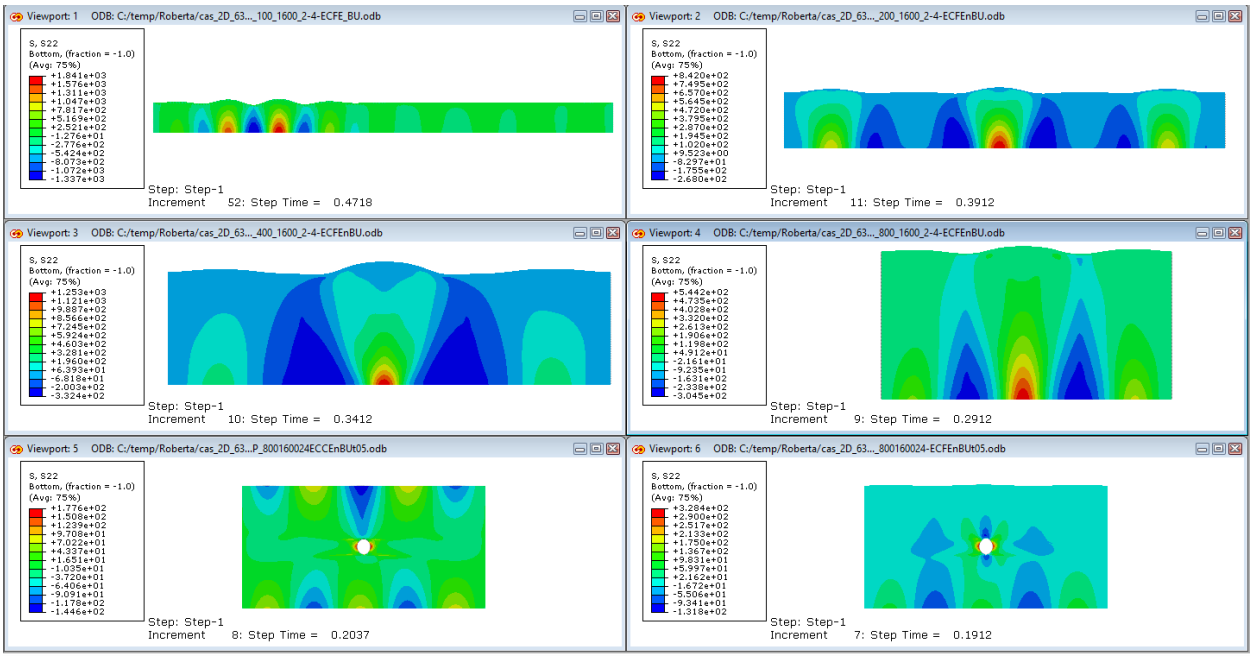

Figure 48: Fields of transverse stress at instability for a unidirectional ply under compression (clamped-free) – bottom left (clamped-clamped)

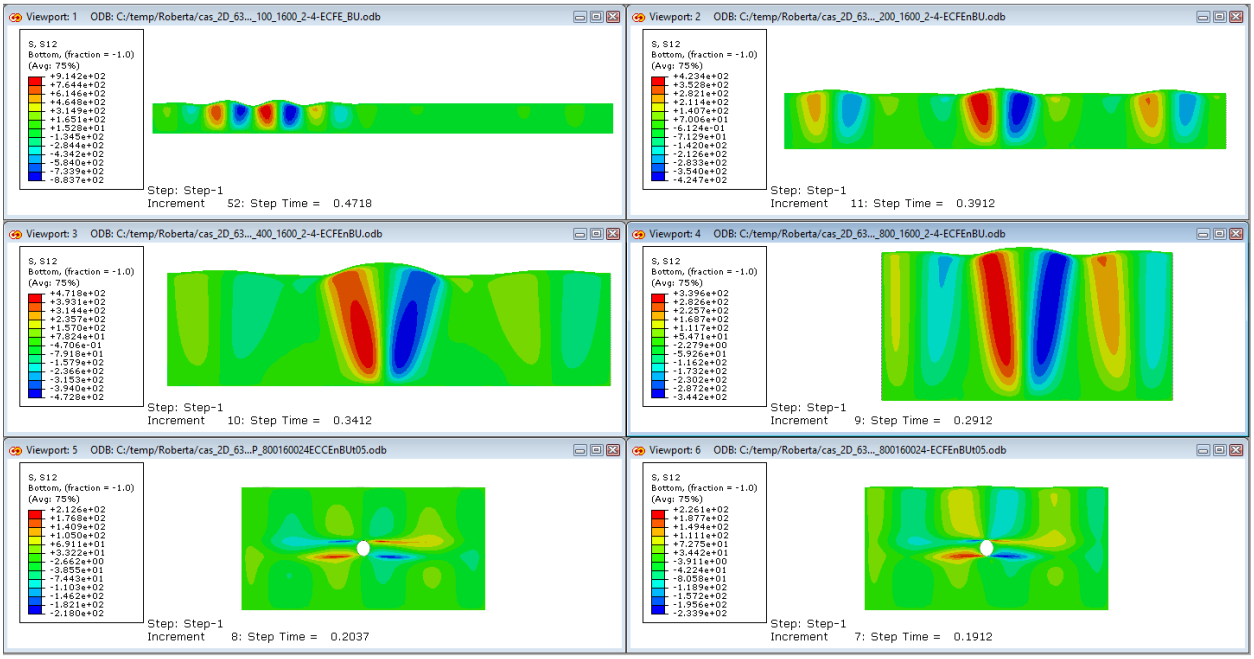

Figure 49: Fields of shear stress at instability for a unidirectional ply under compression (clamped-free) – bottom left (clamped-clamped)

It is clear that the thickness and boundary conditions define the wavelength and consequently the width of kink band. The angle of inclination increases when the thickness increases. This new result has not been obtained by works of Drapier et al., [D3]. The hole influences the instability and disturb the field of shear stress. For clamped-clamped and clamped-free conditions, the kink bands are very similar but transverse load is not the same for a ply inside the laminate and next to the surface. The structural effect influences the field of stress when the instability appears and the critical strain is impacted. These simulations are performed with a particular defect. The question is: does the defect has an effect major in comparison to the structure?

5.2.8.3 *Effect of the shape of an initial undulation defect*

In this part, five sinusoidal defects are considered, they are defined by an amplitude (here 0.001 mm or 0.002mm) and by a number of wave (2, 4 and 8). The distribution is constant in the thickness. One particular case is studied, where the amplitude is variable in function of the length (notation ‘v’). The evolutions of the amplitude in function of the length are described in Figure 50. The angle (in °) of misalignment with longitudinal direction is calculated and shown in Figure 51. These defects are introduced by an initial position of nodes on ply with 200µm thickness and 1600µm length with the upper and lower faces clamped.

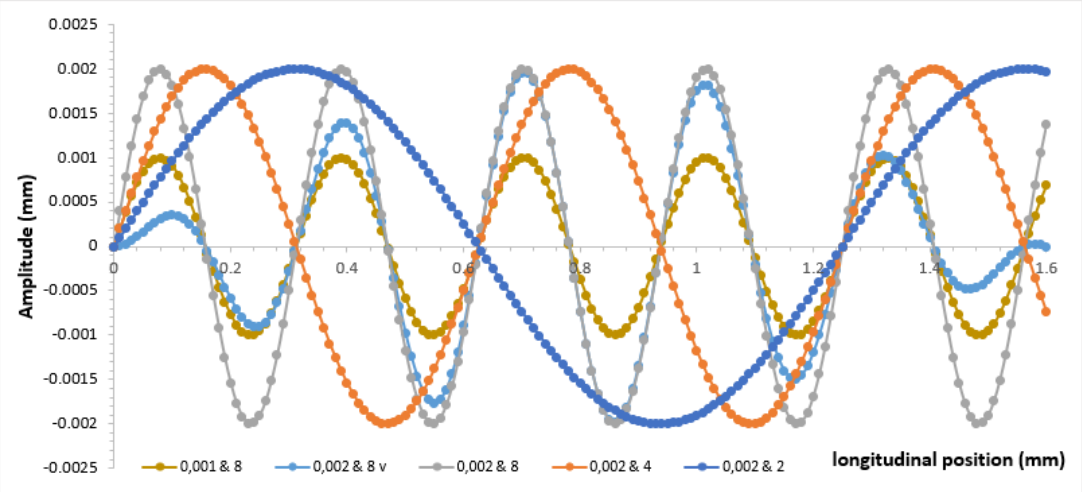

Figure 50: Evolution in the length of amplitude for studying defects

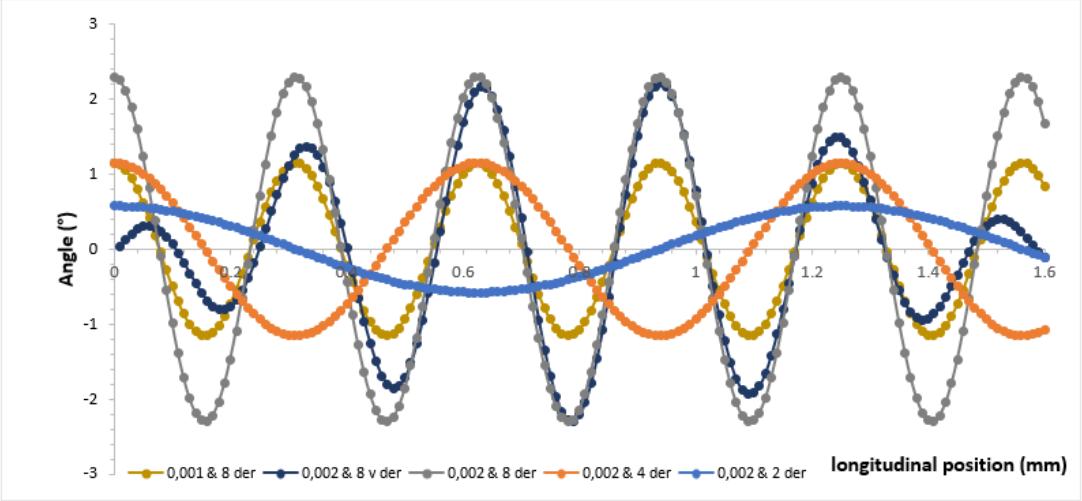

Figure 51: Evolution in the length of angle for studying defects

The graphs in Figure 52 and Figure 53 represent critical strain in function of maximal angle and shape of the defect. The influence on critical strain is equal to 20% in comparison to the structural effect which modifies the critical strain for 50% in internal ply and 37% for an external ply. Consequently, two effects are at the same level. Figure 53 compare the different parameters (a: amplitude, n: number of wave). It is clear that the amplitude alone cannot be just correlated with the critical strain and it is the same for wave number. On the contrary, Figure 52 seems to show that the angle is really a relevant parameter to quantify the influence of misalignment defect due to an undulation. A defect variable in the thickness has an effect at the second order. But this study is not exhaustive and must be completed to improvise the link between the spatial distribution of the defect and the mechanism of plastic instability.

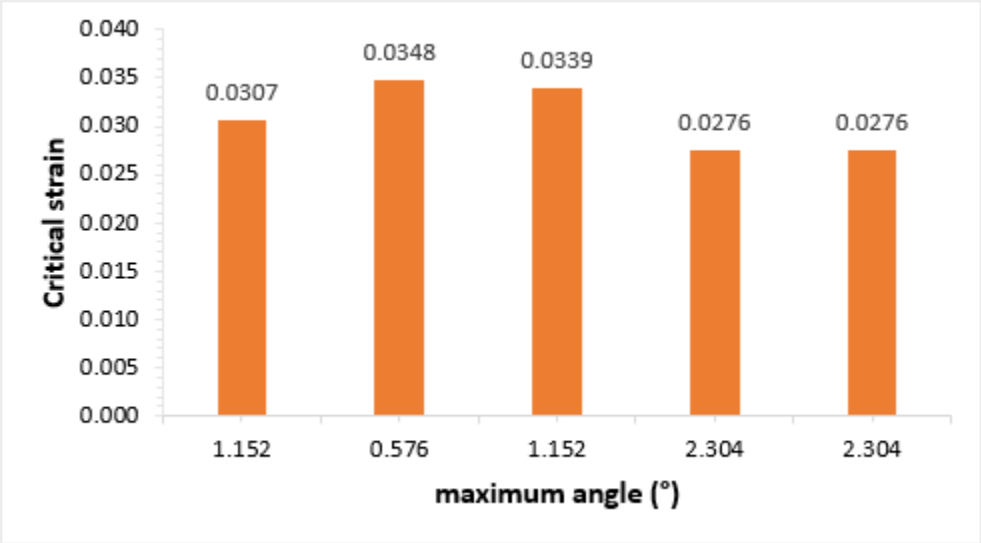

Figure 52: Critical strain in function of maximal angle

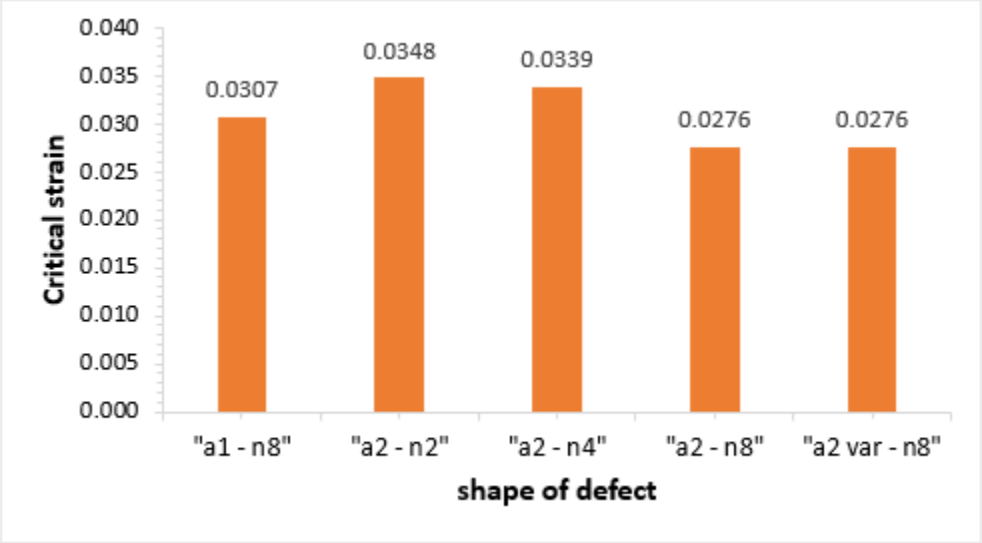

Figure 53: Critical strain in function of parameters of defect

The distribution of stress fields at instability for the unidirectional ply (200µm x 1600µm) considered under compression (clamped-clamped) with different amplitudes and wavenumbers (parameters of defect) are shown in the following figures to demonstrate its influence in the solution.

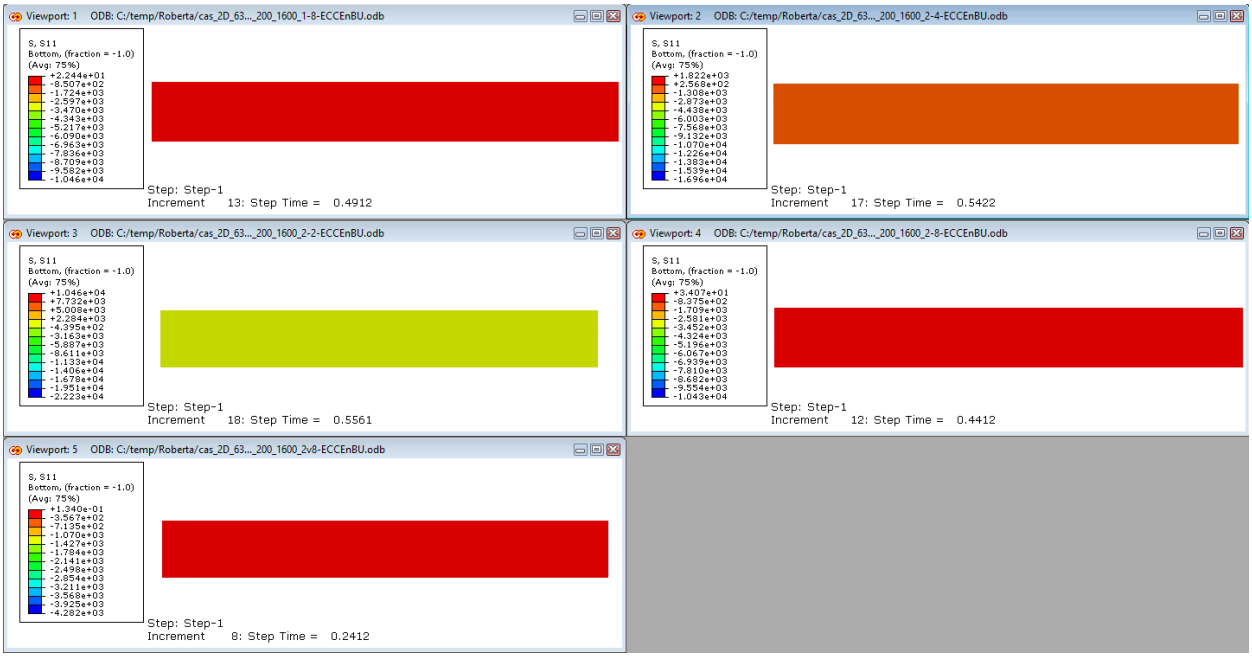

Figure 54: Fields of longitudinal stress at instability for a unidirectional 200µm ply under compression (clamped-clamped)- definition of defect:
up left amplitude =0.001mm, wave number = 8
up right amplitude = 0.002mm, wave number = 4
middle left amplitude = 0.002mm, wave number = 2
middle right amplitude = 0.002mm, wave number = 8
lower left amplitude = 0.002mm variable, wave number = 8

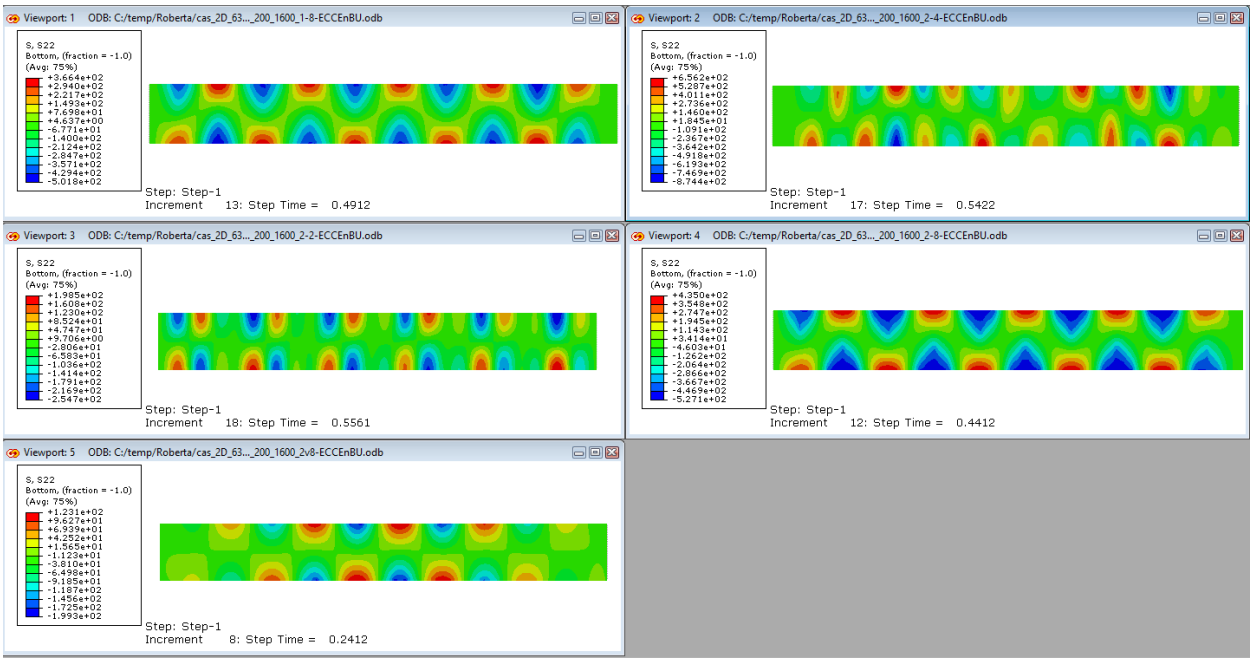

Figure 55: Fields of transverse stress at instability for a unidirectional 200µm ply under compression (clamped-clamped)- definition of defect:
up left amplitude =0.001mm, wave number = 8
up right amplitude = 0.002mm, wave number = 4

middle left amplitude = 0.002mm, wave number = 2
middle right amplitude = 0.002mm, wave number = 8
lower left amplitude = 0.002mm variable, wave number = 8

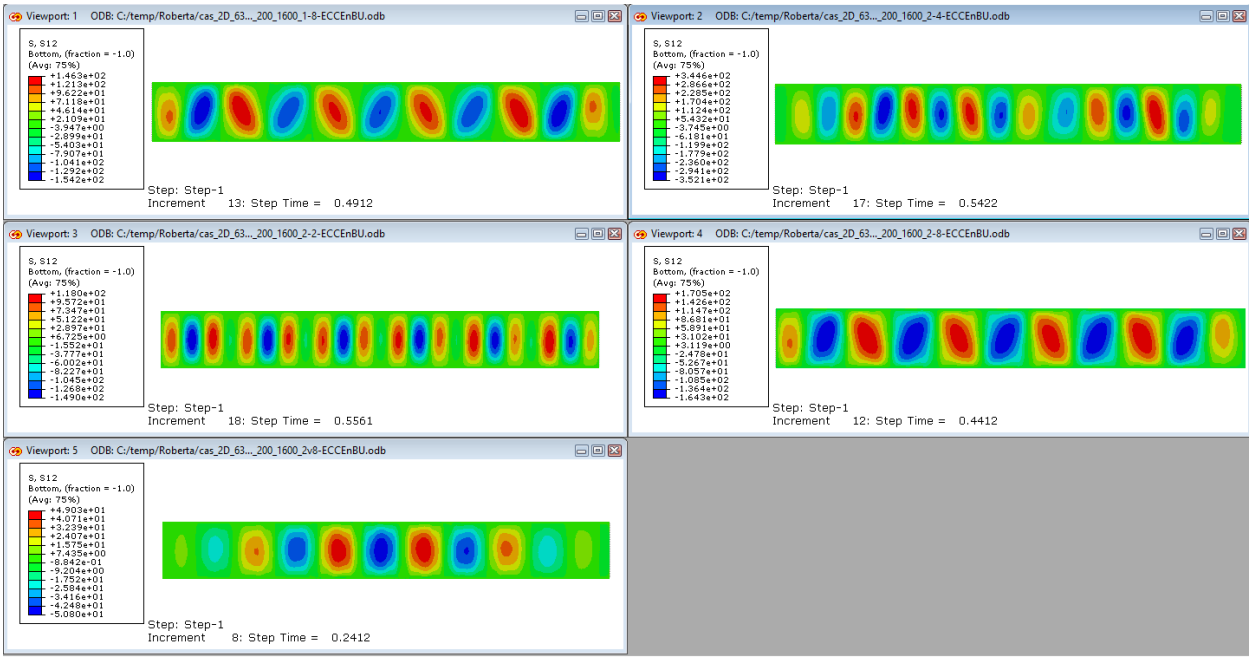

Figure 56: Fields of shear stress at instability for a unidirectional 200µm ply under compression (clamped-clamped)- definition of defect:
up left amplitude =0.001mm, wave number = 8
up right amplitude = 0.002mm, wave number = 4
middle left amplitude = 0.002mm, wave number = 2
middle right amplitude = 0.002mm, wave number = 8
lower left amplitude = 0.002mm variable, wave number = 8

On the distribution of stress fields, the shape of the defect has a major effect. The width and angle of the kink band change with the wavenumber. Greater the increase in wavenumber, the greater the decrease in width of the kink band, and the greater the increase in angle. For the variable amplitude case, localization of two kink band appears in the area where the angle is maximal. This result confirms that the localization of the instability is clearly defined by the shape of the defect.

5.3 Conclusion

BNL model with structural elements of ABAQUS® (2D and 3D) permits to modelize the behavior of UD composites in compression and also predict the failure by taking into account structural effects, defect (initial misalignment) and all non-linearities (geometrical and material).

However, this model is limited to simulate Unidirectional (UD) plies and laminates, it is not possible to simulate composite structures with a complex micro/mesostructure (2D or 3D woven composite). Moreover, it is a discontinuous finite element model. Therefore, it is necessary to develop more generalized model which is continuous and also takes into account structural effects for analysis of woven and more complex architectures.

6 Generalized Non-Local model for UD and Woven composites – numerical model (UEL Abaqus®)

6.1 Introduction

We have seen from the previous chapter that the BNL model (developed with structural elements of ABAQUS®) proved the capability to simulate compressive behavior of UD composites and also gives an idea that the non-local model can be extended to assess more complex cases. In this chapter, various non-local models and finite element approaches (based on non-local theories) developed over the years are presented, which permits to extend our non-local model to simulate compressive behavior of composites with complex architectures. After the bibliography of these models, the development of generalized 3D non-local model for UD and Woven composites is presented with theoretical and numerical parts in detail. And finally, implementation of this model in case of 2D, thereby developing User Element (UEL), "NL U32" for simulation in ABAQUS® is discussed.

6.1.1 Various Non-Local (NL) models and NL Finite Element approaches which permits to modelize compression behavior

6.1.1.1 *Continuum non-local models*

Before going into various non-local models, it is important to know why we need non-local theory and what are its importance, when there are already classical local continuum theories. Various authors have given their definitions and importance of non-local theories, out of which few important ones are discussed here.

The classical (local) elasticity theory has been widely employed in the context of continuum theories to solve with success a large number of engineering problems. However, as known, such *classical (local) theory is unable to capture phenomena which indeed can be reasonably explained only at microstructural level*. Well-known examples are: *the occurrence of size effects (Difference of mechanical behaviors between the micron scale and the macro scale)*; *the dispersion of elastic waves; the singularity of the stress at crack tip*. Application of such theories to realistic engineering problems is computationally unfeasible. This is because, conventional continuum mechanics theories assume that stress at a material point is a function of '*state*' variables, such as *'strain'*, at the same point. This local assumption has long been proved to be adequate when the wavelength of a deformation field is much larger than the dominant micro-structural length scale of the material (Shu et al., 1999). When the dimensions of a structure become comparable to the size of its material micro-structure, size and micro-structural effects are observed. Due to the lack of internal length scale parameters, the classical theory of local continuum theories fails to describe such a behavior. Whereas, *Nonlocal elasticity theories* which include, besides the contact forces between particles (occurring in a local elastic approach), *long-range cohesive forces*, able to catch the capacity of an elastic material to transmit information to neighboring points within a certain distance. This distance, herein named *influence distance, is strictly related to an 'internal length material scale'*, which enters the constitutive material model in different ways (Sofi et al., 2006), i.e.,

1. by considering body couples as in polar elasticity;
2. by gradient operators;
3. by integral operators;
4. by fractional quantities.

Strain gradient theories:
We have understood that, the conventional strain-based mechanics theory does not account for contributions from strain gradients. Or in other words, the difficulties encountered in using classical local theories for capturing well the microstructural phenomenon was due to lack of using the "gradient approach", in which an internal-length scale was properly introduced in the form of higher-order gradients of either the dislocation density (microscale) or the plastic strain(macroscale), so that "size effects" are predicted and characterized. With this introduction of higher order strain gradients, the interaction between macroscopic and microscopic length scales in the constitutive response and the corresponding interpretation of the associated size effects can be properly modelled and predicted well (Aifantis, 1992). The introduction of higher order gradients in the constitutive equations is a measure of the heterogenous character of the deformation field, the overall effect of which may depend on the specimen size.

Starting from the pioneering "*Cosserat couple stress theory***"** (Cosserat and Cosserat, 1909) various '*non-local'* or '*strain gradient'* continuum theories have been proposed. In the full '*Cosserat theory'*, an independent rotation quantity, θ is defined in addition to the material displacement, **u**; *couple stresses* (bending moment per unit area) are introduced as the work conjugate to the micro-curvature (that is, the spatial gradient of θ). Later, "*Toupin"* (Toupin, 1964) and "*Mindlin"* (Mindlin, 1964) proposed a more general theory which includes not only *micro-curvature, but also gradients of normal strain*.

Both the "*Cosserat" and "Toupin – Mindlin"* theories were *developed for linear elastic materials***.** After-wards, *non-local theories for plastic materials* have been developed by, among others, "*Aifantis*"(Aifantis, 1982, 1987, 1992), "*Fleck" and "Hutchinson"* (Fleck, Hutchinson et al., (1993,1994). *Fleck-Hutchinson's strain gradient plasticity theory* falls within the *Toupin-Mindlin framework*. They extended the Toupin-Mindlin theory by including plasticity. Interest in non-local continuum plasticity theories has been rising, due to an increasing number of observed size effects in plasticity phenomena. In general, a brief classification of non-local theories (elastic and plastic) developed over the years is given below:

Elasticity theories:
- Cosserat elastic theory (Cosserat and Cosserat, 1909);
- Cosserat theory with constrained rotations or reduced couple stresses theory/polar gradient elasticity theory (Mindlin and Tiersten, 1962; Koiter, 1964); (Toupin, 1964);
- Multipolar elastic theory/polar functional theory (Green and Rivlin, 1964);
- Higher order strain gradient elastic theory (Mindlin, 1964, 1965);
- Couple stress-based strain gradient theory (concept of RVE) (Yang et al., 2002);
- Couple stress theories for solids (Hadjesfandiari et al., 2011):
    - 1) Couple-stress tensor is skew-symmetric and the skew-symmetric part of the gradient of the rotation tensor is the consistent curvature tensor;

- 2) Modification of the developments of Mindlin and Tiersten (1962) and Koiter (1964).

Framework of non-local (integral type):

- Linear theory of Non-local elasticity (concept of influence/attenuation function) (Eringen, 1972);
- Micromorphic, microstretch and micropolar elastic theories (Eringen, 1999);
- Strain difference based nonlocal elasticity model for macroscopically inhomogenous materials (Extension of Eringen (1972); Vermeer and Brinkgreve(1994) + thermodynamic framework + concept of equivalent distance) (Polizotto et al., 2004).

Only few important theories will be discussed here and more details on the above theories can be found in Pisano et al., (2009), Tiersten and Bleustein (1974), Lakes (1995), Eringen (1999), Exadaktylos and Vardoulakis (2001) and Tekoglu and Onck (2008).

Plasticity theories:

- Strain gradient plasticity theory first suggested by (Aifantis, 1982, 1983, 1984 [b],[c]) and later elaborated by (Aifantis ,1987, 1992, 1995, 1996) and further examined by Zbib and Aifantis (1988a,b);
- Strain gradient plasticity theory (Toupin-Mindlin framework) by Fleck and Hutchinson (1993, 1994, 1997), and also later reformulated by (Fleck and Hutchinson, 2001);
- Theories on Non-Local plasticity based on concept of influence function (Eringen, 1981, 1983);
- Nonlocal strain gradient plasticity theory for finite deformations (Polizotto, 2009).

For more clear details on various gradient theories (plasticity) refer Aifantis (2003) and Polizotto (2009).

In general, it is understood that, in *"gradient type" elasticity* theories, length scales enter the constitutive equations through the elastic strain energy function, which depends not only on the strain tensor, but also on gradients of the rotation and strain tensors. Whereas, in *"gradient type" plasticity theories*, length scales are introduced through the coefficients of spatial gradients of one or more internal variables. Few of the important nonlocal theories (elastic), which pioneered the development of many theories over the years are discussed further.

6.1.1.2 *Cosserat Couple Stress theory*

In the couple stress theory of Cosserat and Cosserat (1909), it is assumed that the surface element *dS* may transmit both a force vector **F***dS* and a couple vector **Q**d*S*. The corollary is that the deformation field of the body is specified by a material rotation $\boldsymbol{\theta}$ in addition to the displacement field, **u**. Note that as mentioned earlier, Toupin (1962), Mindlin and Tiersten (1962) and Koiter (1964) have considered the so called *reduced couple stress theory*, wherein $\boldsymbol{\theta}$ is identified with the rotation of the displacement field, $\boldsymbol{\theta} = \frac{\mathbf{1}}{\mathbf{2}}\text{curl}\,\mathbf{u}$.

Within the framework of general couple stress theory by Cosserat and Cosserat (1909), consider an arbitrary volume **Ω** of the body in the deformed configuration, bounded by a piecewise smooth surface *S*. Equilibrium of forces on the body gives:

$$\int_S \boldsymbol{F}\, dS = 0 \tag{6-1}$$

And the equilibrium of moments gives:

$$\int_S [\boldsymbol{X}\ x\ \boldsymbol{F} + \boldsymbol{Q}]\, dS = 0 \tag{6-2}$$

Where, $\boldsymbol{X}$ is the radius vector from an arbitrary fixed point, $\boldsymbol{F}$ is surface force and $\boldsymbol{Q}$ is surface moment traction. The body forces and body couples have been neglected. The components σ_{ij} of the unsymmetrical Cauchy stress tensor $\boldsymbol{\sigma}$ denote the components of T_j on a plane with a unit normal n_i, such that:

$$T_j = n_i \sigma_{ij} \quad ; \quad i = j = 1{,}2 \tag{6-3}$$

In similar manner, the components μ_{ij} of the couple stress tensor $\boldsymbol{\mu}$ denote the components of Q_j on a plane with a unit normal n_i, such that:

$$Q_j = n_i \mu_{ij} \quad ; \quad i = j = 1{,}2 \tag{6-4}$$

After applying divergence theorem to (Eq. 6-1) and (Eq. 6-2) using (Eq. 6-3) and (Eq. 6-4), leads to the force equilibrium equation:

$$\sigma_{ji,j} = 0 \tag{6-5}$$

And the moment equilibrium equation:

$$\varepsilon_{ijk}\sigma_{jk} + \mu_{ij,j} = 0 \tag{6-6}$$

Where, the (,) denotes differentiation with respect to a component of the spatial co-ordinate $\boldsymbol{X}$. ε_{ijk} denotes the three-dimensional permutation symbol.

The equation of principle of virtual works is formulated as:

$$\int_\Omega \delta W\ d\Omega = \int_S [T_i \delta U_i + Q_i \delta \Theta_i]\ dS \tag{6-7}$$

Where, the volume, Ω is contained within the closed surface, *S*, δw denotes the rate at which work is absorbed internally per unit volume, δU_i denotes virtual displacement and $\delta\Theta_i$ denotes the independent virtual rotations. Using the divergence theorem, the RHS of (Eq. 6-7) can be rearranged to the form:

$$\int_S [T_i \delta U_i + Q_i \delta \Theta_i] \, dS = \int_\Omega [\sigma_{ji,j} \delta U_i + \left(\varepsilon_{ijk}\sigma_{jk} + \mu_{ij,j}\right) \delta\Theta_i + \sigma_{ij}\delta\gamma_{ji} + \mu_{ij}\delta\kappa_{ji}] \, d\Omega \qquad (6\text{-}8)$$

Where, $\delta\gamma_{ij}$ is the 'increment in relative strain', $\delta\gamma_{ij} = \delta U_{i,j} + \varepsilon_{ijk}\delta\Theta_k$, and $\delta\kappa_{ij}$ is the 'curvature increment', $\delta\kappa_{ij} = \delta\Theta_{i,j}$. The first term and second term of RHS of (Eq. 6-8) vanishes by force equilibrium (Eq. 6-5) and moment equilibrium (Eq. 6-6). Finally, the principal of virtual works of (Eq. 6-8) or couple stress theory of Cosserat is formed as:

$$\int_S [T_i \delta U_i + Q_i \delta \Theta_i] \, dS = \int_\Omega [\sigma_{ij}\delta\gamma_{ji} + \mu_{ij}\delta\kappa_{ji}] \, d\Omega \qquad (6\text{-}9)$$

6.1.1.3 *Mindlin's gradient theories (1964, 1965)*

Mindlin (1964), proposed an enhanced general elastic theory to describe linear elastic behavior of isotropic materials with microstructural effects. This was accomplished by considering *the potential energy density as a quadratic form not only of strains but also of gradient of strains* and the *kinetic energy density as a quadratic form of both velocities and gradient of velocities*. However, the use of higher order gradients in the expressions of potential and kinetic energy introduces 16 new intrinsic constants which are very difficult to be determined theoretically or experimentally, thus rendering the new enhanced elastic theory very complicated from physical and mathematical point of view.

In order to make things simpler Mindlin proposed three simplified versions of his theory, known as ***Form I, II and III***, utilizing in the final constitutive equations only two material and five internal length scale constants instead of eighteen employed in his initial model.

- **In Form I**: the strain energy density function (W) is assumed to be a quadratic form of the classical strains and the second gradient of displacement.
- **In Form-II**: the second gradient displacement is replaced by the gradient of strains.
- **In Form-III**: the strain energy function is written in terms of the strain, the gradient of rotation, and the fully symmetric part of the gradient of strain.

Although, three forms are identical and conclude to the same equation of motion, in ***Form- II,*** *the total stresses are symmetric and problems associated with non-symmetric stress tensors as in the case of couple stresses theories are avoided.* Thus, among the aforementioned enhanced elastic theories, *Form-II strain gradient elastic theory of Mindlin is the only with symmetric stresses as in classical elasticity.*

One year later, Mindlin (1965) proposed his "second gradient elastic theory" where**,** *the potential energy density is a quadratic form not only of strains and gradient of strains, as in his first gradient theory, but also of the second gradient of strains.* In the classical higher order strain gradient theory, the strain energy density, W depends on both conventional strain, ε_{ij} (symmetric part of first order deformation gradient) and on the second order deformation gradient, η_{ijk}:

$$W = W(\varepsilon_{ij}, \eta_{ijk}) \tag{6-10}$$

Where, $\varepsilon_{ij} = \frac{1}{2}(\partial_i u_j + \partial_j u_i)$ and $\eta_{ijk} = \partial_{ij} u_k$ are the strain tensor and second order deformation gradient tensor respectively. ∂_i is forward gradient operator and u_i is displacement vector. The Cauchy stress tensor, σ_{ij} and double stress tensor, τ_{ijk} are conjugated with strain tensor and second order deformation tensor via

$$\sigma_{ij} = \frac{\partial W}{\partial \varepsilon_{ij}} \quad ; \quad \tau_{ijk} = \frac{\partial W}{\partial \eta_{ijk}} \tag{6-11}$$

The variation of total strain energy in the volume V of the body can be written as:

$$\int_V \delta W \; dV = \int_S [\sigma_{ij} \delta \varepsilon_{ij} + \tau_{ijk} \delta \eta_{ijk}] \; dV \tag{6-12}$$

For linear elastic isotropic materials, Mindlin (1965) defined the density of strain energy as:

$$W = \frac{1}{2}\lambda \varepsilon_{ii}\varepsilon_{jj} + \mu \varepsilon_{ij}\varepsilon_{ij} + a_1 \eta_{ijj}\eta_{ikk} + a_2 \eta_{iik}\eta_{kjj} + a_3 \eta_{iik}\eta_{jjk} + a_4 \eta_{ijk}\eta_{ijk} + a_5 \eta_{ijk}\eta_{kji} \tag{6-13}$$

Where, λ and μ are the conventional Lamé constants, corresponding to the two invariants of the strain., and $a_n (n = 1 \ldots . 5)$ are the five additional second order elastic constants corresponding to the invariants of the second deformation gradients. The energy density relation contains cross terms for both stretch and rotation gradients in the strain energy density. For more details refer article [L2].

6.1.1.4 *Eringen nonlocal elasticity model*

According to the Eringen model (see Eringen, 1972; Eringen et al., 1977 and Polizotto, 2001), in the framework of nonlocal elasticity (integral type), the long range forces arising in linear (macroscopic) homogenous isotropic elastic materials as a consequence of a strain field, $\boldsymbol{\varepsilon}(\boldsymbol{x}) = \{\varepsilon_{ij}(\boldsymbol{x})\}$, are described by the stress field $\boldsymbol{\sigma}(\boldsymbol{x}) = \{\sigma_{ij}(\boldsymbol{x})\}$, given by:

$$\boldsymbol{\sigma}(\boldsymbol{x}) = \int_V A(\boldsymbol{x}, \boldsymbol{x}') \boldsymbol{D} \; : \boldsymbol{\varepsilon}(\boldsymbol{x}') dV' \quad \forall \boldsymbol{x} \in V \tag{6-14}$$

Where, V is the domain occupied by the material, $dV' = dV\,(\boldsymbol{x}')$, $\boldsymbol{D} = D_{ijkl}$ is the moduli fourth-order tensor of local (homogenous) isotropic elasticity, i.e.

$$D_{ijkl} = \lambda \delta_{ij}\delta_{kl} + \mu(\delta_{ik}\delta_{jl} + \delta_{il}\delta_{jk}) \tag{6-15}$$

Where, λ and μ being the Lamé constants and δ_{ij}, the Kronecker symbol. The scalar function, A is the *influence function, or attenuation function*, related to the nonlocality effects of the (local) strain, a function of Euclidean distance between the source $(\boldsymbol{x}')$ and field $(\boldsymbol{x})$ points, i.e $A = a(r)$ with $r = |\boldsymbol{x}' - \boldsymbol{x}|$. $a(r)$, that is the *attenuation function* in terms of distance, r, is nonnegative and

decays more or less rapidly with increasing r, i.e. $a(r) \to 0$ for $r \to \infty$, but in practice $a(r) \cong 0$ for $r \geq R$, where R is the (finite) *influence distance*. The material stress response $\boldsymbol{\sigma}(\boldsymbol{x})$ of the Eq. (6-14) is referred to as the nonlocal stress, i.e., it is a functional of the local strain, $\boldsymbol{\varepsilon}$, that is, it is expressed as a weighted value of the strain field $\boldsymbol{\varepsilon}(\boldsymbol{x})$ over V.

The attenuation characteristics of the attenuation function $a(r)$, makes sense in relation to *the material internal length scale*, l, i.e., $a = a(\mathcal{R})$, $\mathcal{R} = r/l$ .The *material internal length scale* parameter, l is a positive more or less rapidly decreasing function, such that $a(\mathcal{R}) \cong 0$ for $\mathcal{R} \gg 1$, but $a(\mathcal{R}) \neq 0$ for $\mathcal{R} \leq 1$, or of the same magnitude as 1. The distance r is whether large or small, is only relatively to l. At small distances ($r \cong 0$), the attenuation is moderate and the nonlocality effects can diffuse almost unaltered, whereas at large distances, the attenuation is moderate and the nonlocality effects are sensibly reduced. An essential requisite of the attenuation function arises from the fact that for $l \to 0$, i.e in the limit of local elastic material behavior, the *attenuation function a* must correspondingly become a Direc delta, i.e. $a(r/l) \to \Delta(r)$, and this case, the nonlocal elasticity of Eq. (6-14) transforms into local one, i.e. $\boldsymbol{\sigma} = \boldsymbol{D} : \boldsymbol{\varepsilon}$. To achieve the latter result, it is required to impose the normalization condition:

$$\int_{V_\infty} A(|\boldsymbol{x}' - \boldsymbol{x}|/l)\ dV' = 1 \qquad \textit{(6-16)}$$

In which, V_∞ is the infinite domain embedding V, if V is finite. The major limitation of the model is that it is only applicable for homogenous elastic material, and hence cannot be applied in practical non-homogenous materials.

Later, Polizotto et al., (2001, 2003, 2004, 2006) extended the Eringen's model (in order to curb the limitations of the model, i.e. primarily homogeneity, infinite domain, numerical instability and mesh sensitivity in the solution of boundary value problems), where the energy residual has been evaluated and interpreted as for its thermodynamic role and also addressed nonlocal model for (macroscopically) inhomogenous elastic material, in which stress is the superimposition of two contributions, one coinciding with the local stress, the other is of nonlocal in nature, given by a weighing formula operating on the strain difference. Refer also Pisano et al., (2009) for more details.

6.1.2 Non-local Finite Element Approaches using continuum non-local models

Using the previously discussed non-local theories, many researchers have solved complex 2D and 3D problems involving non-local effects (like cracks, damage, microbuckling, etc.,) occurring at microstructural scale, by implementing the Finite Element (FE) techniques. The finite element implementation of ''strain-gradient'' constitutive models has been the subject of several publications, for instance refer [(Borst et al., 1992, 1996), (Hermann, 1983), (Sternberg and Muki, 1996), (Xia and Hutchinson, 1998), (Zhang et al., 1998)]. Out of many FE implementations and new developments, only few important ones are discussed here. Shu, Fleck et al., (1999), in order to account for strain gradient effects (nonlocality), developed a new set of 2D Finite Elements (C^0-continuous of mixed type- triangular and quadrilateral) to solve the problems using Fleck and Hutchinson (Fleck and Hutchinson, 1997) strain gradient plasticity theory (theory within Toupin-Mindlin framework), where they introduced extra nodal degrees of freedom (D.O.F) along with displacements, and termed as relaxed displacement gradients and the kinematic constraints

between displacement and strain is enforced by using *Lagrange Multipliers*. However, after testing the elements for some boundary value problems, they concluded the limitations of each elements. Similar type of Finite element (mixed type formulation-2D), is developed later by Amanatidou and Aravas (Amanatidou and Aravas, 2002) using Mindlin theories: ‘‘Type I’’ and ‘‘Type III’’ (Mindlin, 1964, 1965), where displacement and the displacement gradients are used as independent unknowns and their relationship is enforced in an ‘‘integral-sense’’ and also they developed new variational formulation which can be used for both linear and non-linear strain-gradient elasticity theories. Following, in the year 2006, Yueguang (Yueguang, 2006), developed a new FE method, based on new variational formulation, using Fleck and Hutchinson (Fleck and Hutchinson, 1997) strain gradient plasticity theory (compressible version) to solve mainly elastic-plastic fracture problems (analyse modes of crack). 3 noded isoparametric triangular elements are used (C^1-continuous type element), where displacements are interpolated using cubic polynomials and derived a new set of cubic shape functions. This new FE concerns only on the displacement gradient terms, and is not related directly to the displacements, so that the new finite element method solutions directly supply the strains, stresses, higher-order strains and stresses.

With these non-local FE models from literature, several problems like simple modal problem, crack (mode I, II and III) and plate with hole are analyzed well, but is limited to only 2D and to solve certain set of problems, cannot be used to study complex structures and phenomenon due to convergence issues. However, it gives an idea about the importance of application of continuum non-local models towards solving gradient related problems and their implementation within the framework of finite elements.

With the understanding and motivation of all these non-local theories and its implementation in various problems, the following sections are dedicated to the development of theoretical and numerical formulation of generalized homogenous non-local model in order to study the compressive behavior of unidirectional and woven composites.

6.2 Theoretical part

Let us consider Eq. 3.6:

$$-\int_{\Omega}\Big\{\underbrace{fE_f r_{gf}^2 v''\delta v''}_{\text{I}}+\underbrace{\mathbf{S}\cdot\delta\boldsymbol{\gamma}}_{\text{II}}\Big\}d\Omega+\underbrace{\langle\mathbf{F},\delta\mathbf{u}\rangle}_{\text{III}}=0\quad\forall\,\delta\mathbf{u}, \tag{6-17}$$

From the above equation, it is understood that, it takes into account only the transverse fiber curvature field along only one direction (UD) as shown in the following figure:

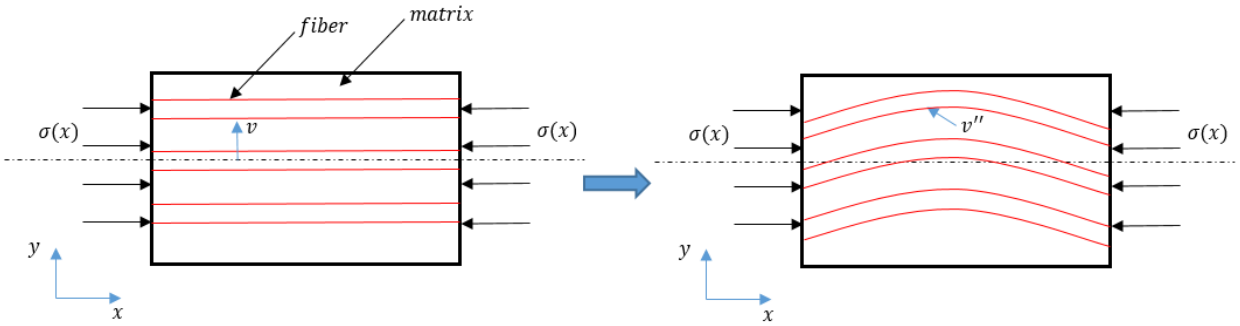

The energy of local bending corresponds to the first term in (Eq. 6-17). This term has been obtained by Gardin et al., [G2] with an asymptotic development. But it is very restrictive, and corresponds to just UD ply under compression. Therefore, it is necessary to extend the model for more general realistic case, taking into account the fiber curvature field in more complex mesostructure, for example: 2D and 3D woven, where fiber curvature field is not only restricted in one direction, but are randomly oriented in multiple directions, during compression or torsion-compression, as shown in fig below:

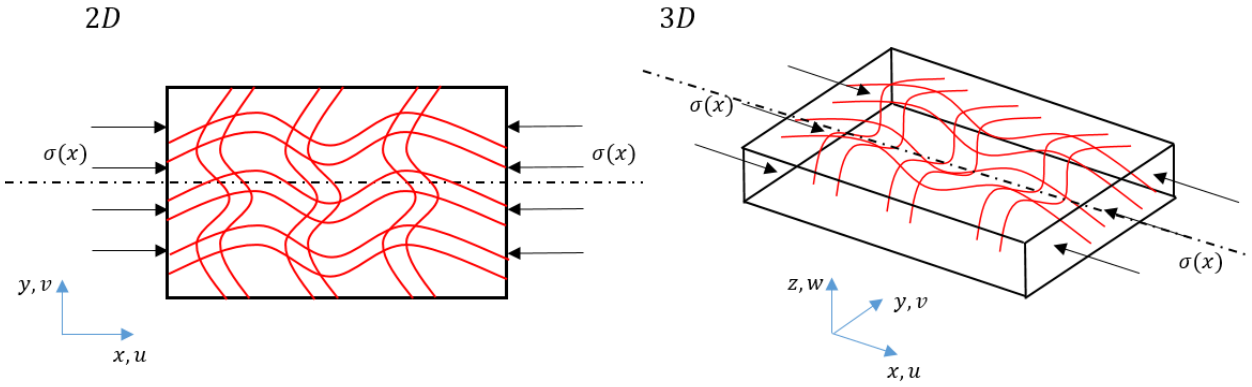

In the Mindlin's strain gradient theory (Form II), curvatures (second gradient of the displacement field) and strain generate an energy of deformation (see Eq. 6-12). Hence it is much more convenient to use this theory to develop our nonlocal model.

The kinematics is defined by the displacement field (classical), $\boldsymbol{u} = u(x,y,z)\boldsymbol{e}_1 + v(x,y,z)\boldsymbol{e}_2 + w(x,y,z)\boldsymbol{e}_3$ and the generalized fiber curvature field is defined by, $\boldsymbol{\kappa}$:

a) 2D

$$\boldsymbol{\kappa} = \left[\frac{\partial^2 u}{\partial x^2}, \frac{\partial^2 u}{\partial y^2}, \frac{\partial^2 u}{\partial x \partial y}, \frac{\partial^2 v}{\partial x^2}, \frac{\partial^2 v}{\partial y^2}, \frac{\partial^2 v}{\partial x \partial y}\right]_{2D}$$

b) 3D

$$\boldsymbol{\kappa} = \left[\frac{\partial^2 u}{\partial x^2}, \frac{\partial^2 u}{\partial y^2}, \frac{\partial^2 u}{\partial z^2}, \frac{\partial^2 u}{\partial x \partial y}, \frac{\partial^2 u}{\partial x \partial z}, \frac{\partial^2 u}{\partial y \partial z}, \frac{\partial^2 v}{\partial x^2}, \frac{\partial^2 v}{\partial y^2}, \frac{\partial^2 v}{\partial z^2}, \frac{\partial^2 v}{\partial x \partial y}, \frac{\partial^2 v}{\partial x \partial z}, \frac{\partial^2 v}{\partial y \partial z}, \frac{\partial^2 w}{\partial x^2}, \frac{\partial^2 w}{\partial y^2}, \frac{\partial^2 w}{\partial z^2}, \frac{\partial^2 w}{\partial x \partial y}, \frac{\partial^2 w}{\partial x \partial z}, \frac{\partial^2 w}{\partial y \partial z}\right]_{3D}$$

The new variables, $\boldsymbol{\kappa} = \kappa_{ijk}$, *the fiber curvature field or higher order bending strains* in multiple directions and $\overline{\overline{\boldsymbol{C_f}}} = C_{f_{\boldsymbol{ijklmn}}}$, *the local fiber bending stiffness matrix* (6th order) are introduced, depends on the complex mesostructure. With an assumption of small displacement or taking into account only linear part of the Green Lagrange strain, i.e. $\boldsymbol{\varepsilon} = \frac{1}{2}[\nabla \boldsymbol{u} + \nabla \boldsymbol{u}^T]$, the new variational formulation of homogenized non-local numerical model in order to assess microbuckling problem at mesoscopic scale is written as:

$$-\int_{\Omega \to 3D} \left\{ \overline{\overline{\boldsymbol{C}_f}}\, \boldsymbol{\kappa}\, \delta\boldsymbol{\kappa} + \boldsymbol{S} : \delta\boldsymbol{\varepsilon} \right\} d\Omega + \langle \boldsymbol{F} \cdot (\delta\boldsymbol{u}\,, \delta\boldsymbol{\kappa}) \rangle = 0 \qquad \forall \delta\boldsymbol{u}, \forall \delta\boldsymbol{\kappa} \tag{6-18}$$

The above equation is also written as:

$$-\int_{\Omega \to 3D} \{ \boldsymbol{\zeta} \cdot \delta\boldsymbol{\kappa} + \boldsymbol{S} : \delta\boldsymbol{\varepsilon} \} d\Omega + \langle \boldsymbol{F} \cdot (\delta\boldsymbol{u}\,, \delta\boldsymbol{\kappa}) \rangle = 0 \qquad \forall \delta\boldsymbol{u}, \forall \delta\boldsymbol{\kappa} \tag{6-19}$$

Where, $\boldsymbol{\zeta} = \zeta_{ijk} = \overline{\overline{\boldsymbol{C}_f}}\, \boldsymbol{\kappa}$ is distributed bending moment (DBM) due to the fiber curvature fields, which leads to bending of fiber. The fiber bending energy term, $'\boldsymbol{\zeta} \cdot \delta\boldsymbol{\kappa} = \overline{\overline{\boldsymbol{C}_f}}\, \boldsymbol{\kappa}\, \delta\boldsymbol{\kappa}\ '$ can be written in 3D as:

$$\begin{aligned}
[\overline{\overline{\boldsymbol{C}_f}}\, \boldsymbol{\kappa}\, \delta\boldsymbol{\kappa}\ ]_{3D} = {} & A\frac{\partial^2 u}{\partial x^2}\delta\left(\frac{\partial^2 u}{\partial x^2}\right) + B\frac{\partial^2 u}{\partial y^2}\delta\left(\frac{\partial^2 u}{\partial y^2}\right) + C\frac{\partial^2 u}{\partial z^2}\delta\left(\frac{\partial^2 u}{\partial z^2}\right) + D\frac{\partial^2 v}{\partial x^2}\delta\left(\frac{\partial^2 v}{\partial x^2}\right) + E\frac{\partial^2 v}{\partial y^2}\delta\left(\frac{\partial^2 v}{\partial y^2}\right) \\
& + F\frac{\partial^2 v}{\partial z^2}\delta\left(\frac{\partial^2 v}{\partial z^2}\right) + G\frac{\partial^2 w}{\partial x^2}\delta\left(\frac{\partial^2 w}{\partial x^2}\right) + H\frac{\partial^2 w}{\partial y^2}\delta\left(\frac{\partial^2 w}{\partial y^2}\right) + I\frac{\partial^2 w}{\partial z^2}\delta\left(\frac{\partial^2 w}{\partial z^2}\right) \\
& + J\frac{\partial^2 u}{\partial x\partial y}\delta\left(\frac{\partial^2 u}{\partial x\partial y}\right) + K\frac{\partial^2 u}{\partial x\partial z}\delta\left(\frac{\partial^2 u}{\partial x\partial z}\right) + L\frac{\partial^2 u}{\partial y\partial z}\delta\left(\frac{\partial^2 u}{\partial y\partial z}\right) + M\frac{\partial^2 v}{\partial x\partial y}\delta\left(\frac{\partial^2 v}{\partial x\partial y}\right) \\
& + N\frac{\partial^2 v}{\partial x\partial z}\delta\left(\frac{\partial^2 v}{\partial x\partial z}\right) + O\frac{\partial^2 v}{\partial y\partial z}\delta\left(\frac{\partial^2 v}{\partial y\partial z}\right) + P\frac{\partial^2 w}{\partial x\partial y}\delta\left(\frac{\partial^2 w}{\partial x\partial y}\right) + Q\frac{\partial^2 w}{\partial x\partial z}\delta\left(\frac{\partial^2 w}{\partial x\partial z}\right) \\
& + R\frac{\partial^2 w}{\partial y\partial z}\delta\left(\frac{\partial^2 w}{\partial y\partial z}\right)
\end{aligned} \tag{6-20}$$

Where, $A, B, C, D, E, F, G, H, I, J, K, L, M, N, O, P, Q, R$ are the local fiber material parameters contained in local fiber bending stiffness matrix, $\overline{\overline{\boldsymbol{C_f}}}$. These parameters in general can also be called as non-local mesoscopic material parameters. Berkache, Ganghoffer et al., [B14] has proposed a methodology to identify these parameters with respect to Representative Volume Element (RVE) of woven materials. The identification protocol of these parameters will be discussed in following chapters.

6.2.1 Principle of virtual work and equilibrium equations (2D)

For the convenience of the derivation, let us rewrite curvatures ($\boldsymbol{\kappa} = \kappa_{ijk}$) as:

$$\frac{\partial^2 u}{\partial x^2} = u_{1,ii}\,;\ \frac{\partial^2 u}{\partial y^2} = u_{1,jj}\,;\ \frac{\partial^2 v}{\partial x^2} = u_{2,ii}\,;\frac{\partial^2 v}{\partial y^2} = u_{2,jj}\,;\ \frac{\partial^2 u}{\partial x\partial y} = u_{1,ij}\ ;\frac{\partial^2 v}{\partial x\partial y} = u_{2,ij}$$

Where, i and j, with (,) denotes the order of partial differentiation.

Let $\delta u_k\ (k = 1,2)$ and $\delta u_{k,ij} (k = 1,2)$ are the virtual displacements, and $\delta\varepsilon_{ij}\,, \delta\kappa_{ijk}$ be the associated virtual strains. After some calculations presented in first appendix(Appendix 13.1), now

using the principle of virtual work (PVW) for case of static analysis, we can write the equilibrium equations (in weak form) of our non-local model for analysis of compressive strength of the composite in 2D as:

$$\Pi = IVW + EVW = 0 \qquad \forall \delta \boldsymbol{u}$$

$$\begin{aligned} IVW = \iint_{\omega} \left[S_{ij,_j} \cdot \delta u_k\right] d\omega - \sum \iint_{\omega} \left[\zeta_{ijk,_{ji}} \cdot \delta u_k\right] d\omega + \\ \left\{ - \oint_S \left[S_{ij} \cdot n_j \cdot \delta u_k\right] dS + \sum \oint_S \left[\zeta_{ijk,_j} \cdot n_\gamma \cdot \delta u_k\right] dS \right. \\ - \oint_S \left[\zeta_{ijk} \cdot n_\gamma \cdot n_\gamma \left(\frac{\partial \delta u_k}{\partial n}\right)\right] dS + \oint_S \left[\frac{\sum_{i=1}^{8} \partial \zeta_{ti}}{\partial S} \cdot \delta u_k\right] dS \\ \left. - \left[\sum_{i=1}^{8} \zeta_{ti} \ \delta u_k\right]_{(Corners)} \right\} \end{aligned} \qquad (6\text{-}21)$$

$$=$$

$$-\left\{ \iint_{\omega} F_k \cdot \delta u_k \, d\omega + \oint_S f_k \cdot \delta u_k \, dS + \sum \iint_{\omega} M_k \cdot \delta u_{k,_i} \, d\omega + \sum \oint_S m_k \cdot \delta u_{k,_i} \, dS + + \sum P \, \delta u_k \right\}$$

The local equilibrium equations in strong form and the boundary conditions can be written as:

Equilibrium equations (Strong Form):

a) *Domain(ω)*:

$$S_{ij,_j} = -F_k \quad \text{and} \quad \zeta_{ijk,_{ji}} = -\sum M_k \qquad \forall point \ \ on \ \in \omega$$

b) Boundary(S):

$$\begin{aligned} -S_{ij} \cdot n_j &= -f_k && \forall point \ \ on \ \in S \\ \zeta_{ijk} \cdot n_\gamma \cdot n_\gamma &= -C_\tau && \forall point \ \ on \ \in S \\ \zeta_{ijk,_j} \cdot n_\gamma + \frac{\sum_{i=1}^{8} \partial \zeta_{ti}}{\partial S} &= -\sum m_k && \forall point \ \ on \ \in S \end{aligned} \qquad (6\text{-}22)$$

Boundary conditions(BC) on S:

Specify:

$$i) \quad u_k \quad or \quad S_{ij} \cdot n_j$$

$$ii) \quad u_{k,_i} \quad or \quad \zeta_{ijk} \cdot n_\gamma \cdot n_\gamma$$

Where, $k = 1,2 \ \ and \ \ \gamma = i, j.$

For example: Clamped or Encastre at the edge of body

$$u_k = 0 \quad \forall\, point \in S$$

$$u_{k,i} = 0 \quad \forall\, point \in S$$

Where, $k = 1,2$.

Note that, at a *corner*, if $\zeta_{ti}[\delta u_k]_{A^-}^{A^+}$ is non-zero, there must be a concentrated load at the corner with: $P = \sum[\zeta_{ti}(A^+) - \zeta_{ti}(A^-)]$.

6.3 Numerical development

6.3.1 Formulation of new element (for 2D UD ply and woven case)

It is important to note that, the strain gradient quantities are the second order spatial derivatives of displacement, where the interpolation of displacement should exhibit actually, C^1- continuity, i.e. both the displacement and its first order derivatives are required to be continuous across inter-element boundaries. Therefore, the elements having C^1- continuity will be more accurate to capture well the nonlocal effects in the structure.

The Lagrange elements (available in ABAQUS ®) are C^0 type continuous elements. The solution field variable (for ex: displacement,U), which is being approximated in Lagrange type of elements are only continuous between element, but not their derivatives. In order to solve the formulation of microbuckling problem using FEM accurately, it is necessary to have C^1 type continuous element (Hermit type), where the solution of field variables and also its derivatives are necessary. Or in other words using Hermit type elements, the continuity between the elements is not only with the solution of field variable, but also with their derivatives (gradients), so that the microbuckling phenomenon (non-local phenomenon) can be captured well at microscopic level.

Therefore, a new element: Non-Local Super-parametric element (NL U32) is formulated, similar to Bogner-Fox-Schmit Rectangle, BFSR (Bogner et al., 1965) as shown in Figure 57, where the degrees of freedom (D.O.F) of the element is not only the displacements, but also their derivatives. BFSR type element is normally used for buckling analysis of plates. See for instance Pifko et al., (1969) and Naik et al., (2001). This NL U32 is implemented in User Element (UEL) subroutine, which is coded using FORTRAN 77 language for analysis in ABAQUS ®.

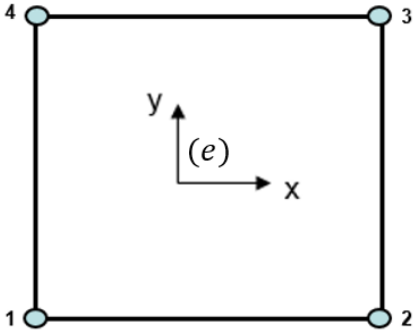

$$Dof, \boldsymbol{d} = \begin{Bmatrix} u \\ \theta_{ux} \\ \theta_{uy} \\ \kappa_{uxy} \\ v \\ \theta_{vx} \\ \theta_{vy} \\ \kappa_{vxy} \end{Bmatrix} = \begin{Bmatrix} u \\ \frac{\partial u}{\partial x} \\ \frac{\partial u}{\partial y} \\ \frac{\partial^2 u}{\partial x \partial y} \\ v \\ \frac{\partial v}{\partial x} \\ \frac{\partial v}{\partial y} \\ \frac{\partial^2 v}{\partial x \partial y} \end{Bmatrix} = \begin{Bmatrix} u \\ u'_x \\ u'_y \\ u'_{xy} \\ v \\ v'_x \\ v'_y \\ v'_{xy} \end{Bmatrix}$$

(8 DOF / node → 32 DOF / Element)

$$\boldsymbol{d}_{(1)} \begin{Bmatrix} \bar{u} = u, \frac{\partial u}{\partial x}, \frac{\partial u}{\partial y}, \frac{\partial^2 u}{\partial x \partial y} \\ \bar{v} = v, \frac{\partial v}{\partial x}, \frac{\partial v}{\partial y}, \frac{\partial^2 v}{\partial x \partial y} \end{Bmatrix}_{(1)}$$

$$\boldsymbol{d} = \sum_{i=1}^{4} \boldsymbol{d}_i$$

Figure 57: Non-Local Super-parametric element (NL U32)

- **Interpolation functions:**
  (a) Displacement: Complete 3rd order cubic polynomial is chosen.

$$\boldsymbol{U(x,y)} \cong \boldsymbol{u_h(x,y)} = \boldsymbol{v_h(x,y)} = c_1 + c_2x + c_3y + c_4x^2 + c_5xy + +c_6y^2 + c_7x^3 + c_8x^2y + c_9xy^2 + c_{10}y^3 + c_{11}x^3y + c_{12}x^2y^2 + c_{13}xy^3 + c_{14}x^3y^2 + c_{15}x^2y^3 + c_{16}x^3y^3$$

$$\boldsymbol{u}_h(\xi,\eta) \cong \sum_{i=1}^{16} N_i^{(e)}(\xi,\eta)\,\bar{\boldsymbol{u}}_i$$

$$\boldsymbol{v}_h(\xi,\eta) \cong \sum_{i=1}^{16} N_i^{(e)}(\xi,\eta)\,\bar{\boldsymbol{v}}_i$$

Where, $\bar{u}_i = \begin{Bmatrix} u_1 \\ u_{1,x} \\ u_{1,y} \\ u_{1,xy} \\ , \\ , \\ , \\ . \\ . \\ . \\ u_{16,xy} \end{Bmatrix}$; $\bar{v}_i = \begin{Bmatrix} v_1 \\ v_{1,x} \\ v_{1,y} \\ v_{1,xy} \\ , \\ , \\ , \\ . \\ . \\ . \\ v_{16,xy} \end{Bmatrix}$

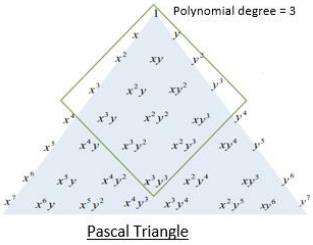

Shape functions

- Obtained using 1D cubic Hermit type polynomials:

$$H_{01}(\xi) = 1 - 3\left(\frac{\xi+1}{2}\right)^2 + 2\left(\frac{\xi+1}{2}\right)^3 \qquad H_{01}(\eta) = 1 - 3\left(\frac{\eta+1}{2}\right)^2 + 2\left(\frac{\eta+1}{2}\right)^3$$

$$H_{02}(\xi) = 3\left(\frac{\xi+1}{2}\right)^2 - 2\left(\frac{\xi+1}{2}\right)^3 \qquad H_{02}(\eta) = 3\left(\frac{\eta+1}{2}\right)^2 - 2\left(\frac{\eta+1}{2}\right)^3$$

$$H_{11}(\xi) = \left(\frac{\xi+1}{2}\right) - 2\left(\frac{\xi+1}{2}\right)^2 + \left(\frac{\xi+1}{2}\right)^3 \qquad H_{11}(\eta) = \left(\frac{\eta+1}{2}\right) - 2\left(\frac{\eta+1}{2}\right)^2 + \left(\frac{\eta+1}{2}\right)^3$$

$$H_{12}(\xi) = \left(\frac{\xi+1}{2}\right)^3 - \left(\frac{\xi+1}{2}\right)^2 \qquad H_{12}(\eta) = \left(\frac{\eta+1}{2}\right)^3 - \left(\frac{\eta+1}{2}\right)^2$$

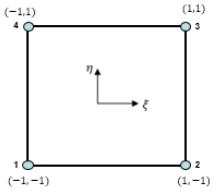

$$N_j = [H_{0i}(\xi)H_{0i}(\eta),\quad H_{1i}(\xi)H_{0i}(\eta),\quad H_{0i}(\xi)H_{1i}(\eta),\quad H_{0i}(\xi)H_{1i}(\eta),]\ ;\ \begin{matrix} j = 1,\dots 16 \\ i = 0,1,2 \end{matrix}$$

$$\downarrow$$

$$N_1 = H_{01}(\xi)\ H_{01}(\eta) = \left[1 - 3\left(\frac{\xi+1}{2}\right)^2 + 2\left(\frac{\xi+1}{2}\right)^3\right]\left[1 - 3\left(\frac{\eta+1}{2}\right)^2 + 2\left(\frac{\eta+1}{2}\right)^3\right]$$

$$N_2 = H_{11}(\xi)\ H_{01}(\eta) = \left[\left(\frac{\xi+1}{2}\right) - 2\left(\frac{\xi+1}{2}\right)^2 + \left(\frac{\xi+1}{2}\right)^3\right]\left[1 - 3\left(\frac{\eta+1}{2}\right)^2 + 2\left(\frac{\eta+1}{2}\right)^3\right]$$

$$N_3 = H_{01}(\xi)\ H_{11}(\eta) = \left[1 - 3\left(\frac{\xi+1}{2}\right)^2 + 2\left(\frac{\xi+1}{2}\right)^3\right]\left[\left(\frac{\eta+1}{2}\right) - 2\left(\frac{\eta+1}{2}\right)^2 + \left(\frac{\eta+1}{2}\right)^3\right]$$

$$N_4 = H_{11}(\xi)\ H_{11}(\eta) = \left[\left(\frac{\xi+1}{2}\right) - 2\left(\frac{\xi+1}{2}\right)^2 + \left(\frac{\xi+1}{2}\right)^3\right]\left[\left(\frac{\eta+1}{2}\right) - 2\left(\frac{\eta+1}{2}\right)^2 + \left(\frac{\eta+1}{2}\right)^3\right]$$

$$N_5 = H_{02}(\xi)\ H_{01}(\eta) = \left[3\left(\frac{\xi+1}{2}\right)^2 - 2\left(\frac{\xi+1}{2}\right)^3\right]\left[1 - 3\left(\frac{\eta+1}{2}\right)^2 + 2\left(\frac{\eta+1}{2}\right)^3\right]$$

$$N_6 = H_{12}(\xi)\ H_{01}(\eta) = \left[\left(\frac{\xi+1}{2}\right)^3 - \left(\frac{\xi+1}{2}\right)^2\right]\left[1 - 3\left(\frac{\eta+1}{2}\right)^2 + 2\left(\frac{\eta+1}{2}\right)^3\right]$$

$$N_7 = H_{02}(\xi)\ H_{11}(\eta) = \left[3\left(\frac{\xi+1}{2}\right)^2 - 2\left(\frac{\xi+1}{2}\right)^3\right]\left[\left(\frac{\eta+1}{2}\right) - 2\left(\frac{\eta+1}{2}\right)^2 + \left(\frac{\eta+1}{2}\right)^3\right]$$

$$N_8 = H_{12}(\xi)\ H_{11}(\eta) = \left[\left(\frac{\xi+1}{2}\right)^3 - \left(\frac{\xi+1}{2}\right)^2\right]\left[\left(\frac{\eta+1}{2}\right) - 2\left(\frac{\eta+1}{2}\right)^2 + \left(\frac{\eta+1}{2}\right)^3\right]$$

$$N_9 = H_{02}(\xi)\ H_{02}(\eta) = \left[3\left(\frac{\xi+1}{2}\right)^2 - 2\left(\frac{\xi+1}{2}\right)^3\right]\left[3\left(\frac{\eta+1}{2}\right)^2 - 2\left(\frac{\eta+1}{2}\right)^3\right]$$

$$N_{10} = H_{12}(\xi)\ H_{02}(\eta) = \left[\left(\frac{\xi+1}{2}\right)^3 - \left(\frac{\xi+1}{2}\right)^2\right]\left[3\left(\frac{\eta+1}{2}\right)^2 - 2\left(\frac{\eta+1}{2}\right)^3\right]$$

$$N_{11} = H_{02}(\xi)\ H_{12}(\eta) = \left[3\left(\frac{\xi+1}{2}\right)^2 - 2\left(\frac{\xi+1}{2}\right)^3\right]\left[\left(\frac{\eta+1}{2}\right)^3 - \left(\frac{\eta+1}{2}\right)^2\right]$$

$$N_{12} = H_{12}(\xi)\ H_{12}(\eta) = \left[\left(\frac{\xi+1}{2}\right)^3 - \left(\frac{\xi+1}{2}\right)^2\right]\left[\left(\frac{\eta+1}{2}\right)^3 - \left(\frac{\eta+1}{2}\right)^2\right]$$

$$N_{13} = H_{01}(\xi)\ H_{02}(\eta) = \left[1 - 3\left(\frac{\xi+1}{2}\right)^2 + 2\left(\frac{\xi+1}{2}\right)^3\right]\left[3\left(\frac{\eta+1}{2}\right)^2 - 2\left(\frac{\eta+1}{2}\right)^3\right]$$

$$N_{14} = H_{11}(\xi)\ H_{02}(\eta) = \left[\left(\frac{\xi+1}{2}\right) - 2\left(\frac{\xi+1}{2}\right)^2 + \left(\frac{\xi+1}{2}\right)^3\right]\left[3\left(\frac{\eta+1}{2}\right)^2 - 2\left(\frac{\eta+1}{2}\right)^3\right]$$

$$N_{15} = H_{01}(\xi)\ H_{12}(\eta) = \left[1 - 3\left(\frac{\xi+1}{2}\right)^2 + 2\left(\frac{\xi+1}{2}\right)^3\right]\left[\left(\frac{\eta+1}{2}\right)^3 - \left(\frac{\eta+1}{2}\right)^2\right]$$

$$N_{16} = H_{11}(\xi)\ H_{12}(\eta) = \left[\left(\frac{\xi+1}{2}\right) - 2\left(\frac{\xi+1}{2}\right)^2 + \left(\frac{\xi+1}{2}\right)^3\right]\left[\left(\frac{\eta+1}{2}\right)^3 - \left(\frac{\eta+1}{2}\right)^2\right]$$

The obtained shape functions correspond to 16 D.O.F of the element. For detailed formulation of shape functions refer for instance (Bogner et al., 1965).

(b) Geometry: Complete 2nd order biquadratic polynomial is chosen.

$$x \cong \sum_{j=1}^{9} N_j^{(e)}(\xi,\eta)x_i \quad ; \quad y \cong \sum_{j=1}^{9} N_j^{(e)}(\xi,\eta)$$

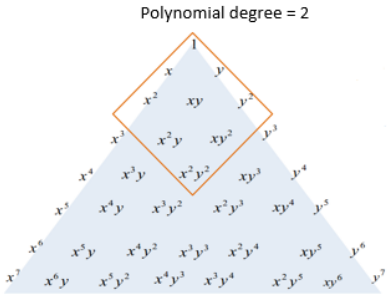

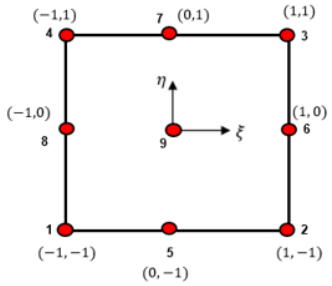

Shape functions

$$N_1 = \frac{1}{4}\xi(1-\xi)\eta(1-\eta) \quad ; \quad N_5 = -\frac{1}{2}(1+\xi)(1-\xi)(1-\eta)\eta$$
$$N_2 = -\frac{1}{4}\xi(1+\xi)\eta(1-\eta) \quad ; \quad N_6 = \frac{1}{2}\xi(1+\xi)(1+\eta)(1-\eta)$$
$$N_3 = \frac{1}{4}\xi(1+\xi)\eta(1+\eta) \quad ; \quad N_7 = \frac{1}{2}(1+\xi)(1-\xi)(1+\eta)\eta$$
$$N_4 = -\frac{1}{4}\xi(1-\xi)\eta(1+\eta) \quad ; \quad N_8 = -\frac{1}{2}\xi(1-\xi)(1-\eta)(\eta+1)$$

$$N_9 = (1-\xi^2)(1-\eta^2)$$

Note that as discussed earlier, element formulated here is *'Super-parametric', not 'iso-parametric', in which the interpolation functions/shape functions for field variable (displacement) and geometry are same.*

And finally using the above formulations, equilibrium equations will be solved for the element to obtain the solutions of unknown field variables, contained in $\bar{\boldsymbol{d}}$:

$$\boldsymbol{K_{ij}^{(e)}} = \iint_{A^{(e)}} \boldsymbol{B_i^T D B_j}\, \boldsymbol{dx\, dy} = \int_{-1}^{1}\int_{-1}^{1} \boldsymbol{B_i^T(\xi,\eta) D B_i(\xi,\eta)}\left|\boldsymbol{J^{(e)}}\right| \boldsymbol{d\xi\, d\eta}\ ;$$

$$\boldsymbol{f_i^{(e)}} = \iint_{A^{(e)}} \boldsymbol{N_i^T F}\, \boldsymbol{dx\, dy} = \int_{-1}^{1}\int_{-1}^{1} \boldsymbol{N_i^T F}\left|\boldsymbol{J^{(e)}}\right| \boldsymbol{d\xi\, d\eta}\ ; \qquad \textit{(6-23)}$$

$$\bar{\bar{\boldsymbol{K}}}\,\bar{\boldsymbol{d}} = \bar{\boldsymbol{f}}$$

i=1...n and j=1..n

Where, $\bar{\bar{\boldsymbol{K}}}$ is global stiffness matrix, $\bar{\boldsymbol{d}}$ is D.O.F vector, which contains unknown displacements and derivatives, whose solution is to be obtained, $\bar{\boldsymbol{f}}$ is force vector, $\boldsymbol{B}$ is the strain matrix, $\boldsymbol{N}$ is the shape function matrix, $\boldsymbol{D}$ corresponds to 4th order constitutive matrix and $\boldsymbol{J}^{(e)}$ corresponds to Jacobian matrix or Jacobi, where physically it relates the quantities/derivatives wrote in the natural/local/parametric coordinate space and the real/global coordinate space. Or in continuum mechanics, Jacobian matrix is Jacobi is an operator that maps the quantities written in current configuration to reference configuration. The $\det(\boldsymbol{J}^{(e)})$ *or* $\left|\boldsymbol{J}^{(e)}\right|$ *or* $J^{(e)}$ is the determinant of Jacobi matrix, $\boldsymbol{J}^{(e)}$, which relates the local stretching/area/volume of the parametric space required to fit onto the global space. Integrals are solved using *Gaussian quadrature rule*.

It is to be noted that, before proceeding to develop UEL subroutine for our non-local element (NL U32), as a part of practice and in order to understand clearly about developing UEL subroutines for performing analysis in ABAQUS®, "*a simple 2D Plane stress linear rectangular element of type (U4)"* similar to ABAQUS® Plane stress element (CPS4) is developed and compared the results (see Appendix section 13.2).

6.3.2 FE Formulation of Non-local model implemented in NL U32

Consider Eq. (6-17),

$$-\int_{\Omega\to 2D}\{\boldsymbol{\zeta}\cdot\delta\boldsymbol{\kappa}\ +\boldsymbol{S}:\delta\boldsymbol{\varepsilon}\}d\Omega+\langle\boldsymbol{F}\cdot(\delta\boldsymbol{u}\,,\delta\boldsymbol{\kappa})\,\rangle=0\qquad\forall\delta\boldsymbol{u}\,,\forall\delta\boldsymbol{\kappa} \tag{6-24}$$

By expanding and neglecting the normal and corner terms, the above equation is written as:

$$\begin{aligned}-\int_{\Omega\to 2D}\{\overline{\overline{\boldsymbol{C_f}}}\,\boldsymbol{\kappa}\,\delta\boldsymbol{\kappa}\ +\ \bar{\bar{\boldsymbol{D}}}\,\boldsymbol{\varepsilon}\ :\ \delta\boldsymbol{\varepsilon}\}d\Omega&\\ =\ \int_{\Omega\to 2D}\boldsymbol{f}_b\ \delta\boldsymbol{u}^T d\Omega+\int_S\boldsymbol{f}_S\ \delta\boldsymbol{u}^T\,dS+\int_{\Omega\to 2D}\boldsymbol{M}_b\ (\delta\boldsymbol{u}')^T d\Omega&\\ +\ \int_S\boldsymbol{M}_S\ (\delta\boldsymbol{u}')^T\,dS\quad\forall\delta\boldsymbol{u}&\end{aligned} \tag{6-25}$$

Where, $\bar{\bar{\boldsymbol{D}}}$ is the 4th order constitutive matrix, 6th order local fiber bending stiffness matrix, $\overline{\overline{\boldsymbol{C_f}}}$ is a diagonal matrix of size (6x6), $\boldsymbol{M}_b$ and $\boldsymbol{M}_S$ are the '*moments*' acting on the body and at the surface/edge and derivatives of displacement or deflection, $\boldsymbol{u}'=\left[\frac{\partial u}{\partial x},\frac{\partial u}{\partial y},\frac{\partial^2 u}{\partial x\partial y},\frac{\partial v}{\partial x},\frac{\partial v}{\partial y},\frac{\partial^2 v}{\partial x\partial y}\right]^{\boldsymbol{T}}$.

Let $\boldsymbol{d}^{(e)}$ be the DOF vector of the element and $\boldsymbol{N}$, the shape function vector for displacement which was developed in the previous sections, then:

$$\begin{gathered}\boldsymbol{u}\cong\boldsymbol{N}\,\boldsymbol{d}^{(e)}\,;\\ \boldsymbol{u}'\cong\boldsymbol{N}'\,\boldsymbol{d}^{(e)}\,;\\ \boldsymbol{\varepsilon}\ \cong\boldsymbol{B}\,\boldsymbol{d}^{(e)}\,;\quad\boldsymbol{B}=B_{ij}=[\boldsymbol{D}]\,\boldsymbol{N}\,;\end{gathered} \tag{6-26}$$

Where, $[\boldsymbol{D}]$ is a derivative operator.

$$\boldsymbol{\kappa} \cong \boldsymbol{B'}\, \boldsymbol{d}^{(e)}$$

Now substituting above approximations in Eq. (6-25), we get system of equations as:

$$\begin{aligned} -\int_{\Omega\to 2D} \left\{\overline{\overline{\boldsymbol{C_f}}}\, \boldsymbol{B'}\, \boldsymbol{d}^{(e)}\, (\boldsymbol{B'})^T \left(\delta \boldsymbol{d}^{(e)}\right)^T + \overline{\overline{\boldsymbol{D}}}\, \boldsymbol{B}\, \boldsymbol{d}^{(e)}\, \boldsymbol{B}^T \left(\delta \boldsymbol{d}^{(e)}\right)^T\right\} d\Omega \\ = \int_{\Omega\to 2D} \boldsymbol{f}_b\, \boldsymbol{N}^T \left(\delta \boldsymbol{d}^{(e)}\right)^T d\Omega + \int_S \boldsymbol{f}_S\, \boldsymbol{N}^T \left(\delta \boldsymbol{d}^{(e)}\right)^T dS \\ + \int_{\Omega\to 2D} \boldsymbol{M}_b\, (\boldsymbol{N'})^T \left(\delta \boldsymbol{d}^{(e)}\right)^T d\Omega + \int_S \boldsymbol{M}_S\, (\boldsymbol{N'})^T \left(\delta \boldsymbol{d}^{(e)}\right)^T dS \qquad \forall \delta \boldsymbol{u} \end{aligned} \tag{6-27}$$

Now taking out the common term, $\left(\delta \boldsymbol{d}^{(e)}\right)^T$, we can obtain the final system of equations to be solved as:

$$\begin{aligned} \left(\delta \boldsymbol{d}^{(e)}\right)^T \Bigg\{ -\int_{\Omega\to 2D} \left\{\overline{\overline{\boldsymbol{C_f}}}\, \boldsymbol{B'}\, \boldsymbol{d}^{(e)}\, (\boldsymbol{B'})^T + \overline{\overline{\boldsymbol{D}}}\, \boldsymbol{B}\, \boldsymbol{d}^{(e)}\, \boldsymbol{B}^T\right\} d\Omega - \int_{\Omega\to 2D} \boldsymbol{f}_b\, \boldsymbol{N}^T\, d\Omega - \int_S \boldsymbol{f}_S\, \boldsymbol{N}^T\, dS \\ - \int_{\Omega\to 2D} \boldsymbol{M}_b\, (\boldsymbol{N'})^T\, d\Omega - \int_S \boldsymbol{M}_S\, (\boldsymbol{N'})^T\, dS \Bigg\} = 0 \end{aligned}$$

Or,

$$\begin{aligned} -\int_{\Omega\to 2D} \left\{\overline{\overline{\boldsymbol{C_f}}}\, \boldsymbol{B'}\, (\boldsymbol{B'})^T + \overline{\overline{\boldsymbol{D}}}\, \boldsymbol{B}\, \boldsymbol{B}^T\right\} \boldsymbol{d}^{(e)}\, d\Omega \\ = \int_{\Omega\to 2D} \boldsymbol{f}_b\, \boldsymbol{N}^T\, d\Omega + \int_S \boldsymbol{f}_S\, \boldsymbol{N}^T\, dS + \int_{\Omega\to 2D} \boldsymbol{M}_b\, (\boldsymbol{N'})^T\, d\Omega + \int_S \boldsymbol{M}_S\, (\boldsymbol{N'})^T\, dS \end{aligned} \tag{6-28}$$

Or, Let $\boldsymbol{B} = \boldsymbol{B}_1$ and $\boldsymbol{B'} = \boldsymbol{B}_2$

$$Now,\ \boldsymbol{K_b} = \int_{\Omega\to 2D} \left\{\overline{\overline{\boldsymbol{C_f}}}\, (\boldsymbol{B}_2)^T\, \boldsymbol{B}_2\right\} d\Omega$$

$$\boldsymbol{K_N} = \int_{\Omega\to 2D} \left\{\left\{\overline{\overline{\boldsymbol{D}}}\, \boldsymbol{B}_1{}^T\, \boldsymbol{B}_1\right\} t\right\} d\Omega$$

$$(\boldsymbol{K_b} + \boldsymbol{K_N})\ \boldsymbol{d}^{(e)} = \boldsymbol{f}$$

Or,

$$\Longrightarrow \boldsymbol{K}\ \boldsymbol{d}^{(e)} = \boldsymbol{f}$$

$$K_{ij}\, d_i{}^{(e)} = f_i$$

$$\boldsymbol{K}_{(32x32)}\ \boldsymbol{d}^{(e)}{}_{(32x1)} = \boldsymbol{f}_{(32x1)}$$

Where, $\boldsymbol{K_b}$ is the fiber bending stiffness and $\boldsymbol{K_N}$ is the normal/ in-plane stiffness, t is the thickness of the 2D composite plate. $\boldsymbol{B_1}$ and $\boldsymbol{B_2}$ are the normal and higher order (bending) strain displacement matrix.

Calculation of strain matrices ($\boldsymbol{B_1}$ and $\boldsymbol{B_2}$):

1. Normal/axial strain matrix ($\boldsymbol{\varepsilon}$) :

$$\boldsymbol{\varepsilon} \cong \boldsymbol{B_1}\, \boldsymbol{d}^{(e)}$$

In a state of plane stress ($\sigma_{zz} = \tau_{xz} = \tau_{yz}$), the linearized tensor of the deformations, $\boldsymbol{\varepsilon} = \frac{1}{2}\left[\nabla \boldsymbol{u} + \nabla \boldsymbol{u}^T\right]$ is written in vector form as:

$$\boldsymbol{\varepsilon} = \begin{Bmatrix} \varepsilon_{xx} \\ \varepsilon_{yy} \\ \gamma_{xy} = 2\varepsilon_{xy} \end{Bmatrix} = \begin{Bmatrix} u'_x \\ v'_y \\ u'_y + v'_x \end{Bmatrix} = \begin{bmatrix} 1 & 0 & 0 & 0 \\ 0 & 0 & 0 & 1 \\ 0 & 1 & 1 & 0 \end{bmatrix} \begin{bmatrix} u'_x \\ u'_y \\ v'_x \\ v'_y \end{bmatrix} = [\boldsymbol{M}_1] \begin{bmatrix} u'_x \\ u'_y \\ v'_x \\ v'_y \end{bmatrix} \qquad \textit{(6-29)}$$

Where ($'$) denotes the derivative, i.e., $u'_x = \frac{\partial u}{\partial x}$, etc.

Or, we can write in local coordinates, ξ and η as:

$$\begin{bmatrix} u'_x \\ u'_y \\ v'_x \\ v'_y \end{bmatrix} = \begin{bmatrix} \frac{\partial u}{\partial x} \\ \frac{\partial u}{\partial y} \\ \frac{\partial v}{\partial x} \\ \frac{\partial v}{\partial y} \end{bmatrix} = \begin{bmatrix} \frac{\partial \xi}{\partial x} & \frac{\partial \eta}{\partial x} & 0 & 0 \\ \frac{\partial \xi}{\partial y} & \frac{\partial \eta}{\partial y} & 0 & 0 \\ 0 & 0 & \frac{\partial \xi}{\partial x} & \frac{\partial \eta}{\partial x} \\ 0 & 0 & \frac{\partial \xi}{\partial y} & \frac{\partial \eta}{\partial y} \end{bmatrix} \begin{bmatrix} \frac{\partial u}{\partial \xi} \\ \frac{\partial u}{\partial \eta} \\ \frac{\partial v}{\partial \xi} \\ \frac{\partial v}{\partial \eta} \end{bmatrix} = [\boldsymbol{M}_2] \begin{bmatrix} \frac{\partial u}{\partial \xi} \\ \frac{\partial u}{\partial \eta} \\ \frac{\partial v}{\partial \xi} \\ \frac{\partial v}{\partial \eta} \end{bmatrix} \qquad \textit{(6-30)}$$

We can observe that, the terms in $\boldsymbol{M}_2$ corresponds to the inverse of Jacobian matrix ($\boldsymbol{J}$), which express the transformation between local/natural coordinates ($\xi \; or \; r$ and $\eta \; or \; s$) and the global coordinates (x and y), i.e.,

$$\boldsymbol{J} = \begin{bmatrix} \frac{\partial x}{\partial \xi} & \frac{\partial y}{\partial \xi} \\ \frac{\partial x}{\partial \eta} & \frac{\partial y}{\partial \eta} \end{bmatrix}$$

By using 2nd order biquadratic polynomial for geometry interpolation, i.e.,

$$x \cong \sum_{j=1}^{9} N_j^{(e)}(\xi, \eta) x_j \quad ; \quad y \cong \sum_{j=1}^{9} N_j^{(e)}(\xi, \eta) y_j$$

Therefore,

$$\boldsymbol{J}_1 = \begin{bmatrix} \frac{\partial x}{\partial \xi} & \frac{\partial y}{\partial \xi} \\ \frac{\partial x}{\partial \eta} & \frac{\partial y}{\partial \eta} \end{bmatrix} = \begin{bmatrix} \sum_{j=1}^{9} \frac{\partial N_j}{\partial \xi}\, x_j & \sum_{j=1}^{9} \frac{\partial N_j}{\partial \xi}\, y_j \\ \sum_{j=1}^{9} \frac{\partial N_j}{\partial \eta}\, x_j & \sum_{j=1}^{9} \frac{\partial N_j}{\partial \eta}\, y_j \end{bmatrix} \qquad \textit{(6-31)}$$

And inverse of Jacobian as $\boldsymbol{J}^{-1}$ is written as:

$$\boldsymbol{J_1}^{-1} = \frac{1}{det(\boldsymbol{J_1})}\begin{bmatrix} J_{22} & -J_{12} \\ -J_{21} & J_{11} \end{bmatrix} = \frac{1}{det(\boldsymbol{J})}\begin{bmatrix} \sum_{j=1}^{9} \frac{\partial N_j}{\partial \eta}\, y_j & -\sum_{j=1}^{9} \frac{\partial N_j}{\partial \xi}\, y_j \\ -\sum_{j=1}^{9} \frac{\partial N_j}{\partial \eta}\, x_j & \sum_{j=1}^{9} \frac{\partial N_j}{\partial \xi}\, x_j \end{bmatrix} = \begin{bmatrix} J_{11}^{*} & J_{12}^{*} \\ J_{21}^{*} & J_{22}^{*} \end{bmatrix} \qquad (6\text{-}32)$$

The derivatives of the above biquadratic shape functions can be found in Appendix section 13.3.2. Now, the updated $\boldsymbol{M_2}$ matrix is written as:

$$\boldsymbol{M_2} = \begin{bmatrix} \left(\frac{\sum_{j=1}^{9} \frac{\partial N_j}{\partial \eta}\, y_j}{det(\boldsymbol{J_1})}\right) & \left(\frac{-\sum_{j=1}^{9} \frac{\partial N_j}{\partial \xi}\, y_j}{det(\boldsymbol{J_1})}\right) & 0 & 0 \\ \left(\frac{-\sum_{j=1}^{9} \frac{\partial N_j}{\partial \eta}\, x_j}{det(\boldsymbol{J_1})}\right) & \left(\frac{\sum_{j=1}^{9} \frac{\partial N_j}{\partial \xi}\, x_j}{det(\boldsymbol{J_1})}\right) & 0 & 0 \\ 0 & 0 & \left(\frac{\sum_{j=1}^{9} \frac{\partial N_j}{\partial \eta}\, y_j}{det(\boldsymbol{J_1})}\right) & \left(\frac{-\sum_{j=1}^{9} \frac{\partial N_j}{\partial \xi}\, y_j}{det(\boldsymbol{J_1})}\right) \\ 0 & 0 & \left(\frac{-\sum_{j=1}^{9} \frac{\partial N_j}{\partial \eta}\, x_j}{det(\boldsymbol{J_1})}\right) & \left(\frac{\sum_{j=1}^{9} \frac{\partial N_j}{\partial \xi}\, x_j}{det(\boldsymbol{J_1})}\right) \end{bmatrix} \qquad (6\text{-}33)$$

Or,

$$\boldsymbol{M_2} = \begin{bmatrix} J_{11}^{*} & J_{12}^{*} & 0 & 0 \\ J_{21}^{*} & J_{22}^{*} & 0 & 0 \\ 0 & 0 & J_{11}^{*} & J_{12}^{*} \\ 0 & 0 & J_{21}^{*} & J_{22}^{*} \end{bmatrix} \qquad (6\text{-}34)$$

Now, using interpolation functions of displacement $(\boldsymbol{u}, \boldsymbol{v})$, as discussed earlier:

$$\boldsymbol{u}_h(\xi,\eta) \cong \sum_{i=1}^{16} N_i^{(e)}\,(\xi,\eta)\,\overline{\boldsymbol{u}}_i$$

$$\boldsymbol{v}_h(\xi,\eta) \cong \sum_{i=1}^{16} N_i^{(e)}\,(\xi,\eta)\,\overline{\boldsymbol{v}}_i$$

We can write,

$$\begin{bmatrix} \frac{\partial u}{\partial \xi} \\ \frac{\partial u}{\partial \eta} \\ \frac{\partial v}{\partial \xi} \\ \frac{\partial v}{\partial \eta} \end{bmatrix} = \begin{bmatrix} N'_{1\xi} & N'_{2\xi} & N'_{3\xi} & N'_{4\xi} & 0 & 0 & 0 & 0 & . & . & N'_{16\xi} & 0 & 0 & 0 & 0 \\ N'_{1\eta} & N'_{2\eta} & N'_{3\eta} & N'_{4\eta} & 0 & 0 & 0 & 0 & . & . & N'_{16\eta} & 0 & 0 & 0 & 0 \\ 0 & 0 & 0 & 0 & N'_{1\xi} & N'_{2\xi} & N'_{3\xi} & N'_{4\xi} & . & . & 0 & N'_{13\xi} & N'_{14\xi} & N'_{15\xi} & N'_{16\xi} \\ 0 & 0 & 0 & 0 & N'_{1\eta} & N'_{2\eta} & N'_{3\eta} & N'_{4\eta} & . & . & 0 & N'_{13\eta} & N'_{14\eta} & N'_{15\eta} & N'_{16\eta} \end{bmatrix}_{(4x32)} \begin{bmatrix} \boldsymbol{d_1} \\ \boldsymbol{d_2} \\ \boldsymbol{d_3} \\ \boldsymbol{d_4} \end{bmatrix}_{(32x1)} \qquad (6\text{-}35)$$

Where $\boldsymbol{d_1}, \boldsymbol{d_2}, \boldsymbol{d_3}$ and $\boldsymbol{d_4}$ corresponds to nodal DOF vector. The derivatives (first order) of the above bicubic (hermit type) 16 shape functions can be found in Appendix section 13.3.3.

$$\boldsymbol{d} = \left[u, \frac{\partial u}{\partial x}, \frac{\partial u}{\partial y}, \frac{\partial^2 u}{\partial x \partial y}, v, \frac{\partial v}{\partial x}, \frac{\partial v}{\partial y}, \frac{\partial^2 v}{\partial x \partial y}\right]^T_{(i=1,..4)} \tag{6-36}$$

Or, Eq. (6-35) can also be written as,

$$\begin{bmatrix} \frac{\partial u}{\partial \xi} \\ \frac{\partial u}{\partial \eta} \\ \frac{\partial v}{\partial \xi} \\ \frac{\partial v}{\partial \eta} \end{bmatrix} = [\boldsymbol{M}_3] \cdot \boldsymbol{d}^{(e)} \tag{6-37}$$

Now substituting, Eq. (6-34) and Eq. (6-37) in Eq. (6-29), the normal/axial strain matrix can be written as:

$$\boldsymbol{\varepsilon} = \begin{Bmatrix} \varepsilon_{xx} \\ \varepsilon_{yy} \\ \gamma_{xy} \end{Bmatrix} = \begin{bmatrix} J^*_{11} & J^*_{12} & 0 & 0 \\ 0 & 0 & J^*_{21} & J^*_{22} \\ J^*_{21} & J^*_{22} & J^*_{11} & J^*_{12} \end{bmatrix} \cdot \boldsymbol{M}_3 \cdot \boldsymbol{d}^{(e)}$$

Or,

$$\boldsymbol{\varepsilon} = \begin{Bmatrix} \varepsilon_{11} \\ \varepsilon_{22} \\ \gamma_{12} \end{Bmatrix} = [\boldsymbol{M}_1]_{(3x4)} \cdot [\boldsymbol{M}_2]_{(4x4)} \cdot [\boldsymbol{M}_3]_{(4x32)} \cdot \boldsymbol{d}^{(e)}{}_{(32X1)} \tag{6-38}$$

$$\Longrightarrow \quad \boxed{\boldsymbol{B}_1 = [\boldsymbol{M}_1]\,[\boldsymbol{M}_2][\boldsymbol{M}_3]}$$

Later, normal stiffness matrix can be calculated using,

$$\boldsymbol{K_N} = t \int_{-1}^{+1}\int_{-1}^{+1} \{\bar{\bar{\boldsymbol{D}}}\, \boldsymbol{B}_1{}^T\, \boldsymbol{B}_1\} \, det(\boldsymbol{J}_1)\, d\xi\, d\eta \tag{6-39}$$

The numerical integration can be performed using Gaussian quadrature rule, using 4 gauss points. For exact integration it is necessary to use 16 Gauss points.

$$\boldsymbol{I} = \int_{-1}^{+1}\int_{-1}^{+1} f(\xi,\eta)\, d\xi\, d\eta = \sum_{j=1}^{n}\sum_{i=1}^{n} w_j\, w_i\, f(\xi,\eta)$$

Gauss points (n)	Local Coordinate values (ξ)	(η)	Weights (w_i)
1	$-1/\sqrt{3}$	$-1/\sqrt{3}$	1
2	$+1/\sqrt{3}$	$-1/\sqrt{3}$	1
3	$+1/\sqrt{3}$	$+1/\sqrt{3}$	1
4	$-1/\sqrt{3}$	$+1/\sqrt{3}$	1

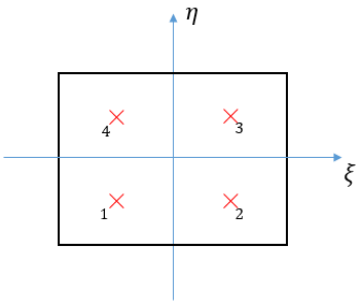

2. Higher order/Bending strain matrix:

$$\boldsymbol{\kappa} \cong \boldsymbol{B}_2\, \boldsymbol{d}^{(e)}$$

$$\boldsymbol{\kappa} = \begin{Bmatrix} \kappa_{111} \\ \kappa_{122} \\ \kappa_{112} \\ \kappa_{211} \\ \kappa_{222} \\ \kappa_{212} \end{Bmatrix} = \begin{bmatrix} u_x'' \\ u_y'' \\ u_{xy}'' \\ v_x'' \\ v_y'' \\ v_{xy}'' \end{bmatrix} \qquad (6\text{-}40)$$

Where, the transformation between local and global coordinates can be written by using chain rule as:

$$u_x'' = \frac{\partial^2 u}{\partial x^2} = \frac{\partial A}{\partial x} = \frac{\partial A}{\partial \xi}\left(\frac{\partial \xi}{\partial x}\right) + \frac{\partial A}{\partial \eta}\left(\frac{\partial \eta}{\partial x}\right)$$

$$A = \frac{\partial u}{\partial x} = \frac{\partial u}{\partial \xi}\left(\frac{\partial \xi}{\partial x}\right) + \frac{\partial u}{\partial \eta}\left(\frac{\partial \eta}{\partial x}\right)$$

$$u_x'' = \frac{\partial^2 u}{\partial x^2} = \frac{\partial A}{\partial x} = \frac{\partial\left(\frac{\partial u}{\partial \xi}\left(\frac{\partial \xi}{\partial x}\right) + \frac{\partial u}{\partial \eta}\left(\frac{\partial \eta}{\partial x}\right)\right)}{\partial \xi}\left(\frac{\partial \xi}{\partial x}\right) + \left(\frac{\partial u}{\partial \xi}\right)\left(\frac{\partial^2 \xi}{\partial x^2}\right) + \frac{\partial\left(\frac{\partial u}{\partial \xi}\left(\frac{\partial \xi}{\partial x}\right) + \frac{\partial u}{\partial \eta}\left(\frac{\partial \eta}{\partial x}\right)\right)}{\partial \eta}\left(\frac{\partial \eta}{\partial x}\right) + \left(\frac{\partial u}{\partial \eta}\right)\left(\frac{\partial^2 \eta}{\partial x^2}\right) \qquad (6\text{-}41)$$

$$u_x'' = \frac{\partial^2 u}{\partial x^2} = \left\{\left[\frac{\partial\left(\frac{\partial u}{\partial \xi}\left(\frac{\partial \xi}{\partial x}\right)\right)}{\partial \xi}\right] + \left[\frac{\partial\left(\frac{\partial u}{\partial \eta}\left(\frac{\partial \eta}{\partial x}\right)\right)}{\partial \xi}\right]\right\}\left(\frac{\partial \xi}{\partial x}\right) + \left(\frac{\partial u}{\partial \xi}\right)\left(\frac{\partial^2 \xi}{\partial x^2}\right) + \left\{\left[\frac{\partial\left(\frac{\partial u}{\partial \xi}\left(\frac{\partial \xi}{\partial x}\right)\right)}{\partial \eta}\right] + \left[\frac{\partial\left(\frac{\partial u}{\partial \eta}\left(\frac{\partial \eta}{\partial x}\right)\right)}{\partial \eta}\right]\right\}\left(\frac{\partial \eta}{\partial x}\right) + \left(\frac{\partial u}{\partial \eta}\right)\left(\frac{\partial^2 \eta}{\partial x^2}\right)$$

$$u'' = \frac{\partial^2 u}{\partial x^2} = \left\{\frac{\partial^2 u}{\partial \xi^2}\left(\frac{\partial \xi}{\partial x}\right) + \frac{\partial^2 u}{\partial \eta \partial \xi}\left(\frac{\partial \eta}{\partial x}\right)\right\}\left(\frac{\partial \xi}{\partial x}\right) + \left(\frac{\partial u}{\partial \xi}\right)\left(\frac{\partial^2 \xi}{\partial x^2}\right) + \left\{\frac{\partial^2 u}{\partial \eta \partial \xi}\left(\frac{\partial \xi}{\partial x}\right) + \frac{\partial^2 u}{\partial \eta^2}\left(\frac{\partial \eta}{\partial x}\right)\right\}\left(\frac{\partial \eta}{\partial x}\right) + \left(\frac{\partial u}{\partial \eta}\right)\left(\frac{\partial^2 \eta}{\partial x^2}\right)$$

$$u''_x = \frac{\partial^2 u}{\partial x^2} = \frac{\partial^2 u}{\partial \xi^2}\left(\frac{\partial \xi}{\partial x}\right)^2 + 2\frac{\partial^2 u}{\partial \eta \partial \xi}\cdot\frac{\partial \eta}{\partial x}\cdot\frac{\partial \xi}{\partial x} + \frac{\partial^2 u}{\partial \eta^2}\left(\frac{\partial \eta}{\partial x}\right)^2 + \frac{\partial u}{\partial \xi}\cdot\frac{\partial^2 \xi}{\partial x^2} + \frac{\partial u}{\partial \eta}\cdot\frac{\partial^2 \eta}{\partial x^2}$$

$$u''_y = \frac{\partial^2 u}{\partial y^2} = \frac{\partial^2 u}{\partial \xi^2}\left(\frac{\partial \xi}{\partial y}\right)^2 + 2\frac{\partial^2 u}{\partial \xi \partial \eta}\cdot\frac{\partial \eta}{\partial y}\cdot\frac{\partial \xi}{\partial y} + \frac{\partial^2 u}{\partial \eta^2}\left(\frac{\partial \eta}{\partial y}\right)^2 + \frac{\partial u}{\partial \xi}\cdot\frac{\partial^2 \xi}{\partial y^2} + \frac{\partial u}{\partial \eta}\cdot\frac{\partial^2 \eta}{\partial y^2}$$

$$u''_{xy} = \frac{\partial^2 u}{\partial x \partial y} = \frac{\partial^2 u}{\partial \xi^2}\cdot\frac{\partial \xi}{\partial x}\cdot\frac{\partial \xi}{\partial y} + \frac{\partial^2 u}{\partial \xi \partial \eta}\cdot\frac{\partial \eta}{\partial x}\cdot\frac{\partial \xi}{\partial y} + \frac{\partial^2 u}{\partial \eta^2}\cdot\frac{\partial \eta}{\partial x}\cdot\frac{\partial \eta}{\partial y} + \frac{\partial^2 u}{\partial \xi \partial \eta}\cdot\frac{\partial \xi}{\partial x}\cdot\frac{\partial \eta}{\partial y} + \frac{\partial u}{\partial \xi}\cdot\frac{\partial^2 \xi}{\partial x\,\partial y} + \frac{\partial u}{\partial \eta}\cdot\frac{\partial^2 \eta}{\partial x\,\partial y}$$

$$v''_x = \frac{\partial^2 v}{\partial x^2} = \frac{\partial^2 v}{\partial \xi^2}\left(\frac{\partial \xi}{\partial x}\right)^2 + 2\frac{\partial^2 v}{\partial \xi \partial \eta}\cdot\frac{\partial \eta}{\partial x}\cdot\frac{\partial \xi}{\partial x} + \frac{\partial^2 v}{\partial \eta^2}\left(\frac{\partial \eta}{\partial x}\right)^2 + \frac{\partial v}{\partial \xi}\cdot\frac{\partial^2 \xi}{\partial x^2} + \frac{\partial v}{\partial \eta}\cdot\frac{\partial^2 \eta}{\partial x^2}$$

$$v''_y = \frac{\partial^2 v}{\partial y^2} = \frac{\partial^2 v}{\partial \xi^2}\left(\frac{\partial \xi}{\partial y}\right)^2 + 2\frac{\partial^2 v}{\partial \xi \partial \eta}\cdot\frac{\partial \eta}{\partial y}\cdot\frac{\partial \xi}{\partial y} + \frac{\partial^2 v}{\partial \eta^2}\left(\frac{\partial \eta}{\partial y}\right)^2 + \frac{\partial v}{\partial \xi}\cdot\frac{\partial^2 \xi}{\partial y^2} + \frac{\partial v}{\partial \eta}\cdot\frac{\partial^2 \eta}{\partial y^2}$$

$$v''_{xy} = \frac{\partial^2 v}{\partial x \partial y} = \frac{\partial^2 v}{\partial \xi^2}\cdot\frac{\partial \xi}{\partial x}\cdot\frac{\partial \xi}{\partial y} + \frac{\partial^2 v}{\partial \xi \partial \eta}\cdot\frac{\partial \eta}{\partial x}\cdot\frac{\partial \xi}{\partial y} + \frac{\partial^2 v}{\partial \eta^2}\cdot\frac{\partial \eta}{\partial x}\cdot\frac{\partial \eta}{\partial y} + \frac{\partial^2 v}{\partial \xi \partial \eta}\cdot\frac{\partial \xi}{\partial x}\cdot\frac{\partial \eta}{\partial y} + \frac{\partial v}{\partial \xi}\cdot\frac{\partial^2 \xi}{\partial x\,\partial y} + \frac{\partial v}{\partial \eta}\cdot\frac{\partial^2 \eta}{\partial x\,\partial y}$$

Therefore,

$$\begin{bmatrix} \frac{\partial^2 u}{\partial x^2} \\ \frac{\partial^2 u}{\partial y^2} \\ \frac{\partial^2 u}{\partial x \partial y} \\ \frac{\partial^2 v}{\partial x^2} \\ \frac{\partial^2 v}{\partial y^2} \\ \frac{\partial^2 v}{\partial x \partial y} \end{bmatrix} = \begin{bmatrix} \left(\frac{\partial \xi}{\partial x}\right)^2 & \left(\frac{\partial \eta}{\partial x}\right)^2 & \left(2\frac{\partial \eta}{\partial x}\frac{\partial \xi}{\partial x}\right) & 0 & 0 & 0 \\ \left(\frac{\partial \xi}{\partial y}\right)^2 & \left(\frac{\partial \eta}{\partial y}\right)^2 & \left(2\frac{\partial \eta}{\partial y}\frac{\partial \xi}{\partial y}\right) & 0 & 0 & 0 \\ \left(\frac{\partial \xi}{\partial x}\frac{\partial \xi}{\partial y}\right) & \left(\frac{\partial \eta}{\partial x}\frac{\partial \eta}{\partial y}\right) & \left(\frac{\partial \eta}{\partial x}\frac{\partial \xi}{\partial y}+\frac{\partial \xi}{\partial x}\frac{\partial \eta}{\partial y}\right) & 0 & 0 & 0 \\ 0 & 0 & 0 & \left(\frac{\partial \xi}{\partial x}\right)^2 & \left(\frac{\partial \eta}{\partial x}\right)^2 & \left(2\frac{\partial \eta}{\partial x}\frac{\partial \xi}{\partial x}\right) \\ 0 & 0 & 0 & \left(\frac{\partial \xi}{\partial y}\right)^2 & \left(\frac{\partial \eta}{\partial y}\right)^2 & \left(2\frac{\partial \eta}{\partial y}\frac{\partial \xi}{\partial y}\right) \\ 0 & 0 & 0 & \left(\frac{\partial \xi}{\partial x}\frac{\partial \xi}{\partial y}\right) & \left(\frac{\partial \eta}{\partial x}\frac{\partial \eta}{\partial y}\right) & \left(\frac{\partial \eta}{\partial x}\frac{\partial \xi}{\partial y}+\frac{\partial \xi}{\partial x}\frac{\partial \eta}{\partial y}\right) \end{bmatrix} \begin{bmatrix} \frac{\partial^2 u}{\partial \xi^2} \\ \frac{\partial^2 u}{\partial \eta^2} \\ \frac{\partial^2 u}{\partial \xi \partial \eta} \\ \frac{\partial^2 v}{\partial \xi^2} \\ \frac{\partial^2 v}{\partial \eta^2} \\ \frac{\partial^2 v}{\partial \xi \partial \eta} \end{bmatrix} + \begin{bmatrix} \frac{\partial^2 \xi}{\partial x^2} & \frac{\partial^2 \eta}{\partial x^2} & 0 & 0 \\ \frac{\partial^2 \xi}{\partial y^2} & \frac{\partial^2 \eta}{\partial y^2} & 0 & 0 \\ \frac{\partial^2 \xi}{\partial x\,\partial y} & \frac{\partial^2 \eta}{\partial x\,\partial y} & 0 & 0 \\ 0 & 0 & \frac{\partial^2 \xi}{\partial x^2} & \frac{\partial^2 \eta}{\partial x^2} \\ 0 & 0 & \frac{\partial^2 \xi}{\partial y^2} & \frac{\partial^2 \eta}{\partial y^2} \\ 0 & 0 & \frac{\partial^2 \xi}{\partial x\,\partial y} & \frac{\partial^2 \eta}{\partial x\,\partial y} \end{bmatrix} \begin{bmatrix} \frac{\partial u}{\partial \xi} \\ \frac{\partial u}{\partial \eta} \\ \frac{\partial v}{\partial \xi} \\ \frac{\partial v}{\partial \eta} \end{bmatrix} \quad (6\text{-}42)$$

Or,

$$\begin{bmatrix} \frac{\partial^2 u}{\partial x^2} \\ \frac{\partial^2 u}{\partial y^2} \\ \frac{\partial^2 u}{\partial x \partial y} \\ \frac{\partial^2 v}{\partial x^2} \\ \frac{\partial^2 v}{\partial y^2} \\ \frac{\partial^2 v}{\partial x \partial y} \end{bmatrix} = [\boldsymbol{M}_4] \begin{bmatrix} \frac{\partial^2 u}{\partial \xi^2} \\ \frac{\partial^2 u}{\partial \eta^2} \\ \frac{\partial^2 u}{\partial \xi \partial \eta} \\ \frac{\partial^2 v}{\partial \xi^2} \\ \frac{\partial^2 v}{\partial \eta^2} \\ \frac{\partial^2 v}{\partial \xi \partial \eta} \end{bmatrix} + [\boldsymbol{M}_5] \begin{bmatrix} \frac{\partial u}{\partial \xi} \\ \frac{\partial u}{\partial \eta} \\ \frac{\partial v}{\partial \xi} \\ \frac{\partial v}{\partial \eta} \end{bmatrix} \quad (6\text{-}43)$$

The matrix $[\boldsymbol{M}_4]$ is equivalent to inverse of Jacobian matrix, $\boldsymbol{J}_2$. Calculating analytically this inverse is not possible. Hence, we need to calculate the inverse numerically.

$$\begin{bmatrix} \frac{\partial u}{\partial \xi} \\ \frac{\partial u}{\partial \eta} \\ \frac{\partial v}{\partial \xi} \\ \frac{\partial v}{\partial \eta} \\ \frac{\partial^2 u}{\partial \xi^2} \\ \frac{\partial^2 u}{\partial \eta^2} \\ \frac{\partial^2 u}{\partial \xi \partial \eta} \\ \frac{\partial^2 v}{\partial \xi^2} \\ \frac{\partial^2 v}{\partial \eta^2} \\ \frac{\partial^2 v}{\partial \xi \partial \eta} \end{bmatrix} = \begin{bmatrix} \boldsymbol{J1} & \mathbf{0}_{(2x2)} & \mathbf{0}_{(2x3)} & \mathbf{0}_{(2x3)} \\ \mathbf{0}_{(2x2)} & \boldsymbol{J1} & \mathbf{0}_{(2x3)} & \mathbf{0}_{(2x3)} \\ \boldsymbol{J2} & \mathbf{0}_{(3x2)} & \boldsymbol{J3} & \mathbf{0}_{(3x3)} \\ \mathbf{0}_{(3x2)} & \boldsymbol{J2} & \mathbf{0}_{(3x3)} & \boldsymbol{J3} \end{bmatrix} \begin{bmatrix} \frac{\partial u}{\partial x} \\ \frac{\partial u}{\partial y} \\ \frac{\partial v}{\partial x} \\ \frac{\partial v}{\partial y} \\ \frac{\partial^2 u}{\partial x^2} \\ \frac{\partial^2 u}{\partial y^2} \\ \frac{\partial^2 u}{\partial x \partial y} \\ \frac{\partial^2 v}{\partial x^2} \\ \frac{\partial^2 v}{\partial y^2} \\ \frac{\partial^2 v}{\partial x \partial y} \end{bmatrix} = [\boldsymbol{M}_6]_{(\mathbf{10x10})} \begin{bmatrix} \frac{\partial u}{\partial x} \\ \frac{\partial u}{\partial y} \\ \frac{\partial v}{\partial x} \\ \frac{\partial v}{\partial y} \\ \frac{\partial^2 u}{\partial x^2} \\ \frac{\partial^2 u}{\partial y^2} \\ \frac{\partial^2 u}{\partial x \partial y} \\ \frac{\partial^2 v}{\partial x^2} \\ \frac{\partial^2 v}{\partial y^2} \\ \frac{\partial^2 v}{\partial x \partial y} \end{bmatrix} \quad \textit{(6-44)}$$

$$\boldsymbol{J}_1 = \begin{bmatrix} \frac{\partial x}{\partial \xi} & \frac{\partial y}{\partial \xi} \\ \frac{\partial x}{\partial \eta} & \frac{\partial y}{\partial \eta} \end{bmatrix}$$

$$\boldsymbol{J}_2 = \begin{bmatrix} \frac{\partial^2 x}{\partial \xi^2} & \frac{\partial^2 y}{\partial \xi^2} \\ \frac{\partial^2 x}{\partial \eta^2} & \frac{\partial^2 y}{\partial \eta^2} \\ \frac{\partial^2 x}{\partial \xi \partial \eta} & \frac{\partial^2 y}{\partial \xi \partial \eta} \end{bmatrix} \quad \textit{(6-45)}$$

$$\boldsymbol{J}_3 = \begin{bmatrix} \left(\frac{\partial x}{\partial \xi}\right)^2 & \left(\frac{\partial y}{\partial \xi}\right)^2 & \left(2\frac{\partial y}{\partial \xi}\frac{\partial x}{\partial \xi}\right) \\ \left(\frac{\partial x}{\partial \eta}\right)^2 & \left(\frac{\partial y}{\partial \eta}\right)^2 & \left(2\frac{\partial y}{\partial \eta}\frac{\partial x}{\partial \eta}\right) \\ \left(\frac{\partial x}{\partial \xi}\frac{\partial x}{\partial \eta}\right) & \left(\frac{\partial y}{\partial \xi}\frac{\partial y}{\partial \eta}\right) & \left(\frac{\partial y}{\partial \xi}\frac{\partial x}{\partial \eta} + \frac{\partial x}{\partial \xi}\frac{\partial y}{\partial \eta}\right) \end{bmatrix}$$

Where, $[\boldsymbol{M}_6]$ corresponds to **"**Jacobian matrix" creating link between first and second derivatives of displacements in local and global coordinates.

By using 2nd order biquadratic polynomial for geometry interpolation, i.e.,

$$x \cong \sum_{j=1}^{9} N_j^{(e)}(\xi, \eta) x_j \quad ; \quad y \cong \sum_{j=1}^{9} N_j^{(e)}(\xi, \eta) y_j$$

Using above interpolation functions for geometry, $[\boldsymbol{M}_6]$ is computed and inverse $[\boldsymbol{M_6}]^{-1}$ is calculated numerically in UEL (Fortran). Let $[\boldsymbol{M_6}]^{-1} = [\boldsymbol{M}_7]$

Now, Eq. (6-44) can be written as:

$$\begin{bmatrix} \frac{\partial u}{\partial x} \\ \frac{\partial u}{\partial y} \\ \frac{\partial v}{\partial x} \\ \frac{\partial v}{\partial y} \\ \frac{\partial^2 u}{\partial x^2} \\ \frac{\partial^2 u}{\partial y^2} \\ \frac{\partial^2 u}{\partial x \partial y} \\ \frac{\partial^2 v}{\partial x^2} \\ \frac{\partial^2 v}{\partial y^2} \\ \frac{\partial^2 v}{\partial x \partial y} \end{bmatrix} = [\boldsymbol{M}_7]_{(\boldsymbol{10x10})} \begin{bmatrix} \frac{\partial u}{\partial \xi} \\ \frac{\partial u}{\partial \eta} \\ \frac{\partial v}{\partial \xi} \\ \frac{\partial v}{\partial \eta} \\ \frac{\partial^2 u}{\partial \xi^2} \\ \frac{\partial^2 u}{\partial \eta^2} \\ \frac{\partial^2 u}{\partial \xi \partial \eta} \\ \frac{\partial^2 v}{\partial \xi^2} \\ \frac{\partial^2 v}{\partial \eta^2} \\ \frac{\partial^2 v}{\partial \xi \partial \eta} \end{bmatrix} \qquad \textit{(6-46)}$$

Notice that, the L.H.S terms contains first derivatives, along with the second and mixed derivatives. Consequently, we are coupling the Normal/axial strain ($\boldsymbol{\varepsilon}$) and Curvatures or bending strain ($\boldsymbol{\kappa}$) . Therefore, the total coupled strain, $\boldsymbol{\varepsilon_T} = \boldsymbol{\varepsilon} + \boldsymbol{\kappa}$.

$$\boldsymbol{\varepsilon_T} = (\boldsymbol{\varepsilon} + \boldsymbol{\kappa}) = \begin{bmatrix} u_x^{'} \\ v_y^{'} \\ (u_y^{'} + v_x^{'}) \\ u_x^{''} \\ u_y^{''} \\ u_{xy}^{''} \\ v_x^{''} \\ v_y^{''} \\ v_{xy}^{''} \end{bmatrix} = \begin{bmatrix} 1 & 0 & 0 & 0 & 0 & 0 & 0 & 0 & 0 & 0 \\ 0 & 0 & 0 & 1 & 0 & 0 & 0 & 0 & 0 & 0 \\ 0 & 1 & 1 & 0 & 0 & 0 & 0 & 0 & 0 & 0 \\ 0 & 0 & 0 & 0 & 1 & 0 & 0 & 0 & 0 & 0 \\ 0 & 0 & 0 & 0 & 0 & 1 & 0 & 0 & 0 & 0 \\ 0 & 0 & 0 & 0 & 0 & 0 & 1 & 0 & 0 & 0 \\ 0 & 0 & 0 & 0 & 0 & 0 & 0 & 1 & 0 & 0 \\ 0 & 0 & 0 & 0 & 0 & 0 & 0 & 0 & 1 & 0 \\ 0 & 0 & 0 & 0 & 0 & 0 & 0 & 0 & 0 & 1 \end{bmatrix} \begin{bmatrix} u_x^{'} \\ u_y^{'} \\ v_x^{'} \\ v_y^{'} \\ u_x^{''} \\ u_y^{''} \\ u_{xy}^{''} \\ v_x^{''} \\ v_y^{''} \\ v_{xy}^{''} \end{bmatrix} = [\boldsymbol{M}_8]_{(\boldsymbol{9x10})} \begin{bmatrix} u_x^{'} \\ u_y^{'} \\ v_x^{'} \\ v_y^{'} \\ u_x^{''} \\ u_y^{''} \\ u_{xy}^{''} \\ v_x^{''} \\ v_y^{''} \\ v_{xy}^{''} \end{bmatrix} \qquad \textit{(6-47)}$$

Hence, we can calculate the total stiffness directly as, $\boldsymbol{K}_T = \boldsymbol{K}_N + \boldsymbol{K}_b$. Now, using interpolation functions of displacement ($\boldsymbol{u}, \boldsymbol{v}$), as discussed earlier:

$$\boldsymbol{u}_h(\xi, \eta) \cong \sum_{i=1}^{16} N_i^{(e)}(\xi, \eta)\, \overline{\boldsymbol{u}}_i \qquad ; \qquad \boldsymbol{v}_h(\xi, \eta) \cong \sum_{i=1}^{16} N_i^{(e)}(\xi, \eta)\, \overline{\boldsymbol{v}}_i$$

We can write,

$$\begin{bmatrix} \frac{\partial u}{\partial \xi} \\ \frac{\partial u}{\partial \eta} \\ \frac{\partial v}{\partial \xi} \\ \frac{\partial v}{\partial \eta} \\ \frac{\partial^2 u}{\partial \xi^2} \\ \frac{\partial^2 u}{\partial \eta^2} \\ \frac{\partial^2 u}{\partial \xi \partial \eta} \\ \frac{\partial^2 v}{\partial \xi^2} \\ \frac{\partial^2 v}{\partial \eta^2} \\ \frac{\partial^2 v}{\partial \xi \partial \eta} \end{bmatrix} = [\boldsymbol{M}_9]_{(\mathbf{10x32})} \begin{bmatrix} \boldsymbol{d_1} \\ \boldsymbol{d_2} \\ \boldsymbol{d_3} \\ \boldsymbol{d_4} \end{bmatrix}_{(\mathbf{32x1})} \qquad \textit{(6-48)}$$

Matrix, $[\boldsymbol{M}_9]$ contains,

$[\boldsymbol{M}_9] =$

$$\begin{bmatrix} N'_{1\xi} & N'_{2\xi} & N'_{3\xi} & N'_{4\xi} & 0 & 0 & 0 & 0 & . & . & N'_{16\xi} & 0 & 0 & 0 & 0 \\ N'_{1\eta} & N'_{2\eta} & N'_{3\eta} & N'_{4\eta} & 0 & 0 & 0 & 0 & . & . & N'_{16\eta} & 0 & 0 & 0 & 0 \\ 0 & 0 & 0 & 0 & N'_{1\xi} & N'_{2\xi} & N'_{3\xi} & N'_{4\xi} & . & . & 0 & N'_{13\xi} & N'_{14\xi} & N'_{15\xi} & N'_{16\xi} \\ 0 & 0 & 0 & 0 & N'_{1\eta} & N'_{2\eta} & N'_{3\eta} & N'_{4\eta} & . & . & 0 & N'_{13\eta} & N'_{14\eta} & N'_{15\eta} & N'_{16\eta} \\ N''_{1\xi} & N''_{2\xi} & N''_{3\xi} & N''_{4\xi} & 0 & 0 & 0 & 0 & . & . & N''_{16\xi} & 0 & 0 & 0 & 0 \\ N''_{1\eta} & N''_{2\eta} & N''_{3\eta} & N''_{4\eta} & 0 & 0 & 0 & 0 & . & . & N''_{16\eta} & 0 & 0 & 0 & 0 \\ N'_{1\eta,\xi} & N'_{2\eta,\xi} & N'_{3\eta,\xi} & N'_{4\eta,\xi} & 0 & 0 & 0 & 0 & . & . & N'_{16\eta,\xi} & 0 & 0 & 0 & 0 \\ 0 & 0 & 0 & 0 & N''_{1\xi} & N''_{2\xi} & N''_{3\xi} & N''_{4\xi} & . & . & 0 & N''_{13\xi} & N''_{14\xi} & N''_{15\xi} & N''_{16\xi} \\ 0 & 0 & 0 & 0 & N''_{1\eta} & N''_{2\eta} & N''_{3\eta} & N''_{4\eta} & . & . & 0 & N''_{13\eta} & N''_{14\eta} & N''_{15\eta} & N''_{16\eta} \\ 0 & 0 & 0 & 0 & N'_{1\eta,\xi} & N'_{2\eta,\xi} & N'_{3\eta,\xi} & N'_{4\eta,\xi} & . & . & 0 & N'_{13\eta,\xi} & N'_{14\eta,\xi} & N'_{15\eta,\xi} & N'_{16\eta,\xi} \end{bmatrix} \qquad \textit{(6-49)}$$

Where,

$$N''_{i\xi} = \frac{\partial^2 N_i}{\partial \xi^2} \;;$$

$$N'_{i\eta,\xi} = \frac{\partial}{\partial \xi}\left(\frac{\partial N_i}{\partial \eta}\right) \qquad i = 1, \ldots, 16$$

The derivatives (first, second and mixed) of the above bicubic (hermit type) shape functions can be found in Appendix section 13.3.3. Now substituting, Eq. (6-46) and Eq. (6-48) in Eq. (6-47), the total coupled curvature-strain matrix ($\boldsymbol{B}_T$) and total coupled strain matrix ($\boldsymbol{\varepsilon_T}$) is written as:

$$\boldsymbol{\varepsilon_T} = [\boldsymbol{M}_8]_{(9x10)} \cdot [\boldsymbol{M}_7]_{(10x10)} \cdot [\boldsymbol{M}_9]_{(10x32)} \cdot \boldsymbol{d}^{(e)}{}_{(32X1)} \qquad \textit{(6-50)}$$

$$\Rightarrow \quad \boxed{\boldsymbol{B}_T = [\boldsymbol{M}_7]\,[\boldsymbol{M}_8]\,[\boldsymbol{M}_9]}$$

Later, Total stiffness can be calculated using,

$$\boldsymbol{K_T} = t \int_{-1}^{+1}\int_{-1}^{+1} \{\bar{\bar{\boldsymbol{D}}}\ (\boldsymbol{B}_T)^T\,\boldsymbol{B}_T + \bar{\bar{\boldsymbol{C}_f}}\,(\boldsymbol{B}_T)^T\,\boldsymbol{B}_T\ \}\ det(\boldsymbol{J}_1)\,d\xi\,d\eta \qquad (6\text{-}51)$$

The numerical integration is performed using Gaussian quadrature rule, using 16 Gauss points for exact integration.

Calculation of Force vectors ($\boldsymbol{f}$) :

1) Body/Volume force($\boldsymbol{f}_b$):

$$\boldsymbol{f}_b = t \iint_{A^{(e)}} \boldsymbol{F}_b\,\boldsymbol{N}^T_{i=1..16}\,dx\,dy = t \int_{-1}^{+1}\int_{-1}^{+1} \boldsymbol{N}^T_{i=1..16}\,\boldsymbol{F}_b\ det(\boldsymbol{J}_1)\,d\xi\,d\eta\ ; \qquad (6\text{-}52)$$

Where,

$$\boldsymbol{F}_b = \begin{Bmatrix} F_{bx} \\ F_{by} \end{Bmatrix}$$

The numerical integration is performed using Gaussian quadrature rule, using 16 gauss points for exact integration.

2) Surface/Traction force($\boldsymbol{f}_s$) :

The second type of distributed forces considered corresponds to pressure forces acting on each face of the element. We have adopted the following convention (see fig below) for a pressure acting on the face, n $(1 < n < 4)$ for identification of Distributed load of type U_n in UEL.

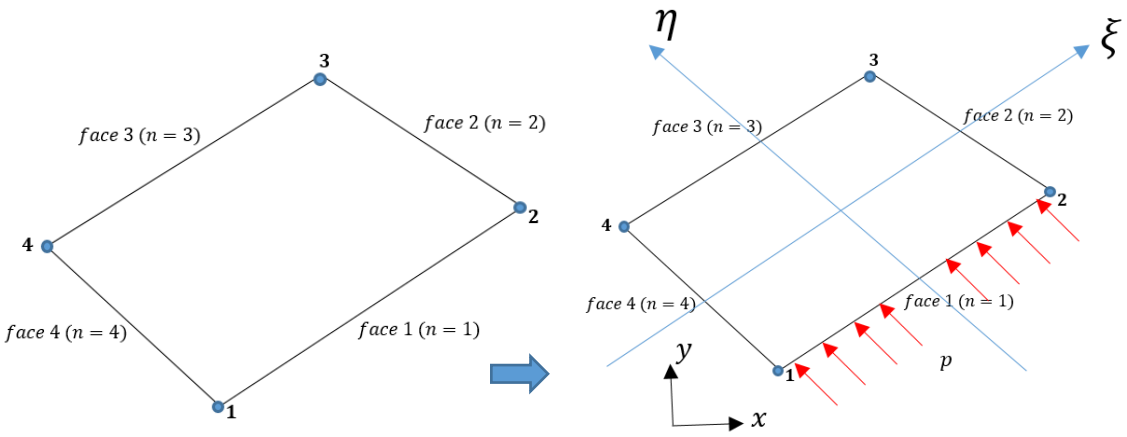

$$\boldsymbol{f_S} = t \iint_{A^{(e)}} \boldsymbol{F_S}\,\boldsymbol{N}^T_{i=1..16}\,dx\,dy = t \int_{-1}^{+1}\int_{-1}^{+1} \boldsymbol{N}^T_{i=1..16}\,\boldsymbol{F_S}\,det\,(J_3)\,d\xi\,d\eta\ ; \qquad (6\text{-}53)$$

With,

$$\boldsymbol{F}_S = \begin{Bmatrix} F_{Sx} \\ F_{Sy} \end{Bmatrix}$$

Where, J_3 is the Jacobi for the edge/face transformation (from global coordinates to local).

For face (n=1 or n=3):

$$\det(J_3) = \sqrt{\left(\sum_{i=1}^{9} \frac{\partial N_i}{\partial \xi}\ x_i\right)^2 + \left(\sum_{i=1}^{9} \frac{\partial N_i}{\partial \xi}\ y_i\right)^2} \qquad (6\text{-}54)$$

For face (n=2 or n=4):

$$\det(J_3) = \sqrt{\left(\sum_{i=1}^{9} \frac{\partial N_i}{\partial \eta}\ x_i\right)^2 + \left(\sum_{i=1}^{9} \frac{\partial N_i}{\partial \eta}\ y_i\right)^2}$$

The components of $\boldsymbol{F}_S$ is given by:

$$F_{Sx} = sgn\ p\ \frac{(y_{(m+1)} - y_m)}{Length\ of\ face}\ ; \qquad (6\text{-}55)$$

$$F_{Sy} = sgn\ p\ \frac{(x_{(m+1)} - x_m)}{Length\ of\ face}$$

Where, p is the pressure in 'Pa (F/L^2)' acting on the face, (x_m, y_m) and $(x_{(m+1)}, y_{(m+1)})$ are the coordinates of face, n and sgn = ± 1 (based on direction of $\boldsymbol{F}_S$ towards the interior of element). Finally, the numerical integration is performed using Gaussian quadrature rule, using 16 gauss points for exact integration.

3) Moments on the body($\boldsymbol{M}_b$):

$$\boldsymbol{M}_b = t \iint_{A^{(e)}} \boldsymbol{M}_b\ [\boldsymbol{N}'_{i=1..16}]^T\ dx\ dy = t \int_{-1}^{+1} \int_{-1}^{+1} [\boldsymbol{N}'_{i=1..16}]^T\ \boldsymbol{M}_b\ \ det(\boldsymbol{J}_1)\ d\xi\ d\eta\ ; \qquad (6\text{-}56)$$

Where,

$$\boldsymbol{M}_b = \begin{Bmatrix} M_{bx} \\ M_{by} \end{Bmatrix}$$

The numerical integration can be performed using Gaussian quadrature rule, using 16 Gauss points for exact integration.

Calculation of Stress components:

1) Second Piola Kirchoff stress**:**

$$\boldsymbol{S} = \begin{bmatrix} S_{11} \\ S_{22} \\ S_{12} \end{bmatrix} = \bar{\bar{\boldsymbol{D}}}\ \boldsymbol{\varepsilon} = \frac{E}{(1 - \nu^2)} \begin{bmatrix} 1 & \nu & 0 \\ \nu & 1 & 0 \\ 0 & 0 & \frac{1-\nu}{2} \end{bmatrix} \begin{bmatrix} \varepsilon_{11} \\ \varepsilon_{22} \\ \gamma_{12} \end{bmatrix} \qquad (6\text{-}57)$$

with,

$$\varepsilon_{33} = -\frac{\nu}{E}(S_{11} + S_{22})$$

Where, E is Elastic Young's modulus, ν is Poisson's ratio for isotropic elastic case. In general, $\bar{\bar{\boldsymbol{D}}}$ should be considered anisotropic.

2) Distributed Bending Moment (DBM):

$$\boldsymbol{\zeta} = \begin{bmatrix} \tau_{111} \\ \tau_{122} \\ \tau_{112} \\ \tau_{211} \\ \tau_{222} \\ \tau_{212} \end{bmatrix} = \bar{\bar{C}}_f \, \boldsymbol{\kappa} = \begin{bmatrix} A & 0 & 0 & 0 & 0 & 0 \\ 0 & B & 0 & 0 & 0 & 0 \\ 0 & 0 & C & 0 & 0 & 0 \\ 0 & 0 & 0 & D & 0 & 0 \\ 0 & 0 & 0 & 0 & E & 0 \\ 0 & 0 & 0 & 0 & 0 & F \end{bmatrix} \begin{Bmatrix} \kappa_{111} \\ \kappa_{122} \\ \kappa_{112} \\ \kappa_{211} \\ \kappa_{222} \\ \kappa_{212} \end{Bmatrix} \quad (6\text{-}58)$$

Where, A, B, C, D, E, F corresponds to fiber material parameters (non-local parameters).

The stress, strain, curvature and DBM components, are calculated in 16 gauss points for exact integration.

Calculation of energy (W):

1) Elastic Deformation energy:

$$W_e = \frac{1}{2}\int_{\Omega} \boldsymbol{\varepsilon}^T \, \bar{\bar{\boldsymbol{D}}} \, \boldsymbol{\varepsilon} \, d\Omega = \frac{1}{2} \; \boldsymbol{d}^{(e)} \, \boldsymbol{K_N} \; \boldsymbol{d}^{(e)} \quad (6\text{-}59)$$

2) Bending energy:

$$W_b = \frac{1}{2}\int_{\Omega} \boldsymbol{\kappa}^T \bar{\bar{\boldsymbol{C}}}_{\boldsymbol{f}} \, \boldsymbol{\kappa} \, d\Omega = \frac{1}{2} \; \boldsymbol{d}^{(e)} \, \boldsymbol{K_b} \; \boldsymbol{d}^{(e)} \quad (6\text{-}60)$$

3) Total Elastic Strain Energy ($\boldsymbol{W}$):

$$W = W_e + W_b \quad (6\text{-}61)$$

***Note:**

Above formulations for the linear case have been implemented in the non-local element:
"NL U32_V1.1" and "NL U32_V1.2"

This completes the development of theoretical and numerical formulation of generalized homogenous non-local model (HOMNL) and user element (NL U32) for linear isotropic elastic case. The following chapter is dedicated to the validation of this model, implemented in NL U32.

7 Validation of NL U32 Element (Linear case)

In this chapter, validation of previously developed Homogenized Non-Local model, implemented in Non-Local Super parametric element (NL U32) for '*linear isotropic elastic*' is performed against ABAQUS® classical elements.

7.1 Linear Geometry and Linear Isotropic Elastic Case

In order to compare the accuracy and validate Non-Local element (NL U32) for linear elastic isotropic case, results are compared with ABAQUS ® linear plane stress element (CPS4), as it is much more convenient reference element at the moment, since it is also built with plane stress formulation. The values of $\overline{\overline{C_f}}$ parameters (A, B, C, D, E, F) is unknown for NL U32 element. Therefore, it is important to understand the influence of these parameters on the solution. Hence, ($\overline{\overline{C_f}}$) parameters value is varied and kept constant in all the cases.

It should be noted that for all the cases, same material properties have been defined for CPS4 element: Elastic Young's modulus, E=2.0E5 MPa, Poisson's ratio, ν=0.3 and thickness, t=1mm. For NL U32 element, material properties are: Composite Effective Elastic Young's modulus, E_c=2.0E5 Mpa, Poisson's ratio, ν_c=0.3, thickness, t=1mm, the values for parameters of local fiber bending stiffness matrix A,B,C,D,E,F: started with initial guess of low value, 0.15 $MPa \cdot mm^2$and varied with the order of 10^2. Analysis is performed on a rectangular plate (100 x 50 mm), meshed with 276 Elements (312 nodes).

7.1.1 Case1: Compression

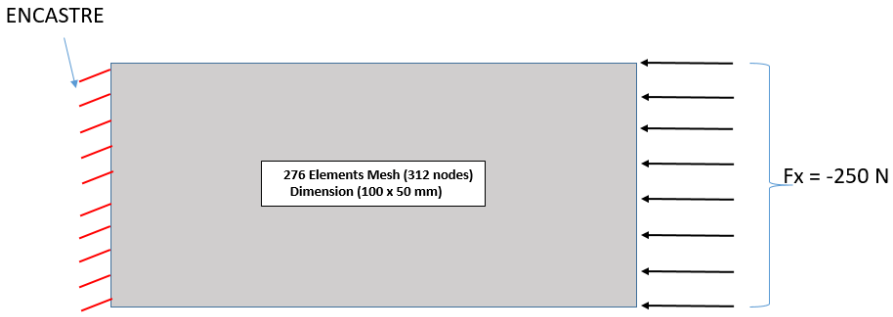

Figure 58: Mesh, Load and Boundary conditions: Case1

In the following figures, displacements U and V of each nodes are plotted. ABAQUS® CPS4 and non-local element (NL U32) with different stiffness of micro bending are compared.

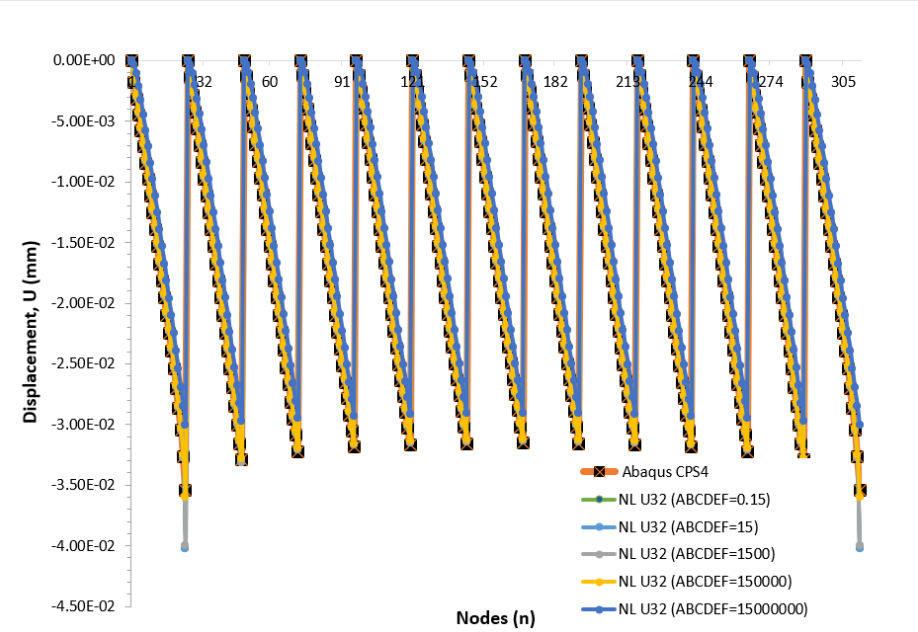

Figure 59: Influence of Cf Parameters (Compression): Displacement, U

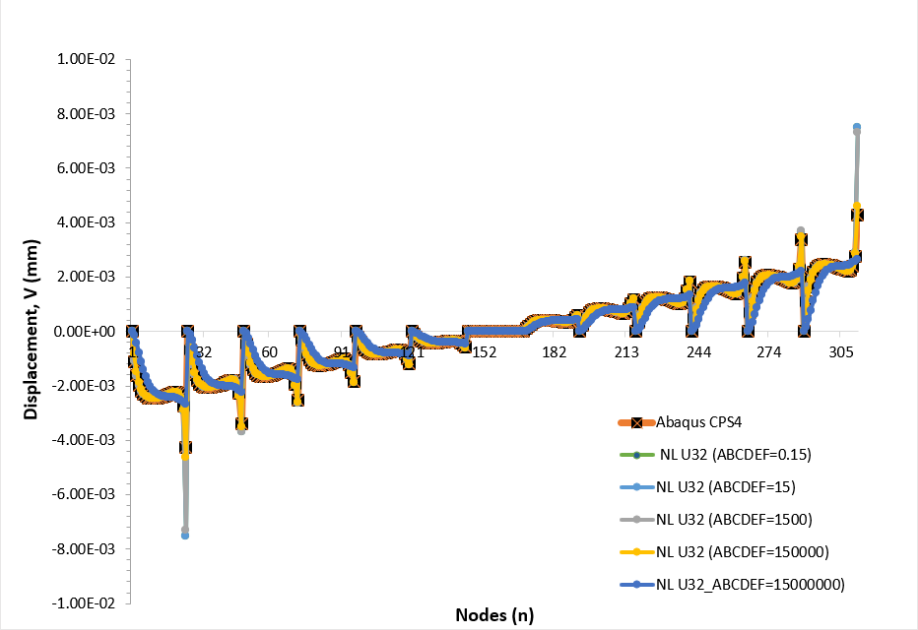

Figure 60: Influence of Cf Parameters (Compression): Displacement, V

In the next figure, the transverse displacement is plotted against the non-local parameters at some particular node to see the evolution clearly.

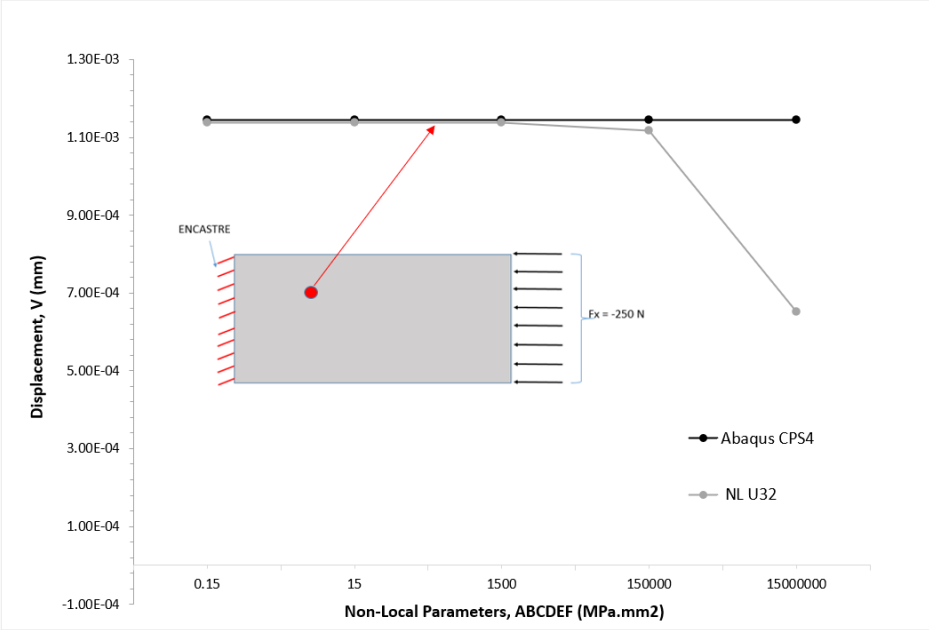

Figure 61: Comparison of Displacement (V) at node 222 for different Cf parameters value (Compression)

7.1.2 Case2: Bending

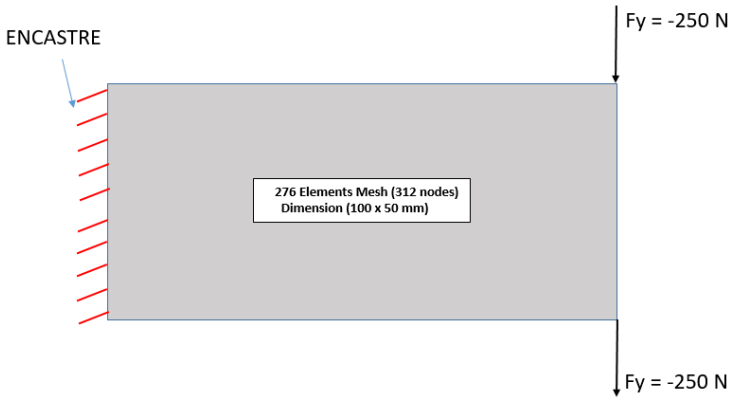

Figure 62: Mesh, Load and Boundary Conditions: Case2

Similar plots as previous case is presented with this specific load in the following figures.

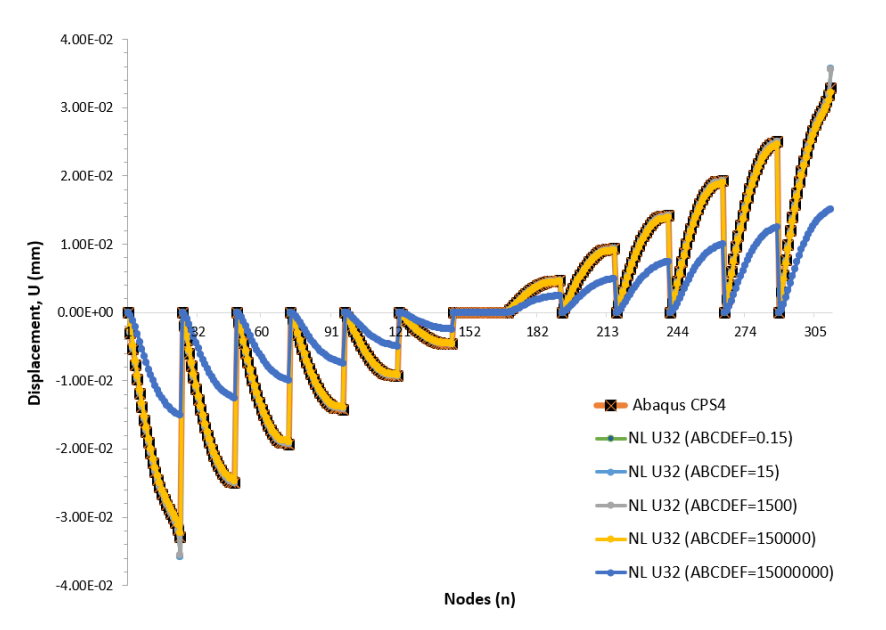

Figure 63: Influence of Cf Parameters (Bending): Displacement, U

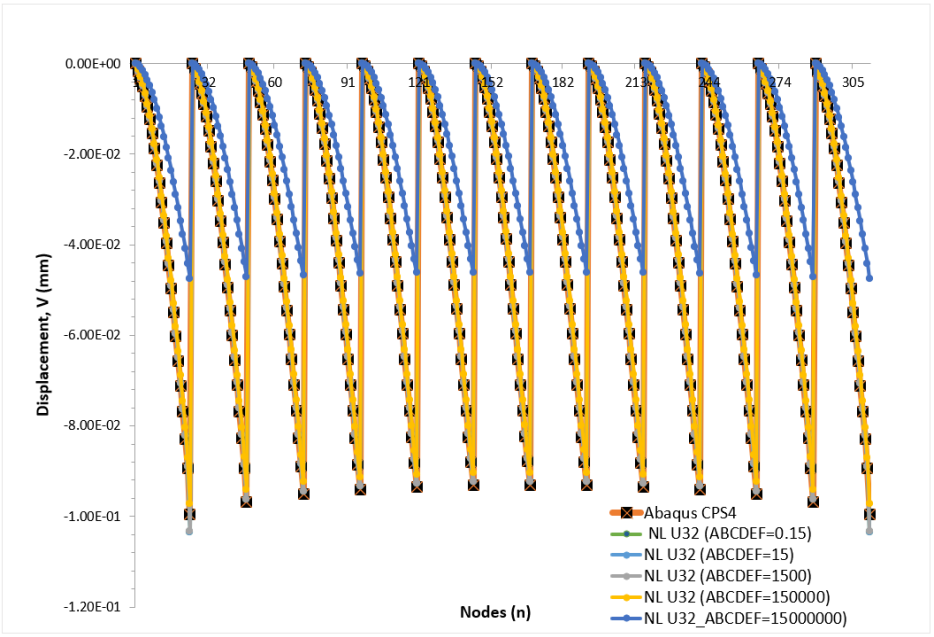

Figure 64: Influence of Cf Parameters (Bending): Displacement, V

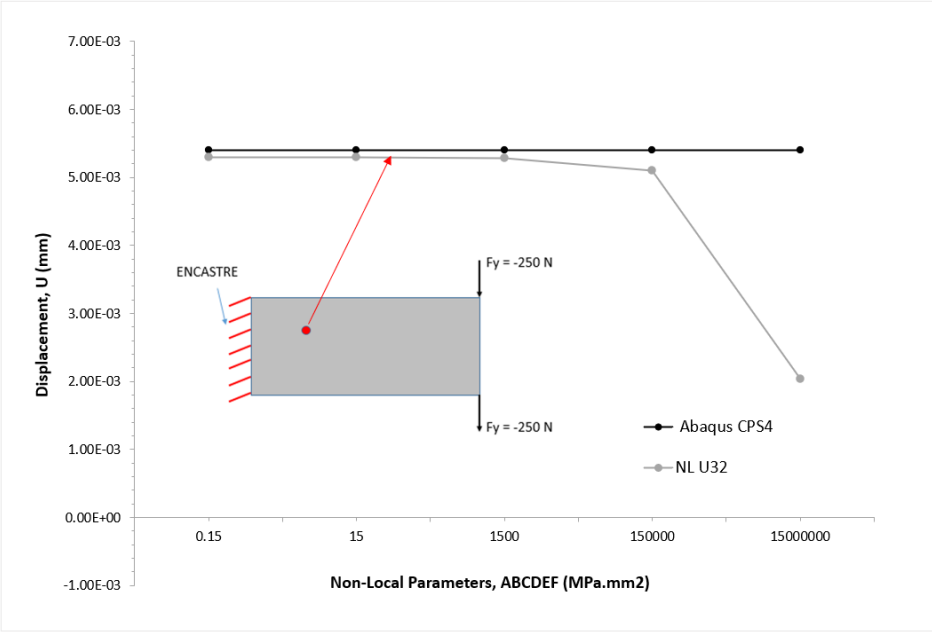

Figure 65: Comparison of Displacement (U) at node 222 for different Cf parameters values (Bending)

7.1.3 Discussion

From both the cases: compression (Figure 59, Figure 60) and bending (Figure 63,Figure 64), it can be observed that, similar response and difference in solution is very less compared to ABAQUS ® CPS4 element when local fiber bending stiffness matrix, $\overline{\overline{\boldsymbol{C_f}}}$ parameters/non-local parameters (ABCDEF) varied up to 1500 $MPa \cdot mm^2$. But, significant difference in solution is observed compared to CPS4 element when ABCDEF value is increased above 1500 $MPa \cdot mm^2$ (see Figure 61 and Figure 65). Much stiffer response can be observed with NL U32 compared to continuum solid CPS4. This is because, for lower order of $\overline{\overline{\boldsymbol{C_f}}}$ ($\leq 10^3$), the order of bending energy ($\boldsymbol{\kappa}^T \overline{\overline{\boldsymbol{C_f}}}\, \boldsymbol{\kappa}$) becomes lower compared to classical strain energy ($\boldsymbol{\varepsilon}^T\, \overline{\overline{\boldsymbol{D}}}\, \boldsymbol{\varepsilon}$), since the order of curvatures is also lower. Consequently, bending energy has negligible contribution to the total energy. So, we tend to obtain similar solution as classical plane stress solution. But, for higher order of $\overline{\overline{\boldsymbol{C_f}}}$ ($> 10^3$), the order of bending energy becomes similar or higher compared to the classical strain energy. Consequently, we can evaluate a significant difference in solution for ABCDEF $>1500\, MPa \cdot mm^2$. The level of stiffness which generates an effect, can be estimated (see Appendix 13.4), and we have also obtained the value of 1500 $MPa \cdot mm^2$. In conclusion, in order to have non-local effects in this particular solution, it is necessary to have $\overline{\overline{\boldsymbol{C_f}}}$ parameters value $> 10^3$. This clearly explains the influence of $\overline{\overline{\boldsymbol{C_f}}}$ parameters value in the solution. In future, it is necessary to obtain proper values for ABCDEF in correspondence to a composite considered by identification protocol. It is also important to note that, the choice of interpolation functions, integration rule for both ABAQUS® CPS4 and NL U32 element are different, which can also cause difference in solution, especially near the points of loading. However, the global response obtained with NL U32 is almost similar compared to ABAQUS® CPS4 element, which validates the non-local element for linear isotropic elastic case.

7.1.4 Mesh Convergence study

In order to understand the convergence of the solution obtained with NL U32 element against mesh size, various mesh size of: $no.of\ elements, n = 8, 32, 66, 128, 276, 512$ is chosen. The material properties, loading and boundary conditions is same as previous (case 2), except that the two values of ABCDEF is chosen: 15 $MPa \cdot mm^2$ and 1500000 $MPa \cdot mm^2$. The solution is compared with ABAQUS® CPS4 element. We can observe from Figure 66, that as the mesh size (n) is increased, we tend to obtain an asymptotic or converged solution for both NL U32 element and ABAQUS® CPS4 element. As discussed earlier, for lower values of ABCDEF with increase in mesh size, we tend to obtain similar solution as classical plane stress element CPS4, and for higher values of ABCDEF, quite significant difference can be observed. However, the convergence is obtained with increase in mesh size. This confirms that for finer mesh, we will obtain a good converged solution with NL U32 element.

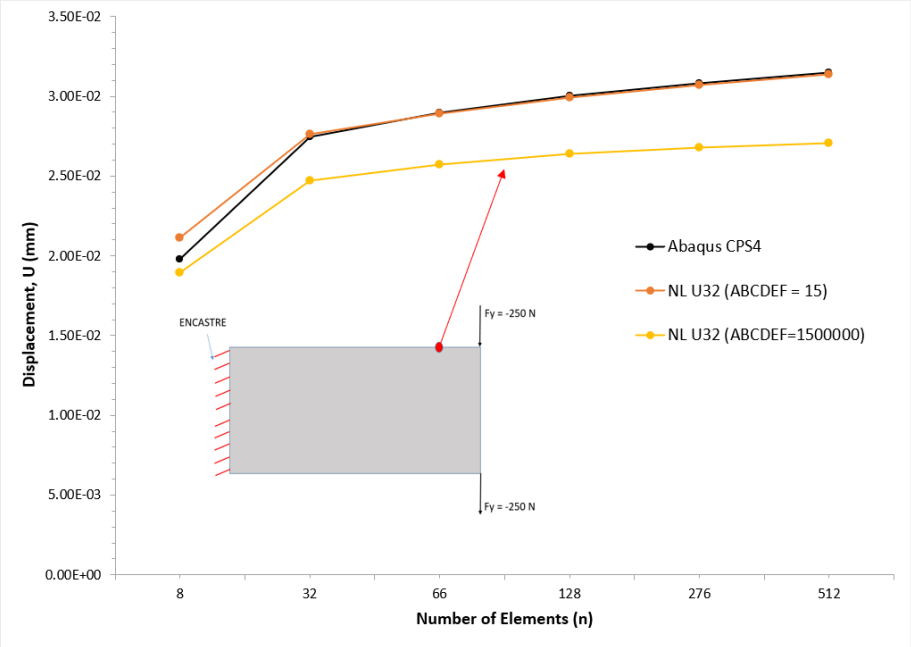

Figure 66: Mesh Convergence Study of NL U32 element

7.1.5 Comparison with 2D heterogenous complete microstructure

7.1.5.1 *Methodology*

As a final step of validation of Non-Local Homogenous model implemented in non-local element (NL U32) for linear elastic case, results are compared with 2D Unidirectional (UD) composite (T300/914 Carbon/epoxy) model built using Abaqus plane stress element (CPS4). The stacking sequence of UD heterogenous composite (with 10 layers) model built in ABAQUS® is as shown in (Figure 67). Mesh size of 200 elements (231 nodes) is used for this comparison.

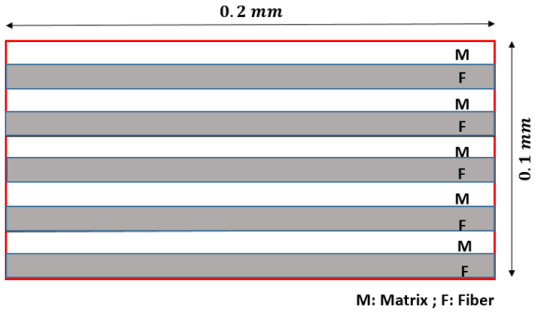

Figure 67: 2D composite stacking sequence: UD plies at 0^0

The elastic properties of T300/914 Carbon/epoxy UD ply obtained from Drapier et al., [D1] as in Table 4 is assigned for both matrix and fiber in heterogenous model of Abaqus and homogenous non-local model. Note that the matrix and fiber is assumed isotropic in both the models.

Table 4: Elastic Material properties of UD ply (Drapier et al., 1996)

Heterogenous model Abaqus (CPS4)		***Homogenous Non-local model (NL U32)***	
matrix	*fiber*	*matrix*	*fiber*
$E_m = 4500\ MPa$	$E_f = 240000\ MPa$	$E_m = 4500\ MPa$	$E_f = 240000\ MPa$
$\nu_m = 0.4$	$\nu_f = 0.3$	$\nu_m = 0.4$	$\nu_f = 0.3$
thickness, $t = 1mm$		*Volume fraction,* $f = 0.625$	
		Diameter of fibers, $d_f = 0.01mm$	
		Local fiber bending stiffness parameter for UD ply, $D = fE_f r_{gf}^2 = 0.09375\ MPa \cdot mm^2$ $r_{gf} = \sqrt{\frac{I}{S_f}}$	
		*ABCEF = 0.001*D*	*thickness,* $t = 1mm$

It is important to note that, for UD ply, since there is just one gradient ($v'' = \frac{\partial^2 v}{\partial x^2}$) along thickness direction, as in case of Drapier et al., 1999 [D3], just one parameter (D) of local bending stiffness matrix, $\overline{\overline{\boldsymbol{C_f}}}$ is considered, values for other parameters (ABCEF) is assigned very low compared to parameter D in homogenous non-local model.

7.1.5.2 ***Results***

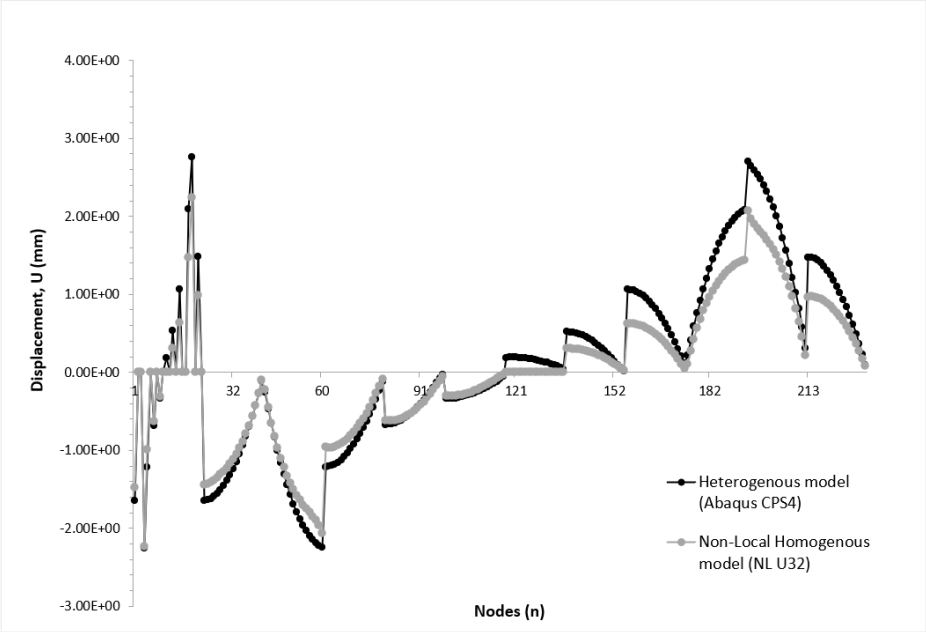

Figure 68: Comparison of variation of displacement (U) over nodes

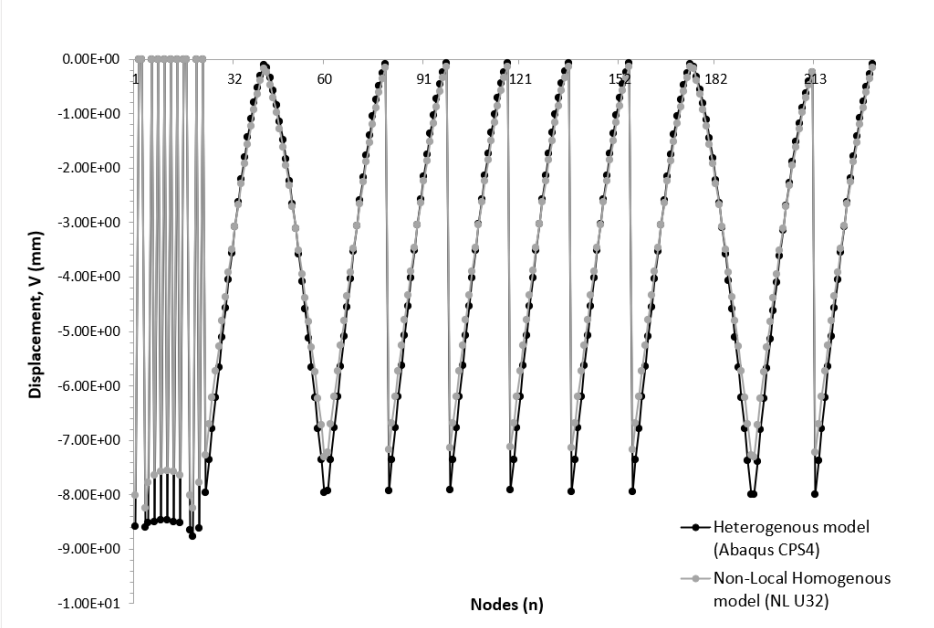

Figure 69: Comparison of variation of displacement (V) over nodes

From Figure 68 and Figure 69, it is clear that the results (displacements: U, V) obtained from homogenous non-local model is in close comparison with the results of heterogenous model of ABAQUS® for the case of UD composite subjected to bending. The slight difference between two solutions are clearly due to the addition of non-local terms and choice of interpolation functions (for displacement and geometry) in homogenous non-local model. With this validation, it can be concluded that the homogenized non-local model (implemented in NL U32 element) can be used for analysis of UD composites (linear isotropic elastic cases).

However, we know that addition of 'non-linear geometrical' effects is one of the important parameters to be considered for prediction of compressive strength of composites as discussed in earlier chapters, the next chapter is devoted to this part, followed by the validation.

8 Geometrical Non-Linearity in NL U32: description and validation

This chapter contains formulation and addition of '*Non-linear geometrical effects*' in previously developed Homogenized Non-Local model, thereby implementing in Non-Local Super parametric element (NL U32). And then finally validation of the results against ABAQUS® classical elements.

8.1 Formulation and addition of Geometrical Non-Linearity

In a state of plane stress ($\sigma_{zz} = \tau_{xz} = \tau_{yz}$) and non-linear geometry, the total Green Lagrange strain tensor is , $\boldsymbol{E} = \boldsymbol{\varepsilon_L} + \boldsymbol{\varepsilon_{NL}} = \frac{1}{2}\left[\left(\nabla \boldsymbol{u} + \nabla \boldsymbol{u}^T\right) + \left(\nabla \boldsymbol{u} \cdot \nabla \boldsymbol{u}^T\right)\right]$ is written in vector form as:

$$\boldsymbol{E} = \begin{Bmatrix} E_{xx} \\ E_{yy} \\ \gamma_{xy} = 2E_{xy} \end{Bmatrix} = \begin{Bmatrix} u'_x \\ v'_y \\ u'_y + v'_x \end{Bmatrix} + \begin{Bmatrix} \frac{1}{2}\left(u'_x{}^2 + v'_x{}^2\right) \\ \frac{1}{2}\left(u'_y{}^2 + v'_y{}^2\right) \\ u'_x \cdot u'_y + v'_x \cdot v'_y \end{Bmatrix} \tag{8-1}$$

Now the total couple strain, $\boldsymbol{\varepsilon_T}$ can be written as:

$$\boldsymbol{\varepsilon_T} = (\boldsymbol{\varepsilon_L} + \boldsymbol{\varepsilon_{NL}}) + \boldsymbol{\kappa} = \boldsymbol{E} + \boldsymbol{\kappa} \tag{8-2}$$

Total Strain displacement matrix, $\boldsymbol{B}_T$ can be written as:

$$\boldsymbol{B}_T = \boldsymbol{B}_{LT}{}^1 + \boldsymbol{B}_{NLT}(\boldsymbol{d}) \tag{8-3}$$

Where, $\boldsymbol{B}_{LT}{}^1$ and $\boldsymbol{B}_{NLT}(\boldsymbol{d})$ corresponds to total linear and non-linear strain displacement matrix.

We know from previous formulation for linear geometry (Eq. 6-47):

$$\boldsymbol{\varepsilon_T} = (\boldsymbol{\varepsilon_L} + \boldsymbol{\kappa}) = \begin{bmatrix} u'_x \\ v'_y \\ \left(u'_y + v'_x\right) \\ u''_x \\ u''_y \\ u''_{xy} \\ v''_x \\ v''_y \\ v''_{xy} \end{bmatrix} = \boldsymbol{B}_{LT}{}^1 \cdot \boldsymbol{d}^{(e)}{}_{(32X1)} = [\boldsymbol{M}_7]\,[\boldsymbol{M}_8]\,[\boldsymbol{M}_9] \cdot \boldsymbol{d}^{(e)} \tag{8-4}$$

Therefore, the Total linear stiffness matrix can be written as:

$$\boldsymbol{K_{LT}}^{1} = t \int_{-1}^{+1}\int_{-1}^{+1} \left\{ \overline{\overline{\boldsymbol{D}}} \left(\boldsymbol{B_{LT}}^{1}\right)^{T} \boldsymbol{B_{LT}}^{1} + \overline{\overline{\boldsymbol{C_f}}} \left(\boldsymbol{B_{LT}}^{1}\right)^{T} \boldsymbol{B_{LT}}^{1} \right\} det(\boldsymbol{J}_1)\, d\xi\, d\eta \qquad \textit{(8-5)}$$

Or,

$$\boldsymbol{K_{LT}}^{1} = \boldsymbol{K_N} + \boldsymbol{K_b}$$

With addition of geometrical non-linearity, the Total Tangent Stiffness matrix now takes the form:

$$\boldsymbol{K_T} = \boldsymbol{K_{LT}}^{1} + (\boldsymbol{K_{NLT}}^{1}(\boldsymbol{d}) + \boldsymbol{K_S}) \qquad \textit{(8-6)}$$

Where, $\boldsymbol{K_{NLT}}^{1}(\boldsymbol{d})$ is a non-linear tangent stiffness matrix and $\boldsymbol{K_S}$ is a Tangent stiffness matrix depending on the Second Piola Kirchoff Stress, ($\boldsymbol{S}$).

1) <u>Non-linear tangent stiffness matrix, $\boldsymbol{K_{NLT}}^{1}(\boldsymbol{d})$:</u>

Let's consider total coupled non-linear strain, $\boldsymbol{\varepsilon_{NL}}$

$$\boldsymbol{\varepsilon_{NL}}_{(9X1)} = \begin{Bmatrix} \frac{1}{2}({u'_x}^2 + {v'_x}^2) \\ \frac{1}{2}({u'_y}^2 + {v'_y}^2) \\ u'_x \cdot u'_y + v'_x \cdot v'_y \\ 0 \\ 0 \\ 0 \\ 0 \\ 0 \\ 0 \end{Bmatrix} = \boldsymbol{B_{NL}}(\boldsymbol{d}) \qquad \textit{(8-7)}$$

Differentiating Eq. (8-7)

$$d\boldsymbol{\varepsilon_{NL}} = \boldsymbol{B_{NL}}(\boldsymbol{d})\, \mathrm{d}\,(\boldsymbol{d})$$

$$\mathrm{d}\boldsymbol{\varepsilon_{NL}} = \begin{Bmatrix} u'_x \cdot \mathrm{d}(u'_x) + v'_x \cdot \mathrm{d}(v'_x) \\ u'_y \cdot \mathrm{d}(u'_y) + v'_y \cdot \mathrm{d}(v'_y) \\ \mathrm{d}\,(u'_x) \cdot u'_y + u'_x \cdot \mathrm{d}\,(u'_y) + \mathrm{d}(v'_x) \cdot v'_y + v'_x \cdot \mathrm{d}(v'_y) \\ 0 \\ 0 \\ 0 \\ 0 \\ 0 \\ 0 \end{Bmatrix} \qquad \textit{(8-8)}$$

Or it can also be re-written as:

$$d_{\boldsymbol{NL}} = \boldsymbol{B}_{NLT}(\boldsymbol{d})\, \mathrm{d}\,(\boldsymbol{d})$$

$$\mathrm{d}\boldsymbol{\varepsilon_{NL}} = \begin{bmatrix} u'_x & 0 & v'_x & 0 & 0 & 0 & 0 & 0 & 0 & 0 \\ 0 & u'_y & 0 & v'_y & 0 & 0 & 0 & 0 & 0 & 0 \\ u'_y & u'_x & v'_y & v'_x & 0 & 0 & 0 & 0 & 0 & 0 \\ 0 & 0 & 0 & 0 & 0 & 0 & 0 & 0 & 0 & 0 \\ 0 & 0 & 0 & 0 & 0 & 0 & 0 & 0 & 0 & 0 \\ 0 & 0 & 0 & 0 & 0 & 0 & 0 & 0 & 0 & 0 \\ 0 & 0 & 0 & 0 & 0 & 0 & 0 & 0 & 0 & 0 \\ 0 & 0 & 0 & 0 & 0 & 0 & 0 & 0 & 0 & 0 \\ 0 & 0 & 0 & 0 & 0 & 0 & 0 & 0 & 0 & 0 \end{bmatrix} \cdot \begin{bmatrix} \mathrm{d}(u'_x) \\ \mathrm{d}(u'_y) \\ \mathrm{d}(v'_x) \\ \mathrm{d}(v'_y) \\ 0 \\ 0 \\ 0 \\ 0 \\ 0 \\ 0 \end{bmatrix} = [\boldsymbol{M}_{10}]_{(\boldsymbol{9x10})} \cdot \begin{bmatrix} \mathrm{d}(u'_x) \\ \mathrm{d}(u'_y) \\ \mathrm{d}(v'_x) \\ \mathrm{d}(v'_y) \\ 0 \\ 0 \\ 0 \\ 0 \\ 0 \\ 0 \end{bmatrix}$$

$\Rightarrow$

$$\mathrm{d}\boldsymbol{\varepsilon_{NL}}_{(9X1)} = [\boldsymbol{M}_{10}]_{(\boldsymbol{9x10})} \cdot \mathrm{d}\left\{[\boldsymbol{M}_7]_{(10x10)} \cdot [\boldsymbol{M}_9]_{(10x32)} \cdot \boldsymbol{d}^{(e)}{}_{(32X1)}\right\}$$

$$= [\boldsymbol{M}_{10}]_{(9x10)} \cdot [\boldsymbol{M}_7]_{(10x10)} \cdot [\boldsymbol{M}_9]_{(10x32)} \cdot \mathrm{d}\,(\boldsymbol{d}^{(e)}{}_{(32X1)})$$

$\therefore$

$$\mathrm{d}\boldsymbol{\varepsilon_{NL}} = [\boldsymbol{M}_{10}] \cdot \boldsymbol{B}_T{}^2 \cdot \mathrm{d}\,(\boldsymbol{d}^{(e)}) \qquad \textit{(8-9)}$$

Therefore, the non-linear tangent stiffness matrix, $\boldsymbol{K}_{NLT}{}^1$ can be now written as:

$$\boldsymbol{K}_{NLT}{}^1 = t \iint_{-1\,-1}^{+1\,+1} \left\{\overline{\overline{\boldsymbol{D}}}\ (\boldsymbol{B}_{NLT}(\boldsymbol{d}))^T\, \boldsymbol{B}_{NLT}(\boldsymbol{d}) \ + \ \overline{\overline{\boldsymbol{C}_f}}\, (\boldsymbol{B}_{NLT}(\boldsymbol{d}))^T\, \boldsymbol{B}_{NLT}(\boldsymbol{d})\right\} det(\boldsymbol{J}_1)\, d\xi\, d\eta \qquad \textit{(8-10)}$$

2) <u>Tangent stiffness matrix depending on the Stress, $\boldsymbol{K_S}$:</u>

$$\boldsymbol{K_S} = t \iint_{-1\,-1}^{+1\,+1} \{\, \mathrm{d}(\boldsymbol{B}_T)^T \cdot \boldsymbol{S}\,\}\ det(\boldsymbol{J}_1)\, d\xi\, d\eta \qquad \textit{(8-11)}$$

We know that, $\boldsymbol{B}_T = \boldsymbol{B}_{LT}{}^1 + \boldsymbol{B}_{NL}(\boldsymbol{d})$. By Differentiating $\boldsymbol{B}_T$ we get:

$$\mathrm{d}\,(\boldsymbol{B}_T) = \ \mathrm{d}\,(\boldsymbol{B}_{NLT}(\boldsymbol{d})) = \mathrm{d}\big([\boldsymbol{M}_{10}] \cdot \boldsymbol{B}_T{}^2\big) = \ \mathrm{d}\,[\boldsymbol{M}_{10}\,(\boldsymbol{d})] \cdot \boldsymbol{B}_T{}^2 \qquad \textit{(8-12)}$$

Therefore,

$$\boldsymbol{K_S} = t \iint_{-1\,-1}^{+1\,+1} \left\{ \left(\boldsymbol{B}_T{}^2\right)^T \cdot (\mathrm{d}\,[\boldsymbol{M}_{10}])^T \cdot \boldsymbol{S}\right\} det(\boldsymbol{J}_1)\, d\xi\, d\eta \qquad \textit{(8-13)}$$

Where,

$$(\mathrm{d}\,[\boldsymbol{M}_{10}])^T \cdot \boldsymbol{S} = \begin{bmatrix} \mathrm{d}(u'_x) & 0 & \mathrm{d}(u'_y) & 0 & 0 & 0 & 0 & 0 & 0 \\ 0 & \mathrm{d}(u'_y) & d(u'_x) & 0 & 0 & 0 & 0 & 0 & 0 \\ \mathrm{d}(v'_x) & 0 & \mathrm{d}(v'_y) & 0 & 0 & 0 & 0 & 0 & 0 \\ 0 & \mathrm{d}(v'_y) & \mathrm{d}(v'_x) & 0 & 0 & 0 & 0 & 0 & 0 \\ 0 & 0 & 0 & 0 & 0 & 0 & 0 & 0 & 0 \\ 0 & 0 & 0 & 0 & 0 & 0 & 0 & 0 & 0 \\ 0 & 0 & 0 & 0 & 0 & 0 & 0 & 0 & 0 \\ 0 & 0 & 0 & 0 & 0 & 0 & 0 & 0 & 0 \\ 0 & 0 & 0 & 0 & 0 & 0 & 0 & 0 & 0 \\ 0 & 0 & 0 & 0 & 0 & 0 & 0 & 0 & 0 \end{bmatrix} \cdot \begin{bmatrix} S_{11} \\ S_{22} \\ S_{12} \\ 0 \\ 0 \\ 0 \\ 0 \\ 0 \\ 0 \end{bmatrix}$$

Or,

$$(\mathrm{d}\,[\boldsymbol{M}_{10}])^T \cdot \boldsymbol{S} = \begin{bmatrix} \mathrm{d}(u'_x)\, S_{11} + \mathrm{d}(u'_y)\, S_{12} \\ \mathrm{d}(u'_y)\, S_{22} + \mathrm{d}(u'_x)\, S_{12} \\ \mathrm{d}(v'_x)\, S_{11} + \mathrm{d}(v'_y)\, S_{12} \\ \mathrm{d}(v'_y)\, S_{22} + \mathrm{d}(v'_x)\, S_{12} \\ 0 \\ 0 \\ 0 \\ 0 \\ 0 \end{bmatrix} \qquad \textit{(8-14)}$$

Or,

$$= \begin{bmatrix} S_{11} & S_{12} & 0 & 0 & 0 & 0 & 0 & 0 & 0 & 0 \\ S_{12} & S_{22} & 0 & 0 & 0 & 0 & 0 & 0 & 0 & 0 \\ 0 & 0 & S_{11} & S_{12} & 0 & 0 & 0 & 0 & 0 & 0 \\ 0 & 0 & S_{12} & S_{22} & 0 & 0 & 0 & 0 & 0 & 0 \\ 0 & 0 & 0 & 0 & 0 & 0 & 0 & 0 & 0 & 0 \\ 0 & 0 & 0 & 0 & 0 & 0 & 0 & 0 & 0 & 0 \\ 0 & 0 & 0 & 0 & 0 & 0 & 0 & 0 & 0 & 0 \\ 0 & 0 & 0 & 0 & 0 & 0 & 0 & 0 & 0 & 0 \\ 0 & 0 & 0 & 0 & 0 & 0 & 0 & 0 & 0 & 0 \\ 0 & 0 & 0 & 0 & 0 & 0 & 0 & 0 & 0 & 0 \end{bmatrix} \cdot \begin{bmatrix} \mathrm{d}(u'_x) \\ \mathrm{d}(u'_y) \\ \mathrm{d}(v'_x) \\ \mathrm{d}(v'_y) \\ 0 \\ 0 \\ 0 \\ 0 \\ 0 \\ 0 \end{bmatrix} = [\boldsymbol{M}_{11}]_{(\mathbf{10x10})} \cdot \begin{bmatrix} \mathrm{d}(u'_x) \\ \mathrm{d}(u'_y) \\ \mathrm{d}(v'_x) \\ \mathrm{d}(v'_y) \\ 0 \\ 0 \\ 0 \\ 0 \\ 0 \\ 0 \end{bmatrix}$$

$\Rightarrow$

$$(\mathrm{d}\,[\boldsymbol{M}_{10}])^T \cdot \boldsymbol{S} = [\boldsymbol{M}_{11}]_{(10x10)} \cdot \mathrm{d}\left\{[\boldsymbol{M}_7]_{(10x10)} \cdot [\boldsymbol{M}_9]_{(10x32)} \cdot \boldsymbol{d}^{(e)}{}_{(32X1)}\right\}$$

$$= [\boldsymbol{M}_{11}]_{(10x10)} \cdot [\boldsymbol{M}_7]_{(10x10)} \cdot [\boldsymbol{M}_9]_{(10x32)} \cdot \mathrm{d}\,(\boldsymbol{d}^{(e)}{}_{(32X1)})$$

$\therefore$

$$(\mathrm{d}\,[\boldsymbol{M}_{10}])^T \cdot \boldsymbol{S} = [\boldsymbol{M}_{11}] \cdot \boldsymbol{B}_T{}^2 \cdot \mathrm{d}\,(\boldsymbol{d}^{(e)})$$

Now substituting $(\mathrm{d}\,[\boldsymbol{M}_{10}])^T \cdot \boldsymbol{S}$ in Eq. (8-13), Tangent matrix depending on the Stress, $\boldsymbol{K_S}$ can be written as:

$$\boldsymbol{K} = t \int_{-1}^{+1}\int_{-1}^{+1} \left\{ \left(\boldsymbol{B}_T{}^2\right)^T \cdot [\boldsymbol{M}_{11}] \cdot \boldsymbol{B}_T{}^2 \right\} det(\boldsymbol{J}_1)\, d\xi\, d\eta \qquad (8\text{-}15)$$

Above non-linear geometry (isotropic elastic) formulations have been implemented in the non-local element: "NL U32_V1.4".

8.2 Validation of Geometrical Non-Linearity

Similar to Linear case, for Non-Local element (NL U32) with geometrical non-linearity (Isotropic Elastic case), results are compared with ABAQUS® plane stress element (CPS4) by turning on the non-linear geometry in the STEP module (NLGEOM = YES). Same material properties, mesh size and studies are performed as of linear case to validate the NL U32 element under compression and bending.

As previous, compression and bending loads are investigated and compared to classical elements.

8.2.1 Case1: Compression

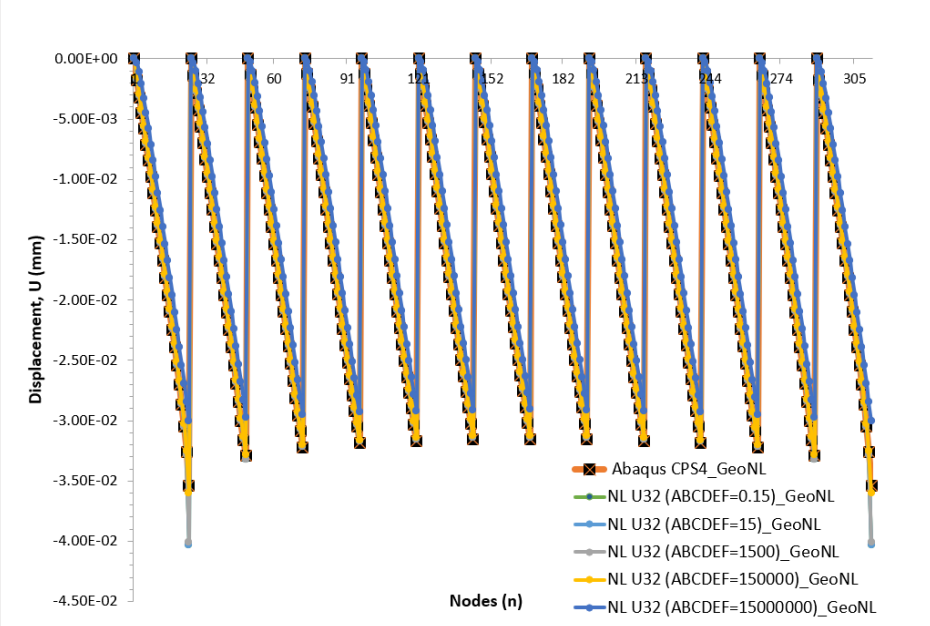

Figure 70: Influence of Cf Parameters (Compression) with geometrical non-linearity: Displacement (U)

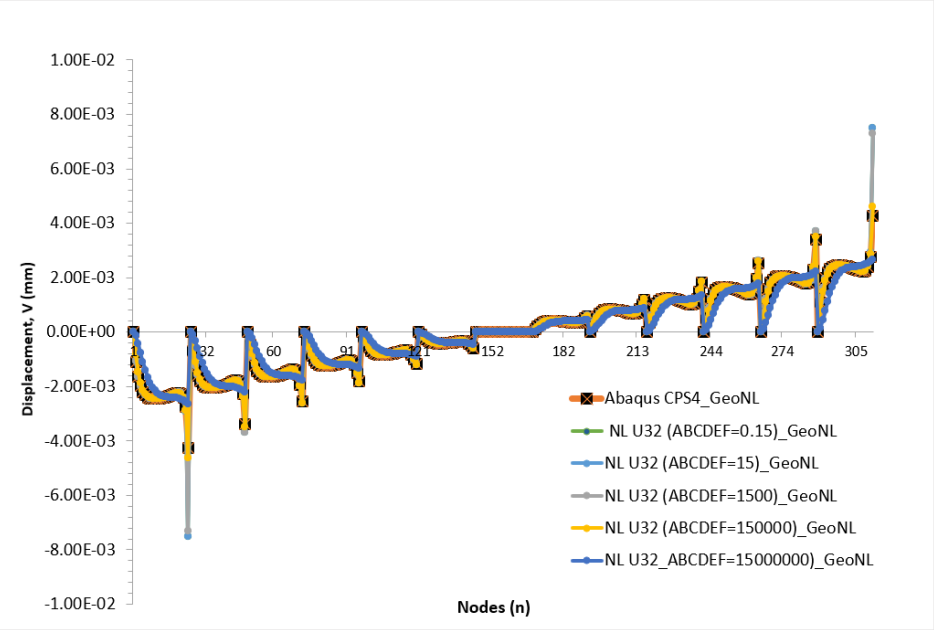

Figure 71: Influence of Cf Parameters (Compression) with geometrical non-linearity: Displacement (V)

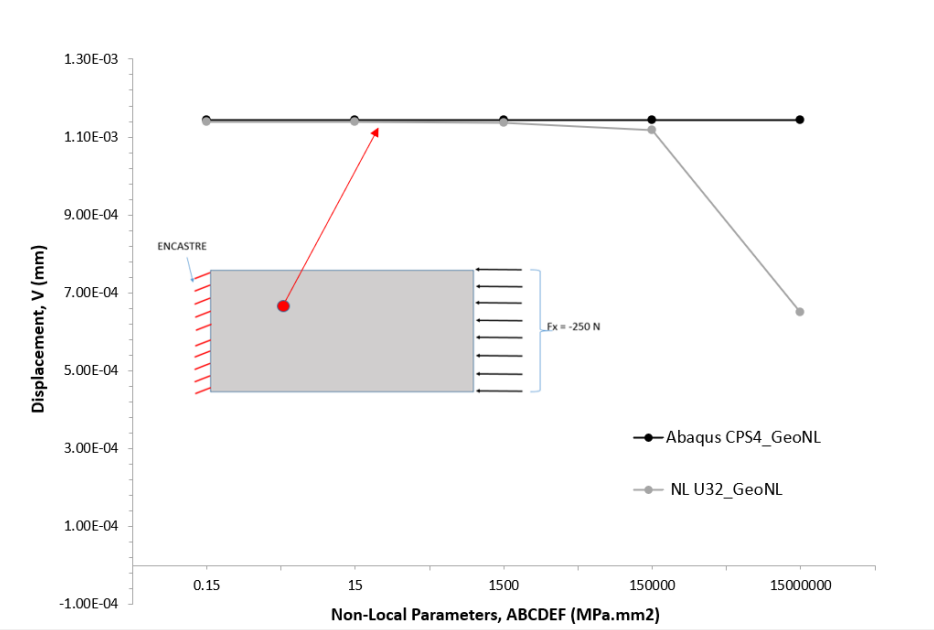

Figure 72: Comparison of Displacements (V) at node 222 for different Cf parameters value (Compression) with geometrical non-linearity

8.2.2 Case2: Bending

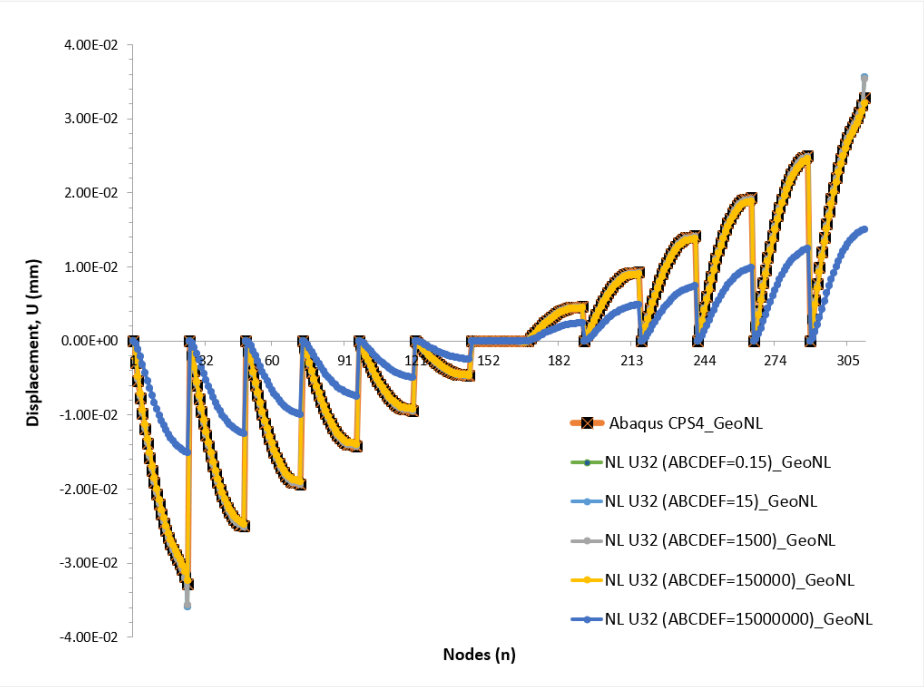

Figure 73: Influence of Cf Parameters (Bending) with geometrical non-linearity: Displacement (U)

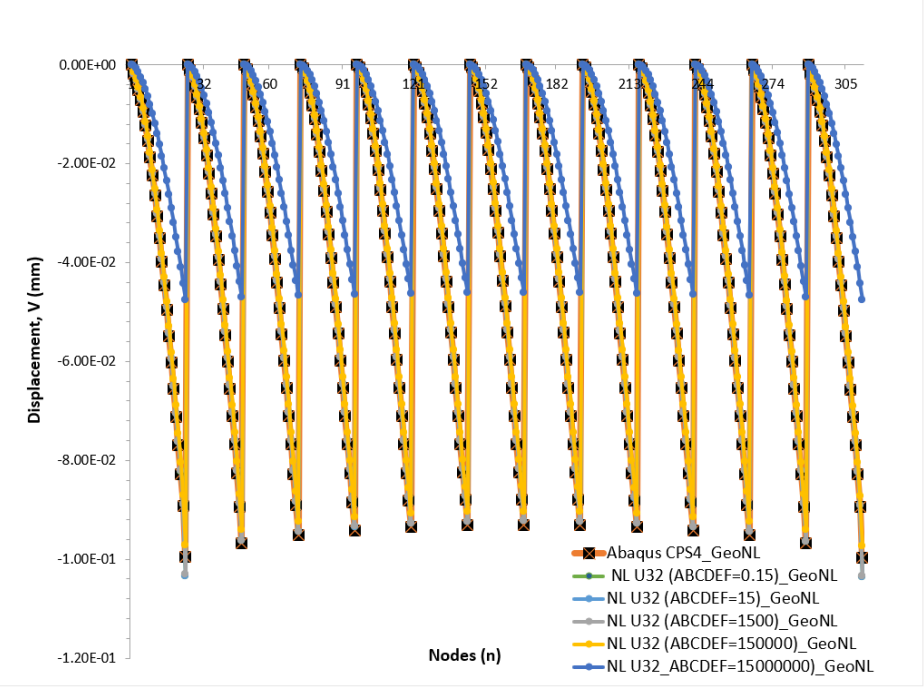

Figure 74: Influence of Cf Parameters (Bending) with geometrical non-linearity: Displacement (V)

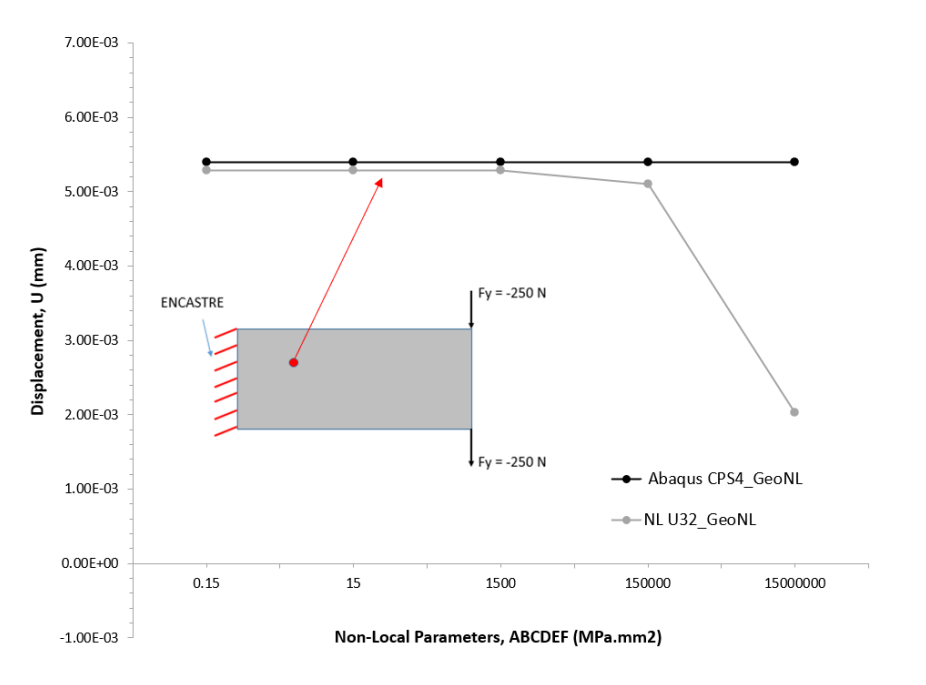

Figure 75: Comparison of Displacement (U) at node 222 for different Cf parameters values (Bending) with geometrical non-linearity

From both the cases: compression (Figure 70, Figure 71) and bending (Figure 73, Figure 74), it can be observed that, similar response and difference in solution is very less compared to ABAQUS® CPS4 element when local fiber bending stiffness matrix, $\overline{\overline{\boldsymbol{C_f}}}$ parameters (ABCDEF) varied up to 1500 $MPa \cdot mm^2$. But, significant difference in solution is observed compared to CPS4 element when ABCDEF value is increased above 1500 $MPa \cdot mm^2$ (see Figure 72 and Figure 75). Much stiffer response can be observed with NL U32 compared to continuum solid CPS4. The reason for the difference is same as of *linear geometry case*. Clearly, it can be observed that it is giving same response as of linear geometry case with the variation of local fiber bending stiffness matrix, $\overline{\overline{\boldsymbol{C_f}}}$ parameters (ABCDEF). The global response obtained with NL U32 is almost similar compared to ABAQUS® CPS4 element, which validates the non-local element for non-linear geometry with isotropic elasticity. Mesh convergence study is also performed and observed that as the mesh size (n) is increased, we tend to obtain an asymptotic or converged solution for both NL U32 element and ABAQUS® CPS4 element with non-linear geometry.

Another, important parameter to be considered in the model to predict well the compressive strength of composites, particularly unidirectional is 'matrix material non-linearity', which is discussed in detail in the following chapter.

9 Matrix Material Non-Linearity in NL U32: description of the law and validation

This chapter focus on formulation and addition of '*Non-linear material effects*' in Homogenized Non-Local model, thereby integrating inside Non-Local Super parametric element (NL U32). And then finally validating the results against ABAQUS® classical in-built elements and material law.

9.1 Formulation and addition of matrix material non-linearity (Isotropic)

Matrix material non-linear behavior is taken into account by an elasto-plastic constitutive law based on the Ramberg-Osgood (Isotropic) relation, which is written in the 3D case in the following form (ABAQUS® 2017 theory manual *(section 4.3.9))*:

$$E\,\boldsymbol{\varepsilon} = (1+\nu)\,\boldsymbol{S}^d - (1-2\nu)p\,\mathbf{I} + \frac{3}{2}\,\alpha\left[\frac{q}{\sigma_y}\right]^{n-1}\boldsymbol{S}^d \qquad (9\text{-}1)$$

Where, E, ν, α, n and σ_y denote, the Young's modulus, Poisson's ratio, yield offset, hardening exponent and the yield stress. Equivalent hydrostatic stress, $p = -\frac{1}{3}\boldsymbol{S} : \mathbf{I} = -\frac{1}{3}\,trace(\boldsymbol{S})$, $\boldsymbol{S}^d$ is the stress deviator defined by, $\boldsymbol{S}^d = \boldsymbol{S} + p\,\mathbf{I}$ and the Von-Mises equivalent stress defined by: $q = \sqrt{\frac{3}{2}\boldsymbol{S} : \boldsymbol{S}}$.

Since our non-local element is developed based on the plane stress assumption ($S_{33} = S_{13} = S_{23} = 0\,; \varepsilon_{13} = \varepsilon_{23} = 0\,, \varepsilon_{33} \neq 0$ and $S^d{}_{33} = p$) , the above law can be modified in 2D (plane stress) case as follows:

In 2D space and with the assumption of plane stress, Ramberg-Osgood law is deduced from the Eq. (9-1). Equivalent hydrostatic stress, Von-Mises equivalent stress and stress deviator is written as:

$$p = -\frac{1}{3}\,(S_{11} + S_{22})$$

$$q = \sqrt{{S_{11}}^2 + {S_{22}}^2 - S_{11}\,S_{22} + 3{S_{12}}^2} \qquad (9\text{-}2)$$

$$\boldsymbol{S}^d = \boldsymbol{S} + p\,\mathbf{I} = \begin{bmatrix} \left(\frac{2}{3}S_{11} - \frac{1}{3}S_{22}\right) & S_{12} & 0 \\ S_{12} & \left(-\frac{1}{3}S_{11} + \frac{2}{3}S_{22}\right) & 0 \\ 0 & 0 & \left(-\frac{1}{3}S_{11} - \frac{1}{3}S_{22}\right) \end{bmatrix}$$

Now expanding Eq. (9-1), we can re-write:

$$E\,\varepsilon_{11} = (1+\nu)\,S^{d}{}_{11} - (1-2\nu)p + \tfrac{3}{2}\,\alpha\left[\frac{q}{\sigma_y}\right]^{n-1} S^{d}{}_{11} \qquad \text{(i)}$$

$$E\,\varepsilon_{22} = (1+\nu)\,S^{d}{}_{22} - (1-2\nu)p + \tfrac{3}{2}\,\alpha\left[\frac{q}{\sigma_y}\right]^{n-1} S^{d}{}_{22} \qquad \text{(ii)}$$

$$E\,\varepsilon_{12} = (1+\nu)\,S^{d}{}_{12} - (1-2\nu)p + \tfrac{3}{2}\,\alpha\left[\frac{q}{\sigma_y}\right]^{n-1} S^{d}{}_{12} \qquad \text{(iii)}$$

and,

$$E\,\varepsilon_{33} = (1+\nu)\,S^{d}{}_{33} - (1-2\nu)p + \tfrac{3}{2}\,\alpha\left[\frac{q}{\sigma_y}\right]^{n-1} S^{d}{}_{33} \qquad \text{(iv)}$$

(9-3)

$$\text{Since, } S^{d}{}_{33} = p$$

⇒

$$E\,\varepsilon_{33} = (1+\nu)\,p - (1-2\nu)p + \tfrac{3}{2}\,\alpha\left[\frac{q}{\sigma_y}\right]^{n-1} p \qquad \text{(v)}$$

∴

$$\varepsilon_{33} = \frac{3\nu}{E}p + \frac{3}{2}\,\frac{\alpha}{E}\left[\frac{q}{\sigma_y}\right]^{n-1} p$$

Now substituting $S^{d}{}_{11}$, $S^{d}{}_{22}$ and $S^{d}{}_{12}$ in Eq. (9-1) we obtain:

$$E\,\varepsilon_{11} = (1+\nu)\left(\frac{2}{3}S_{11} - \frac{1}{3}S_{22}\right) - (1-2\nu)p + \frac{3}{2}\,\alpha\left[\frac{q}{\sigma_y}\right]^{n-1}\left(\frac{2}{3}S_{11} - \frac{1}{3}S_{22}\right)$$

⇒

$$E\,\varepsilon_{11} = S_{11}\left(1 + \alpha\left[\frac{q}{\sigma_y}\right]^{n-1}\right) + S_{22}\left(-\nu - \frac{\alpha}{2}\left(\left[\frac{q}{\sigma_y}\right]^{n-1}\right)\right) \qquad \text{(i)}$$

Similarly,

$$E\,\varepsilon_{22} = S_{11}\left(-\nu - \frac{\alpha}{2}\left(\left[\frac{q}{\sigma_y}\right]^{n-1}\right)\right) + S_{22}\left(1 + \alpha\left[\frac{q}{\sigma_y}\right]^{n-1}\right) \qquad \text{(ii)}$$

(9-4)

$$E\,\varepsilon_{12} = S_{12}\left((1+\nu) + \tfrac{3}{2}\,\alpha\left[\frac{q}{\sigma_y}\right]^{n-1}\right) \qquad \text{(iii)}$$

We can observe from the above equation that, the system is non-linear in S_{11}, S_{22} and S_{12} and we have written the system in function of stress, $\boldsymbol{f}(\boldsymbol{S})$, with residual, $\boldsymbol{R} = E\,\boldsymbol{\varepsilon} - \boldsymbol{f}(\boldsymbol{S})$, which can be solved using Newton Raphson/Newton's method.

$$\boldsymbol{S}_{i+1} = \boldsymbol{S}_i + \boldsymbol{c}_{\boldsymbol{S}}$$

Where,

$$corrector, \boldsymbol{c}_{\boldsymbol{S}} = \frac{\boldsymbol{R}}{\boldsymbol{f}'(\boldsymbol{S})} = \boldsymbol{R} \cdot [\boldsymbol{f}'(\boldsymbol{S})]^{-1}$$

(9-5)

Note that: $[\boldsymbol{f}'(\boldsymbol{S})]^{-1} = Jacobi\ or\ Jacobian\ or\ Tangent\ stiffness\ matrix\ (\boldsymbol{DDSDDE})$ *in ABAQUS ® User material subroutine (UMAT), which is output to ABAQUS® solver, has to be updated along with* $(\boldsymbol{STRESS})$, $\boldsymbol{S}$ *during each iteration, until the convergence is achieved.* For

Newton's method, it is necessary to provide the initial guess for stress, $\mathbf{S}_0$, which is calculated using constitutive relation: $\boldsymbol{S}_0 = \boldsymbol{D}_{el}\,\boldsymbol{\varepsilon}_{el}$ in the UMAT.

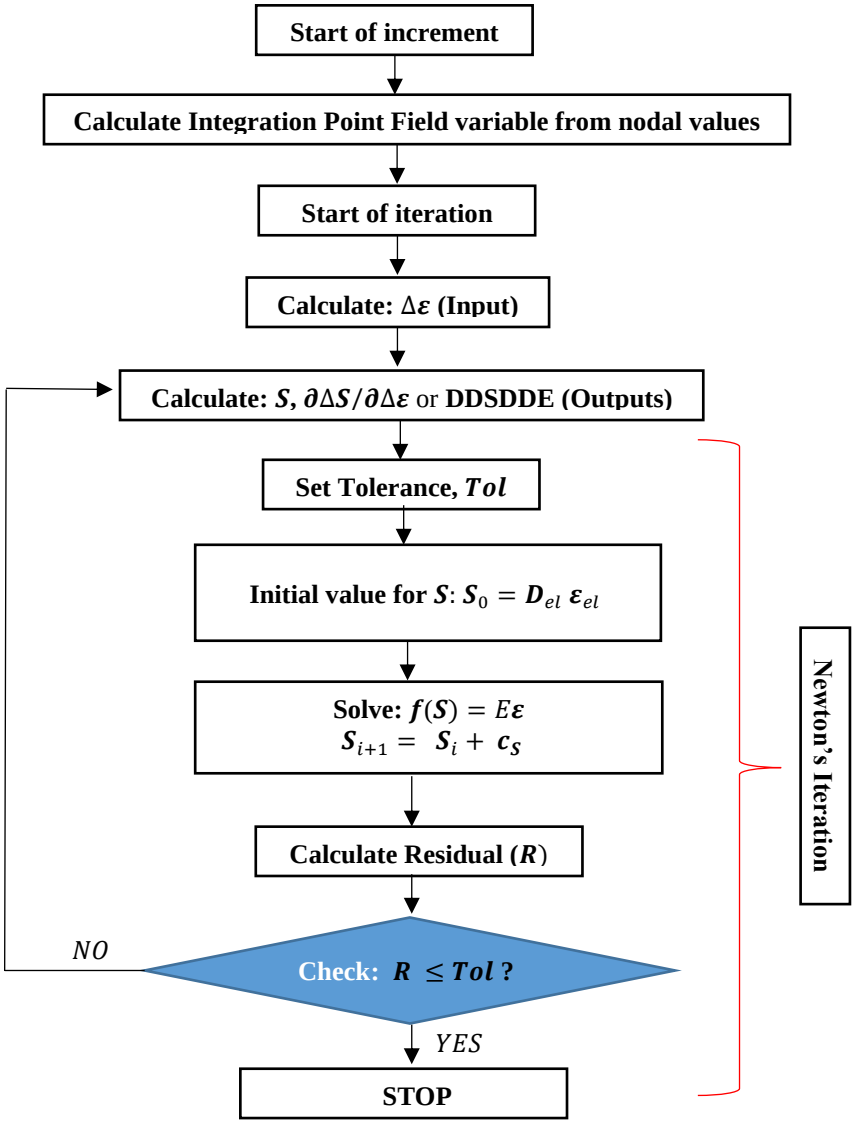

Figure 76: Workflow of ABAQUS® UMAT subroutine

The tangent matrix for the material ($\boldsymbol{DDSDDE}$ *or* $\bar{\bar{\boldsymbol{D}}} = \partial\Delta\boldsymbol{S}/\partial\Delta\boldsymbol{\varepsilon}$) is required when *ABAQUS/Standard® is being used for 'Implicit time integration' and Newton's method is being used to solve the equilibrium equations.* The flowchart in Figure 76 gives the detail workflow of ABAQUS® UMAT subroutine.

All the above formulations are coded in UMAT subroutine of ABAQUS ® and has been integrated inside non-local user element ("NL U32_V1.3" and "NL U32_V1.5") with subroutine named 'KUMAT'. Also, a separate user material subroutine, called 'KURMAT' is also integrated inside the

NL U32 to take into account tangent material behavior of fiber non-local stiffness (elastic at the moment).

9.2 Validation of matrix material non-linearity

Validation of matrix material non-linearity (Isotropic Ramberg Osgood Elastoplastic law in 2D plane stress) is performed by two steps:

1) Comparison of the results obtained by User Material (UMAT) subroutine, developed for Isotropic Ramberg-Osgood (RO) law with respect to ABAQUS ® in-built Isotropic Ramberg-Osgood (RO), using CPS4 element in both the cases with non-linear geometry.
2) Comparison of the results obtained by Ramberg-Osgood UMAT integrated within NL U32 (KUMAT) with respect to ABAQUS ® in-built Isotropic Ramberg-Osgood (RO) using CPS4 element with non-linear geometry.

9.2.1 Validation of UMAT (RO Law) with CPS4

Material Properties used: $E = 8000\,MPa,\ \nu = 0.4,\ \sigma_y = 60MPa, \alpha = 0.015\ and\ n = 4.$ All loading test cases (traction, compression and shear) are performed on square plate of dimension 0.1 x 0.1 mm with 1 Elem mesh. Displacements are applied in 10 time steps.

a) Uniaxial Traction/Compression in longitudinal or X direction:

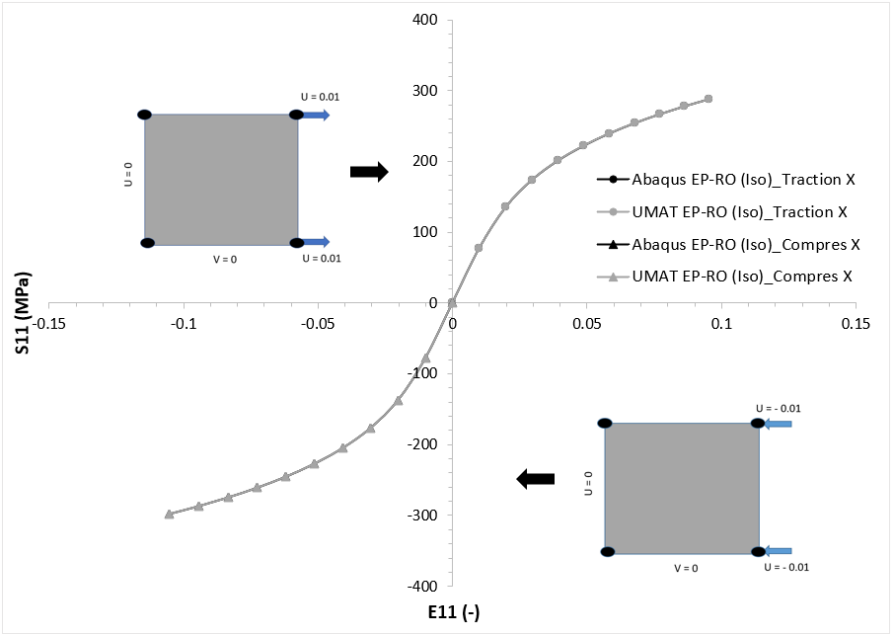

Figure 77: Comparison of UMAT EP-RO (Iso) with Abaqus EP-RO (Iso): Uniaxial Traction/Compression in X direction

b) Uniaxial Traction/Compression in transverse or Y direction:

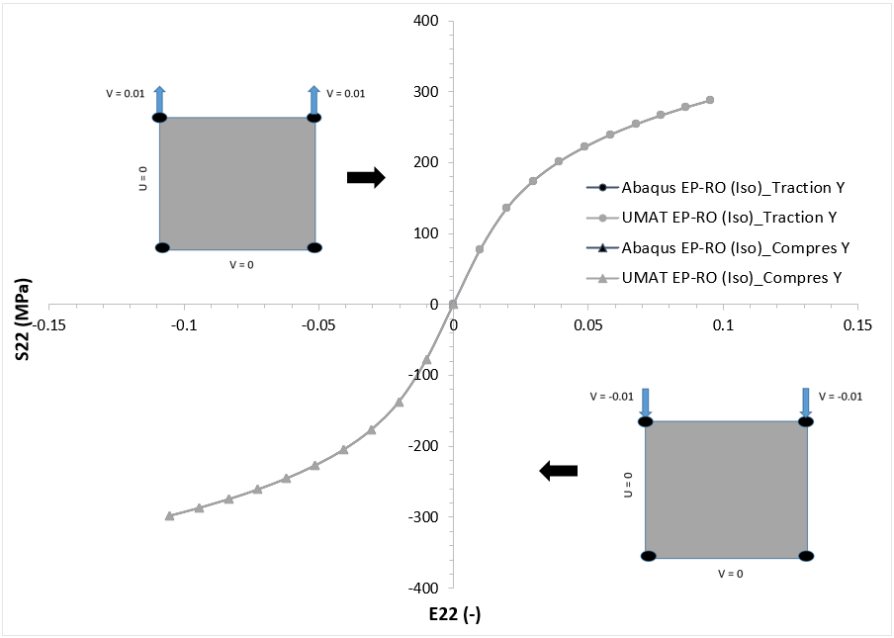

Figure 78: Comparison of UMAT EP-RO (Iso) with Abaqus EP-RO (Iso): Uniaxial Traction/Compression in Y direction

c) Shear in X / Y direction

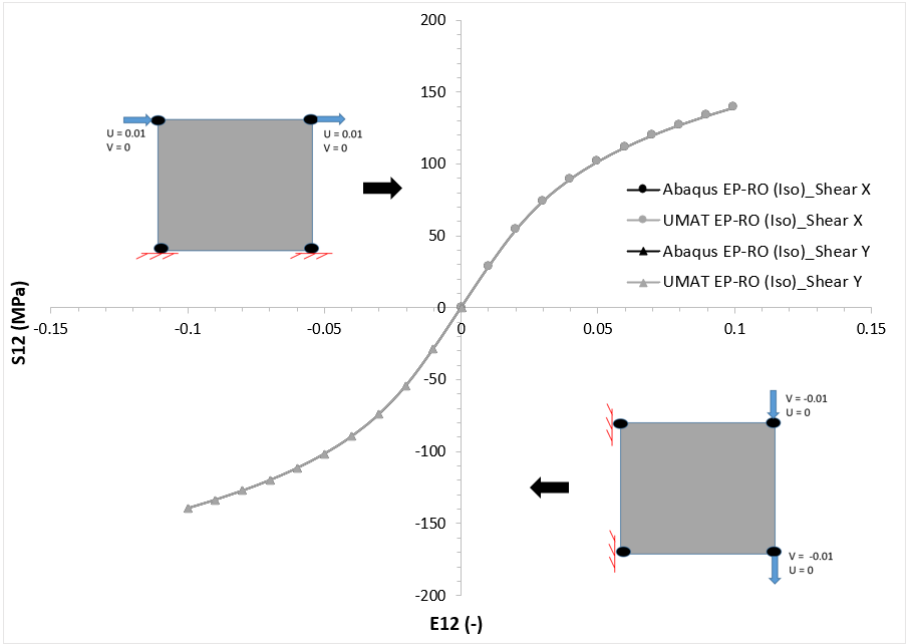

Figure 79: Comparison of UMAT EP-RO (Iso) with Abaqus EP-RO (Iso): Shear in X / Y direction

Figure 77 - Figure 79 depict the evolution of stress v/s strain components with both RO law UMAT and ABAQUS® built-in RO law for different loading cases(traction, compression and shear). It is clearly justified from figures that the response with RO law UMAT and ABAQUS® RO-law is exactly same, thereby validating the development.

9.2.2 Validation of matrix material non-linearity (RO Law) in NL U32

Validation is performed with respect to ABAQUS® built-in RO Law and CPS4 element (Non-linear geometry). The isotropic elasto-plastic matrix material properties are taken from Nezamabadi et al.,[N1]:$E = 4500\ MPa,\ \nu = 0.4,\ \sigma_y = 60MPa,\ \alpha = 0.002\ and\ n = 3$. Similar to Linear and Non-Linear Isotropic Elastic cases, the validation is performed by the values for parameters of local fiber bending stiffness matrix (non-local parameters) A,B,C,D,E,F are started with initial guess of low value, 0.15 $MPa \cdot mm^2$and varied with the order of 10^2. And also, same mesh, load and boundary conditions are used.

It is important to note that field of the results (Ex: Displacements/Stress-Strain) obtained with User Elements (UEL's) cannot be visualized with the standard post-processing tool, ABAQUS/Viewer as it does not support. The main reason for this is that the element topology is hidden inside the element subroutine. The ABAQUS/Viewer only supports the visualization of built-in elements of the ABAQUS® element library (standard elements). There is no interface to specify user defined elements in the viewer. Hence it is necessary to user external post-processing tool like "PARAVIEW", which is an open source data visualization software for the field outputs, developed by SANDIA National Laboratories, Los Alamos National Laboratory and the company Kitware Inc. Therefore, all the results of field output of User Element (NL U32) shown in this chapter is obtained through "PARAVIEW", by defining a specific script.

As previous, compression and bending loads are investigated and the solution is compared to ABAQUS®CPS4 with different values of micro-bending stiffness. In Appendix section 13.5, fields of displacements, strains and stress are plotted.

For small values of non-local stiffness, the fields are identical to ABAQUS® CPS4, consequently the tool is validated with all non-linearities need to solve the problem. Further, another result, which is interesting is that, when the non-local stiffness increase, the gradients generated by the boundary conditions spread out in the structure. The length of the influence generated by the support is thus directly linked with the stiffness. We have obtained correctly the expected results.

9.2.3 Comparison with 2D heterogenous complete microstructure (Non-linear Matrix material and Non-linear geometry)

As a final step of validation of Non-Local Homogenous model implemented in non-local element (NL U32) for Non-Linear Matrix material and non-linear geometry case, results are compared with 2D Unidirectional (UD) composite (T300/914 Carbon/epoxy) model built using ABAQUS® plane stress element (CPS4). The stacking sequence of UD heterogenous composite (with 10 layers) model built in ABAQUS® is as shown in Figure 67.

The elastic fiber and elasto-plastic matrix properties of T300/914 Carbon/epoxy UD ply obtained from Drapier et al., [D1] and Nezamabadi et al., [N1] as in Table 5 is assigned for both matrix and fiber in heterogenous model of ABAQUS® and homogenous non-local model. Note that the matrix and fiber is assumed isotropic in both the models.

Table 5: Elastic fiber and Elasto-plastic matrix material properties of UD ply

<table>
<tr><th colspan="2">Heterogenous model Abaqus (CPS4)</th><th colspan="2">Homogenous Non-local model (NL U32)</th></tr>
<tr><td>matrix</td><td>fiber</td><td>matrix</td><td>fiber</td></tr>
<tr><td>$E_m = 4500\ MPa$</td><td>$E_f = 240000\ MPa$</td><td>$E_m = 4500\ MPa$</td><td>$E_f = 240000\ MPa$</td></tr>
<tr><td>$\nu_m = 0.4$</td><td>$\nu_f = 0.3$</td><td>$\nu_m = 0.4$</td><td>$\nu_f = 0.3$</td></tr>
<tr><td>$\sigma_y = 60\ MPa$</td><td></td><td>$\sigma_y = 60\ MPa$</td><td></td></tr>
<tr><td>$n = 3$</td><td></td><td>$n = 3$</td><td></td></tr>
<tr><td>$\alpha = 0.002$</td><td></td><td>$\alpha = 0.002$</td><td></td></tr>
<tr><td colspan="2" rowspan="4">thickness, $t = 1mm$</td><td colspan="2">Volume fraction, $f = 0.625$</td></tr>
<tr><td colspan="2">Diameter of fibers, $d_f = 0.01mm$</td></tr>
<tr><td colspan="2">Local fiber bending stiffness parameter for UD ply, $D = fE_f r_{gf}^2 = 0.09375\ MPa \cdot mm^2$
$r_{gf} = \sqrt{\frac{I}{S_f}}$</td></tr>
<tr><td>ABCEF = 0.001*D</td><td>thickness, $t = 1mm$</td></tr>
</table>

As previous it is important to note that, for UD ply, since there is just one gradient ($v'' = \frac{\partial^2 v}{\partial x^2}$) along thickness direction, as in case of Drapier et al., (1999) [D3], just one parameter (D) of local bending stiffness matrix, $\overline{\overline{\boldsymbol{C_f}}}$ is considered, values for other parameters (ABCEF) is assigned very low compared to parameter D in homogenous non-local model.

From Figure 81 and Figure 91 , it is clear that the results (displacements: u, v) obtained from homogenous non-local model is in close comparison with the results of heterogenous model of ABAQUS ® for the case of UD composite subjected to compression and bending. The slight difference between two solutions are clearly due to the addition of non-local terms and choice of interpolation functions (for displacement and geometry) in homogenous non-local model.

With this validation, it can be concluded that the homogenized non-local model with matrix plasticity (implemented in NL U32 element) can be used for analysis of UD composites (Non-Linear matrix material with Linear and Non-Linear Geometry). The comparison of fields of different components of stress, strain, curvatures and distributed bending moments are shown in Figure 82 - Figure 99 for both the cases of compression and bending. We can observe that the behavior of homogenous non-local composite is in good comparison with the heterogenous

composite. And also, first results of curvatures and distributed bending moments can be seen in Figure 88 - Figure 89 for compression and Figure 98 - Figure 99 for bending.

9.2.3.1 *Case1: Compression*

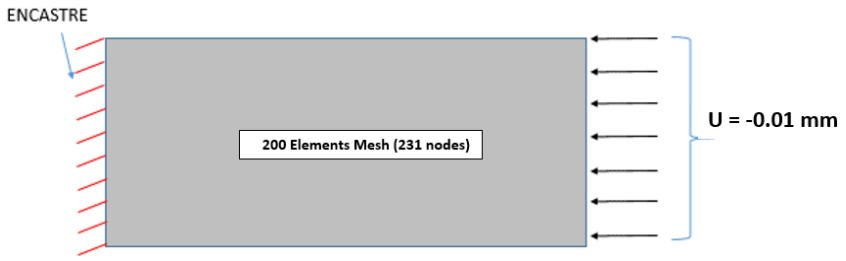

Figure 80: Mesh, Load and Boundary conditions (Validation w.r.t hetero UD composite – matrix plasticity) in case of compression

1) Displacement fields:

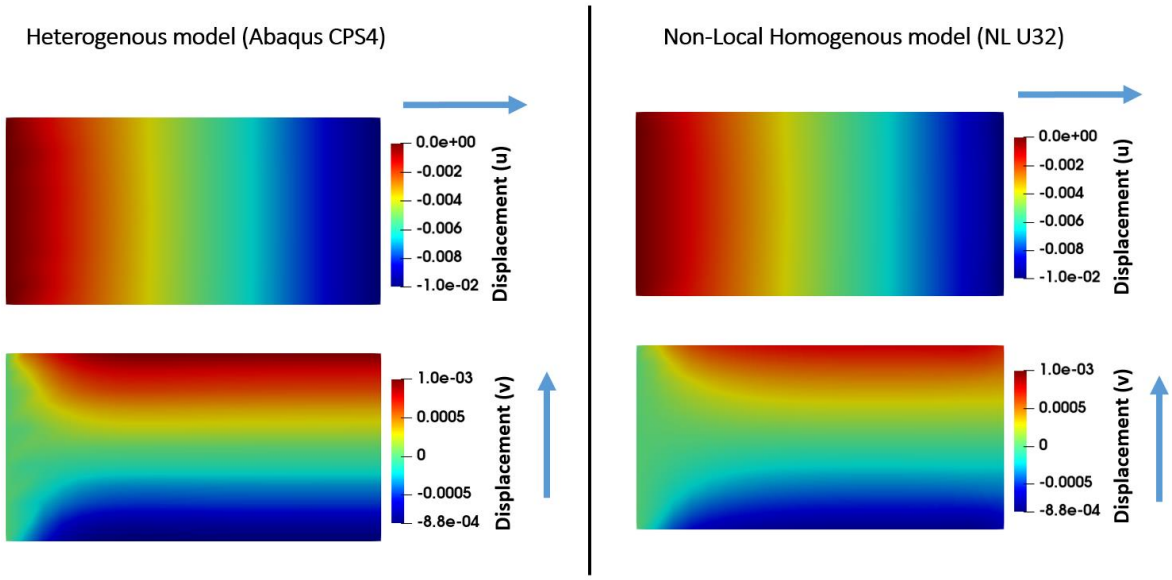

Figure 81: Comparison of displacement fields (u,v) w.r.t hetero UD composite (Matrix plasticity and Non-Linear geometry) – compression

2) Stress Fields (***S***):

S11

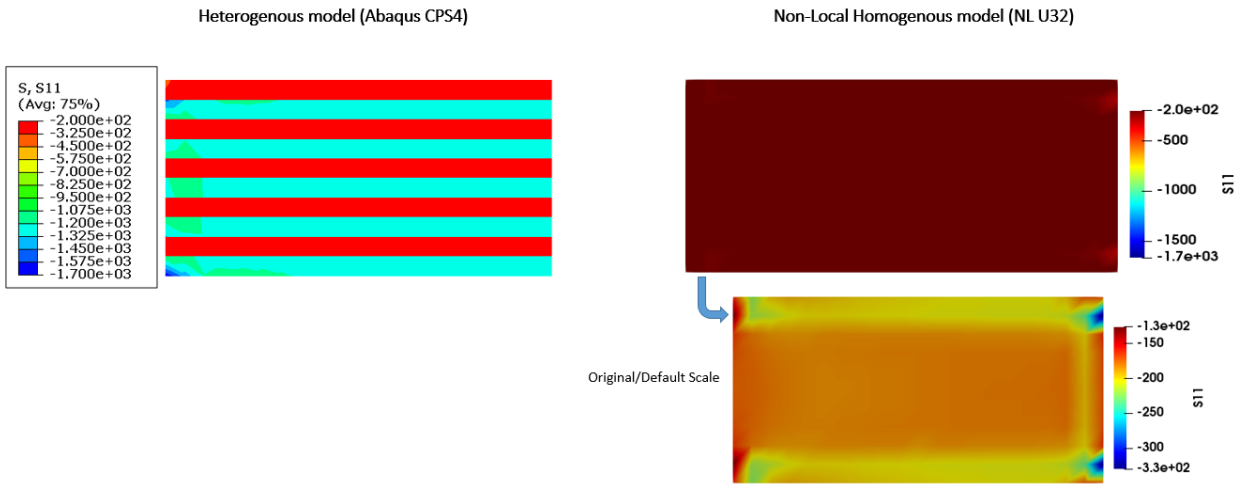

Figure 82: Comparison of S11 component – Non-linear Material and Non-Linear Geometry – compression

S22

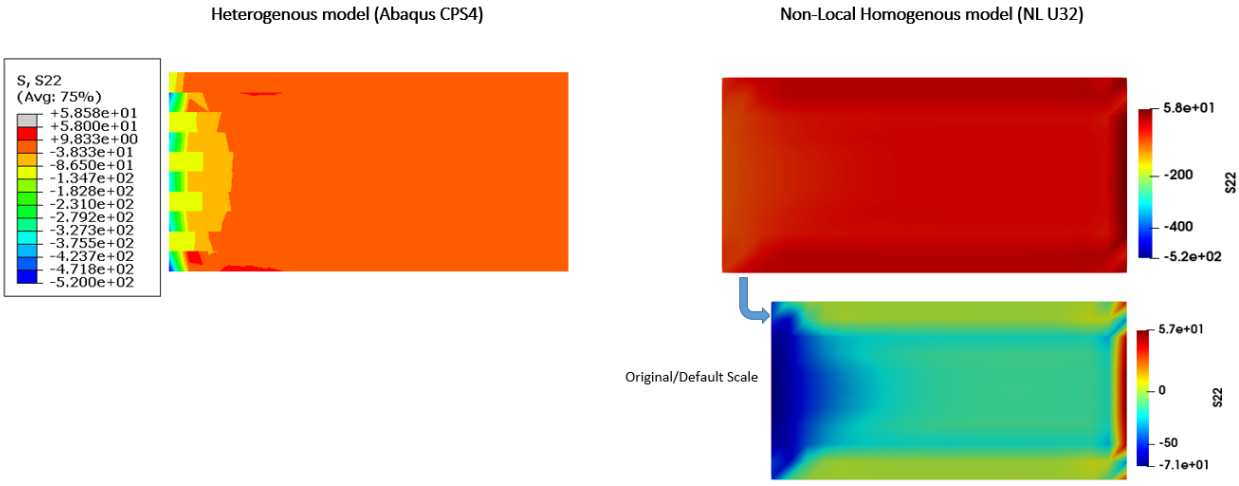

Figure 83: Comparison of S22 component – Non-linear Material and Non-Linear Geometry- compression

S12

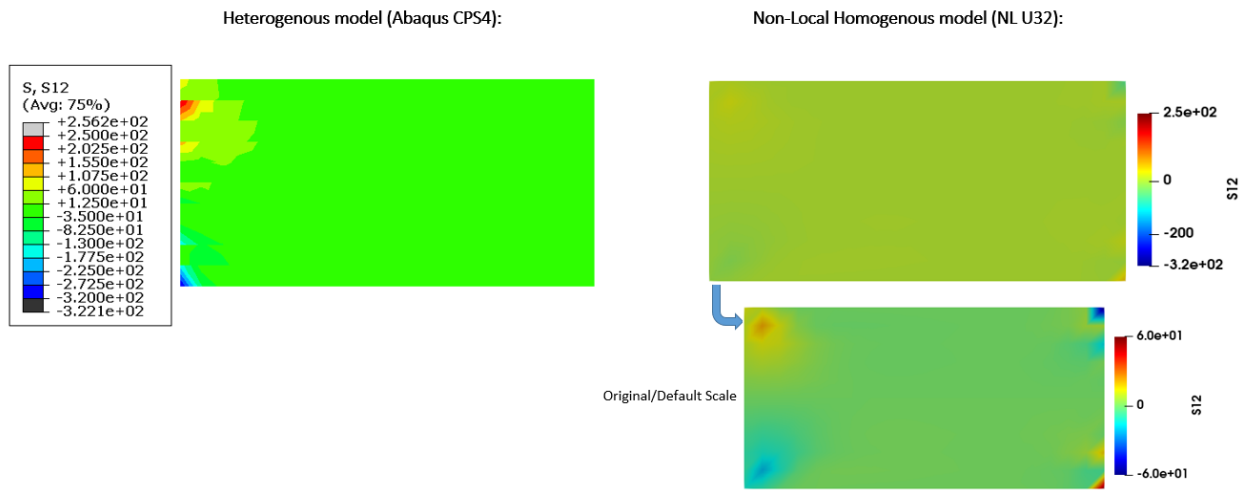

Figure 84: Comparison of S12 component – Non-linear Material and Non-Linear Geometry- compression

3) Strain Fields (***E***):

E11

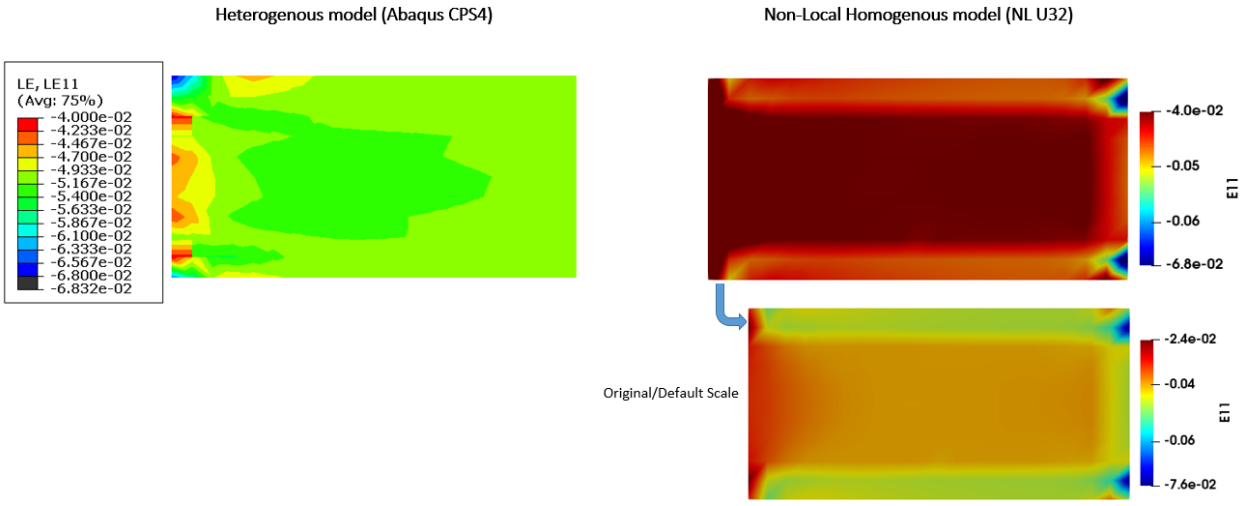

Figure 85: Comparison of E11 component – Non-linear Material and Non-Linear Geometry- compression

E22

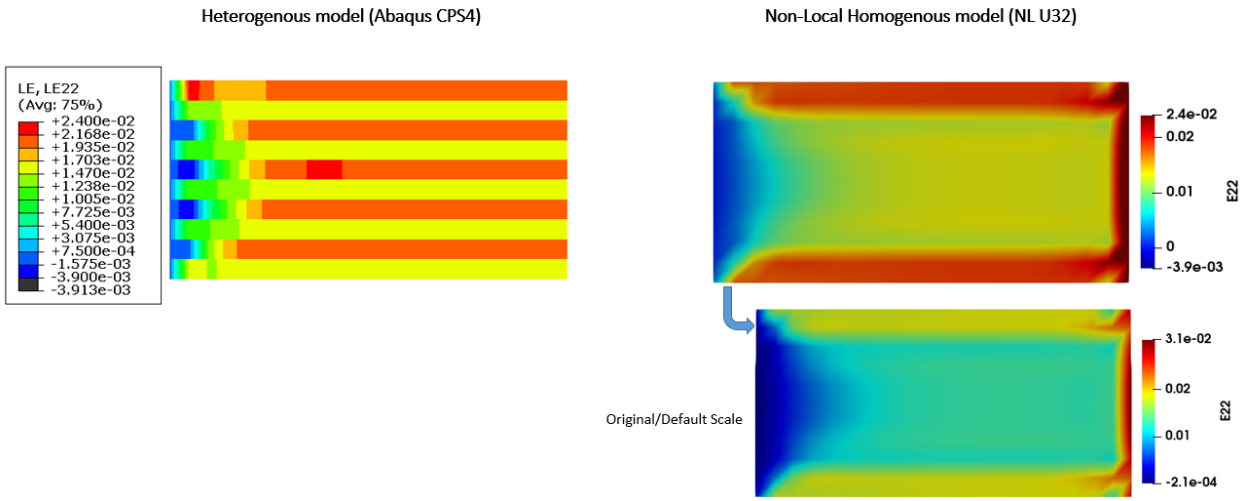

Figure 86: Comparison of E22 component – Non-linear Material and Non-Linear Geometry- compression

E12

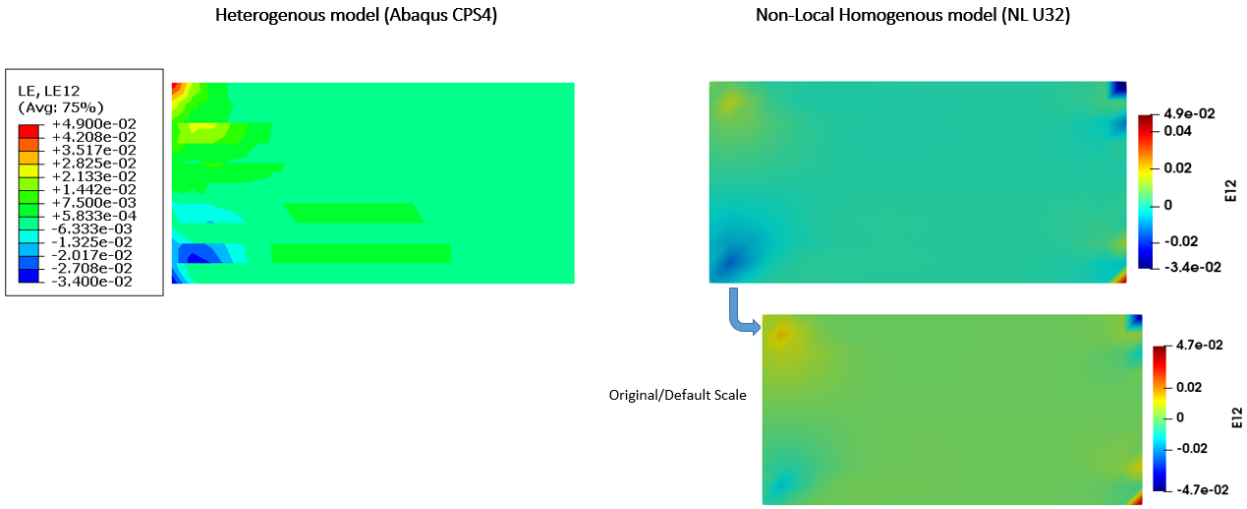

Figure 87: Comparison of E12 component – Non-linear Material and Non-Linear Geometry- compression

4) Curvature/higher order bending strain fields **(κ)**:

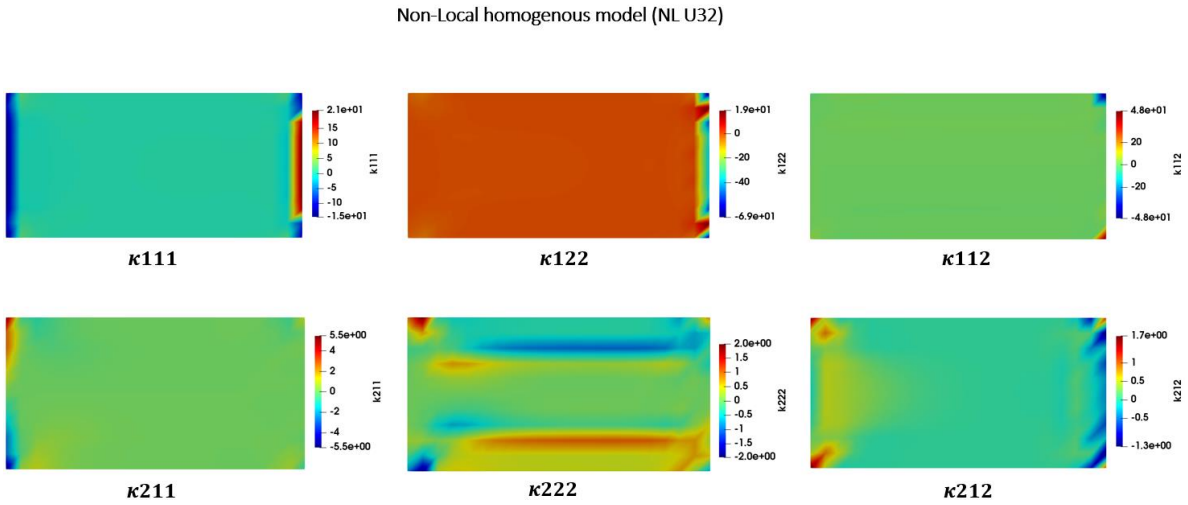

Figure 88: Curvature components fields – Non-linear Material and Non-Linear Geometry- compression

5) Distributed bending moment fields **(τ)**:

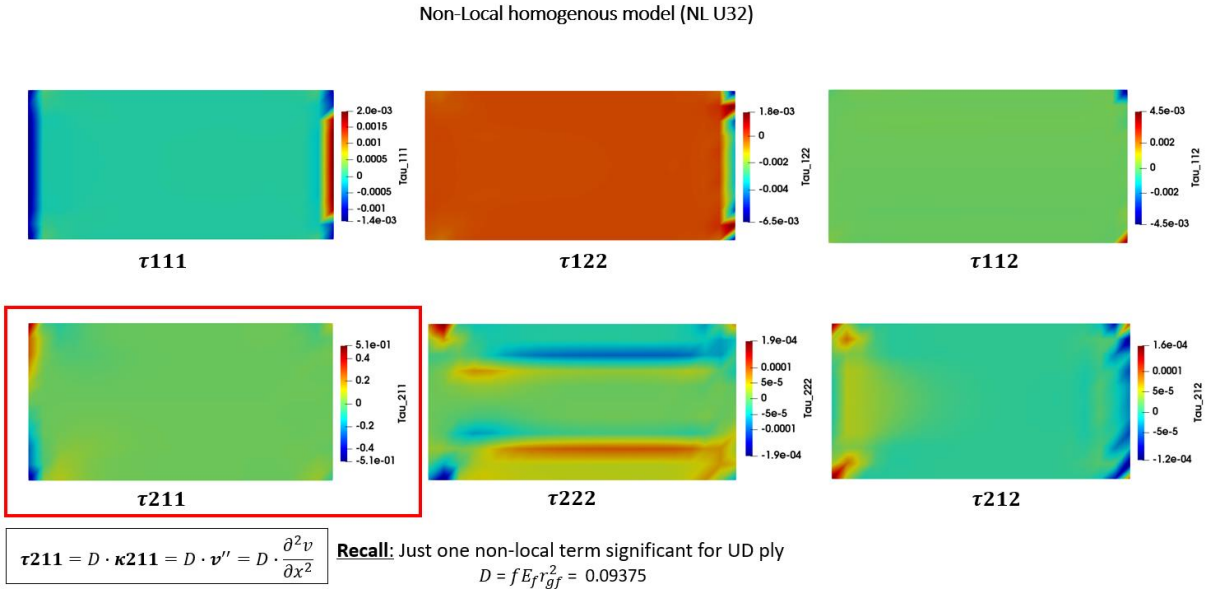

Figure 89: Distributed bending moment components fields – Non-linear Material and Non-Linear Geometry – compression

9.2.3.2 *Case2: Bending*

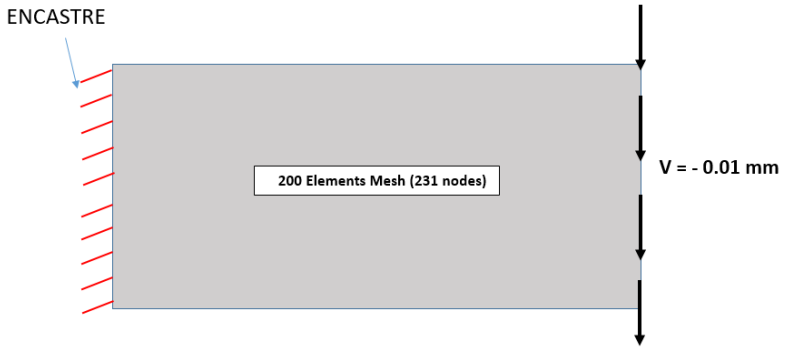

Figure 90: Mesh, Load and Boundary conditions (Validation w.r.t hetero UD composite – matrix plasticity) in case of bending

1) Displacement fields:

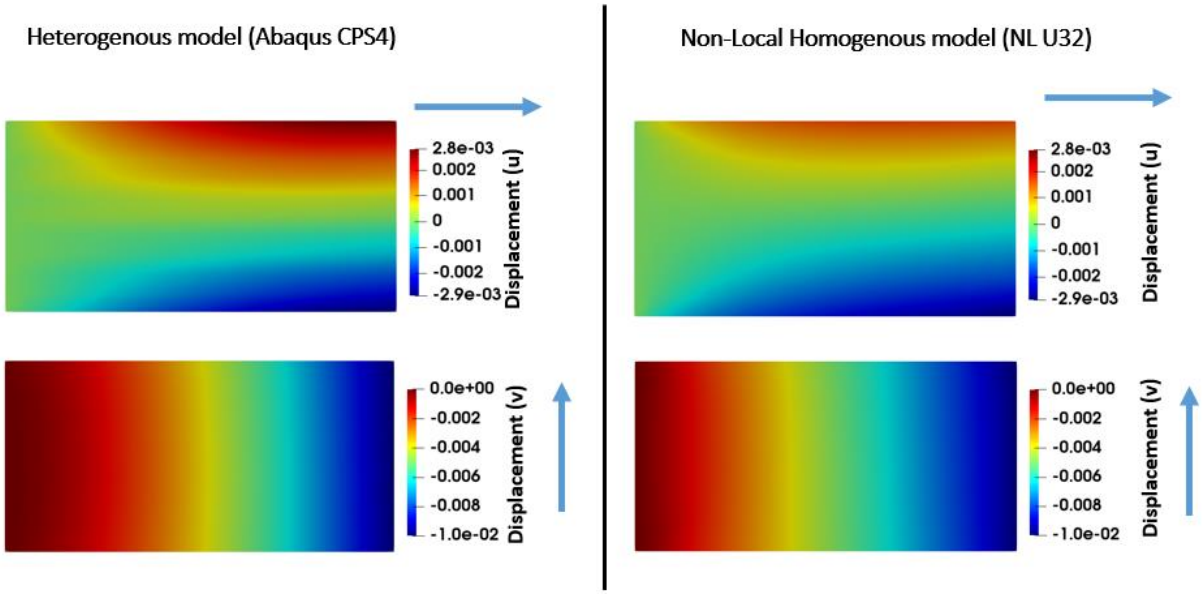

Figure 91: Comparison of displacement fields (u,v) w.r.t hetero UD composite (Matrix plasticity and Non-Linear geometry) – bending

2) Stress Fields (***S***):

S11

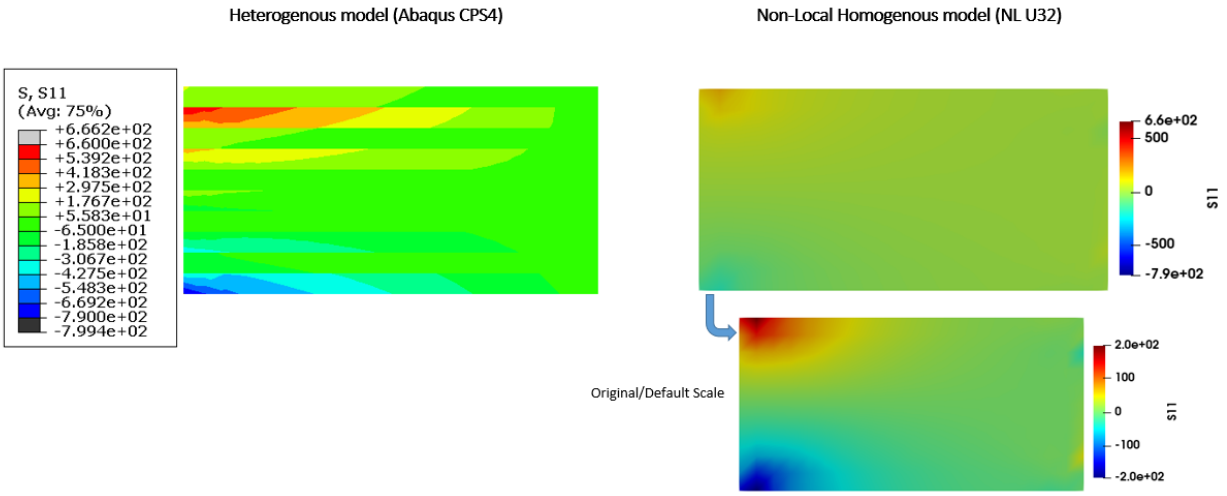

Figure 92: Comparison of S11 component – Non-linear Material and Non-Linear Geometry – bending

S22

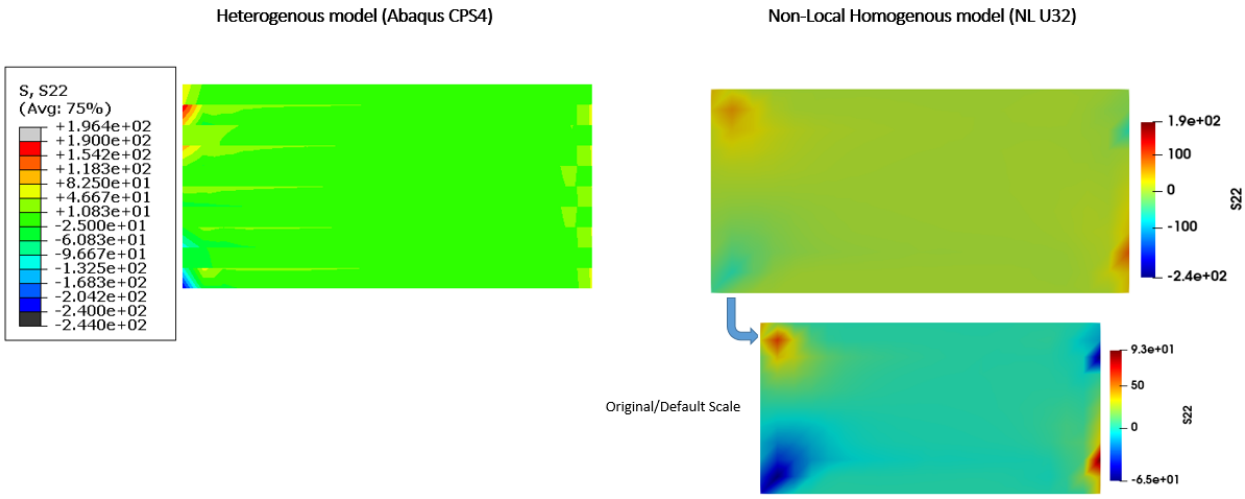

Figure 93: Comparison of S22 component – Non-linear Material and Non-Linear Geometry – bending

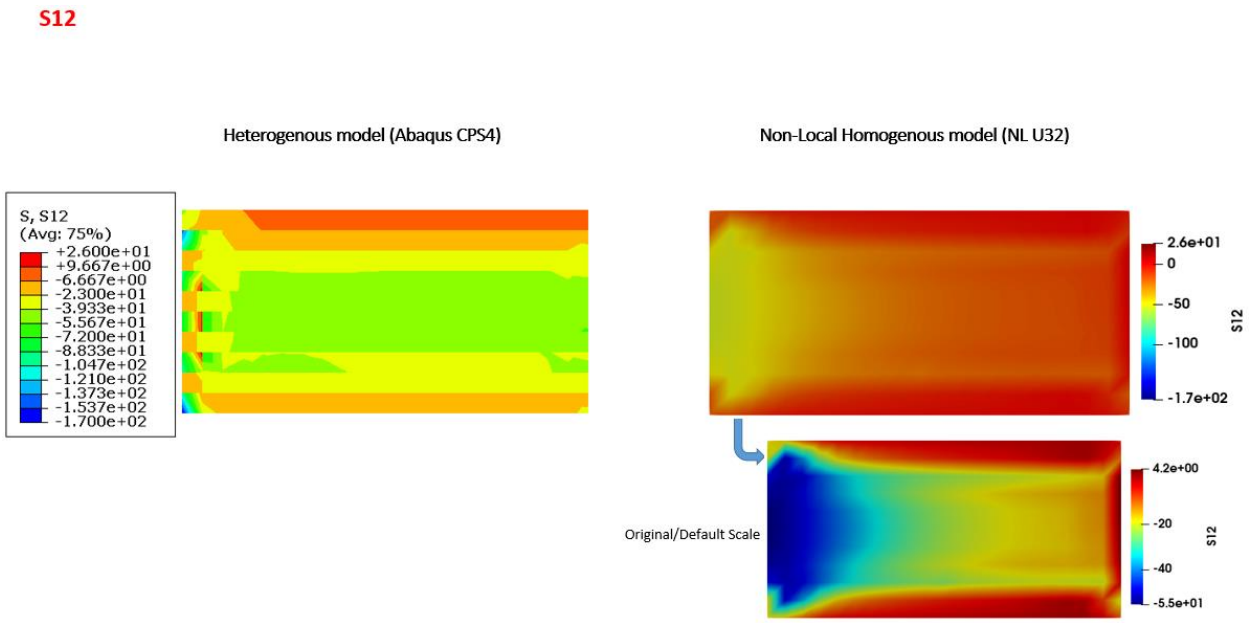

Figure 94: Comparison of S12 component – Non-linear Material and Non-Linear Geometry – bending

3) Strain Fields (***E***):

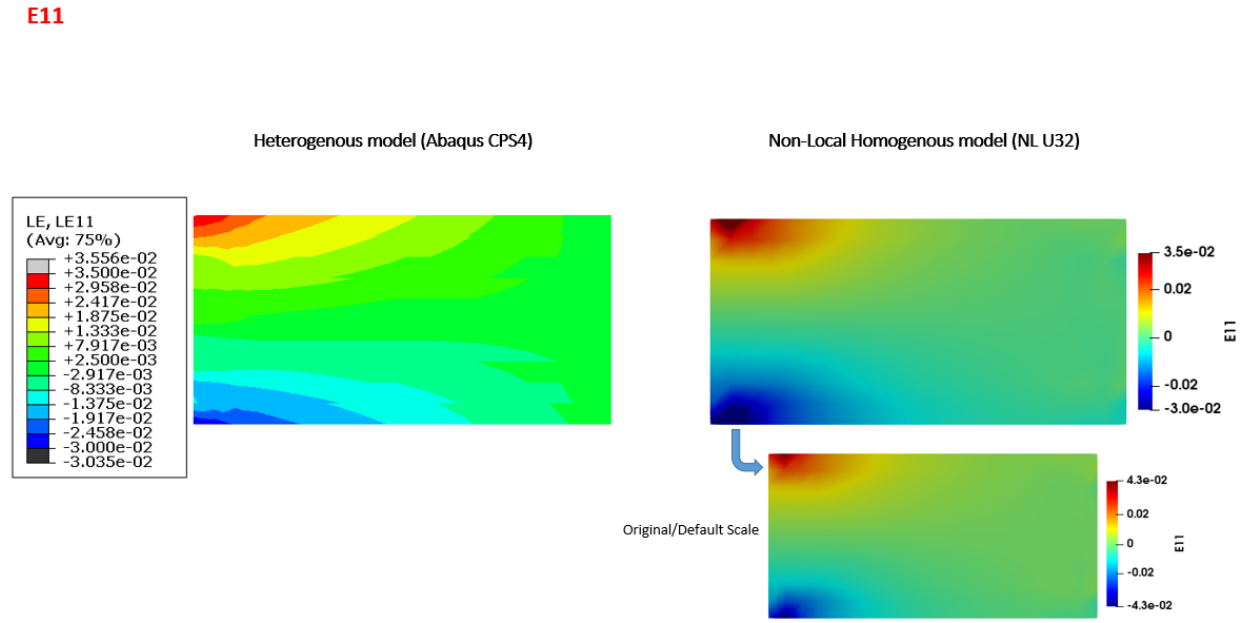

Figure 95: Comparison of E11 component – Non-linear Material and Non-Linear Geometry- bending

E22

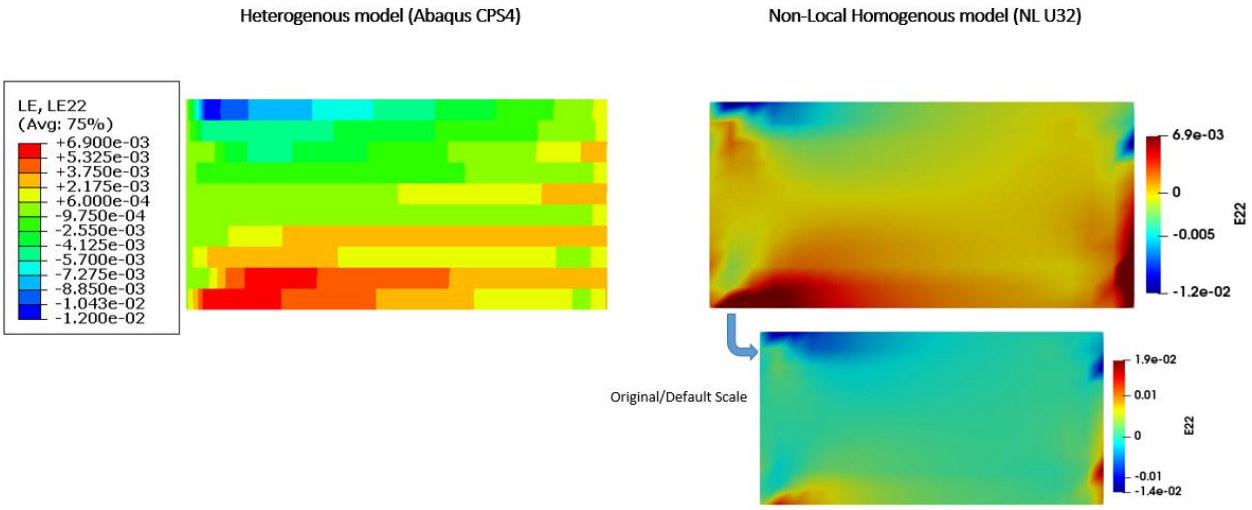

Figure 96: Comparison of E22 component – Non-linear Material and Non-Linear Geometry- bending

E12

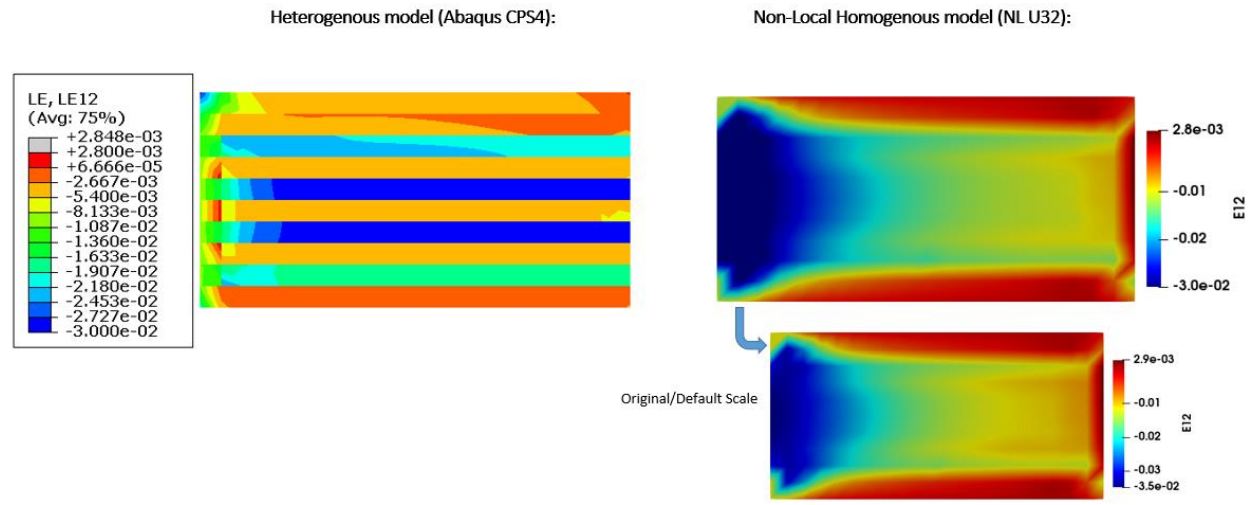

Figure 97: Comparison of E12 component – Non-linear Material and Non-Linear Geometry- bending

4) Curvature/higher order bending strain fields **($\boldsymbol{\kappa}$)**:

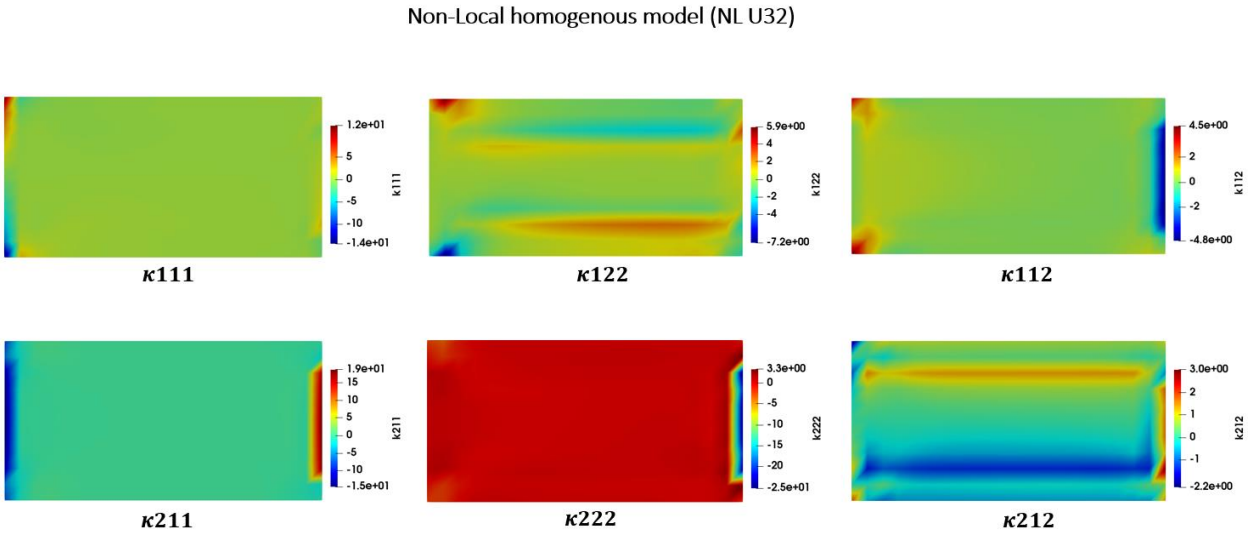

Figure 98: Curvature components fields – Non-linear Material and Non-Linear Geometry – bending

5) Distributed bending moment fields **($\boldsymbol{\tau}$):**

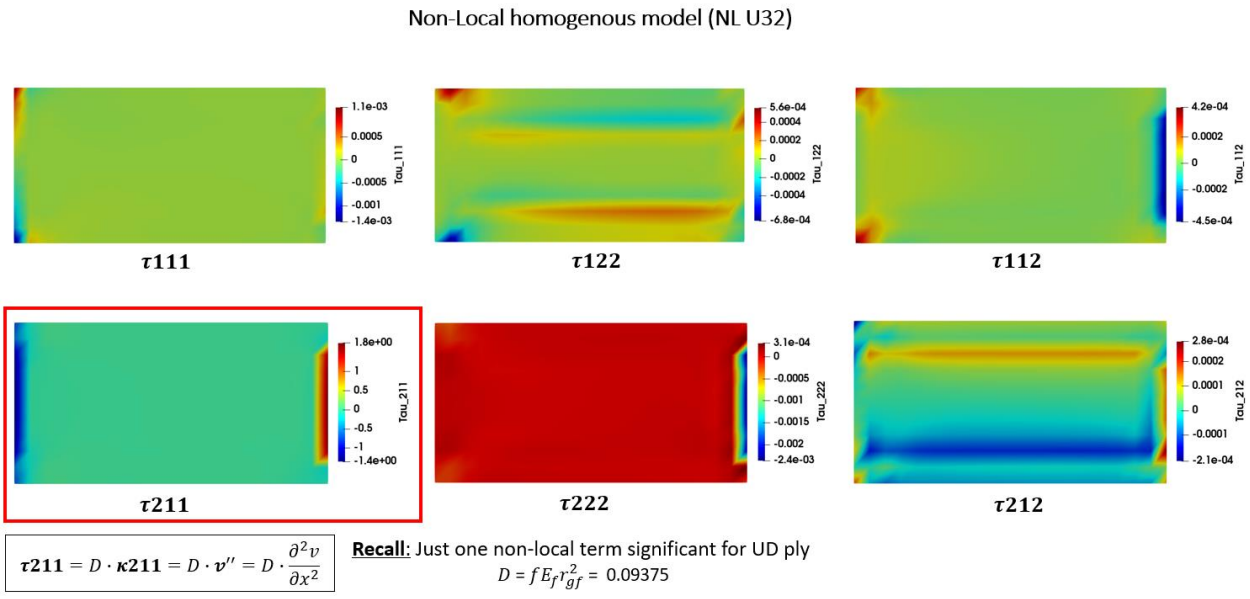

Figure 99: Distributed bending moment components fields – Non-linear Material and Non-Linear Geometry – compression

At this point, we have implemented isotropic Ramberg-Osgood material behavior law to take into account matrix non-linear behavior and also validated against ABAQUS® in-built elements and law. A UMAT subroutine is validated to simulate the behavior of the matrix. However, in order to replicate same behavior as real heterogenous UD composite, it is necessary to develop material

law(elasto-plasticity) of anisotropic type. Therefore, Anisotropic Ramberg-Osgood (RO) law is developed in following section and integrated in HOMNL model (NL U32).

9.2.4 Anisotropic Ramberg-Osgood (RO) Law (2D Plane stress) - unidirectional composite

In this part, the Ramberg Osgood law is generalized to represent unidirectional behavior. Since our non-local element (NL U32) is developed based on the plane stress assumption ($\sigma_{33} = \sigma_{13} = \sigma_{23} = 0$; $\varepsilon_{13} = \varepsilon_{23} = 0$, $\varepsilon_{33} \neq 0$), the isotropic law can be modified in 2D (plane stress) under anisotropic form by a separation between transverse and shear components. It is assumed that the non-linearity has not the same expression for transverse and shear components, although the non-linear behavior comes from the matrix which exhibit visco-elastic behavior:

$$\begin{aligned}\boldsymbol{\varepsilon} = \boldsymbol{L}\cdot\boldsymbol{\sigma} &+ \frac{\alpha_{22}}{E2}\left(\frac{\sqrt{{\sigma_{22}}^2}}{\sigma_{22}^0}\right)^{(n_{22}-1)} \sigma_{22}\,(e_2 \otimes e_2) \\ &+ \alpha_{12}\,\frac{\alpha_{22}}{E2}\left(\frac{\sqrt{{\sigma_{11}}^2 + {\sigma_{22}}^2}}{\sigma_{22}^0}\right)^{(n_{22}-1)} \sigma_{11}\,(e_2 \otimes e_1) \\ &+ \alpha_{12}\,\frac{\alpha_{22}}{E2}\left(\frac{\sqrt{{\sigma_{11}}^2 + {\sigma_{22}}^2}}{\sigma_{22}^0}\right)^{(n_{22}-1)} \sigma_{22}\,(e_1 \otimes e_2) \\ &+ \frac{\alpha_6}{G12}\left(\frac{\sqrt{3{\sigma_6}^2}}{\sigma_6^0}\right)^{(n_6-1)} \sigma_6\,(e_6 \otimes e_6)\end{aligned} \qquad (9\text{-}6)$$

$$e_2 \otimes e_2 = \begin{bmatrix}0 & 0\\ 0 & 1\end{bmatrix};\ e_1 \otimes e_2 = \begin{bmatrix}0 & 1\\ 0 & 0\end{bmatrix};\ e_2 \otimes e_1 = \begin{bmatrix}0 & 0\\ 1 & 0\end{bmatrix}$$

With this specific notation:

$$\begin{aligned}A &= \frac{\alpha_{22}}{E2}\left(\frac{\sqrt{{\sigma_{22}}^2}}{\sigma_{22}^0}\right)^{(n_{22}-1)} \\ B &= \frac{\alpha_6}{G12}\left(\frac{\sqrt{3{\sigma_6}^2}}{\sigma_6^0}\right)^{(n_6-1)} \\ C &= \frac{\alpha_{22}}{E2}\left(\frac{\sqrt{{\sigma_{11}}^2 + {\sigma_{22}}^2}}{\sigma_{22}^0}\right)^{(n_{22}-1)}\end{aligned} \qquad (9\text{-}7)$$

The law can be written under this form:

$$\begin{bmatrix}\varepsilon_{11}\\ \varepsilon_{22}\\ \varepsilon_{12}\end{bmatrix} = \begin{bmatrix}L_{11} & [L_{12} + \alpha_{12}C] & 0\\ [L_{21} + \alpha_{12}C] & [L_{22} + A] & 0\\ 0 & 0 & [L_{66} + B]\end{bmatrix}\cdot\begin{bmatrix}\sigma_{11}\\ \sigma_{22}\\ \sigma_{12}\end{bmatrix}$$

where, $E2, G12$ denote, the Young's modulus in the transverse direction, shear stiffness in plane, and $\boldsymbol{L} = [\boldsymbol{D}]^{-1}$ is a compliance tensor (anisotropic). α_{22}, α_6, $\sigma_{22}^0, \sigma_6^0$, n_{22} , n_6 are the yield offset, the yield stress and hardening exponent in direction 22 and 6. α_{12} is material parameter similar to yield offset in direction 12 and is very close to ν_{12} . Therefore, this law contains total 7 non-linear material parameters. Note that when $\alpha_{12}, \alpha_{22}\ and\ \alpha_6 \simeq 0$, anisotropic RO law tends towards anisotropic elastic.

Taking the variation (δ) on Eq. (9-6),

$$\delta\boldsymbol{\varepsilon} = \mathbf{L}\cdot\boldsymbol{\sigma} + \left[\frac{\alpha_{22}}{E2}\left(\frac{\sqrt{{\sigma_{22}}^2}}{\sigma_{22}^0}\right)^{(n_{22}-1)}\right]\delta\sigma_{22}\,(e_2 \otimes e_2)$$

$$+\frac{\alpha_{22}}{E2}\sigma_{22}(n_{22}-1)\left(\frac{\sqrt{{\sigma_{22}}^2}}{\sigma_{22}^0}\right)^{(n_{22}-2)}\frac{1}{\sigma_{22}^0}\left[\frac{1}{2}({\sigma_{22}}^2)^{-\frac{1}{2}}2\sigma_{22}\right]\delta\sigma_{22}\,(e_2 \otimes e_2)$$

$$+\alpha_{12}\left[\frac{\alpha_{22}}{E2}\left(\frac{\sqrt{{\sigma_{11}}^2+{\sigma_{22}}^2}}{\sigma_{22}^0}\right)^{(n_{22}-1)}\right]\delta\sigma_{11}\,(e_2 \otimes e_1) + \alpha_{12}\frac{\alpha_{22}}{E2}\sigma_{11}(n_{22} \qquad (9\text{-}8)$$

$$-1)\left(\frac{\sqrt{{\sigma_{11}}^2+{\sigma_{22}}^2}}{\sigma_{22}^0}\right)^{(n_{22}-2)}\frac{1}{\sigma_{22}^0}\left[\left({\sigma_{11}}^2+{\sigma_{22}}^2\right)^{-\frac{1}{2}}\sigma_{11}\right]\delta\sigma_{11}\,(e_2 \otimes e_1)$$

$$+\alpha_{12}\left[\frac{\alpha_{22}}{E2}\left(\frac{\sqrt{{\sigma_{11}}^2+{\sigma_{22}}^2}}{\sigma_{22}^0}\right)^{(n_{22}-1)}\right]\delta\sigma_{22}\,(e_1 \otimes e_2) + \alpha_{12}\frac{\alpha_{22}}{E2}\sigma_{11}(n_{22}$$

$$-1)\left(\frac{\sqrt{{\sigma_{11}}^2+{\sigma_{22}}^2}}{\sigma_{22}^0}\right)^{(n_{22}-2)}\frac{1}{\sigma_{22}^0}\left[\left({\sigma_{11}}^2+{\sigma_{22}}^2\right)^{-\frac{1}{2}}\sigma_{22}\right]\delta\sigma_{22}\,(e_1 \otimes e_2)$$

$$+\left[\frac{\alpha_6}{G12}\left(\frac{\sqrt{3{\sigma_6}^2}}{\sigma_6^0}\right)^{(n_6-1)}\right]\delta\sigma_6\,(e_6 \otimes e_6) + \frac{\alpha_6}{G12}\sigma_6(n_6 -$$

$$1)\left(\frac{\sqrt{3{\sigma_6}^2}}{\sigma_6^0}\right)^{(n_6-2)}\frac{1}{\sigma_6^0}\left[\frac{1}{2}(3{\sigma_6}^2)^{-1/2}\,6\sigma_6\right]\delta\sigma_6\,(e_6 \otimes e_6)$$

Derivatives (using chain rule):

$$f'_{22}(\sigma_{22}) = \left[\frac{\alpha_{22}}{E2}\left(\frac{\sqrt{{\sigma_{22}}^2}}{\sigma_{22}^0}\right)^{(n_{22}-1)}\right] + \frac{\alpha_{22}}{E2}\sigma_{22}(n_{22}-1)\left(\frac{\sqrt{{\sigma_{22}}^2}}{\sigma_{22}^0}\right)^{(n_{22}-2)}\frac{1}{\sigma_{22}^0}\left[\frac{1}{2}({\sigma_{22}}^2)^{-1/2}\,2\sigma_{22}\right]$$

$$f'_{12}(\sigma_{11}) = \left[\frac{\alpha_{22}}{E2}\left(\frac{\sqrt{{\sigma_{11}}^2+{\sigma_{22}}^2}}{\sigma_{22}^0}\right)^{(n_{22}-1)}\right] + \frac{\alpha_{22}}{E2}\sigma_{11}\,(n_{22} - 1)\left(\frac{\sqrt{{\sigma_{11}}^2+{\sigma_{22}}^2}}{\sigma_{22}^0}\right)^{(n_{22}-2)}\frac{1}{\sigma_{22}^0}\left[({\sigma_{11}}^2+{\sigma_{22}}^2)^{-\frac{1}{2}}\,\sigma_{11}\right] \quad (9\text{-}9)$$

$$f'_{12}(\sigma_{22}) = \left[\frac{\alpha_{22}}{E2}\left(\frac{\sqrt{{\sigma_{11}}^2+{\sigma_{22}}^2}}{\sigma_{22}^0}\right)^{(n_{22}-1)}\right] + \frac{\alpha_{22}}{E2}\sigma_{22}\,(n_{22} - 1)\left(\frac{\sqrt{{\sigma_{11}}^2+{\sigma_{22}}^2}}{\sigma_{22}^0}\right)^{(n_{22}-2)}\frac{1}{\sigma_{22}^0}\left[({\sigma_{11}}^2+{\sigma_{22}}^2)^{-1/2}\,\sigma_{22}\right]$$

$$f'_{6}(\sigma_{6}) = \frac{\alpha_{6}}{G12}\left(\frac{\sqrt{3{\sigma_{6}}^2}}{\sigma_{6}^0}\right)^{(n_{6}-1)} + \frac{\alpha_{6}}{G12}\sigma_{6}(n_{6}-1)\left(\frac{\sqrt{3{\sigma_{6}}^2}}{\sigma_{6}^0}\right)^{(n_{6}-2)}\frac{1}{\sigma_{6}^0}\left[\frac{1}{2}(3{\sigma_{6}}^2)^{-1/2}\,6\sigma_{6}\right]$$

Eq. (9-8) can be written as,

$$\Delta\boldsymbol{\varepsilon} = \boldsymbol{L}\cdot\Delta\boldsymbol{\sigma} + f'_{22}(\sigma_{22})\,\Delta\sigma_{22}\,(e_2\otimes e_2) + \alpha_{12}\,f'_{12}(\sigma_{11})\,\Delta\sigma_{11}\,(e_2\otimes e_1) + \alpha_{12}\,f'_{12}(\sigma_{22})\,\Delta\sigma_{22}\,(e_1\otimes e_2) + f'_{6}(\sigma_{6})\,\Delta\sigma_{6}\,(e_6\otimes e_6) \quad (9\text{-}10)$$

Or in matrix form,

$$\Delta\boldsymbol{\varepsilon} = \begin{bmatrix} L_{11} & [L_{12} + \alpha_{12}f'_{12}(\sigma_{22})] & 0 \\ [L_{21} + \alpha_{12}\,f'_{12}(\sigma_{11})] & [L_{22} + f'_{22}(\sigma_{22})] & 0 \\ 0 & 0 & [L_{66} + f'_{6}(\sigma_{6})] \end{bmatrix}\cdot\Delta\boldsymbol{\sigma} \quad (9\text{-}11)$$

$$\Delta\boldsymbol{\varepsilon} = \boldsymbol{L}(\sigma) \cdot \Delta\boldsymbol{\sigma}$$

The Jacobian or Tangent matrix can be written as:

$$\boldsymbol{DDSDDE} = \frac{\partial\Delta\boldsymbol{\sigma}}{\partial\Delta\boldsymbol{\varepsilon}} = [\boldsymbol{L}(\boldsymbol{\sigma})]^{-1}$$

It can be observed from the above equation that, the system is non-linear in σ_{11}, σ_{22} and $\sigma_6(\sigma_{12})$ and we have written the system in function of stress. For each increment, the stress is defined at beginning and UMAT should calculate the increment, the problem to solve can be written under this form:

$$\Delta\boldsymbol{\varepsilon} = \begin{bmatrix} L_{11} & [L_{12} + \alpha_{12} f'_{12}(\sigma_{22}^{o} + \Delta\sigma_{22})] & 0 \\ [L_{12} + \alpha_{12} f'_{12}(\sigma_{11}^{o} + \Delta\sigma_{11})] & [L_{22} + f'_{22}(\sigma_{22}^{o} + \Delta\sigma_{22})] & 0 \\ 0 & 0 & [L_{66} + f'_{6}(\sigma_{6}^{o} + \Delta\sigma_{6})] \end{bmatrix} \cdot \Delta\boldsymbol{\sigma}$$

$$\Delta\boldsymbol{\varepsilon} = \boldsymbol{L}(\sigma^{o} + \Delta\sigma) \cdot \Delta\boldsymbol{\sigma}$$

$$\Delta\boldsymbol{\varepsilon} - \boldsymbol{L}(\sigma^{o} + \Delta\sigma) \cdot \Delta\boldsymbol{\sigma} = \mathbf{0}$$

The increment of strain (DSTRAN) is given by ABAQUS®. Then using Newton-Raphson algorithm, actual stress (STRESS) and tangent matrix (DDSDDE) matrix is calculated. Following steps are followed in UMAT to solve this constitutive relation:

a) Prediction of Initial Stress using Elastic relation:

Solve

$$\Delta\boldsymbol{\sigma^{p}} = [\boldsymbol{D}_{el}] \cdot \Delta\boldsymbol{\varepsilon}$$

$$\boldsymbol{D}_{el} = \begin{bmatrix} \frac{E_1}{(1-\nu_{12}\nu_{21})} & \frac{\nu_{21}E_1}{(1-\nu_{12}\nu_{21})} & 0 \\ \frac{\nu_{12}E_2}{(1-\nu_{12}\nu_{21})} & \frac{E_2}{(1-\nu_{12}\nu_{21})} & 0 \\ 0 & 0 & G_6 \end{bmatrix}$$

b) Correction:

Correction 1

$$\boldsymbol{R^{p}} = \Delta\boldsymbol{\varepsilon} - \boldsymbol{L}(\sigma^{o} + \Delta\sigma^{p}) \cdot \Delta\boldsymbol{\sigma^{p}}$$

$$\Delta\boldsymbol{\varepsilon} - \boldsymbol{L}(\sigma^{o} + \Delta\sigma^{p}) \cdot (\Delta\boldsymbol{\sigma^{p}} + \cdot \Delta\boldsymbol{\sigma^{c1}}) = \mathbf{0}$$

Solve

$$\boldsymbol{L}(\sigma^{o} + \Delta\sigma^{p}) \cdot \Delta\boldsymbol{\sigma^{c1}} = \Delta\boldsymbol{\varepsilon} - \boldsymbol{L}(\sigma^{o} + \Delta\sigma^{p})\, \Delta\boldsymbol{\sigma^{p}} = \boldsymbol{R^{p}}$$

Correction 2

$$\boldsymbol{R^{c1}} = \Delta\boldsymbol{\varepsilon} - \boldsymbol{L}(\sigma^o + \Delta\sigma^p + \Delta\sigma^{c1}) \cdot (\Delta\boldsymbol{\sigma^p} + \Delta\boldsymbol{\sigma^{c1}})$$

$$\Delta\boldsymbol{\varepsilon} - \boldsymbol{L}(\sigma^o + \Delta\sigma^p + \Delta\sigma^{c1}) \cdot (\Delta\boldsymbol{\sigma^p} + \cdot\Delta\boldsymbol{\sigma^{c1}} + \cdot\Delta\boldsymbol{\sigma^{c2}}) = \boldsymbol{0}$$

Solve

$$\boldsymbol{L}(\sigma^o + \Delta\sigma^p + \Delta\sigma^{c1}) \cdot \Delta\boldsymbol{\sigma^{c2}} = \Delta\boldsymbol{\varepsilon} - \boldsymbol{L}(\sigma^o + \Delta\sigma^p + \Delta\sigma^{c1}) (\Delta\boldsymbol{\sigma^p} + \cdot\Delta\boldsymbol{\sigma^{c1}}) = \boldsymbol{R^{c1}}$$

Correction 3

$$\boldsymbol{R^{c1}} = \Delta\boldsymbol{\varepsilon} - \boldsymbol{L}(\sigma^o + \Delta\sigma^p + \Delta\sigma^{c1} + \Delta\sigma^{c2}) \cdot (\Delta\boldsymbol{\sigma^p} + \Delta\boldsymbol{\sigma^{c1}} + \Delta\boldsymbol{\sigma^{c2}})$$

$$\Delta\boldsymbol{\varepsilon} - \boldsymbol{L}(\sigma^o + \Delta\sigma^p + \Delta\sigma^{c1} + \Delta\sigma^{c2}) \cdot (\Delta\boldsymbol{\sigma^p} + \cdot\Delta\boldsymbol{\sigma^{c1}} + \cdot\Delta\boldsymbol{\sigma^{c2}} + \Delta\boldsymbol{\sigma^{c3}}) = \boldsymbol{0}$$

Solve

$$\boldsymbol{L}(\sigma^o + \Delta\sigma^p + \Delta\sigma^{c1} + \Delta\sigma^{c2}) \cdot \Delta\boldsymbol{\sigma^{c3}} = \Delta\boldsymbol{\varepsilon} - \boldsymbol{L}(\sigma^o + \Delta\sigma^p + \Delta\sigma^{c1} + \Delta\sigma^{c2}) (\Delta\boldsymbol{\sigma^p} + \cdot\Delta\boldsymbol{\sigma^{c1}} + \Delta\boldsymbol{\sigma^{c2}}) = \boldsymbol{R^{c2}}$$

Until convergence on Residual, ($\|\boldsymbol{R}\| <$ Tol)
After it is possible to calculate the tangent matrix:

$$\boldsymbol{DDSDDE} = \frac{\partial\Delta\boldsymbol{\sigma}}{\partial\Delta\boldsymbol{\varepsilon}} = [\boldsymbol{L}(\sigma^o + \Delta\sigma^p + \Delta\sigma^{c1} + \Delta\sigma^{c2} + \cdots \ldots \ldots)]^{-1}$$

And update stress to get the actual value,

$$\boldsymbol{\sigma} = \boldsymbol{\sigma^o} + \Delta\boldsymbol{\sigma^p} + \Delta\boldsymbol{\sigma^{c1}} + \Delta\boldsymbol{\sigma^{c2}} + \cdots$$

Above formulation is implemented in UMAT subroutine, validated against Isotropic RO-Law of ABAQUS® and is integrated within NL U32 element.

9.2.5 Validation of Anisotropic Ramberg-Osgood (RO) Law

Validation of Anisotropic Ramberg Osgood Elastoplastic law in 2D plane stress) law is performed by comparing the results obtained by User Material (UMAT) subroutine, developed for anisotropic RO law with respect to ABAQUS® in-built Isotropic Ramberg-Osgood (RO), using CPS4 element with non-linear geometry.

Material Properties used: $E_1 = E_2 = 8000\,MPa,\ G_{12}\ or\ G_6 = 1600\,MPa,\ \nu_{12} = 0.4, \sigma_{22}^0 = \sigma_6^0 = 60MPa,\ \alpha_{22} = \alpha_6 = \alpha_{12} = 0.015\ and\ n_{22} = n_6 = 4$. For isotropic RO law of ABAQUS® same material properties are used as previous. All loading test cases (traction, compression and shear)

are performed on square plate of dimension 0.1 x 0.1 mm with 1 Elem mesh. Displacements are applied in 10 time steps.

- Uniaxial Traction/Compression in longitudinal or X direction:

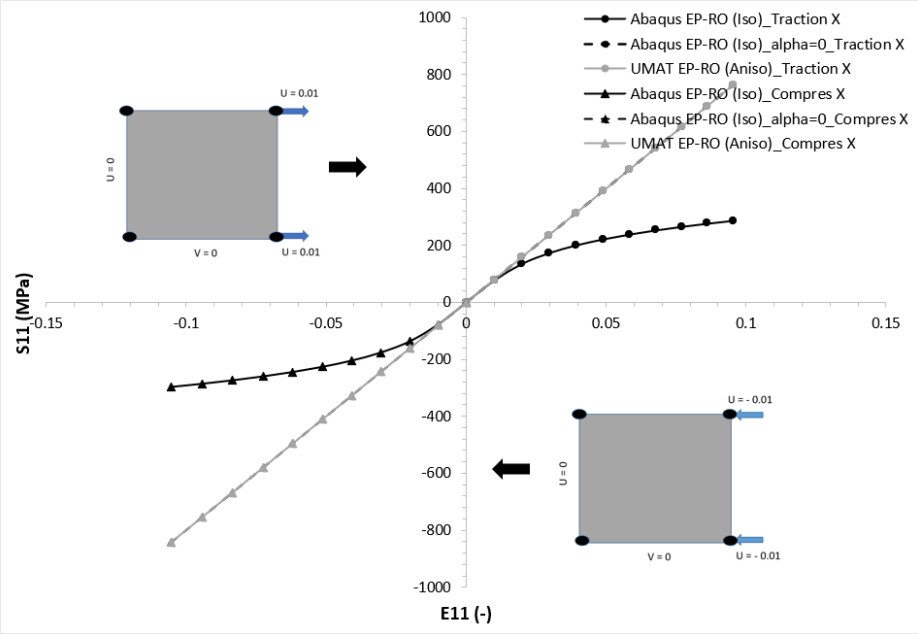

Figure 100: Comparison of UMAT EP-RO (Aniso) with Abaqus EP-RO (Iso): Uniaxial Traction/Compression in X direction

- Uniaxial Traction/Compression in transverse or Y direction:

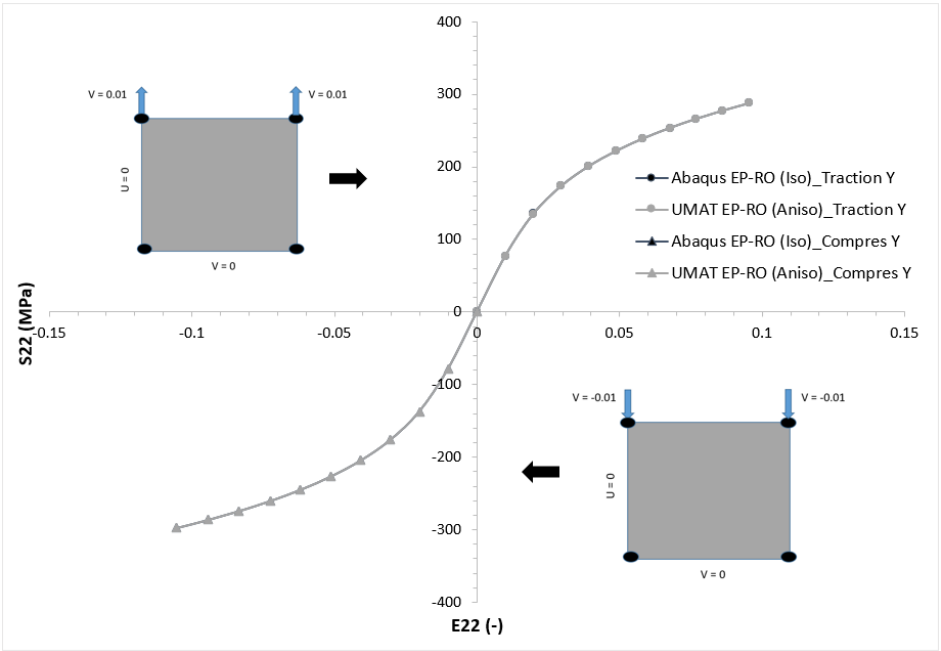

Figure 101: Comparison of UMAT EP-RO (Aniso) with Abaqus EP-RO (Iso): Uniaxial Traction/Compression in Y direction

- Shear in X / Y direction:

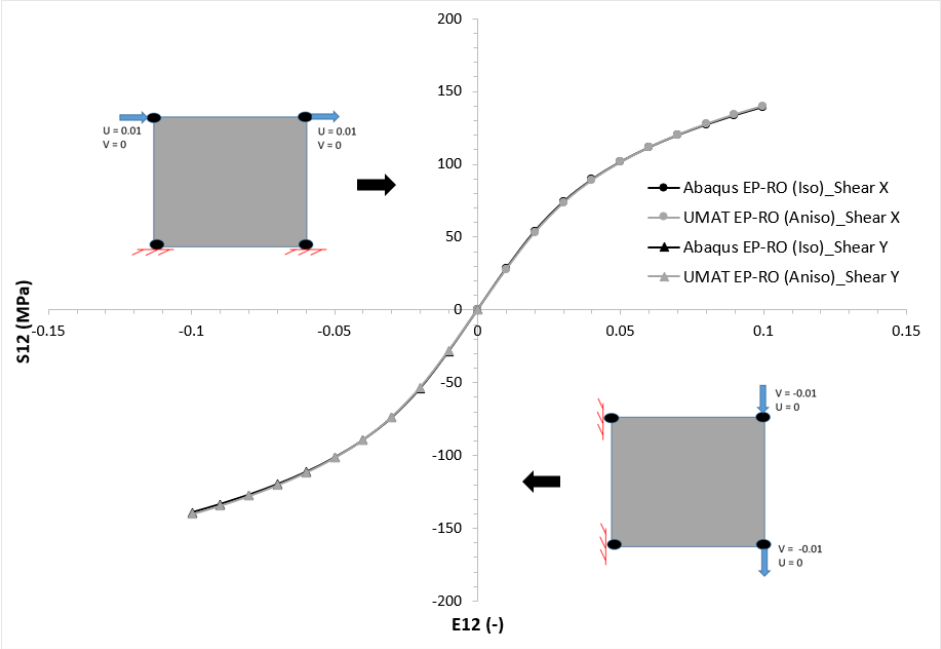

Figure 102: Comparison of UMAT EP-RO (Aniso) with Abaqus EP-RO (Iso): Shear in X / Y direction

From Figure 100 - Figure 102, it is depicted that Anisotropic RO law with isotropic properties leads to the same solution as ABAQUS® isotropic RO law. However, we can notice that for the case of traction/compression in longitudinal direction, it is necessary to use " $\alpha = 0$ " for isotropic RO law of ABAQUS® to match with anisotropic RO law, since the latter one does not have non-linear effect in X or longitudinal direction.

10 Identification of Parameters

In this chapter, a detailed procedure or protocol is developed to identify the elastic, non-local and non-linear material parameters with geometrical non-linearity in 2D case and is realized. It is to be noted that, since there are no experimental data (for ex: Stress/Strain or Force/Displacement curves) under different loading conditions are available at the moment, the identification of parameters is performed with respect to the numerical model developed in ABAQUS® using its in-built structural elements/by developing replica of its elements using User Element (UEL) subroutine and material behavior law by providing some experimentally investigated material parameters from bibliography.

10.1 Identification of Elastic and Non-Local parameters

The parameters of classical elastic modulus, $\boldsymbol{D}$ and non-local parameters of local fiber bending stiffness matrix, $\overline{\overline{\boldsymbol{C_f}}}$ of Homogenized Non-Local model (HOMNL) is unknown and should be identified. As $\boldsymbol{D}$ is assumed to be anisotropic elastic (transversely isotropic) for homogenized non-local model, in order to represent 2D heterogenous UD/woven composite, we have 4 parameters: D_{11}, D_{22}, D_{12} and D_{33}. And, in local fiber bending stiffness matrix, $\overline{\overline{\boldsymbol{C_f}}}$, we have 6 parameters: A, B, C, D, E and F. Therefore, a total of 10 parameters need to be identified. Parameters are identified using an open-source optimization tool called, DAKOTA (Design Analysis Kit for Optimization and Terascale Applications), which is developed by Sandia National Laboratories, which can be linked with ABAQUS® using an external python script.

10.1.1 A brief description about DAKOTA

- The DAKOTA toolkit provides a flexible and extensible interface between simulation codes and iterative analysis methods [D6];
- DAKOTA contains algorithms for:
    - optimization with gradient and non-gradient based methods;
    - uncertainty quantification with sampling, reliability, and stochastic expansion methods;
    - parameter estimation with non-linear least squares methods;
    - sensitivity/variance analysis with design of experiments and parameter study methods.
- Different simulation codes, for example: Finite Element solver (ABAQUS®) can be linked to DAKOTA for parametric study and optimization.

DAKOTA version 6.10 and ABAQUS® 2017 with Python 3.7.3 is used for this part.

The detailed workflow of DAKOTA during the optimization loop can be observed in Figure 103. A standard input file (.in) must be provided to DAKOTA which contains the type of optimization methods (Ex: gradient free/Genetic algorithm or gradient based/Least-square method), parameters initial values, bounds, interface with simulation codes and number of objective functions (calibration terms) to minimized should be defined inside this. An example of input file for "non-linear least square (nl2sol)" method is shown below:

```
***** Input File for DAKOTA ******
environment,
        #single_method
     #graphics
     tabular_data
         results_output

method,

        nl2sol
        max_iterations = 200
          convergence_tolerance = 1e-2
          #function_precision = 1e-5
          output quiet

variables,
        continuous_design = 10
          cdv_initial_point =  123210.77  4081.86   10894.11  3859.46  1.139E-03  4.04847  0.40069  9.19324   13.74507  9.11084
          cdv_lower_bounds  =  100000  2000   10000  2500  1.139E-03  1E-03  1E-03  1E-03   1E-03   1E-03
          cdv_upper_bounds  =  150000  6000   15000  5000  1.139E-03  2E+01  2E+01  2E+01   2E+01   2E+01
          cdv_descriptor    =  'D11' 'D12' 'D22' 'D33' 'A' 'B' 'C' 'D' 'E' 'F'

interface,
        fork,
      parameters_file = 'params.in'
      results_file    = 'results.out'
      analysis_driver = 'abaqus.bat'
      file_save

responses,
        calibration_terms = 1
        numerical_gradients
      interval_type central
      method_source dakota
          fd_gradient_step_size = 0.001
    no_hessians
```

With the supply of this input file, DAKOTA performs the optimization with the selected methods by varying the parameters within the defined range/bounds. For each iteration, a new parameters set is supplied to ABAQUS® simulation input file (.inp) through a python script ("dako_to_aba.py") to run the structural calculation and corresponding output files (.odb / .dat) are generated. And then the output from ".odb" or ".dat" files (Ex: Force v/s displacement curve) is extracted using another python script ("identAba.py"), which is linked with "dako_to_aba.py". The user has to calculate the error (relative/absolute) by comparing experimental and simulation values. This error can be also be called as "objective function" to be minimized. This objective function is then supplied to DAKOTA though result file ("results.out"). If the objective function is minimized to reach defined tolerance within the maximum number of iterations set, the loop terminates and optimal parameters are generated. If not, then it is necessary to change the maximum number of iterations and also the initial values or bounds depending upon the selected methods.

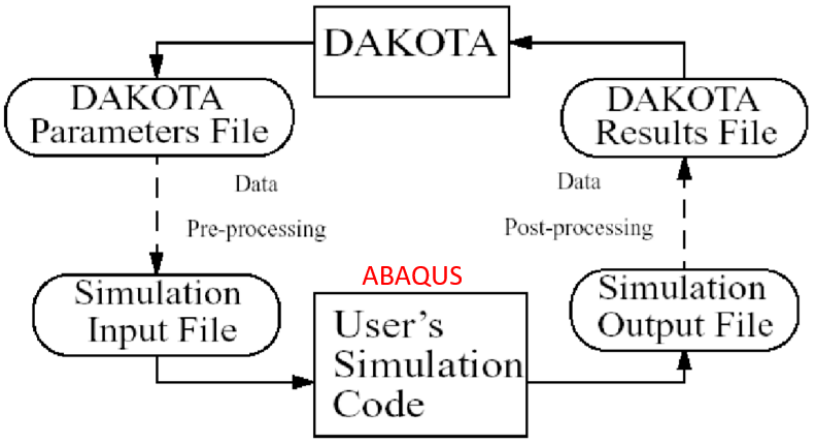

Figure 103: "Black-box" interface between Dakota and a user-supplied simulation code. [D6]

10.1.2 Strategy/Protocol to identify parameters

In order to identify the parameters of HOMNL model, following steps need to be followed:

1) Choose Representative Volume Element (RVE)
2) Choose proper Boundary Conditions (BC's)
3) Optimization in DAKOTA

10.1.2.1 *Representative Volume Element (RVE)*

In our case, three RVE's of 2D heterogenous models are chosen: Microstructure1 (0^0 ply), Microstructure2 (90^0 ply) and Microstructure3 (Woven (plain)), as shown in the Figure 104 and parameters are identified with respect to each RVE's. A Volume fraction, f = 0.5 is used in heterogenous models. Isotropic Elastic material properties (fiber and matrix) for heterogenous models are taken form Drapier et al., (1996) as shown in the Table 4. Size of homogenous and heterogenous RVE's is set to: 0.1 x 0.1 mm. Heterogenous models are meshed with ABAQUS® CPS4 element with geometrical non-linearity. One of the important points to be noted here is that for geometrical non-linear analysis, ABAQUS® CPS4 use for outputs Logarithmic Strain tensor (**LE**) and the Cauchy Stress tensor ($\boldsymbol{\sigma}$). Whereas, in NLU32 we use II Piola Kirchoff stress tensor(**S**) and Green Strain tensor(**E**). And also, the constitutive relation (formulations given in ABAQUS® user's manual for non-linear geometry part has some additional steps in calculating Logarithmic Strain tensor, which is not exactly same as NL U32, which might lead to some variations in few components on some particular loading cases (verified). Therefore, in order to avoid this discrepancy and match exactly the same constitutive relation as NL U32, a new user element: "CPS4 UEL (with non-linear geometry)" is developed and used for the calculation of heterogenous models and consequently for optimization. A mesh size of 100 elements are chosen in order to reduce to calculation and optimization time.

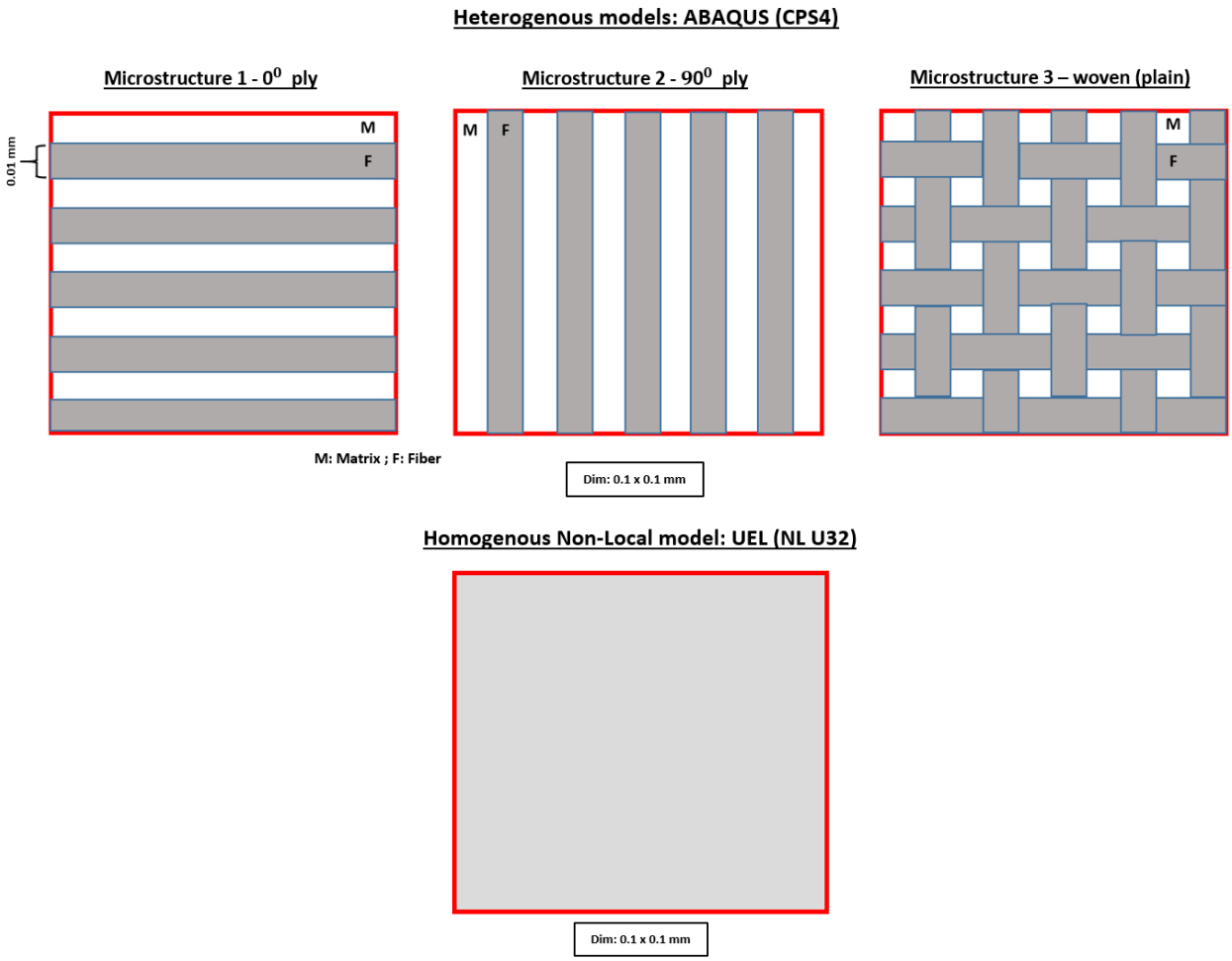

Figure 104: Heterogenous and Homogenous RVE's

Initial material properties for HOMNL model (NL U32):

Initial values for components of equivalent homogenous composite elastic constitutive matrix, ***D*** are calculated using a "Rule of Mixtures law" (Voigt[V3] and Reuss[R3]) based on the properties from Drapier et al., [D1] for UD ply as shown in Table 6.

Table 6: Mechanical Characteristics of UD ply – epoxy T300/914 (Drapier et al., 1996)

Isotropic matrix	***Anisotropic fiber***
$E_m = 4500\ MPa$	$E_{f1} = 240000\ Mpa$
	$E_{f2} = 15000\ Mpa$
$G_m = 1600\ MPa$	$G_f = 92000\ MPa$
$\nu_m = 0.4$	$\nu_f = 0.3$

We know that that,

$$\boldsymbol{S} = \begin{bmatrix} S_{11} \\ S_{22} \\ S_{12} \end{bmatrix} = \bar{\bar{\boldsymbol{D}}}\,\boldsymbol{\varepsilon} = \begin{bmatrix} \frac{E_1}{(1-\nu_{12}\nu_{21})} & \frac{\nu_{21}E_1}{(1-\nu_{12}\nu_{21})} & 0 \\ \frac{\nu_{21}E_2}{(1-\nu_{12}\nu_{21})} & \frac{E_2}{(1-\nu_{12}\nu_{21})} & 0 \\ 0 & 0 & G_{12} \end{bmatrix} \begin{bmatrix} \varepsilon_{11} \\ \varepsilon_{22} \\ \gamma_{12} \end{bmatrix} \qquad (10\text{-}1)$$

$$\begin{bmatrix} S_{11} \\ S_{22} \\ S_{12} \end{bmatrix} = \begin{bmatrix} D_{11} & D_{12} & 0 \\ D_{21} & D_{22} & 0 \\ 0 & 0 & D_{33} \end{bmatrix} \begin{bmatrix} \varepsilon_{11} \\ \varepsilon_{22} \\ \gamma_{12} \end{bmatrix}$$

Now using the Rule of Mixtures, the effective composite (homogenous continuum medium) properties are calculated as:

$$E_1 = E_{C1} = fE_{f1} + (1-f)\,E_m = 122250\ MPa$$

$$E_2 = E_{C2} = \frac{E_{f2}\,E_m}{fE_m + (1-f)\,E_{f2}} = 6923.08\ MPa$$

$$G_{12} = G_{C12} = \frac{G_m G_f}{fG_m + (1-f)\,G_f} = 3145.30 \qquad (10\text{-}2)$$

$$\nu_{12} = \nu_{C12} = f\nu_f + (1-f)\,\nu_m = 0.35$$

$$\nu_{21} = \frac{\nu_{12}\,E_2}{E_1} = 0.01982$$

With, $f = 0.5$

Now, after substituting Eq. (10-2) in Eq. (10-1), the initial values for $\boldsymbol{D}$ matrix can be calculated as,

$$\begin{gathered} D_{11} = 123104\ MPa \\ D_{22} = 6971.44\ MPa \\ D_{33} = 3145.3\ MPa \\ D_{12} = D_{21} = 2440\ MPa \end{gathered} \qquad (10\text{-}3)$$

Regarding the $\bar{\bar{\boldsymbol{C}}}_{\boldsymbol{f}}$ parameters: A, B, C, D, E and F, since there are no experimental measured values at the moment, a detailed study to identify the initial values will be discussed in following section.

10.1.2.2 *Boundary Conditions (BC's)*

To define the boundary conditions, we follow a similar methodology proposed by Berkache, Ganghoffer et al., [B14] to identify the first and second gradient continuum moduli with respect to Representative Volume Element (RVE) of different heterogenous microstructures.

One of the most important and difficult part in identifying the unknown parameters numerically is to define good BC's. As we have 10 parameters, it is necessary to define 10 boundary conditions (BC's). Following BC's needs to be defined to identify the respective parameters.

Case1: Traction in X direction for D_{11} – Uniform strain, $\varepsilon_{11} = 1$

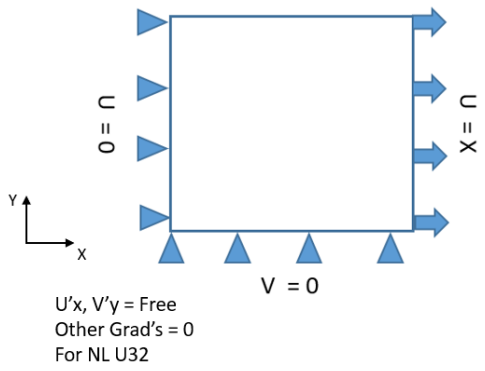

Case2: Traction in Y direction for D_{22} – Uniform strain, $\varepsilon_{22} = 1$

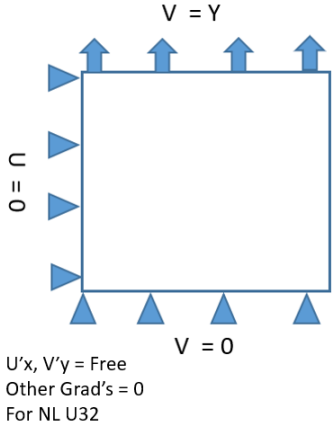

Case3: Biaxial Extension in XY direction for D_{12} – Uniform strain, $\varepsilon_{11} = \varepsilon_{22} = 1$

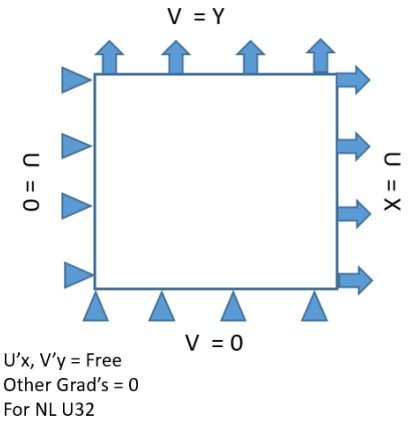

Case4: Mixed Shear for D_{33} – Dominant shear strain, $\gamma_{12} = 1$. Here all the Gradients (Grad's) for NL U32 is set free as it was observed that with this BC, we obtain good shear dominant behavior in comparison with ABAQUS® heterogenous model.

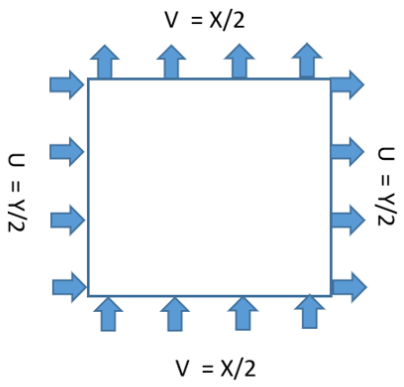

All Grad's = Free
For NL U32

For the cases of Non-Local parameters, it is not very easy to choose the BC's equivalent to ABAQUS® heterogenous model, since we cannot apply "gradient" degrees of freedom (dof) for ABAQUS® CPS4 element as it contains just displacement dof's. So, it is necessary to impose gradients using displacements (U, V) to generate non-local effects. For NL U32 element, all gradients ($U'x$, $U'y$, $U'xy$, $V'x$, $V'y$ and $U'xy$) are set free at all nodes, as it was observed that only with this condition, it was possible obtain dominant effects (but not constant) of corresponding curvature components: κ_{111}, κ_{122}, κ_{112}, κ_{211}, κ_{222} and κ_{212}. After testing different possible combinations of BC's, the following BC's are selected, which generates dominant non-local effects to identify the respective non-local parameters.

Case5: Traction in X direction with gradient for 'A ' - $\kappa_{111} = \frac{\partial^2 u}{\partial x^2} = 1$

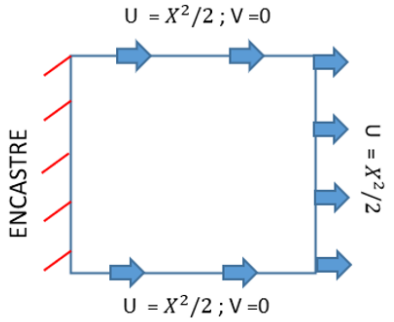

All Grad's = Free
For NL U32

Case6: Traction in Y direction with gradient for 'E ' - $\kappa_{222} = \frac{\partial^2 v}{\partial y^2} = 1$

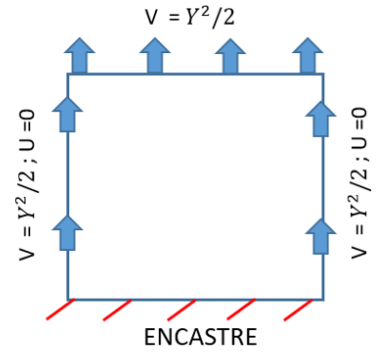

All Grad's = Free
For NL U32

Case7: Shear in X direction with gradient for 'B ' - $\kappa_{122} = \frac{\partial^2 u}{\partial y^2} = 1$

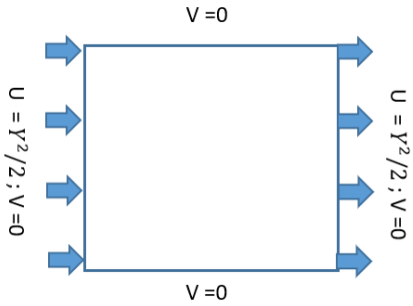

All Grad's = Free
For NL U32

Case8: Shear in Y direction with gradient for 'D ' - $\kappa_{211} = \frac{\partial^2 v}{\partial x^2} = 1$

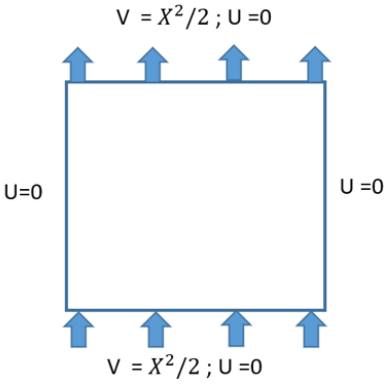

All Grad's = Free
For NL U32

Case9: Traction in X along Shear with gradient for 'C ' - $\kappa_{112} = \frac{\partial^2 u}{\partial x \partial y} = 1$

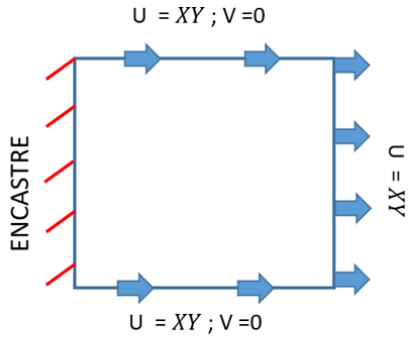

All Grad's = Free
For NL U32

Case10: Traction in Y along Shear with gradient for 'F ' - $\kappa_{212} = \frac{\partial^2 v}{\partial x \partial y} = 1$

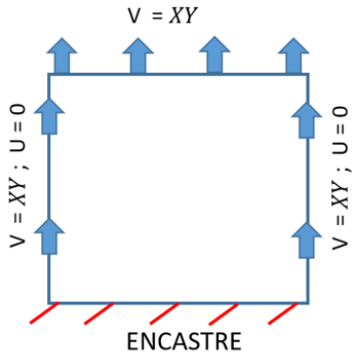

All Grad's = Free
For NL U32

10.1.2.3 ***Optimization in DAKOTA***

As it is discussed earlier, one of the important steps in DAKOTA is to define an objective function (Error Criteria) to be minimized to obtain optimal parameters. Since we are dealing with elastic problem, we know that the Total Strain Energy (W) remains constant, hence, "*Global Total Strain Energy Error (ETot)*" is chosen as an objective function, which is the sum of relative global energy error between heterogenous model and homogenous non-local model of 10 cases.

$$ETot = \sum_{i=1}^{10} \frac{\{Abs[EHET^{(i)} - EHOM^{(i)}]\}}{EHET^{(i)}} \qquad (10\text{-}4)$$

Where, $EHET$ is global total strain energy of heterogenous model and $EHOM$ is global total strain energy of homogenous non-local model. Now, with the definition of objective function, the optimization loop in DAKOTA is defined as shown in Figure 105:

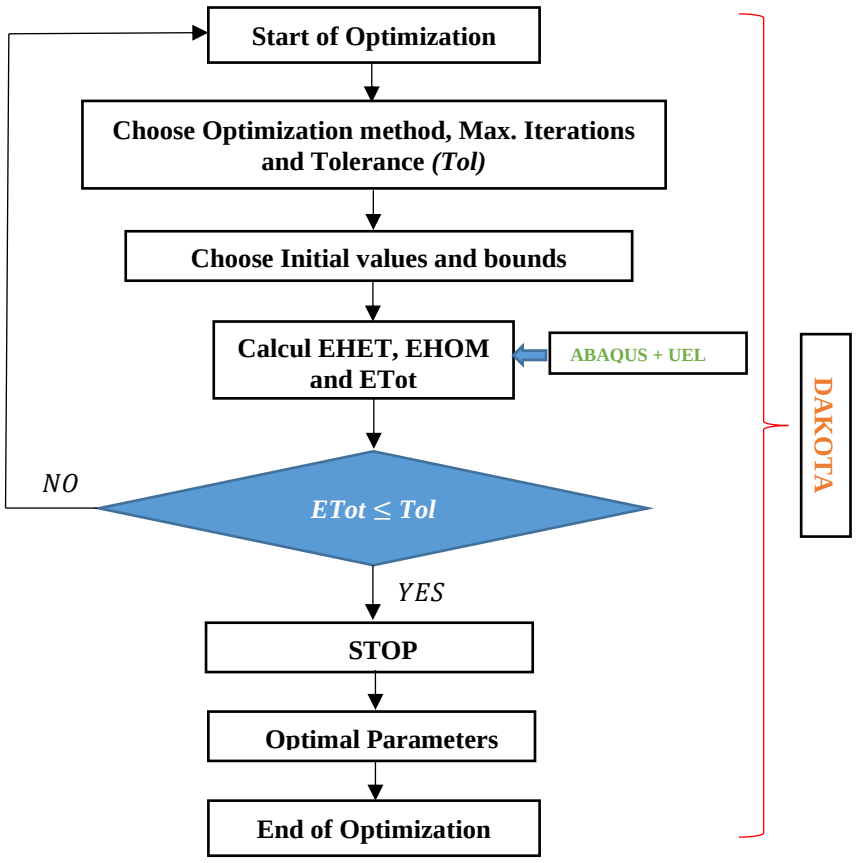

Figure 105: Optimization loop - DAKOTA

Optimal Parameters (Microstructure 1):

A sensitivity analysis is performed to choose good initial values for non-local parameters. As mentioned earlier, we have calculated good initial parameter values for elastic constitutive moduli, but we do not have proper estimation of initial values for non-local parameters (A, B, C, D, E and F), it is necessary to consider individual cases and obtain good initial guess respectively by minimizing the individual Energy Error difference with respect to heterogenous model in order to avoid the increase in optimization loop time. For this study/analysis, "Absolute Energy Error Criteria" between EHET and EHOM is chosen (ETot=Abs [EHET – EHOM]), in order to get close parameter value, which results in minimum error. In DAKOTA, "Genetic/Evolutionary algorithm" is chosen with 200 function evaluations/iterations and population size of 50 in order to perform optimization with all possible combination of values within the defined range/bounds. Some random initial guess values are provided and the optimal

values given by DAKOTA will be selected as initial values for final optimization considering all cases together.

1) Parameter "A / $\frac{\partial^2 u}{\partial x^2}$": We can observe that, since we apply traction in X direction with gradient for "A", there is also a dependency of parameter "D11" in reducing energy error. Therefore, D11 is also varied and other parameters kept constant. Other non-local parameters are set to low values (1E-8) in order to have dominant effect of energy corresponding to just "A".

Parameters	Initial Value	Initial Global Abs Energy Error	Optimal Value	Global Abs Energy Error after Optimization	Bounds	
					Lower	Upper
A	4.0		3.18		1E-02	1E+01
D11	123104		131527.82		100000	200000
		ETot = 0.718443		ETot = 0.000007		

Fix :
D22 = 6971.44
D12 = 2440
D33 = 3145.30
BCDEF = 1E-08

2) Parameter "E / $\frac{\partial^2 v}{\partial y^2}$": We can observe that, since we apply traction in Y direction with gradient for "E", there is also a dependency of parameter "D22" in reducing energy error. Therefore, D22 is also varied and other parameters kept constant. Other non-local parameters are set to low values (1E-8) in order to have dominant effect of energy corresponding to just "E".

Parameters	Initial Value	Initial Global Abs Energy Error	Optimal Value	Global Abs Energy Error after Optimization	Bounds	
					Lower	Upper
E	3.3		2.819		1E-02	1E+01
D22	6971.44		10460		6000	20000
		ETot = 0.020734		ETot = 0.00001		

Fix :
D11 = 123104
D12 = 2440
D33 = 3145.30
ABCDF = 1E-08

3) Parameter "B / $\frac{\partial^2 u}{\partial y^2}$": We can observe that, since we apply shear in X direction with gradient for "B", there is also a dependency of parameter "D33" in reducing energy error. Therefore, D33 is also varied and other parameters kept constant. Other non-local parameters are set to low values (1E-8) in order to have dominant effect of energy corresponding to just "B".

Parameters	Initial Value	Initial Global Abs Energy Error	Optimal Value	Global Abs Energy Error after Optimization	Bounds	
					Lower	Upper
B	2.9		9.67		1E-03	1E+01
D33	3145.30		7136.68		3000	10000
		ETot = 0.23140		ETot = 0.000006		

Fix :
D11 = 123104
D22 = 6971.44
D12 = 2440
ACDEF = 1E-08

4) Parameter "D / $\frac{\partial^2 v}{\partial x^2}$": We can observe that, since we apply shear in Y direction with gradient for "D", there is also a dependency of parameter "D33" in reducing energy error. Therefore, D33 is also varied and other parameters kept constant. Other non-local parameters are set to low values (1E-8) in order to have dominant effect of energy corresponding to just "D".

Parameters	Initial Value	Initial Global Abs Energy Error	Optimal Value	Global Abs Energy Error after Optimization	Bounds	
					Lower	Upper
D	5.8		3.18E-02		1E-02	1E+01
D33	3145.30		8604.65		3000	10000
		ETot = 0.088740		ETot = 0.000001		

Fix :
D11 = 123104
D22 = 6971.44
D12 = 2440
ABCEF = 1E-08

5) Parameter "C / $\frac{\partial^2 u}{\partial x \partial y}$": We can observe that, since we apply traction in X direction along shear with gradient for "C", there is also a dependency of parameters: "D11" and "D33" in reducing energy error. Therefore, D11 and D33 are also varied and other parameters kept constant. Other non-local parameters are set to low values (1E-8) in order to have dominant effect of energy corresponding to just "C".

Parameters	Initial Value	Initial Global Abs Energy Error	Optimal Value	Global Abs Energy Error after Optimization	Bounds	
					Lower	Upper
C	0.4		1.59		1E-02	1E+01
D11	123104		107406.90		100000	200000
D33	3145.30		6208.24		3000	10000
		ETot = 1.353979		ETot = 0.00002		

Fix :
D22 = 6971.44
D12 = 2440
ABDEF = 1E-08

6) Parameter "F / $\frac{\partial^2 v}{\partial x \partial y}$": We can observe that, since we apply traction in Y direction along shear with gradient for "F", there is also a dependency of parameters: "D22" and "D33" in reducing energy error. Therefore, D22 and D33 are also varied and other parameters kept constant. Other non-local parameters are set to low values (1E-8) in order to have dominant effect of energy corresponding to just "F".

Parameters	Initial Value	Initial Global Abs Energy Error	Optimal Value	Global Abs Energy Error after Optimization	Bounds	
					Lower	Upper
F	0.038		8.88		1E-02	1E+01
D22	6971.44		12085.42		5000	15000
D33	3145.30		14064.32		3000	15000
		ETot = 1.353979		ETot = 0.00002		

Fix :
D11 = 123104
D12 = 2440
ABCDE = 1E-08

With this study, the first estimated good initial values of non-local parameters to be used in final optimization loop are:

$$\begin{aligned} A &= 3.18\ MPa \cdot mm^2 \\ E &= 2.819\ MPa \cdot mm^2 \\ B &= 9.67\ MPa \cdot mm^2 \\ D &= 3.18\text{E-}02\ MPa \cdot mm^2 \\ C &= 1.59\ MPa \cdot mm^2 \\ F &= 8.88\ MPa \cdot mm^2 \end{aligned} \qquad (10\text{-}5)$$

Now the final optimization considering all cases can be carried out with these good initial parameters values for both classical and non-local part. We choose "Non-linear least-square (nl2sol)" available in DAKOTA for the final optimization since we are close to the solution and also it is less expensive compared to non-gradient based/genetic algorithm. The maximum number of iterations is set to 200 and tolerance is set to 1E-02 with objective function, "*Global Total Strain Energy Error (ETot)*", as mentioned earlier. The final parameters given by DAKOTA are shown in Figure 106.

Parameters	Cases	Initial Value	Initial Global Relative Energy Error	Optimal Value	Global Relative Energy Error after Optimization	Bounds	
						Lower	Upper
D11	1	123104	0.00002	123210.77	0.004671	120000	140000
D22	2	6971.44	0.35523	10894.11	0.002012	6000	12000
D12	3	2440	0.05140	4081.86	0.000003	2000	5000
D33	4	3145.30	0.20921	3859.46	0.002938	3000	6000
A	5	3.18	0.04248	0.001139	0.000643	1E-03	2E+01
E	6	2.819	0.56747	9.72208	0.000899	1E-03	2E+01
B	7	9.67	0.05049	4.04847	0.000093	1E-03	2E+01
D	8	3.18E-02	0.38345	9.19324	0.000120	1E-03	2E+01
C	9	1.59	0.18285	6.48397	0.001427	1E-03	2E+01
F	10	8.88	0.46311	9.11084	0.000440	1E-03	2E+01
			ETot = 2.30570		ETot = 0.013248		

Figure 106: Initial and Optimal parameters for Microstructure 1

From Figure 106, it is realized that with initial values we obtain an ETot=2.3057, but after optimization, we were able to achieve the order of global error, ETot =1E-02 with the optimal parameters, which is really compromising. Figure 107 depict the evolution of relative total strain energy error with initial and optimal parameters over different loading cases used to identify parameters.

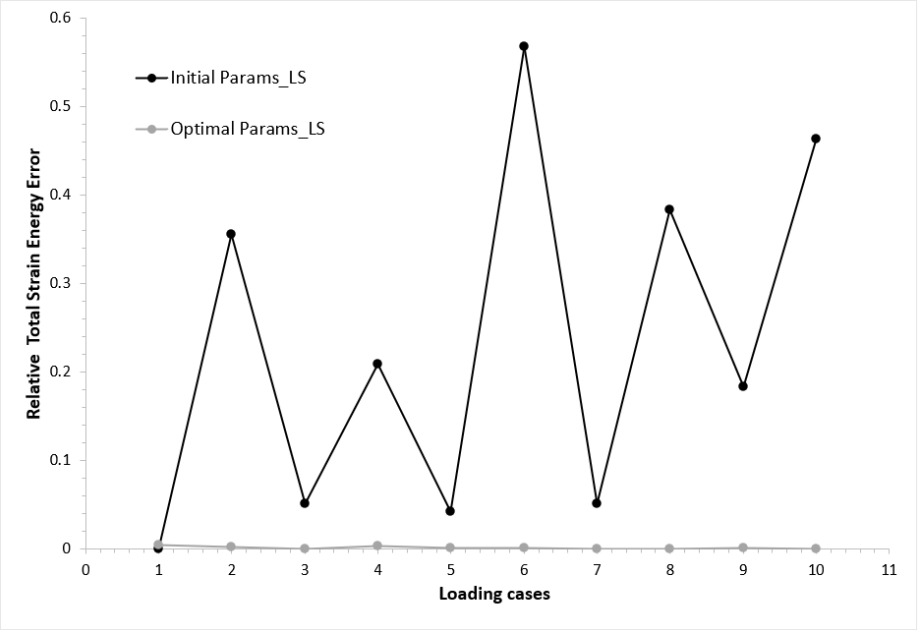

Figure 107: Evolution of Relative Total Strain Energy Error with initial and optimal values over loading cases for Microstructure 1

Optimal Parameters (Microstructure 2):

In this case, the initial values are chosen by interchanging the cross principal directional components, for Ex: D11(Micro1) = D22(Micro2), A (Micro1) = E (Micro2), etc., since we just change the orientation of fibers from 0^0 to 90^0. So, the initial values for Microstructure 2 is same as Microstructure 1 with the interchange of cross principal directional components (compare the Figure 106 and Figure 108). Optimization method, maximum number of iterations and tolerance used is same as Microstructure 1. The final parameters given by DAKOTA are shown in the Figure 108.

From Figure 108, it is realized that after optimization, we were able to achieve the order of global error, ETot =1E-02 with the optimal parameters, which is exactly same as Microstructure 1, thereby proving the robustness of DAKOTA and also validating our HOMNL model and NL U32. Because, when we change the orientation of fibers from 0^0 to 90^0, it is expected that we should be obtain same global energy with identical cross principal component values. Figure 109 depicts the evolution of relative total strain energy error with initial and optimal parameters over different loading cases used to identify parameters.

Parameters	Cases	Initial Value	Initial Global Relative Energy Error	Optimal Value	Global Relative Energy Error after Optimization	Bounds	
						Lower	Upper
D11	1	6971.44	0.35523	10894.11	0.002012	6000	12000
D22	2	123104	0.00002	123210.77	0.004671	120000	140000
D12	3	2440	0.05140	4081.86	0.000004	2000	5000
D33	4	3145.30	0.20921	3859.46	0.002938	3000	6000
A	5	2.819	0.56747	9.72208	0.000899	1E-03	2E+01
E	6	3.18	0.04248	0.001139	0.000642	1E-03	2E+01
B	7	3.18E-02	0.38345	9.19324	0.000120	1E-03	2E+01
D	8	9.67	0.05049	4.04847	0.000093	1E-03	2E+01
C	9	8.88	0.46311	9.11084	0.000440	1E-03	2E+01
F	10	1.59	0.18285	6.48397	0.001427	1E-03	2E+01
			ETot = 2.30570		ETot = 0.013248		

Figure 108: Initial and Optimal parameters for Microstructure 2

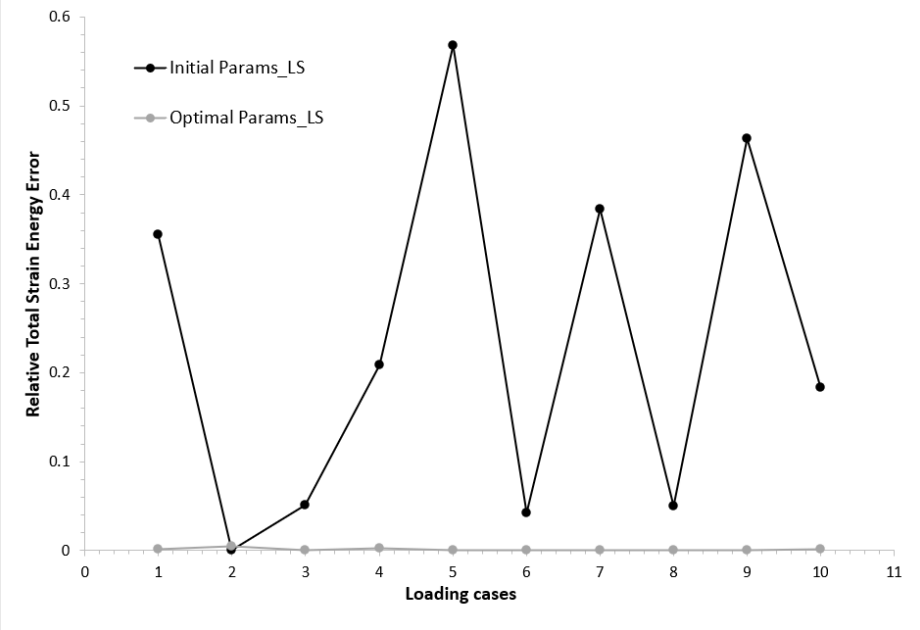

Figure 109: Evolution of Relative Total Strain Energy Error with initial and optimal values over loading cases for Microstructure 2

Optimal Parameters (Microstructure 3):

For the case of Microstructure 3 (woven plain), it was decided to choose the initial values for HOMNL model based on performing sensitivity analysis considering individual loading cases which permits to identify respective parameters, with minimization of energy error using "Absolute Energy Error Criteria", similar to the case of Microstructure 1. For the final optimization (considering all cases together), optimization method, maximum number of iterations and tolerance used is same as Microstructure 1 and 2. The initial values and optimal parameters values obtained can be seen in Figure 110. The evolution of relative total strain energy error with initial and optimal parameters over different loading cases used to identify the parameters can be seen in Figure 111.

Parameters	Cases	Initial Value	Initial Global Relative Energy Error	Optimal Value	Global Relative Energy Error after Optimization	Bounds	
						Lower	Upper
D11	1	194527.75	0.011699	192282.17	0.000940	190000	200000
D22	2	194527.75	0.011904	192282.17	0.000737	190000	200000
D12	3	38537.98	0.003578	38537.98	0.006092	35000	50000
D33	4	61678.98	0.230224	57858.51	0.001559	50000	60000
A	5	8.32E-01	0.068234	8.5012	0.000158	1E-03	1E+01
E	6	8.54	0.032547	9.867	0.000660	1E-03	1E+01
B	7	7.97E-01	0.331099	2.7765E-01	0.000709	1E-03	1E+01
D	8	7.48	0.087791	9.988	0.000615	1E-03	1E+01
C	9	3.49	0.057971	4.151E-03	0.000929	1E-03	1E+01
F	10	3.77	0.023379	5.680	0.001314	1E-03	1E+01
			ETot = 0.858425		ETot = 0.013713		

Figure 110: Initial and Optimal parameters for Microstructure 3

The final optimal values of the components of classical elastic moduli, $\boldsymbol{D}$ in MPa and local fiber bending stiffness matrix/non-local moduli, $\overline{\overline{\boldsymbol{C_f}}}$ in $MPa \cdot mm^2$ of HOMNL model for the considered heterogenous RVE's with geometrical non-linearity are given in Table 7.

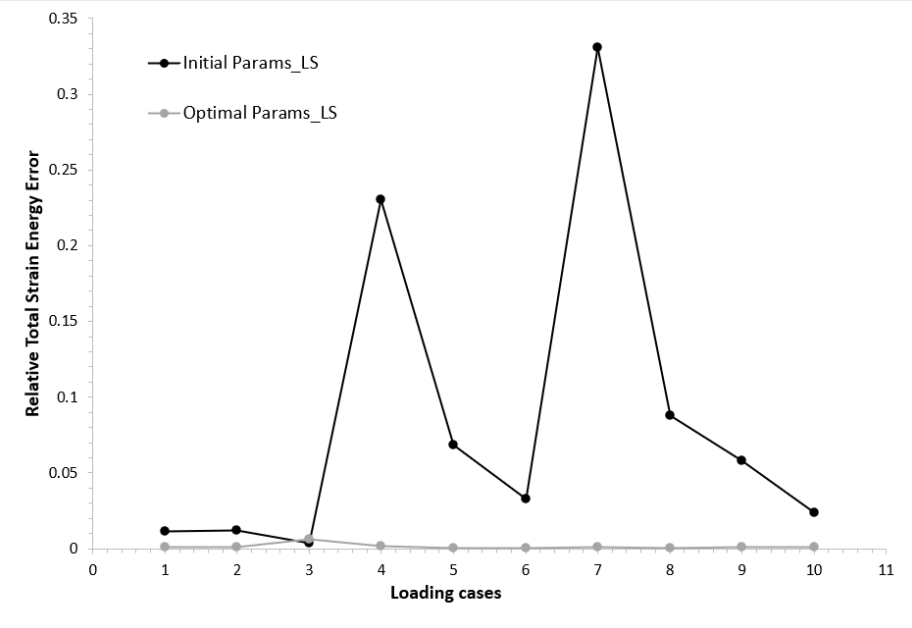

Figure 111: Evolution of Relative Total Strain Energy Error with initial and optimal values over loading cases for Microstructure 3

Table 7: Optimal values of classical elastic moduli and non-local moduli of HOMNL model for the heterogenous RVE's

Parameters	***Microstructure* 1**	***Microstructure 2***	***Microstructure* 3**
$D11$	123210.77	10894.11	192282.17
$D22$	10894.11	123210.77	192282.17
$D33$	3859.46	3859.46	57858.51
$D12$	4081.86	4081.86	38537.98
A	0.001139	9.72208	8.5012
B	4.04847	9.19324	0.27765
C	6.48397	9.11084	0.004151
D	9.19324	4.04847	9.988
E	9.72208	0.001139	9.867
F	9.11084	6.48397	5.680

Anisotropic elastic and non-local properties of HOMNL model have been identified with respect to considered heterogenous RVE's. Next part is to identify the parameters of matrix material non-linearity (anisotropic RO law) in HOMNL model (NL U32) developed in chapter 9, which is discussed in detail in the following section.

10.2 Identification of Non-Linear material parameters

In the earlier chapter 9, we have developed anisotropic Ramberg-Osgood material behavior to replicate same behavior as real heterogenous UD composites. In this section, identification of material law parameters with non-linear geometry is performed.

10.2.1 Influence of α_{12} parameter

In order to evaluate the influence of α_{12} parameter, one loading case (traction in longitudinal or X direction) is considered. All other material parameters are kept same as previous (see chapter section 9.2.5), including mesh and loading. Following figure depicts the influence of this parameter in the solution for the considered loading case.

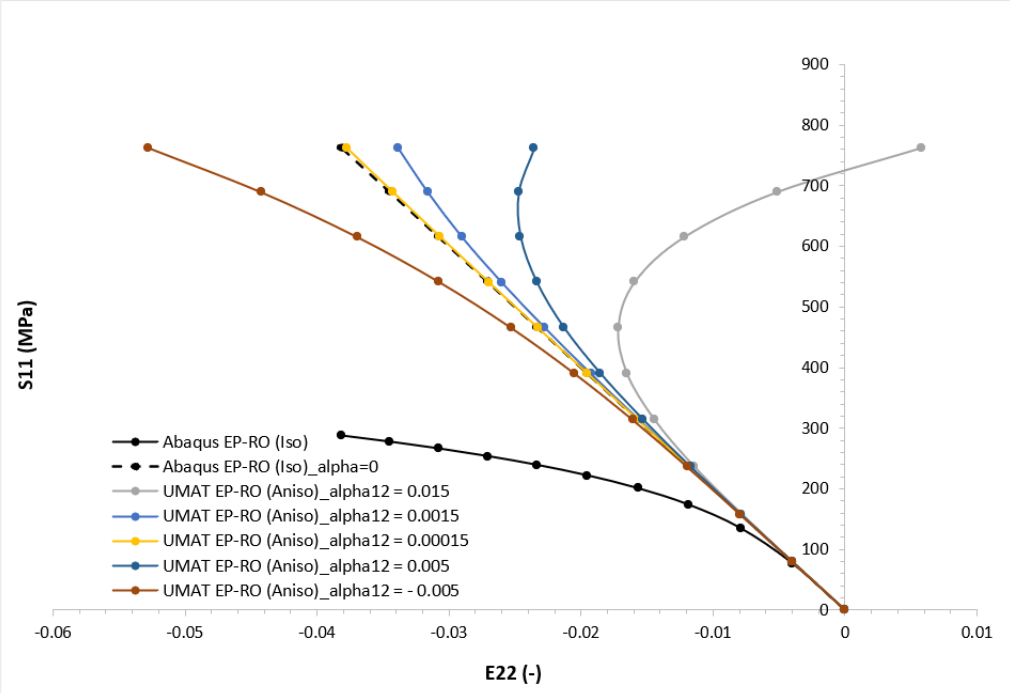

Figure 112: Influence of α_{12} parameter in case of traction along X direction

We can observe from Figure 112 that, how the parameter α_{12} affects the solution in case of uniaxial traction. When $\alpha_{12} = 0.00015$, solution with Anisotropic RO law tends closer to the solution of isotropic RO law of ABAQUS® with $\alpha = 0$ (to represent linearity). This parameter introduced in the law to reproduce a non-linear Poisson's effect. It is necessary to do several numerical tests to obtain the good value for α_{12} for the respective cases considered.

10.2.2 Identification of parameters

Before proceeding to identification of Anisotropic RO law parameters of HOMNL model (NL U32), it was decided to first study the sensitivity analysis of parameters introduced in the material behavior law developed, in order to understand better the influence of the parameters. It is to be

noted that, for all the cases in this part, RVE of Microstructure 1 (0^0 ply) is chosen as reference heterogenous model. The fiber(elastic) and matrix(elastic and plastic) parameters for heterogenous RVE are taken from Drapier et al., [D1] and Nezamabadi et al., [N1] as in Table 5.

10.2.2.1 *Sensitivity Analysis of Anisotropic RO-Law parameters in HOMNL model (NL U32)*

First study is performed on α_{12} parameter as it is also important to choose the initial value of this parameter for further studies. Study is performed with loading condition of uniaxial traction in X direction. Initial parameters for HOMNL model: Elastic and Plastic/RO law material parameters for HOMNL model used for the study can be seen in Table 8. Note that the Elastic and Non-local parameters (Table 7) are optimal parameters obtained with DAKOTA for Microstructure 1.

Table 8: Initial Anisotropic Elasto-plastic RO law parameters of Homogenous Non-local model

Elastic parameters		***Plastic/Anisotropic RO law parameters***
$D11 = 123210.77$	$E_1 = 121681\ MPa$	$\sigma_{22}^0 = \sigma_6^0 = 60\ MPa$
$D22 = 10894.11$	$E_2 = 10758.88\ MPa$	$n_{22} = n_6 = 4$
$D33 = 3859.46$	$G_{12}/G_6 = 3859.40\ MPa$	$\alpha_{22} = \alpha_6 = 0.015$
$D12 = 4081.86$	$\nu_{12} = 0.37$	
		Thickness, t =1mm

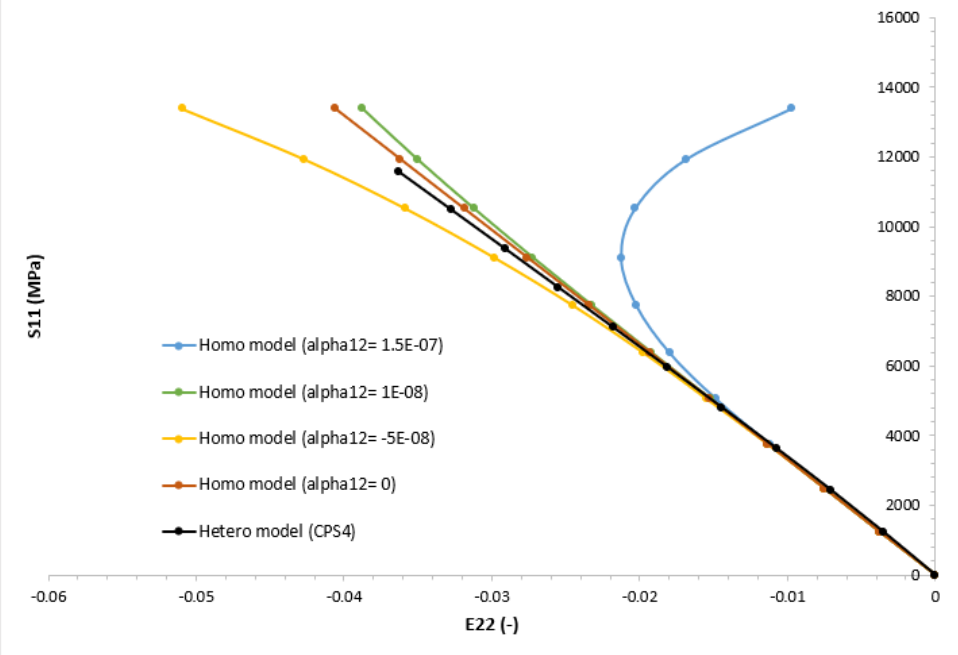

Figure 113: Influence of α_{12} parameter in case of traction along X direction for HOMNL model – Microstructure 1

For this analysis, many parameters set values are studied and finally 4 set of values (0, 1.5E-07, 1E-08 and -5E-08) are chosen to demonstrate significant effects, relevant for this particular model. From Figure 113, it is evident that, even though the value of α_{12} is very low, we can observe the significant effect of this parameter in the solution. With $\alpha_{12} = 0$, solution with Anisotropic RO law of HOMNL model tends closer to the solution of ABAQUS® heterogenous model (which is

almost linear due to higher elastic stiffness of fiber in loading direction). However, we can observe that, with α_{12} = -5E-08 non-linear effect of Poisson appears, therefore, it was decided to use, α_{12} = -5E-08 for further studies/analysis in order to avoid numerical problems (divide by zero).

Next part is to study the influence of α_{22}, n_{22}, and σ_{22}^{0} (parameters defined in transverse direction in RO law). For this case, loading condition of 'Uniaxial traction in Y or transverse direction' is chosen. For each sensitivity study of parameters: α_{22}, n_{22}, and σ_{22}^{0} all other RO law parameters are kept constant as in Table 8 respectively. Following Figure 114 - Figure 116, depicts the evolution of Global Total Strain Energy(W) over Time steps(T) with the variation of these parameters.

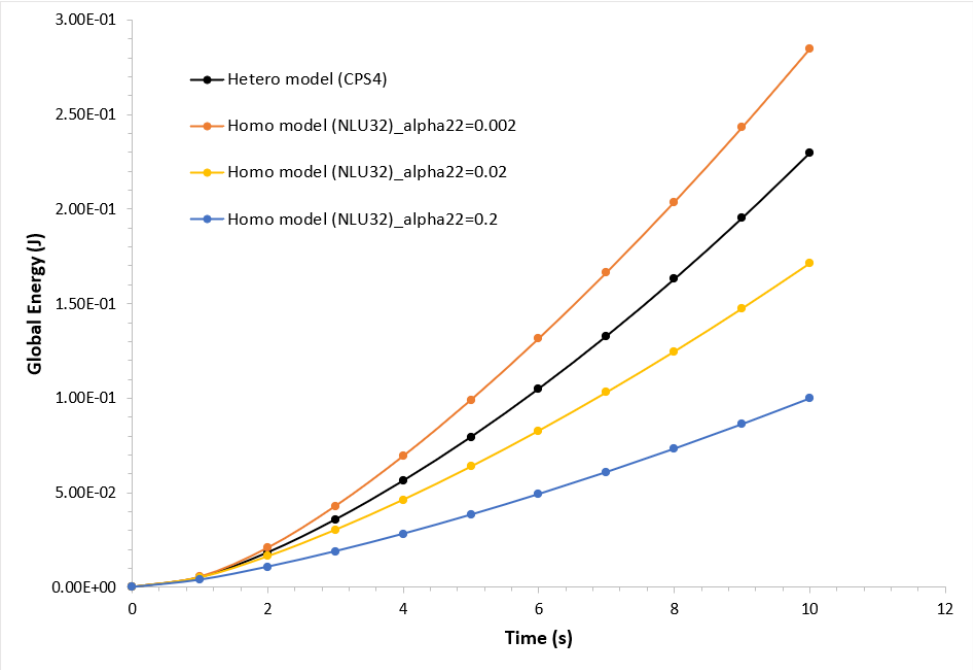

Figure 114: Influence of α_{22} parameter

From Figure 114, it can be realized that for lower value of α_{22}, i.e. 0.002, we can observe stiffer response, whereas for $\alpha_{22} = 0.02$, softer and for $\alpha_{22} = 0.2$ more softer, almost linear solution with HOMNL model(NL U32) in comparison to heterogenous model(CPS4) respectively. Similar trend can be observed with the variation of n_{22} parameter, but with greater difference in the solution against heterogenous model for $n_{22} = 2$, compared to other values of n_{22} (see Figure 115). In general, it can be concluded that with increase in value of α_{22} and n_{22} parameters, response is softer and the trend tends towards linear in comparison against heterogenous RVE of Microstructure 1. For parameter, σ_{22}^{0} the response is exact opposite (Figure 116).

Note that similar study was also carried out even for α_{6}, n_{6} and σ_{6}^{0} parameters using shear loading case (not shown here) and observed identical trends in the solution with respect to heterogenous model.

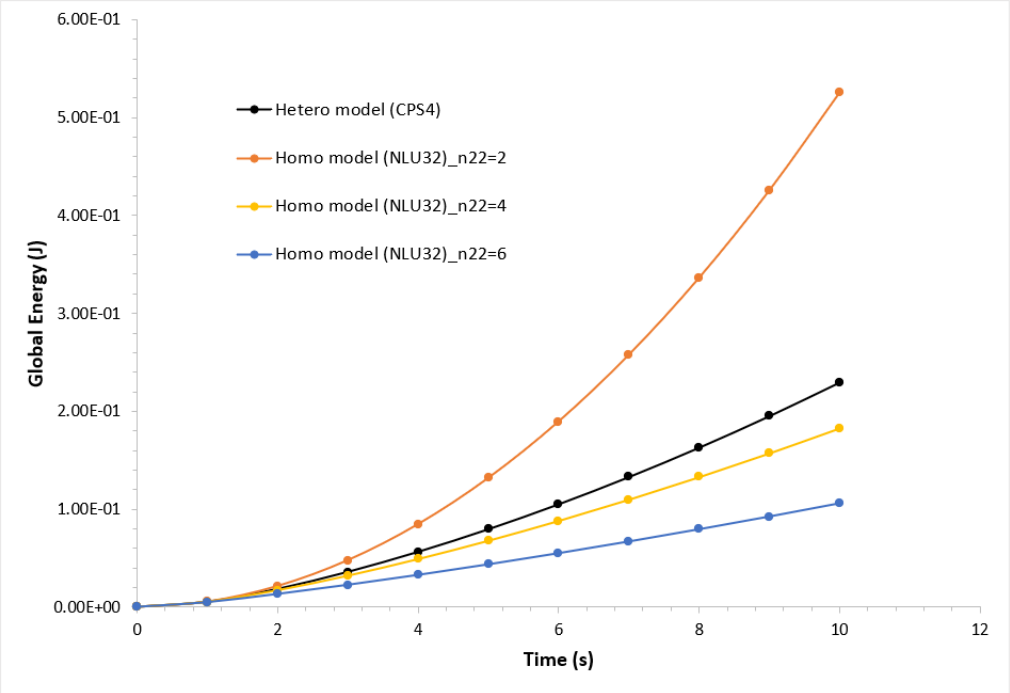

Figure 115: Influence of n_{22} parameter

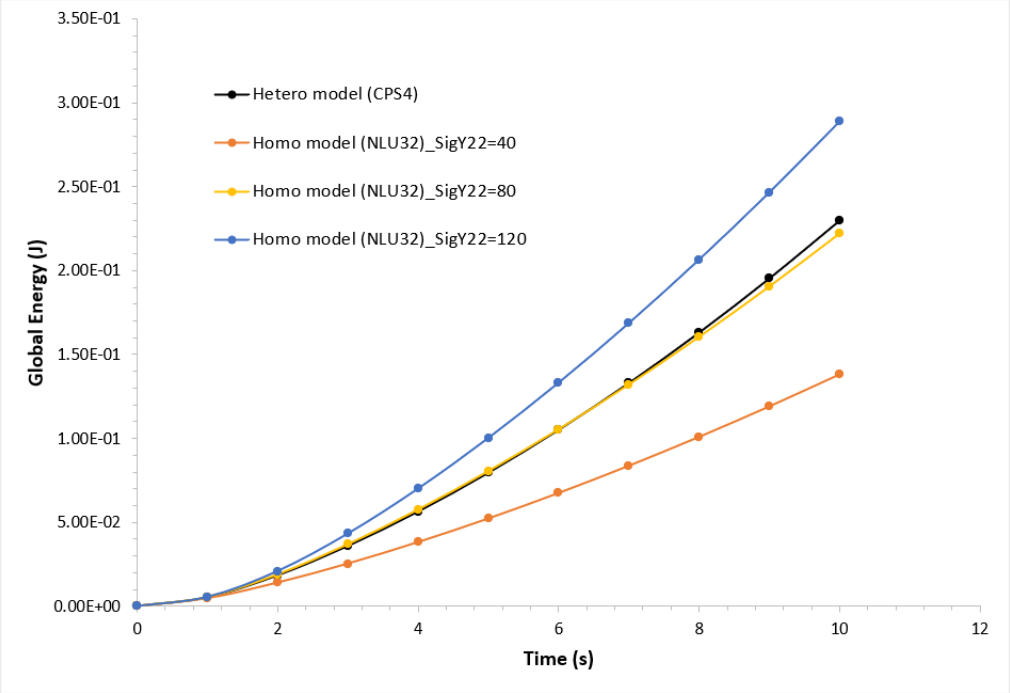

Figure 116: Influence of σ_{22}^{0} parameter

At this stage, we have understood the influence of each parameters of Anisotropic RO law of HOMNL model. Now the next part is dedicated to identification of these parameters with respect

to RVE of heterogenous model, taking into account all 10 loading cases, as in identification of elastic parameters (section 10.1).

10.2.2.2 *Identification of optimal parameters (Microstructure 1)*

As mentioned earlier, the initial values for Anisotropic RO law of HOMNL model considered is as in Table 8 with α_{12}= -5E-08. RVE size, mesh and loading conditions are same as the one used for elastic case (Figure 104). It is important to note that for this part, Global Total Strain Energy(W) over Time steps(T) is considered as a global criterion. The objective is to minimize the gap or error between two energy curves (generated from RVE of heterogenous and homogenous non-local model) to obtain the final optimal non-linear material law parameters. DAKOTA is not used for this optimization as it is time consuming when used with non-linear material laws, since it runs 'n' number of simulations with numerous sets of parameter values defined within range and moreover there can be convergence issues with some random set of values too. Therefore, optimal parameters values are obtained by varying parameters manually, thereby studying and understanding the behavior with each parameter set to curb time. The final optimal parameters of anisotropic Ramberg-Osgood law of HOMNL model for heterogenous RVE of Microstructure1 obtained are as in Table 9.

Table 9: Optimal material parameters of Anisotropic Ramberg-Osgood law of HOMNL model for heterogenous RVE of Microstructure1

Plastic/Anisotropic RO law parameters
$\sigma_{22}^0 = \sigma_6^0 = 60\ MPa$
$n_{22} = 4$
$n_6 = 3$
$\alpha_{22} = 0.006$
$\alpha_6 = 0.002$
$\alpha_{12} =$ *-5E-08*

Figure 117 and Figure 118 shows graphically how close the homogenized model (HOMNL) is to the heterogenous RVE model of Microstructure1 with the set of optimal parameters obtained for different loading cases. A good compromising fit is obtained for all the loading cases with the set of optimal parameters. However, slight differences are observed especially for the loading cases involving shear, which is expected since it is not very easy to fit the curve exactly with plasticity in the model involving complex loading cases. And also, it can be possible that the heterogenous RVE considered with 10 layers of matrix-fiber may be not a good reference with plasticity, since there can be localized effects of stress/strain for example in the model. But it is sufficient to demonstrate the protocol to obtain these parameters. Further, it is interesting to note that the optimal elastic and non-local parameters obtained previously (chapter section 10.1) is also validated accordingly here. In future, it is necessary to vary the volume fraction or increase the number of layers, and also change the RVE dimension and perform the optimization to understand the influence of these parameters to use in more general cases. Due to limited time-frame and resources it was not possible to study many cases.

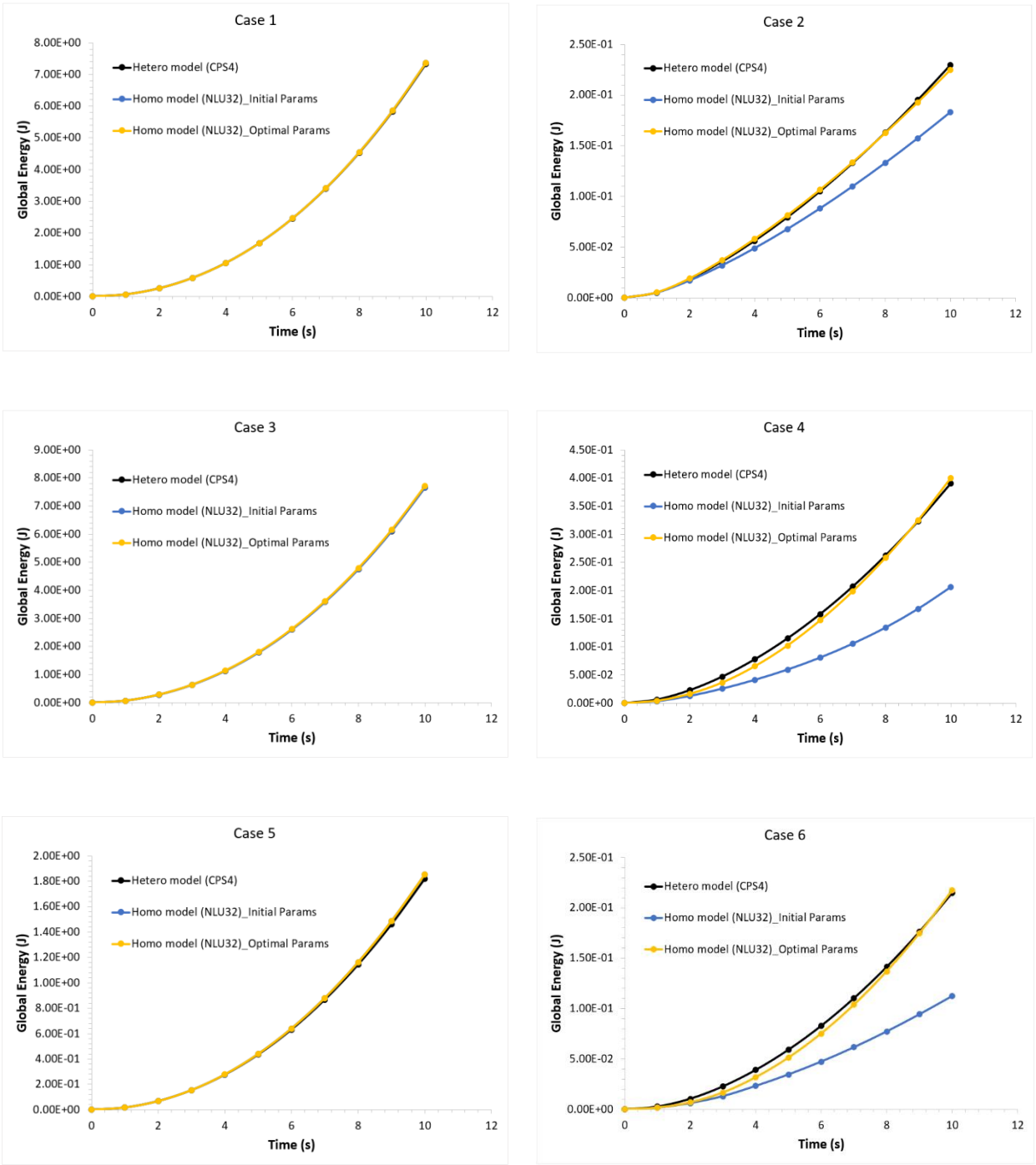

Figure 117: Comparison of Global Energy of Homogenous Non-Local and Heterogenous RVE's of Microstructure1 with optimal parameters of Anisotropic RO law for loading cases: 1 - 6

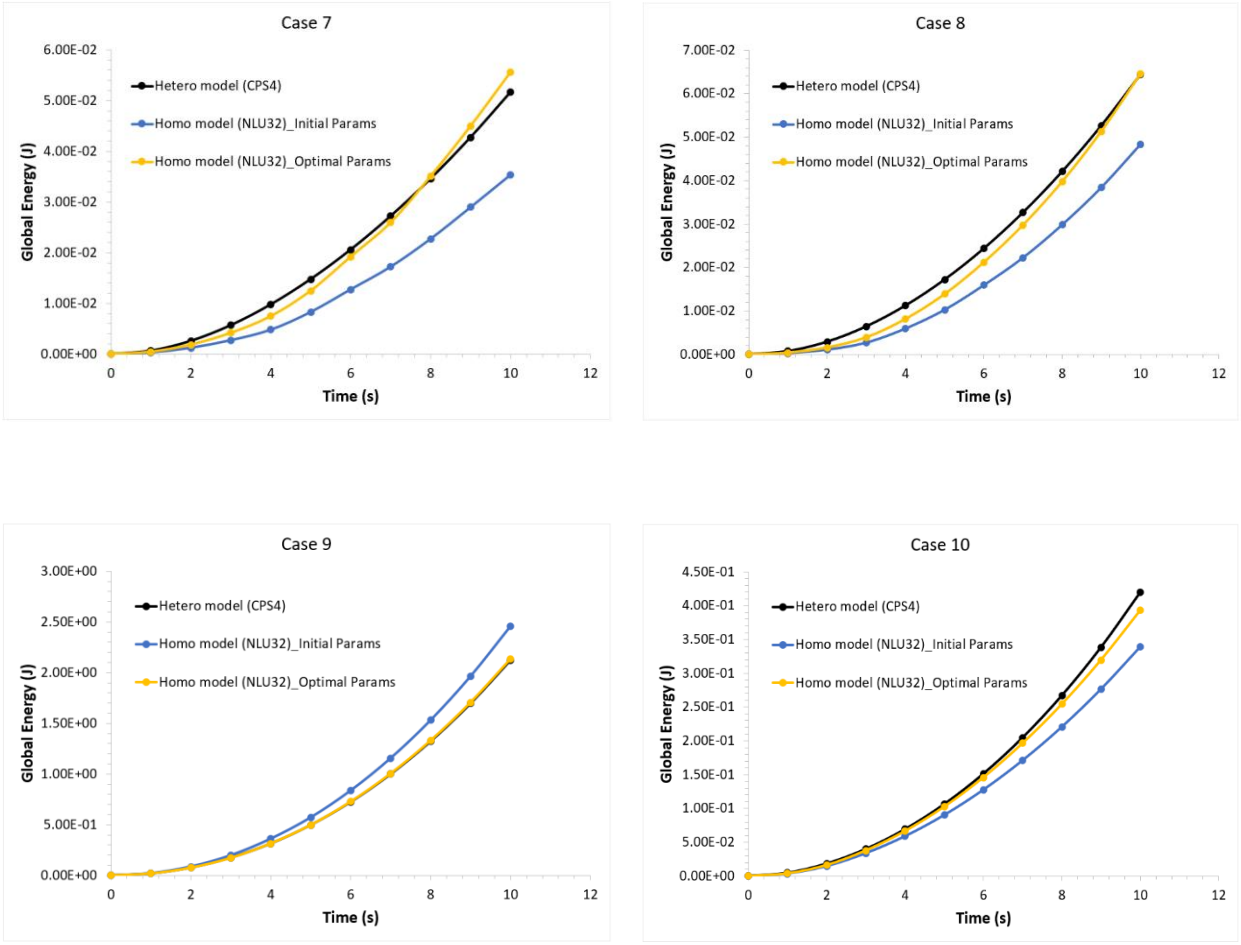

Figure 118: Comparison of Global Energy of Homogenous Non-Local and Heterogenous RVE's of Microstructure1 with optimal parameters of Anisotropic RO law for loading cases: 7 - 10

11 Compressive Response of Non-Local composites

In this chapter, the compressive response of Homogenized Non-Local model (HOMNL) for UD (0^0 ply) and woven cases (plain) are investigated. The optimal material parameters (elastic and non-linear) obtained in the previous chapter (Chapter 10) is used for HOMNL model implemented in NL U32 element. The aim is not to compare with experimental characterizations as it needs a specific identification for each kind of materials. The results obtained with HOMNL model are compared with previously developed BNL model (Chapter 5) and also with Heterogenous model built using CPS4 elements in ABAQUS®. It is important to note that it is not possible to obtain the microbuckling modes using HOMNL model for UD and woven cases since it is not clear or no enough information is available on ABAQUS® user's manual at the moment regarding the integration of "BUCKLING" STEP inside the UEL (NL U32). A complete specific solver should be built. And also, no initial misalignment/defect is taken to into account in HOMNL model because of lack of time frame and information. The main objective here is to show the capability of the model in prediction of compressive strength by observing the compressive response at the critical stage (when ABAQUS® aborts the calculation, i.e., until divergence or instability occurs).

11.1 Unidirectional case

11.1.1 Comparison with BNL model: Effect of thickness of ply

The results are compared for a non-linear case (geometry and material). A rectangular model of UD ply of length (1600µm) with a variable thickness under compression with two loading cases: Clamped-Clamped (CC) and Clamped-Free (CF) (see Figure 30) are investigated similar to BNL model. As discussed earlier, critical displacement is recorded when ABAQUS® aborts the calculation i.e., when instability occurs. Consequently, critical strain is calculated. Critical strain for different ply thickness for both the models under two loading cases can be seen in Figure 119.

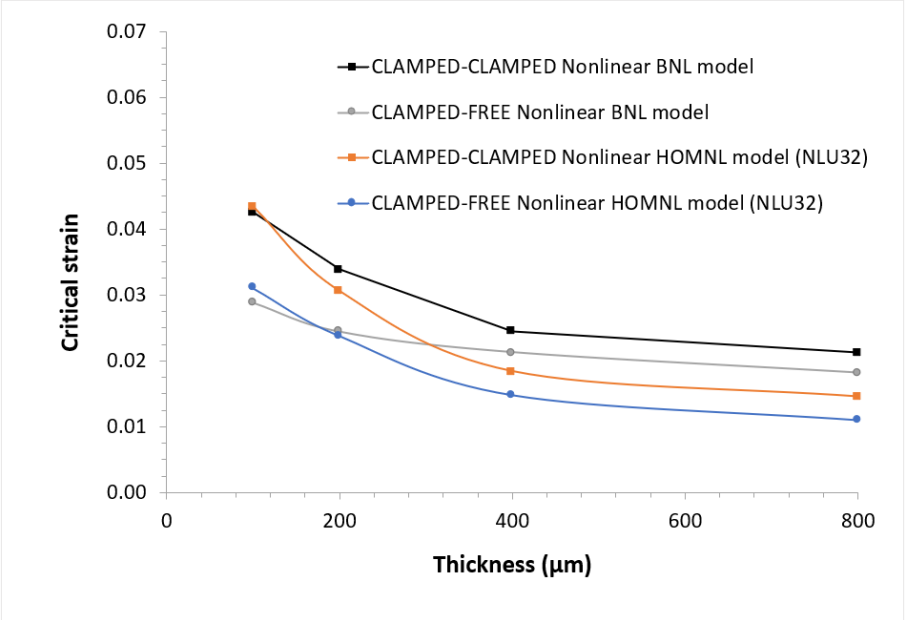

Figure 119: Comparison of critical strain versus ply thickness under compression of UD ply for BNL and HOMNL model with two boundary conditions

From Figure 119 it is evident that similar to BNL model, HOMNL model (NL U32) is also able to confirm the 'structural effect' with critical value in the order of experimental data. As the thickness increase, the critical value decreases and tends to be asymptotic. We can also notice that we do not obtain a similar solution as BNL model since the material parameters are not exactly same and also negligence of initial misalignment/defect in HOMNL model. However, the order of critical value is satisfying and proves that capability of HOMNL model (NL U32). In future, it is necessary to integrate initial defect inside NL U32 element and perform many calculations to investigate more on the influence of the effect of the defect along with matrix plasticity.

11.1.2 Comparison with heterogenous model

In this part, the compressive response of HOMNL model (NL U32) is compared with the heterogenous model built using ABAQUS® CPS4 element with geometrical and material non-linearity. The effect of length and thickness are studied under clamped-clamped and clamped-free boundary conditions. Material parameters for HOMNL model is used as in Table 7 and Table 9. The heterogenous model is built with a volume fraction, $f = 0.5$ similar to Figure 67 but with matrix at the top and bottom layer. The layers of matrix and fibers is also varied when the thickness of ply is varied to maintain the constant volume fraction. The fiber(elastic) and matrix (elastic and plastic) parameters for the heterogenous model is used as in Table 5. As discussed earlier, the solution is compared when ABAQUS® aborts the calculation. The evolution of transverse displacement fields at last increment, just before the divergence in the calculation (critical value) with variable length and thickness is shown in the following figures.

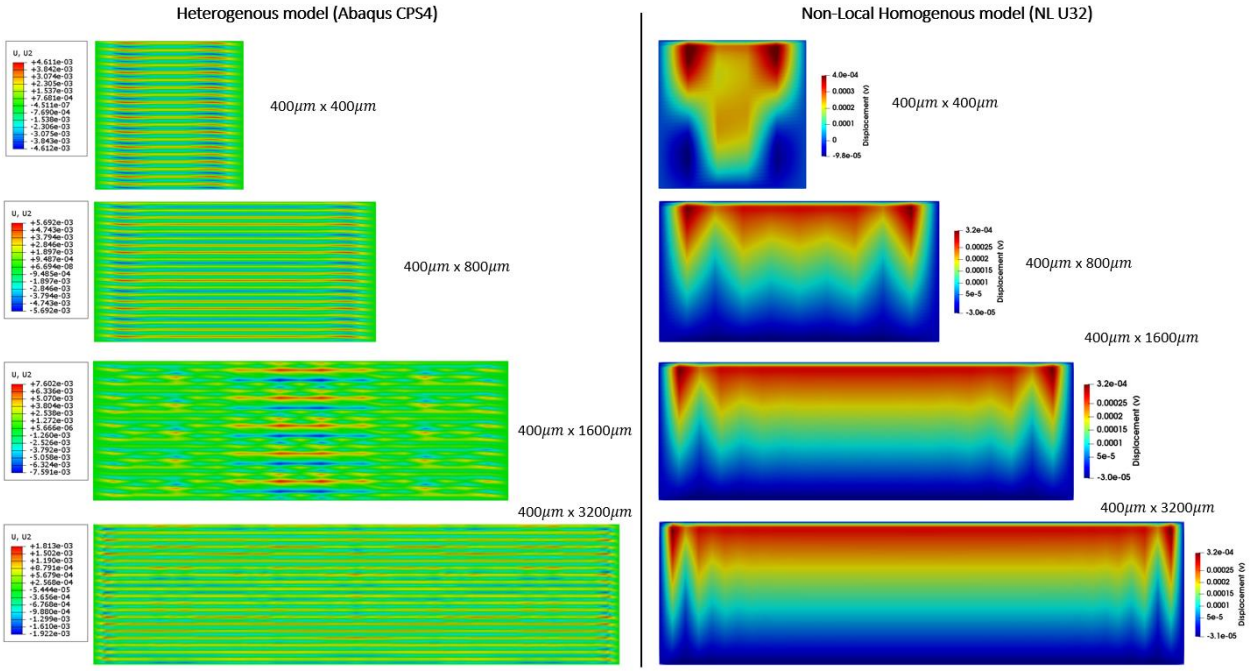

Figure 120: Comparison of transverse displacement field for different lengths with constant ply thickness of 400µm under clamped-clamped boundary condition for UD case

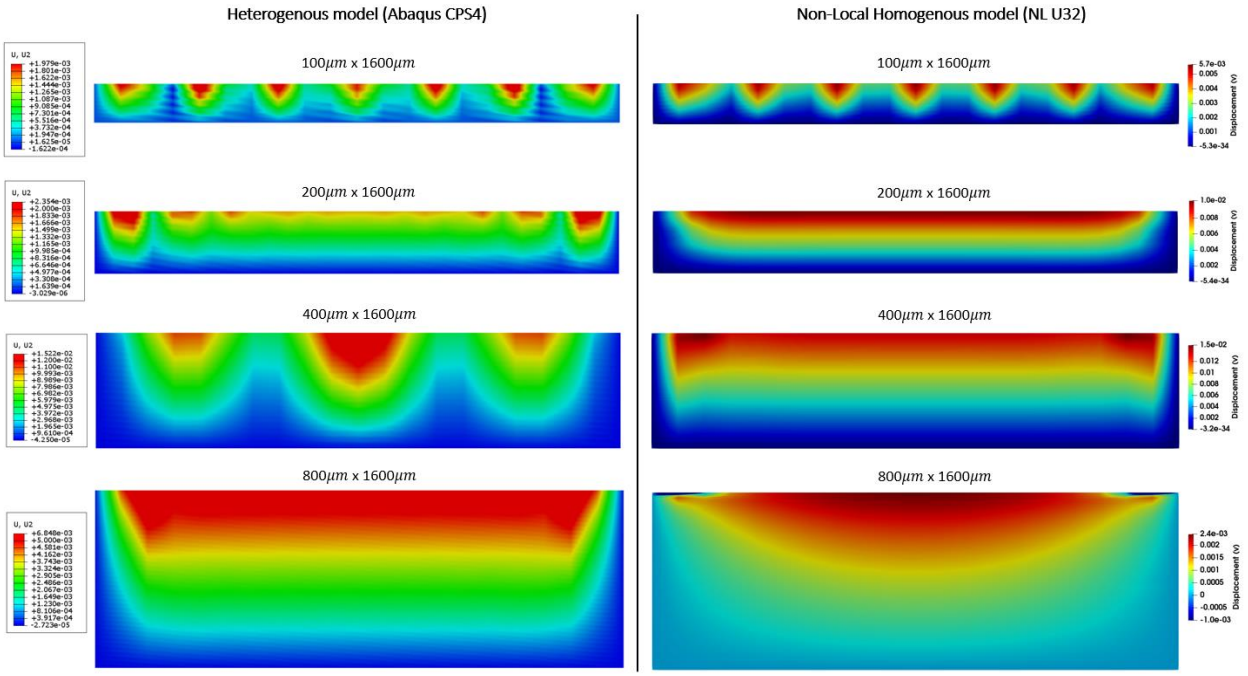

Figure 121: Comparison of transverse displacement field for different ply thickness with constant length of 1600μm under clamped-free boundary condition for UD case

Figure 120 depicts the evolution of the transverse displacement field for different lengths: 400μm, 800μm, 1600μm and 3200μm with constant thickness of 400μm under clamped-clamped boundary condition. It is clear that the heterogenous model and non-local homogenous model does not resemble the same distribution of displacement field. However, the evolution of field can be observed clearly with HOMNL model, showing that as the length increases, no significant changes in the distribution of displacement occurs or in other words, the critical value does not get affected much with the increase in ply length. Figure 121 represents the evolution of transverse displacement field for different ply thickness: 100μm, 200μm, 400μm and 800μm with constant length of 1600μm under clamped-free boundary condition. In this case, we can observe that HOMNL model represents the similar distribution of displacement field over the thickness as the heterogenous model. As the thickness of ply increases, the maximum displacement field (critical) becomes more uniform near the free edge/face(top). It is difficult to apprehend the post microbuckling, the kink band does not appear as observed with BNL model. Perhaps is due to Newton-Raphson algorithm or also negligence of the initial defect which facilitate the instability since it plays role of a perturbation? The comparison of critical strain is not good and this result confirms the former remarks. This point should be investigated.

11.2 Woven case

In this part, results are discussed only for the elastic case, since we do not have anisotropic elasto-plastic law developed for woven material and also there is no experimental data available for woven material. Consequently, the number of cases is also limited. The heterogenous model for woven (plain) is built similar to Figure 104 (Microstructure 3) using ‘partition by sketch’ option in ABAQUS® and meshed with CPS4 elements. Isotropic elastic material properties (fiber and matrix) for the woven heterogenous model is used as in Table 4, which is originally obtained for

UD ply. For HOMNL model (NL U32), the optimal parameters (elastic and non-local) obtained as in Table 7 for woven is used. Similar to the UD case, the evolution of displacement field at divergence with length and thickness of the woven ply is studied under clamped-clamped and clamped-free boundary conditions. The simulation is carried out with geometrical non-linearity.

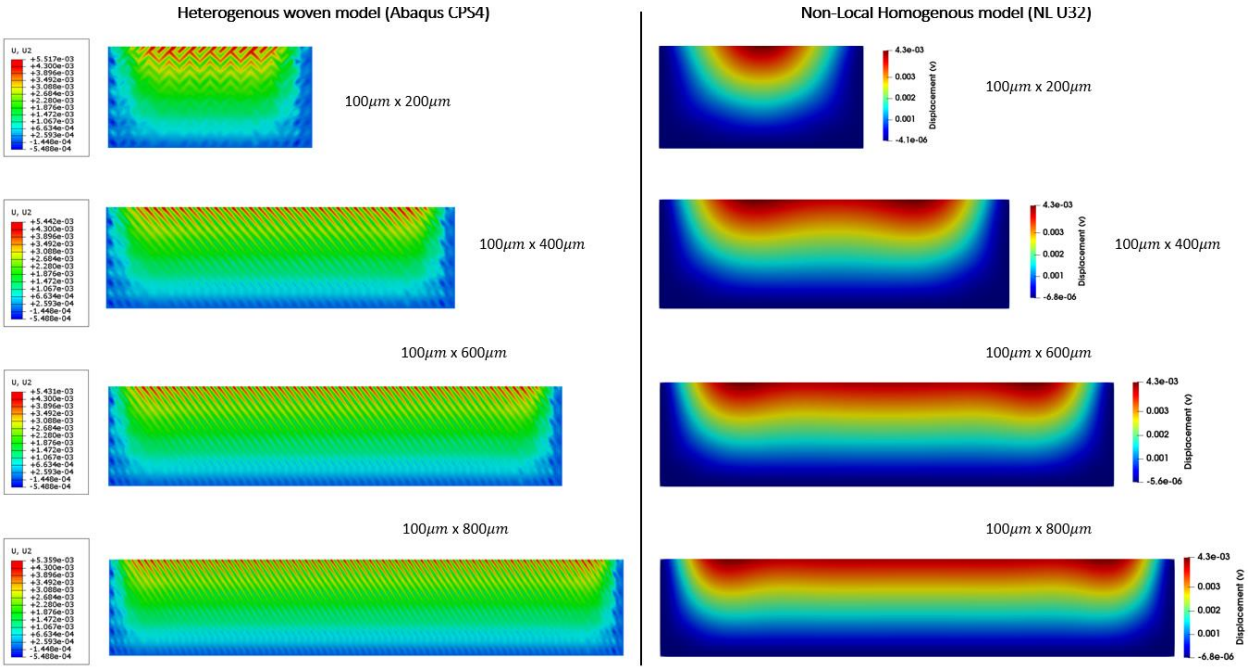

Figure 122: Comparison of transverse displacement field for different lengths with constant ply thickness of 100μm under clamped-free boundary condition for woven case

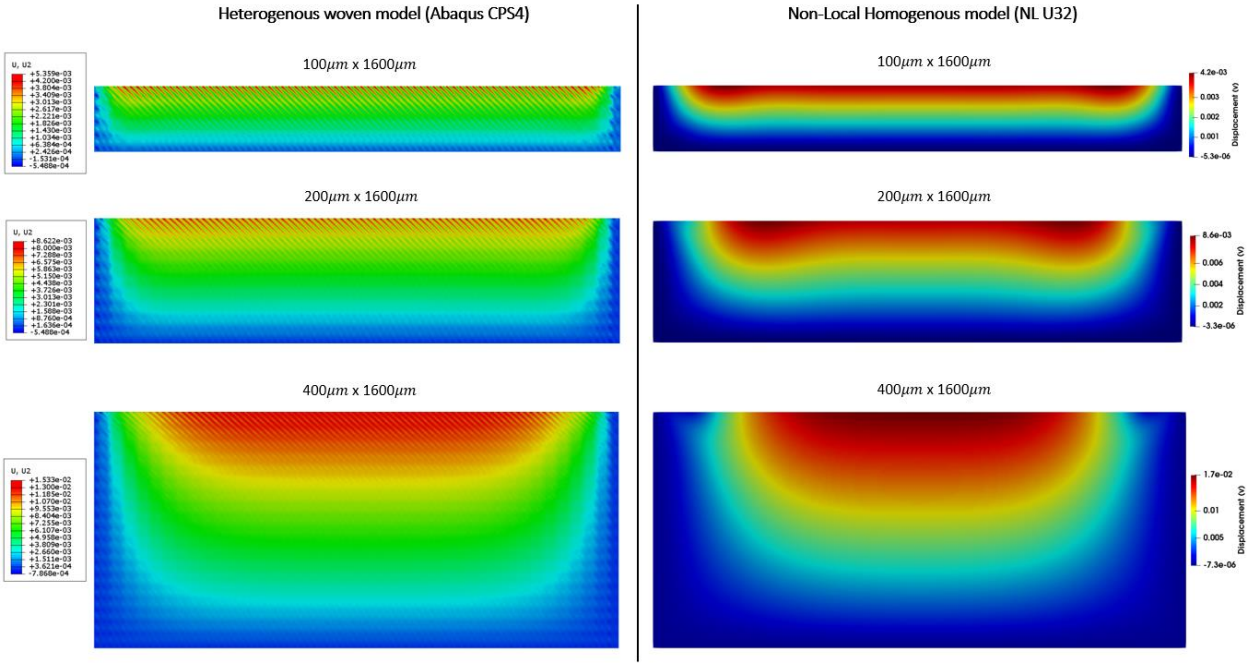

Figure 123: Comparison of transverse displacement field for different ply thickness with constant length of 1600μm under clamped-free boundary condition for woven case

Figure 122 portrays the evolution of the transverse displacement field for different lengths: 200μm, 400μm, 600μm and 800μm with constant thickness of 100μm under clamped-free boundary condition. We can observe that the HOMNL model (NL U32) replicate alike behavior as heterogenous woven model. Similar to the UD case, increase in the length has a negligible effect on the critical solution. Figure 123 depicts the evolution of the transverse displacement field for different ply thickness: 100μm, 200μm and 400μm with constant length of 1600μm. Better comparison is obtained, thereby proving the capability of HOMNL model for complex architecture. Figure 124 show the evolution of critical strain versus the ply thickness. We can observe that the effect of thickness is confirmed with HOMNL model, but negligible effect on critical strain with heterogenous model of ABAQUS® with the increase in thickness for both the boundary conditions. It is not well understood at the moment why the heterogenous model did not have the effect of thickness. Perhaps it might be due to one of the previous remarks mentioned for the case of heterogenous UD ply, which should be investigated in future.

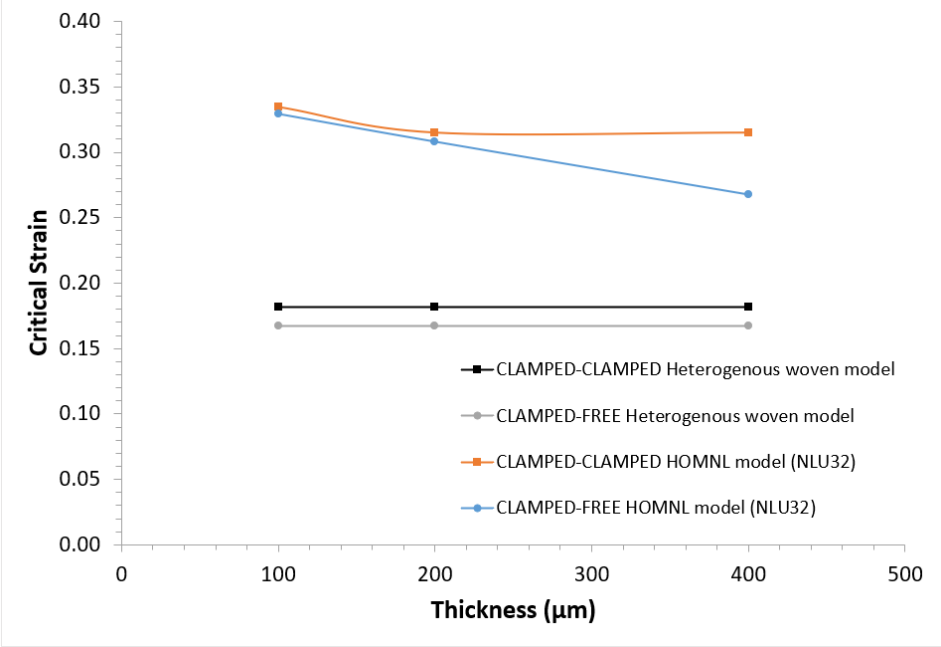

Figure 124: Comparison of critical strain versus ply thickness under compression of woven ply for Abaqus Heterogenous model and HOMNL model with two boundary conditions

It will be really interesting to study many cases but due to limited time frame, resources and data available at the moment it is difficult to perform many studies. Besides, we could have obtained a much more realistic comparison if we had experimental results on woven cases.

12 Conclusion and Perspectives

With an aim to extend the works of Grandidier, Drapier et al., ([D1],[D3],[G1],[G4]), non-local finite element models have been proposed: one with structural elements of ABAQUS®, named Beam Non-Local (BNL) model and the other with User Element subroutine (UEL) of ABAQUS®, named Homogenized Non-Local Model (HOMNL) to assess compressive strength of UD plies/laminates and also for woven composites (2D and 3D). Both the non-linear geometrical and material effects are taken into account in these models.

BNL model is a coupling of continuum media and beams (2D or 3D). It is similar to a model developed by Wisnom [W3]. The interest of this model is the capability to simulate the microbuckling phenomenon which appears in unidirectional ply under compression in the structure and take into account the effect of neighbouring plies. It permits to predict the elastic local instability of unidirectional plies inside a structure in case of complex loads. The 'structural effect' explained in the literature is confirmed and new results are obtained, for example, the elastic mode in 3D or the mechanism under bending. To predict the failure in compression under complex load, a non-linear behavior is developed and implemented in the model with the user subroutine (USDFLD). The plasticity is introduced in the behavior of continuum media and the defect (fiber misalignment) in the initial position of the beams. The quantification of the different parameters (plasticity, initial defects, structural effects) is obtained with the BNL model which can be used to study the strength of compression in complex composite structures. But this model is limited to simulate just Unidirectional (UD) plies and laminates, it is not possible to simulate composite structures with a complex micro/mesostructure (2D or 3D woven composite). Moreover, it is a discontinuous finite element model.

Therefore, with the need to extend the model in the framework of more general (to assess complex composite structures, for example: woven) and also to build a continuous finite element, a homogenized non-local numerical model (HOMNL) is proposed, similar to Mindlin's II gradient theory [M4]. In comparison with the previous model of Drapier et al., [D3], micro-curvatures in all the directions have been taken into account to assess microbuckling phenomenon in UD and woven composites. The non-local model has been implemented for 2D case in User Element (UEL) subroutine (coded in FORTRAN 77), named NL U32, which is *superparametric* and C^1 *type continuous* for analysis in ABAQUS®, which permits to simulate the complex structures. Non-linear geometrical effects are taken into account in this non-local user element (NL U32) as well as the non-linear behavior of the matrix (Ramberg-Osgood elastoplastic law) with a User Material subroutine (KUMAT), which permits to model all family of behavior. The tangent behavior of the non-local stiffness of microstructure is apprehended by integrating another User material subroutine (KURMAT) within the element which permits to modulate the non-localities (for example when micro damage appears).

The validation of the NL U32 element has been performed with respect to ABAQUS® classical element (CPS4) for both linear and non-linear (geometry and material) cases. The classical (elastic and plastic) and non-local material properties (elastic) are identified in comparison to the responses of a Representative Volume Element (RVE) of full heterogenous microstructures built using CPS4 element. A detailed protocol is proposed which is sufficient to understand the influence and identification of the parameters in the model. In future, it is necessary to vary the volume fraction

or increase the number of layers in the heterogenous model and also change the RVE dimension and perform the optimization to understand the influence of these parameters to use in more general cases. Due to limited time-frame and resources, it was not possible to study many cases.

From the investigation of the compressive response of 2D UD (0^0 ply) composite in the last chapter, it is clear that the 'structural effect' is again confirmed with HOMNL model with non-linearities. The order of critical strain is of the experimental data for UD ply similar to BNL model. The effect of length and thickness of the ply is studied for both UD and woven cases. Microbuckling modes could not be obtained using HOMNL model for UD and woven cases since it is not clear or no enough information is available on ABAQUS® user's manual at the moment regarding the integration of "BUCKLING" STEP inside the UEL (NL U32) to perform eigenvalue buckling analysis. And also, no initial misalignment/defect is taken into account in HOMNL model as it is not well understood at the moment how to integrate this effect in the model, as well as in the element. Therefore, it limits to study many cases and comparison with the past results obtained in the literature. Nevertheless, the HOMNL model (NL U32) showed the capability in the prediction of compressive strength even without the former effects for UD and woven composites.

Besides, one of the major advantages of using this non-local super parametric C^1 type continuous element (NL U32) is that it does not require to have a finer mesh in the structure as of classical Lagrange elements in ABAQUS® to simulate and capture well the non-local phenomenon (for ex: microbuckling) at the microscopic level, thereby saving a lot of computational time.

Perspectives

The HOMNL model (NL U32) showed us some compromising results in simulating compressive strength of 2D composite structures. However, still there are several parameters needed to be integrated to ameliorate the model and the element to assess many complex structures under complex loading situations. Following are the future perspectives which are to be taken into account for the developments proposed:

- Introduce initial defect/misalignment in the HOMNL (NL U32) model;
- Introduce "BUCKLING" STEP inside NL U32 element;
- Parametric study on microbuckling should be performed to evaluate the possibilities of the models;
- Parameters identification of HOMNL model has been performed with respect to the numerical model with material parameters from the literature. It will be interesting and more realistic if this identification could be performed with respect to experimental data if possible;
- The developed non-local user element (NL U32) is 2D in this thesis and it should be extended to a 3D case, consequently identification of parameters;
- Study many cases on different woven architectures;
- A work should be also focussed on the development of good post-processing tool for results of NL U32 element, especially for plotting stress/strain and curvature fields as it is difficult and time consuming to plot some results using PARAVIEW for finer mesh at the moment.

13 APPENDIX

13.1 Principle of virtual work and equilibrium equations (2D)

For the convenience of the derivation, let us rewrite curvatures ($\boldsymbol{\kappa} = \kappa_{ijk}$) as:

$$\frac{\partial^2 u}{\partial x^2} = u_{1,ii}\ ;\ \frac{\partial^2 u}{\partial y^2} = u_{1,jj}\ ;\ \frac{\partial^2 v}{\partial x^2} = u_{2,ii}\ ;\frac{\partial^2 v}{\partial y^2} = u_{2,jj}\ ;\ \frac{\partial^2 u}{\partial x \partial y} = u_{1,ij}\ ;\frac{\partial^2 v}{\partial x \partial y} = u_{2,ij}$$

Where, i and j, with (,) denotes the order of partial differentiation.

Let $\delta u_k\ (k = 1,2)$ and $\delta u_{k,ij} (k = 1,2)$ be the virtual displacements, and $\delta\varepsilon_{ij}\ , \delta\kappa_{ijk}$ be the associated virtual strains. Thus, the Internal Virtual Work (IVW) of 2D composite plate is given by:

$$IVW = -\iint\limits_{\omega\to 2D} \boldsymbol{S} : \boldsymbol{\varepsilon}\, d\omega - \iint\limits_{\omega\to 2D} \boldsymbol{\zeta}\cdot\boldsymbol{\kappa}\, d\omega \tag{13-1}$$

Or,

$$\begin{aligned} IVW = & -\iint\limits_{\omega\to 2D} S_{ij}\ \delta\varepsilon_{ij}\, d\omega - \iint\limits_{\omega\to 2D} \zeta_{ijk}\ \delta\kappa_{ijk}\, d\omega \\ & = -\iint_{\omega\to 2D} S_{ij}\cdot\delta\left\{\frac{1}{2}\left(u_{i,j}+u_{j,i}\right)\right\} d\omega - \iint_{\omega\to 2D}\zeta_{ijk}\cdot \\ & \qquad \delta\left\{u_{1,ii}\ ,\ u_{1,jj}\ , u_{1,ij}\ ,\ \ u_{2,ii}\ , u_{2,jj}\ ,\ u_{2,ij}\right\} d\omega \end{aligned} \tag{13-2}$$

After performing integration by parts of both the terms in the above equation, we obtain:

$$\begin{aligned} IVW = & +\iint_{\omega} S_{ij,j}\cdot\delta u_k\, d\omega - \oint_S S_{ij}\cdot n_j\cdot\delta u_k\, dS + && \text{(I)} \\ & \iint_{\omega}\zeta_{ii1,i}\cdot\delta u_{1,i}\, d\omega - \oint_S \zeta_{ii1}\cdot n_i\cdot\delta u_{1,i}\, dS + && \text{(II)} \\ & \iint_{\omega}\zeta_{jj1,j}\cdot\delta u_{1,j}\, d\omega - \oint_S \zeta_{jj1}\cdot n_j\cdot\delta u_{1,j}\, dS + && \text{(III)} \\ & \iint_{\omega}\zeta_{ij1,j}\cdot\delta u_{1,i}\, d\omega - \oint_S \zeta_{ij1}\cdot n_j\cdot\delta u_{1,i}\, dS + && \text{(IV)} \\ & \iint_{\omega}\zeta_{ji1,i}\cdot\delta u_{1,j}\, d\omega - \oint_S \zeta_{ji1}\cdot n_i\cdot\delta u_{1,j}\, dS + && \text{(V)} \\ & \iint_{\omega}\zeta_{ii2,i}\cdot\delta u_{2,i}\, d\omega - \oint_S \zeta_{ii2}\cdot n_i\cdot\delta u_{2,i}\, dS + && \text{(VI)} \\ & \iint_{\omega}\zeta_{jj2,j}\cdot\delta u_{2,j}\, d\omega - \oint_S \zeta_{jj2}\cdot n_j\cdot\delta u_{2,j}\, dS + && \text{(VII)} \\ & \iint_{\omega}\zeta_{ij2,j}\cdot\delta u_{2,i}\, d\omega - \oint_S \zeta_{ij2}\cdot n_j\cdot\delta u_{2,i}\, dS + && \text{(VIII)} \\ & \iint_{\omega}\zeta_{ji2,i}\cdot\delta u_{2,j}\, d\omega - \oint_S \zeta_{ji2}\cdot n_i\cdot\delta u_{2,j}\, dS && \text{(IX)} \end{aligned} \tag{13-3}$$

Let us consider "first term" of Eq. (13-3 II) and apply integrating by parts again, we obtain:

$$\iint_{\omega} \zeta_{ii1,i} \cdot \delta u_{1,i}\, d\omega = -\iint_{\omega} \zeta_{ii1,ii} \cdot \delta u_1\, d\omega + \oint_S \zeta_{ii1,i} \cdot n_i \cdot \delta u_1\, dS \qquad (13\text{-}4)$$

Let us consider "second term" of Eq. (13-3 II):

$$\oint_S \zeta_{ii1} \cdot n_i \cdot \delta u_{1,i}\, dS = \oint_S \zeta_{ii1} \cdot n_i \cdot \left\{\frac{\partial \delta u_1}{\partial S}\tau_i + \frac{\partial \delta u_1}{\partial n} n_i\right\} dS$$
$$= \oint_S \zeta_{ii1} \cdot n_i \cdot \tau_i \left(\frac{\partial \delta u_1}{\partial S}\right) dS + \oint_S \zeta_{ii1} \cdot n_i \cdot n_i \left(\frac{\partial \delta u_1}{\partial n}\right) dS \qquad (13\text{-}5)$$

Where, $\vec{\tau}$ and $\vec{n}$ are the tangent and normal vectors. τ_i, τ_j and n_i, n_j are their components respectively along x_i, x_j and y_i, y_j directions. We can observe that $\left(\frac{\partial \delta u_1}{\partial n}\right) = \delta u_{1,n}$ can be varied independently of δu along boundary, S, but not $\left(\frac{\partial \delta u_1}{\partial S}\right)$.

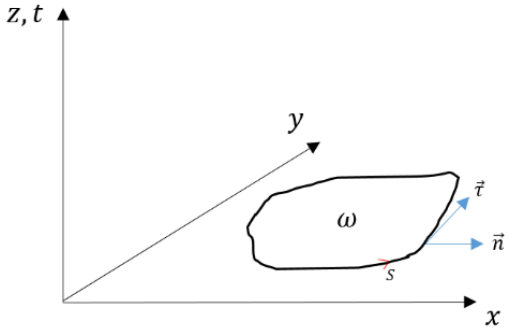

Therefore, integrating first term of Eq. (13-5) by parts again to permit identification of independent variations of components, we get:

$$\oint_S \zeta_{ii1} \cdot n_i \cdot \tau_i \left(\frac{\partial \delta u_1}{\partial S}\right) dS = \left(\zeta_{ii1} \cdot n_i \cdot \tau_i\right) \cdot [\delta u_1]_{A^-}^{A^+} - \oint_S \frac{\partial \zeta_{ii1} \cdot n_i \cdot \tau_i}{\partial S} \cdot \delta u_1\, dS$$

Let, $\zeta_{t1} = \zeta_{ii1} \cdot n_i \cdot \tau_i$ (13-6)

$$\Rightarrow \oint_S \zeta_{t1} \left(\frac{\partial \delta u_1}{\partial S}\right) dS = (\zeta_{t1}) \cdot [\delta u_1]_{A^-}^{A^+} - \oint_S \frac{\partial \zeta_{t1}}{\partial S} \cdot \delta u_1\, dS$$

Where, the contributions of $'A'$ are meant to represent the points along S, such as corners at which $\vec{\tau}$ is discontinuous. Substituting Eq. (13-5) in Eq. (13-6), we get:

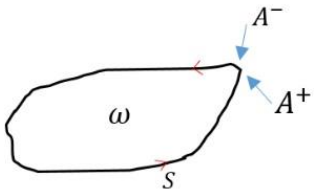

$$\oint_S \zeta_{ii1} \cdot n_i \cdot \delta u_{1,i}\, dS = \oint_S \zeta_{ii1} \cdot n_i \cdot n_i \left(\frac{\partial \delta u_1}{\partial n}\right) dS - \oint_S \frac{\partial \zeta_{t1}}{\partial S} \cdot \delta u_1\, dS + (\zeta_{t1}) \cdot [\delta u_1]_{A^-}^{A^+} \qquad (13\text{-}7)$$

We can also write as:

$$\oint_S \zeta_{ii1} \cdot n_i \cdot \delta u_{1,i} \, dS = \oint_S \left[\zeta_{ii1} \cdot n_i \cdot n_i \left(\frac{\partial \delta u_1}{\partial n} \right) dS - \frac{\partial \zeta_{t1}}{\partial S} \cdot \delta u_1 \right] dS + \left[\zeta_{t1} \, \delta u_1 \right]_{(Corners)}$$

Now Substituting Eq. (13-4) and Eq. (13-7) in Eq. (13-3 II), we obtain:

$$\underline{\text{II}^*}$$

$$\begin{aligned} &\iint_\omega \zeta_{ii1,i} \cdot \delta u_{1,i} \, d\omega - \oint_S \zeta_{ii1} \cdot n_i \cdot \delta u_{1,i} \, dS \\ &\quad = -\iint_\omega \zeta_{ii1,ii} \cdot \delta u_1 \, d\omega + \oint_S \zeta_{ii1,i} \cdot n_i \cdot \delta u_1 \, dS \\ &\quad - \oint_S \left[\zeta_{ii1} \cdot n_i \cdot n_i \left(\frac{\partial \delta u_1}{\partial n} \right) - \frac{\partial \zeta_{t1}}{\partial S} \cdot \delta u_1 \right] dS - \left[\zeta_{t1} \, \delta u_1 \right]_{(Corners)} \end{aligned} \qquad \textit{(13-8)}$$

Following similar steps for other terms, i.e., III-IX in Eq. (13-3), we obtain:

$$\underline{\text{III}^*}$$

$$\begin{aligned} &\iint_\omega \zeta_{jj1,j} \cdot \delta u_{1,j} \, d\omega - \oint_S \zeta_{jj1} \cdot n_j \cdot \delta u_{1,j} \, dS \\ &\quad = -\iint_\omega \zeta_{jj1,jj} \cdot \delta u_1 \, d\omega + \oint_S \zeta_{jj1,j} \cdot n_j \cdot \delta u_1 \, dS \\ &\quad - \oint_S \left[\zeta_{jj1} \cdot n_j \cdot n_j \left(\frac{\partial \delta u_1}{\partial n} \right) - \frac{\partial \zeta_{t2}}{\partial S} \cdot \delta u_1 \right] dS - \left[\zeta_{t2} \, \delta u_1 \right]_{(Corners)} \end{aligned}$$

$$\boxed{\zeta_{t2} = \zeta_{jj1} \cdot n_j \cdot \tau_j}$$

$$\underline{\text{IV}^*}$$

$$\begin{aligned} &\iint_\omega \zeta_{ij1,j} \cdot \delta u_{1,i} \, d\omega - \oint_S \zeta_{ij1} \cdot n_j \cdot \delta u_{1,i} \, dS \\ &\quad = -\iint_\omega \zeta_{ij1,ji} \cdot \delta u_1 \, d\omega + \oint_S \zeta_{ij1,j} \cdot n_i \cdot \delta u_1 \, dS \\ &\quad - \oint_S \left[\zeta_{ij1} \cdot n_j \cdot n_i \left(\frac{\partial \delta u_1}{\partial n} \right) - \frac{\partial \zeta_{t3}}{\partial S} \cdot \delta u_1 \right] dS - \left[\zeta_{t3} \, \delta u_1 \right]_{(Corners)} \end{aligned}$$

$$\boxed{\zeta_{t3} = \zeta_{ij1} \cdot n_j \cdot \tau_i}$$

Note: *Here (*) refers to the updated terms after performing some mathematical steps.*

V*

$$\iint_{\omega} \zeta_{ji1_{,i}} \cdot \delta u_{1_{,j}}\, d\omega - \oint_{S} \zeta_{ji1} \cdot n_i \cdot \delta u_{1_{,j}}\, dS$$

$$= - + \oint_{S} \zeta_{ji1_{,i}} \cdot n_j \cdot \delta u_1\, dS$$

$$- \oint_{S} \left[\zeta_{ji1} \cdot n_i \cdot n_j \left(\frac{\partial \delta u_1}{\partial n} \right) - \frac{\partial \zeta_{t4}}{\partial S} \cdot \delta u_1 \right] dS - \left[\zeta_{t4}\, \delta u_1 \right]_{(Corners)}$$

$$\boxed{\zeta_{t4} = \zeta_{ji1} \cdot n_i \cdot \tau_j}$$

VI*

$$\iint_{\omega} \zeta_{ii2,_i} \cdot \delta u_{2,_i}\, d\omega - \oint_{S} \zeta_{ii2} \cdot n_i \cdot \delta u_{2,_i}\, dS$$

$$= - \iint_{\omega} \zeta_{ii2,_{ii}} \cdot \delta u_2\, d\omega + \oint_{S} \zeta_{ii2,_i} \cdot n_i \cdot \delta u_2\, dS$$

$$- \oint_{S} \left[\zeta_{ii2} \cdot n_i \cdot n_i \left(\frac{\partial \delta u_2}{\partial n} \right) - \frac{\partial \zeta_{t5}}{\partial S} \cdot \delta u_2 \right] dS - \left[\zeta_{t5}\, \delta u_2 \right]_{(Corners)} \qquad \textit{(13-9)}$$

$$\boxed{\zeta_{t5} = \zeta_{ii2} \cdot n_i \cdot \tau_i}$$

VII*

$$\iint_{\omega} \zeta_{jj2_{,j}} \cdot \delta u_{2_{,j}}\, d\omega - \oint_{S} \zeta_{jj2} \cdot n_j \cdot \delta u_{2_{,j}}\, dS$$

$$= - \iint_{\omega} \zeta_{jj2_{,jj}} \cdot \delta u_2\, d\omega + \oint_{S} \zeta_{jj2_{,j}} \cdot n_j \cdot \delta u_2\, dS$$

$$- \oint_{S} \left[\zeta_{jj2} \cdot n_j \cdot n_j \left(\frac{\partial \delta u_2}{\partial n} \right) - \frac{\partial \zeta_{t6}}{\partial S} \cdot \delta u_2 \right] dS - \left[\zeta_{t6}\, \delta u_2 \right]_{(Corners)}$$

$$\boxed{\zeta_{t6} = \zeta_{jj2} \cdot n_j \cdot \tau_j}$$

VIII*

$$\iint_{\omega} \zeta_{ij2,_j} \cdot \delta u_{2,_i}\, d\omega - \oint_S \zeta_{ij2} \cdot n_j \cdot \delta u_{2,_i}\, dS$$
$$= -\iint_{\omega} \zeta_{ij2,_{ji}} \cdot \delta u_2\, d\omega + \oint_S \zeta_{ij2,_j} \cdot n_i \cdot \delta u_2\, dS$$
$$- \oint_S \left[\zeta_{ij2} \cdot n_j \cdot n_i \left(\frac{\partial \delta u_2}{\partial n}\right) - \frac{\partial \zeta_{t7}}{\partial S} \cdot \delta u_2\right] dS - \left[\zeta_{t7}\, \delta u_2\right]_{(Corners)}$$

$$\zeta_{t7} = \zeta_{ij2} \cdot n_j \cdot \tau_i$$

IX*

$$\iint_{\omega} \zeta_{ji2,_i} \cdot \delta u_{2,_j}\, d\omega - \oint_S \zeta_{ji2} \cdot n_i \cdot \delta u_{2,_j}\, dS$$
$$= -\iint_{\omega} \zeta_{ji2,_{ij}} \cdot \delta u_2\, d\omega + \oint_S \zeta_{ji2,_i} \cdot n_j \cdot \delta u_2\, dS$$
$$- \oint_S \left[\zeta_{ji2} \cdot n_i \cdot n_j \left(\frac{\partial \delta u_2}{\partial n}\right) - \frac{\partial \zeta_{t8}}{\partial S} \cdot \delta u_2\right] dS - \left[\zeta_{t8}\, \delta u_2\right]_{(Corners)}$$

$$\zeta_{t8} = \zeta_{ji2} \cdot n_i \cdot \tau_j$$

And after rearranging the identical terms at domain and boundary we may finally write the internal virtual work as:

$$IVW = \iint_{\omega} \left[S_{ij,_j} \cdot \delta u_k\right] d\omega - \sum \iint_{\omega} \left[\zeta_{ijk,_{ji}} \cdot \delta u_k\right] d\omega +$$
$$\left\{ - \oint_S \left[S_{ij} \cdot n_j \cdot \delta u_k\right] dS + \sum \oint_S \left[\zeta_{ijk,_j} \cdot n_\gamma \cdot \delta u_k\right] dS \right.$$
$$\left. - \oint_S \left[\zeta_{ijk} \cdot n_\gamma \cdot n_\gamma \left(\frac{\partial \delta u_k}{\partial n}\right)\right] dS + \oint_S \left[\frac{\sum_{i=1}^{8} \partial \zeta_{ti}}{\partial S} \cdot \delta u_k\right] dS - \left[\sum_{i=1}^{8} \zeta_{ti}\, \delta u_k\right]_{(Corners)} \right\}$$

Or,

$$IVW = \iint_{\omega} \left\{\left[S_{ij,_j} \cdot \delta u_k\right] - \sum \left[\zeta_{ijk,_{ji}} \cdot \delta u_k\right]\right\} d\omega \qquad \zeta_n = \zeta_{ijk} \cdot n_\gamma \cdot n_\gamma \qquad \textit{(13-10)}$$
$$- \oint_S \left\{\left[S_{ij} \cdot n_j \cdot \delta u_k\right] - \sum \left[\zeta_{ijk,_j} \cdot n_\gamma \cdot \delta u_k\right] + \left[\zeta_n \cdot \left(\frac{\partial \delta u_k}{\partial n}\right)\right] - \left[\frac{\sum_{i=1}^{8} \partial \zeta_{ti}}{\partial S} \cdot \delta u_k\right]\right\} dS$$
$$- \left[\sum_{i=1}^{8} \zeta_{ti}\, \delta u_k\right]_{(Corners)}$$

Where, $k = 1,2$ and $\gamma = i \ or \ j$

Note: For the term: $[\zeta_{ti}\ \delta u_k\ ]_{(Corners)}=(\zeta_{ti})\cdot[\delta u_k\ ]_{A^-}^{A^+}$, there are 2 possible cases:

i) If the contour, S is a smooth closed curve, the value at $A^- = A^+, i.e.,$

$$[\zeta_{ti}(A^+) - \zeta_{ti}(A^-)] = 0$$

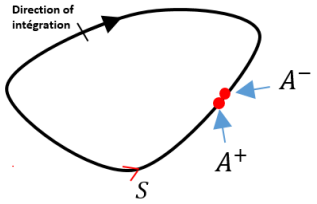

And hence the term $[\sum_{i=1}^{8}\zeta_{ti}\ \delta u_k\ ]_{(Corners)}$ can be neglected.

ii) If the contour, S is piece-wise linear or composed of finite number, k_n, of smooth curves with discontinuity, the integration should be made in a piecewise manner. Thus, the continuation of A^+ and A^- should be added, i.e.,

$$\sum_{k_n}(\zeta_{ti})\cdot[\delta u_k\ ]_{A^-}^{A^+}$$

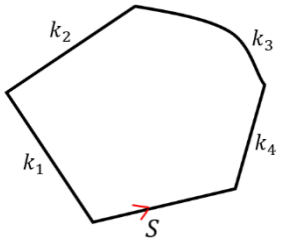

Now, corresponding external virtual work (EVW) is defined as:

$$EVW = \iint_{\omega} F_k\cdot\delta u_k\, d\omega + \oint_S f_k\cdot\delta u_k\, dS + \sum\iint_{\omega} M_k\cdot\delta u_{k_{,i}}\, d\omega + \sum\oint_S m_k\cdot\delta u_{k_{,i}}\, dS + \oint_S C_\tau\cdot\frac{\partial\delta u_k}{\partial n}\, dS + \sum P\,\delta u_k$$

Or, *(13-11)*

$$EVW = \iint_{\omega} F_k\cdot\delta u_k\, d\omega + \oint_S f_k\cdot\delta u_k\, dS + \sum\iint_{\omega} M_k\cdot\delta\theta_k\, d\omega + \sum\oint_S m_k\cdot\delta\theta_k\, dS + \oint_S C_\tau\cdot\frac{\partial\delta u_k}{\partial n}\, dS + \sum P\,\delta u_k$$

Where,

F_k = Body/Volume force;
f_k = Traction/surface force ;
M_k = Couple force on the plane/body;
m_k = Couple force on the edge/surface of the plane/body;
C_τ = Couple spread on the edge of the plane/body, only normal at the edge of plate;
P = Contributions of concentrated load at the corner/edge.

Now using the principle of virtual work (PVW) for case of static analysis, we can write the equilibrium equations (in weak form) of our non-local model for analysis of compressive strength of the composite in 2D as:

$$\Pi = IVW + EVW = 0 \qquad \forall \delta \boldsymbol{u}$$

$$IVW = \iint_{\omega} \left[S_{ij,j} \cdot \delta u_k\right] d\omega - \sum \iint_{\omega} \left[\zeta_{ijk,ji} \cdot \delta u_k\right] d\omega + \left\{ - \oint_S \left[S_{ij} \cdot n_j \cdot \delta u_k\right] dS + \sum \oint_S \left[\zeta_{ijk,j} \cdot n_\gamma \cdot \delta u_k\right] dS - \oint_S \left[\zeta_{ijk} \cdot n_\gamma \cdot n_\gamma \left(\frac{\partial \delta u_k}{\partial n}\right)\right] dS + \oint_S \left[\frac{\sum_{i=1}^{8} \partial \zeta_{ti}}{\partial S} \cdot \delta u_k\right] dS - \left[\sum_{i=1}^{8} \zeta_{ti} \, \delta u_k\right]_{(Corners)} \right\} \quad (13\text{-}12)$$

$$= -\left\{ \iint_{\omega} F_k \cdot \delta u_k \, d\omega + \oint_S f_k \cdot \delta u_k \, dS + \sum \iint_{\omega} M_k \cdot \delta u_{k,i} \, d\omega + \sum \oint_S m_k \cdot \delta u_{k,i} \, dS + + \sum P \, \delta u_k \right\}$$

The local equilibrium equations in strong form and the boundary conditions can be written as:

<u>*Equilibrium equations (Strong Form):*</u>

c) *Domain(ω)*:

$$S_{ij,j} = -F_k \quad \text{and} \quad \zeta_{ijk,ji} = -\sum M_k \qquad \forall point \ \ on \ \in \omega$$

d) Boundary(S):

$$-S_{ij} \cdot n_j = -f_k \qquad \forall point \ \ on \ \in S$$

$$\zeta_{ijk} \cdot n_\gamma \cdot n_\gamma = -C_\tau \qquad \forall point \ \ on \ \in S$$

$$\zeta_{ijk,j} \cdot n_\gamma + \frac{\sum_{i=1}^{8} \partial \zeta_{ti}}{\partial S} = -\sum m_k \qquad \forall point \ \ on \ \in S \quad (13\text{-}13)$$

<u>*Boundary conditions(BC) on S:*</u>

Specify:

$$i) \quad u_k \quad or \quad S_{ij} \cdot n_j$$

$$ii) \quad u_{k,i} \quad or \quad \zeta_{ijk} \cdot n_\gamma \cdot n_\gamma$$

Where, $k = 1,2 \ \ and \ \ \gamma = i, j.$

For example: Clamped or Encastre at the edge of body

$$u = 0 \quad \forall\, point \in S$$

$$u_{k_i} = 0 \quad \forall\, point \in S$$

Where, $k = 1,2$.

Note that, at a *corner*, if $\zeta_{ti}[\delta u_k]_{A^-}^{A^+}$ is nonzero, there must be a concentrated load at the corner with: $P = \sum[\zeta_{ti}(A^+) - \zeta_{ti}(A^-)]$.

13.2 2D Plane Stress User Element (U4)

In order to understand how to develop *'User Element'* (using UEL subroutine, written in FORTRAN 77), and to know the standard conventions/keys that can be defined on UEL, which can be called, accepted and used in ABAQUS® calculations, a UEL of 2D Plane stress isoparametric linear rectangular element (U4) with 2 DOF (u and v) globally (8 nodal DOF/element locally) has been developed (using FORTRAN 77) and compared the results of some test cases with ABAQUS® CPS4 element for square plate. U4 is developed using the guidelines from ABAQUS® 6.10 user's manual *(Abaqus 6.10 section 1.1.23)* and FE course book by JC Grandidider(2017-18),ENSMA and FE book by K.J Bathe (1982).

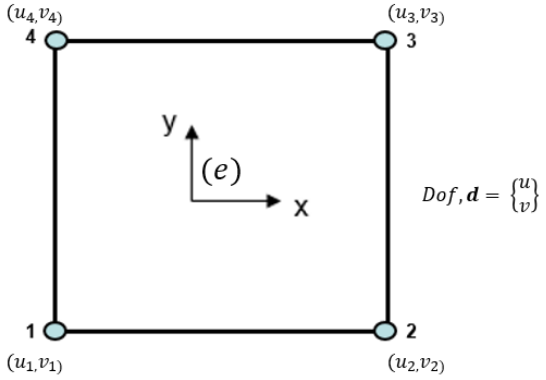

Figure 125: 2D Plane stress User element (U4)

13.2.1 Abaqus UEL implementation

UEL (User Elements) subroutine is a programming interface provided with Abaqus/Standard using which one can define customized finite elements. Figure 126 shows the detailed workflow of Abaqus/Standard. In order to work with UEL, one must start by using the default UEL header (as shown in Figure 127) from the Abaqus 6.10 User Subroutines Reference Guide, Section 1.1.23 in Abaqus 6.10 documentation. The user specified program is contained under this header and the end of the UEL is marked by the 'END' syntax. It is very important to understand the overall operation of the 'UEL' block. Figure 128 shows a schematic describing the 'input' and 'output' flow from the UEL subroutine, that is called for every element. For a current time, increment, Abaqus provides the incremental and final nodal point displacements. State variables at the start of that time increment are also provided. UEL is then required to return the updated element stiffness matrix, internal force and state variables all at the end of the current time step.

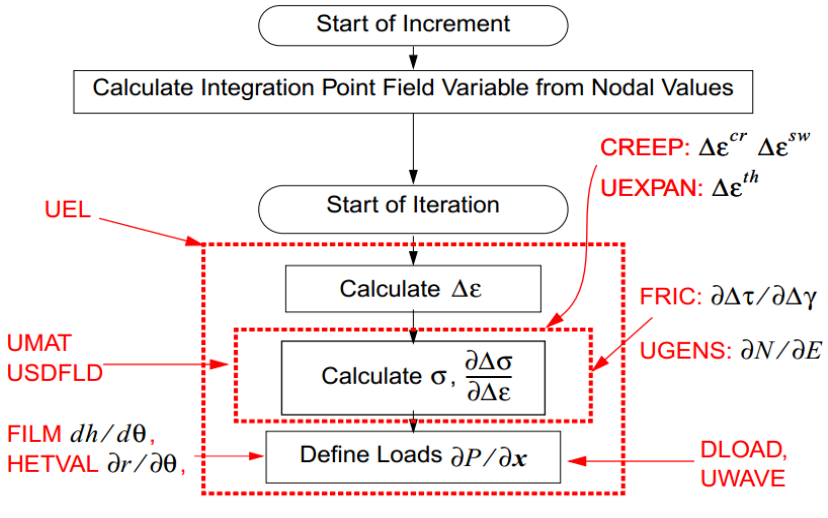

Figure 126: Detailed workflow of Abaqus/Standard (Abaqus user's manual)

```
      SUBROUTINE UEL(RHS,AMATRX,SVARS,ENERGY,NDOFEL,NRHS,NSVARS,
     1 PROPS,NPROPS,COORDS,MCRD,NNODE,U,DU,V,A,JTYPE,TIME,DTIME,
     2 KSTEP,KINC,JELEM,PARAMS,NDLOAD,JDLTYP,ADLMAG,PREDEF,NPREDF,
     3 LFLAGS,MLVARX,DDLMAG,MDLOAD,PNEWDT,JPROPS,NJPROP,PERIOD)
C
      INCLUDE 'ABA_PARAM.INC'
C
      DIMENSION RHS(MLVARX,*),AMATRX(NDOFEL,NDOFEL),PROPS(*),
     1 SVARS(*),ENERGY(8),COORDS(MCRD,NNODE),U(NDOFEL),
     2 DU(MLVARX,*),V(NDOFEL),A(NDOFEL),TIME(2),PARAMS(*),
     3 JDLTYP(MDLOAD,*),ADLMAG(MDLOAD,*),DDLMAG(MDLOAD,*),
     4 PREDEF(2,NPREDF,NNODE),LFLAGS(*),JPROPS(*)


      user coding to define RHS, AMATRX, SVARS, ENERGY, and PNEWDT


      RETURN
      END
```

Figure 127: UEL subroutine header (Abaqus user's manual 6.10, section 1.1.23)

Figure 128: I/O block diagram for UEL subroutine

UEL input variables:

a) $\boldsymbol{U}$**:** is a vector of size number-of-element-nodes×degrees-of-freedom-per-node, and contains the degree of freedom values at each node at the end of the current time increment. This is shown as $\boldsymbol{U}_{new}$ in Figure 128.

b) $\boldsymbol{DU}$**:** is a vector of size number-of-nodes×degrees-of-freedom-per-node and contains the incremental degree of freedom values for all the nodes in the previous increment.

c) $\boldsymbol{COORDS}$**:** is an array containing the original coordinates of the nodes of the element. It contains the coordinates of the nodes of an element, expressed in (x, y, z) format. COORDS (K1, K2) is the K1th coordinate of the K2th node of the element.

UEL output variables:

a) $\boldsymbol{SVARS}$**:** is a user defined solution dependent state variable associated with the element and needs to be passed back to Abaqus after being updated. Typically stress and strains at all integration points within element are stored in this array.

b) $\boldsymbol{AMATRX}$**:** is the stiffness matrix for an element. For our case, small deformation and linear elasticity, the stiffness matrix is constant, however, if there are non-linear effects then the stiffness matrix needs to be updated before returning to Abaqus.

d) $\boldsymbol{RHS}$**:** is an array containing the contributions of the element to the right-hand side vectors (Force vectors,$\boldsymbol{f}$) of the overall system of equations. RHS (K1, K2) is the entry for the K1th degree of freedom of the element in the K2th right hand side vector.

For case of linear static analysis (LFLAGS (1) =1, 2), one must define $\boldsymbol{AMATRX}$ and $\boldsymbol{RHS}$, and update the state variables ($\boldsymbol{SVARS}$)**.** For more detailed information on usage of various parameters/variables of UEL, please refer Abaqus 6.10 user's manual *(Abaqus 6.10 section 1.1.23).*

13.2.2 Formulation of element U4

Using the principle of virtual work (PVW), i.e IVW+EVW=0, the governing equation for 2D plane stress ($\sigma_{zz} = \tau_{xz} = \tau_{yz}$) problem is given by:

$$-\int_{\Omega\to 2D} \{\boldsymbol{S} : \delta\boldsymbol{\varepsilon}\} d\Omega + \langle \boldsymbol{F} \cdot \delta\boldsymbol{u} \rangle = 0 \qquad \forall \delta\boldsymbol{u} \tag{13-14}$$

Where, the displacement field, $\boldsymbol{u} = u(x,y,)\boldsymbol{e}_1 + v(x,y,)\boldsymbol{e}_2$, $\delta\boldsymbol{u}$ is the virtual displacement and $\delta\boldsymbol{\varepsilon}$ is the associated virtual strain. We can also rewrite above equation by expanding the terms:

$$-\int_{\Omega\to 2D} \{\bar{\bar{\boldsymbol{D}}}\ \boldsymbol{\varepsilon} \ :\ \delta\boldsymbol{\varepsilon}\} d\Omega = \int_{\Omega\to 2D} \boldsymbol{F}_b\ \delta\boldsymbol{u}^T d\Omega + \int_S \boldsymbol{F}_S\ \delta\boldsymbol{u}^T\, dS \quad \forall \delta\boldsymbol{u} \tag{13-15}$$

Where, $\boldsymbol{S}$ is Second Piola Kirchoff stress tensor, $\bar{\bar{\boldsymbol{D}}}$ is the 4th order constitutive matrix (elastic isotropic in this case), the Green Lagrange strain tensor,$\boldsymbol{\varepsilon} = \frac{1}{2}(\nabla \boldsymbol{u} + \nabla \boldsymbol{u}^T)$, $\boldsymbol{F}_b$ is external body force and $\boldsymbol{F}_S$ is external surface/traction force.

Let $\boldsymbol{d}^{(e)}$ be the DOF vector of the element, which contains nodal displacements ($u_n, v_n \; with \; n = 1,..4$), $\boldsymbol{N}$, the shape function matrix (in our case Bilinear shape functions are used, which will be discussed in the following steps) for displacement and $\boldsymbol{B}$ is the strain displacement/shape functions derivative matrix, then:

$$\boldsymbol{u} \cong \boldsymbol{N}\, \boldsymbol{d}^{(e)} ;$$
$$\boldsymbol{\varepsilon} \cong \boldsymbol{B}\, \boldsymbol{d}^{(e)} ; \quad \boldsymbol{B} = B_{ij} = [\boldsymbol{D}]\, \boldsymbol{N} ; \tag{13-16}$$

Where, $[\boldsymbol{D}]$ is a derivative operator.

Now substituting above approximations in Eq. (13-15), we get system of equations as:

$$-\int_{\Omega \to 2D} \left\{ \bar{\bar{\boldsymbol{D}}}\, \boldsymbol{B}\, \boldsymbol{d}^{(e)}\, \boldsymbol{B}^T \left(\delta \boldsymbol{d}^{(e)}\right)^T \right\} d\Omega = \int_{\Omega \to 2D} \boldsymbol{F}_b\; \delta \boldsymbol{N}^T \left(\delta \boldsymbol{d}^{(e)}\right)^T d\Omega + \int_S \boldsymbol{F}_S\; \delta \boldsymbol{N}^T \left(\delta \boldsymbol{d}^{(e)}\right)^T dS \qquad \forall \delta \boldsymbol{u} \tag{13-17}$$

Now taking out the common term, $\left(\delta \boldsymbol{d}^{(e)}\right)^T$, we can obtain the final system of equations to be solved as:

$$\left(\delta \boldsymbol{d}^{(e)}\right)^T \left\{ -\int_{\Omega \to 2D} \{\bar{\bar{\boldsymbol{D}}}\, \boldsymbol{B}\, \boldsymbol{B}^T\} \boldsymbol{d}^{(e)}\, d\Omega - \int_{\Omega \to 2D} \boldsymbol{F}_b\; \delta \boldsymbol{N}^T\; d\Omega - \int_S \boldsymbol{F}_S\; \delta \boldsymbol{N}^T\; dS \right\} = 0$$

$$\Rightarrow -\int_{\Omega \to 2D} \{\bar{\bar{\boldsymbol{D}}}\, \boldsymbol{B}\, \boldsymbol{B}^T\} \boldsymbol{d}^{(e)}\, d\Omega - \int_{\Omega \to 2D} \boldsymbol{F}_b\; \delta \boldsymbol{N}^T\; d\Omega - \int_S \boldsymbol{F}_S\; \delta \boldsymbol{N}^T\; dS = 0$$

Or,

$$\int_{\Omega \to 2D} \{\bar{\bar{\boldsymbol{D}}}\, \boldsymbol{B}\, \boldsymbol{B}^T\} \boldsymbol{d}^{(e)}\, d\Omega = \int_{\Omega \to 2D} \boldsymbol{F}_b\; \delta \boldsymbol{N}^T\; d\Omega + \int_S \boldsymbol{F}_S\; \delta \boldsymbol{N}^T\; dS$$

Let,

$$\boldsymbol{K} = t \int_{\Omega \to 2D} \bar{\bar{\boldsymbol{D}}}\, \boldsymbol{B}\, \boldsymbol{B}^T\, d\Omega \tag{13-18}$$

$$\boldsymbol{f} = t \int_{\Omega \to 2D} \boldsymbol{F}_b\; \delta \boldsymbol{N}^T\; d\Omega + \int_S \boldsymbol{F}_S\; \delta \boldsymbol{N}^T\; dS$$

Or,

$$\Rightarrow \boldsymbol{K}\; \boldsymbol{d}^{(e)} = \boldsymbol{f}$$
$$K_{ij}\, d_i^{(e)} = f_i$$
$$\boldsymbol{K}_{(8x8)}\; \boldsymbol{d}^{(e)}{}_{(8x1)} = \boldsymbol{f}_{(8x1)}$$

Where, $\boldsymbol{K}$ is the stiffness matrix of the element and t is the thickness of the plate.

Calculation of strain displacement matrix ($\boldsymbol{B}$):

We know that,

$$\boldsymbol{\varepsilon} \cong \boldsymbol{B}\, \boldsymbol{d}^{(e)}$$

In a state of plane stress, the linearized tensor of the deformations, $\boldsymbol{\varepsilon} = \frac{1}{2}\left[\nabla \boldsymbol{u} + \nabla \boldsymbol{u}^T\right]$ is written in vector form as:

$$\boldsymbol{\varepsilon} = \begin{Bmatrix} \varepsilon_{xx} \\ \varepsilon_{yy} \\ \gamma_{xy} = 2\varepsilon_{xy} \end{Bmatrix} = \begin{Bmatrix} u'_x \\ v'_y \\ u'_y + v'_x \end{Bmatrix} = \begin{bmatrix} 1 & 0 & 0 & 0 \\ 0 & 0 & 0 & 1 \\ 0 & 1 & 1 & 0 \end{bmatrix} \begin{bmatrix} u'_x \\ u'_y \\ v'_x \\ v'_y \end{bmatrix} = [\boldsymbol{M}_1] \begin{bmatrix} u'_x \\ u'_y \\ v'_x \\ v'_y \end{bmatrix} \qquad \textit{(13-19)}$$

Where ($'$) denotes the derivative, i.e., $u'_x = \frac{\partial u}{\partial x}$, etc. Or, we can write in local coordinates, $'\xi' \; or \; 'r'$ and $'\eta' \; or \; 's'$ as:

$$\begin{bmatrix} u'_x \\ u'_y \\ v'_x \\ v'_y \end{bmatrix} = \begin{bmatrix} \frac{\partial u}{\partial x} \\ \frac{\partial u}{\partial y} \\ \frac{\partial v}{\partial x} \\ \frac{\partial v}{\partial y} \end{bmatrix} = \begin{bmatrix} \frac{\partial \xi}{\partial x} & \frac{\partial \eta}{\partial x} & 0 & 0 \\ \frac{\partial \xi}{\partial y} & \frac{\partial \eta}{\partial y} & 0 & 0 \\ 0 & 0 & \frac{\partial \xi}{\partial x} & \frac{\partial \eta}{\partial x} \\ 0 & 0 & \frac{\partial \xi}{\partial y} & \frac{\partial \eta}{\partial y} \end{bmatrix} \begin{bmatrix} \frac{\partial u}{\partial \xi} \\ \frac{\partial u}{\partial \eta} \\ \frac{\partial v}{\partial \xi} \\ \frac{\partial v}{\partial \eta} \end{bmatrix} = [\boldsymbol{M}_2] \begin{bmatrix} \frac{\partial u}{\partial \xi} \\ \frac{\partial u}{\partial \eta} \\ \frac{\partial v}{\partial \xi} \\ \frac{\partial v}{\partial \eta} \end{bmatrix} \qquad \textit{(13-20)}$$

We can observe that, the terms in $\boldsymbol{M}_2$ corresponds to the inverse of Jacobian matrix ($\boldsymbol{J}$), which express the transformation between local coordinates (ξ and η or r and s) and the global coordinates (x and y), i.e.,

$$\boldsymbol{J} = \begin{bmatrix} \frac{\partial x}{\partial \xi} & \frac{\partial y}{\partial \xi} \\ \frac{\partial x}{\partial \eta} & \frac{\partial y}{\partial \eta} \end{bmatrix}$$

By using 2nd order bilinear polynomial for geometry interpolation, i.e.,

$$x \cong \sum_{j=1}^{9} N_j^{(e)}(\xi, \eta) x_i \quad ; \quad y \cong \sum_{j=1}^{9} N_j^{(e)}(\xi, \eta) y_i$$

with linear shape functions,

$$\begin{aligned} N_1 &= \frac{1}{4}(1-\xi)(1-\eta) \\ N_2 &= \tfrac{1}{4}(1+\xi)(1-\eta) \\ N_3 &= \frac{1}{4}(1+\xi)(1+\eta) \\ N_4 &= \frac{1}{4}(1-\xi)\eta(1+\eta) \end{aligned} \qquad \textit{(13-21)}$$

Shape function vector,

$$\boldsymbol{N} \;\; = \; [N_1 \;\; N_2 \; N_3 \;\; N_4 \;]^T$$

Now we can write,

$$\boldsymbol{J} = \begin{bmatrix} \frac{\partial x}{\partial \xi} & \frac{\partial y}{\partial \xi} \\ \frac{\partial x}{\partial \eta} & \frac{\partial y}{\partial \eta} \end{bmatrix} = \begin{bmatrix} \sum_{j=1}^{4} \frac{\partial N_j}{\partial \xi}\, x_j & \sum_{j=1}^{4} \frac{\partial N_j}{\partial \xi}\, y_j \\ \sum_{j=1}^{4} \frac{\partial N_j}{\partial \eta}\, x_j & \sum_{j=1}^{4} \frac{\partial N_j}{\partial \eta}\, y_j \end{bmatrix} \tag{13-22}$$

And inverse of Jacobian as $\boldsymbol{J}^{-1}$ as:

$$\boldsymbol{J}^{-1} = \frac{1}{det(\boldsymbol{J})} \begin{bmatrix} J_{22} & -J_{12} \\ -J_{21} & J_{11} \end{bmatrix} = \frac{1}{det(\boldsymbol{J})} \begin{bmatrix} \sum_{j=1}^{4} \frac{\partial N_j}{\partial \eta}\, y_j & -\sum_{j=1}^{4} \frac{\partial N_j}{\partial \xi}\, y_j \\ -\sum_{j=1}^{4} \frac{\partial N_j}{\partial \eta}\, x_j & \sum_{j=1}^{4} \frac{\partial N_j}{\partial \xi}\, x_j \end{bmatrix} = \begin{bmatrix} J_{11}^* & J_{12}^* \\ J_{21}^* & J_{22}^* \end{bmatrix} \tag{13-23}$$

Now the updated $\boldsymbol{M}_2$ matrix is written as:

$$\boldsymbol{M}_2 = \begin{bmatrix} \left(\frac{\sum_{j=1}^{4} \frac{\partial N_j}{\partial \eta}\, y_j}{det(\boldsymbol{J})} \right) & \left(\frac{-\sum_{j=1}^{4} \frac{\partial N_j}{\partial \xi}\, y_j}{det(\boldsymbol{J})} \right) & 0 & 0 \\ \left(\frac{-\sum_{j=1}^{4} \frac{\partial N_j}{\partial \eta}\, x_j}{det(\boldsymbol{J})} \right) & \left(\frac{\sum_{j=1}^{4} \frac{\partial N_j}{\partial \xi}\, x_j}{det(\boldsymbol{J})} \right) & 0 & 0 \\ 0 & 0 & \left(\frac{\sum_{j=1}^{4} \frac{\partial N_j}{\partial \eta}\, y_j}{det(\boldsymbol{J})} \right) & \left(\frac{-\sum_{j=1}^{4} \frac{\partial N_j}{\partial \xi}\, y_j}{det(\boldsymbol{J})} \right) \\ 0 & 0 & \left(\frac{-\sum_{j=1}^{4} \frac{\partial N_j}{\partial \eta}\, x_j}{det(\boldsymbol{J})} \right) & \left(\frac{\sum_{j=1}^{4} \frac{\partial N_j}{\partial \xi}\, x_j}{det(\boldsymbol{J})} \right) \end{bmatrix} \tag{13-24}$$

Or,

$$\boldsymbol{M}_2 = \begin{bmatrix} J_{11}^* & J_{12}^* & 0 & 0 \\ J_{21}^* & J_{22}^* & 0 & 0 \\ 0 & 0 & J_{11}^* & J_{12}^* \\ 0 & 0 & J_{21}^* & J_{22}^* \end{bmatrix} \tag{13-25}$$

Now, using bilinear interpolation functions (same as geometry) for displacements (u, v):

$$\boldsymbol{u}_h(\xi, \eta) \cong \sum_{i=1}^{4} N_i^{(e)}\,(\xi, \eta)\, \overline{\boldsymbol{u}}_i$$

$$\boldsymbol{v}_h(\xi, \eta) \cong \sum_{i=1}^{4} N_i^{(e)}\,(\xi, \eta)\, \overline{\boldsymbol{v}}_i$$

We can write,

$$\begin{bmatrix} \frac{\partial u}{\partial \xi} \\ \frac{\partial u}{\partial \eta} \\ \frac{\partial v}{\partial \xi} \\ \frac{\partial v}{\partial \eta} \end{bmatrix} = \begin{bmatrix} N'_{1\xi} & 0 & N'_{2\xi} & 0 & N'_{3\xi} & 0 & N'_{4\xi} & 0 \\ N'_{1\eta} & 0 & N'_{2\xi} & 0 & N'_{3\eta} & 0 & N'_{4\eta} & 0 \\ 0 & N'_{1\xi} & 0 & N'_{2\xi} & 0 & N'_{3\eta} & 0 & N'_{4\xi} \\ 0 & N'_{1\eta} & 0 & N'_{2\xi} & 0 & N'_{3\eta} & 0 & N'_{4\eta} \end{bmatrix}_{(4x8)} \begin{bmatrix} \boldsymbol{d_1} \\ \boldsymbol{d_2} \\ \boldsymbol{d_3} \\ \boldsymbol{d_4} \end{bmatrix}_{(8x1)} = [\boldsymbol{M}_3] \cdot \boldsymbol{d}^{(e)} \qquad (13\text{-}26)$$

Where $\boldsymbol{d_1}, \boldsymbol{d_2}, \boldsymbol{d_3}$ and $\boldsymbol{d_4}$ corresponds to nodal DOF vector with $\boldsymbol{d_i} = [u_i, v_i]^T,\ i = 1,..4$. The derivatives of bilinear shape function can be found in Appendix section 13.3.1.

Now substituting, Eq. (13-25) and Eq. (13-26) in Eq. (13-19), we can write the normal/axial strain matrix as:

$$\boldsymbol{\varepsilon} = \begin{Bmatrix} \varepsilon_{xx} \\ \varepsilon_{yy} \\ \gamma_{xy} \end{Bmatrix} = \begin{bmatrix} J^*_{11} & J^*_{12} & 0 & 0 \\ 0 & 0 & J^*_{21} & J^*_{22} \\ J^*_{21} & J^*_{22} & J^*_{11} & J^*_{12} \end{bmatrix} \cdot \boldsymbol{M}_3 \cdot \boldsymbol{d}^{(e)}$$

Or,

$$\boldsymbol{\varepsilon} = \begin{Bmatrix} \varepsilon_{11} \\ \varepsilon_{22} \\ \gamma_{12} \end{Bmatrix} = [\boldsymbol{M}_1]_{(3x4)} \cdot [\boldsymbol{M}_2]_{(4x4)} \cdot [\boldsymbol{M}_3]_{(4x8)} \cdot \boldsymbol{d}^{(e)}{}_{(8X1)} \qquad (13\text{-}27)$$

$$\Longrightarrow \quad \boxed{\boldsymbol{B} = [\boldsymbol{M}_1]\,[\boldsymbol{M}_2][\boldsymbol{M}_2]}$$

Later, the stiffness matrix can be calculated using,

$$\boldsymbol{K} = t \int_{x=a}^{b} \int_{y=a}^{b} \{\bar{\bar{\boldsymbol{D}}}\, \boldsymbol{B}^T(x,y)\, \boldsymbol{B}(x,y)\}\, dx\, dy = t \int_{-1}^{+1} \int_{-1}^{+1} \{\bar{\bar{\boldsymbol{D}}}\, \boldsymbol{B}^T(\xi,\eta)\, \boldsymbol{B}(\xi,\eta)\}\, det(\boldsymbol{J})\, d\xi\, d\eta \qquad (13\text{-}28)$$

Where, $det(\boldsymbol{J})$ relates the differential of area in the two coordinate systems. The numerical integration is performed using Gaussian quadrature rule, using 4 gauss points.

$$\boldsymbol{I} = \int_{-1}^{+1} \int_{-1}^{+1} f(\xi,\eta)\, d\xi\, d\eta = \sum_{j=1}^{n} \sum_{i=1}^{n} w_j\, w_i\, f(\xi,\eta) \qquad (13\text{-}29)$$

Gauss points (n)	Local Coordinate values (ξ)	(η)	Weights (w_i)
1	$-1/\sqrt{3}$	$-1/\sqrt{3}$	1
2	$+1/\sqrt{3}$	$-1/\sqrt{3}$	1
3	$-1/\sqrt{3}$	$+1/\sqrt{3}$	1
4	$+1/\sqrt{3}$	$+1/\sqrt{3}$	1

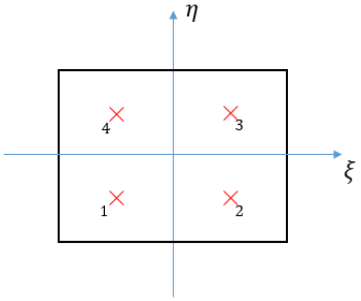

Calculation of Force vectors ($\boldsymbol{f}_b$ and $\boldsymbol{f}_S$) :

1) Body/Volume force($\boldsymbol{F}_b$):

$$\boldsymbol{f_b} = t \iint_{A^{(e)}} \boldsymbol{F}_b \, \boldsymbol{N}^T \, dx \, dy = t \int_{-1}^{+1} \int_{-1}^{+1} \boldsymbol{N}^T \boldsymbol{F}_b \, det(\boldsymbol{J}) \, d\xi \, d\eta \, ; \qquad (13\text{-}30)$$

Where,

$$\boldsymbol{F}_b = \begin{Bmatrix} F_{bx} \\ F_{by} \end{Bmatrix}$$

The numerical integration is performed using Gaussian quadrature rule, using 4 gauss points.

2) Surface/Traction force($\boldsymbol{f}_s$) :

The second type of distributed forces considered corresponds to pressure forces acting on each face of the element. We have adopted the following convention (see fig below) for a pressure acting on the face, n $(1 < n < 4)$ for identification of Distributed load of type U_n in UEL.

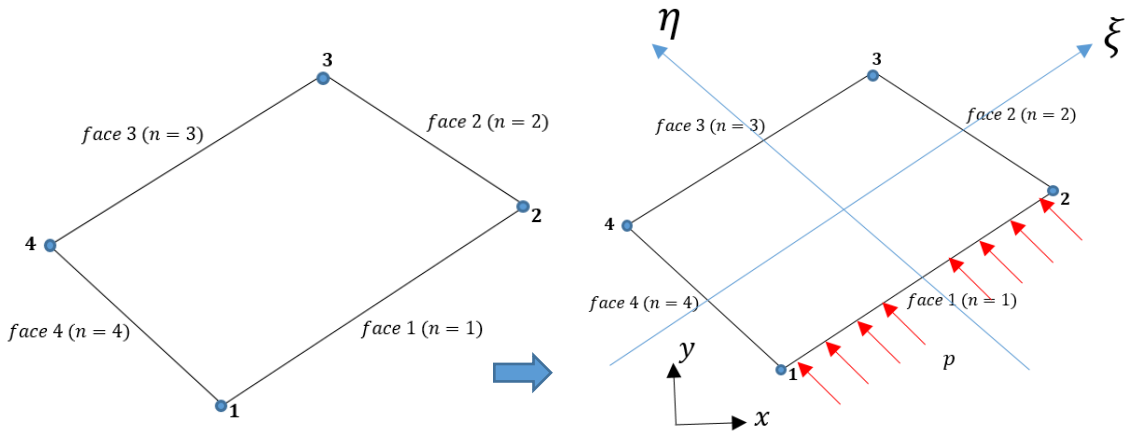

$$\boldsymbol{f_S} = t \iint_{A^{(e)}} \boldsymbol{F}_S \, \boldsymbol{N}^T \, dx \, dy = t \int_{-1}^{+1} \int_{-1}^{+1} \boldsymbol{N}^T \boldsymbol{F}_S \, det\,(J_2) \, d\xi \, d\eta \, ; \qquad (13\text{-}31)$$

Where,

$$\boldsymbol{F}_S = \begin{Bmatrix} F_{Sx} \\ F_{Sy} \end{Bmatrix}$$

Where, J_2 is the Jacobi for the edge/face transformation (from global coordinates to local).

For face (n=1 or n=3):

$$\det\,(J_2) = \sqrt{\left(\sum_{i=1}^{4} \frac{\partial N_i}{\partial \xi} \, x_i\right)^2 + \left(\sum_{i=1}^{4} \frac{\partial N_i}{\partial \xi} \, y_i\right)^2} \qquad (13\text{-}32)$$

For face (n=2 or n=4):

$$\det(J_2)=\sqrt{\left(\sum_{i=1}^{4}\frac{\partial N_i}{\partial \eta}\ x_i\right)^2+\left(\sum_{i=1}^{4}\frac{\partial N_i}{\partial \eta}\ y_i\right)^2}$$

The components of $\boldsymbol{F_S}$ is given by:

$$F_{Sx}=sgn\,p\,\frac{\left(y_{(m+1)}-y_m\right)}{Length\ of\ face}\ ;\qquad F_{Sy}=sgn\,p\,\frac{\left(x_{(m+1)}-x_m\right)}{Length\ of\ face}\ ; \tag{13-33}$$

Where, p is the pressure in 'Pa (F/L^2)' acting on the face, (x_m, y_m) and $(x_{(m+1)}, y_{(m+1)})$ are the coordinates of face, n and sgn = ± 1 (based on direction of $\boldsymbol{F_S}$ towards the interior of element). Finally, the numerical integration is performed using Gaussian quadrature rule, using 2 gauss points.

Calculation of Stress components:

$$\begin{bmatrix}S_{11}\\S_{22}\\S_{12}\end{bmatrix}=\bar{\bar{\boldsymbol{D}}}\,\boldsymbol{\varepsilon}=\frac{E}{(1-\nu^2)}\begin{bmatrix}1&\nu&0\\\nu&1&0\\0&0&\frac{1-\nu}{2}\end{bmatrix}\begin{bmatrix}\varepsilon_{11}\\\varepsilon_{22}\\\gamma_{12}\end{bmatrix} \tag{13-34}$$

And,

$$\varepsilon_{33}=-\frac{\nu}{E}(S_{11}+S_{22})$$

Where, E is Elastic Young's modulus, ν is Poisson's ratio. Totally 28 variables (stress and strain components) are calculated in 4 gauss points.

Calculation of Elastic deformation energy (W):

$$W=\frac{1}{2}\int_{\Omega}\boldsymbol{\varepsilon}^T\,\bar{\bar{\boldsymbol{D}}}\,\boldsymbol{\varepsilon}\,d\Omega=\frac{1}{2}\ \boldsymbol{d}^{(e)}\,\boldsymbol{K}\ \boldsymbol{d}^{(e)} \tag{13-35}$$

13.2.3 Comparison of UEL (U4) with ABAQUS® CPS4

In order to compare the accuracy of results obtained from UEL (U4) with ABAQUS® CPS4 element (Linear static analysis), some test cases have been created, which can be found below. It should be noted that for all the cases, same material properties have been defined: 1) Elastic Young's modulus, $E=2.0E5\ MPa$, Poisson's ratio,$\nu=0.3$ and thickness of plate,$t=1mm$.

Case1: Concentrated nodal loads, $F_y = 100\ N$ (100x100 square plate, meshed with 1 element)

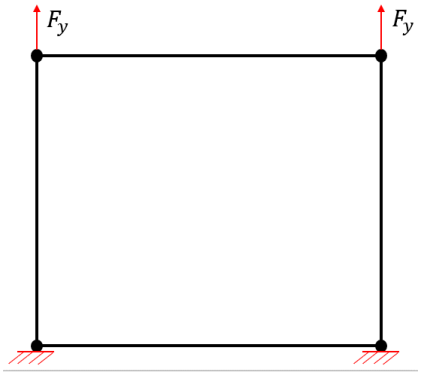

Figure 129: Loading and Boundary conditions for Case 1 (U4)

Table 10: Comparison of strain components and Max.nodal displacements (Case1)

Integration Points (n)	$\boldsymbol{\varepsilon_{11}}$		$\boldsymbol{\varepsilon_{22}}$		$\boldsymbol{\tau_{12}}$		$\boldsymbol{U_{(max)}}$	
	U4	*CPS4*	*U4*	*CPS4*	*U4*	*CPS4*	*U4*	*CPS4*
1	−1.5E-36	−1.5E-36	2.27E-05	2.27E-05	−8.84E-22	8.84E-22		
2	−1.5E-36	−1.5E-36	2.27E-05	2.27E-05	−8.84E-22	8.84E-22	2.28E-03	2.28E-03
3	−1.5E-36	−1.5E-36	2.27E-05	2.27E-05	3.38E-22	3.38E-22		
4	−1.5E-36	−1.5E-36	2.27E-05	2.27E-05	3.38E-22	3.38E-22		

Case2: Concentrated nodal loads, $F_x = 250\ N$ (100x100 square plate, meshed with 1 element)

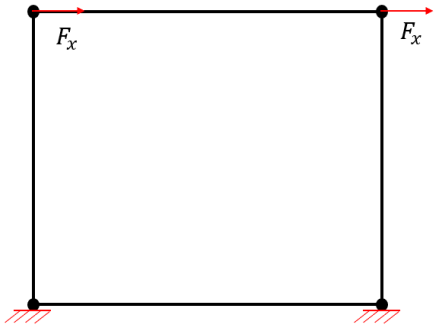

Figure 130: Loading and Boundary conditions for Case 2 (U4)

Table 11: Comparison of strain components and Max.nodal displacements for Case2 (U4)

Integration Points (n)	$\boldsymbol{\varepsilon_{11}}$		$\boldsymbol{\varepsilon_{22}}$		$\boldsymbol{\tau_{12}}$		$\boldsymbol{U_{(max)}}$	
	U4	*CPS4*	*U4*	*CPS4*	*U4*	*CPS4*	*U4*	*CPS4*
1	3.38E-21	0	−6.68E-52	0	6.50E-05	6.50E-05		
2	3.38E-21	0	−1.17E-51	6.68E-52	6.50E-05	6.50E-05	6.50E-03	6.50E-03
3	1.35E-20	0	−6.68E-52	0	6.50E-05	6.50E-05		
4	1.35E-20	0	−1.17E-51	6.68E-52	6.50E-05	6.50E-05		

Case3: Concentrated nodal loads, $F = 250\ N$ (100x100 square plate, meshed with 1 element)

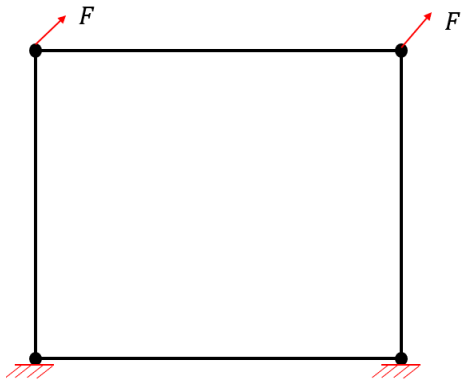

Figure 131: Loading and Boundary conditions for Case 3 (U4)

Table 12: Comparison of strain components and Max.nodal displacements Case3 (U4)

Integration Points (n)	ε_{11}		ε_{22}		τ_{12}		$U_{(max)}$	
	U4	*CPS4*	*U4*	*CPS4*	*U4*	*CPS4*	*U4*	*CPS4*
1	2.65E-23	0	2.34E-07	2.34E-07	7.54E-07	7.54E-07		
2	2.64E-23	0	−2.34E-07	−2.34E-07	7.54E-07	7.54E-07	9.24E-05	9.24E-05
3	1.06E-22	0	2.34E-07	2.34E-07	2.86E-07	2.86E-07		
4	1.06E-22	0	−2.34E-07	−2.34E-07	2.86E-07	2.86E-07		

Case4: Concentrated nodal loads, $F = 250\ N$ (100x100 square plate with a hole, meshed with 20 elements)

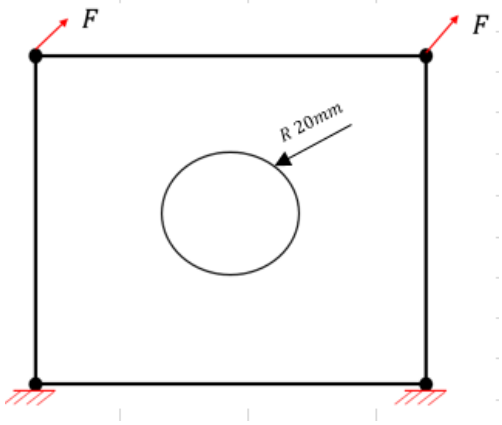

Figure 132: Loading and Boundary conditions for Case 4 (U4)

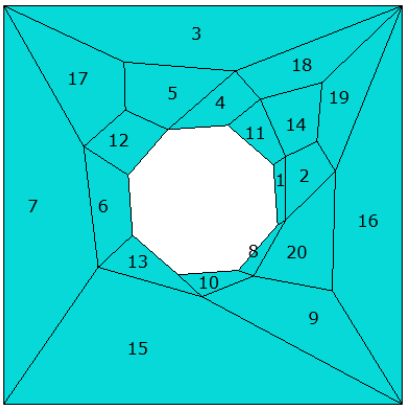

Figure 133: Mesh for case4 (generated in Abaqus)

a) Element label 1:

Table 13: Comparison of strain components for Case4 (U4)

Integration Points (n)	$\boldsymbol{\varepsilon_{11}}$		$\boldsymbol{\varepsilon_{22}}$		$\boldsymbol{\tau_{12}}$	
	U4	*CPS4*	*U4*	*CPS4*	*U4*	*CPS4*
1	7.22E-09	7.22E-09	−3.67E-07	−3.67E-07	5.20E-07	5.20E-07
2	3.20E-08	3.20E-08	−3.77E-07	−3.77E-07	3.77E-07	3.77E-07
3	9.56E-09	9.56E-09	−3.48E-07	−3.48E-07	5.03E-07	5.03E-07
4	3.49E-08	3.49E-08	−3.50E-07	−3.50E-07	3.56E-07	3.56E-07

b) Element label 10:

Integration Points (n)	$\boldsymbol{\varepsilon_{11}}$		$\boldsymbol{\varepsilon_{22}}$		$\boldsymbol{\tau_{12}}$	
	U4	*CPS4*	*U4*	*CPS4*	*U4*	*CPS4*
1	−4.30E-09	−4.30E-09	2.40E-07	2.40E-07	3.05E-07	3.05E-07
2	8.83E-08	8.83E-08	2.05E-07	2.05E-07	6.51E-07	6.51E-07
3	4.20E-08	4.20E-08	2.24E-07	2.24E-07	4.58E-07	4.58E-07
4	−3.60E-08	−3.60E-08	1.99E-07	1.99E-07	7.08E-07	7.08E-07

Discussions:

We can observe from all the considered test cases that, we obtain a good compromise and very negligible errors in the output parameters calculated between user element ‘U4’ and the ‘ABAQUS® CPS4’ element (see Table 10 - Table 13). And also it is a very good practice to understand how to create our own user elements using UEL subroutine (written in FORTRAN 77), that will be called in ABAQUS® for our calculations and also to understand the importance of various standard parameters or keys to define in UEL, that is accepted and passed to Abaqus for various calculations, using our own user elements.

13.3 Derivatives of shape functions

13.3.1 Bilinear shape functions

1)

$$\frac{\partial N_1}{\partial \xi} = -\frac{1}{4}(1-\eta) \quad ; \quad \frac{\partial N_1}{\partial \eta} = -\frac{1}{4}(1-\xi)$$

(2)

$$\frac{\partial N_2}{\partial \xi} = \frac{1}{4}(1-\eta) \quad ; \quad \frac{\partial N_2}{\partial \eta} = -\frac{1}{4}(1+\xi)$$

(3) *(13-36)*

$$\frac{\partial N_3}{\partial \xi} = \frac{1}{4}(1+\eta) \quad ; \quad \frac{\partial N_3}{\partial \eta} = \frac{1}{4}(1+\xi)$$

(4)

$$\frac{\partial N_4}{\partial \xi} = -\frac{1}{4}(1+\eta) \quad ; \quad \frac{\partial N_4}{\partial \eta} = \frac{1}{4}(1-\xi)$$

13.3.2 Biquadratic shape functions

(1)

$$\frac{\partial N_1}{\partial \xi} = \frac{1}{4}[\,(1-2\xi)(\eta-\eta^2)\,]$$

$$\frac{\partial N_1}{\partial \eta} = \frac{1}{4}[(\xi-\xi^2)(1-2\eta)]$$

(2)

$$\frac{\partial N_2}{\partial \xi} = \frac{-1}{4}[\,(1+2\xi)(\eta-\eta^2)\,]$$

$$\frac{\partial N_2}{\partial \eta} = \frac{-1}{4}[(\xi+\xi^2)(1-2\eta)] \qquad \textit{(13-37)}$$

(3)

$$\frac{\partial N_3}{\partial \xi} = \frac{1}{4}[\,(1+2\xi)(\eta+\eta^2)\,]$$

$$\frac{\partial N_3}{\partial \eta} = \frac{1}{4}[(\xi+\xi^2)(1+2\eta)]$$

(4)

$$\frac{\partial N_4}{\partial \xi} = \frac{-1}{4}[\,(1-2\xi)(\eta+\eta^2)\,]$$

$$\frac{\partial N_4}{\partial \eta} = \frac{-1}{4}[(\xi - \xi^2)\,(1 + 2\eta)]$$

(5)

$$\frac{\partial N_5}{\partial \xi} = \xi\,(\eta - \eta^2)$$

$$\frac{\partial N_5}{\partial \eta} = \frac{-1}{2}[(\,\xi - 1)(\,\xi + 1)(2\eta - 1)]$$

(6)

$$\frac{\partial N_6}{\partial \xi} = -\frac{1}{2}[\,(1 + 2\xi)\,(\eta - 1)(\eta + 1)\,\,]$$

$$\frac{\partial N_6}{\partial \eta} = -\xi\,(\xi + 1)\eta$$

(7)

$$\frac{\partial N_7}{\partial \xi} = -\eta\,(\eta + 1)\xi$$

$$\frac{\partial N_7}{\partial \eta} = -\frac{1}{2}[\,(\xi - 1)(\xi + 1)(2\eta + 1)\,]$$

(8)

$$\frac{\partial N_8}{\partial \xi} = \frac{-1}{2}[\,(2\xi - 1)\,(\eta - 1)\,(\eta + 1)\,]$$

$$\frac{\partial N_8}{\partial \eta} = (\xi - \xi^2)\eta$$

(9)

$$\frac{\partial N_9}{\partial \xi} = 2\xi\,(\eta^2 - 1)$$

$$\frac{\partial N_9}{\partial \eta} = 2\eta\,(\xi^2 - 1)$$

13.3.3 Bicubic shape functions (Hermit type)

(1)

$$\frac{\partial N_1}{\partial \xi} = \frac{3}{16}[(\eta^3 - 3\eta + 2)\,(\xi - 1)\,(\xi + 1)] \quad ; \quad \frac{\partial^2 N_1}{\partial \xi^2} = \frac{1}{8}[(3\eta^3 - 9\eta + 6)\xi]$$

$$\frac{\partial N_1}{\partial \eta} = \frac{3}{16}[(\xi^3 - 3\xi + 2)\,(\eta - 1)\,(\eta + 1)\,] \quad ; \quad \frac{\partial^2 N_1}{\partial \eta^2} = \frac{1}{8}[(3\xi^3 - 9\xi + 6)\,\eta]$$

$$\frac{\partial^2 N_1}{\partial \xi\, \partial \eta} = \frac{\partial}{\partial \xi}\left(\frac{\partial N_1}{\partial \eta}\right) = \frac{9}{16}[(\xi^2 - 1)\,(\eta^2 - 1)]$$

(2)

$$\frac{\partial N_2}{\partial \xi} = \frac{1}{32}[(\eta^3 - 3\eta + 2)(3\xi^2 - 2\xi - 1)]$$

$$\frac{\partial^2 N_2}{\partial \xi^2} = \frac{1}{32}[(\eta^3 - 3\eta + 2)(6\xi - 2)]$$

$$\frac{\partial N_2}{\partial \eta} = \frac{3}{32}[(\xi + 1)(\xi^2 - 2\xi + 1)(\eta - 1)(\eta + 1)]$$

$$\frac{\partial^2 N_2}{\partial \eta^2} = \frac{3}{16}[(\xi + 1)(\xi^2 - 2\xi + 1)\,\eta] \qquad \textit{(13-38)}$$

$$\frac{\partial^2 N_2}{\partial \xi\, \partial \eta} = \frac{\partial}{\partial \xi}\left(\frac{\partial N_2}{\partial \eta}\right) = \frac{3}{32}[(3\xi^2 - 2\xi - 1)(\eta^2 - 1)]$$

(3)

$$\frac{\partial N_3}{\partial \xi} = \frac{3}{32}[\,(\eta + 1)(\eta^2 - 2\eta + 1)(\xi - 1)(\xi + 1)]$$

$$\frac{\partial^2 N_3}{\partial \xi^2} = \frac{3}{16}[(\eta + 1)(\eta^2 - 2\eta + 1)\,\xi]$$

$$\frac{\partial N_3}{\partial \eta} = \frac{1}{32}[(\xi^3 - 3\xi + 2)(3\eta^2 - 2\eta - 1)]$$

$$\frac{\partial^2 N_3}{\partial \eta^2} = \frac{1}{32}[(\xi^3 - 3\xi + 2)(6\eta - 2)\,]$$

$$\frac{\partial^2 N_3}{\partial \xi\, \partial \eta} = \frac{\partial}{\partial \xi}\left(\frac{\partial N_3}{\partial \eta}\right) = \frac{3}{32}[(\xi^2 - 1)(\eta - 1)(3\eta + 1)]$$

(4)

$$\frac{\partial N_4}{\partial \xi} = \frac{1}{64}[(\eta + 1)(\eta^2 - 2\eta + 1)\,(3\xi^2 - 2\xi - 1)]$$

$$\frac{\partial^2 N_4}{\partial \xi^2} = \frac{1}{64}[(\eta + 1)(\eta^2 - 2\eta + 1)(6\xi - 2)]$$

$$\frac{\partial N_4}{\partial \eta} = \frac{1}{64}[\,(\xi+1)\,(\xi^2-2\xi+1)\,(3\eta^2-2\eta-1)]$$

$$\frac{\partial^2 N_4}{\partial \eta^2} = \frac{1}{64}[(\xi+1)\,(\xi^2-2\xi+1)\,(6\eta-2)]$$

$$\frac{\partial^2 N_4}{\partial \xi\,\partial \eta} = \frac{\partial}{\partial \xi}\left(\frac{\partial N_4}{\partial \eta}\right) = \frac{1}{64}[(3\xi^2-2\xi-1)(\eta-1)(3\eta+1)]$$

(5)

$$\frac{\partial N_5}{\partial \xi} = \frac{-3}{16}[(\eta^3-3\eta+2)(\xi-1)(\xi+1)] \quad ; \quad \frac{\partial^2 N_5}{\partial \xi^2} = \frac{-3}{8}[(\eta^3-3\eta+2)\,]$$

$$\frac{\partial N_5}{\partial \eta} = \frac{-3}{16}[(\xi+1)^2\,(\xi-2)(\eta-1)(\eta+1)] \quad ; \quad \frac{\partial^2 N_5}{\partial \eta^2} = \frac{-3}{8}[(\xi+1)^2\,(\xi-2)\,\eta]$$

$$\frac{\partial^2 N_5}{\partial \xi\,\partial \eta} = \frac{\partial}{\partial \xi}\left(\frac{\partial N_5}{\partial \eta}\right) = \frac{-9}{16}[(\xi^2-1)(\eta^2-1)]$$

(6)

$$\frac{\partial N_6}{\partial \xi} = \frac{1}{32}[(\eta^3-3\eta+2)\,(\xi+1)(3\xi-1)] \quad ; \quad \frac{\partial^2 N_6}{\partial \xi^2} = \frac{1}{16}[(\eta^3-3\eta+2)\,(3\xi+1)]$$

$$\frac{\partial N_6}{\partial \eta} = \frac{3}{32}[(\xi+1)^2\,(\xi-1)(\eta-1)(\eta+1)] \;\; ; \;\; \frac{\partial^2 N_6}{\partial \eta^2} = \frac{3}{16}[(\xi+1)^2\,(\xi-1)\,\eta]$$

$$\frac{\partial^2 N_6}{\partial \xi\,\partial \eta} = \frac{\partial}{\partial \xi}\left(\frac{\partial N_6}{\partial \eta}\right) = \frac{3}{32}[(3\xi^2+2\xi-1)(\eta^2-1)]$$

(7)

$$\frac{\partial N_7}{\partial \xi} = \frac{-3}{32}[\,(\eta+1)(\eta^2-2\eta+1)\,(\xi-1)(\xi+1)]$$

$$\frac{\partial^2 N_7}{\partial \xi^2} = \frac{-3}{16}[(\eta+1)(\eta^2-2\eta+1)\,\xi\,]$$

$$\frac{\partial N_7}{\partial \eta} = \frac{-1}{32}[(\xi+1)^2\,(\xi-2)\,(3\eta^2-2\eta-1)]$$

$$\frac{\partial^2 N_7}{\partial \eta^2} = \frac{-1}{32}[(\xi+1)^2\,(\xi-2)\,(6\eta-2)]$$

$$\frac{\partial^2 N_7}{\partial \xi\,\partial \eta} = \frac{\partial}{\partial \xi}\left(\frac{\partial N_7}{\partial \eta}\right) = \frac{-3}{32}[(\xi^2-1)(\eta-1)(3\eta+1)]$$

(8)

$$\frac{\partial N_8}{\partial \xi} = \frac{1}{64}[\,(\eta+1)(\eta^2-2\eta+1)\,(\xi+1)(3\xi-1)]\;;$$

$$\frac{\partial^2 N_8}{\partial \xi^2} = \frac{1}{32}[(\eta+1)(\eta^2-2\eta+1)(3\xi+1)]$$

$$\frac{\partial N_8}{\partial \eta} = \frac{1}{64}[(\xi-1)\,(\xi+1)^2\,(3\eta^2-2\eta-1)] \quad ; \quad \frac{\partial^2 N_8}{\partial \eta^2} = \frac{1}{64}[(\xi+1)^2\,(\xi-1)(6\eta-2)]$$

$$\frac{\partial^2 N_8}{\partial \xi\,\partial \eta} = \frac{\partial}{\partial \xi}\left(\frac{\partial N_8}{\partial \eta}\right) = \frac{1}{64}[(3\xi^2+2\xi-1)(\eta-1)(3\eta+1)]$$

(9)

$$\frac{\partial N_9}{\partial \xi} = \frac{3}{16}[(\eta+1)^2\,(\eta-2)\,(\xi-1)(\xi+1)] \quad ; \quad \frac{\partial^2 N_9}{\partial \xi^2} = \frac{3}{8}[(\eta+1)^2\,(\eta-2)\,\xi]$$

$$\frac{\partial N_9}{\partial \eta} = \frac{3}{16}[(\xi+1)^2\,(\xi-2)(\eta-1)(\eta+1)] \quad ; \quad \frac{\partial^2 N_9}{\partial \eta^2} = \frac{3}{8}[(\xi+1)^2\,(\xi-2)\,\eta]$$

$$\frac{\partial^2 N_9}{\partial \xi\,\partial \eta} = \frac{\partial}{\partial \xi}\left(\frac{\partial N_9}{\partial \eta}\right) = \frac{9}{16}[(\xi^2-1)(\eta^2-1)]$$

(10)

$$\frac{\partial N_{10}}{\partial \xi} = \frac{-1}{32}[(\eta+1)^2\,(\eta-2)(\xi+1)(3\xi-1)]$$

$$\frac{\partial^2 N_{10}}{\partial \xi^2} = \frac{-1}{16}[(\eta+1)^2\,(\eta-2)(3\xi+1)\,]$$

$$\frac{\partial N_{10}}{\partial \eta} = \frac{-3}{32}[(\xi+1)^2\,(\xi-1)(\eta-1)(\eta+1)]$$

$$\frac{\partial^2 N_{10}}{\partial \eta^2} = \frac{-3}{16}[(\xi+1)^2\,(\xi-1)\,\eta\,]$$

$$\frac{\partial^2 N_{10}}{\partial \xi\,\partial \eta} = \frac{\partial}{\partial \xi}\left(\frac{\partial N_{10}}{\partial \eta}\right) = \frac{-3}{32}[(3\xi^2+2\xi-1)(\eta^2-1)]$$

(11)

$$\frac{\partial N_{11}}{\partial \xi} = \frac{-3}{32}[(\eta+1)^2\,(\eta-1)\,(\xi-1)(\xi+1)]$$

$$\frac{\partial^2 N_{11}}{\partial \xi^2} = \frac{-3}{16}[(\eta+1)^2\,(\eta-1)\,\xi]$$

$$\frac{\partial N_{11}}{\partial \eta} = \frac{-1}{32}[(\xi+1)^2\,(\xi-2)(\eta+1)(3\eta-1)]$$

$$\frac{\partial^2 N_{11}}{\partial \eta^2} = \frac{-1}{16}[(\xi+1)^2\,(\xi-2)(3\eta+1)]$$

$$\frac{\partial^2 N_{11}}{\partial \xi\,\partial \eta} = \frac{\partial}{\partial \xi}\left(\frac{\partial N_{11}}{\partial \eta}\right) = \frac{-3}{32}[(\xi^2-1)(\eta+1)(3\eta-1)]$$

(12)

$$\frac{\partial N_{12}}{\partial \xi} = \frac{1}{64}[(\eta+1)^2\,(\eta-1)\,(\xi+1)(3\xi-1)]$$

$$\frac{\partial^2 N_{12}}{\partial \xi^2} = \frac{1}{32}[(\eta+1)^2\,(\eta-1)(3\xi+1)]$$

$$\frac{\partial N_{12}}{\partial \eta} = \frac{1}{64}[(\xi-1)\,(\xi+1)^2(\eta+1)(3\eta-1)]$$

$$\frac{\partial^2 N_{12}}{\partial \eta^2} = \frac{1}{32}[(\xi-1)\,(\xi+1)^2\,(3\eta+1)]$$

$$\frac{\partial^2 N_{12}}{\partial \xi\,\partial \eta} = \frac{\partial}{\partial \xi}\left(\frac{\partial N_{12}}{\partial \eta}\right) = \frac{1}{64}[(3\xi^2+2\xi-1)(\eta+1)(3\eta-1)]$$

(13)

$$\frac{\partial N_{13}}{\partial \xi} = \frac{-3}{16}[(\eta+1)^2\,(\eta-2)(\xi-1)(\xi+1)]$$

$$\frac{\partial^2 N_{13}}{\partial \xi^2} = \frac{-3}{8}[(\eta+1)^2\,(\eta-2)\,\xi]$$

$$\frac{\partial N_{13}}{\partial \eta} = \frac{-3}{16}[(\xi^3-3\xi+2)(\eta-1)(\eta+1)]$$

$$\frac{\partial^2 N_{13}}{\partial \eta^2} = \frac{-3}{8}[(\xi^3 - 3\xi + 2)\,\eta\,]$$

$$\frac{\partial^2 N_{13}}{\partial \xi\,\partial \eta} = \frac{\partial}{\partial \xi}\left(\frac{\partial N_{13}}{\partial \eta}\right) = \frac{-9}{16}[(\xi^2 - 1)(\eta^2 - 1)]$$

(14)

$$\frac{\partial N_{14}}{\partial \xi} = \frac{-1}{32}[(\eta + 1)^2\,(\eta - 2)(3\xi^2 - 2\xi - 1)]$$

$$\frac{\partial^2 N_{14}}{\partial \xi^2} = \frac{-1}{32}[(\eta + 1)^2\,(\eta - 2)(6\xi - 2)]$$

$$\frac{\partial N_{14}}{\partial \eta} = \frac{-3}{32}[\,(\xi + 1)(\xi^2 - 2\xi + 1)(\eta - 1)(\eta + 1)]$$

$$\frac{\partial^2 N_{14}}{\partial \eta^2} = \frac{-3}{16}[(\xi + 1)(\xi^2 - 2\xi + 1)\,\eta]$$

$$\frac{\partial^2 N_{14}}{\partial \xi\,\partial \eta} = \frac{\partial}{\partial \xi}\left(\frac{\partial N_{14}}{\partial \eta}\right) = \frac{-3}{32}[(3\xi^2 - 2\xi - 1)(\eta^2 - 1)]$$

(15)

$$\frac{\partial N_{15}}{\partial \xi} = \frac{3}{32}[(\eta + 1)^2\,(\eta - 1)\,(\xi + 1)(\xi - 1)]$$

$$\frac{\partial^2 N_{15}}{\partial \xi^2} = \frac{3}{16}[(\eta + 1)^2\,(\eta - 1)\,\xi]$$

$$\frac{\partial N_{15}}{\partial \eta} = \frac{1}{32}[(\xi^3 - 3\xi + 2)\,(\eta + 1)(3\eta - 1)]$$

$$\frac{\partial^2 N_{15}}{\partial \eta^2} = \frac{1}{16}[(\xi^3 - 3\xi + 2)(3\eta + 1)]$$

$$\frac{\partial^2 N_{15}}{\partial \xi\,\partial \eta} = \frac{\partial}{\partial \xi}\left(\frac{\partial N_{15}}{\partial \eta}\right) = \frac{3}{32}[(\xi^2 - 1)(\eta + 1)(3\eta - 1)]$$

(16)

$$\frac{\partial N_{16}}{\partial \xi} = \frac{1}{64}[(\eta + 1)^2\,(\eta - 1)\,(3\xi^2 - 2\xi - 1)]$$

$$\frac{\partial^2 N_{16}}{\partial \xi^2} = \frac{1}{64}[(\eta + 1)^2\,(\eta - 1)\,(6\xi - 2)]$$

$$\frac{\partial N_{16}}{\partial \eta} = \frac{1}{64}[(\xi+1)(\xi^2-2\xi+1)(\eta+1)(3\eta-1)]$$

$$\frac{\partial^2 N_{16}}{\partial \eta^2} = \frac{1}{32}[(\xi+1)(\xi^2-2\xi+1)\,(3\eta+1)]$$

$$\frac{\partial^2 N_{16}}{\partial \xi\,\partial \eta} = \frac{\partial}{\partial \xi}\left(\frac{\partial N_{16}}{\partial \eta}\right) = \frac{1}{64}[(3\xi^2-2\xi-1)\,(\eta+1)(3\eta-1)]$$

13.4 Why order of Cf Parameters should be higher than 10^3?

Let us consider the example of rectangular plate of dimension (100mmx50mm) subjected to bending:

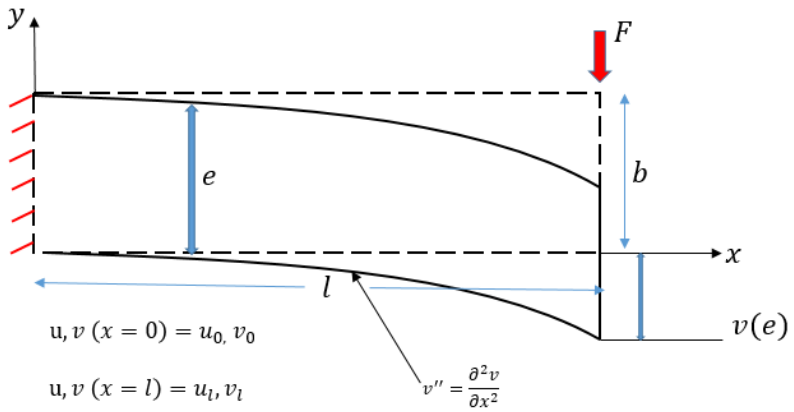

Let, u is the axial/longitudinal displacement, v is transverse displacement and $v''(x)$ corresponds to the curvature/gradient. For the above problem,

$$v(x,y) = v(x) = \frac{v_l}{l^2}\,x^2$$

$$u(x,y) = y\frac{dv}{dx} = y\frac{v_l}{l^2}\,2x \qquad (13\text{-}39)$$

$$v''(x) = \frac{\partial^2 v}{\partial x^2} = 2\frac{v_l}{l^2}$$

So, for example, if we obtain the value of v_l (after deformation) as $v_l = 0.1\ mm$,

$$v''(x) = \boldsymbol{\kappa} = 2\frac{0.1}{100^2} = 2\cdot 10^{-5}$$

We know that the local fiber bending energy is,

$$W_b = \frac{1}{2}\int_{\Omega} \boldsymbol{\kappa}^T \overline{\overline{\boldsymbol{C_f}}}\,\boldsymbol{\kappa} = \frac{1}{2}\int_{\Omega} \boldsymbol{\kappa}^T D\,\boldsymbol{\kappa} = \frac{1}{2}\int_{\Omega} D\,\boldsymbol{\kappa^2} \qquad (13\text{-}40)$$

If we keep the order of $D \leq 10^3$,

$$D\,\boldsymbol{\kappa^2} = 10^3 \cdot 2 \cdot (10^{-5})^{\mathbf{2}} = 2 \cdot 10^{-7} \tag{13-41}$$

Now let's calculate the order the classical strain energy:

$$W_e = \frac{1}{2}\int_{\Omega} \boldsymbol{\varepsilon}^T\, \overline{\overline{\boldsymbol{D}}}\, \boldsymbol{\varepsilon} = \frac{1}{2}\int_{\Omega} E\, \boldsymbol{\varepsilon^2} \tag{13-42}$$

Let's assume that the order Young's Modulus, $E = 10^5\ MPa$. We know that,

$$\varepsilon_{xx} = \frac{du}{dx} = 2y\frac{v_l}{l^2} = \frac{2\ x\ 25\ x\ 0.1}{100^2} = 5 \cdot 10^{-4} \tag{13-43}$$

Therefore,

$$E\,\boldsymbol{\varepsilon^2} = E\ {\varepsilon_{xx}}^2 = 10^5 \cdot 5 \cdot (10^{-4})^{\mathbf{2}} = 5 \cdot 10^{-3} \tag{13-44}$$

From Eq. (13-41) and Eq. (13-44), it is clear that for $D \leq 10^3$:

Or,

$$D\,\boldsymbol{\kappa^2} < E\,\boldsymbol{\varepsilon^2}$$
$$\mathcal{O}(W_b) < \mathcal{O}(W_e) \tag{13-45}$$

Consequently, for $\overline{\overline{\boldsymbol{C_f}}}$ ($\leq 10^3$) bending energy has negligible contribution to the total energy. So, we tend to obtain similar solution as classical plane stress solution. Therefore, it is necessary to have $\overline{\overline{\boldsymbol{C_f}}}$ ($> 10^3$) , so that the order of bending energy becomes similar or higher compared to the classical strain energy. And hence we can observe the non-local effects in the solution.

13.5 Validation of RO laws

Case1: Compression

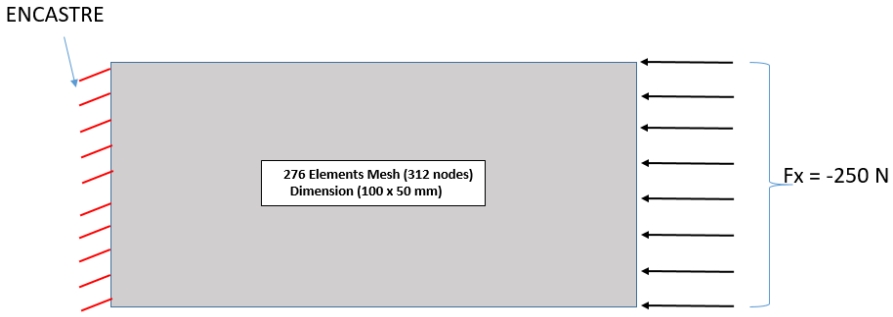

Figure 134: Mesh, Load and Boundary conditions (compression) – Material Non-linearity

1) Displacements:

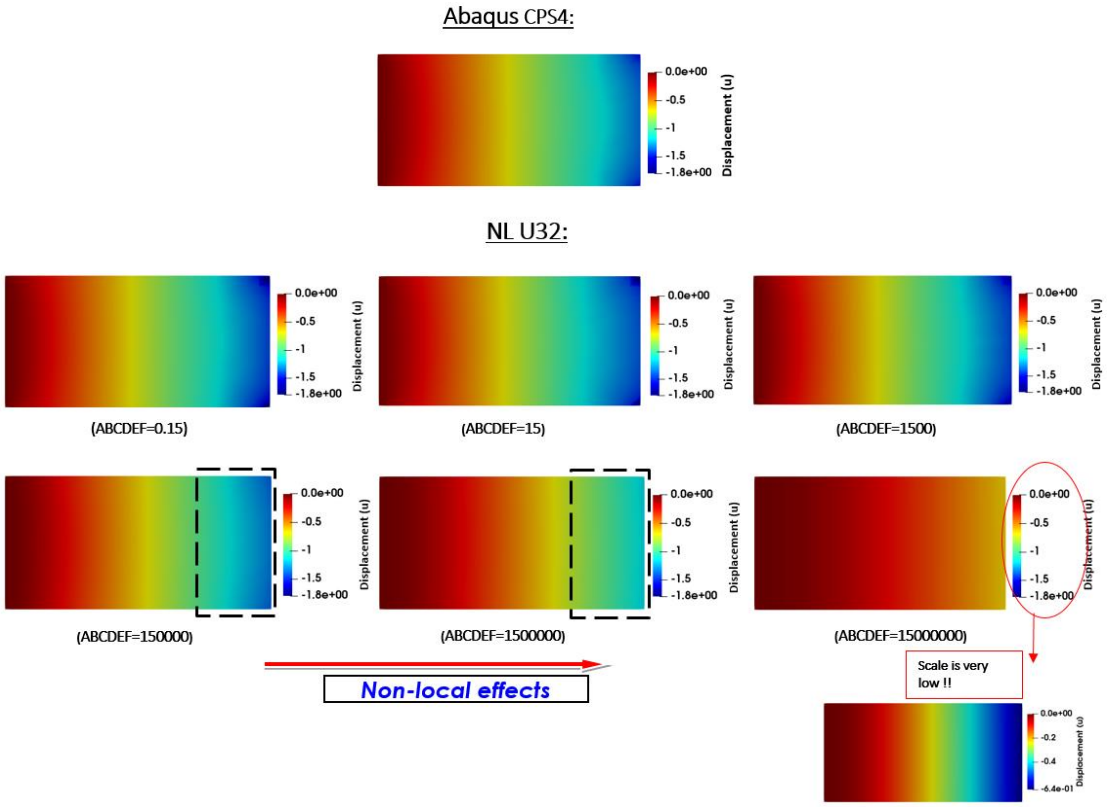

Figure 135: Comparison of Displacement Field (u) for different Cf parameters value (Compression) – Non-linear Material and Non-Linear Geometry

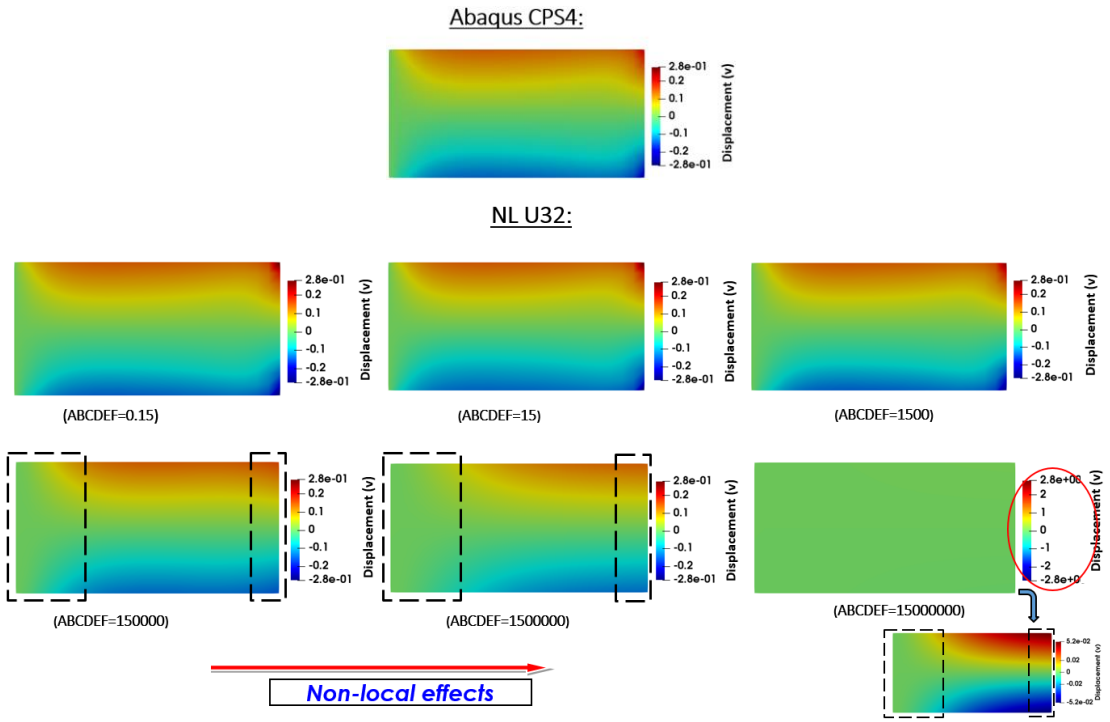

Figure 136: Comparison of Displacement Field (v) for different Cf parameters value (Compression) – Non-linear Material and Non-Linear Geometry

2) Stress Fields (***S***):

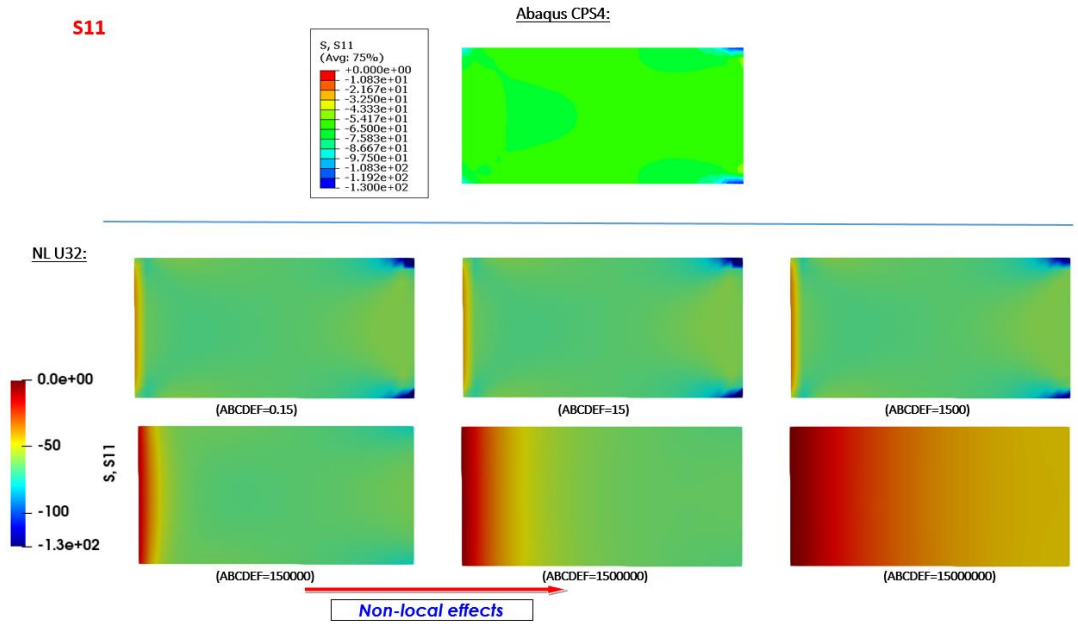

Figure 137: Comparison of S11 component for different Cf parameters values (Compression) – Non-linear Material and Non-Linear Geometry

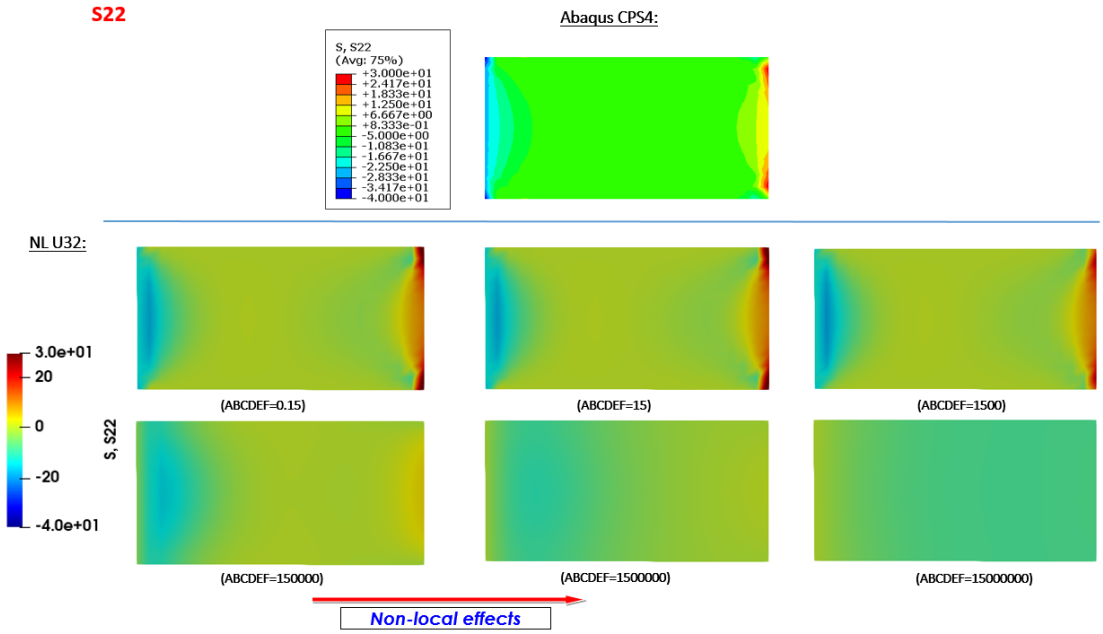

Figure 138: Comparison of S22 component for different Cf parameters values (Compression) – Non-linear Material and Non-Linear Geometry

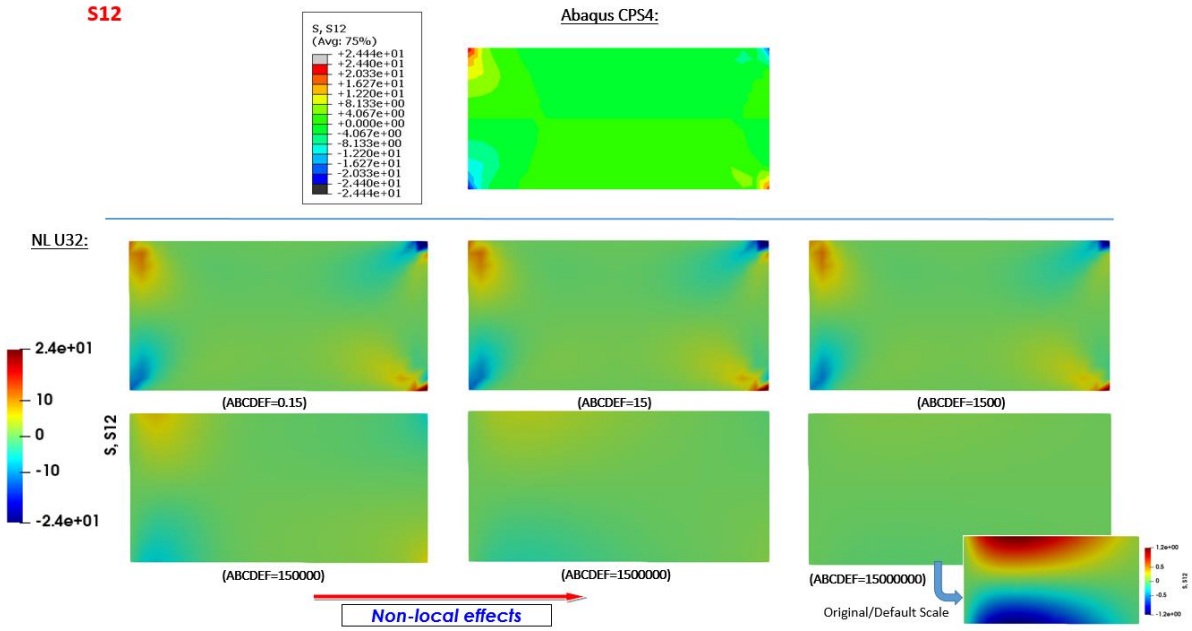

Figure 139: Comparison of S12 component for different Cf parameters values (Compression) – Non-linear Material and Non-Linear Geometry

3) Strain Fields (***E***):

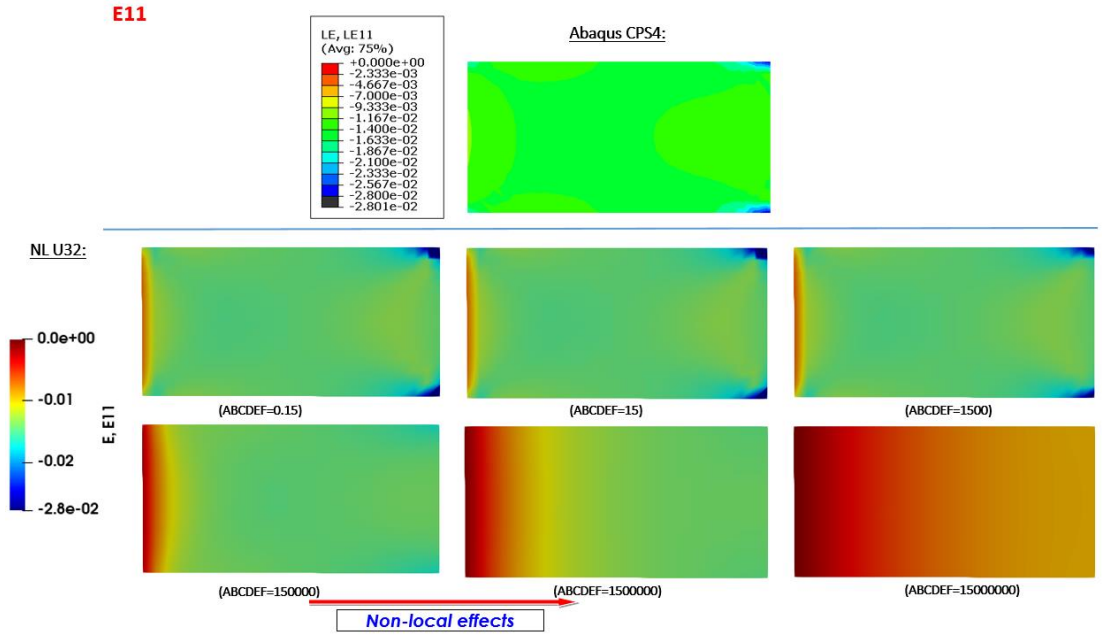

Figure 140: Comparison of E11 component for different Cf parameters values (Compression) – Non-linear Material and Non-Linear Geometry

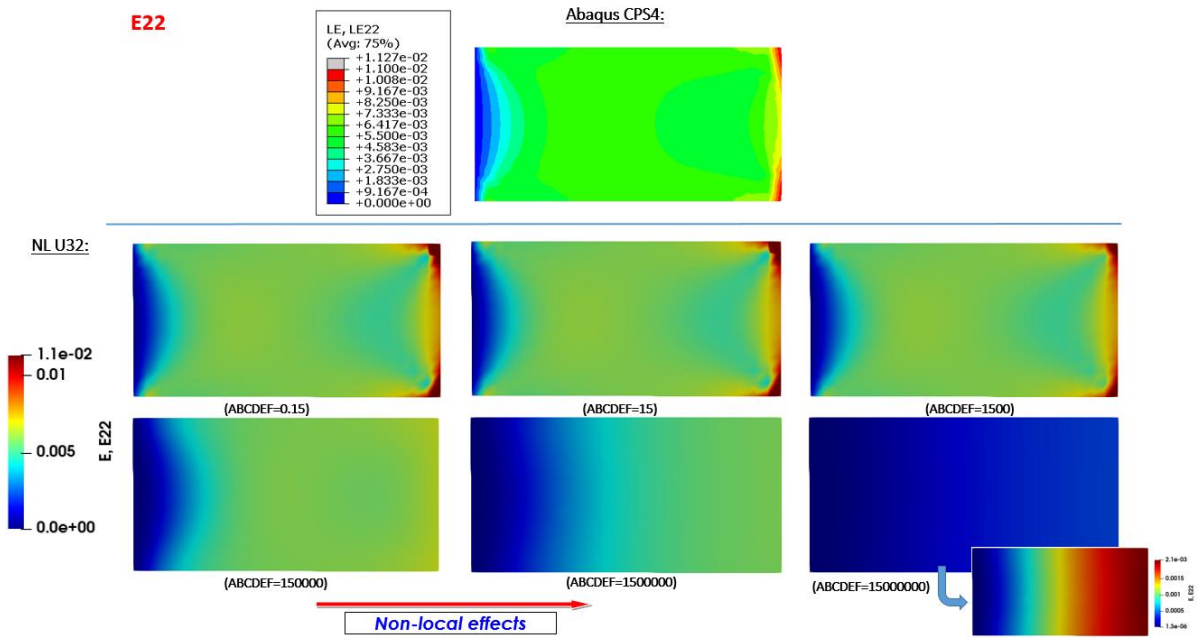

Figure 141: Comparison of E22 component for different Cf parameters values (Compression) – Non-linear Material and Non-Linear Geometry

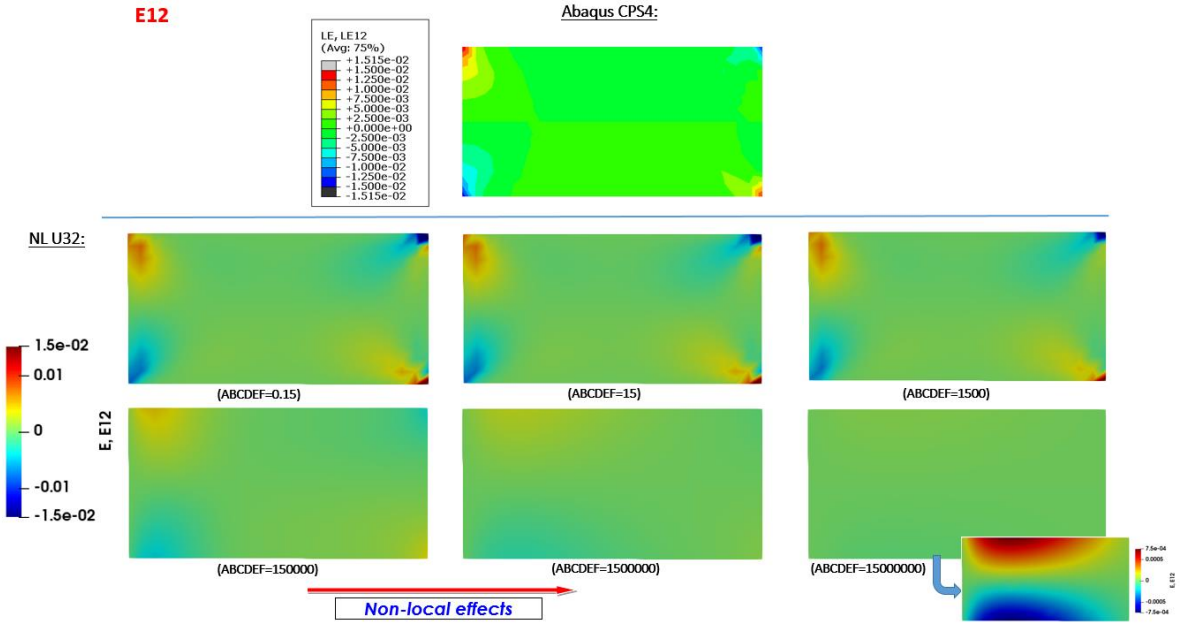

Figure 142: Comparison of E12 component for different Cf parameters values (Compression) – Non-linear Material and Non-Linear Geometry

4) Curvature/higher order bending strain fields **(*κ*)**:

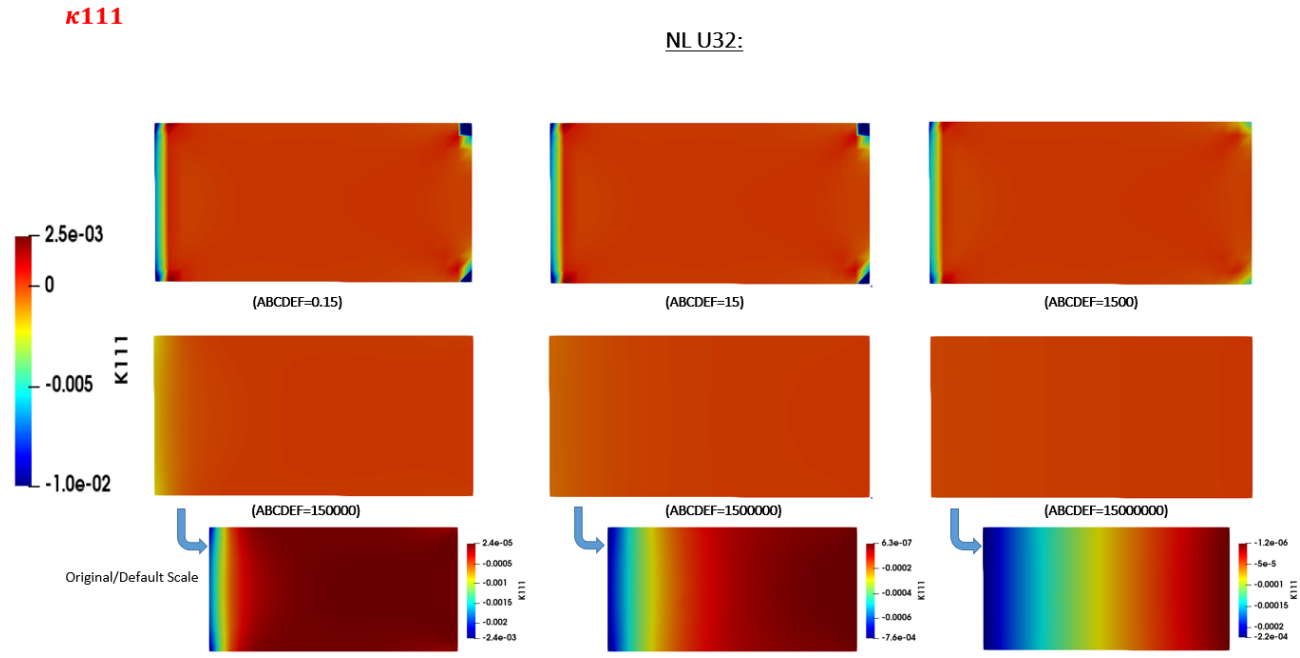

Figure 143: k111 component for different Cf parameters values (Compression) – Non-linear Material and Non-Linear Geometry

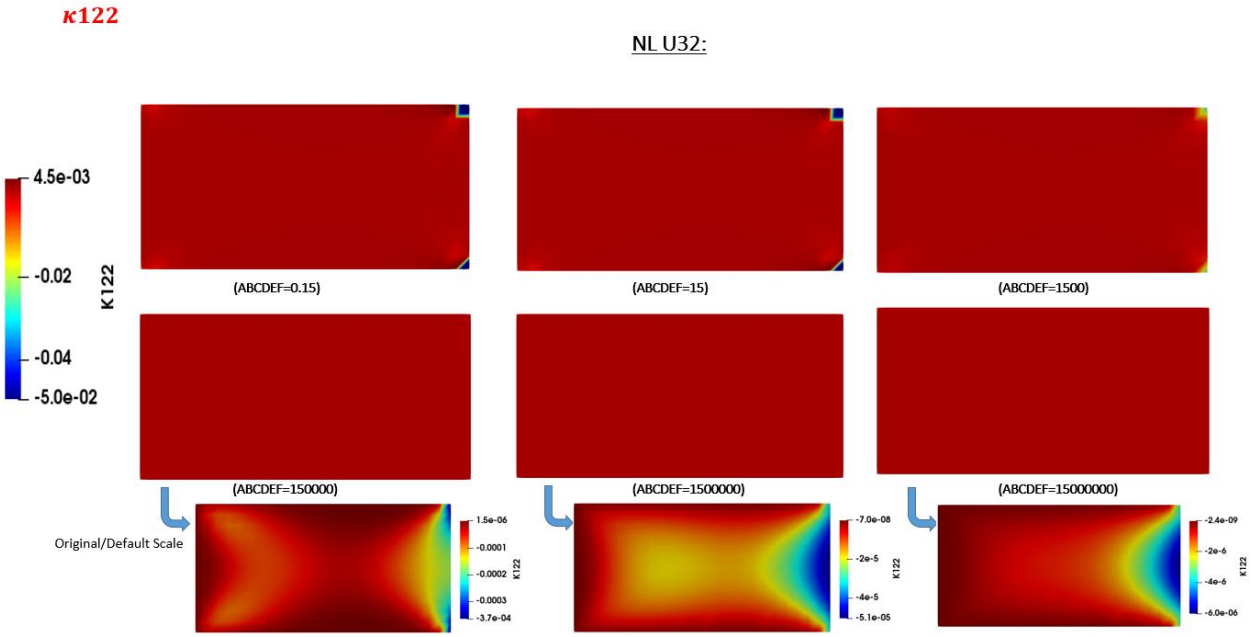

Figure 144: k122 component for different Cf parameters values (Compression) – Non-linear Material and Non-Linear Geometry

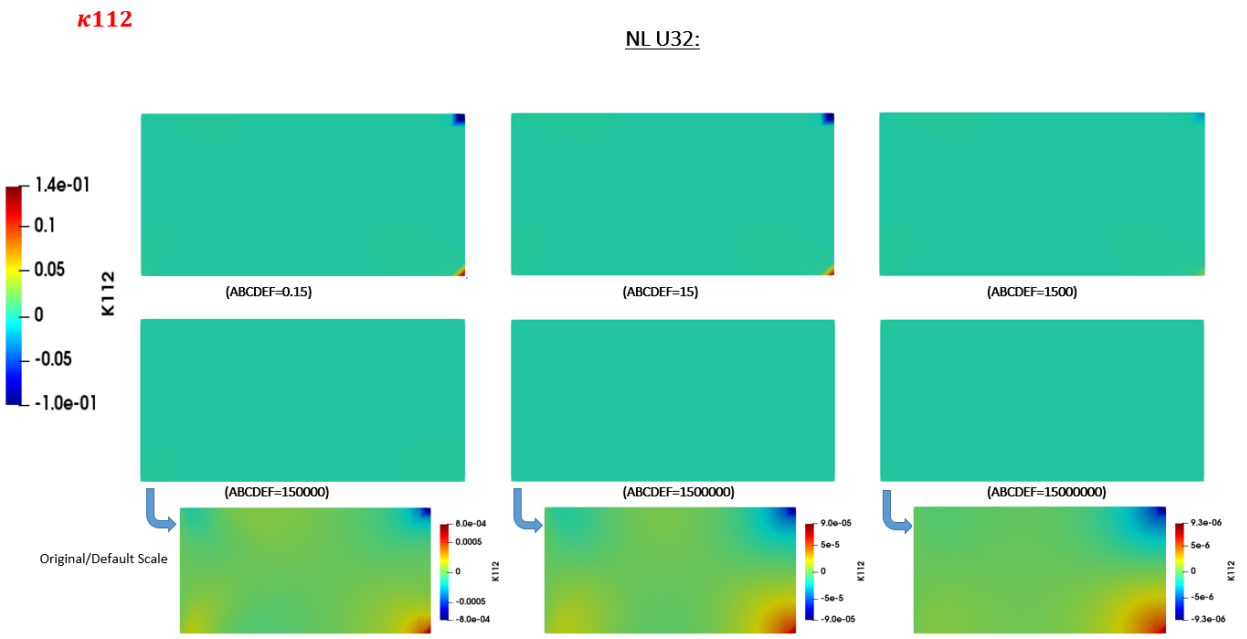

Figure 145: k112 component for different Cf parameters values (Compression) – Non-linear Material and Non-Linear Geometry

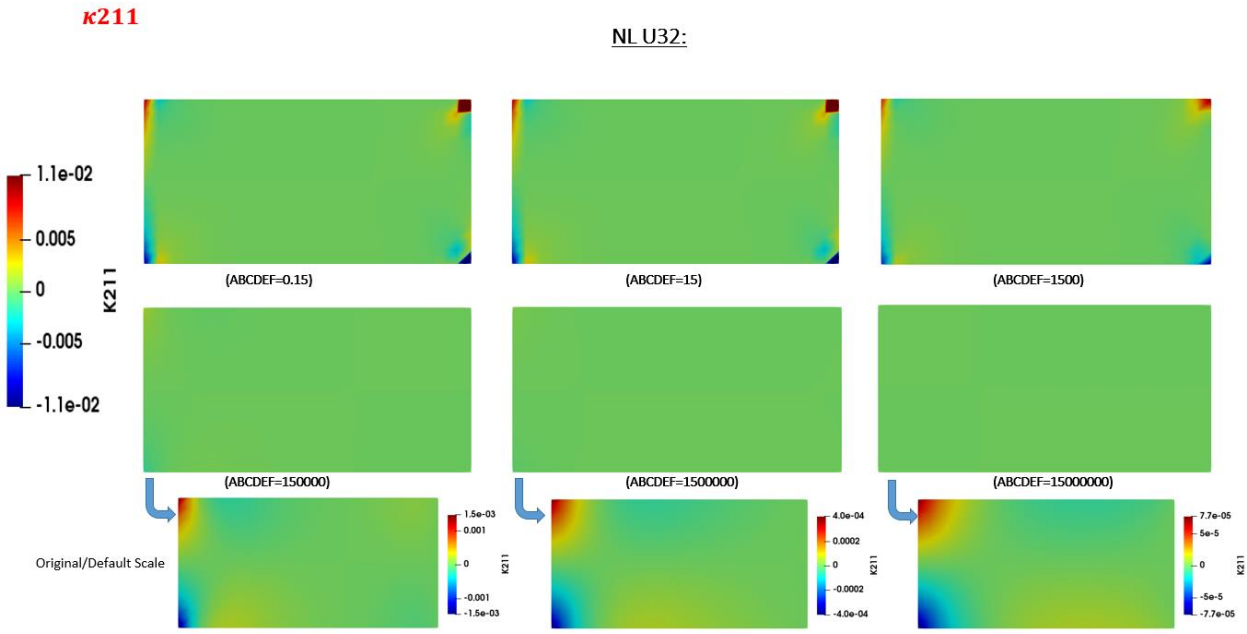

Figure 146: k211 component for different Cf parameters values (Compression) – Non-linear Material and Non-Linear Geometry

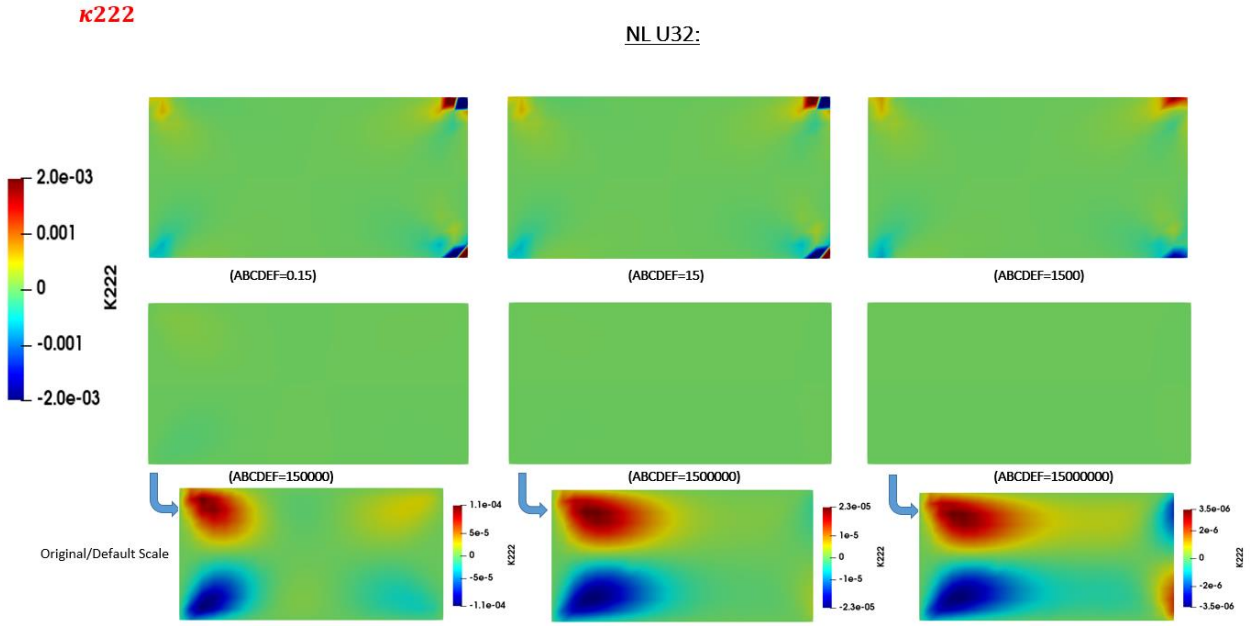

Figure 147: k222 component for different Cf parameters values (Compression) – Non-linear Material and Non-Linear Geometry

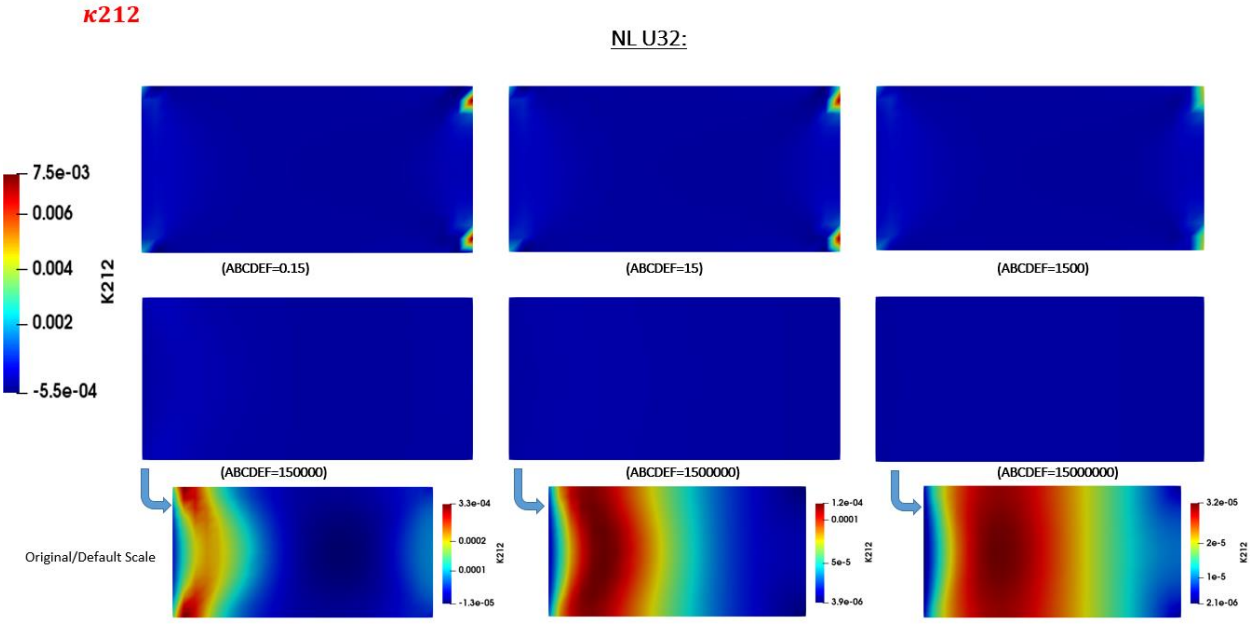

Figure 148: k212 component for different Cf parameters values (Compression) – Non-linear Material and Non-Linear Geometry

5) Distributed bending moment fields **(τ)**:

$\tau 111$

NL U32:

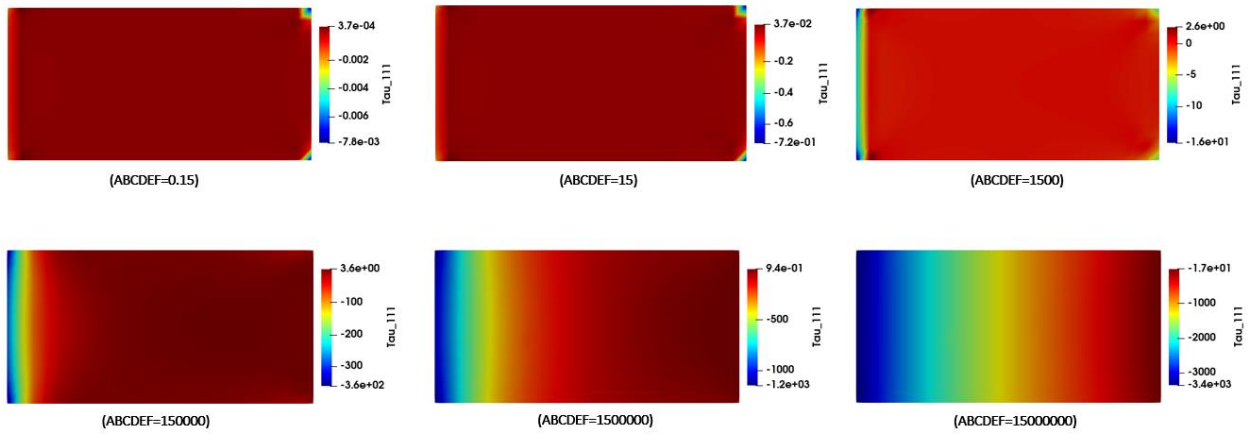

Figure 149: τ111 component for different Cf parameters values (Compression) – Non-linear Material and Non-Linear Geometry

$\tau 122$

NL U32:

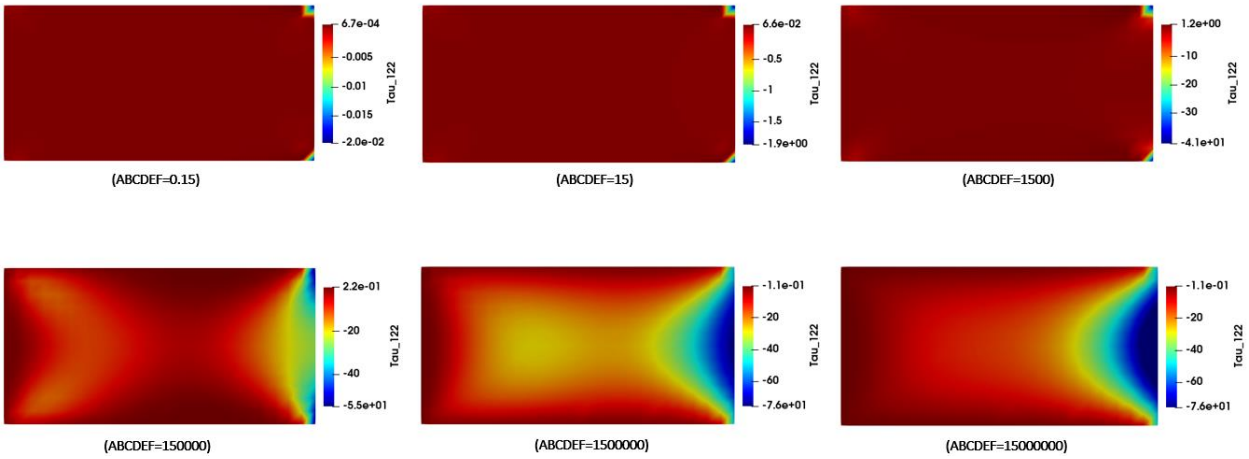

Figure 150: τ122 component for different Cf parameters values (Compression) – Non-linear Material and Non-Linear Geometry

$\tau 112$

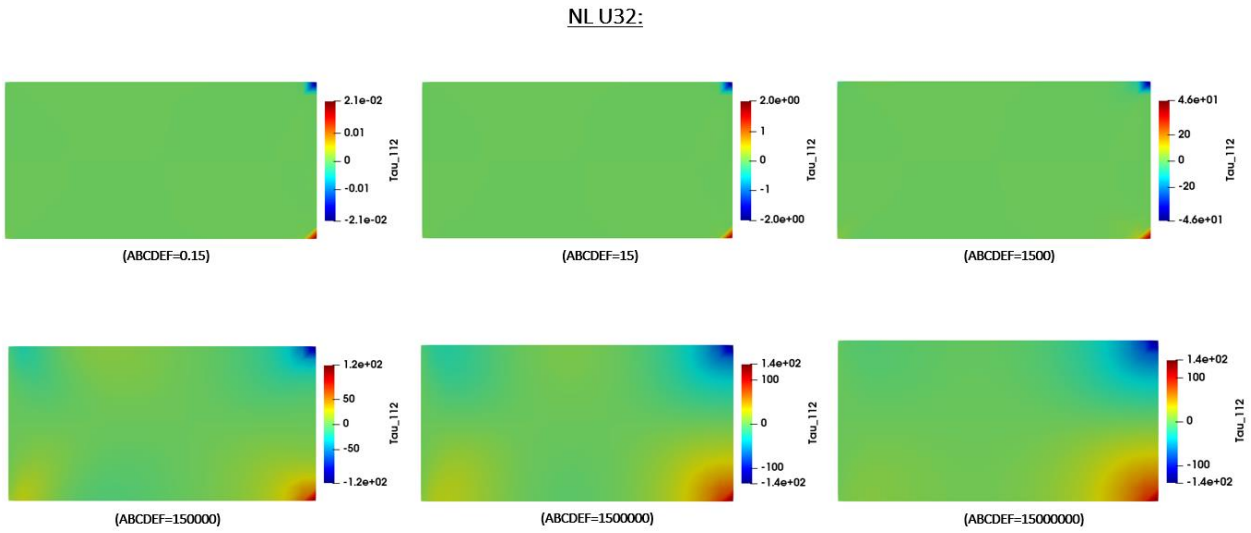

Figure 151: τ112 component for different Cf parameters values (Compression) – Non-linear Material and Non-Linear Geometry

$\tau 211$

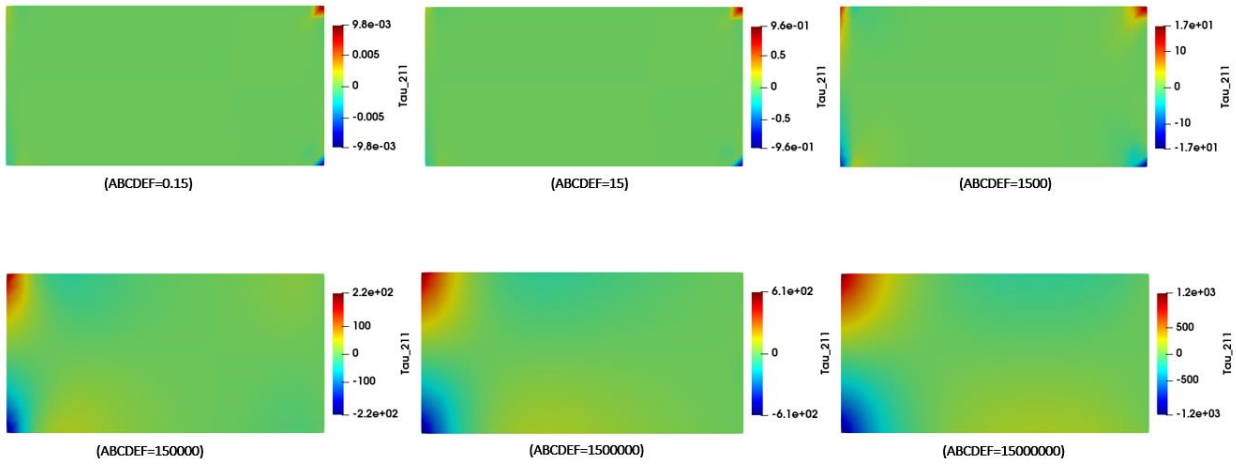

Figure 152: τ211 component for different Cf parameters values (Compression) – Non-linear Material and Non-Linear Geometry

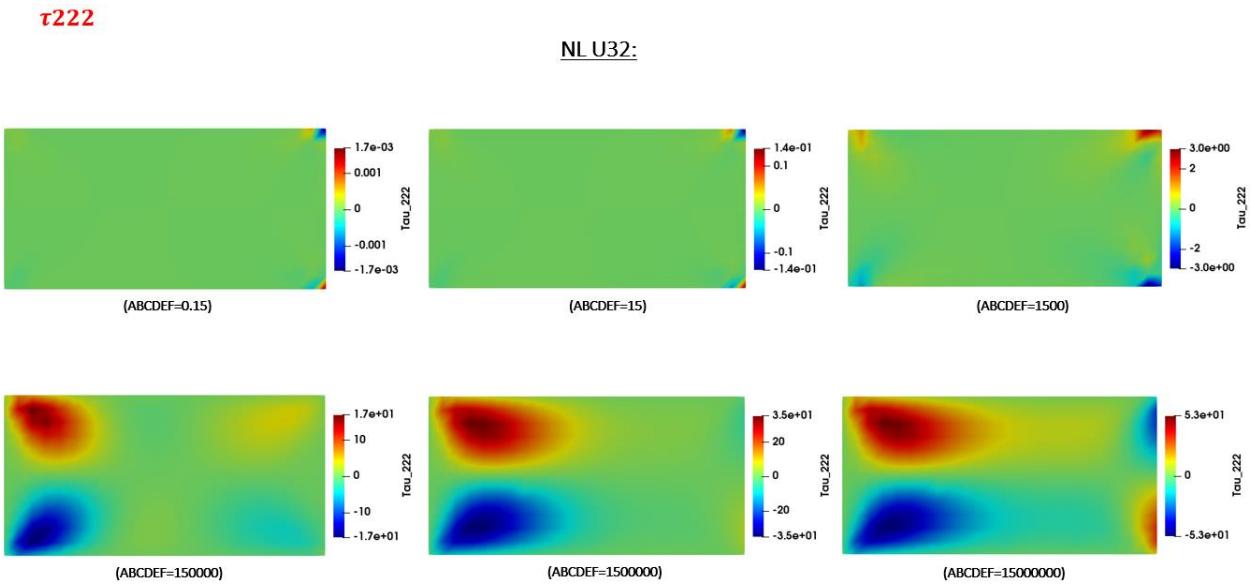

Figure 153: τ222 component for different Cf parameters values (Compression) – Non-linear Material and Non-Linear Geometry

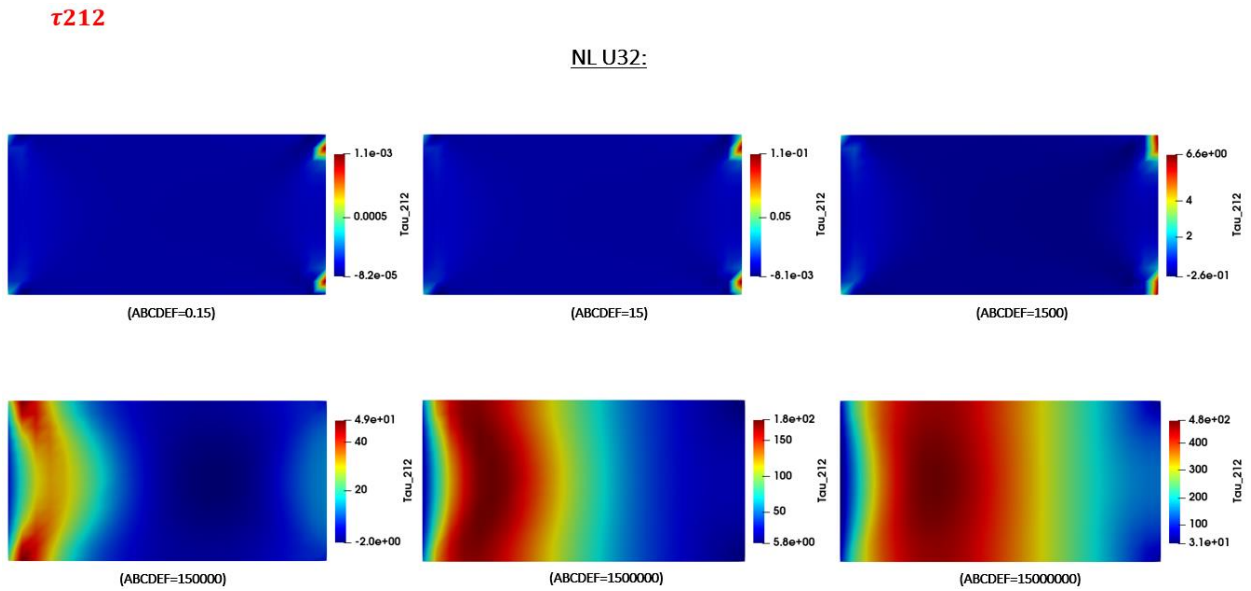

Figure 154: τ212 component for different Cf parameters values (Compression) – Non-linear Material and Non-Linear Geometry

Case2: Bending

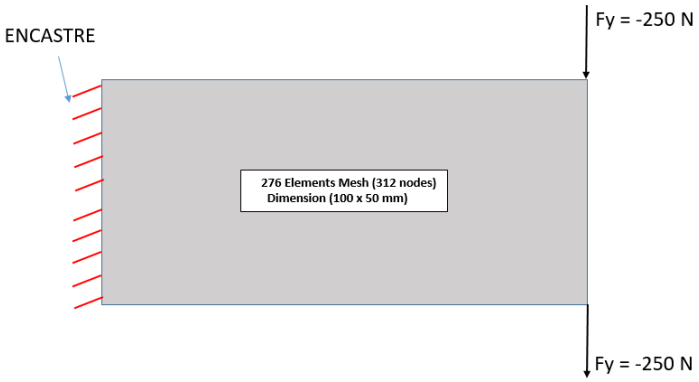

Figure 155: Mesh, Load and Boundary conditions (bending) – Material Non-linearity

1) Displacements:

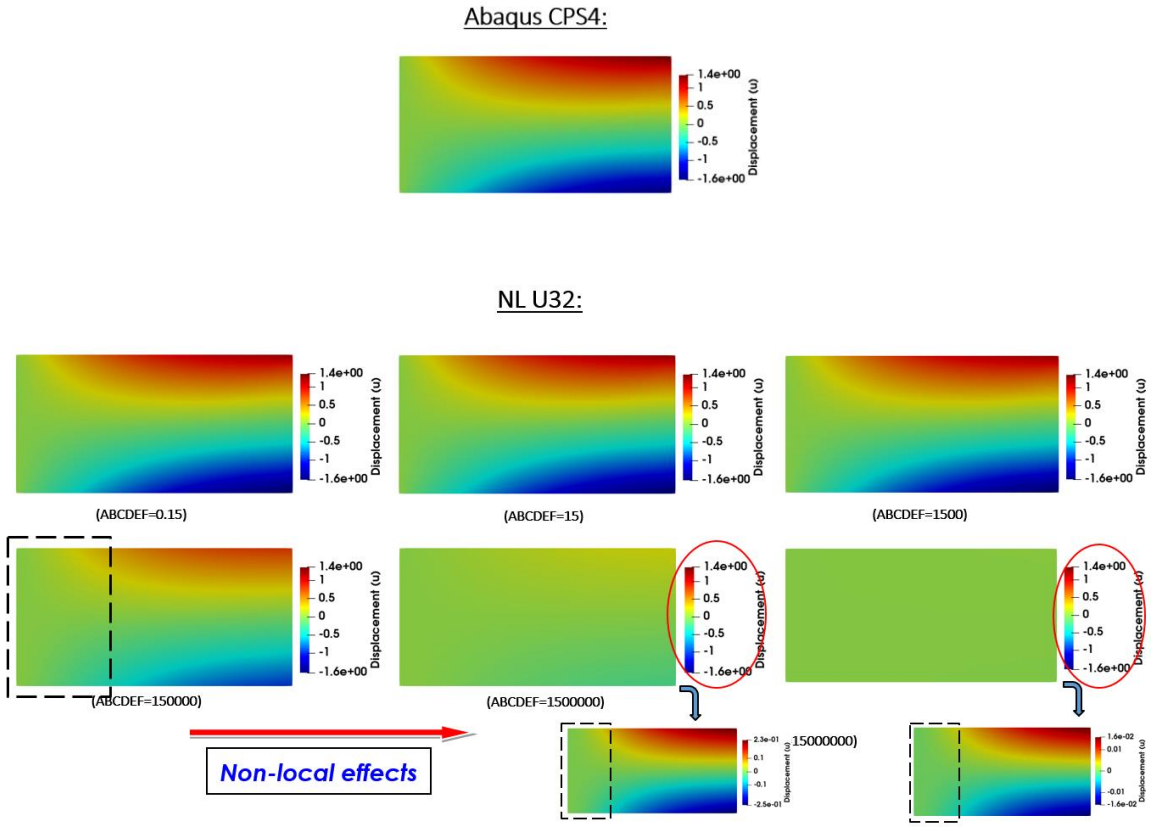

Figure 156: Comparison of Displacement Field (u) for different Cf parameters value (bending) – Non-linear Material and Non-Linear Geometry

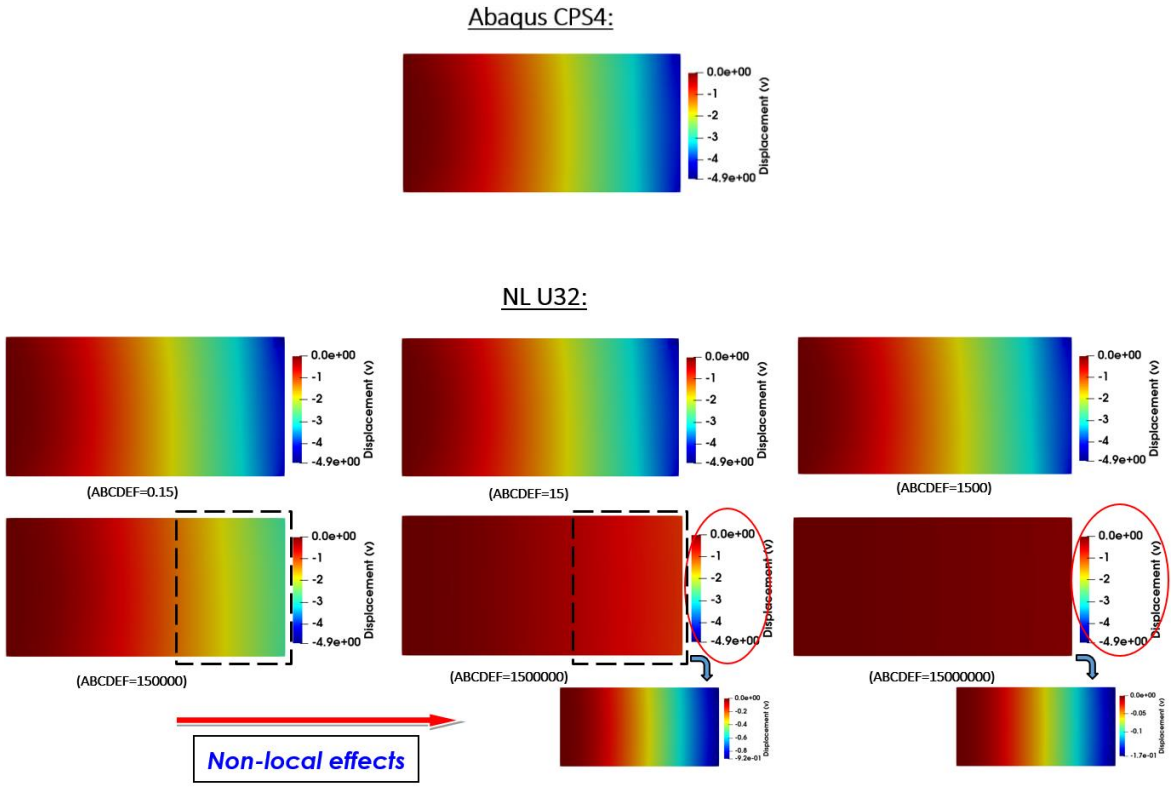

Figure 157: Comparison of Displacement Field (v) for different Cf parameters value (bending) – Non-linear Material and Non-Linear Geometry

2) Stress Fields (***S***):

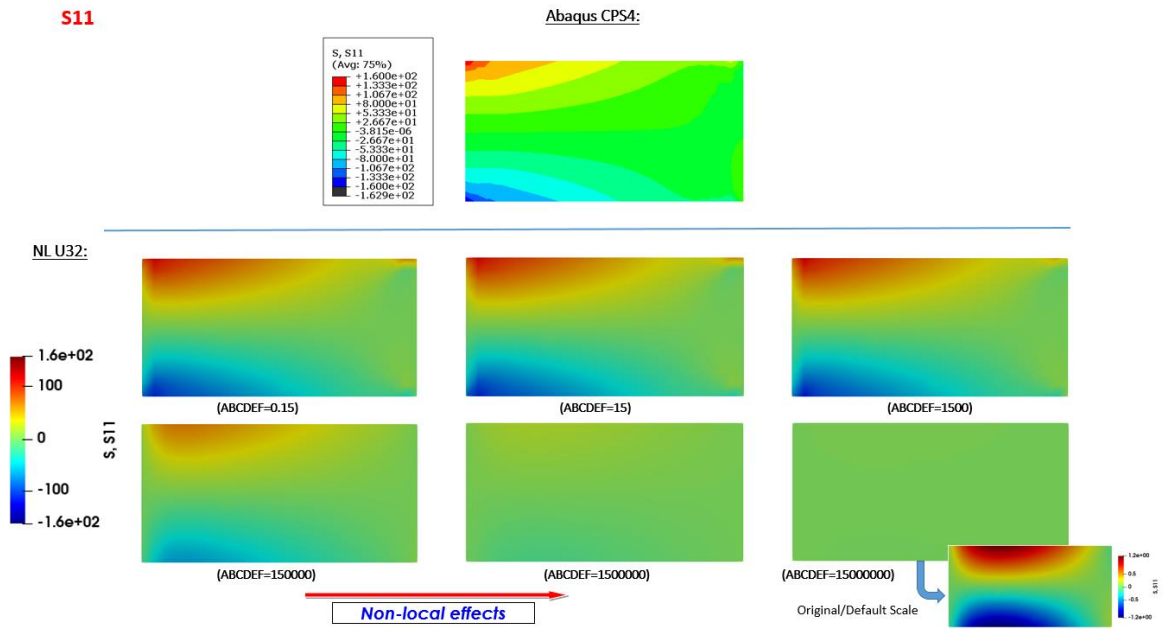

Figure 158: Comparison of S11 component for different Cf parameters values (Bending) – Non-linear Material and Non-Linear Geometry

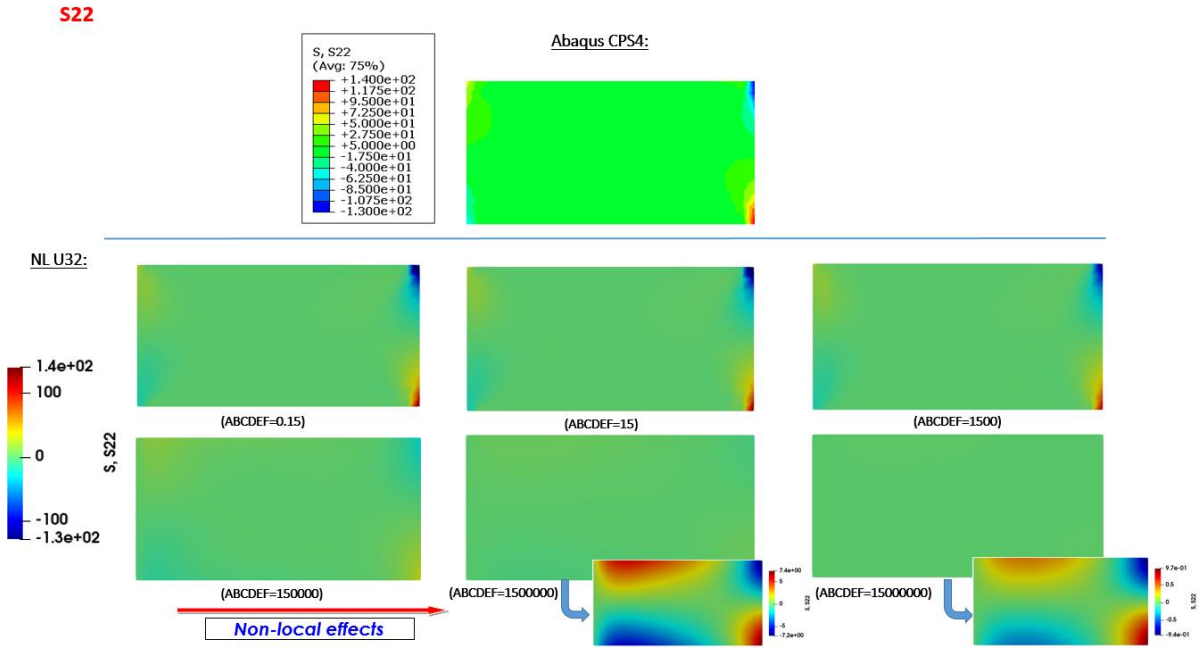

Figure 159: Comparison of S22 component for different Cf parameters values (Bending) – Non-linear Material and Non-Linear Geometry

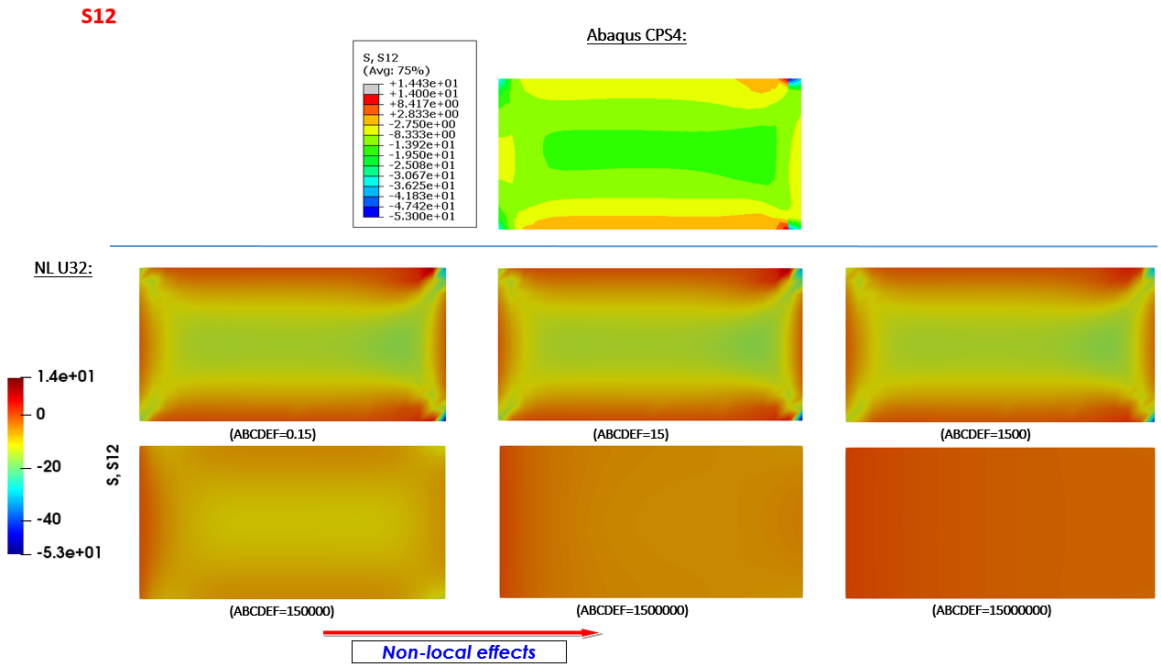

Figure 160: Comparison of S12 component for different Cf parameters values (Bending) – Non-linear Material and Non-Linear Geometry

3) Strain Fields (***E***):

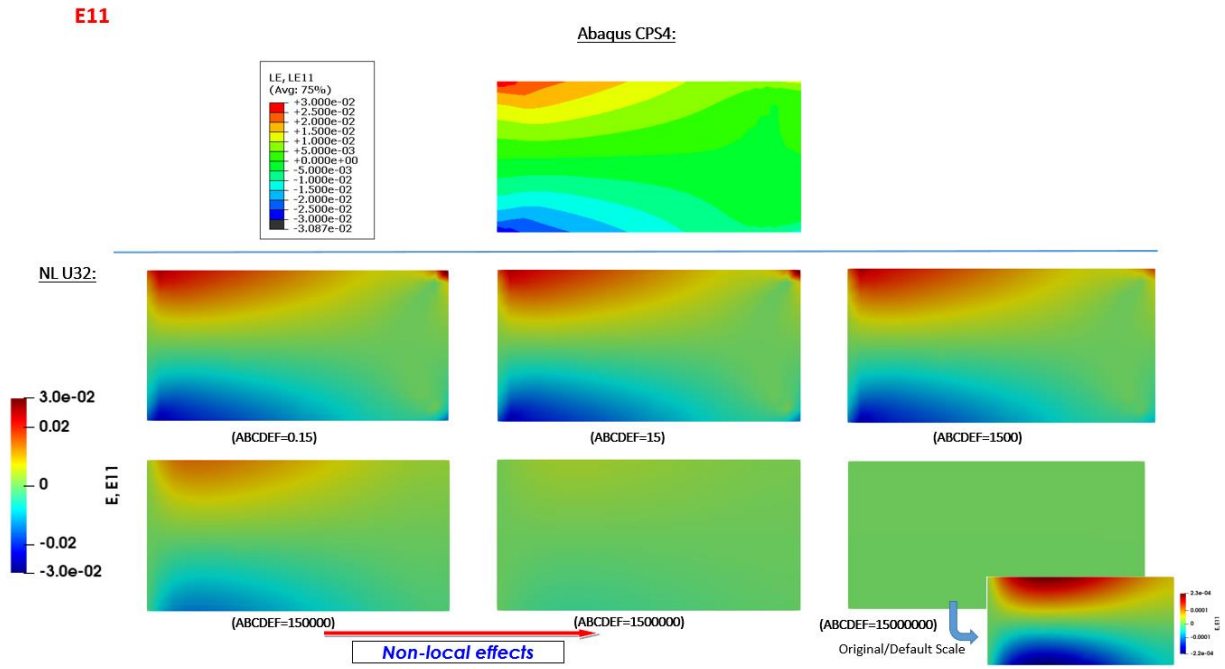

Figure 161: Comparison of E11 component for different Cf parameters values (Bending) – Non-linear Material and Non-Linear Geometry

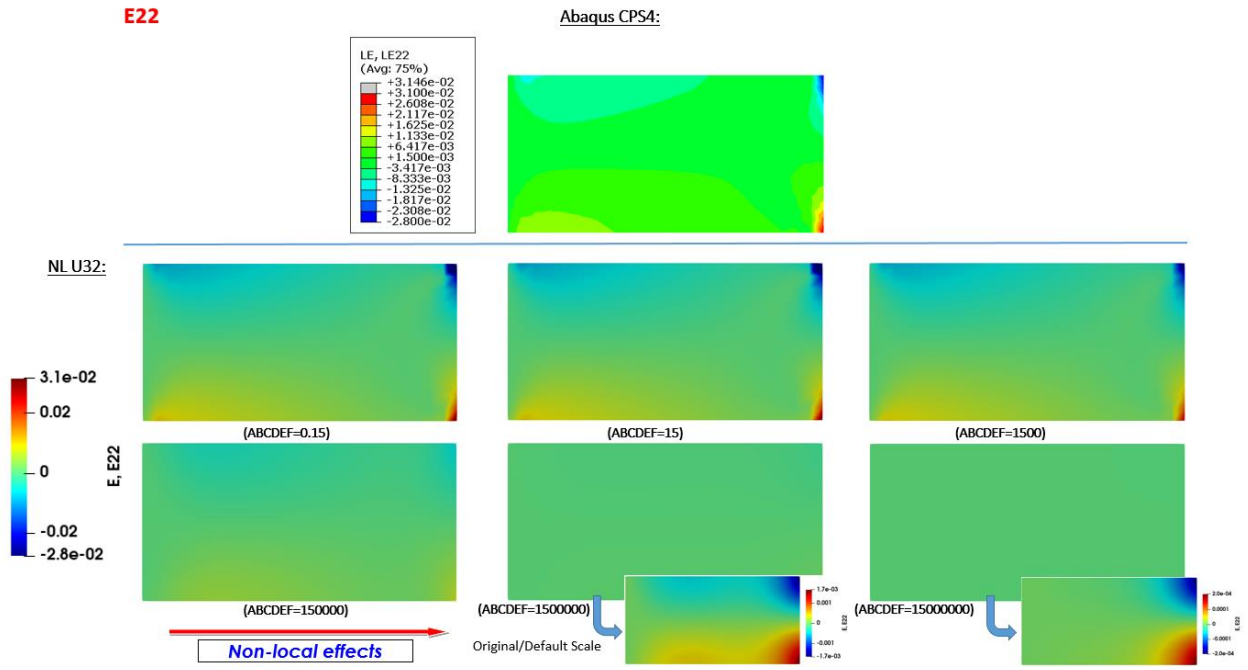

Figure 162: Comparison of E22 component for different Cf parameters values (Bending) – Non-linear Material and Non-Linear Geometry

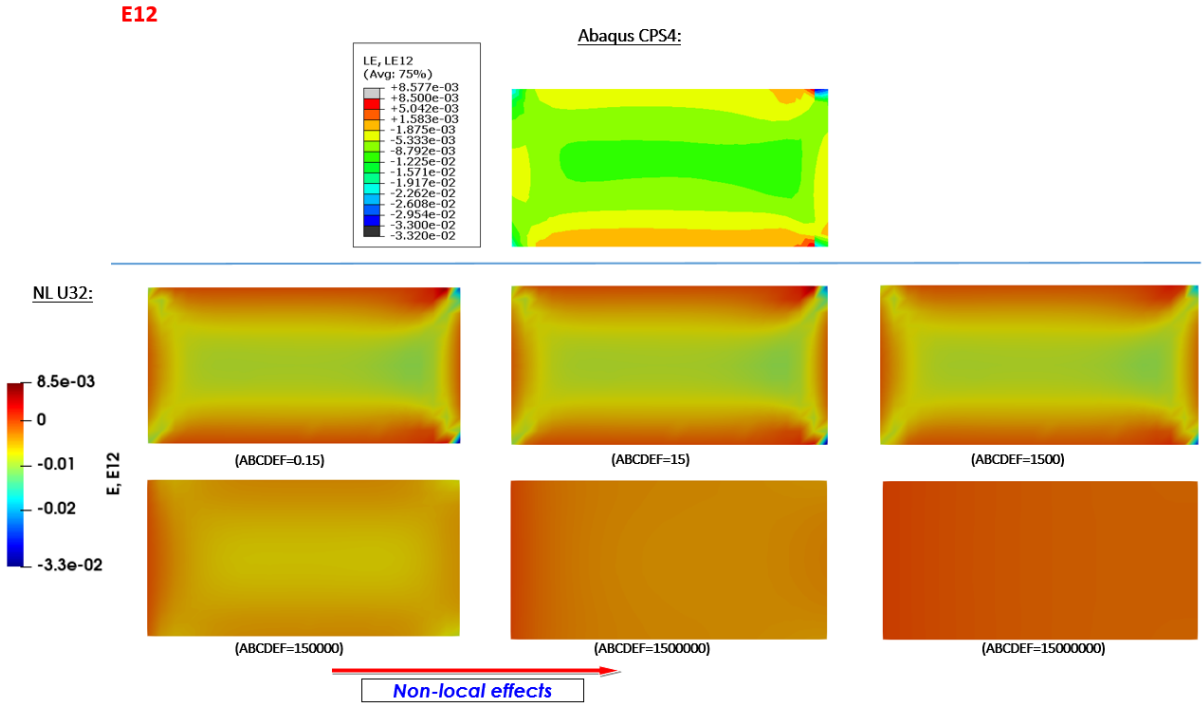

Figure 163: Comparison of E12 component for different Cf parameters values (Bending) – Non-linear Material and Non-Linear Geometry

4) Curvature/higher order bending strain fields **(*κ*)**:

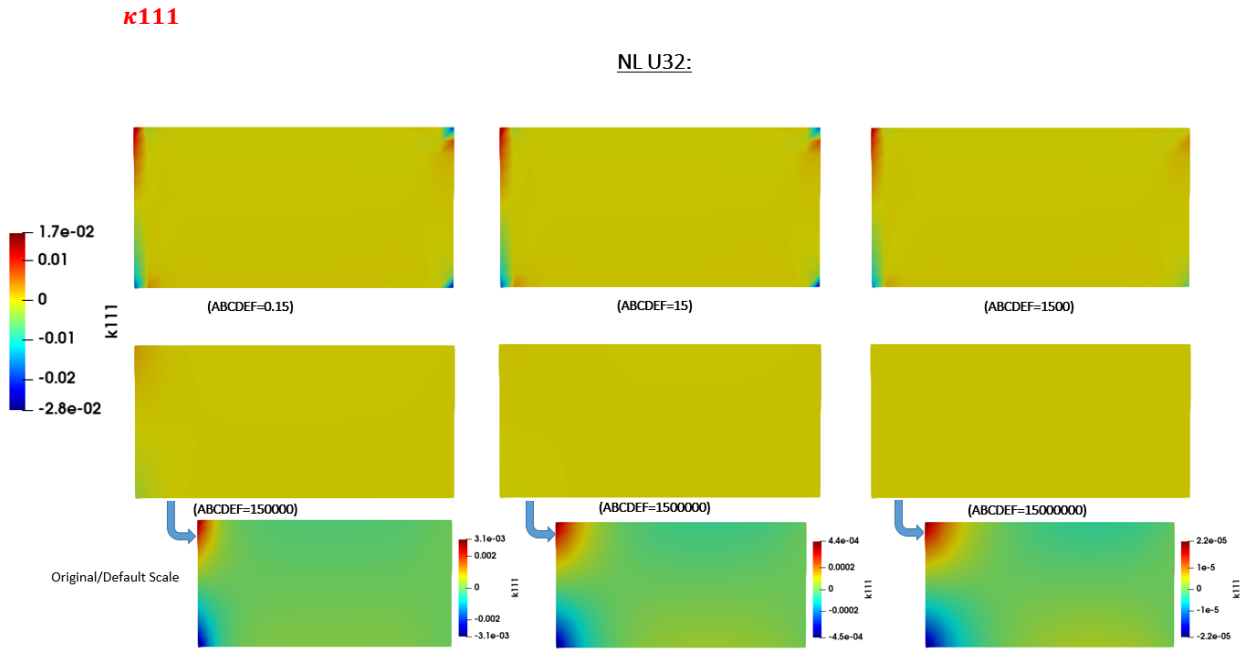

Figure 164: k111 component for different Cf parameters values (bending) – Non-linear Material and Non-Linear Geometry

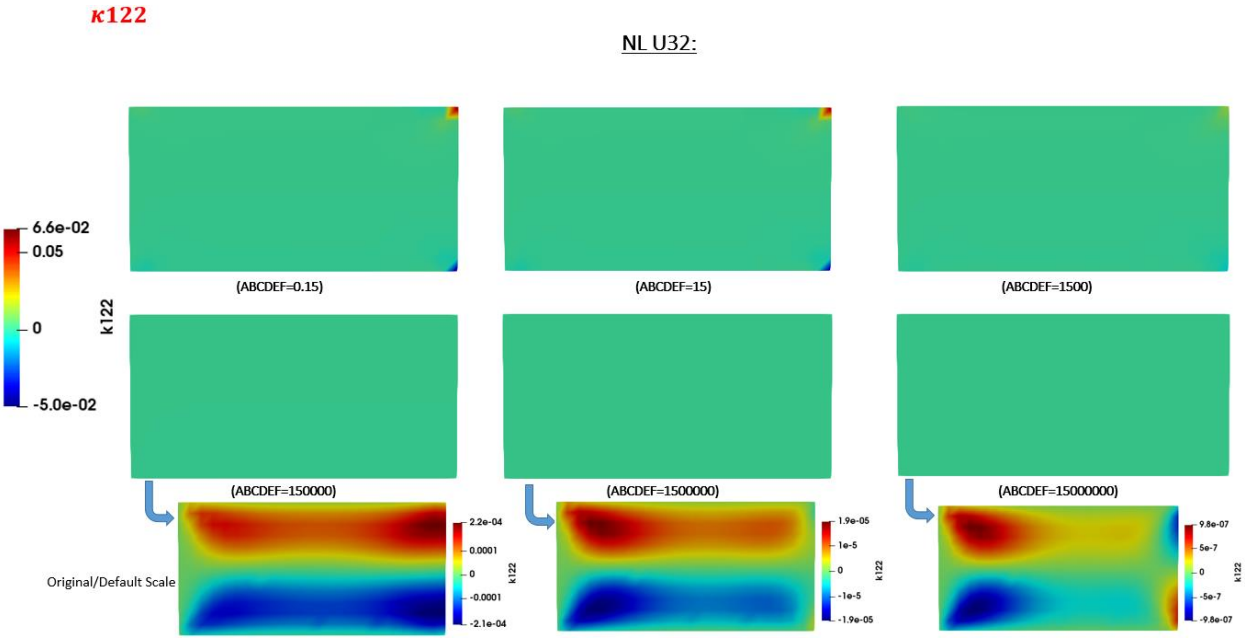

Figure 165: k122 component for different Cf parameters values (bending) – Non-linear Material and Non-Linear Geometry

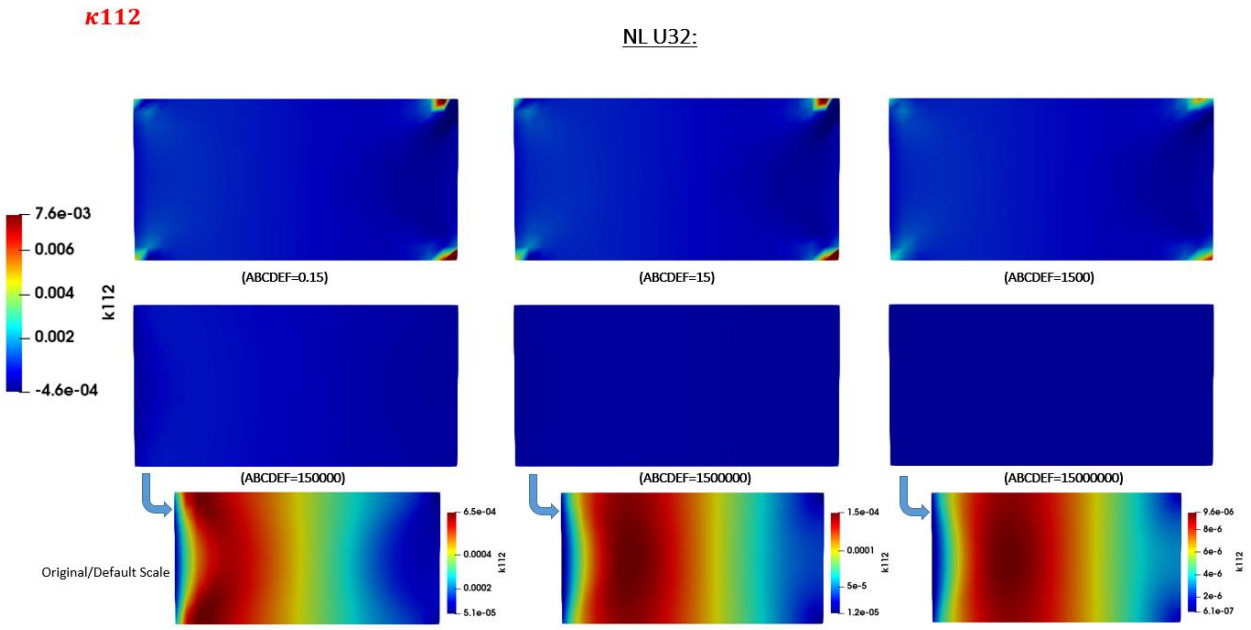

Figure 166: k112 component for different Cf parameters values (bending) – Non-linear Material and Non-Linear Geometry

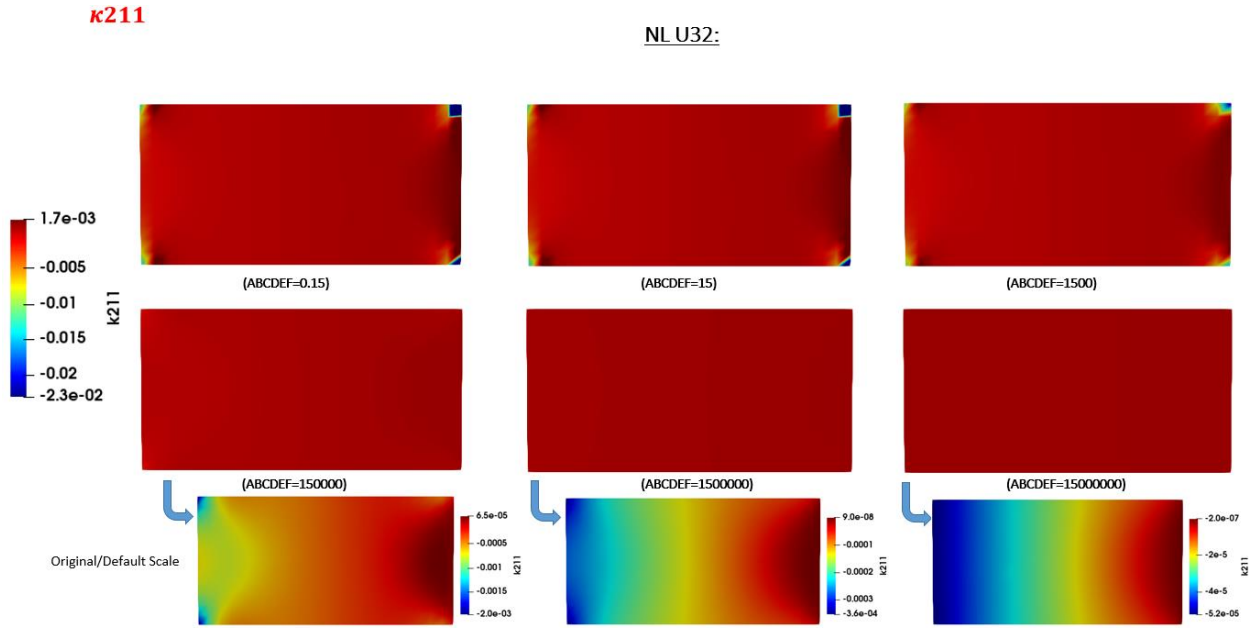

Figure 167: k211 component for different Cf parameters values (bending) – Non-linear Material and Non-Linear Geometry

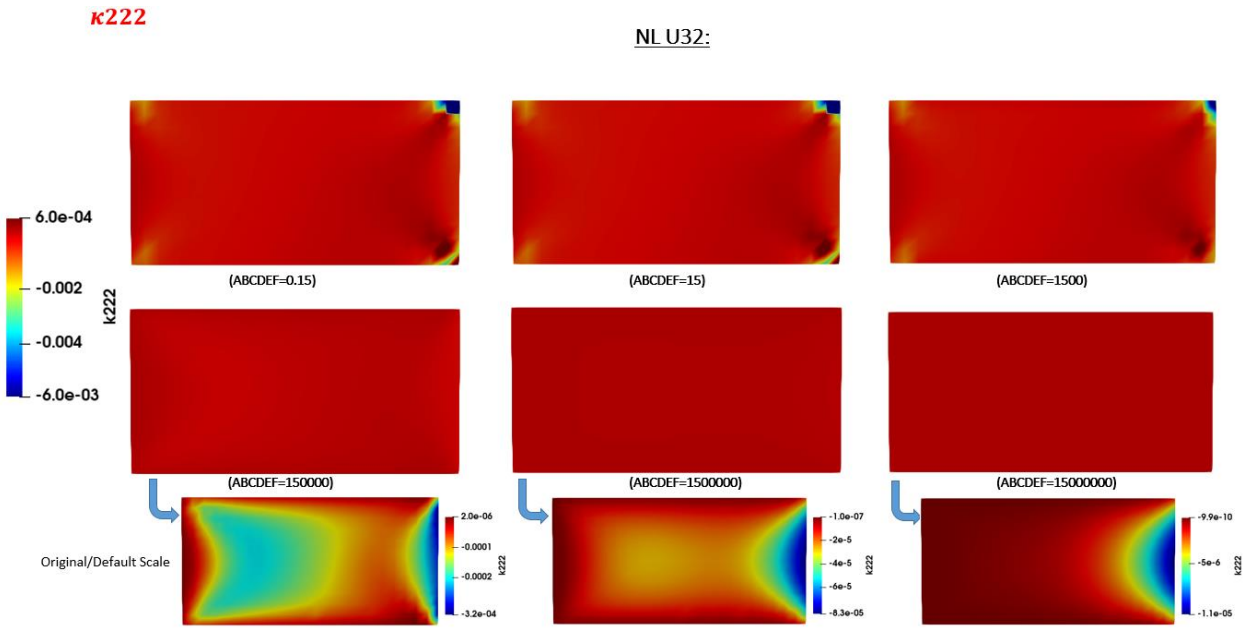

Figure 168: k222 component for different Cf parameters values (bending) – Non-linear Material and Non-Linear Geometry

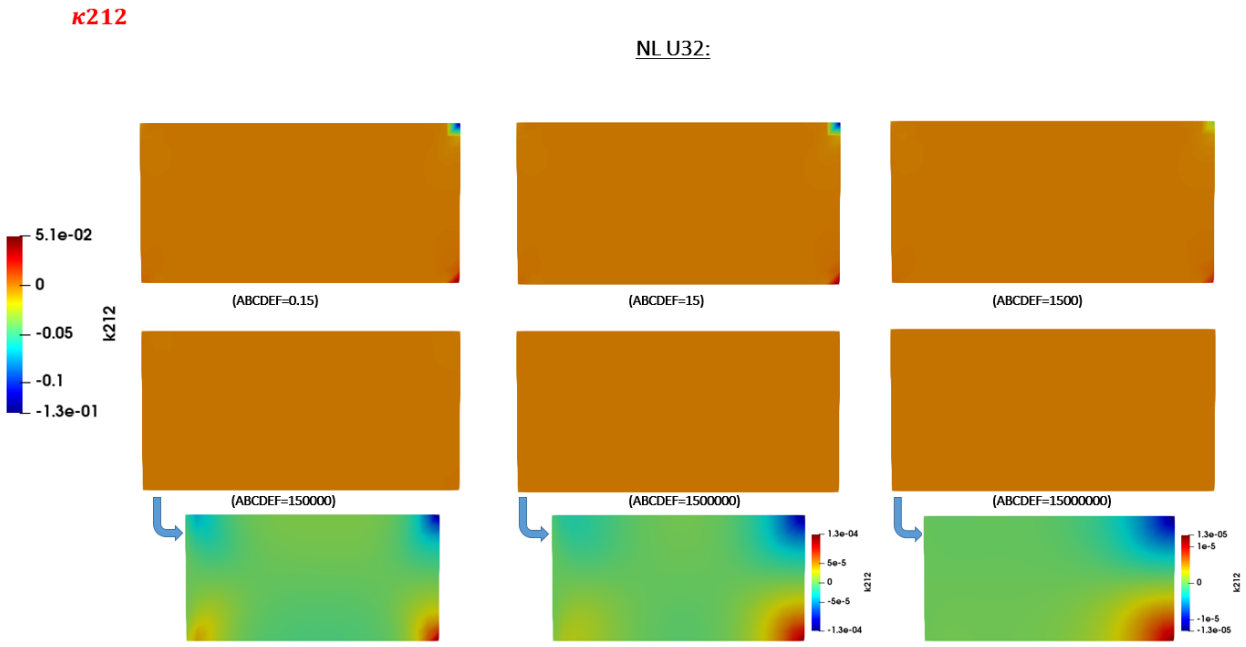

Figure 169: k212 component for different Cf parameters values (bending) – Non-linear Material and Non-Linear Geometry

5) Distributed bending moment fields **(τ)**:

τ111

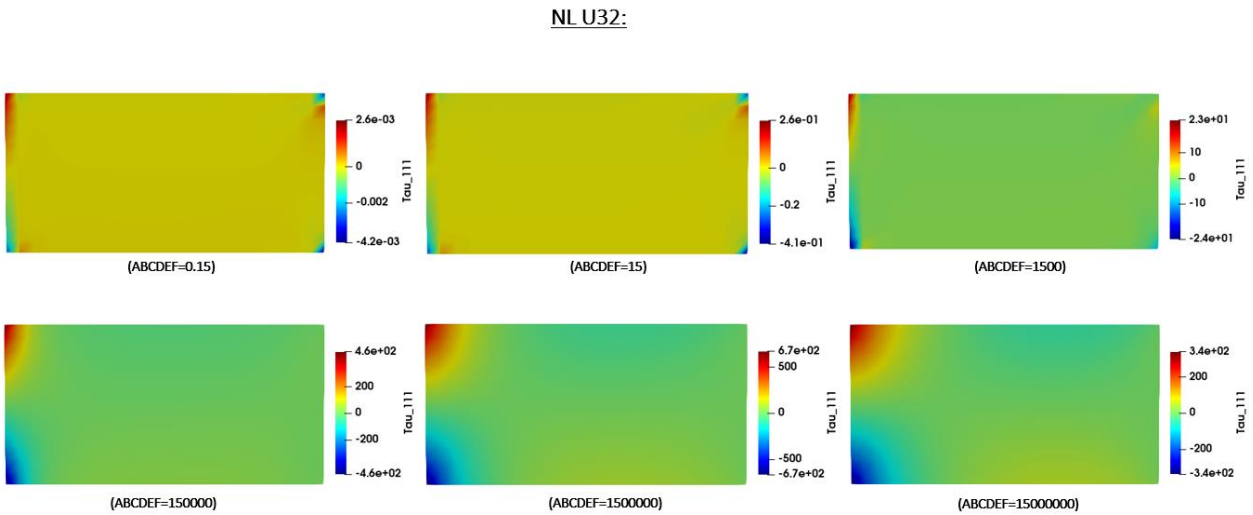

Figure 170: τ111 component for different Cf parameters values (bending) – Non-linear Material and Non-Linear Geometry

τ122

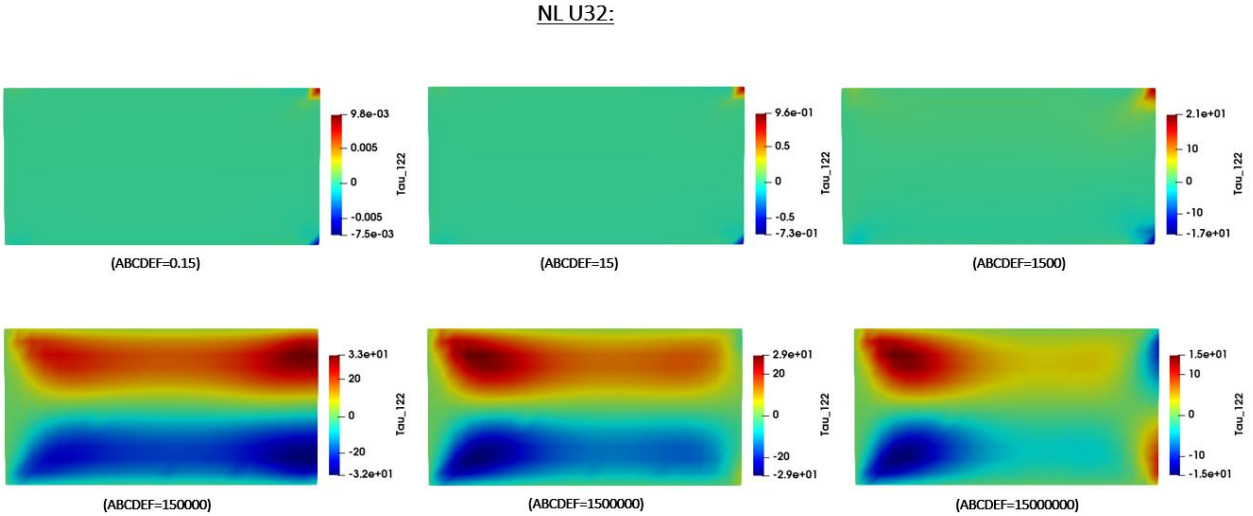

Figure 171: τ122 component for different Cf parameters values (bending) – Non-linear Material and Non-Linear Geometry

$\tau 112$

NL U32:

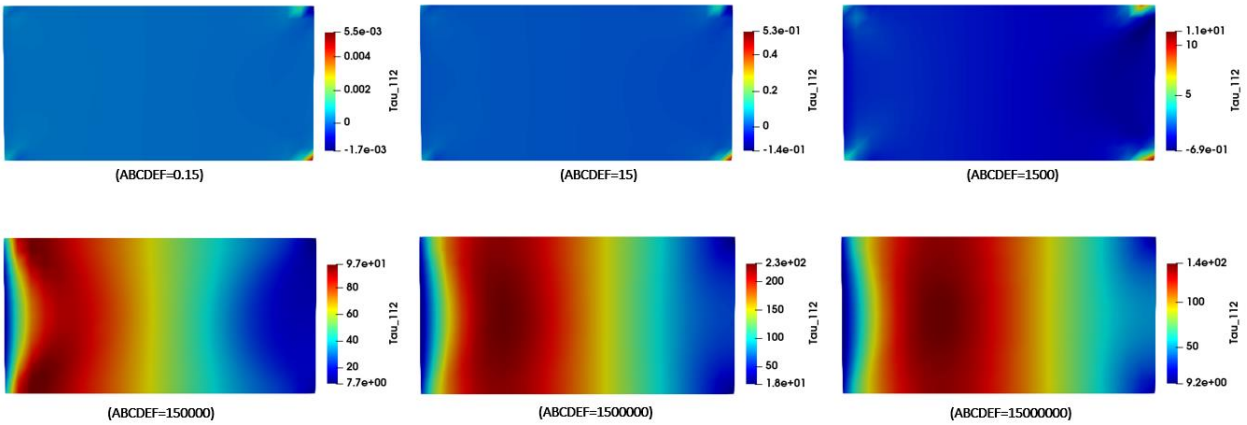

Figure 172: τ112 component for different Cf parameters values (bending) – Non-linear Material and Non-Linear Geometry

$\tau 211$

NL U32:

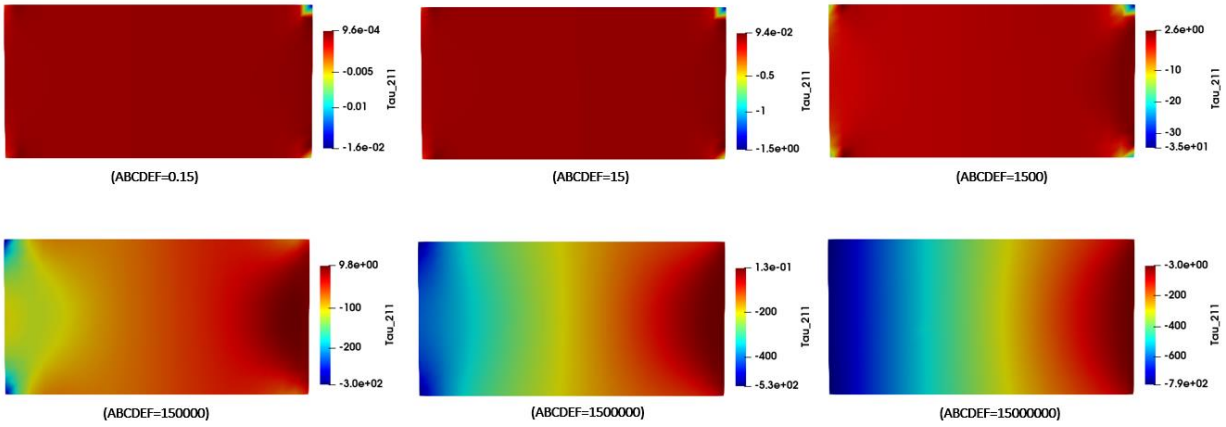

Figure 173: τ211 component for different Cf parameters values (bending) – Non-linear Material and Non-Linear Geometry

$\tau 222$

NL U32:

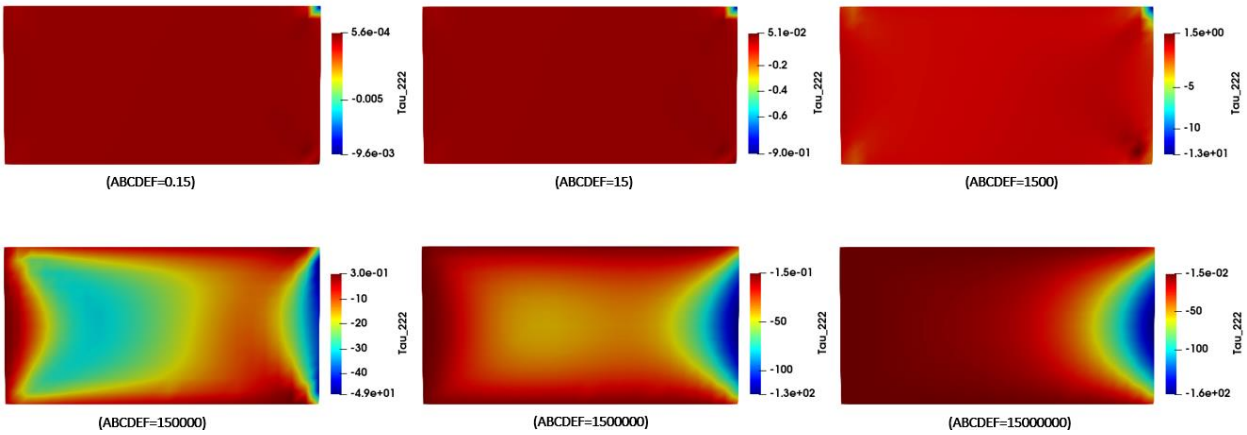

Figure 174: τ222 component for different Cf parameters values (bending) – Non-linear Material and Non-Linear Geometry

$\tau 212$

NL U32:

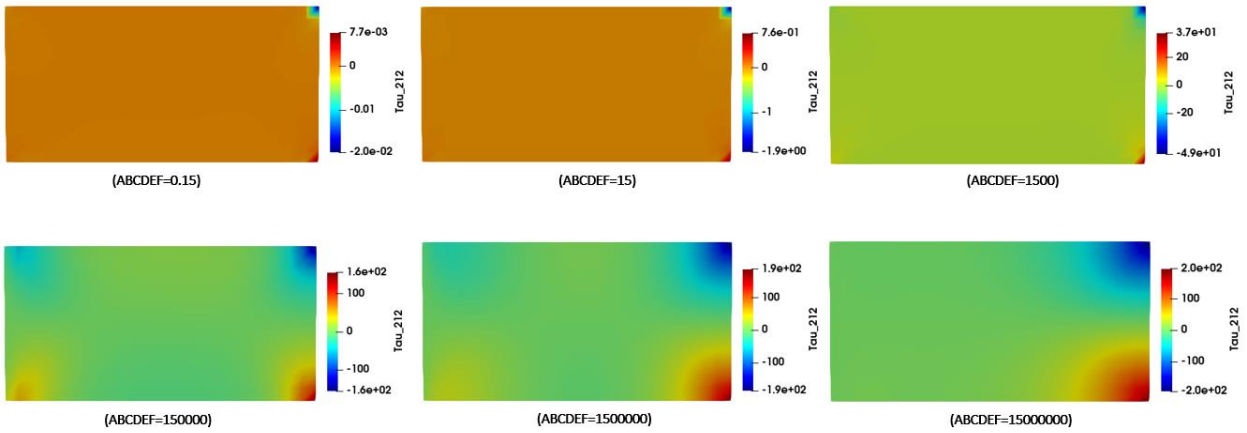

Figure 175: τ212 component for different Cf parameters values (bending) – Non-linear Material and Non-Linear Geometry

References

[A] [1] Argon, A.S., (1972). Fracture of Composites. Treatise of Materials Science and Technology, vol.1, Academic Press, New York.

[2] Adams, D., (2005). Test methods and fixtures currently available to test the compressive strength of composites [Internet blog post]. Retrieved from: https://www.compositesworld.com/articles/current-compression-test-methods

[3] Automated Dynamics company.[Internet]. (2018). Composite-basics. Retrieved from: http://www.automateddynamics.com/article/composite-basics/thermoset-vs-thermoplastic-composites.

[4] Abdel Ghafaar, M., Mazen, A.A., El-Mahallawy, N.A., (2006). Behavior of woven fabirc reinforced epoxy composites under bending and compressive loads. Journal of Engg. Sci., 34(2), 453-469.

[5] Aifantis, E.C., Bammann, D.J., (1982). On a proposal for a continuum with microstructure. Acta Mechanica. 45, 91-121.

[6] Aifantis, E.C., Serrin, J.B., (1983). The mechanical theory of fluid interfaces and Maxwell's rule. J. Coll. Int. Sci. 96, 517–529.

[7] Aifantis, E.C., (1984 a). Maxwell and van der Waals revisited. In: Tsakalakos, T. (Ed.), Phase Transformations in Solids. North-Holland, pp. 37–49.

[8] Aifantis, E.C., (1984 b). On the microstructural origin of certain inelastic models. Journal of Engg. Mater. Tech. 106(4), 326-330.

[9] Aifantis, E.C., (1987). The physics of plastic deformation. Int. J. Plasticity 3, 211–247.

[10] Aifantis, E.C., (1992). On the role of gradients in the localization of deformation and fracture. Int. Journal of Engg. Sci., 30(10), 1279-1299.

[11] Aifantis, E.C., (1995). Pattern formation in plasticity. Int. J. Engg. Sci. 33, 2161–2178.

[12] Aifantis, E.C., (1996). Non-linearity, periodicity and patterning in plasticity and fracture. Int. J. Non-Linear Mech. 31, 797–809.

[13] Aifantis, E.C., (2003). Update on a class of gradient theories. Mech. of Materials, 35, 259-280.

[14] Amanatidou, E., Aravas., N., (2002). Mixed finite element formulations of strain gradient elasticity problems. Comput. Methods Appl. Mech. Engg. 191, 1723-1751.

[15]Abaqus 6.10 user's manual (Section 1.1.23 and 29.16.1). Retrieved from https://www.sharcnet.ca/Software/Abaqus610/Documentation/docs/v6.10/books/sub/default.htm?startat=ch01s01asb23.html#sub-rtn-uuel

[16] Abaqus theory manual, version 2017 (Section 4.3.9).

[17] Aboudi, J., Gilat., R., (2006). Buckling analysis of fibers in composite materials by wave propagation analogy. Int. Journal of Solids and Structures. 43, 5168-5181.

[B] [1] Berhe, G. [Internet]. (2015). Textile Reinforced Composites. Retreived from: https://www.slideshare.net/GranchBerheTseghai/2-textile-reinforced-composites-52380588.

[2] Bilisik, K., Sahbaz Karaduman, N., Bilisik, N.E., Bilisik, H.E., (2014). Three dimensional (3D) circular various weave patterns in woven preform structures. Textile Research Journal. 84, 638-654.

[3] Budiansky, B., (1983) Micromechanics, Computers and Structures, 16 (1), 3-12.

[4] Budiansky, B., Fleck, N.A., (1993) Compressive failure of fiber composite, J. Mech. Phys. Solids, 41 (1), 183-211.

[5] Bouvet, C., (2017). Mechanics of Aeronautical Composite Meaterials. Retrieved from: http://books.google.com.

[6] Borst, R. de., Muhlhaus, H.B., (1992). Gradient dependent plasticity: formulation and algorithmic aspects, Int. J. Numer. Methods Engg. 35, 521-540.

[7] Borst, R. de., Pamin, J., (1996). Some novel developments in finite element procedures for greadient-dependent plasticity, Int. J. Numer. Methods Engg. 39, 2477-2505.

[8] Bogner, F. K., Fox, R. L. and. Schmit, L. A., (1965). The Generation of Inter-element Compatible Stiffness and Mass Matrices by the Use of Interpolation Formulas, Proceedings of the Conference on Matrix Methods in Structural Mechanics, Wright-Patterson Air Force Base, Ohio, October 1965, pp. 397-444.

[9] Bathe, K.J., (1982). The Finite Element Procedures in Engineering Analysis. Prentice-Hall.

[10] Biomomentum., (2016). Mach-1 -3-point or 4-point bending test [Internet company test setup Report]. Retrieved from: https://biomomentum.com/wpcontent/themes/biomomentum/library/images/zoho/Publications/MA056-SOP11-D%20v2%20Mach-1%20-%203-point%20or%204-point%20Bending%20Test.pdf

[11] Boisse, P., Borr, M.,Buet, K., Cherouat, A., (1997). Finite element simulations of textile composite forming including the biaxial fabric behavior. Composites: Part B 28B, 453-464.

[12] Boisse, P., Buet, K., Gasser, A., Launay, J., (2001). Meso/macro-mechanical behavior of textile reinforcements for thin composites. Composites Science and Technology. 61 (3), 395-401.

[13] Boise, P., Zouari, B., Daniel, J., (2006). Importance of in-plane rigidity in finite element analysis of woven fabric composite preforming. Composites: Part A 37, 2201-2212.

[14] Berkache, K., Deogekar, S., Goda, I., Picu, R.C., Ganghoffer., J.-F. (2017). Construction of second gradient continuum models for random fibrous networks and analysis of size effects. Composites structures 181, 347-357.

[15] Breiman, U., Aboudi, J., Haj-Ali, R., (2017). Semianalytical compressive strength criteria for unidirectional composites. Journal of Reinforced Plastics and Composites, 37(4), 238-246.

[16] Basu, S., Waas, A.M., Ambur, D.R., (2006). A macroscopic model for kink banding instabilities in fiber composites. Journal oof Mechanics of Materials and Structures, 1(6).

[17] Basu, S., (2005). Computational modeling of progressive failure and damage in composite laminates. Ph.D thesis, Aerospace Engineering Department, University of Michigan, Ann Arbor.

[18] Bishara, M., Rofles., R, Allix., O., (2017). Revealing complex aspects of compressive failure of polymer composites - Part I: Fiber kinking at microscale. Composites structures, 169, 105-115.

[19] Bishara, M., Vogler., Rofles., R., (2017). Revealing complex aspects of compressive failure of polymer composites - Part II: Failure interactions in multidirectional laminates and validation. Composites structures, 169, 116-128.

[20] Brandt J., Drechsler K., and Arendts F. J., (1996). Mechanical performance of composites based on various three-dimensional woven-fiber preforms. Composite Science and Technology. 56, 381-386.

[21] BMW i3 passenger compartment made of composites, BMW group®.
Retreived from: http://www.bmw.com/com/de/insights/corporation/bmwi/concept.html

[22] Boat Building Plans [Pinterest Post].
Retreived from: https://www.pinterest.fr/pin/745275438309528227/

[C] [1] Cosserat, E., Cosserat, F., (1909). Therie des Corps Deformables. Paris: Hermann & Fils.

[2] Cox, B.N., Dadkhah, M.S., Morris, W.L., Flintoff, J.G., (1994). Failure mechanisms of 3D woven composites in tension, compression and bending. Acta. metall. mater. 42(12), 3967-3984.

[3] Chen, X., Taylor, L.W., Tsai, L.J., (2011). An overview on fabrication of three-dimensional woven textile preforms for composites. Text Res Journal. 81(9), 932-944.

[D] [1] Drapier S., Grandidier, J.-C., Gardin, C., Potier-Ferry, M., (1996). Structure effect and microbuckling, Composite Science and Technology, 56, 861-867;

[2] Drapier S., Grandidier, J.-C., Gardin, C., Potier-Ferry, M., (1996). Theoretical study of structural effects on the compressive failure of laminate composites. Compt. Rend. de l'Acad. des Sci. Paris, Série II b 324, 279-227

[3] Drapier S., Grandidier, J.-C., Potier-Ferry, M., (1999). A non-linear numerical approach to the analysis of microbuckling, Composite Science and Technology, 58, 785-790;

[4] Drapier S., Grandidier, J.-C., Potier-Ferry, M., (2001). A structural approach of plastic microbuckling in long fiber composites: comparison with theoretical and experimental results, International Journal of Solids and Structures, 38, 3877-3904;

[5] Dixit, A., Mali H. S., (2013). Modelling techniques for predicting the mechanical properties of woven -fabric textile composites: A review. Mechanics of Composite Materials 49, 1-20.

[6] DAKOTA 6.10 user's manual, Sandia National Laboratories, New Mexico. Retrieved from https://dakota.sandia.gov/content/manuals/Version6.10

[7] Daniel, IM, Ishai, O., (1994). Engineering Mechanics of Composite Structures, Oxford University Press.

[8] Demboski, G., Bogoeva-Gaceva, G., (2005). Textiles structures for technical textiles. II part: Types and Features of Textile assemblies. Bulletin of the Chemists and Technologists of Macedonia. 24(1), 77-86.

[E] [1] Eringen, A.C., (1972). Linear theory of Nonlocal Elasticity. Int. Journal of Engg. Sci. 10, 425-435.

[2] Eringen, A.C., Speziale, C.G., Kim, B.S., (1977). Crack tip problem in nonlocal elasticity. Journal of Mech. Phy. Solids. 25, 339-355.

[3] Eringen, A.C., (1981). On nonlocal plasticity. Int. Journal of Engg. Sci. 19, 1461-1474.

[4] Eringen, A.C., (1983). Theories of nonlocal plasticity. Int. Journal of Engg. Sci. 21(7), 741-751.

[5] Eringen, A.C., (1999). Microcontinuum Field Theories I: Foundations and Solids. Springer-Verlag, New York.

[6] Exadaktylos, G.E., Vardoulakis, I., (2001). Microstructure in linear elasticity and scale effects: a reconsideration of basic rock mechanics and rock fracture mechanics. Tectonophysics 335, 81–109.

[7] Ernst, G., Vogler, M., Huhne, C., Rofle, R., (2010). Multiscale progrssive failure analysis of textile composites. Compos Sci Technol. 70(1), 61-72.

[8] Elsaid, B., Green, S., Hallett, R.S., (2014). Kinematic modelling of 3D woven fabric deformation for structural scale features. Compos. Part A Appl. Sci. and Manu. 107, 57-95.

[F] [1] Fleck, N.A., Hutchinson, J.W., (1993). A phenomenological theory for strain gradient effects in plasticity. J. Mech. Phys.Solids., 41, 1825–1857.

[2] Fleck, N.A., Muller, G.M., Ashby, G.M., Hutchinson, J.W., (1994). Strain gradient plasticity: Theory and experiment. Acta metall. mater. 42(2), 475-487.

[3] Fleck, N.A., Deng, L., Budiansky, B., (1995a). Prediction of kink width in fiber composite. J. Appl. Mech. 62, 329-337.

[4] Fleck, N.A., Shu, J.Y., (1995b). Microbuckle initiate in fiber composites: A finite element study. J. Appl. Mech. Phys. Solids 43(12), 1887-1918.

[5] Fleck, N.A., Hutchinson, J.W., (1997). Strain gradient plasticity. In: Hutchinson, J.W., Wu, T.W. (Eds.), Advances in Applied Mechanics, 33, 295–361.

[6] Fleck, N.A., Hutchinson, J.W., (2001). A reformulation of strain gradient plasticity. Journal of Mech. and Phy. Of Solids. 49, 2245-2271.

[7] Fleck, N.A., Liu, D., Sutcliffe, M.P.F., (2004). Compressive strength of fiber composites with random fiber waviness. Journal of Mech. and Phy. Of Solids. 52, 1481-1505.
[8] Fredrik, S., and Hallstrom, S., (2009). Assessment of the mechanical properties of a new 3D woven fiber composite material, Compos. Sci. Technol. 69, 1686-1692.

[9] Fleck, N.A., Jelf, P.M., (1995). Deformation and failure of a carbon fiber composite under combined shear and transverse loading. J. Composite Materials, 43(8), 3001–3007.

[G] [1] Grandidier, J.-C., (1991). Compression et microflambage dans les materiaux composites a fibers Longues, Doctoral thesis, Université de Metz-France.

[2] Gardin, C., Poitier-Ferry, M., (1992). Microflambage des fibers dans un matériaux composite à fibers longues: analyse asymptotique 2-D. Compt. Rend. de l'Acad. des Sci. Paris, Série II 315, 1159-1164.

[3] Grandidier, J.-C., Potier-Ferry, M., (1990). Microflambage des fibers dans un matériaux composite à fibers longues. Compt. Rend. de l'Acad. des Sci. Paris, Série II 310, 1-6

[4] Grandidier, J.-C., Ferron, G., Potier-Ferry, M., (1992). Microbuckling and strength in long-fiber composites: theory and experiments. Int. J. Solids Struct. 29(14/15), 1753-1761.

[5] Grandsire-Vincon, I., (1993). Compression des Composites Unidirectionnels: Méthodes d'Essais et Approche Micromécanique. Thése de Doctorat de l'ENS Cachan.

[6] Gokarneshan, N., Alagirusamy, R., (2009). Weavingh of 3D fabrics: A critical appreciation of the developments. 41(1), 1-58.

[7] Green, A.E., Rivlin, R.S., (1964). Multipolar Continuum Mechanics. Arch. for Rat. Mech. and Anal. 17(2), 113-147.

[8] Grandidier, J.-C., (2017). COURS EF pour les structures 2017-18, ENSMA.

[9] Gornet, L., (2008). “Géneralités sur les matériaux composites”, Engineering school.

[10] Gerlach R., (2012). In-plane and through-thickness properties, failure modes, damage and delamination in 3D woven carbon fiber composites subjected to impact loading. Composites Science and Technology. 72(3), 397-411.

[11] Grandidier, J.-C., Casari, P., Jochum, C., (2012). A fibre direction compressive failure criterion for long fibre laminates at ply scale, including stacking sequence and laminate thickness effects. Composite Structures. 94, 3799-3806.

[H] [1] Hutchinson, J.W., (1974). Plastic buckling. Adv. Appl. Mech. 14(12), 67-144.

[2] Hutchinson, J.W., Wu, T.Y. (Eds), (1997). Advances in applied mechanics. Academic Press. 33, 296-361.

[3] Hsiao, H.M., Daniel, I.M., (1984). Effect of fiber waviness on stiffness and strength reduction of unidirectional composites under compressive loading. Comp. Sci. Tech. 56, 581-593.

[4] Hadjesfandiari, A.R., Dargush, G.F., (2011). Couple stress theory for solids. Int. J. Solids Struct. 48, 2496-2510.

[5] Herrmann, L.R., (1983). Mixed finite elements for couple-stress analysis, in: S.N. Atluri, R.H. Gallagher, O.C. Zienkiewicz (Eds.), Hybrid and Mixed Finite Element Methods, Wiley, New York, pp. 1–17.

[6] Hahn, H.T and Williams, J.G., (1984). Compression failure mechanisms in unidirectional composites. Tech. rep., NASA TM-85834, NASA Langley Research Center, Hampton, VA.

[7] Hashin, Z., (1980). Failure criteria for unidirectional fiber composites. J Appl Mech. 47, 329-34

[8] Huang, T., Wang, Y., Wang, G., (2017). A Review of the Mechanical properties of a 3D Woven Composite and its Applications. J Polymer-Plastics Technology and Engineering. 57, 740-756.

[9] Huang G., Zhong Z.L. (2002). Tensile behavior of 3D woven composites by using different fabric structures. Materials and Design, 23(7), 671-674

[I] [1] Interik. (2018). Flexural Test Composites Four-Point Bending by ASTM D6272 [Internet]. Retrieved from: http://www.intertek.com/polymers/composites/flexural-test-composites-four-point-bending-astm-d6272/

[J] [1] Jones, R.M., (1999). Mechanics of Composite Materials, Edition 2, Taylor and Francis Inc., Philadelphia.

[2] Jollivet, T., Peyrac, C., Lefebvre, F., (2013). Damage of composite materials. 5th Fatigue Design Conference, Fatigue Design. 66, 746-758.

[K] [1] Kyriakides, S., Arseculeratne, R., Perry, E.J., Liechti, K.M., (1995). On the compressive failure of fiber reinforced composites. Int. J. Solids Struct. 32(6/7), 689-738.

[2] Karaduman, N.S., Karaduman, Y., Ozdemir, H., and Ozdemir, O., (2017). Textile Reinforced Structural Composites for Advanced Applications, Textiles for Advanced Applications, Dr. Bipin Kumar (Ed.), InTech, Available from: https://mts.intechopen.com/books/textiles-for-advanced-applications/textile-reinforced-structural-composites-for-advanced-applications

[3] Khokar, N., (1996). 3D fabric-forming process: Distinguishing between 2D-weaving, 3D-weaving and an unspecified non-interlacing process. Journal of the Textile Institute, 87(1), 97–106.

[4] Khokar, N., (2001). 3D-weaving: Theory and practice. Journal of the Textile Institute, 92(1), 193–207.

[5] Koiter, W.T., (1964). Couple stresses in the theory of elasticity, I and II. Proc. Ned. Akad. Wet. Ser B. 67, 17-44.

[6] King, M.J., Jearanaisilawong, P., Socrate, S., (2005). A constitutive model for the mechanical behavior of woven fabrics. 42, 3867-3896.

[7] Kuo W-S, Ko T-H (2000). Compressive damage in 3-axis orthogonal fabric composites. Compos Part A: Appl Sci Manuf. 31(10):1091–105. ISSN 1359-835X

[8] Kaddour, A.S., Hinton, M.J., Smith, P.A., Li, S., (2013). Mechanical properties and details of composite laminates for the test cases used in the third world-wide failure exercise. J Compos Mater. 47(20-21), 2427-42.

[9] Kawabata, S., Niwa, M., Kawai, H., (1973a). The finite deformation theory of plain weave fabrics. Part I: The biaxial deformation theory. Journal of Textile Institute. 64(1), 21-46.

[L] [1] Lakes, R., (1995). Experimental methods for study of Cosserat elastic solids and other generalized elastic continua. In: Mühlhaus, H.B. (Ed.), Continuum Models for Materials with Microstructure. John Wiley & Sons, Chichester, pp. 1–25.

[2] Lam, D.C.C., Yang, F., Chong, A.C.M., Wang, J., Tong, P., (2003). Experiments and theory in strain gradient elasticity. Journal of Mech. and Phy. of Solids. 51, 1477-1508.

[3] Lo, KH., Chim, ES., (1992). Compressive strength of unidirectional composites. Journal of Reinforced Plastics and Composites. 11, 838-896.

[4] Lee, J., Soutis, C., (2007). A study on the compressive strength of thick carbon fiber epoxy laminates. Compos Sci Technol. 67(10), 2015-26.

[M] [1] Maziotta, R. (2017). Analysis of elastic microbuckling and post-buckling in T300/914 material (2D and 3D)", Internship Report, Institute Pprime.

[2] Mindlin, R.D., (1964). Microstructure in linear elasticity. Arch. Rat. Mech. Anal. 16, 57-78.

[3] Mindlin, R.D., Tiersten, H.F., (1962). Effects of couple stress in linear elasticity. Arch. Rat. Mech. Anal. 11, 415-448.

[4] Mindlin, R.D., (1965). Second gradient of strain and surface-tension in linear elasticity. Int. J. Solids Struct. 1, 417-438.

[5] Méchin P.-Y., Keryvin V., Grandidier J.-C., Glehen D., (2019). An experimental protocol to measure the parameters affecting the compressive strength of CFRP with a fiber micro-buckling failure criterion, Composite Structures. 211, 154-162.

[6] Materials Common House (MATCH) company.[Internet]. (2016). Textile-based composite design and application of the multi-scale modelling approach. Retrieved from: http://www.match-a4m.eu/index.php/latest/news/145-textilemodelling

[N] [1] Nezamabadi, S., Poitier-Ferry, M., Zahrouni, H., Yvonnet, J., (2015). Compressive failure of composites: A computational homogenization approach, Composites structures. 127, 60-68.

[2] Naik, N.K., Ramasimha, R., (2001). Estimation of compressive strength of delaminated composites. Composites structures. 52(2), 199-204.

[3] Naya, F., Herraez, M., Lopes, C.S., Gonzalez, C., Van der Veen, S., Pons, F., (2017). Computational micromechanics of fiber kinking in unidirectional FRP under different environmental conditions. Composites Science and Technology. 144, 26-35.

[O]

[P] [1] Pisano, A. A., Sofi, A., Fuschi, P., (2009). A Finite Element Approach for Nonhomogeneous Nonlocal Elastic Problems. Mechanics Research Communications, 36, 755-761.

[2] Pisano, A. A., Sofi, A., Fuschi, P., (2009). Nonlocal integral elasticity: 2D finite element based solutions. Int. Joural of Solids and Struct. 46, 3836-3849.

[3] Polizzotto, C., (2001). Nonlocal elasticity and related variational principles. Int. Journal of Solids and Struct. 38, 7359–7380.

[4] Polizzotto, C., (2003). Unified thermodynamic framework for nonlocal/gradient continuum theories. European Journal of Mechanics A/Solids 22, 651–668.

[5] Polizotto, C., Fuschi, P., Pisano, A.A., (2004). Strain diffference based nonlocal elasticity model. Int. Journal of Solids and Struct. 41, 2383-2401.

[6] Polizzotto, C., (2009). A nonlocal strain gradient plasticity theory for finite deformations. Int. Journal of Plasticity. 25, 1280–1300.

[7] Pifko, A., Isakson, G., (1969). A Finite element method for plastic buckling analysis of plates. AIAA Journal, 7(10), 1950-1957.

[8] Pimenta, S., Gutkin, R., Pinho, S.T. and Robinson, P., (2009). A micromechanical model for kink-band formation: Part II - Analytical modelling. Composites Science and Technology, 69(7-8), 956-964.

[9] Puck, A., Schurmann, H., (1998). Failure analysis of FRP laminates by means of physically based phenomenological models. Compos Sci. Technol. 58, 45-1067.

[10] Pinho, S.T., Robinson, P., Iannucci, L., (2006). Fracture toughness of the tensile and compressive fiber failure modes in laminated composites. Compos Sci. Technol. 66(13), 2069-79.

[11] Polizotto, C., Fuschi, P., Pisano, A.A., (2006). A nonhomogeneous nonlocal elasticity model. European Journal of Mechanics A/Solids 25, 308–333.

[Q]

[R] [1] Rosen, B.W., (1964). Mechanics of Composite Strengthening, Fiber Composite Materials, American Society of Metals Seminar, Metals Parks, Ohio,37-75.

[2] Rosen, W., (1972). AGARD Lecture series no. 55 on Composite Materials. Retreived from: https://apps.dtic.mil/dtic/tr/fulltext/u2/744596.pdf.

[3] Reuss, A., (1929). Determination of the yield point of Polycrystals based on the yield condition of single crystals, Z. Angew. Math. Mech. 9, 49–58.

[S] [1] Schaffrers, W.J., (1977). Buckling in fiber reinforced elastomer. Text. Res. J. 502-512

[2] Swanson, S.R., (1992). A micromechanics model for in-situ compression strength of fiber composite laminates. ASME J. Engng. Mat. Technol. 114, 8-12.

[3] Stig, F., (2009). An introduction to Mechanics of 3D Woven Fiber Reinforced Composites (Licentiate thesis). Retreived from: https://www.diva-portal.org/smash/get/diva2:211960/FULLTEXT01.pdf

[4] Sun, C.T., Wanki Jun, A., (1994). Compressive strength of unidirectional fiber composites with matrix non-linearity. Comp. Sci. Tech. 52(4), 577-587.

[5] Sun, W., Guan, Z., Zengshan LI, Mi Zhang, Huang, Y., (2017). Compressive failure analysis of unidirectional carbon/epoxy composite based on micro-mechanical models. Chinese Journal of Articles. 30(6), 1907-1918.

[6] Shu, John Y., King, Wayne E., Fleck, Norman A., (1999). Finite Elements for materials with strain gradient effects. Int. Journal for Numerical Methods in Engg. 44, 373-391.

[7] Sofi, A., Pisano, A.A., Fuschi, P., (2006). Nonhomogeneous nonlocal elasticity: a finite element approach. Retrieved from: http://www.dipmat.univpm.it/aimeta2009/Atti%20Congresso/MECCANICA_STRUTTURE/Sofi_paper62.pdf

[8] Sternberg, E., Muki, R., (1996). The effect of couple-stresses on the stress concentration around a crack, Int. J. Solids Struct. 3, 69–95.

[9] Schapery, R.A., (1995). Prediction of compressive strength and kink bands in composites using a work potential. Int. J. Solids and Structures. 32(6/7), 739-765.

[10] Smith, R.A., (2009). Composite defects and their detection. Materials Science and Engineering – Vol. III. Retrieved from: http://www.eolss.net/samplechapters/c05/e6-36-04-03.pdf

[T] [1] Toupin, R.A., (1964). Theories of elasticity with couple-stress. Arch. Rat. Mech. Anal. 17, 85-112.

[2] Tiersten, H.F., Bleustein, J.L., (1974). Generalized elastic continua. In: Herrmann, G.(Ed.), R.D. Mindlin and Applied Mechanics. Rergamon Press, New York, pp. 67–103.

[3] Tekoglu, C., Onck, P.R., (2008). Size effects in two-dimensional Voronoi foams: a comparison between generalized continua and discrete models. J. Mech. Phys.Solids. 56, 3541–3564.

[4] Turner, P., Liu, T., Zeng, X., (2016). Collapse of 3D orthogonal woven carbon fiber composites under in-plane tension/compression and out of plane bending. Comp. Struct. 142, 286-297.

[5] Tsai K.H., Chiu C.H., Wu T.H. (2000). Fatigue behavior of 3D multi-layer angle interlock woven composite plates. Composite Science Technology, 60(2), 241-248.

[6] Thirumalai Kumaran, S., Jo Ko, T., Utahayakumar, M., Mofizul Islam, Md., (2017). Prediction of surface roughness in abrasive water jet machining of CFRP composites using regression analysis. J. Alloys and Compounds. 724, 1037-1045.

[7] Huang, T., Wang, Y., Wang, G., (2017). A Review of the Mechanical Properties of a 3D Woven Composite and Its Applications. Polymer-Plast. Tech. and Engg. 57, 740-756.

[U]

[V] [1] Vermeer, P.A., Brinkgreve, R.B.J., (1994). A new effective nonlocal strain measure for softening plasticity. In: R., Chambon, Desrues, J., Vardoulakis, I., (Eds.), Localisation and Bifurcation Theory for Soils and Rocks, Balkema, Rotterdam, 89–100.

[2] Vogler, M., Rolfes, R., Camanho, PP., (2013). Modeling the inelastic deformation and fracture of polymer composites - Part I: plasticity model. Mech Mater. 59, 50-64.

[3] Voigt, W., (1889). On the relation between the elasticity constants of isotropic bodies, Ann. Phys. Chem. 274, 573–587

[W] [1] Wisnom, M. R., (1991). The effect of the specimen size on the bending strength of unidirectional carbon fiber-epoxy. Comp. Struct. 18, 47-63.

[2] Wisnom, M. R., (1992). On the high compressive strains achieved in bending tests on unidirectional carbon fiber-epoxy. Comp. Sci. Tech. 43, 229-235.

[3] Wisnom, M. R., (1993). Analysis of shear instability in compression due to fiber waviness, Journal of Reinforced Plastic and Composites, 12(11), 1171-1189.

[4] Warren, K.C., Lopez-Anido, R.A., Goering, J., (2015a). Experimental investigation of three-dimensional woven composites. Composites Part A Applied sci. and Manufact. 73, 242-259.

[5] Wang, B., Zhong, S., Lee, T., Fancey, K.S., Mi, J., (2020). Non-destructive testing and evaluation of composite materials/structure: A state-of-the-art review. Advances in Mechanical Engineering, 12(4), 1-28.

[X] [1] Xia, Z.C., Hutchinson, J.W., (1998). Crack tip fields in strain gradient plasticity, Int. J. Fracture 92, 325–348.

[Y] [1] Yang, F., Chong, A.C.M., Lam, D.C.C., Tong P.,(2002). Couple stress based strain gradient theory for elasticity. Int. J. Solids Struct. 39, 2731-2743.

[2] Yueguang, W., (2006). A new finite element method for strain gradient theories and applications to fracture analyses. European Journal of Mech. A/Solids. 25, 897-913.

[Z] [1] Zbib, H.M., Aifantis, E.C., (1988 a). On the structure and width of shear bands. Scripta Met. 22, 703–708.

[2] Zbib, H.M., Aifantis, E.C., (1988 b). On the localization and post-localization behavior of plastic deformation—I, II, III. Res. Mech. 23, 261–305.

[3] Zhang, L., Huang, Y., Chen, J.Y., Hwang, K.C. (1998). The mode III full-field solution in elastic materials with strain gradient effects, J. Mech. Phys. Solids. 44, 1621–1648.

Summary of chapters in French (Résumé des chapitres en français)

Chapitre 1: Introduction

Le contexte général de ce travail est la modélisation du comportement en compression des tissus stratifiés et tissés unidirectionnels. Ce sujet a fait l'objet de nombreuses recherches depuis de nombreuses années (à partir de 1964) et régulièrement des articles apportent de nouveaux résultats ou confirment les résultats des précédents. La difficulté de ce problème réside dans le mécanisme même de la ruine. Sa particularité est que la résistance à la compression ne peut pas être seulement une quantité "matérielle", mais que le mécanisme est la conséquence conjointe de non-linéarités matérielles de l'état initial du matériau (défauts initiaux) et de paramètres structurels à l'échelle mésoscopique. Pour illustrer ce point, les essais de compression pure sont très difficiles à réaliser car la défaillance du matériau ne dépend pas seulement des concentrations de contraintes dans les mâchoires, de leur intensité mais aussi certainement de leurs gradients. La résistance à la compression sous contrainte de flexion est plus élevée que celle mesurée sous compression pure.
D'un point de vue plus concret, face à ce constat rapide, les ingénieurs dimensionnent en compression avec des coefficients qui ne sont pas toujours en accord avec ce que le matériau est capable de supporter. Grandidier et al., (2012) ont proposé un critère simple pour améliorer le dimensionnement en compression. En outre, des questions supplémentaires se posent sur les notions de tolérance aux dommages ou de fatigue. Comment pouvons-nous prédire la résistance à la compression de structures fatiguées ou présentant des dommages inhérents à un usage intensif? Ce sont autant de questions ouvertes qui demandent un travail supplémentaire pour modéliser le comportement et prédire la résistance en compression. Les travaux de cette thèse devraient contribuer à cette problématique. Sur la base de cette réflexion et des connaissances actuelles, il est apparu comme une opportunité de créer des outils théoriques et numériques pour répondre aux questions des ingénieurs.

Plus précisément, l'objectif global de la thèse est donc de: '*Développer un modèle/outil d'éléments finis non-locaux homogénéisés en continu (2D et 3D), capable de prédire la résistance à la compression des structures composites complexes*'. L'objectif défini est en fait lié aux travaux de recherche antérieurs de Grandidier, Drapier et al., (1992, 1996, 1999). Les définitions claires des objectifs locaux et la nécessité de développer ce modèle sont expliquées en détail au Chapitre 4. Pour avoir une vision claire des problèmes et de la définition des objectifs, il est recommandé au lecteur d'avoir une compréhension préalable de la revue de la littérature sur le comportement mécanique général des composites, en particulier sous compression (Chapitre section 2.6), des diverses investigations expérimentales, des modèles théoriques et numériques développés par de nombreux chercheurs au fil des ans pour modéliser et prédire la résistance à la compression (Chapitre 3).

Chapitre 2: À propos des composites

Ce chapitre se concentre sur les avantages, les inconvénients, les applications, les composants, la classification générale et les méthodes de production des matériaux composites utilisés dans les structures industrielles. Un focus spécifique sur les défauts résultant du processus des composites. Le cas spécifique des composites renforcés par des fibres de carbone longues est traité, en expliquant leurs avantages et leurs limites, tout en se focalisant dans ce présent travail sur *le composite à fibres de carbone longues et à matrice époxy thermodurcissable: T300/914*, largement utilisé dans les industries aéronautiques dans le passé avec de nombreuses données de la littérature proposées sans restriction par l'industrie. Enfin, une section est consacrée à la compréhension du comportement mécanique général des composites, suivie par des cas spécifiques de composites UD et tissés. Le chapitre se termine par la section expliquant le problème spécifique de la compression dans les composites afin de comprendre la nécessité de modéliser la résistance à la compression des composites.

L'important dans ce chapitre est de comprendre le problème de la compression dans les composites et la motivation à les modéliser. En bref, les dommages causés aux matériaux composites sont une combinaison de fissures dans la matrice, de décollement de l'interface et de rupture des fibres. L'endommagement des fils est la conséquence de ces modes. Sous des charges complexes, l'endommagement d'un composite ou d'une structure doit être décrit par un scénario compte tenu de l'évolution, de la localisation et de la propagation de chaque mode. La délamination est une fissure qui traverse la résine de l'interface et saute parfois sur l'interface entre les fibres et la matrice, qui sont proches de chaque lèvre de l'interface. Il en est de même pour la rupture sous une compression appliquée dans le sens des fibres. C'est la conséquence d'un mécanisme complexe, qui est discuté en détail dans le chapitre suivant (Chapitre 3). La connaissance de ces mécanismes est importante pour la conception des structures composites [Méchin et al., (2019)], car la résistance à la compression et la rigidité des laminés sont supposées inférieures à leur résistance à la traction.

Deux exemples sont présentés à la Figure 13, pour expliquer la nécessité de modéliser le comportement en compression/la défaillance des composites. Le premier exemple correspond à une aile d'avion, qui est soumise à une charge de compression constante pendant le vol, ce qui peut entraîner une rupture en compression près de la jonction (comme souligné dans la figure) sur la période de temps. Le second exemple est un voilier de course. Le mât d'un voilier de course peut s'attendre à une rupture en compression en raison de l'application continue d'une charge verticale induite par la tension du gréement (étai / pataras) et la masse du mât et du gréement lui-même. De même, il existe de nombreux exemples de défaillances en compression survenant à l'échelle de la structure qui confirme la nécessité de modéliser finement ce comportement et prédire la défaillance en compression. De nombreuses recherches menées au fil des ans ont confirmé que l'une des principales causes de cette défaillance en compression, en particulier dans les composites à fibres de carbone longues, est due au '*phénomène de microflambage plastique local*', qui est abordé explicitement dans le chapitre suivant (Chapitre 3). Toutefois, ces exemples montrent la nécessité d'encore mieux comprendre et modéliser ce comportement en compression des composites, pour améliorer les prévisions de résistance.

Chapitre 3: Résistance des matériaux composites sous compression (expériences et modèles)

Ce chapitre se concentre sur les divers tests de compression disponibles et sur la bibliographie des résultats expérimentaux de divers chercheurs, puis sur les modèles analytiques et numériques développés au fil des ans à différentes échelles pour modéliser la résistance à la compression des composites UD et tissés, en particulier la rupture.

Plus concrètement la défaillance en compression des composites à fibres longues est une préoccupation majeure pour la conception des structures composites, puisque la résistance à la compression des stratifiés est nettement inférieure à leur résistance à la traction [Méchin et al., (2019)]. Il existe des modes multiples de rupture en compression, notamment *la délamination, la rupture des fibres et le microflambage élastique et plastique*. Le *'microflambage élastique'* est une instabilité de flambage par cisaillement et la matrice qui se déforme en cisaillement simple, tandis que le '*microflambage plastique*' est une instabilité de flambage aussi par cisaillement, mais qui se produit à des contraintes suffisamment importantes pour que la matrice se déforme de manière non linéaire. De nombreuses études expérimentales menées par différents chercheurs au fil des ans ont confirmé que les principaux paramètres qui influencent le micro flambage et la formation de bandes de pliage sont: a) la non-linéarité physique de la matrice et b) la présence d'une imperfection ondulatoire initiale de la fibre. D'autres facteurs importants jouent un rôle majeur sur ce mécanisme, ce sont: i) *Les effets de la séquence d'empilement* ii) *Le type de charge flexion compression pure* et iii) *l'épaisseur des plis*, qui représentent " l'effet structurel*"*, terme inventé au cours des recherches expérimentales de Wisnom (1991), Grandidier et al., (1992) et Grandsire-Vinçon (1993), qui s'est avéré par la suite être la clé pour améliorer les critères de défaillance. Les études expérimentales sur la résistance à la compression de différentes architectures tissées sont également examinées en détail. En tenant compte de tous les paramètres mentionnés précédemment, plusieurs modèles de rupture/microflambage ont été développés au fil des ans pour prédire la rupture du composite sous compression.

Dans la partie modélisation, à partir du premier modèle de microflambage de Rosen (Rosen, 1960), plusieurs modèles locaux et non-locaux à différentes échelles de longueur sont rappelés, leurs limites sont discutées en détail. Parmi eux, seuls quelques chercheurs ont modélisé le mécanisme de microflambage en UD à l'échelle mésoscopique, par exemple Drapier et al., (1996), qui ont clairement établi l'influence de l'épaisseur des plis, de la séquence d'empilement et de la charge sur le microflambage élastique. Ils ont développé un modèle numérique hétérogène en 2D, dans lequel ils ont discrétisé la microstructure complète en 2D du stratifié et calculé exactement les modes de microflambage élastique, qui est influencée par les effets structurels. Les limites étaient que l'augmentation des degrés de liberté, qui a entraîné une augmentation du temps de calcul. De plus, leur modèle numérique ne prend pas en compte les défauts initiaux des fibres et la plasticité de la matrice et se limite uniquement à l'instabilité/ microflambage élastique. Afin d'éliminer ces limitations, Drapier et al., (1999) ont proposé un *'Modèle Homogénéisé (HOM)'* en 2D, qui prend en compte les défauts d'alignement initiaux des fibres, la plasticité de la matrice et les paramètres structurels. Le comportement microstructural est représenté par un milieu continu homogène, dans lequel la rigidité en flexion des fibres est distribuée. La modélisation/formulation numérique homogénéisée du problème de microflambage plastique, construite à l'échelle mésoscopique à l'aide des travaux de Grandidier et al., (1992) sous forme de formulation variationnelle utilisant le

principe des travaux virtuels. Cependant, même si le modèle a réussi à prédire les modes de microflambage élastique, à l'aide du modèle hétérogène complet de Drapier et al., (1996), le modèle est en 2D et suppose que le microflambage est périodique dans la direction des fibres (un seul gradient dans la direction de l'épaisseur). Par conséquent, il n'est pas possible de comparer directement, les résultats des tests obtenus avec des structures réelles. De plus, la prédiction de la 'distribution' et 'des amplitudes' de 'l'imperfection initiale de la fibre' n'est pas encore bien connue, ce qui a été confirmé plus tard par Drapier et al., (2001), qui ont comparé les prédictions obtenues par ce modèle HOM avec les résultats expérimentaux et théoriques de la littérature, et ont également étudié et affiné la compréhension du microflambage plastique. En outre, diverses autres approches supplémentaires au cours des années suivantes à différentes échelles sont discutées en détail.

Cependant, chaque modèle ne fait que prouver ses résultats avec les documents précédents et a ses propres limites. Il est entendu que certaines stratégies de modélisation se limitent aux structures 2D, que certaines se limitent aux plis/laminés UD et que d'autres sont coûteuses en termes de calcul pour les structures micro/méso complexes (composites tissés). Il n'existe pas de modèle général unique qui puisse prédire avec précision le comportement en compression des micro/mésostructures composites complexes, tant en UD qu'en tissé (impliquant des gradients de déformation complexes dans toutes les directions possibles), tout en tenant compte des 'effets structurels'. Compte tenu de tous ces facteurs, le chapitre suivant (Chapitre 4) est consacré à la définition du '*Champ d'application du travail de thèse*', avec des informations précises sur les objectifs globaux et locaux.

Chapitre 4: Champ d'application et aperçu

Bien que de nombreuses théories non locales et diverses approches des éléments finis, basées sur les théories non locales (pour évaluer le phénomène non local), aient été développées au fil des ans pour résoudre les problèmes à l'échelle microscopique/mésoscopique, chaque modèle est limité à certaines limites et seuls quelques modèles ont été développés pour évaluer la résistance à la compression (en particulier le phénomène de microflambage/instabilité locale) des matériaux composites carbone/époxy à fibres longues à l'échelle structurelle/mésoscopique. Par exemple, Drapier et al., (1999) ont proposé un modèle homogénéisé en 2D (comme discuté au Chapitre 3), qui prend en compte les défauts d'alignement initial des fibres, la plasticité de la matrice et les paramètres structurels. Le modèle réussit à prédire les modes de microflambage élastique, mais le modèle est en 2D et suppose que le microflambage est périodique dans la direction des fibres, un seul gradient dans la direction de l'épaisseur est pris en compte. Par conséquent, il n'est pas possible de comparer les résultats des tests obtenus avec des structures complexes réelles (par exemple : composites tissés, structure avec trou près d'un bord encastré). De plus, la prédiction de la "distribution" et des "amplitudes" des imperfections initiales des fibres n'est pas encore bien appréhendée [Drapier et al., (2001)]. Il est donc nécessaire d'étendre les modèles et, plus spécifiquement, celui proposé par Drapier et al., (1999), car tous les paramètres ont été pris en compte.

En outre, il n'existe pas de travaux particuliers dans la littérature, qui traite d'une modélisation générique non locale du comportement en compression des plis UD et des composites tissés (2D et 3D) et aucune simulation des instabilités à l'échelle d'une structure réelle n'a été réalisée. Par conséquent, un modèle unique devrait être développé pour évaluer la résistance à la compression sur une structure complexe avec des composites UD et tissés (2D et 3D), qui prend en compte les effets des gradients dans toutes les directions possibles. Avec ce modèle théorique, il est nécessaire de développer un modèle numérique non local à l'échelle structurelle qui peut évaluer/simuler le phénomène de micro flambage des composites à fibres longues carbone/époxy, en tenant compte de la plasticité de la matrice (époxy) et de l'énergie de flexion des fibres due aux ondulations des fibres (les principales causes de la rupture en compression des composites à fibres longues carbone/époxy).

Par conséquent, sur les bases des travaux de Grandidier, Drapier et al., (1992, 1996, 1999), l'objet de la thèse est de "*Développer un modèle/outil d'éléments finis non-locaux homogénéisés continus (2D et 3D), capable de prédire la résistance à la compression des structures composites complexes"*. Plus de détails:

- Construire une nouvelle modélisation du microflambage, plus générale que celle des travaux précédents de Drapier et al., (1996,1999);
- Prendre en compte:
    - Comportement non linéaire de la résine/matrice;
    - Effets géométriques non-linéaires;
    - Défauts dans la modélisation (ex : désalignement initial des fibres).
- Développer les paramètres de contrôle pour le calcul 2D et 3D;
- Étendre le modèle pour évaluer les structures mésoscopiques complexes (ex : composites tissés).

4.1 Tâches / Plan

Les tâches du travail de recherche comprennent principalement deux parties:

1. Développement d'un modèle non-local avec des éléments structurels d'ABAQUS® pour les composites UD afin d'évaluer la possibilité de résoudre le micro flambage en structure 2D et 3D;
2. Développement d'un modèle/outil généralisé d'éléments finis non-locaux homogénéisés utilisant le sous-programme d'éléments utilisateur (UEL) d'ABAQUS® pour évaluer les composites UD et tissés:
    a. Formulation et validation pour le cas élastique isotrope linéaire;
    b. Formulation et validation pour le cas de géométrie non-linéaire (isotrope élastique);
    c. Formulation et validation pour les cas de matériaux non-linéaires et de géométrie non-linéaire;
    d. Identification des paramètres élastiques et non-locaux;
    e. Identification des paramètres des matériaux non-linéaires.

En particulier, le Chapitre 5 est associé à la première partie de la thèse, où il comprend les informations détaillées concernant le développement du modèle non-local à l'aide des éléments intégrés d'ABAQUS®, le protocole de la validation par rapport aux résultats de certains travaux de recherche antérieurs. Le Chapitre 6 est consacré à certains des fondements théoriques importants et des travaux de recherche développés au fil des ans sur divers modèles non-locaux et ses applications en ce qui concerne les éléments finis qui permettent de modéliser le comportement en compression des composites avec des architectures complexes. Partie suivie par le développement théorique et numérique du modèle généralisé d'éléments finis non-locaux homogénéisés (HOMNL), et sa mise en œuvre pour le cas 2D dans le sous-programme d'éléments utilisateur (UEL) d'ABAQUS® pour évaluer les composites UD et tissés.

Les Chapitres 7, 8 et 9 traitent de la validation du modèle HOMNL, implémenté dans l'élément utilisateur 2D (NL U32) pour respectivement les cas : linéaire isotrope élastique, non-linéaire géométrie isotrope élastique et non-linéaire géométrie en abordant les matériaux UD et un tissé. Les résultats sont comparés aux éléments classiques intégrés d'ABAQUS®.

Le Chapitre 10 est associé à une procédure ou un protocole détaillé pour identifier les paramètres élastiques, non-locaux et non-linéaires du matériau avec la non-linéarité géométrique dans le modèle HOMNL 2D respectivement. Le Chapitre 11 comprend quelques résultats de la réponse en compression des composites avec le modèle HOMNL, suivi d'un chapitre de clôture, à savoir le Chapitre 12, qui comprend des conclusions et des perspectives d'avenir.

Chapitre 5: Modèle non-local pour les composites UD avec éléments structurels d'ABAQUS®

Le modèle numérique proposé dans cette partie est construit afin de déterminer le champ tridimensionnel d'instabilité généré par une contrainte de compression. Ce modèle a la capacité de prendre en compte de manière plus réaliste tous les effets mentionnés précédemment, et d'analyser le phénomène de compression à l'échelle mésoscopique. Il s'inspire du modèle homogène de Gardin et al., (1992) et Drapier et al., (1996) où la formulation non-linéaire du problème de micro flambage peut être vue comme un raidisseur sous la forme d'une poutre (beams) liée à un milieu continu (appelé Beam Non-Local Model avec la contraction BNL). L'énergie de flexion par rapport aux fibres, induit l'effet de non-localité. Le modèle BNL est similaire à un modèle développé par Wisnom, (1993), qui consistait en une analyse bidimensionnelle d'une couche composite UD modélisée par ABAQUS®. Le modèle de Wisnom convient à la modélisation précise de l'instabilité de cisaillement, même s'il présente certaines limites. En effet, cet auteur a entrepris une analyse limitée dans le domaine bidimensionnel et a donc considéré l'ondulation uniquement dans un plan. De plus, une seule onde a été prise en compte et, pour des raisons de symétrie, il a fallu modéliser la moitié de la longueur d'onde. La largeur modélisée n'a pas affecté les résultats puisqu'un domaine continu a été représenté, par conséquent un seul élément a été utilisé dans cette direction, alors que, dans la direction des fibres, 17 éléments ont été considérés comme suffisants pour obtenir des résultats précis. Pour le besoin d'une modélisation plus avancée, le modèle BNL est développé afin de: i) prendre en compte la rigidité à la flexion ; ii) prendre en compte l'effet de largeur, par conséquent il n'y a pas un seul élément dans cette direction ; iii) étendre la modélisation au tridimensionnel ; iv) permettre d'évaluer le phénomène de micro flambage, non seulement à l'échelle micro mais aussi à l'échelle de la structure (macro-échelle), en utilisant des hypothèses classiques sur les conditions limites, qui permettent d'évaluer l'effet structurel ; v) permettre d'évaluer le phénomène de micro flambage grâce au protocole d'extraction de valeurs propres proposé par le solveur d'ABAQUS.

Le modèle BNL est développé dans le logiciel ABAQUS® sans sous-programme utilisateur pour le cas élastique et le simple sous-programme USDFLD ("USerDefinedFieLD") pour le comportement non linéaire. Il est constitué par la superposition d'un milieu continu, qui peut être un solide homogène (3D) ou une hypothèse de contrainte plane ou de déformation plane (2D) et de poutres : éléments unidimensionnels dans l'espace ou dans le plan, représentant la rigidité des fibres. Dans le cas 2D, un maillage est choisi avec la superposition de CPS8 (un quadrilatère biquadratique à 8 nœuds de contrainte plane), représentant le milieu continuum, et B22 (une poutre quadratique à 3 nœuds dans un plan), représentant les fibres en moyenne. Alors que, dans le cas 3D, la superposition de C3D8 (une brique linéaire à 8 nœuds), représentant le milieu du continuum, et B33 (une poutre linéaire à 2 nœuds dans l'espace avec une formulation cubique) pour les raidisseurs en 3D. Les propriétés du matériau sont identifiées par rapport à la réponse du modèle hétérogène construit dans ABAQUS® avec les propriétés de la littérature.

Le modèle permet de prédire l'instabilité locale élastique des couches unidirectionnelles à l'intérieur d'une structure sous des charges complexes. "L'effet structurel" expliqué dans la littérature est confirmé et de nouveaux résultats sont obtenus, comme par exemple le mode élastique en 3D ou le mécanisme sous flexion. Pour prédire la défaillance en compression sous une charge complexe, un comportement non linéaire est développé et mis en œuvre dans le modèle

avec le sous-programme utilisateur (USDFLD). La plasticité est introduite dans le comportement des milieux continus et le défaut (désalignement des fibres), dans la position initiale des poutres. La quantification des différents paramètres (plasticité, défauts initiaux, effets structurels) est obtenue avec le modèle BNL qui peut être utilisé pour étudier la résistance à la compression dans des structures complexes avec des plis stratifiés UD.

Bien que le modèle BNL permette de modéliser le comportement des composites UD en compression et de prédire la défaillance en tenant compte des effets structurels, du défaut (désalignement initial) et de toutes les non-linéarités (géométriques et matérielles), il se limite à simuler uniquement des plis unidirectionnels (UD) de stratifiés, il n'est pas possible de simuler des structures composites avec une micro/mésostructure complexe (composite tissé en 2D ou 3D). De plus, il s'agit d'un modèle d'éléments finis discontinus pas simple à générer parfois. Par conséquent, il est nécessaire de développer un modèle plus généralisé qui soit continu et qui tienne également compte des effets structurels pour l'analyse des architectures tissées et plus complexes, ce qui reste la conclusion de ce chapitre.

Chapitre 6: Modèle non-local généralisé pour les composites UD et tissés - modèle numérique (UEL ABAQUS®)

Ce chapitre présente divers modèles non-locaux et approches par éléments finis (basées sur des théories non locales) développés au fil des ans, ce qui permet d'étendre notre modèle non-local pour simuler le comportement en compression des composites à architecture complexe. Après la bibliographie de ces modèles, le développement d'un modèle non-local 3D généralisé pour les composites UD et tissés est présenté avec des parties théoriques et numériques en détail. Et enfin, l'implémentation de ce modèle dans le cas de la 2D, développant ainsi l'élément utilisateur (UEL), "NL U32" pour la simulation dans ABAQUS® est discutée.

En bref, divers modèles non-locaux de continuum sont examinés, expliquant les inconvénients des théories de continuum local et la nécessité de modèles non-locaux pour saisir des phénomènes qui ne peuvent en effet être raisonnablement expliqués qu'au niveau microstructurel, par exemple: *l'apparition d'effets de taille, la dispersion d'ondes élastiques, la singularité de la contrainte à la pointe de la fissure* et *le phénomène de microflambage dans les composites*. En particulier, une bonne compréhension des différentes théories de ‘gradient de contrainte’ (élastique et plastique) est réalisée, dans laquelle une échelle de longueur interne a été correctement introduite sous la forme de gradients d'ordre supérieur, l'interaction entre les échelles de longueur macroscopique et microscopique dans la réponse constitutive et l'interprétation correspondante des effets de taille associés peuvent être correctement modélisées et bien prédites (Aifantis, 1992). Quelques-unes des théories non locales les plus importantes, par exemple : la théorie élastique de Cosserat/Couple stress (Cosserat et Cosserat, 1909) ; les théories de l'élasticité du gradient de déformation d'ordre supérieur (Mindlin, 1964, 1965) et le modèle élastique non-local d'Eringen (Eringen, 1972, 1977) sont discutées de façon exhaustive.

Avec la compréhension et la motivation inhérentes toutes ces théories non-locales et leur mise en œuvre dans divers problèmes, les sections suivantes sont consacrées au développement de la formulation théorique et numérique d'un modèle homogène non-local généralisé afin d'étudier le comportement en compression des composites unidirectionnels et tissés. Dans la partie théorique, en utilisant la théorie des gradients de Mindlin II (Mindlin, 1965), le modèle de Drapier et al. (1999) est étendu pour prendre en compte les microcourbures (champ de courbure des fibres) dans toutes les directions, ce qui conduit au développement d'un nouveau modèle généralisé non-local en 3D appelé modèle non-local homogénéisé (HOMNL) à l'échelle mésoscopique (Eq. (6-18)) pour bien simuler le comportement en compression de toute mésostructure complexe. Le principe des travaux virtuels et des équations d'équilibre est formulé pour le cas 2D en utilisant les hypothèses de Kirchhoff, suivi par des formulations d'éléments finis implémentées dans l'élément utilisateur (UEL) en utilisant FORTRAN 77, nommé "Non-Local Super-paramétrique élément (NL U32)" pour la simulation dans ABAQUS®. L'élément formulé est similaire au rectangle de Bogner-Fox-Schmit, BFSR (Bogner et al., 1965), où les degrés de liberté (D.O.F) de l'élément ne sont pas seulement les déplacements, mais aussi leurs dérivés. Les fonctions d'interpolation pour le déplacement sont un polynôme cubique complet d'ordre 3 et pour la géométrie il est choisi un polynôme biquadratique complet d'ordre 2. Les chapitres suivants sont consacrés à la validation de l'élément développé (NL U32) dans différentes situations.

Chapitre 7: Validation de l'élément NL U32 (cas linéaire)

Dans ce chapitre, la validation du modèle non-local homogénéisé précédemment développé, mis en œuvre dans l'élément super paramétrique non local (NL U32) pour '*l'élastique isotrope linéaire*' est effectuée par rapport aux éléments classiques d'ABAQUS®. et plus spécifiquement l'élément linéaire à contrainte plane (CPS4) d'ABAQUS®. Les valeurs des rigidités de flexion des fibres locales/des paramètres non-locaux (A, B, C, D, E, F) introduites dans le modèle HOMNL au Chapitre 6 sont inconnues pour l'élément NL U32. Pour comprendre l'influence de ces paramètres matériaux sur la solution, la valeur des paramètres non-locaux est variée dans la plage 0,15 à 15000000 et les réponses des cas particuliers sont comparées. Les propriétés élastiques classiques prises en compte pour les deux éléments sont les suivantes : module d'Young, E=2.0E5 MPa, coefficient de Poisson, ν=0.3 et épaisseur, t=1mm. L'analyse est effectuée sur une plaque rectangulaire (100 mm x 50 mm), maillée avec 276 éléments (312 nœuds) sous compression et flexion. Il a été observé qu'une réponse similaire mais des différences de solution sont observées avec des flèches très inférieures à celles de l'élément ABAQUS® CPS4 lorsque les paramètres non-locaux (ABCDEF) atteignent 1500 $MPa \cdot mm^2$. Cette différence significative de solution est dû au fait que, pour des ordres inférieurs des paramètres non-locaux ($\leq 10^3$), l'énergie de flexion devient plus faible par rapport à l'énergie de déformation classique, puisque l'ordre des courbures sont faibles. En conclusion, il est entendu que pour avoir des effets non-locaux dans cette solution particulière, il est nécessaire d'avoir la valeur des paramètres non-locaux $> 10^3$. L'analyse de la sensibilité des paramètres non-locaux est alors menée pour les différents cas envisagés, ce qui permet de valider le fonctionnement de l'élément (NL U32).

En plus, l'étude de convergence des mailles a été réalisée pour évaluer la convergence de la solution obtenue avec l'élément NL U32 par rapport à un maillage différent (nombre d'éléments, n=8, 32, 66, 128, 276, 512) sous flexion. Les propriétés du matériau sont supposées être les mêmes que précédemment, sauf que seules les deux valeurs de ABCDEF sont choisies : 15 $MPa \cdot mm^2$ et 1500000 $MPa \cdot mm^2$. La solution a été comparée à l'élément ABAQUS® CPS4 et il a été observé que plus le maillage (n) augmente en densité, plus on a tendance à obtenir une solution asymptotique que l'on suppose convergente, ceci à la fois pour l'élément NL U32 et l'élément ABAQUS® CPS4 avec une valeur d'ABCDEF plus faible, ce qui quantifie l'influence du maillage dans la solution. Comme étape finale de la validation du modèle HOMNL, mise en œuvre dans l'élément NL U32, les résultats sont comparés avec le modèle hétérogène composite 2D unidirectionnel (UD) (T300/914 carbone/époxy) construit à l'aide de l'élément à contrainte plane ABAQUS® (CPS4). La séquence d'empilement du modèle composite hétérogène UD à fraction volumique f=0,5 (avec 10 couches: matrice et fibre) est construite dans ABAQUS®. La matrice et les fibres sont supposées être élastiques isotropes linéaires. Les propriétés des matériaux élastiques sont celles du papier de Drapier et al., (1996) pour les deux approches homogène et hétérogène. De la comparaison des résultats (les déplacements : U,V), il est clair que nous avons obtenu une des résultats très proches entre le modèle hétérogène d'ABAQUS® et le modèle homogène pour un composite UD soumis à la flexion, validant ainsi notre outil numérique NL U32 implémenté dans ABAQUS® pour le cas élastique linéaire.

Chapitre 8: Non-linéarité géométrique en NL U32: description et validation

Ce chapitre contient la formulation étendue avec l'ajout '*d'effets géométriques non linéaires*' dans le modèle non-local homogénéisé précédemment développé, mettant ainsi en œuvre l'élément super paramétrique non local (NL U32). Enfin, le protocole de validation des résultats par rapport aux éléments classiques d'ABAQUS® est similaire au cas linéaire. Les étapes détaillées de la formulation de la géométrie non-linéaire sont présentées et implémentées dans l'élément NL U32. Ensuite, pour valider, les résultats sont comparés à l'élément ABAQUS® avec la non-linéarité géométrique sous les cas de compression et de flexion. Comme dans le cas linéaire précédent, les mêmes propriétés des matériaux, la même taille de maille sont choisies et les mêmes études sont réalisées pour les éléments NL U32 et CPS4. Il a été observé à nouveau des réponses similaires et les différences de solution sont très inférieures à celles de l'élément CPS4 d'ABAQUS® lorsque les paramètres non locaux (ABCDEF) varient jusqu'à 1500 $MPa \cdot mm^2$. En revanche, une différence significative de solution est observée par rapport à l'élément CPS4 lorsque la valeur ABCDEF est augmentée au-dessus de 1500 $MPa \cdot mm^2$. La raison est identique à celle du cas de l'élastique isotrope linéaire. Une étude de convergence des mailles est également réalisée et on observe que lorsque la taille des mailles (n) est augmentée, on tend à obtenir une solution asymptotique ou convergente à la fois pour l'élément NL U32 et l'élément CPS4 ABAQUS® avec une hypothèse de non-linéarité géométrique. Ainsi, la validation du cas de l'élément NL U32 à géométrie non-linéaire est confirmée dans ce chapitre.

Chapitre 9: Non-linéarité des matériaux de la matrice en NLU32: description de la loi et validation

Nous savons, grâce à la bibliographie, que l'un des paramètres importants à prendre en compte dans le modèle pour bien prédire la résistance à la compression des composites, en particulier unidirectionnels est la 'non-linéarité du matériau de la matrice'. Dans ce chapitre, les '*effets matériels non-linéaires*' sont injectée dans la formulation le modèle non-local homogénéisé (NL U32). Enfin, la validation des résultats par rapport aux éléments intégrés classiques d'ABAQUS® avec cette loi matériaux spécifique est examinée en détail.

La première partie se concentre sur le développement de la formulation de la loi élasto-plastique isotrope de Ramberg Osgood (RO), similaire à la loi du matériau RO intégré d'ABAQUS® pour prendre en compte le comportement non-linéaire du matériau de la matrice. La loi de matériau est développée pour le cas de contrainte plane 2D, puisque l'élément non-local (NL U32) est développé sous cette hypothèse particulière. La formulation est codée en utilisant FORTRAN dans la sous-routine User Material (UMAT) d'ABAQUS® qui a été intégrée dans l'élément NL U32. De plus, un sous-programme de matériau utilisateur séparé, appelé 'KURMAT', est également intégré dans l'élément NL U32 pour prendre en compte toutes sortes de comportement du matériau pour la partie non locale des fibres (élastique pour l'instant). La validation de la loi est effectuée en deux étapes : 1) Comparaison des résultats obtenus par le sous-programme UMAT, développé pour la loi RO isotrope, par rapport à la loi RO isotrope intégrée de base dans ABAQUS®, en utilisant l'élément CPS4 dans ces deux cas avec l'hypothèse de nonlinéarité géométrique. 2) Comparaison des résultats obtenus par l'UMAT RO intégré maintenant dans NL U32 combiné à KUMAT par rapport à l'élément CPS4et la loi RO isotrope intégré dans ABAQUS® en non linéaire géométrique. Les propriétés des matériaux de la matrice sont choisies dans Nezamabadi et al., (2015). Pour les petites valeurs de rigidité non-locale, les champs (contrainte/déformation) sont identiques à ceux d'ABAQUS® avec les CPS4, en conséquent l'outil est jugé validé avec toutes les non-linéarités nécessaires pour résoudre le problème. De plus, un autre résultat intéressant est que, lorsque la rigidité non-locale augmente, les gradients générés par les conditions aux limites se propagent dans la structure. La longueur de l'influence générée par le support est donc directement liée à cette rigidité. Nous avons obtenu correctement les résultats escomptés. Ensuite, les résultats sont finalement validés par rapport à un modèle hétérogène construit à l'aide d'ABAQUS® et toujours des éléments CPS4 pour le cas de la compression et de la flexion. Les propriétés des fibres élastiques et de la matrice élasto-plastique de la couche UD carbone/époxy T300/914 obtenues de Drapier et al., (1996) et Nezamabadi et al., (2015). Cependant, il a été réalisé que pour reproduire le même comportement qu'un composite UD hétérogène réel, il est nécessaire de développer une loi de matériau (élasto-plasticité) de type anisotrope. Par conséquent, la loi de Ramberg-Osgood anisotrope sous l'hypothèse de contrainte plane pour les composites UD est développée dans la section suivante et intégrée dans le modèle HOMNL (NL U32). On suppose que la non-linéarité n'ait pas la même expression pour les composantes transversales et de cisaillement, bien que le comportement non-linéaire provienne de la matrice. Cette loi introduit 7 paramètres matériaux, qui doivent être identifiés. La validation de la loi est effectuée par rapport à la loi de Ramberg-Osgood (RO) isotrope intégrée à ABAQUS®, en utilisant un élément CPS4 en non linéaire géométrique et suivant les trajets particuliers de charge de traction, de compression et de cisaillement.

Chapitre 10: Identification des paramètres

Dans ce chapitre, une procédure est proposée pour identifier les paramètres élastiques, non locaux et non linéaires des matériaux du modèle HOMNL avec la non-linéarité géométrique dans le cas 2D et elle est mise en œuvre. Il est à noter que, puisqu'il n'y a pas de données expérimentales disponibles spécifiques (par exemple: les courbes de contrainte/déformation ou de force/déplacement) sous différentes conditions de charge, l'identification des paramètres est effectuée en comparant des réponse d'un milieu hétérogène avec des propriétés locales issues de la littérature et le modèle homogène non local.

Plus concrètement dans la première partie, un protocole d'identification des paramètres élastiques et non-locaux est établi. Pour cela, l'outil d'optimisation, nommé DAKOTA, est utilisé car il peut être facilement relié à ABAQUS® en utilisant un script python externe. Comme les modules élastiques classiques, $\boldsymbol{D}$ est supposé être élastique anisotrope (transversalement isotrope) pour le modèle non-local homogénéisé, afin de représenter le composite UD/tissé hétérogène 2D, nous avons au final 4 paramètres: D_{11}, D_{22}, D_{12} et D_{33}. Dans la matrice locale micro-flexion des fibres ($\overline{\overline{\boldsymbol{C_f}}}$), nous avons 6 paramètres : A, B, C, D, E et F. Il faut donc identifier un total de 10 paramètres. Pour réaliser cela, 3 étapes sont définies : 1) Choisir l'élément de volume représentatif (VER) ; 2) Choisir les conditions limites appropriées (BC) ; 3) Optimisation dans DAKOTA. Trois RVE de modèles hétérogènes 2D sont choisis: Microstructure 1 (pli à 0°), Microstructure 2 (pli à 90°) et Microstructure 3 (Tissé (uni)) avec des dimensions de 0,1mm x 0,1 mm, et sont construits en utilisant des éléments ABAQUS® CPS4. Une taille de maille de 100 éléments est choisie afin de réduire le temps de calcul et d'optimisation. Les propriétés des matériaux élastiques isotropes (fibre et matrice) pour les modèles hétérogènes sont issues de Drapier et al., (1996). Les valeurs initiales des composants de la matrice D du modèle HOMNL sont calculées à l'aide d'une "loi des mélanges" basée sur les propriétés de Drapier et al., (1996) pour le pli UD. Les valeurs initiales des paramètres non-locaux ont été obtenues par une analyse de sensibilité dans DAKOTA. Ensuite, la partie la plus importante et la plus difficile a été de définir les conditions limites. Comme nous avons 10 paramètres à identifier, 10 conditions limites différentes sont proposées, ce qui permet d'identifier les paramètres respectivement. Enfin, l'optimisation a été réalisée en utilisant DAKOTA avec la méthode '*Non-linear least-square/gradient method (nl2sol)'* avec un maximum d'itérations de 200. Le critère d'erreur/fonction objective défini était "*l'erreur énergétique globale totale (ETot)*", qui est la somme de l'erreur énergétique globale relative entre le modèle hétérogène et le modèle homogène non local de 10 cas. Les paramètres optimaux finaux (élastiques et non-locaux) sont obtenus en minimisant '*l'ETot*' dans la DAKOTA pour les VERs considérées.

La partie suivante a consisté à identifier les paramètres non-linéaires du matériau de la matrice (c'est-à-dire 7 paramètres plastiques) de la loi RO anisotrope développée dans le chapitre précédent (Chapitre 9) pour le composite UD (pli à 0°). Pour cette partie, le VER de la microstructure 1 (pli à 0°) est choisie. Les paramètres élastiques et non-locaux optimaux obtenus précédemment sont utilisés. Il a d'abord été décidé d'étudier l'analyse de sensibilité de chacun des paramètres de la loi RO anisotrope et de choisir les bonnes valeurs initiales. Ensuite, les paramètres plastiques optimaux finaux sont obtenus en tenant compte de 10 cas de chargement ensemble. Il est important de noter que pour cette partie, l'énergie de déformation totale globale (W) sur les pas de temps (T) est considérée comme un critère global. L'objectif est de minimiser l'écart ou l'erreur entre deux

courbes d'énergie (générées à partir du VER d'un modèle hétérogène et non-local homogène) pour obtenir les paramètres finaux optimaux de la loi des matériaux non-linéaire. DAKOTA n'est pas utilisé pour cette optimisation car il prend beaucoup de temps lorsqu'il est utilisé avec des lois matérielles non-linéaires et aussi pour éviter les problèmes de convergence avec un ensemble de valeurs aléatoires. Un ensemble de paramètres optimaux est obtenu pour tous les cas de chargement il permet un bon compromis. Toutefois, de légères différences sont observées, en particulier pour les cas de charge impliquant un cisaillement, car il n'a pas été très facile de faire correspondre exactement la courbe de plasticité dans le modèle impliquant des cas de charge aussi divers. De plus, il est possible que le VER hétérogène considéré avec 10 couches de fibre-matrice ne soit pas une bonne référence avec la plasticité, car il peut y avoir des effets plus ou moins localisés en contrainte/déformation dépendant de la taille. Mais il suffisait ici de démontrer la faisabilité du protocole pour obtenir ces paramètres. À l'avenir, il est nécessaire de faire varier la fraction volumique ou d'augmenter le nombre de couches, et aussi de changer la dimension du VER et d'effectuer l'optimisation pour comprendre l'influence de ces paramètres à utiliser dans des cas plus généraux. En raison des délais et des ressources limités, il n'a pas été possible d'étudier de nombreux cas.

Chapitre 11: Réponse en compression des composites non-locaux

Dans ce chapitre, la réponse en compression du modèle non local homogénéisé (HOMNL) pour l'UD (plis à 0°) et les cas tissés (uni) sont étudiés. Les paramètres optimaux du matériau (élastique et non-linéaire) obtenus dans le chapitre précédent (Chapitre 10) sont utilisés pour le modèle HOMNL mis en œuvre dans l'élément U32 NL. L'objectif n'est pas de comparer avec des caractérisations expérimentales car il faut une identification spécifique pour chaque type de matériaux. Les résultats obtenus avec le modèle HOMNL sont confrontés aux résultats du modèle BNL développé précédemment (Chapitre 5) et également avec le modèle Hétérogène construit à l'aide des éléments CPS4 dans ABAQUS®. Il est important de noter qu'il n'est pas possible d'obtenir les modes de microflambage en utilisant le modèle HOMNL pour les cas UD et tissées car il n'y a pas assez d'informations disponibles sur le manuel d'utilisation d'ABAQUS® sur la manière d'intégrer l'étape "BUCKLING" à l'intérieur de la UEL (NL U32). Un solveur spécifique complet devrait être construit. De plus, aucun désalignement ou défaut initial n'est pris en compte dans le modèle HOMNL en raison du manque de temps et d'informations. L'objectif principal ici est de montrer la capacité du modèle à prédire la résistance à la compression en observant la réponse à la compression au stade critique (lorsqu'ABAQUS® interrompt le calcul, c'est-à-dire jusqu'à ce qu'une divergence ou une instabilité se produise).

Pour le cas UD, les résultats sont comparés au modèle BNL précédemment développé et au modèle hétérogène construit à l'aide d'ABAQUS® CPS4 avec toutes les non-linéarités. L'effet de l'épaisseur et de la longueur de la couche est étudié, ce qui est réalisé sous deux cas de chargement: bloqué-bloqué et bloqué-libre (conditions aux limites sur les faces supérieures et inférieures des plis voir Figure 30). Pour étudier l'effet de l'épaisseur, un modèle rectangulaire de pli UD de longueur (1600µm) avec une épaisseur variable (100µm, 200µm, 400µm et 800µm) est considéré. L'évolution de la déformation critique obtenue avec le modèle HOMNL (NL U32) est similaire au modèle BNL, confirmant ainsi 'l'effet structurel' avec une valeur critique de l'ordre des données expérimentales. Mais nous n'avons pas obtenu des solutions identiques au modèle BNL car les paramètres matériaux ne sont pas exactement les mêmes et aussi par non prise en compte du désalignement initial/défaut dans le modèle HOMNL. Cependant, l'ordre de grandeur de la valeur critique est satisfaisant et prouve les capacités du modèle HOMNL (NL U32). D'après la comparaison avec le modèle hétérogène d'ABAQUS® CPS4, il est entendu que la longueur du VER (400µm, 800µm, 1600µm et 3200µm) avec une épaisseur de pli constante de 400µm a un effet négligeable sur la solution critique. Mais pour différentes épaisseurs, le champ transversal de déplacement maximum (critique) devient plus uniforme près du bord/face libre (en haut), une distribution similaire du champ est observée pour le modèle hétérogène et le modèle homogène non-local. Cependant, il est difficile d'appréhender le post microflambage, la bande de pliage n'apparaît pas comme observé avec le modèle BNL. Peut-être est-ce dû à l'algorithme de Newton-Raphson ou aussi à la non prise en compte du défaut initial qui a la propriété de faciliter l'instabilité puisqu'il joue le rôle d'une perturbation ? La comparaison de la contrainte critique n'est pas bonne et ce résultat confirme les remarques précédentes. Ce point devrait être étudié à l'avenir.

Pour la partie du tissage en 2D, seul le cas élastique est pris en compte puisque nous n'avons pas de loi élasto-plastique anisotropie développée pour le matériau tissé et que nous n'avons pas non plus de données expérimentales exhaustives pour le matériau tissé. Par conséquent, le nombre de cas est également limité. Le modèle hétérogène pour le tissé (uni) est construit en utilisant

ABAQUS® CPS4. Comme dans le cas de l'UD, l'évolution du champ de déplacement à la divergence numérique avec la longueur et l'épaisseur de la couche tissée est étudiée dans des conditions limites avec et sans blocage. La simulation est réalisée avec une non-linéarité géométrique. Nous avons obtenu une bonne comparaison des champs par rapport au modèle hétérogène, et l'effet de l'épaisseur est également confirmé avec le modèle HOMNL. Mais le modèle hétérogène n'a pas montré cet effet et la raison n'est pas claire pour le moment, ce qui devrait être étudié à l'avenir. Il sera vraiment intéressant d'étudier de nombreux cas, mais en raison du temps, des ressources et des données disponibles limités, il est difficile de réaliser des études paramétriques. En outre, nous aurions pu obtenir une comparaison beaucoup plus réaliste si nous avions eu des résultats expérimentaux exhaustifs sur des cas tissés.

Chapitre 12: Conclusion et perspectives

Dans le but d'étendre les travaux de Grandidier, Drapier et al., (1991, 1992, 1996, 1999), des modèles d'éléments finis non-locaux ont été proposés: l'un avec les éléments structurels d'ABAQUS®, appelé modèle Beam Non-Local (BNL) et l'autre avec le sous-programme User Element (UEL) d'ABAQUS®, appelé Homogenized Non-Local Model (HOMNL) pour évaluer la résistance à la compression des plis/laminés UD et également pour les composites tissés (2D et 3D). Ces modèles prennent en compte les effets géométriques et matériels non-linéaires.

Le modèle BNL est un couplage d'un milieu continu et des poutres (2D ou 3D). Il est similaire à un modèle développé par Wisnom (1993). L'intérêt de ce modèle est la capacité à simuler le phénomène de microflambage qui apparaît dans un pli unidirectionnel sous compression dans la structure et à prendre en compte l'effet des plis voisins. Il permet de prédire l'instabilité locale élastique des couches unidirectionnelles à l'intérieur d'une structure en cas de charges complexes. 'L'effet structurel' expliqué dans la littérature est confirmé et de nouveaux résultats sont obtenus, par exemple, le mode élastique en 3D ou le mécanisme en flexion. Pour prédire la défaillance en compression sous une charge complexe, un comportement non linéaire est développé et mis en œuvre dans le modèle avec le sous-programme utilisateur (USDFLD). La plasticité est introduite dans le comportement des milieux continus et le défaut (désalignement des fibres) dans la position initiale des poutres. La quantification des différents paramètres (plasticité, défauts initiaux, effets structurels) est obtenue avec le modèle BNL qui peut être utilisé pour étudier la résistance à la compression dans les structures composites complexes. Mais ce modèle se limite à simuler uniquement des plis et des stratifiés unidirectionnels (UD), il n'est pas possible de simuler toutes les structures composites avec une micro/mésostructures complexe (composite tissé en 2D ou 3D). De plus, il s'agit d'un modèle d'éléments finis discontinu encore un peu difficile à mettre en œuvre.

Par conséquent, avec la nécessité d'étendre le modèle aux cas de structures plus générales (pour évaluer des structures composites complexes, par exemple : tissées) et aussi pour construire un élément fini continu de géométrie classique, un modèle numérique non-local homogénéisé (HOMNL) est proposé, similaire à la théorie du gradient II de Mindlin (Mindlin, 1965). En comparaison avec le modèle précédent de Drapier et al., (1999), les micro-courbures dans toutes les directions ont été prises en compte pour évaluer le phénomène de microflambage dans les composites UD et tissés. Le modèle non-local a été implémenté pour le cas 2D dans le sous-programme User Element (UEL) (codé en FORTRAN 77), nommé NL U32, qui est *superparamétrique* et de *type* C^1 *continu* pour l'analyse dans ABAQUS®, ce qui permet de simuler les structures complexes. Les effets géométriques non linéaires sont pris en compte dans cet élément utilisateur non-local (NL U32) ainsi que le comportement non-linéaire de la matrice (loi élastoplastique de Ramberg-Osgood) avec deux sous-programmes User Material (UMAT et KUMAT), qui permettent de modéliser toutes les familles de comportement. Le comportement tangent de la rigidité non-locale de la microstructure est appréhendé en intégrant le sous-programme de matériau utilisateur (KURMAT) au sein de l'élément qui permet de moduler les non-localités (par exemple lorsque des micro-dommages apparaissent).

La validation de l'élément NL U32 a été effectuée par rapport à l'élément classique ABAQUS® (CPS4) pour les cas linéaires et non linéaires (géométrie et matériau). Les propriétés classiques (élastiques et plastiques) et non-locales des matériaux (élastiques) sont identifiées par rapport aux

réponses d'un élément de volume représentatif (VER) de microstructures entièrement hétérogènes construites à l'aide de l'élément CPS4. Un protocole détaillé est proposé, qui est suffisant pour comprendre l'influence et l'identification des paramètres dans le modèle. À l'avenir, il est nécessaire de faire varier la fraction volumique ou augmenter le nombre de couches dans le modèle hétérogène et aussi changer la dimension VER et effectuer l'optimisation pour comprendre l'influence de ces paramètres à utiliser dans des cas plus généraux. En raison des délais et des ressources limités, il n'a pas été possible d'étudier de nombreux cas.
L'étude de la réponse en compression du composite 2D UD (pli à 0°) dans le dernier chapitre montre clairement que 'l'effet structurel' est à nouveau confirmé par le modèle HOMNL avec des non-linéarités géométriques. L'ordre de grandeur de la contrainte critique est du même ordre que celui des données expérimentales pour un UD et celles obtenues avec le modèle BNL. L'effet de la longueur et de l'épaisseur du pli est étudié pour les cas UD et tissés. Les modes de microflambage n'ont pas pu être obtenus en utilisant le modèle HOMNL pour les cas UD et tissés car il n'y a pas assez d'informations disponibles sur le manuel d'utilisation d'ABAQUS® pour le moment sur l'intégration de l'étape "BUCKLING" à l'intérieur du UEL (NL U32) pour effectuer une analyse d'extraction des modes et valeurs propres. De plus, aucun désalignement ou défaut initial n'est pris en compte dans le modèle HOMNL car il n'est pas encore bien établi comment intégrer cet effet dans le modèle, ainsi que dans l'élément fini. Par conséquent, il est limité à l'étude de quelques cas et la comparaison avec quelques résultats obtenus dans le passé dans la littérature est restreinte. Néanmoins, le modèle HOMNL (NL U32) a montré la capacité de prédire la résistance à la compression même sans prendre en compte tous les paramètres actifs pour les composites UD et tissés.
Par ailleurs, un des avantages majeurs de l'utilisation de cet élément continu non-local super paramétrique de type C^1 (NL U32) est qu'il ne nécessite pas d'avoir un maillage plus fin dans la structure que les éléments de Lagrange classiques dans ABAQUS® pour simuler et bien capturer le phénomène non-local (par ex : microflambage) à l'échelle microscopique, ce qui permet de gagner beaucoup de temps de calcul.

Les perspectives

Le modèle HOMNL (NL U32) nous a montré des résultats prometteurs dans la simulation de la résistance à la compression des structures composites 2D. Cependant, il reste plusieurs paramètres à intégrer pour améliorer le modèle et l'élément permettant d'évaluer de nombreuses structures complexes dans des situations de chargements complexes. Voici les perspectives d'avenir qui doivent être prises en compte pour les développements proposés:

- Introduire le défaut initial/le désalignement dans le modèle HOMNL (NL U32) ;
- Introduire l'étape "BUCKLING" dans l'élément NL U32 ;
- Une étude paramétrique sur le microflambage doit être effectuée pour évaluer les possibilités des modèles ;
- L'identification des paramètres du modèle HOMNL a été effectuée par rapport au modèle numérique avec des paramètres matériaux tirés de la littérature. Il serait intéressant et plus réaliste que cette identification puisse être effectuée par rapport à des données expérimentales si possible;
- L'élément utilisateur non local développé (NL U32) est en 2D dans cette thèse et il devrait être étendu à un cas en 3D, par conséquent l'identification des paramètres;
- Étudier de nombreux cas sur différentes architectures tissées;